



SEAL TECHNOLOGY FOR LIQUID OXYGEN (LOX) TURBOPUMPS

by Wilbur Shapiro and Robert Hamm

MECHANICAL TECHNOLOGY INCORPORATED

Prepared for

NATIONAL AERONAUTICS AND SPACE ADMINISTRATION

NASA Lewis Research Center
Contract NAS3-23260

(NASA-CR-174866) SEAL TECHNOLOGY FOR LIQUID
OXYGEN (LOX) TURBOPUMPS Final Report, Feb.
1982 - Nov. 1985 (Mechanical Technology)
388 p Avail: NTIS HC A17/MF A01 CSCL 11A

N88-13603

Unclas
G3/37 0114097

1. Report No. NASA CR-174866		2. Government Accession No.		3. Recipient's Catalog No.	
4. Title and Subtitle Seal Technology for Liquid Oxygen (LOX) Turbopumps				5. Report Date November 1985	
				6. Performing Organization Code	
7. Author(s) Wilbur Shapiro Robert Hamm				8. Performing Organization Report No. 85TR20	
				10. Work Unit No.	
9. Performing Organization Name and Address Mechanical Technology Incorporated Research and Development Division 968 Albany-Shaker Road Latham, New York 12110				11. Contract or Grant No. NAS3-23260	
				13. Type of Report and Period Covered FINAL 2/82 - 11/85	
12. Sponsoring Agency Name and Address National Aeronautics and Space Administration Lewis Research Center Cleveland, OH 44135				14. Sponsoring Agency Code	
15. Supplementary Notes Project Manager: J. A. Hemminger, NASA-Lewis Research Center, Cleveland, OH 44135					
16. Abstract Two types of advanced seals for liquid oxygen (LOX) turbopumps were investigated. One was a spiral-groove face seal whose function is to seal high-pressure LOX at the impeller end of the turbopump. The other was a floating-ring, Rayleigh-step, helium buffered seal used to prevent LOX ingress to the turbine side of the unit. For each seal type, two sizes were investigated - 50 and 20 mm. A turbine-driven test rig was designed and manufactured, and a test program was completed on the 50-mm floating-ring, Rayleigh-step, helium buffered seal. Significant results of the program were: <u>Spiral-Groove LOX Seal</u> <ul style="list-style-type: none"> • Vaporization in the flow path could cause seal failure by overheating; therefore, the spiral-groove pumping portion of the seal that provides the fluid film must circulate fluid without disruption if vaporization occurs in the sealing dam. This is successfully accomplished by a pressure-balanced spiral-groove concept that is described in the text. • The spiral-groove configuration is affected by turbulence in the fluid film and pressure drops due to fluid inertia at sudden contractions. The net result of these effects are deep grooves, large operating films, and high power loss when compared against seals operating with laminar films. Turbulence and inertia are induced by the high-density and low-viscosity characteristics of LOX. 					
17. Key Words (Suggested by Author(s)) Rotating Shaft Seals Spiral-Groove Seals Floating-Ring Seals Liquid-Oxygen Seals Self-Acting Seals Helium Buffer Seals Turbopump Shaft Seals Rayleigh Step Seals			18. Distribution Statement		
19. Security Classif. (of this report)		20. Security Classif. (of this page)		21. No. of Pages	
				22. Price*	

- Computed flow levels for the 50-mm seal are approximately $30 \text{ mm}^3/\text{s}$ (4.7 gpm) at pressure levels of 5.17 MPa (750 psi). Film thickness is 0.0236 mm (0.93 mils) and the interface speed is 183 m/s (600 ft/s).

The floating-ring, Rayleigh-step seals were exposed to an extensive testing program. Successful operation was demonstrated at speeds up to 5760 m/s (55,000 r/min), and buffer fluid pressure levels of 1379 kPa (200 psia). Average leakage rates per ring were 0.0016 kg/s (20.2 scfm). Multiple high acceleration starts at 152 m/s^2 (500 ft/s^2) were accomplished without incident. Several seal failures did occur, but were attributed to external influences such as excessive rig vibration and contamination of the helium supply system.

The program clearly pointed out the need to consider system environmental factors such as thermal and centrifugal distortions and rotor vibrations in the seal design. More liberal seal clearances would probably have permitted operation to 7330 rad/s (70,000 r/min), but rig changes made to improve dynamic response altered the seal environment and caused greater than anticipated clearance closure due to thermal growth.

ACKNOWLEDGMENTS

The work reported upon herein was due to the contribution of several key individuals at Mechanical Technology Incorporated (MTI). Their efforts, which are presented below, are gratefully acknowledged.

<u>Individual</u>	<u>Description</u>
Dr. Jed Walowit	Spiral-Groove Seal Analysis
Mr. Antonio Artilles	Rayleigh-Step Helium Seal Analysis
Mr. Henry Jones	Seal Design
Mr. John Dunne	Test Rig Design

MTI expresses appreciation to Mr. Jeffrey Frazier of Wyle Laboratories, Norco, California, for his efforts during the testing phase of the program. In addition, MTI expresses sincere gratitude to Messrs. Joseph Hemminger and J. P. Wanhainen of NASA/LeRC for their consistent support and assistance throughout the course of the program. MTI also acknowledges, posthumously, the efforts of Mr. Lawrence Ludwig of NASA/LeRC who was responsible for advanced seal development and conceived the seal configurations discussed in this report.

TABLE OF CONTENTS

<u>SECTION</u>		<u>PAGE</u>
	ACKNOWLEDGMENTS	ii
	LIST OF FIGURES	viii
	LIST OF TABLES	
1.0	INTRODUCTION	1-1
2.0	SUMMARY OF SIGNIFICANT RESULTS AND CONCLUSIONS	2-1
	2.1 Configuration and Principle of Operation of a 50-mm Helium Buffer Seal	2-1
	2.2 Test Results of the 50-mm Rayleigh-Step Helium Buffer Seal .	2-2
	2.3 Conclusions and Recommendations for the 50-mm Rayleigh-Step Seal	2-4
	2.4 Results and Conclusions for the 20-mm Rayleigh-Step Helium Buffer Seal	2-7
	2.5 Description and Principle of Operation of the Spiral-Groove LOX Seals	2-8
	2.5.1 Special Considerations for LOX	2-8
	2.5.2 Pressure-Balanced Spiral-Groove Seal	2-10
	2.6 50-mm Spiral-Groove Seal	2-11
	2.6.1 Groove Geometry	2-11
	2.6.2 Summary of Performance	2-12
	2.7 20-mm Spiral-Groove Seal	2-13
	2.7.1 Geometry	2-13
	2.7.2 Summary of Performance	2-13
	2.8 Test Rig	2-14
	2.8.1 Design Philosophy	2-14
	2.8.2 General Configuration	2-14
	2.8.3 Summary of Test Rig Performance	2-15
	2.9 Instrumentation	2-17
3.0	TEST RESULTS	3-1
	3.1 Introduction	3-1
	3.2 Steady-State Test Results	3-3
	3.2.1 Seal Set No. 1	3-3
	3.2.2 Seal Set No. 2	3-6
	3.2.3 Seal Set No. 3	3-10
	3.2.4 Seal Set No. 4	3-11
	3.3 Dynamic Behavior During Seal Testing	3-17
	3.3.1 Seal Set No. 2	3-18
	3.3.2 Seal Set No. 3	3-19
	3.3.3 Seal Set No. 4	3-20
	3.4 Acceleration Testing	3-22
	3.4.1 Seal Set No. 2	3-22
	3.4.2 Seal Set No. 3	3-23

PRECEDING PAGE BLANK NOT FILMED

TABLE OF CONTENTS (CONTINUED)

<u>SECTION</u>		<u>PAGE</u>
3.5	Post-Test Hardware Inspections and Failure Analysis	3-23
3.5.1	Seal Set No. 1	3-24
3.5.2	Seal Set No. 2	3-25
3.5.3	Seal Set No. 3	3-26
3.5.4	Seal Set No. 4	3-27
3.6	Discussion Of The Results	3-27
3.6.1	Steady-State Operation	3-28
3.6.2	Start-Up Performance	3-29
3.6.3	Seal Life	3-30
3.6.4	Leakage Rates	3-32
3.6.5	Parametric Effects.	3-33
3.6.6	Dynamic Performance	3-41
3.6.7	Material Considerations	3-42
4.0	ANALYSIS AND DESIGN OF RAYLEIGH-STEP, HELIUM BUFFER SEALS	4-1
4.1	Operating Conditions	4-1
4.2	Design Considerations	4-1
4.3	Analysis and Design of the 50-mm Floating-Ring Helium Purge Seal	4-2
4.3.1	Rayleigh Step Optimization Studies	4-2
4.3.2	General Configuration and Design	4-4
4.3.3	Fluid-Film Performance	4-5
4.3.4	Thermal Analysis	4-7
4.3.5	Seal Ring Dynamic Response	4-9
4.3.6	Summary of Results and Conclusions of Analytical Studies	4-12
4.4	Analysis and Design of the 20-mm Floating-Ring Helium Purge Seal	4-13
4.4.1	General Configuration and Operating Conditions	4-13
4.4.2	Fluid-Film Performance	4-13
4.4.3	Dynamic Response	4-15
5.0	ANALYSIS AND DESIGN OF SPIRAL-GROOVE LOX SEALS	5-1
5.1	General Discussion	5-1
5.2	Analytical Approach	5-1
5.3	Configuration for the 50-mm Seal	5-2
5.4	Calculated Fluid-Film Performance of the 50-mm Spiral-Groove Seal	5-4
5.5	Dynamic Analysis of the 50-mm Spiral-Groove Seal	5-6
5.6	Elastic and Thermal Distortions of the 50-mm Spiral-Groove Seal	5-8
5.7	Design of the 20-mm Spiral-Groove Seal	5-9
6.0	TEST RIG	6-1
6.1	General Configuration	6-1
6.2	Fluid Systems	6-2

TABLE OF CONTENTS (CONTINUED)

<u>SECTION</u>		<u>PAGE</u>
6.3	Test Seal Arrangement	6-5
6.4	Turbine Design and Performance	6-5
6.4.1	Acceleration	6-6
6.4.2	Stress	6-7
6.4.3	Design	6-7
6.5	Bearing Design and Performance	6-7
6.5.1	Journal Bearings	6-7
6.5.2	Thrust Bearings	6-8
6.6	Rotor Dynamics	6-9
6.6.1	Rotor Model for the 50-mm LOX Seal Shaft	6-12
6.6.2	Undamped Critical Speeds for the 50-mm LOX Seal Rotor	6-12
6.6.3	Synchronous Unbalance Response of the 50-mm LOX Seal Rotor	6-13
6.6.4	Stability Analysis for the 50-mm LOX Seal Rotor	6-14
6.7	Thermal Analysis	6-15
7.0	TEST FACILITY	7-1
7.1	Fluid Supply Systems	7-1
7.1.1	Helium Seal Supply System	7-1
7.1.2	LN ₂ Bearing Supply System	7-2
7.1.3	GN ₂ Turbine Supply System	7-4
7.1.4	Helium Supply to Labyrinth Seal	7-5
7.1.5	GN ₂ Purge	7-5
7.2	Controls	7-6
7.3	Instrumentation	7-9
7.3.1	Film Thickness and Shaft Displacement	7-9
7.3.2	Seal Film Thickness Probes	7-10
7.3.3	Shaft Displacement Probes	7-12
7.3.4	Shaft Speed	7-12
7.3.5	Vibration	7-12
7.3.6	Pressures	7-13
7.3.7	Flows	7-13
7.3.8	Temperatures	7-13
7.3.9	Data Acquisition Equipment	7-13
8.0	TEST PLAN FOR THE RAYLEIGH-STEP, HELIUM BUFFER SEAL	8-1
8.1	Test Description	8-1
8.1.1	Steady-State Tests	8-1
8.1.2	Acceleration Tests	8-4
8.2	Test Schedules	8-5
8.3	Test Procedures	8-5
8.3.1	Preparation of Test Rig at MTI	8-5
8.3.2	Preparation of Test Facility and Test Rig at Wyle Laboratories	8-6
8.3.3	Test Facility Operating Procedures	8-6
8.3.4	Pre- and Post-Test Inspection and Assembly Procedures	8-11
8.3.5	Instrument Calibration	8-11
8.3.6	Data Reduction	8-12
9.0	REFERENCES	9-1

LIST OF FIGURES

NUMBER		PAGE
1-1	LOX Turbopump Cross Section	1-5
2-1	Floating-Ring Seal Schematic	2-18
2-2	Developed View of 50-mm Rayleigh-Step Pad	2-19
2-3	50-mm Rayleigh-Step Floating Rings	2-20
2-4	Operating Map for 50-mm Helium Buffer Seal - Seal Set No. 2	2-21
2-5	Outboard Seal Flow, 103 kPa Drain Pressure - Seal Set No. 2	2-22
2-6	Zero Speed versus Pressure Drop - Seal Set No. 4	2-23
2-7	Flow versus Pressure Drop - Seal Set No. 4	2-23
2-8	Seal Leakage Envelope Data at Varying Speeds	2-24
2-9	Seal Leakage Envelope Data at Constant Speed	2-25
2-10	Operating Range Map for 20-mm Helium Buffer Seal	2-26
2-11	Pressure-Balanced, Outward Pumping, Spiral-Groove Concept	2-27
2-12	Seal Face Pressure Profile	2-28
2-13	Groove Geometry	2-29
2-14	50-mm Pressure-Balanced LOX Seal	2-30
2-15	50-mm Spiral-Groove Seal, Mating Ring, and Face Seal	2-31
2-16	Operating Range Map for 50-mm Spiral-Groove Seal	2-32
2-17	20-mm Pressure-Balanced LOX Seal	2-33
2-18	Operating Range Map for 20-mm Spiral-Groove Seal	2-34
2-19	Test Rig Cross Section	2-35
2-20	Test Rig Components	2-36
2-21	Helium Seal Rotor	2-37
2-22	Modified Test Rig Configuration - Seal Set No. 4	2-38
2-23	Details of Embedded Probe Installation	2-39
2-24	Instrumented Seal Ring with Embedded Capacitance Probes	2-40
3-1	Pressure History - Seal Set No. 1	3-48
3-2	Speed History - Seal Set No. 1	3-48
3-3	Operating Map for Seal Set No. 1	3-49
3-4	Failure of No. 1 Outboard Seal Ring	3-50
3-5	Zero Speed Flow versus Pressure Drop - Seal Set No. 1	3-51
3-6	Zero Speed Seal Temperatures versus Pressure Drop - Seal Set No. 1	3-51
3-7	Flow versus Pressure Drop - Seal Set No. 1	3-52
3-8	Inboard Seal Temperature versus Pressure Drop - Seal Set No. 1	3-53
3-9	Outboard Seal Temperature versus Pressure Drop - Seal Set No. 1	3-53
3-10	Inboard and Outboard Seal Temperature versus Pressure Drop - Seal Set No. 1	3-54
3-11	First Day Pressure History - Seal Set No. 2	3-55
3-12	First Day Speed History - Seal Set No. 2	3-55
3-13	Second Day Pressure History - Seal Set No. 2	3-56
3-14	Second Day Speed History - Seal Set No. 2	3-56
3-15	Third Day Pressure History - Seal Set No. 2	3-57
3-16	Third Day Speed History - Seal Set No. 2	3-57
3-17	Operating Map for Seal Set No. 2	3-58
3-18	Inboard Seal Flow versus Pressure Drop, Zero Speed - Seal Set No. 2	3-59

LIST OF FIGURES (CONTINUED)

3-19	Outboard Seal Flow versus Pressure Drop, Zero Speed - Seal Set No. 2	3-59
3-20	Zero Speed Seal Temperatures versus Pressure Drop - Seal Set No. 2	3-60
3-21	Inboard Seal Flow versus Pressure Drop - Seal Set No. 2 . .	3-61
3-22	Inboard Seal Temperature versus Pressure Drop - Seal Set No. 2	3-61
3-23	Outboard Seal Flow, 517 kPa Drain Pressure - Seal Set No. 2	3-62
3-24	Outboard Seal Flow, 310 kPa Drain Pressure - Seal Set No. 2	3-63
3-25	Outboard Seal Temperature, 517 kPa Drain Pressure - Seal Set No. 2	3-64
3-26	Outboard Seal Temperature, 310 kPa Drain Pressure - Seal Set No. 2	3-65
3-27	Outboard Seal Temperature, 103 kPa Drain Pressure - Seal Set No. 2	3-66
3-28	Outboard Seal Temperature and Flow versus Pressure Drop - Seal Set No. 2	3-67
3-29	Outboard Seal Temperature and Flow versus Supply Pressure - Seal Set No. 2	3-67
3-30	First Day Seal Film Thickness History, Seal Set No. 2 . .	3-68
3-31	Second Day Film Thickness History - Seal Set No. 2	3-69
3-32	Third Day Film Thickness History - Seal Set No. 2	3-70
3-33	Pressure History - Seal Set No. 3	3-71
3-34	Speed History - Seal Set No. 3	3-71
3-35	Operating Map - Seal Set No. 3	3-72
3-36	Failure of No. 3 Inboard Seal Ring	3-73
3-37	Inboard Seal Flow versus Pressure Drop - Seal Set No. 3 . .	3-74
3-38	Inboard Seal Temperature versus Pressure Drop - Seal Set No. 3	3-74
3-39	Outboard Seal Flow, 517 kPa Drain Pressure - Seal Set No. 3	3-75
3-40	Outboard Seal Flow, 310 kPa Drain Pressure - Seal Set No. 3	3-76
3-41	Outboard Seal Flow, 103 kPa Drain Pressure - Seal Set No. 3	3-77
3-42	Outboard Seal Temperature, 517 kPa Drain Pressure - Seal Set No. 3	3-78
3-43	Outboard Seal Temperature, 310 kPa Drain Pressure - Seal Set No. 3	3-79
3-44	Outboard Seal Temperature, 103 kPa Drain Pressure - Seal Set No. 3	3-80
3-45	Operating Map of Seal Set No. 4	3-81
3-46	Pressure History - Seal Set No. 4	3-82
3-47	Speed History - Seal Set No. 4	3-82
3-48	Failure of No. 4 Inboard Seal Ring	3-83
3-49	Flow History - Seal Set No. 4	3-84

LIST OF FIGURES (CONTINUED)

3-50	Seal Temperature History - Seal Set No. 4	3-85
3-51	Outboard Seal Film Thickness History - Seal Set No. 4 . . .	3-86
3-52	Outboard Seal Eccentricity History - Seal Set No. 4	3-86
3-53	Outboard Seal Film Thickness versus Shaft Speed - Seal Set No. 4	3-87
3-54	Seal and Runner Motion - Seal Set No. 2 at 3665 rad/s . . .	3-88
3-55	Seal and Runner Motion - Seal Set No. 2 at 4188 rad/s . . .	3-88
3-56	Seal and Runner Motion - Seal Set No. 2 at 4712 rad/s . . .	3-88
3-57	Seal and Runner Motion - Seal Set No. 3 at 3665 rad/s . . .	3-89
3-58	Seal and Runner Motion - Seal Set No. 3 at 3665 rad/s . . .	3-89
3-59	Seal and Runner Motion - Seal Set No. 3 at 3665 rad/s . . .	3-90
3-60	Seal and Runner Motion - Seal Set No. 3 at 3665 rad/s . . .	3-90
3-61	Seal and Runner Motion - Seal Set No. 3 at 4188 rad/s . . .	3-91
3-62	Seal and Runner Motion - Seal Set No. 3 at 4712 rad/s . . .	3-91
3-63	Seal and Runner Motion - Seal Set No. 4 at 3665 rad/s . . .	3-92
3-64	Seal and Runner Motion - Seal Set No. 4 at 4188 rad/s . . .	3-92
3-65	Seal and Runner Motion - Seal Set No. 4 at 4712 rad/s . . .	3-92
3-66	Seal and Runner Motion - Seal Set No. 4 at 5235 rad/s . . .	3-93
3-67	Seal and Runner Motion - Seal Set No. 4 at 5759 rad/s . . .	3-93
3-68	Embedded Probe Oscilloscope Display Format	3-94
3-69	Seal Probe Time Trace - Seal Set No. 4 at 5759 rad/s . . .	3-95
3-70	Speed-Time Curve for Typical Acceleration Run	3-96
3-71	Damaged Seal; Outboard Ring - Seal Set No. 1	3-97
3-72	Undamaged Seal; Inboard Ring - Seal Set No. 1	3-97
3-73	Damaged Runner; Inboard Left, Outboard Right - Seal Set No. 1	3-98
3-74	Magnified View (X11.4) of Damaged Runner - Seal Set No. 1 .	3-98
3-75	Undamaged Seal; Outboard Ring - Seal Set No. 2	3-99
3-76	Damaged Seal; Outboard Ring - Seal Set No. 3	3-100
3-77	Undamaged Seal; Inboard Ring - Seal Set No. 3	3-100
3-78	Damaged No. 2 Runner; Inboard Left, Outboard Right - Seal Set No. 3	3-101
3-79	Magnified View (X11.5) of Damaged No. 2 Runner	3-101
3-80	Damaged Seal; Inboard Ring - Seal Set No. 4	3-102
3-81	Damaged No. 3 Runner; Inboard Left, Outboard Right - Seal Set No. 4	3-102
3-82	Parametric Variations as a Function of Pressure Drop and Supply Pressure	3-103
4-1	Dimensionless Direct Stiffness versus Step Depth	4-22
4-2	Axial Step-Length Optimization	4-23
4-3	Optimization of Circumferential Pocket Extent	4-24
4-4	50-mm Rayleigh-Step Pad	4-25
4-5	50-mm Runner Seal Installation	4-26
4-6	50-mm Helium Seal Runner Centrifugal Distortions	4-27
4-7	50-mm Helium Purge Bushing Seal Assembly	4-29
4-8	Bushing Seal, CCW	4-31
4-9	Concentric Clearance versus Speed Including Centrifugal Growth	4-33
4-10	50-mm Fluid-Film Radial Force and Seal Friction Force . . .	4-34

LIST OF FIGURES (CONTINUED)

4-11	50-mm Viscous Power Loss as a Function of Speed and Pressure, $\epsilon = 0.5$	4-35
4-12	50-mm Seal Leakage versus Speed and Pressure	4-36
4-13	50-mm Fluid Temperature Rise	4-37
4-14	50-mm Thermal Analysis Model	4-38
4-15	50-mm Fluid Film Forces versus Eccentricity Ratio; 1379 kPa Helium Pressure; 7330 rad/s	4-39
4-16	50-mm Ring Orbital Response; 1379 kPa, 7330 rad/s, 7.62 μ m Shaft Runout	4-40
4-17	50-mm Ring Orbital Response, 345 kPa Absolute (50 psia), 2094 rad/s (20,000 r/min), 0.0102 mm (0.0004 in.) Shaft Runout	4-41
4-18	50-mm Ring Orbital Response; 689 kPa Absolute (100 psia); 2094 rad/s (20,000 r/min); 0.0102 mm (0.0004 in.) Shaft Runout	4-42
4-19	50-mm Ring Orbital Response; 1379 kPa Absolute (200 psia); 3142 rad/s (30,000 r/min); 0.0254 mm (0.0004 in.) Shaft Runout	4-43
4-20	50-mm Composite Metal Ring, Orbital Response; 1379 kPa Absolute (200 psia), 7330 rad/s (70,000 r/min); 0.00635 mm (0.00025 in.) Shaft Runout	4-44
4-21	50-mm Ring Response versus Shaft Orbit	4-45
4-22	50-mm Composite and All Carbon Ring Orbit Summary versus Shaft Runout	4-46
4-23	20-mm Helium Purge Seal	4-47
4-24	20-mm Helium Seal; Force versus Eccentricity at Different Pressures and Speeds	4-49
4-25	20-mm Helium Seal; Pressure versus Eccentricity to Balance Frictional Force	4-50
4-26	20-mm Helium Seal; Effect of Clearance on Fluid Film Force; 10,472 rad/s (100,000 r/min); 1379 kPa Absolute (200 psia)	4-51
4-27	20-mm Helium Seal; Force versus Eccentricity at Larger Clearance ($CO = 0.0254$ mm)	4-52
4-28	20-mm Helium Buffer Seal at 0.5 Eccentricity Ratio; Leakage versus Helium Pressure	4-53
4-29	20-mm Helium Seal; Leakage versus Eccentricity at 1379 kPa (200 psia)	4-54
4-30	20-mm Helium Seal, Power Loss versus Speed	4-55
4-31	20-mm Helium Buffer Seal at 0.5 Eccentricity Ratio; Temperature Rise versus Speed	4-56
4-32	20-mm Helium Seal, Fluid Film Force versus Eccentricity at 1379 kPa Absolute (200 psi), 10,472 rad/s (100,000 r/min)	4-57
4-33	20-mm Helium Seal; Transient Response Summary; 0.0025 mm Shaft Runout	4-58
4-34	20-mm Helium Seal; Transient Response Summary versus Buffer Pressure; 0.0025 mm Shaft Runout	4-59

LIST OF FIGURES (CONTINUED)

5-1	50-mm LOX Spiral-Groove Seal Assembly	5-11
5-2	50-mm Spiral-Groove Face Seal	5-13
5-3	50-mm Spiral-Groove Seal Mating Ring	5-15
5-4	50-mm Spiral-Groove Secondary Seal	5-17
5-5	Split Spiral-Groove Secondary Seal	5-19
5-6	50-mm Spiral-Groove Seal; Film Thickness versus Speed and Pressure	5-20
5-7	50-mm Spiral-Groove Seal; Axial Stiffness versus Speed and Pressure	5-21
5-8	50-mm Spiral-Groove Seal; Spiral Groove Circulating Flow versus Speed and Pressure	5-22
5-9	50-mm Spiral-Groove Seal; Leakage Flow versus Speed and Pressure	5-23
5-10	50-mm Spiral-Groove Seal; Power Loss versus Speed and Pressure	5-24
5-11	50-mm Spiral-Groove Seal; Spiral-Groove Temperature Rise versus Speed and Pressure	5-25
5-12	50-mm Spiral-Groove Seal; Temperature Rise versus Speed and Pressure	5-26
5-13	50-mm Spiral-Groove Seal; Angular Amplitude Ratio versus Speed and Pressure	5-27
5-14	50-mm Spiral-Groove Seal; Thermoelastic Distortion	5-28
5-15	20-mm Spiral-Groove Seal; Film Thickness versus Speed	5-29
5-16	20-mm Spiral-Groove Seal; Axial Stiffness versus Speed	5-30
5-17	20-mm Spiral-Groove Seal; Leakage Flow versus Speed	5-31
5-18	20-mm Spiral-Groove Seal; Groove Flow versus Speed	5-32
5-19	20-mm Spiral-Groove Seal; Power Loss versus Speed	5-33
5-20	20-mm Spiral-Groove Seal; Seal Temperature Rise versus Speed	5-34
5-21	20-mm Spiral-Groove Seal; Seal Temperature Rise versus Speed	5-35
5-22	20-mm Spiral-Groove Seal; Axial Natural Frequency versus Speed	5-36
5-23	20-mm Spiral-Groove Seal; Angular Natural Frequency versus Speed	5-37
5-24	20-mm Spiral-Groove Seal; Axial Amplitude Ratio versus Speed	5-38
5-25	20-mm Spiral-Groove Seal; Angular Amplitude Ratio versus Speed	5-39
5-26	Spiral-Groove Seal - Elastic Distortions	5-40
6-1	Cross Section of Seal Test Rig; Housing Sections Identified	6-16
6-2	Test Rig Housings	6-17
6-3	Test Rig Nozzle Box	6-18
6-4	Test Rig Fluid Systems	6-19
6-5	Supply and Drainage - Turbine-Side Bearing Housing.	6-20
6-6	Supply and Drainage - Seal-Side Bearing Housing	6-21
6-7	Supply and Drainage - Labyrinth Seal and Shim Plate Housings	6-22

LIST OF FIGURES (CONTINUED)

6-8	Test Rig Power Losses	6-23
6-9	Turbine Design Schematic	6-24
6-10	Assembled Test Rig Shaft	6-25
6-11	Turbine Output Power versus Inlet Pressure	6-26
6-12	Turbine Efficiency Ratio versus Speed	6-27
6-13	Turbine Wheel	6-29
6-14	Test Rig Journal Bearing Recess Geometry	6-31
6-15	Test Rig Thrust Bearing Recess Geometry	6-32
6-16	Test Rig Thrust Loading	6-33
6-17	Thrust Bearing Load Capacity versus Displacement	6-34
6-18	Thrust Bearing Flow versus Displacement	6-35
6-19	Thrust Bearing Power Loss - Single Side	6-36
6-20	Thrust Bearing Recess Pressure	6-37
6-21	Thrust Bearing Temperature Rise versus Film Thickness	6-38
6-22	Rotor Dynamics Model of Test Rig	6-39
6-23	Undamped Critical Speed Map - 50-mm LOX Seal Shaft	6-40
6-24	Half Amplitude Response, Stations 8, 10, 11; In-Phase Unbalance, $C = 0.0191$ mm	6-41
6-25	50-mm Seal Half-Amplitude Response, Stations 9, 10, 15; In-Phase Unbalance, $C = 0.0191$ mm	6-42
6-26	50-mm Seal Half-Amplitude Response, Stations 1, 16, 20; In-Phase Unbalance, $C = 0.0191$ mm	6-43
6-27	50-mm Seal Half-Amplitude Response, Stations 8, 10, 11; Out-of-Phase Unbalance, $C = 0.0191$ mm	6-44
6-28	50-mm Seal Half-Amplitude Response, Stations 9, 10, 15; Out-of-Phase Unbalance, $C = 0.0191$ mm	6-45
6-29	50-mm Seal Half-Amplitude Response, Stations 1, 16, 20; Out-of-Phase Unbalance, $C = 0.0191$ mm	6-46
6-30	LOX Seal Test Rig	6-47
6-31	Test Rig Drain Pressure versus Saturation Temperature	6-48
7-1	Overall View of Helium Seal Test Facility	7-15
7-2	Close-Up View of LN ₂ Manifold and Bearing Supply Valves	7-16
7-3	Close-Up View of Test Rig Drain Valves	7-17
7-4	Close-Up View of Helium Seal Test Rig	7-18
7-5	Overhead View of Helium Seal Test Rig	7-19
7-6	Overall View of Control Room	7-20
7-7	Close-Up View of System Control Panel	7-21
7-8	Fluid Supply System Schematic	7-23
7-9	Test Rig Instrumentation	7-25
7-10	Capacitance Probe Construction	7-26
7-11	50-mm Helium Seal Probe Configuration	7-27
7-12	Capacitance Probes, LOX Seal, and Shaft Probes Configurations	7-28
7-13	Simplified Schematic of Data Acquisition Equipment	7-29
8-1	Typical Seal Operating Sequence	8-14
8-2	Typical Data Logger Scan from Seal Test No. 4	8-15
8-3	Typical Computer-Generated Plot	8-16

LIST OF TABLES

<u>NUMBER</u>		<u>PAGE</u>
1-1	REQUIREMENTS AND OPERATING CONDITIONS	1-6
2-1	SUMMARY OF TEST RESULTS	2-41
2-2	DIMENSIONS OF PRESSURE-BALANCED, 50-MM, OUTWARD PUMPING, SPIRAL-GROOVE SEAL	2-42
2-3	STEADY-STATE PERFORMANCE OF 50-MM SPIRAL-GROOVE SEAL . . .	2-43
2-4	DIMENSIONS OF PRESSURE-BALANCED, 20-MM, OUTWARD PUMPING, SPIRAL-GROOVE SEAL	2-44
2-5	STEADY-STATE PERFORMANCE OF 20-MM SPIRAL-GROOVE SEAL . . .	2-45
3-1	SEAL DIMENSION SUMMARY	3-44
3-2	ACCELERATION RUN PERFORMANCE DATA - SEAL SET NO. 2	3-45
3-3	ACCELERATION RUN PERFORMANCE DATA - SEAL SET NO. 3	3-46
3-4	SEAL INSPECTION SUMMARY	3-47
4-1	PROPERTIES OF HELIUM	4-17
4-2	REQUIRED ECCENTRICITY AND FLM THICKNESS TO OVERCOME FRICTIONAL RESISTANCE	4-18
4-3	MAXIMUM OPERATING SPEED FOR $\Delta T = 22^{\circ}\text{C}$	4-18
4-4	RESULTS OF 50-MM THERMAL ANALYSIS	4-19
4-5	RECOMMENDED DIMENSIONS ACCOUNTING FOR CENTRIFUGAL GROWTH AND THERMAL CONTRACTIONS	4-19
4-6	50-MM SEAL TRANSIENT ANALYSIS: SUMMARY OF RESULTS	4-20
4-7	20-MM SEAL TRANSIENT ANALYSIS: SUMMARY OF RESULTS	4-21
5-1	50-MM PRESSURE-BALANCED SEAL	5-41
5-2	20-MM PRESSURE-BALANCED SEAL	5-42
6-1	SUMMARY OF CONCENTRIC JOURNAL BEARING PERFORMANCE	6-49
6-2	SUMMARY OF THRUST BEARING PERFORMANCE (7329 RAD/S; ORIFICE ($d_o = 2.08$ MM)	6-50
6-3	SUMMARY OF THRUST BEARING PERFORMANCE (10,470 RAD/S; ORIFICE ($d_o = 1.93$ MM)	6-51
6-4	50-MM LOX SEAL ROTOR PARAMETERS	6-52
6-5	50-MM LOX SEAL STABILITY ANALYSIS	6-53
7-1	INSTRUMENTATION MATRIX	7-30
7-2	MTI ACCUMEASURE TM SYSTEM 1000 REQUIREMENTS AND SPECIFICATIONS	7-31
8-1	SEAL SET NO. 1 STEADY-STATE TEST SCHEDULE	8-17
8-2	SEAL SET NO. 2 STEADY-STATE TEST SCHEDULE	8-19
8-3	SEAL SET NO. 3 STEADY-STATE TEST SCHEDULE	8-22
8-4	SEAL SET NO. 4 STEADY-STATE TEST SCHEDULE	8-24
8-5	SEAL SET NO. 2 ACCELERATION TEST SCHEDULE	8-26

1.0 INTRODUCTION

Liquid oxygen (LOX) turbopumps are high-speed, high-pressure, and high-power density machines that require effective sealing between the high-pressure LOX being pumped at the impeller end of the machine and the gaseous steam at the turbine end of the unit.

Under NASA Contract NAS3-23260, Mechanical Technology Incorporated (MTI) conducted a technology program for seals to be used in advanced LOX turbopumps. Two types of seals were examined; a primary spiral-groove LOX seal and a floating-ring helium buffer seal with Rayleigh step, hydrodynamic lift pads. Two shaft sizes of 20 mm and 50 mm were considered for each seal type. The function of the spiral-groove LOX seal is to limit leakage of high-pressure LOX generated by the pump impeller. It seals LOX fluid in a seal chamber in which the pressure is typically maintained at 3 to 5 MPa (435 to 725 psig). The function of the floating-ring helium buffer seal is to separate the gaseous steam that drives the turbine from the LOX end of the machine. Helium is used as a buffer fluid at a maximum pressure of 1.38 MPa (200 psia).

Figure 1-1* is a cross section of a LOX turbopump that incorporates both types of seals. Other configurations that utilize a double suction impeller obviate the need for the LOX end seal, but still require the helium buffer seal.

In Figure 1-1, the flow path through the spiral-groove face seal is as follows. From the discharge of the impeller, the flow that does not enter the volute leaks to the backside of the impeller and into the bearing compartment through two orifices formed by the clearance space between the impeller and the housing. These orifice openings adjust as a function of the thrust loading and direction and form an integral component of the thrust balancing system. After flowing through the bearings (for cooling purposes), the flow passes through a labyrinth seal to break down the pressure from approximately 29.6 MPa to 3.45 MPa maintained in the seal chamber. Upon entering the seal

*For ease of readership, illustrations throughout this report are included at the end of each section. In this section, they begin on page 1-5.

chamber, the flow takes two paths. One path is the leakage through the face type seal; the other is a recirculation line to the pump inlet. These separate flow paths are indicated on Figure 1-1. It is important that there is a constant injection flow circulating through the seal chamber to carry away heat developed by the face seal.

At the turbine end of the machine, helium buffer fluid is introduced between the opposed pair of rings of the floating-ring seals at a maximum pressure of approximately 1379 kPa (200 psia). The leakage from the face seal and LOX side of the floating-ring seal discharge from the machine through a common drain.

The seal development program was not directed toward a specific machine, but was intended to cover a broad range of sizes and conditions. Two seal sizes were investigated, one for a 20-mm diameter shaft and the other for a 50-mm diameter shaft. Table 1-1 identifies targeted requirements and operating conditions.

Although leakage requirements were not specified, they were to be as small as practicable because leakage reduction translates directly into increased vehicle payload. The 183 m/s (600 ft/s) interface speed was a target requirement that could not practically be met with the 20-mm shaft diameter. It necessitates operating shaft speeds of approximately 18,326 rad/s (175,000 r/min). The maximum design speed of the rig was 10,472 rad/s (100,000 r/min).

The program that was accomplished included the following:

1. Analysis, design, manufacture, and test of 50-mm Rayleigh-step helium buffer seals.
2. Analysis and design of 20-mm Rayleigh-step helium buffer seals.
3. Analysis, design, and manufacture of 50-mm spiral-groove LOX seals.
4. Analysis and design of 20-mm spiral-groove LOX seals.

5. Analysis, design, and manufacture of a seal test rig designed for maximum speeds of 7330 rad/s (70,000 r/min) for 50-mm seal testing and 10,472 rad/s (100,000 r/min) for 20-mm seal testing.
6. Design and installation of a seal test facility at Wyle Laboratories, Norco, California.
7. Completion of a test program for the 50-mm, helium buffered Rayleigh-step seal.
8. The program produced extensive documentation. In addition to this final report and separate Executive Summary, References [1]*, [2], and [3] are interim reports concerned with the analysis and design of the LOX spiral-groove seals, Rayleigh-step helium buffer seals, and the test rig, respectively. Reference [4] describes the test plan including the design of the test facility.

Several sets of spiral-groove face seals and Rayleigh-step floating ring seals were manufactured in the 50-mm size, by Stein Seal Company of Philadelphia, Pennsylvania. Stein completed manufacturing drawings and contributed to the final designs.

In addition to the tasks described above, MTI supplied to NASA/LeRC for internal use a series of computer codes for analyzing the spiral-groove and Rayleigh-step seals. Brief descriptions of these codes follow.

- Spiral-Groove Seal Codes

SPIRALTI - is used for establishing the geometry and fluid-film performance of spiral-groove seals. Turbulence and inertia are included and the geometry can be optimized on the basis of stiffness.

*Numbers in brackets denote references that can be found in Section 9.0.

DSEALBI2 - establishes complete seal performance of a given geometry including film thickness, flow, power loss, temperature rise, elastic thermal distortions and stresses, and dynamic response characteristics.

- Floating-Ring Seal Codes

RASTEPCO - is used for optimizing the geometry of the shrouded Rayleigh-step compressible fluid seal configuration and producing steady state performance. The code also produces fluid-film forces as a function of eccentricity ratio for use in the dynamics code described below.

RINGDY - determines dynamic response of a fluid-film (compressible fluid) floating-ring seal as a function of given shaft excursions. Coulomb friction occurring along the side walls is taken into account. The program produces orbital response of the ring and establishes whether the ring is properly following the shaft.

FLOWCAL - was written to provide more accurate leakage predictions for the floating-ring seal. The RASTEPCO code computes flow on the basis of viscous laminar theory. FLOWCAL computes gas flow through an annular clearance of finite length exposed to an axial pressure gradient, including combined inertia, viscous effects, and seal ring eccentricity. The thermodynamic behavior of the fluid can be preselected to be isothermal or adiabatic.

This report has been organized so that significant results, conclusions, and recommendations are presented up front. For those involved in the details of seal technology including analysis, design, testing, instrumentation, etc., subsequent sections of the report would be informative. Also, an Executive Summary (MTI 85TR21) has been generated that concisely presents the more significant results of the program effort.

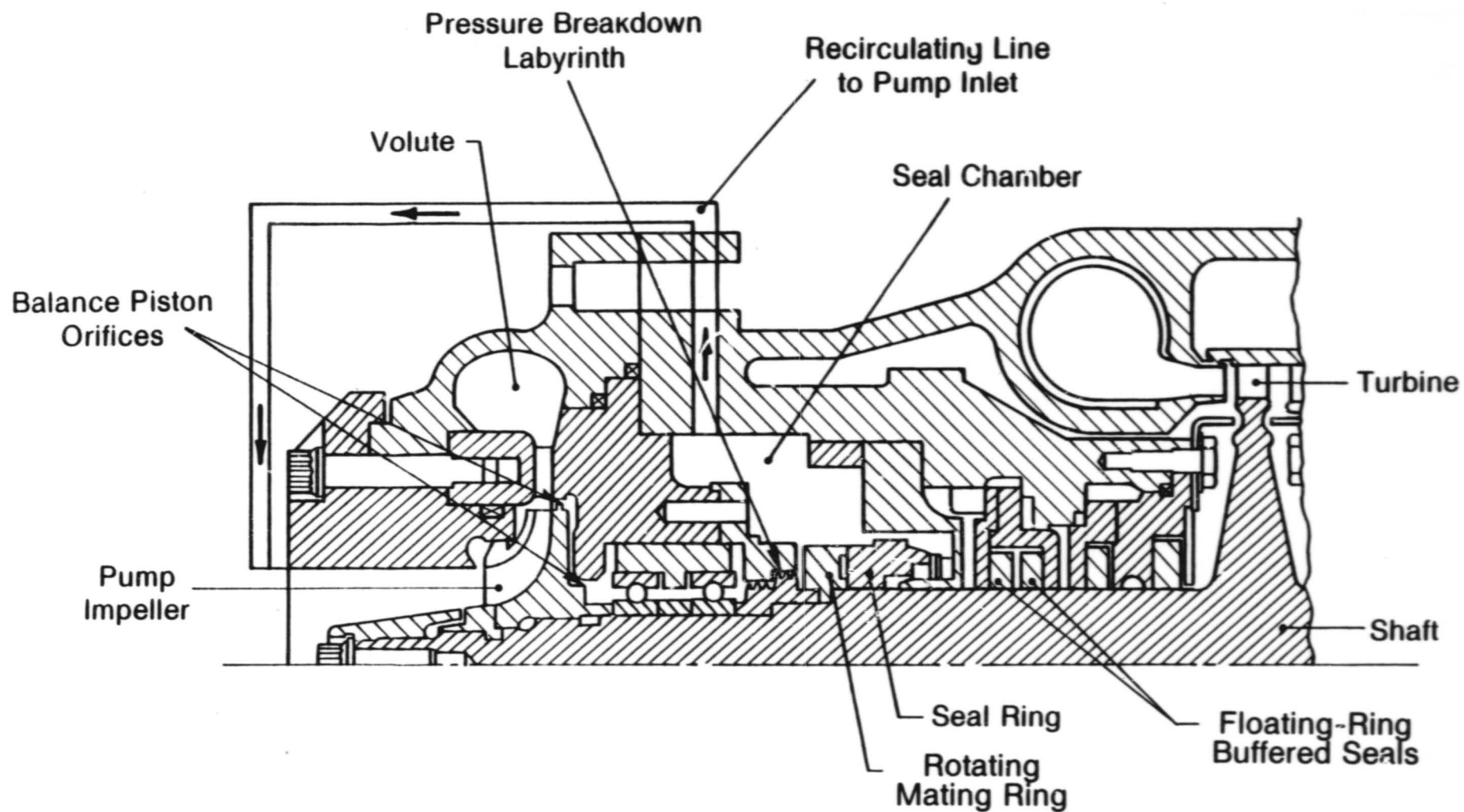


Fig. 1-1 LOX Turbopump Cross Section

TABLE 1-1
REQUIREMENTS AND OPERATING CONDITIONS

Spiral Groove Seals

Shaft Diameter (mm):	50/20
Maximum Pressure (MPa):	5.17/5.17 (750 psia)
Fluid:	LOX
Interface Speed:	183 m/s (600 ft/s ²)
Start-Up Acceleration:	152.4 m/s ² (500 ft/s ²)
Minimum Operating Life (h):	10
Minimum Number of Starts:	300

Helium Buffer Seals

Shaft Diameter (mm):	50/20
Maximum Pressure (MPa):	1.38/1.38 (200 psia)
Fluid:	Helium Gas
Interface Speed:	183 m/s (600 ft/s)
Start-Up Acceleration:	152.4 m/s ² (500 ft/s ²)
Minimum Operating Life (h):	10
Minimum Number of Starts:	300

2.0 SUMMARY OF SIGNIFICANT RESULTS AND CONCLUSIONS

In this section, a broad summary of the results of the program are presented with relevant descriptive material, conclusions, and recommendations. Both types of seals are discussed as well as the test rig and instrumentation.

2.1 Configuration and Principle of Operation of a 50-mm Helium Buffer Seal

Figure 2-1* shows a schematic representation of the helium buffered, floating-ring seal. The seal consists of two rings that are mounted back-to-back. The helium buffer fluid enters between the rings and forces the rings up against the stationary housing. The buffer fluid leaks in the clearance annulus between the shaft and the seal and prevents ingress of exterior fluid on either side of the floating-ring assembly.

The rings are held in equilibrium by a number of forces as shown in Figure 2-1. F_C is a pressure force from the inlet buffer fluid that forces the rings up against the housings. This pressure force is balanced part way on the housing sides of the rings indicated by F_B . F_H represents a hydrodynamic force that is generated by rotation between the shaft and the ring. The net hydrodynamic force is zero when the shaft and rings are in the concentric position. However, when the ring becomes eccentric with respect to the shaft, a hydrodynamic force is built up that opposes the eccentricity. There is also a normal force, F_N , acting on the ring at the contact area between the ring and the housing. Generally, F_N is maintained as small as possible to minimize frictional resistance forces. To minimize F_N , the balance force, F_B , should be as large as possible. Therefore, the contact area is small and is located as close to the shaft as is practicable, but with sufficient housing clearance to permit the necessary shaft excursions. In addition to the equilibrium forces mentioned above, there is a friction force, F_f , between the seal ring and housing.

*Figures are presented consecutively, beginning on page 2-18.

Figure 2-2 shows the hydrodynamic geometry that is incorporated into the bore of the seal rings. A portion of the length of the bore is segregated into sectors and these sectors are separated from one another by axial grooves. A circumferential groove that goes completely around the bore is incorporated before the seal dam region. At the interior of the sectors, Rayleigh-step pockets are machined. Hydrodynamic pressures are generated by viscous pumping of the fluid over the Rayleigh step. Surrounding the Rayleigh-step gas bearing by the high-pressure ambient, results in increased load capability. The sealing occurs across the dam which is a narrow annulus of low clearance exposed to high pressure at its interior circumferential groove and to lower pressure at its outboard end. The shaded regions on Figure 2-2 indicate depressions from grooves and Rayleigh-step pockets. Figure 2-3 is a photograph of a carbon ring seal set with embedded thermocouples for temperature measurement.

2.2 Test Results of the 50-mm Rayleigh-Step Helium Buffer Seal

Four helium seal sets and three runners were tested during the course of the program. All were subjected to steady-state tests while two sets additionally underwent high acceleration rate tests. The tests resulted in 613 min of cumulative running time and 90 high acceleration rate starts. Table 2-1* provides a brief summary of the tests performed.

The seals performed successfully over a broad range of conditions, including the full design pressure of 1379 kPa absolute (200 psia). The design speed of 7330 rad/s (70,000 r/min) was not achieved. The first three seal tests were limited to about 5235 rad/s (50,000 r/min) due to a dynamics problem in the test rig. After modifications were made to correct the problem, a fourth seal test was run.

Seal set No. 2 completed the test program to the maximum speed capability of the rig without damage, including 50 high acceleration start-ups.

*Tables are presented consecutively, beginning on page 2-41.

The failure of seal set No. 1 was directly attributable to large amplitude motions of the seal runner. The estimated amplitude was 0.038 to 0.098 mm (1.5 to 2 mils) peak to peak which was well beyond the acceptable range. Seal set No. 3 failed because of contamination in the helium supply system that infiltrated the ring clearance.

Testing of seal set No. 4 was accomplished subsequent to modification made to the rig to achieve full speed. The changes clearly had a beneficial effect and allowed operation to proceed to 5968 rad/s (57,000 r/min) with much lower vibration levels. The modification, however, resulted in a higher temperature seal environment. Seal failure resulted by consumption of available clearance at a speed of 5968 rad/s (57,000 r/min). The rig did not show evidence of excessive vibrations. The indications were that full speed operation of 7330 rad/s (70,000 r/min) could be achieved, and seal failure would not have occurred if larger installed clearances were incorporated.

Figure 2-4 indicates the steady-state data points for seal set No. 2, as a function of speed and helium supply pressure superimposed upon a theoretical operating range map. Analytically, there are two limitations on performance:

1. Insufficient hydrodynamic forces to overcome friction forces - a low-speed, high-pressure constraint identified by the high friction region on the figure
2. Insufficient friction to counteract inertia forces - a high-speed, low-pressure constraint identified as the low friction region on the figure.

Figure 2-4 shows an operating range map for the 50-mm seal that accounts for all constraints. If the pressure follows a speed squared relationship to a maximum of 1379 kPa (200 psia) at 7330 rad/s (70,000 r/min), it was expected that seal performance would be satisfactory. The majority of the data points fall into the high friction region where friction forces on the seal ring exceed hydrodynamic fluid-film forces. Most of the testing revealed that the seal ring remained stationary and shaft movement was contained inside the

clearance region. Any movement of the ring was to another stationary position to accommodate variation in shaft eccentricity at the seal ring location.

Figure 2-5 shows flow data versus pressure drop for the outboard seal ring on seal set No. 2 at various operating speeds. The solid lines represent theoretically predicted flows at various radial clearances. Theoretical flow is independent of speed. Speed increases cause clearance reduction because of centrifugal runner growth and thermal expansions. Consequently, flow generally decreased with speed.

The most accurate film thickness measurements were obtained from the outboard seal ring of seal set No. 4. Four probes were embedded in this ring and directly measured the film thickness between the seal ring and the shaft. Flow versus pressure drop data are shown on Figures 2-6 and 2-7. The results indicate that measured clearances are lower than theoretical predictions for equal flows and pressures. However, there are indications of bypass flow between the seal rings and housing that could account for some of the differences noted.

2.3 Conclusions and Recommendations for the 50-mm Rayleigh-Step Seal

The general conclusions drawn from the 50-mm Rayleigh-step floating-ring helium buffer seal program are as follows:

- The program results confirm the capability of the seals to perform well in cryogenic turbomachines. Seal set No. 2 went through its complete test program unscathed and could be readily inserted into a machine and rerun. Eight steady-state runs were made resulting in a accumulative test time of 261 min. Also, a total of 50 fast starts were completed with average acceleration rates of over 152.4 m/s^2 (500 ft/s^2). Although full design interface speed of 183 m/s (600 ft/s) was not achieved, the seals performed very satisfactorily up to an interface speed of approximately 144 m/s (472 ft/s) which is 1.53 times faster than previously reported results for cryogenic applications [5]. In addition, full pressure drop of 1379 kPa absolute (200 psia) was accomplished up to a speed of 126 m/s (412 ft/s). There was

every indication that a greater machined clearance for seal set No. 4 would have permitted full speed, full pressure operation.

- Leakage flow ranges per seal ring averaged between 0.001 and 0.002 kg/s (13 to 25 scfm) and were not significantly affected by pressure drop and speed. The most sensitive parameter is clearance. Examination of Figure 2-7 reveals that the measured flow varies approximately as the 2.5 power of clearance at a constant pressure drop. Figure 2-8 shows a maximum flow envelope for each seal set as a function of pressure drop. Each flow curve represents the higher of the two rings (inboard or outboard) flows at a given operating point. The highest flow recorded was 0.0026 kg/s (33 scfm). However, typical flows ranged between 0.001 and 0.002 kg/s (13 and 25 scfm). Figure 2-9 shows flow data for a single speed of 4712 rad/s (45,000 r/min). While it was not the highest speed tested, it is the highest speed at which a wide range of supply pressures were applied to each seal set. Seal Sets No. 2 and No. 3 had maximum pressure drops of 1365 kPa (198 psia) and 1250 kPa (181 psia). Maximum flow levels are 0.0019 kg/s (24 scfm).
- Two of the three seals that failed by high-speed contact did so because of external factors unrelated to seal design and performance. One failure occurred because of excessive shaft vibrations and another by a contaminated helium supply.
- The seal design process requires integration with the machine environment. Thermal expansions and contractions and centrifugal growth of the runner are important considerations. To correct test rig vibrations, changes were made that altered the seal environment. The program did not permit detail studies to be made to determine the effects of the environmental changes on seal set No. 4. As a result, the seals were installed with insufficient clearance. More liberal clearances would have permitted successful full speed operation.
- The material combination (P-5N carbon graphite rings versus tungsten carbide coated runner) was not tolerant of high-speed rubs. The runner, in particular, performed badly. It retained carbon transfer, closing up seal clearances. Localized heating caused upset and flaking of the tungsten

carbide coating. Large surface area rubs also caused "wipe-out" of the Rayleigh steps machined into the carbon rings. Investigation of alternate material combinations was beyond the scope of the program, but more suitable materials should be a future consideration.

- The analytical tools used in the design process were very effective in predicting fluid-film performance and dynamic response. Initially, leakage was computed using viscous flow theory which proved to be difficult to correlate with experimental results. It was necessary to modify the flow theory to include entrance and film inertia losses (see Appendix A). This improved correlation and interpretation, however, discrepancies still exist. For the same flow and pressure, theoretical clearances are larger than measured by a factor of approximately 1.6. This is not a large factor considering the sensitivity of flow with film thickness. There was also evidence of bypass leakage along the end walls that was not accounted for by theory. However, further effort remains to explore in depth the reasons for the variations.
- Dynamic response of the rings did not appear to be a serious problem. Analysis indicated that the rings should have low mass to dynamically track runner excursions. Consequently, they were made of carbon without composite metallic rings on the outer circumferences. In most instances, the rings were maintained in a static position. Test rig speed limitations caused most test points to be in the high friction region of the operating range map (Figure 2-4), but there appeared to be sufficient hydrodynamic capability to move the rings when necessary. Dynamic response of the seal rings probably would have been more active at full design speed.

Seal motions did arise on several occasions. The principal occurrence was with the inboard ring of the seal set No. 3. The seal ring developed an in-phase, generally elliptical orbit. The orbit was observed at all three test speeds of 3665, 4188, and 4712 rad/s (35,000, 40,000, and 45,000 r/min) and became larger in amplitude as the supply pressure was increased. The maximum orbit diameter was approximately 0.025 to 0.030 mm (0.001 to 0.0012 in.). The runner orbit was approximately 0.010 to 0.013 mm (0.0004 to 0.0005 in.) so that some amplification was taking place. This

ring did not fail nor make contact with the runner and attest to the excellent dynamic qualities of the seal system. It is speculated that a fluid film existed between the rings and end walls, minimizing frictional resistance of the rings to shaft-induced motions.

2.4 Results and Conclusions for the 20-mm Rayleigh-Step Helium Buffer Seal

For this seal, theoretical and design investigations were made and the following is a summary of the significant results and conclusions:

The maximum test rig speed is 10,472 rad/s (100,000 r/min). This limits the surface speed of a 20-mm diameter shaft to 104.5 m/s (343 ft/s). Thus, it would not be possible to test the 20-mm seal at the specified condition of 163 m/s (600 ft/s). Surface speed limitations also restrict fluid-film hydrodynamic force generation necessary to overcome seal ring friction. It was determined that the maximum buffer fluid pressure at 10,472 rad/s (100,000 r/min) would be 689 kPa (100 psia). Figure 2-10 shows the operating range map for the 20-mm seal, indicating the high and low friction regions that would cause difficulty. The operating range is narrower than for the 50-mm design. Also indicated on the curve is the speed squared relationship with pressure to be used in test. Regions of low friction are encountered as the shaft comes up to speed where excessive ring motions would occur if operation was sustained. However, if the seal system does not dwell at these conditions, it could pass through them without endangering seal operation.

- Centrifugal expansion for the 20-mm seal runner is negligible because the runner is integral with the small diameter shaft. Thermal contractions, however, require very close installation clearances of 0.0102 to 0.0229 mm (0.0004 to 0.0009 in.) diametral clearance. Mating the rings directly against the shaft is desirable since it removes the uncertainties of runner growth and distortions. Material combinations should be such that the shaft survive high-speed rubs.
- As with the 50-mm seals, low mass and all carbon rings are required for dynamic tracking.

2.5 Description and Principle of Operation of the Spiral-Groove LOX Seals

The spiral-groove face seal is a prime candidate for application to LOX turbo-pumps. It is a fluid-film seal that can effectively inhibit leakage and avoid rubbing contact that could cause catastrophic explosion failure in a LOX environment. As described in Section 1.0, the function of the LOX seal is to aid in preventing leakage of LOX from the pump end of the machine.

Originally, MTL examined a conventional type of spiral-groove seal that was labeled the straight-through design. The spiral grooves extended to the outside diameter and the fluid was pumped inward to a dam region at the interior ID of the seal. Although excellent performance characteristics were predicted, the straight-through designs were ultimately abandoned because of the probability of vaporization in the flow path.

The pressure-balanced concept selected was conceived by NASA/LeRC and recommended for the LOX turbopump application because it obviated vaporization problems and reduced net axial loading.

2.5.1 Special Considerations for LOX

2.5.1.1 Fluid Vaporization. Because of the many restrictions the fluid passes through before it reaches the seal compartment, it enters relatively hot. However, since it is at high pressure, it is still a liquid. When passing through the seal, it is further heated by viscous shear and simultaneously the pressure drops to the seal exhaust ambient. Thus, upon discharging from the seal interface, it is in a mixed vapor state. At ambient pressure, the saturation temperatures of LOX is -183°C (-297.4°F); the discharge temperature in the seal interface can be significantly higher and is generally around -115°C (-175°F). Therefore, vaporization is likely. Vaporization in the spiral-groove leakage path can block the through-flow which assists in carrying away the heat generated in the interface. This leads to further vaporization, reduction in fluid viscosity, and consequently load capacity. Ultimately, the seal fails due to overload and overheating. Therefore, an adequate seal design must handle vaporization without seriously jeopardizing performance.

2.5.1.2 Fluid Turbulence. The criterion for turbulence is that the ratio of inertia to viscous fluid forces, which is the commonly applied Reynolds number, be greater than 1000 [6]. The Reynolds number is a dimensionless quantity defined as follows:

$$Re = \rho U_0 h / \mu$$

where:

- ρ = fluid density
- U_0 = surface velocity
- h = film thickness
- μ = absolute viscosity

The characteristics of LOX are such that the mass density approaches that of water, while the viscosity is close to that of a gas. From the definition of the Reynolds number, this combination of fluid properties is conducive to the promotion of turbulence. The load on the seal would have to be great enough so that the operating film thickness was only 6.1×10^{-7} m (24×10^{-6} in.) for the flow to be laminar. This film thickness is too small to be practical and would produce heat generation that would vaporize the fluid and cause failure by contact and overheating. The final seal design operated with film thicknesses near 2.54×10^{-5} m (0.001 in.) with resulting Reynolds numbers in the vicinity of 42,500. The effects of turbulence upon fluid-film performance is the same as if the seal were operating in the laminar regime with a greatly increased viscosity. It produces a greater load carrying capability and higher viscous power losses than a laminar operating seal. With respect to the spiral-groove geometry, turbulence results in much deeper and wider grooves than a laminar counterpart, so that sufficient fluid of apparent high viscosity could be pumped through the large clearance.

2.5.1.3 Fluid Inertia. Because of the large operating film thickness and high-pressure gradients, the flow restriction through the seal is not entirely viscous. Inertia forces are another significant consideration. Inertia produces steep pressure drops at flow restrictions, or sudden contractions in the path of the flow. At the sudden contractions, pressure head is converted

to velocity head. Such contractions occur at the spiral-groove dam upon fluid entrance into the seal land, and also upon fluid entrance into the spiral-groove seal from the high-pressure fluid at the outer periphery. Another inertia influence is centrifugal forces acting on the fluid. These were not considered because of the complexity of the analyses; their general effect is to retard flow. It was estimated they would not have more than a 10% influence on the predicted rates.

2.5.1.4 Two-Phase Flow. Once the fluid vaporizes, it enters the mixed flow regime and a considerable amount of energy is required to boil the liquid. When it is in the mixed regime, the performance of the seal is not precisely known although it was speculated that leakage would be close to that of a pure liquid. Because of this, most of the seal interface is in the spiral-groove region where the fluid is at high pressure and in a purely liquid state. It is only at the latter end of the seal dam where the pressure is low that vaporization generates. Two-phase flow may be a significant phenomenon for future LOX seals and is an area where further effort should be devoted.

2.5.2 Pressure-Balanced Spiral-Groove Seal

The pressure-balanced concept is schematically pictured on Figure 2-11. The spiral-groove region is fed by an interior groove that communicates through passages (drilled holes) with the pressurized fluid to be sealed. In this instance, the term pressure-balance implies that the high-pressure fluid to be sealed resides at both the inside and outside perimeters of the spiral-groove region. The grooves pump outward to a dam region on the outer periphery of the seal. Leakage flows from the interior groove inward through a sealing land to the ambient low-pressure region.

A principal advantage of this configuration over the straight-inflow design is that the spiral-groove pumping circuit operates independently of the leakage circuit. Thus, if the fluid flashes or vaporizes in the leakage dam interface, it will not affect the pumping action of the spiral-groove and the ability of the faces to maintain separation. From a leakage point of view, flashing is beneficial since it significantly reduces mass flow. The one

major problem with the pressure-balanced concept is the possibility of overheating.

Consider a control volume surrounding the seal, as represented by the dashed lines on Figure 2-11. What leaves and enters the control volume is leakage flow. However, internal to the control volume, there is a significant amount of viscous shear. If we presume that all the heat generated by viscous shear is carried away by the leakage flow, then the temperature rise inside the control volume can become very high. However, if external cooling flow is circulated through the control volume, it can carry away the heat generated by viscous friction and prevent excessive temperature rises. Fortunately, excess flow is forced into the seal cavity of many LOX turbopumps and recirculated into the impeller inlet (refer to Figure 1-1). This circulating flow can prevent overheating.

A typical pressure distribution across the face of the pressure-balanced concept is shown on Figure 2-12. The pressure is normalized with respect to the high pressure being sealed on the outer periphery. The radial distance or span is indicated nondimensionally along the abscissa. The origin in the radial direction is at the inlet of the spiral-groove region. The pressure increases from the interior of the grooved region outboard until the spiral-groove dam is reached. Then, there is a sudden inertia pressure drop at the entrance to the dam, followed by a linear pressure drop through the dam to the outer periphery of the seal. From the origin at the interior of the spiral-groove region, proceeding inward, there is a constant pressure in the grooved annulus followed by a significant pressure drop at the entrance to the sealing dam and then a linear drop across the sealing dam to ambient pressure. The inertia pressure drop is high across the sealing dam because of the high-pressure gradient across it.

2.6 50-mm Spiral-Groove Seal

2.6.1 Groove Geometry

The general groove geometry is shown on Figure 2-13. Note that deep and wide grooves are necessary to pump the highly turbulent fluid because of its high

effective viscosity. Table 2-2 defines the principal nominal dimensions of the pressure-balanced design.

The original MTI design layout of the 50-mm pressure-balanced seal is shown on Figure 2-14. In the test rig, the seal will be installed in a back-to-back configuration as shown on the bottom left corner of the drawing. This was done to eliminate excessive thrust loading on the test rig thrust bearing. The outboard seal is the test seal, while the inboard seal is the thrust balancing seal. The nonrotating member of the spiral-groove seal is made from carbon graphite (P-5N) and contains the interior high-pressure inlet annulus and feed holes.

The seal rings do not have metal shrouds or interface pieces. The intent is to maintain the mass of the seal ring members as low as possible for improved dynamic response. Figure 2-15 is a photograph of one face seal and a mating ring. Because of the back-to-back installation, the mating ring incorporates grooving on both sides, but of opposite hand.

2.6.2 Summary of Performance

The principal advantage of the pressure-balanced design is that it separates the spiral-groove and leakage circuits, and reduces the consequences of fluid vaporization in the seal region interface.

Disadvantages of the pressure-balanced design are high power loss including viscous friction and windage of the rotating mating ring, relatively large collar diameter, poor low-speed performance, and high lift-off speed. Also, without external cooling or recirculation of LOX inlet supply, there is a good possibility the seal will overheat. A summary of calculated performance results at design operating conditions is indicated on Table 2-3. The table provides information for both the cooled and uncooled inlet conditions.

The factors that influence safe operation of pressure-balanced seals are film-thickness, fluid temperature rise, and dynamic response or ability of the seal ring to follow excursions of the rotating collar. Based on the analysis, an acceptable operating range was established. This is shown in Figure 2-16.

At low rotational speeds, low film thickness and excessive temperatures are limiting factors. At lower pressures and high speeds, the limiting factor is dynamic response. The safe operating range lies within these boundaries. Note that a pressure versus speed squared relationship will produce safe start-up operation. The relatively large operating clearance provides a greater tolerance to distortions and dynamic response than laminar seals that typically operate in the film thickness range of 0.0025 to 0.0051 mm (0.0001 to 0.0002 in.)

The effects of turbulence are increased film thickness and power consumption. Geometrically, the seal requires deep and wide pumping grooves. The magnitude of the turbulence is large, producing Reynolds numbers in the 40,000 to 50,000 range.

2.7 20-mm Spiral-Groove Seal

2.7.1 Geometry

Figure 2-17 is a layout drawing of the 20-mm pressure-balanced design. The concept is very similar to the 50-mm design except it is a scaled down version consistent with the size reduction, but optimized to operate at similar surface speeds of 183 m/s (600 ft/s). Table 2-4 indicates the pertinent nominal dimensions of the 20-mm design; the spiral-groove geometry is also indicated on Figure 2-17.

2.7.2 Summary of Performance

Performance of the 20-mm seal is summarized on Table 2-5 and Figure 2-18. The table presents performance at the design point condition, while the figure is an operating range map. The map indicates low-speed, high-pressure operation is to be avoided because of marginal film thickness and high temperature rise of the fluid. At high-speed, low-pressure operation, dynamic response problems are encountered. A pressure increase proportional to the square of the operating speed produces safe operation.

2.8 Test Rig

2.8.1 Design Philosophy

The general design of the test rig was guided by several fundamental principals generated at the outset of the program.

1. The rig was to have the capability to test both 50- and 20-mm seals. The 50-mm seals were to be tested at a maximum speed of 7,330 rad/s (70,000 r/min); the 20-mm seals were to be tested at a maximum speed of 10,472 rad/s (100,000 r/min).
2. Different shafts could be installed for the 50- and 20-mm seal tests, but the same set of bearings were to be employed. A journal size of 30 mm was selected as a compromise for testing both size seals and for providing acceptable rotordynamic response and bearing power losses.
3. Hydrostatic fluid-film bearings were to be employed to enable friction-free start/stops, whirl-free operation, good damping qualities, and freedom of adjustment through flow and restrictor element alterations.

2.8.2 General Configuration

A cross section of the test rig is shown on Figure 2-19. The right-hand portion of the rig is the drive where the nitrogen turbine is located. The central portion is the bearing region where the journal and thrust bearings are located. The left end of the rig is the test seal section; the 50-mm helium buffer seal is shown installed.

Locating the thrust bearing in the center of the rotor avoids excessive overhang at either end and provides for a more uniform distribution of mass along the rotor. This arrangement alleviates rotordynamic difficulties due to large overhung masses which would occur if the test seals and thrust bearing were mounted in tandem at one end of the rotor. The helium buffers are installed in a back-to-back configuration, and mate against a common runner.

The 30-mm shaft journal diameter provides sufficient stiffness to be below the bending critical speed, and prevents excessive bearing and windage power losses for operation at 7330 rad/s (70,000 r/min). At the turbine end of the shaft, a heat dam is located between the turbine wheel and shaft. This dam prevents high temperature at the turbine wheel from conducting heat into the cold shaft regions. The outside periphery of the heat dam is machined with a labyrinth that provides one half of a buffer seal that prevents turbine gas from entering the bearing region. At the seal end of the shaft, the helium seal runner is secured to the shaft by a spring sleeve that is pressed onto the shaft. This compensates for bore growth of the runner. Figure 2-20 shows disassembled components of the test rig and Figure 2-21 is a photograph of an assembled rotor. Details concerning the rig design are presented in Section 6.0.

Because of problems uncovered during the first three tests, three modifications were made prior to the fourth seal test. Perhaps the most significant alteration was the addition of a small labyrinth seal between the inboard helium seal ring and the nearby journal bearing as shown in Figure 2-22. Helium leaking from the seal and an additional flow of helium entering through a new external port, were maintained at a slightly higher than bearing drain pressure, preventing LN₂ from flowing through the new labyrinth seal and bathing the inboard end of the runner. This was done to reduce the heat generation from windage losses that was causing vaporization in the adjacent bearing film, reducing bearing effective stiffness and damping and resulting in unacceptable rotor response at speeds below design speed. The insertion of the labyrinth seal insured that only gaseous helium would run against the seal runner with significantly lower windage losses than that produced by LN₂.

2.8.3 Summary of Test Rig Performance

In general, the test rig performed well with the principal exception of not achieving full speed. As mentioned above, this problem was traced to vaporization in the seal end journal bearing reducing its stiffness and damping characteristics which resulted in high vibration levels at approximately 5236 rad/s (50,000 r/min). Corrections were made to the rig to eliminate this

problem, but a seal failure at 5969 rad/s (57,000 r/min) prevented further speed increases.

The testing program surfaced several other characteristics of the test rig that are significant and peculiar to cryogenic testing. These are mentionable because they have general applicability to cryogenic test rigs and are important to understand for future applications of the rig.

1. Initial Cooldown. The hydrostatic bearings are energized early in the start-up process in order to float the shaft prior to rotation. Initially, the rig is at ambient temperature and the cryogenic fluid supply to the bearings (LN₂ or LOX) is in a gaseous state. Since there are deep recesses in the bearings, the bearing rotor system is prone to pneumatic hammer until the cryogenic fluid is liquefied. It was necessary to manually hold the shaft from vibrating by forcing it axially against the thrust bearing surface during the chill-down period (~20-min time span). For LN₂ testing, this requirement presented an inconvenience but no serious problems. For LOX testing, however, personnel are not permitted in the vicinity of the test rig, and a remote holding device is required. For future hydrostatic bearing designs, the recess volume should be as small as practicable to avoid pneumatic hammer at startup.
2. Recess Pressure Measurement. Measurement of recess pressures provides information on the state of health of the rotor-bearing system while operating. Unfortunately, the measurement system introduced problems and ultimately had to be abandoned. What occurred was vaporization of the cryogen in the pressure sensor lines emanating from the rig to the pressure transducers. This deteriorated bearing stiffness because the fluid column stiffness in the instrument line is significantly less when vapor is present. Also, heat is transferred from the line fluid into the recess promoting bubbling. It was necessary to plug all pressure tap lines at the tester and operate without recess pressure information.
3. Isolation of the seal test area from the seal end journal bearing was required to prevent heat transfer into the bearing and causing vaporization and bubbling of the cryogen in the bearing. The installation of a

labyrinth seal between the bearing and seal compartment and an additional source of helium buffer fluid prevented ingress of LOX to the bearing side surface of the seal runner. A substantial reduction in windage heat generation was accomplished, which effectively eliminated excessive heat transfer into the bearing from the seal compartment.

4. Nitrogen was not an acceptable buffer fluid at the turbine end buffered labyrinth seal because it liquefied rapidly. It was necessary to use helium as the buffer fluid.

2.9 Instrumentation

There is one area regarding instrumentation that is worthy of mentioning in this summary of significant results. The original method of measuring seal film thickness was to trace the movement of the seal rings and runner separately and obtain clearance by electronically subtracting signals. It was originally determined that embedding probes directly into the seal ring would impose restraint by cables that would prevent dynamic tracking. It was subsequently discovered that a very thin coaxial cable (0.76 mm in diameter) existed, that would not impose excessive restraint on the seal rings. It was decided to make probes and embed them directly into one of the seal rings for test No. 4. Direct measurement of film thickness rather than the differential approach would produce more accurate measurement and errors due to large temperature gradients in the housing could be avoided. The probes performed very well.

Figure 2-23 shows details of the probe installation and Figure 2-24 is a photograph of the instrumented ring. The two original probes observing the seal runner were kept and used to monitor runner motion. The embedded probes were not subject to error due to thermal distortions of the seal housings.

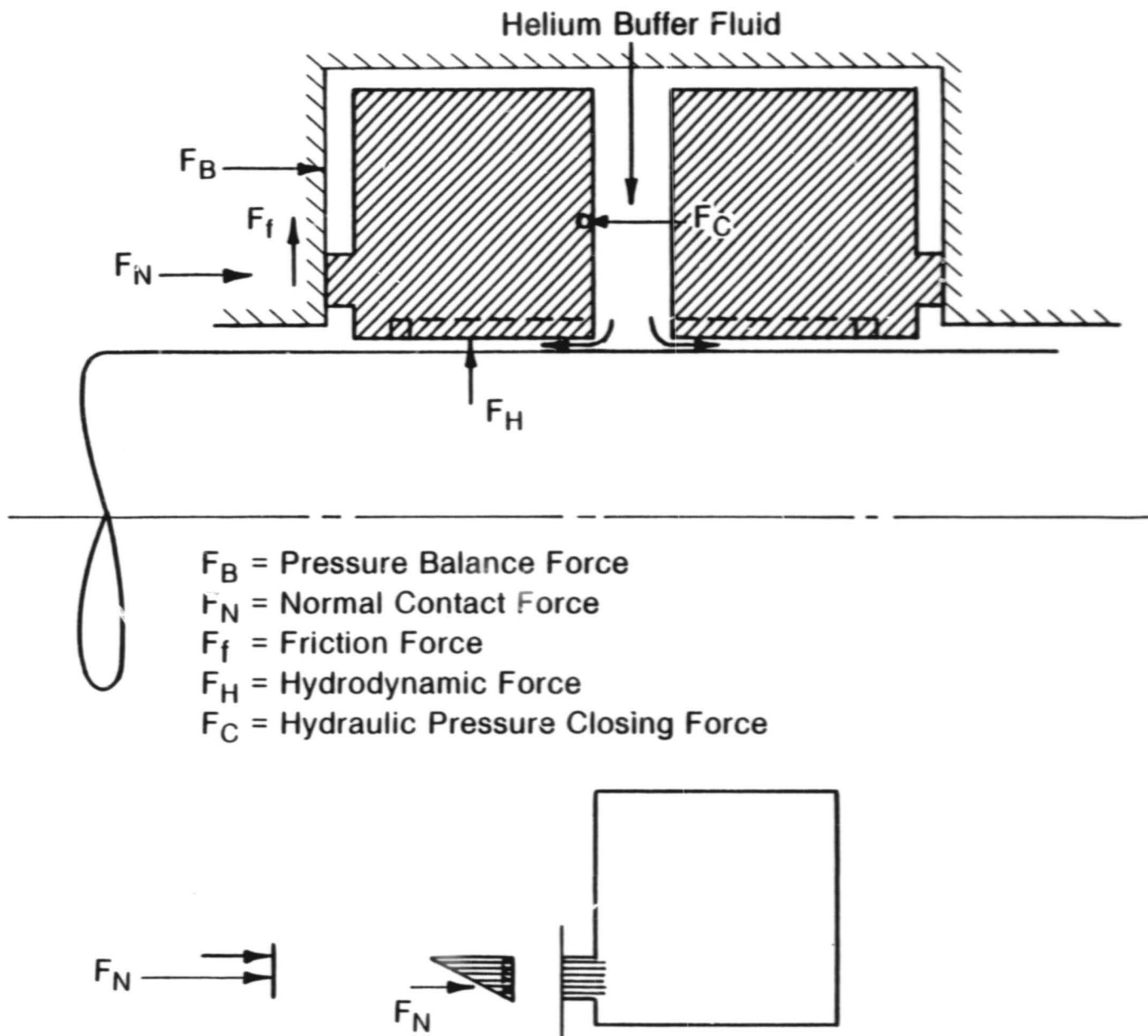
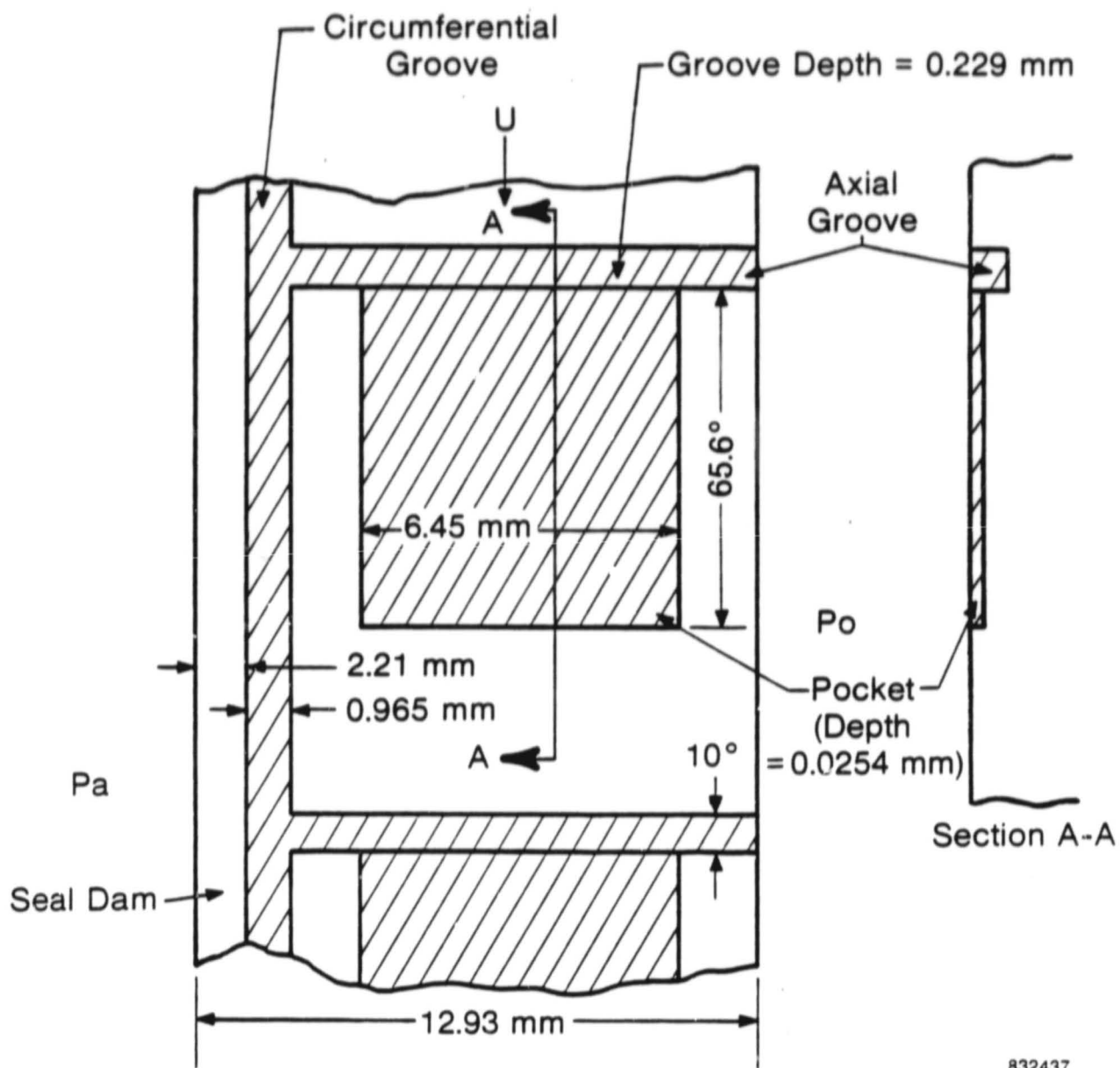


Fig. 2-1 Floating-Ring Seal Schematic



832437

Fig. 2-2 Developed View of 50-mm Rayleigh-Step Pad

ORIGINAL PAGE IS
OF POOR QUALITY

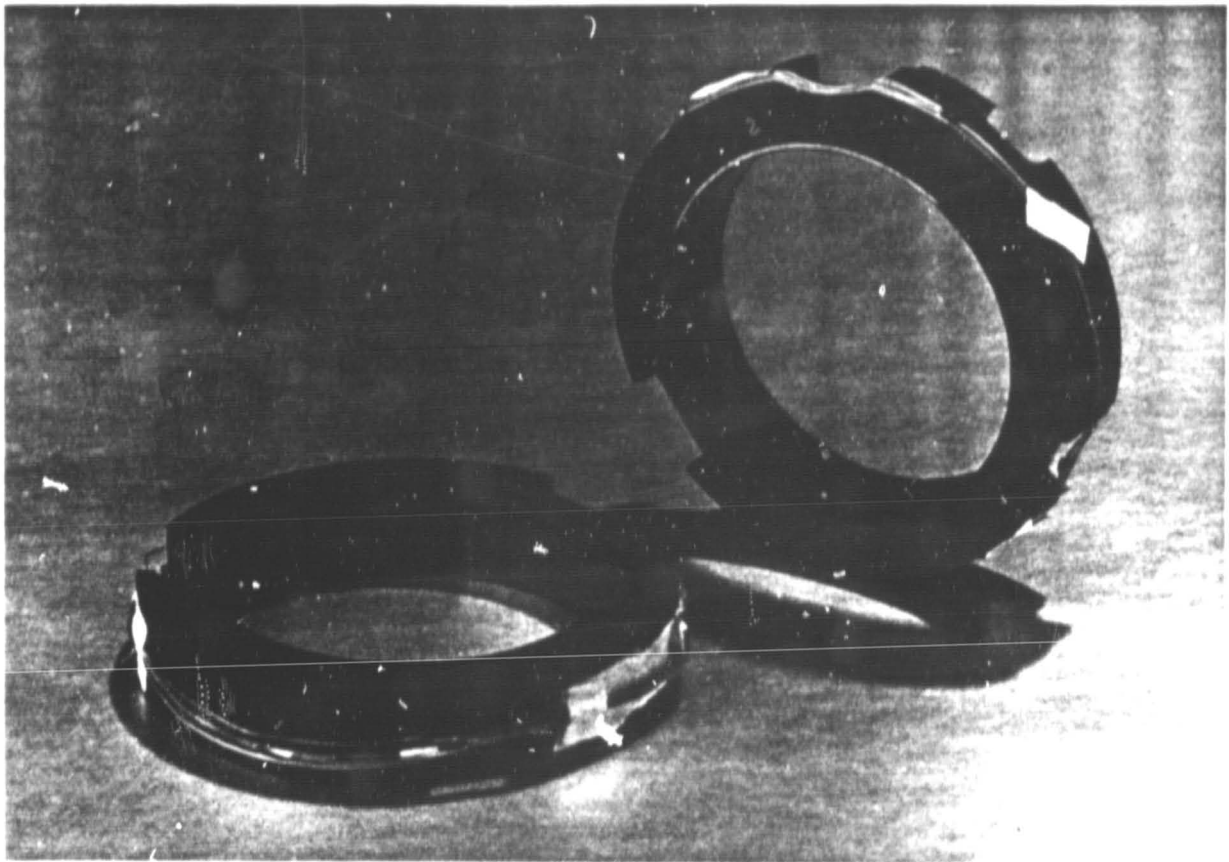


Fig. 2-3 50-mm Rayleigh-Step Floating Ring.

ORIGINAL PAGE IS
OF POOR QUALITY

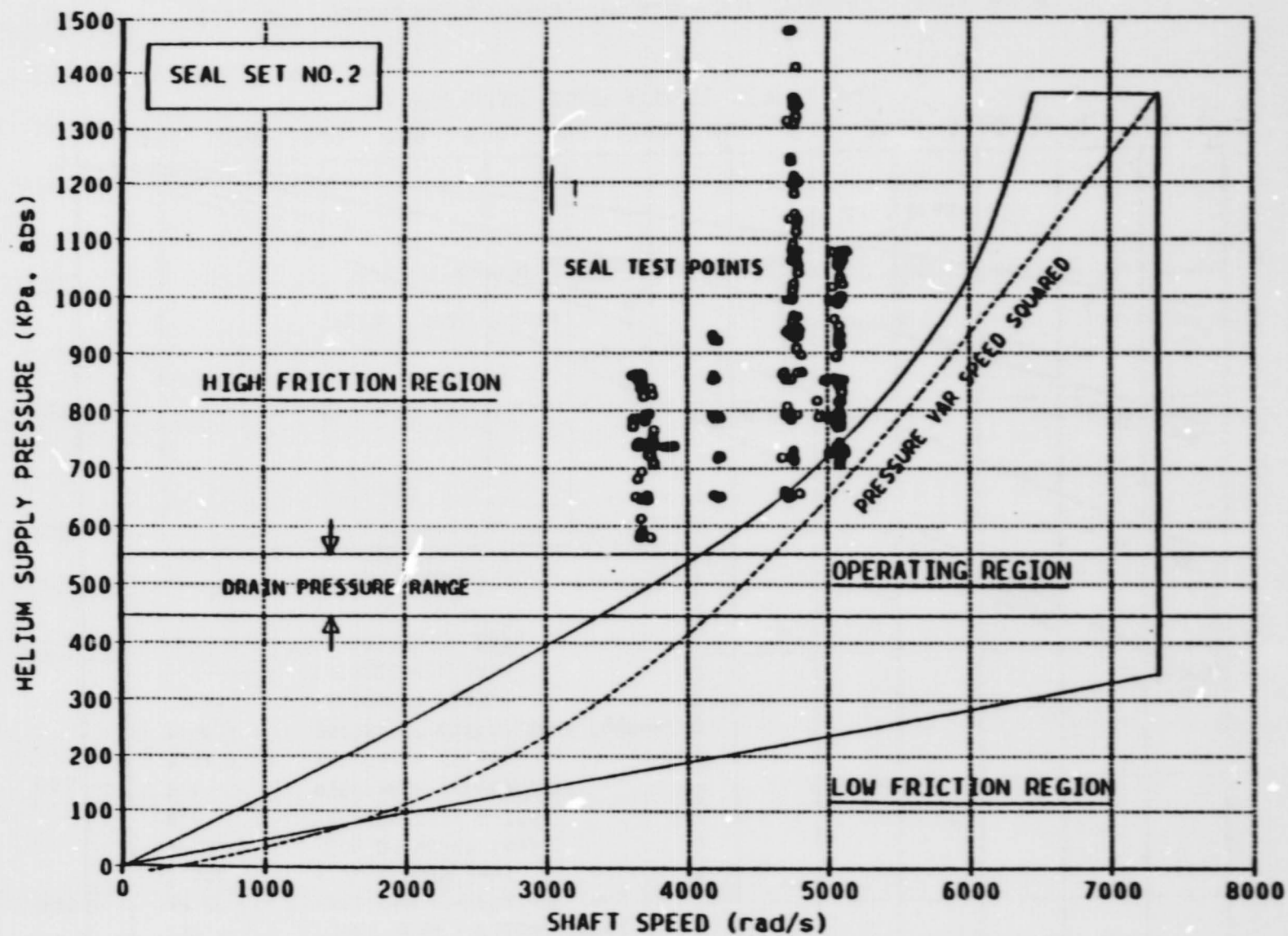


Fig. 2-4 Operating Map for 50-mm Helium Buffer Seal - Seal Set No. 2

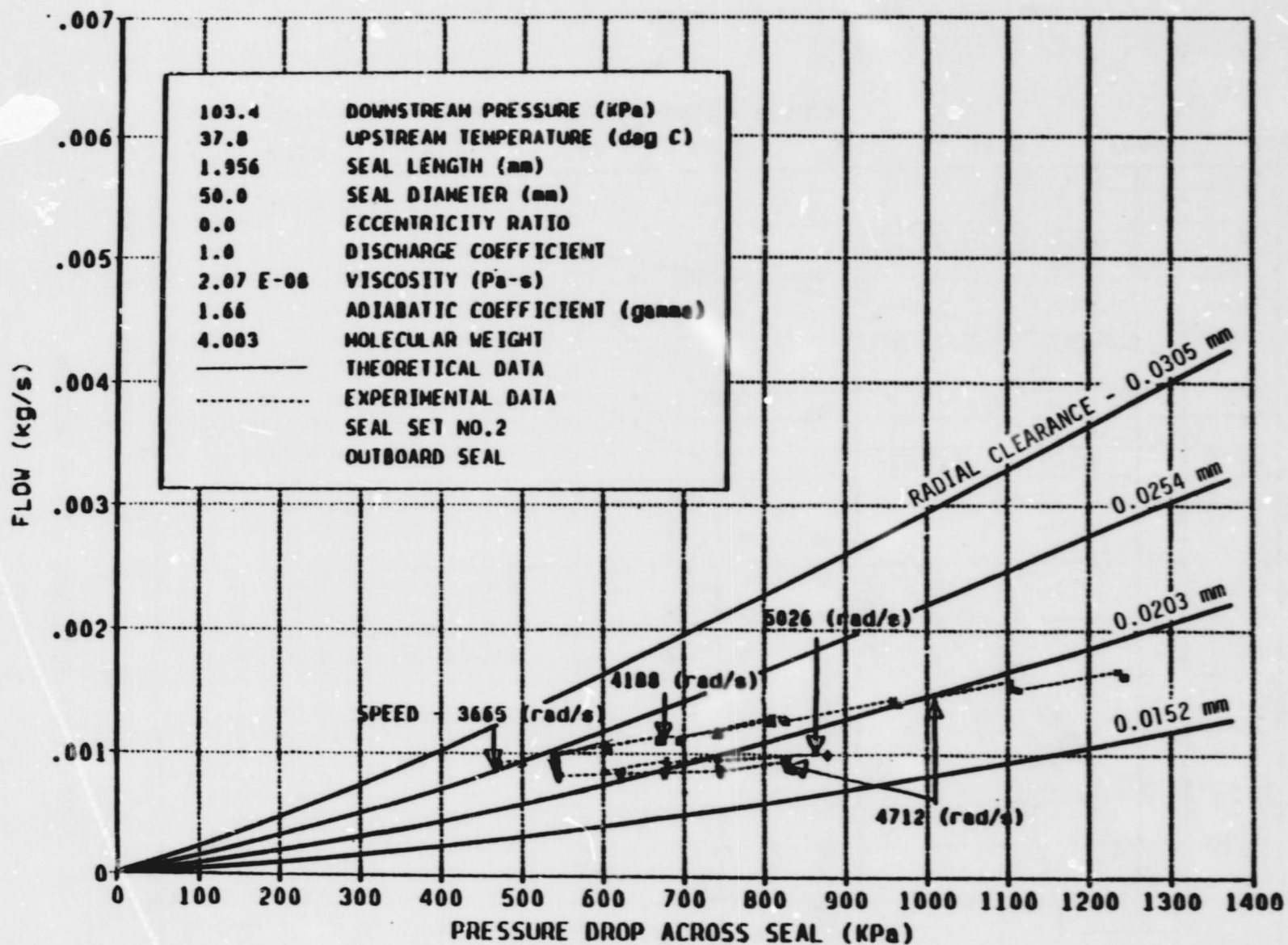


Fig. 2-5 Outboard Seal Flow, 103 kPa Drain Pressure - Seal Set No. 2

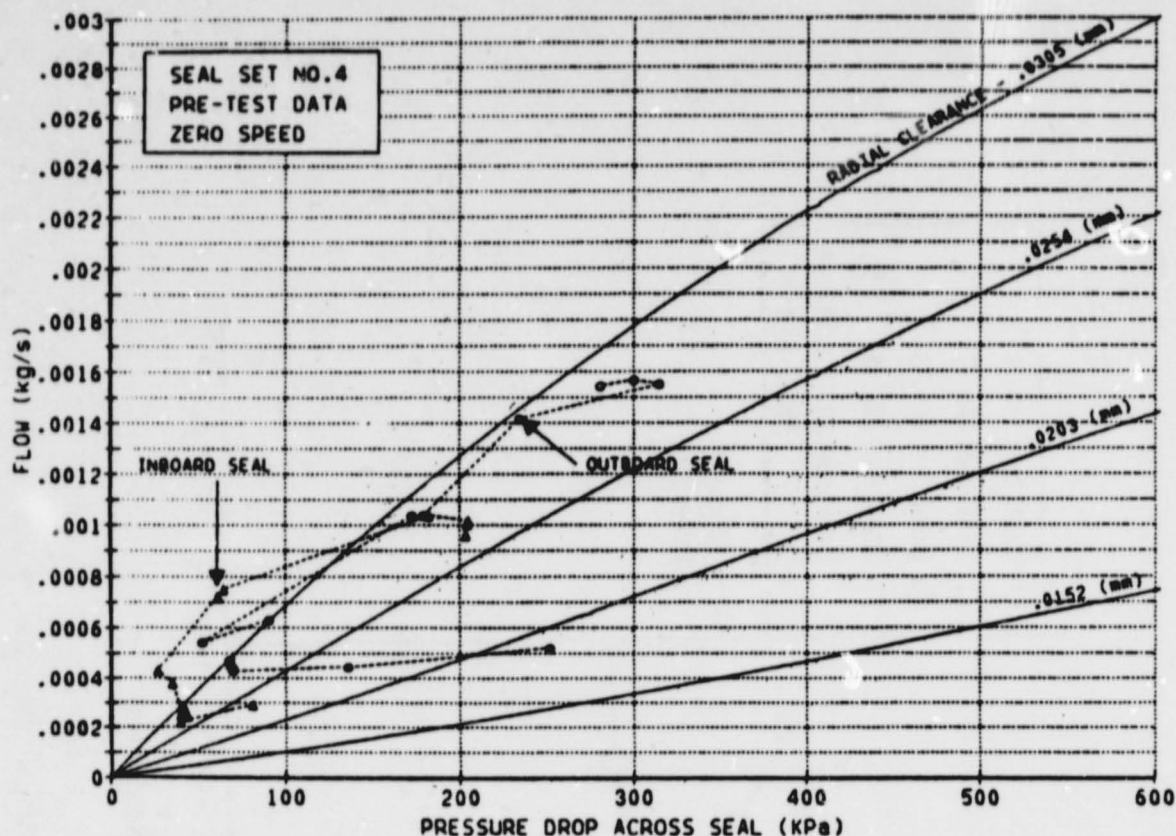


Fig. 2-6 Zero Speed versus Pressure Drop - Seal Set No. 4

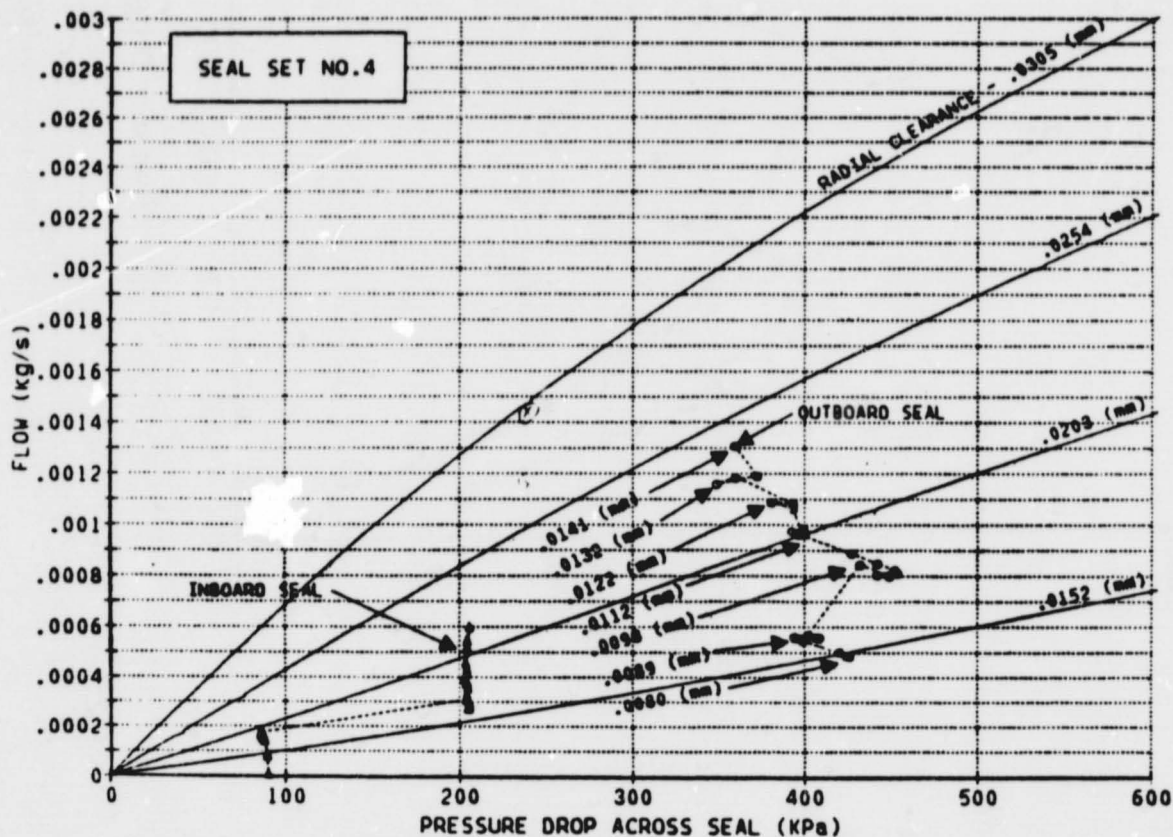


Fig. 2-7 Flow versus Pressure Drop - Seal Set No. 4

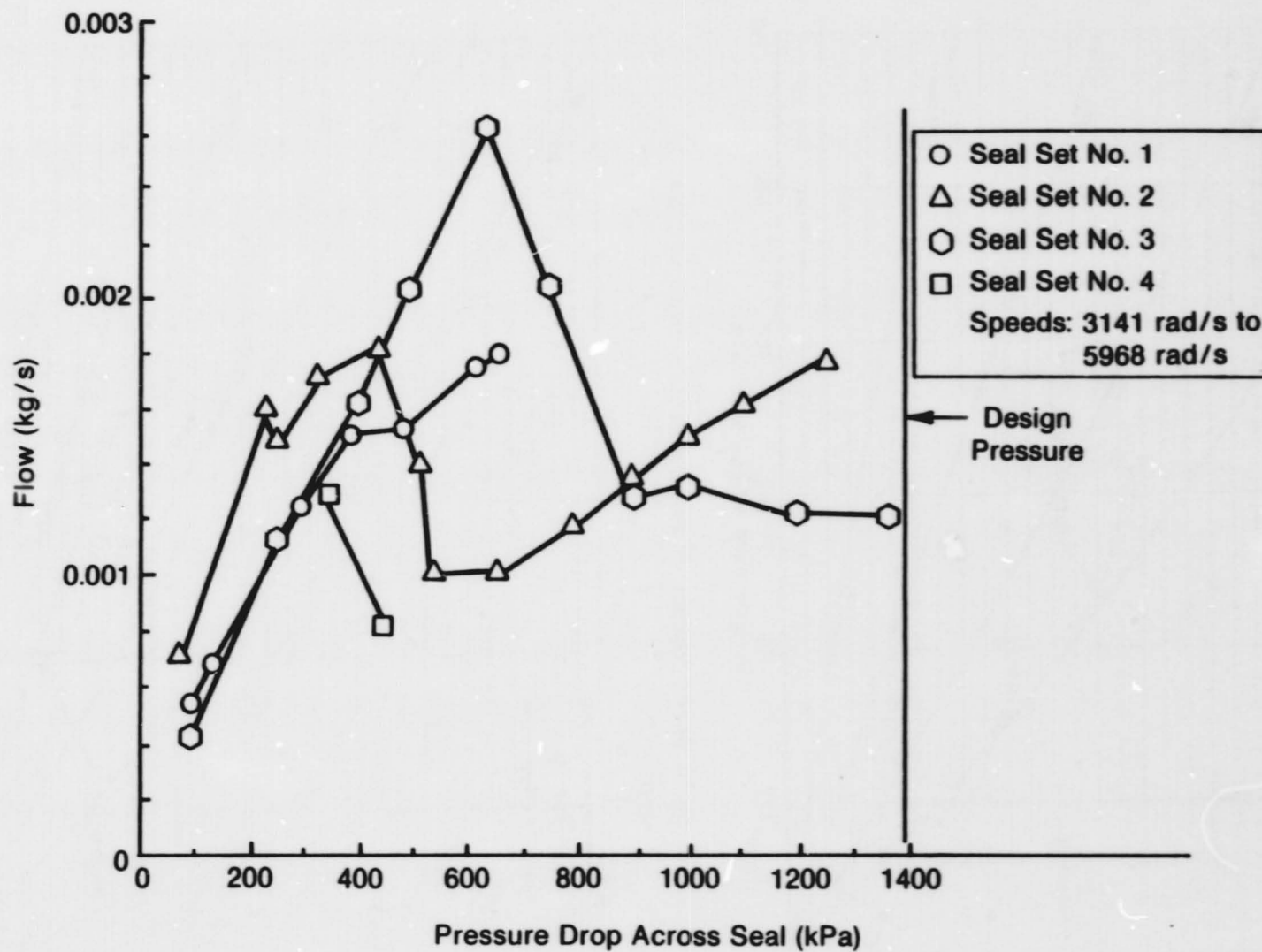


Fig. 2-8 Seal Leakage Envelope Data at Varying Speeds

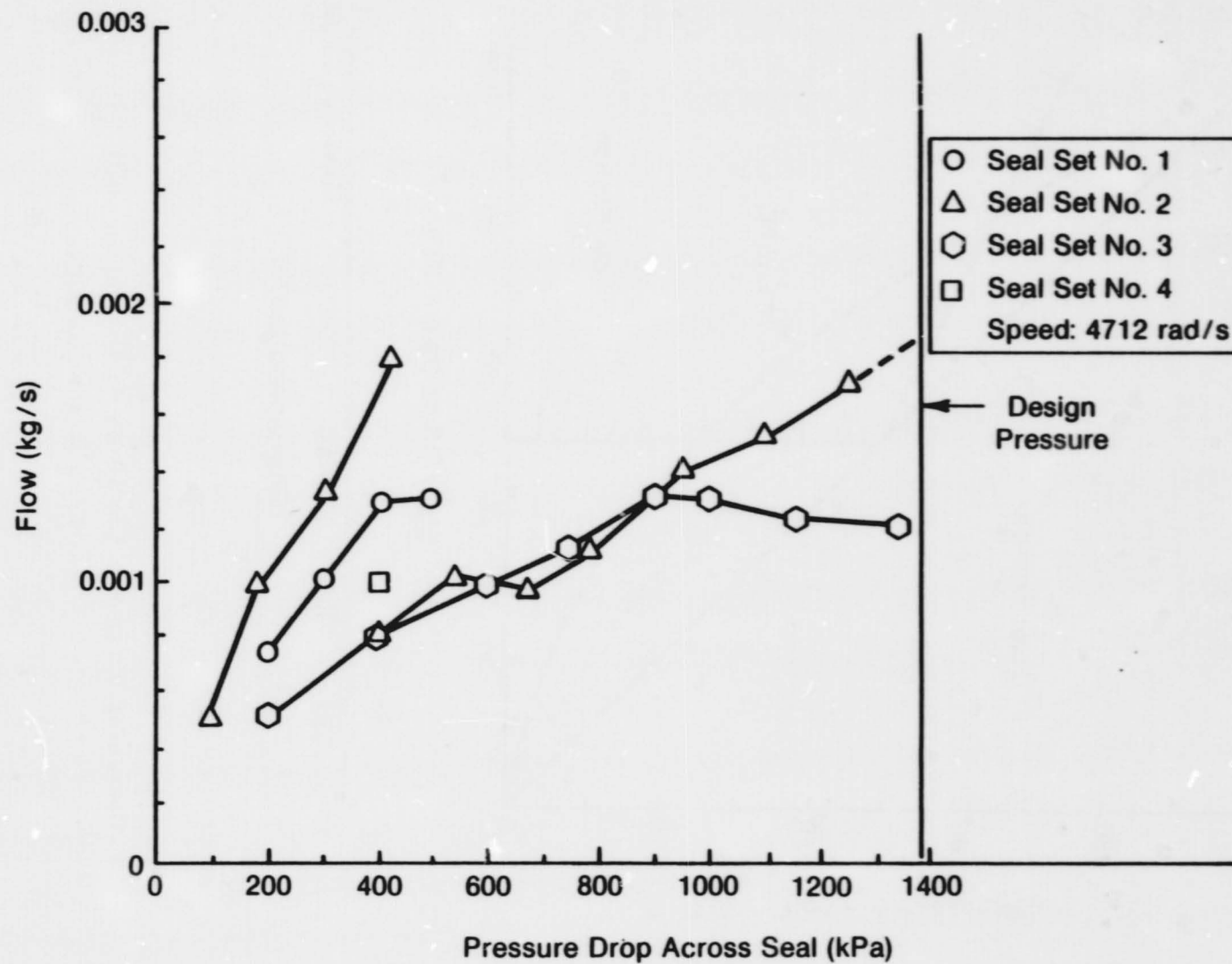


Fig. 2-9 Seal Leakage Envelope Data at Constant Speed

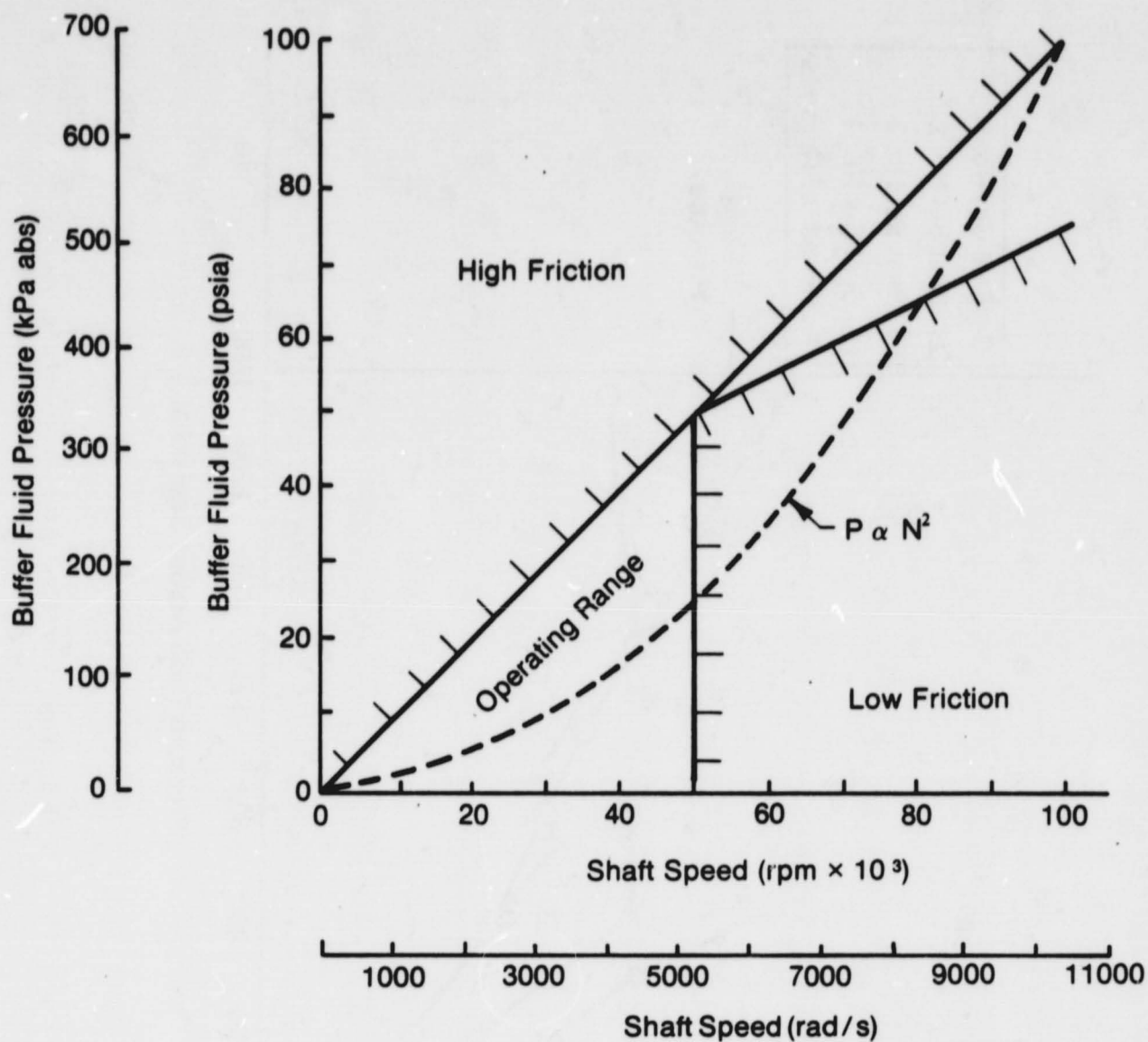
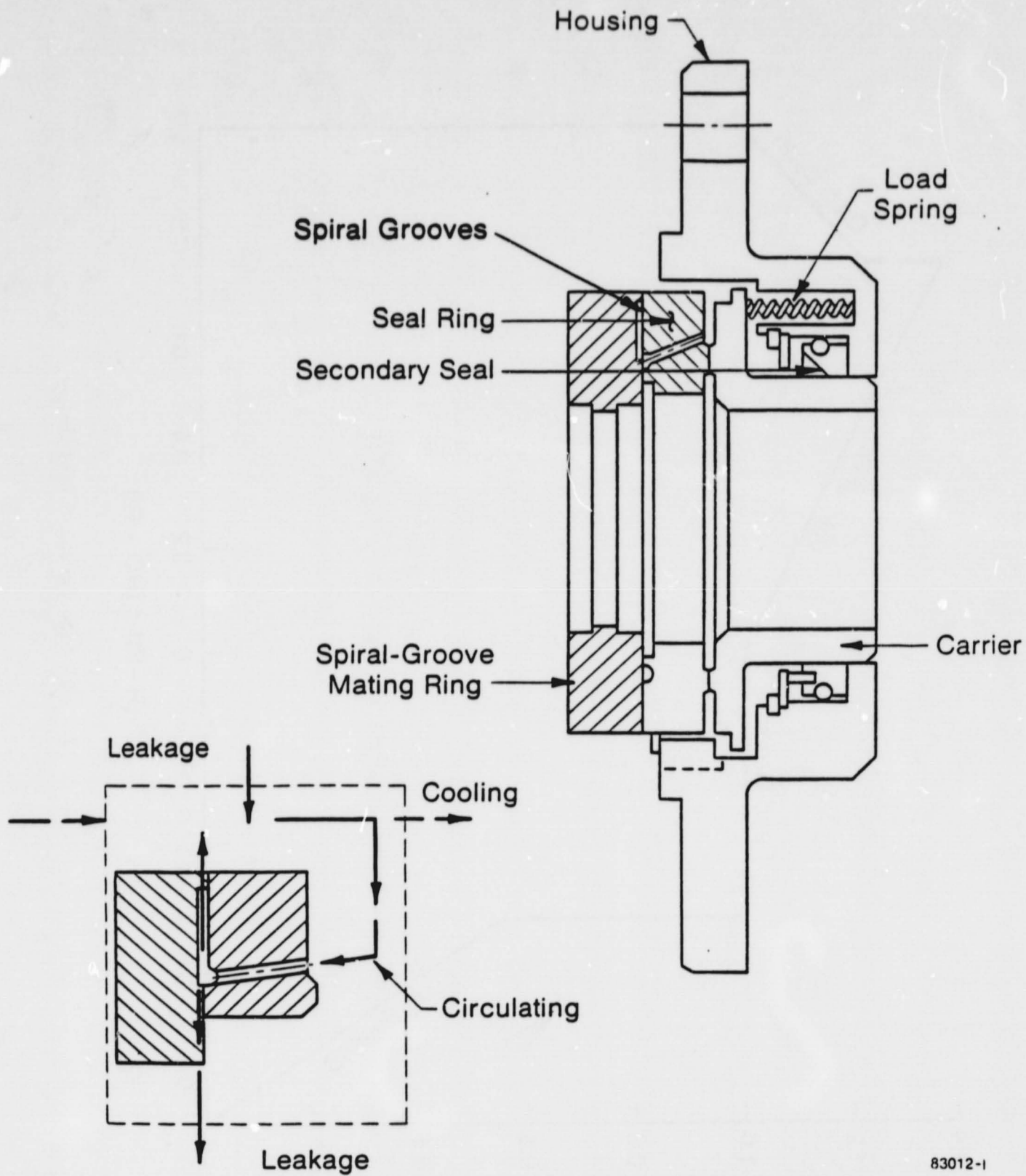
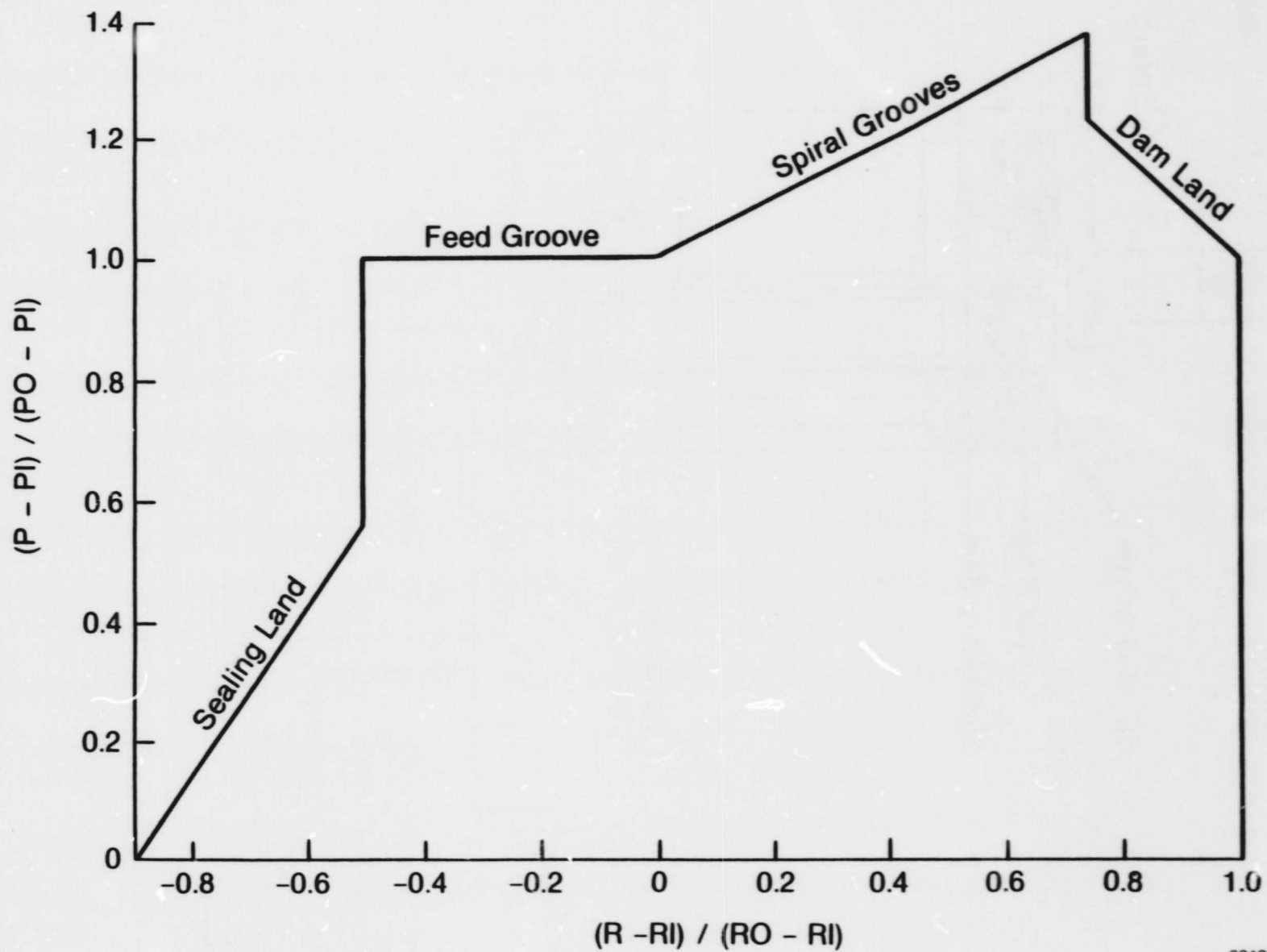


Fig. 2-10 Operating Range Map for 20-mm Helium Buffer Seal



83012-1

Fig. 2-11 Pressure-Balanced, Outward Pumping, Spiral-Groove Concept



83109

Fig. 2-12 Seal Face Pressure Profile

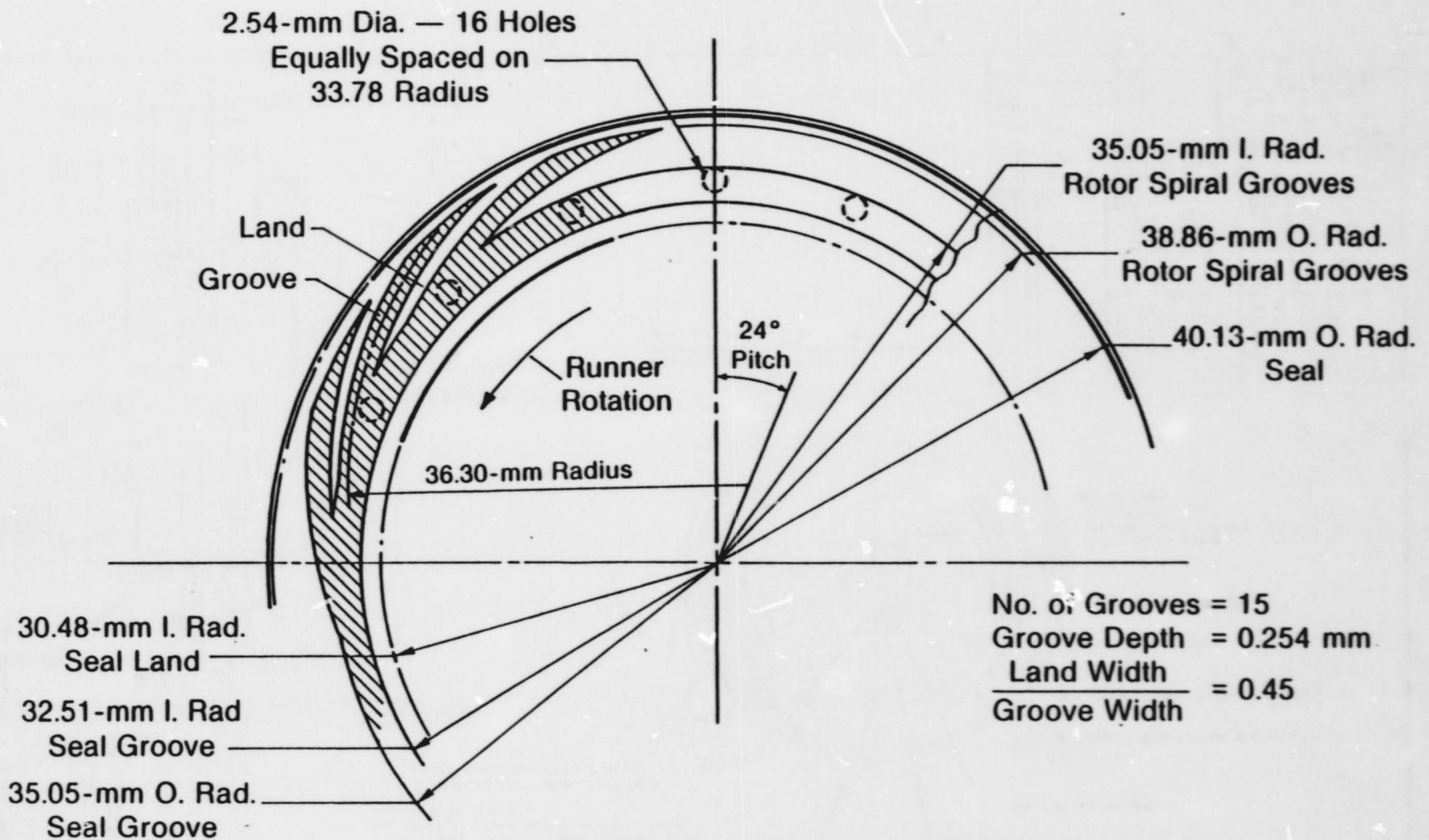


Fig. 2-13 Groove Geometry



ORIGINAL PAGE IS
OF POOR QUALITY.

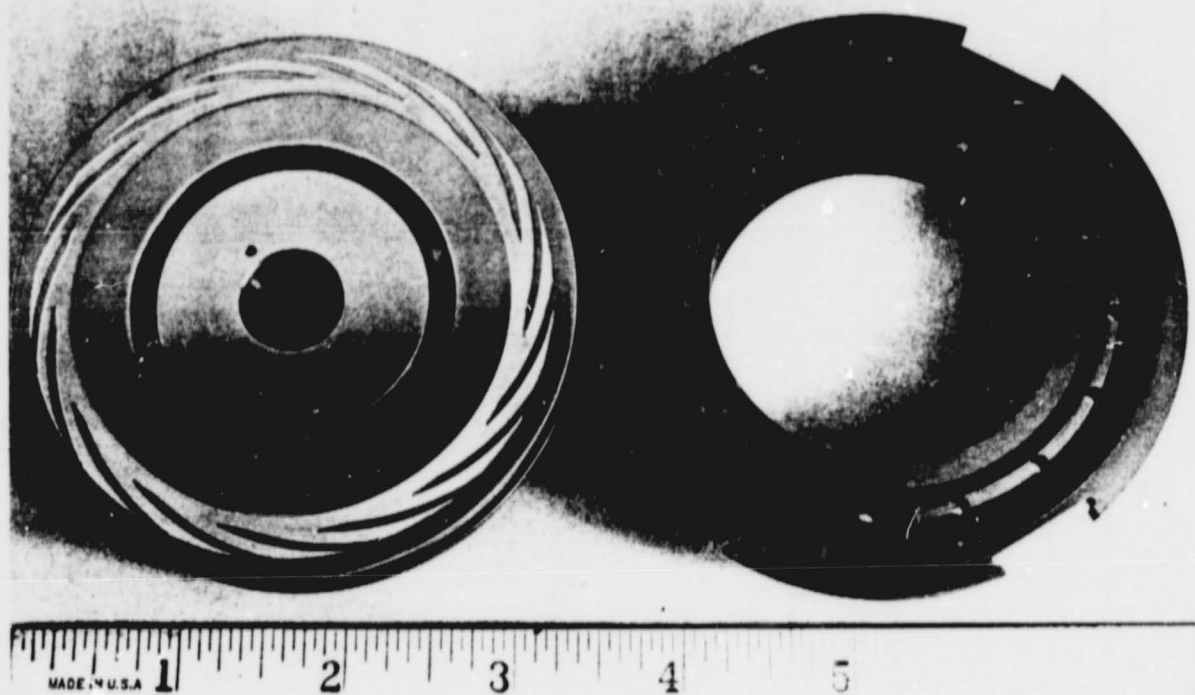
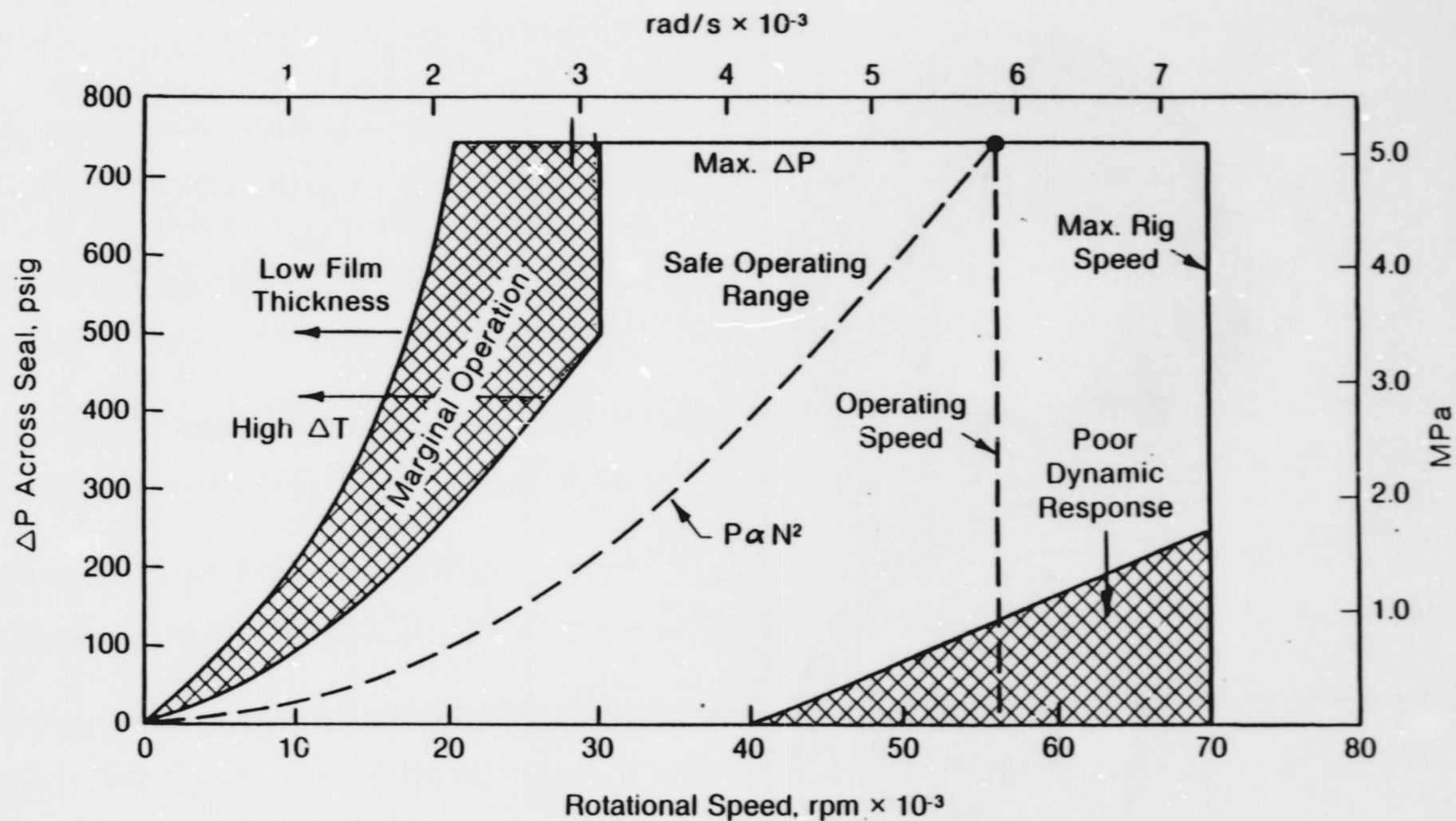


Fig. 2-15 50-mm Spiral-Groove Seal, Mating Ring, and Face Seal



83019

Fig. 2-16 Operating Range Map for 50-mm Spiral-Groove Seal

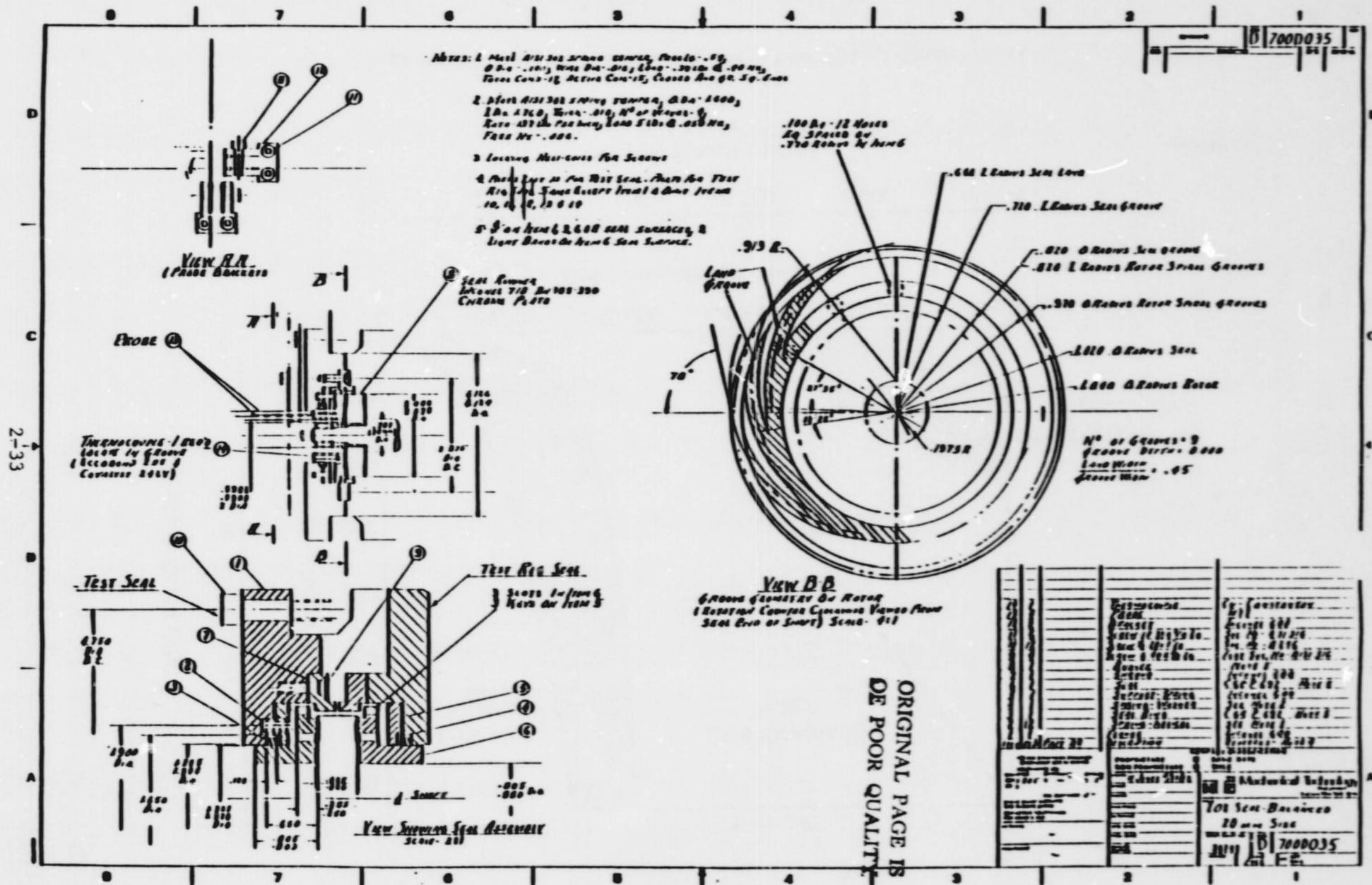
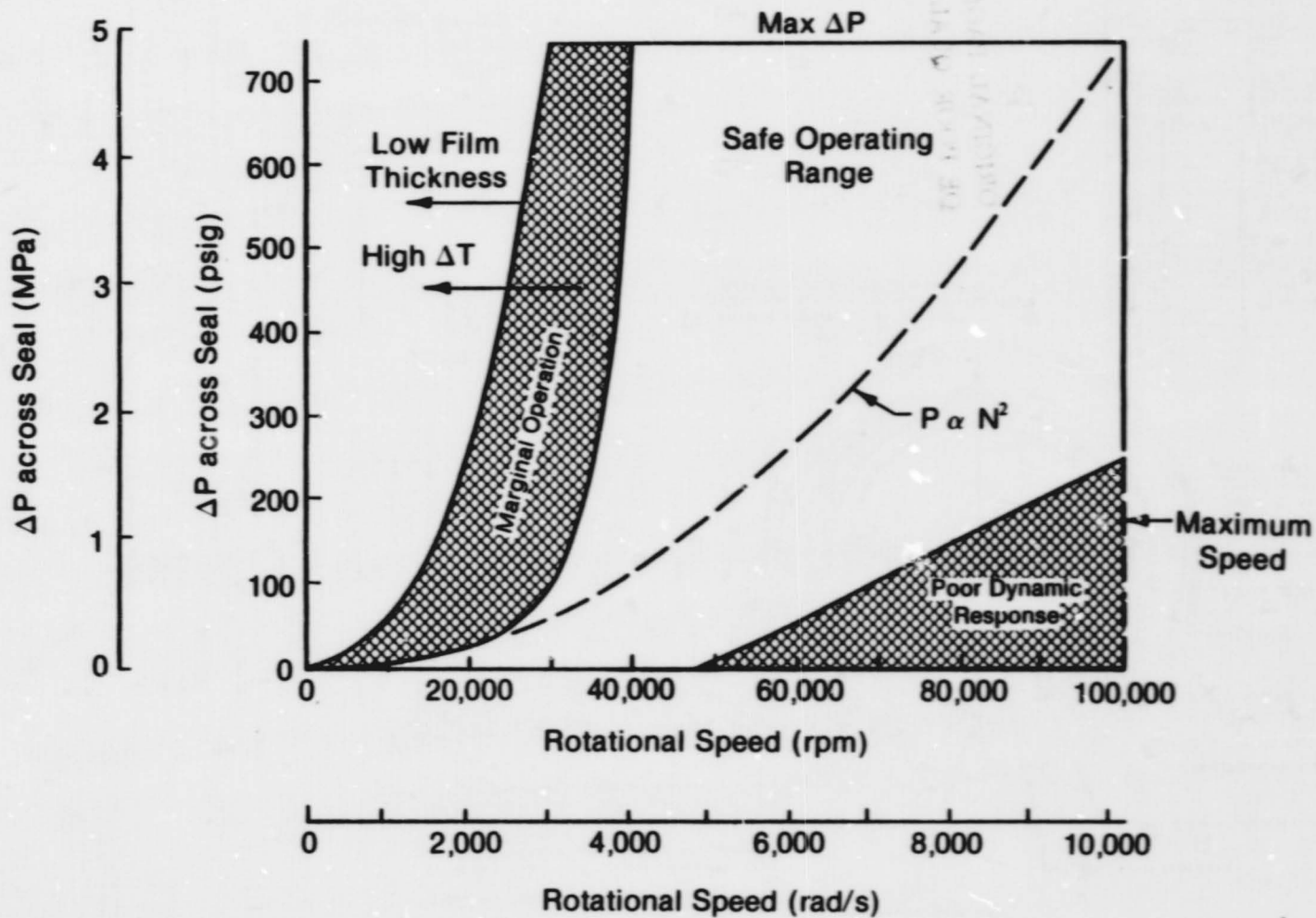


Fig. 2-17 20-mm Pressure-Balanced LOX Seal



83020-1

Fig. 2-18 Operating Range Map for 20-mm Spiral-Groove Seal

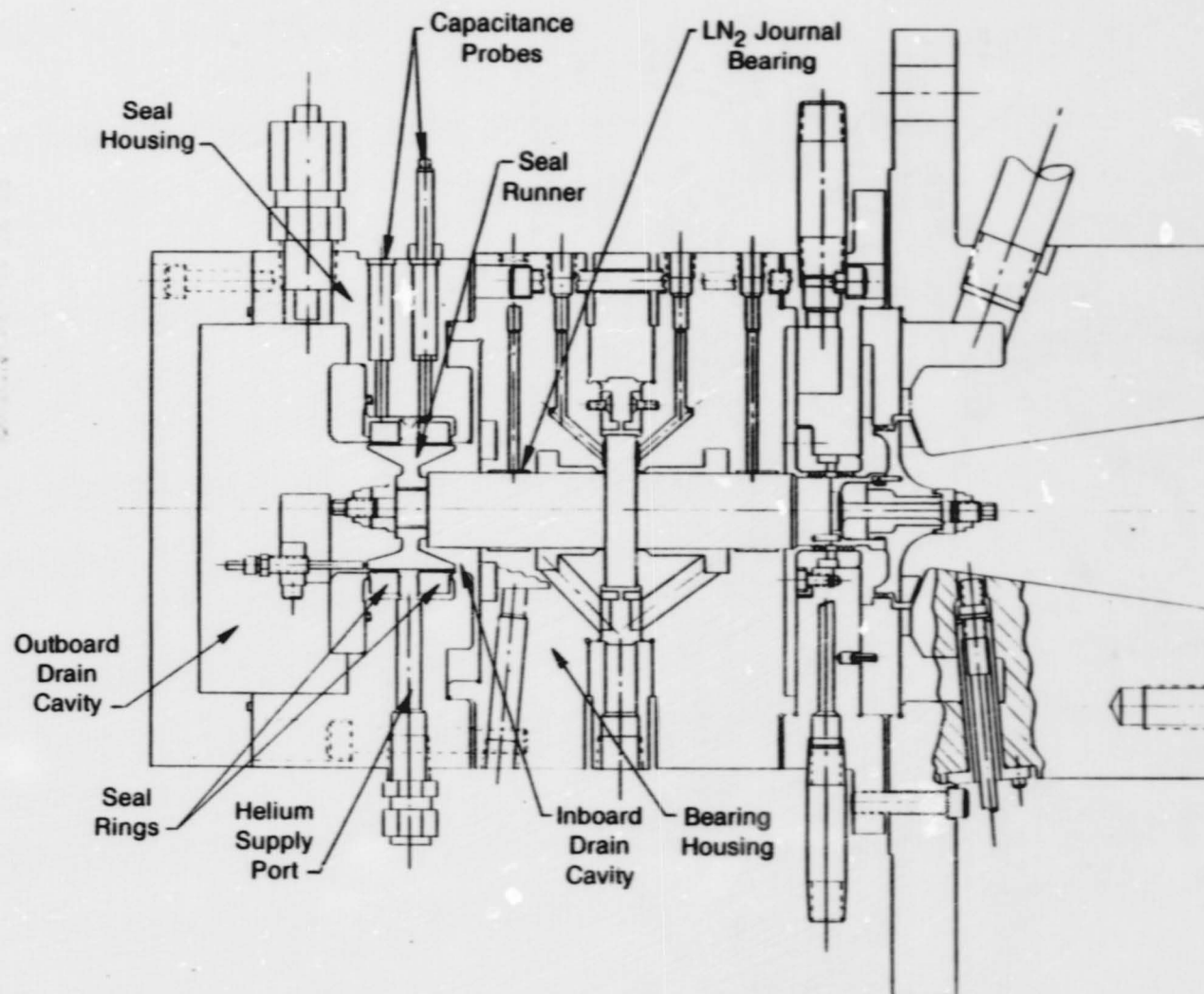


Fig. 2-19 Test Rig Cross Section

ORIGINAL PAGE IS
OF POOR QUALITY

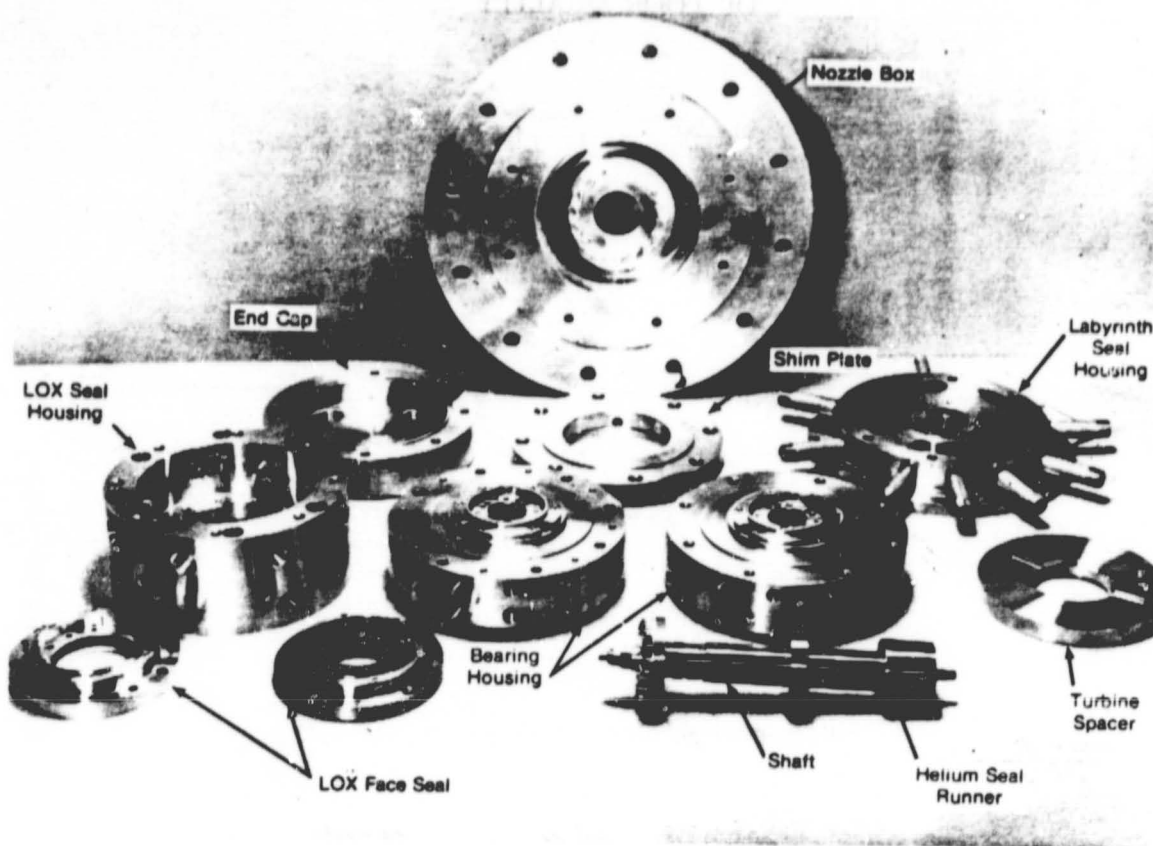


Fig. 2-20 Test Rig Components

**ORIGINAL PAGE IS
OF POOR QUALITY**

ORIGINAL PAGE IS
OF POOR QUALITY

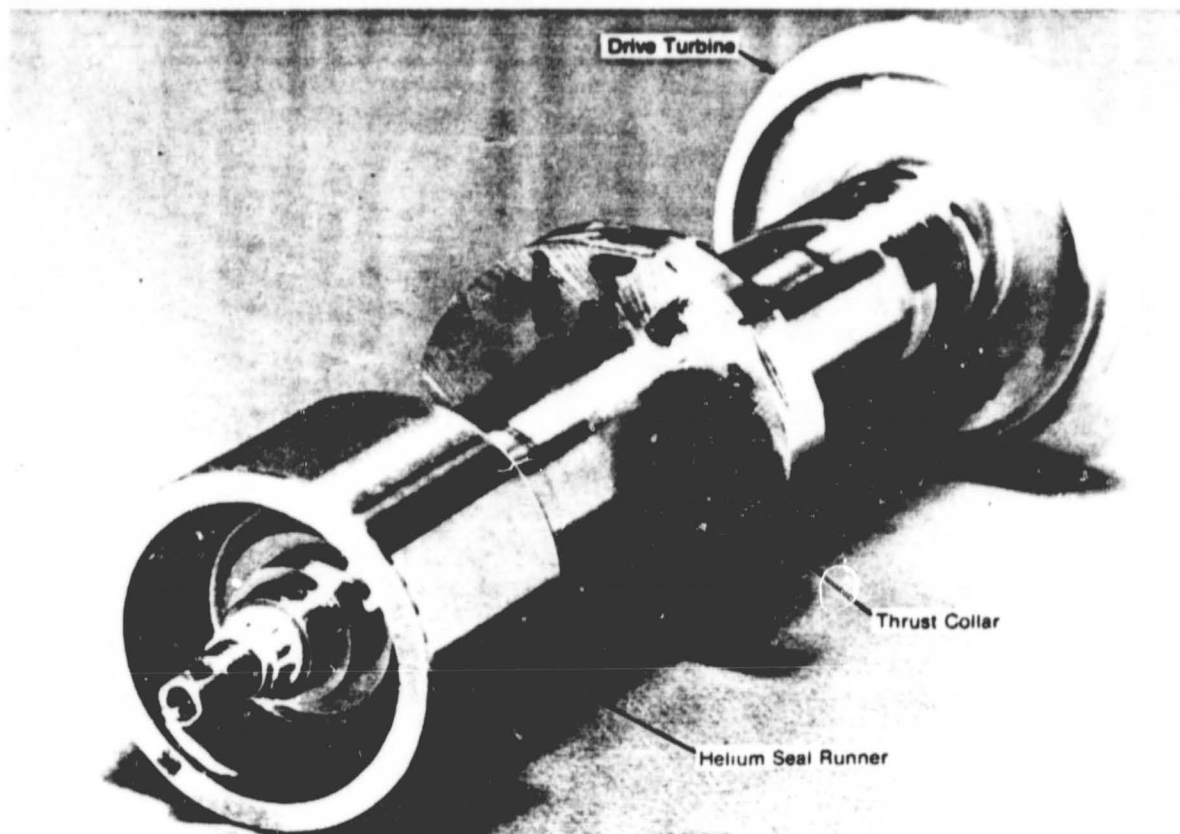


Fig. 2-21 Helium Seal Rotor

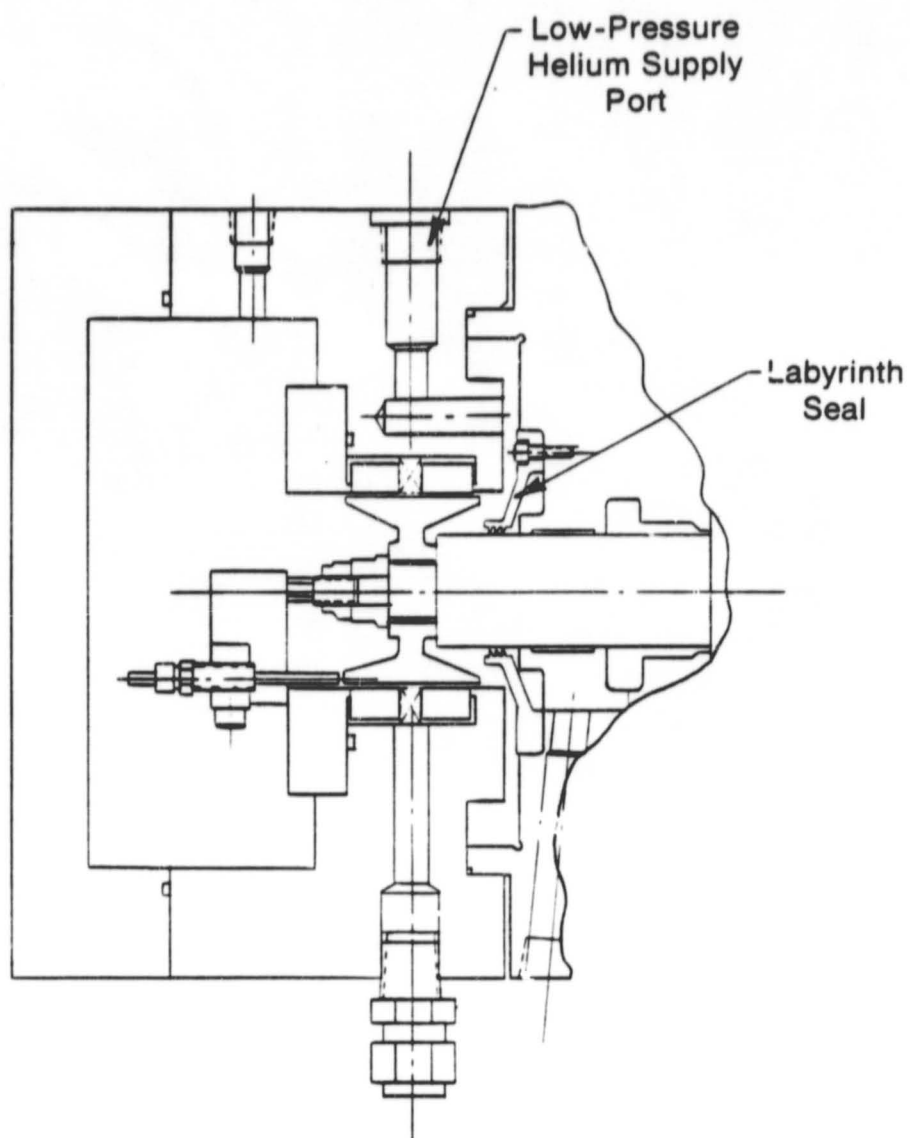


Fig. 2-32 Modified Test Rig Configuration - Seal Set No. 4

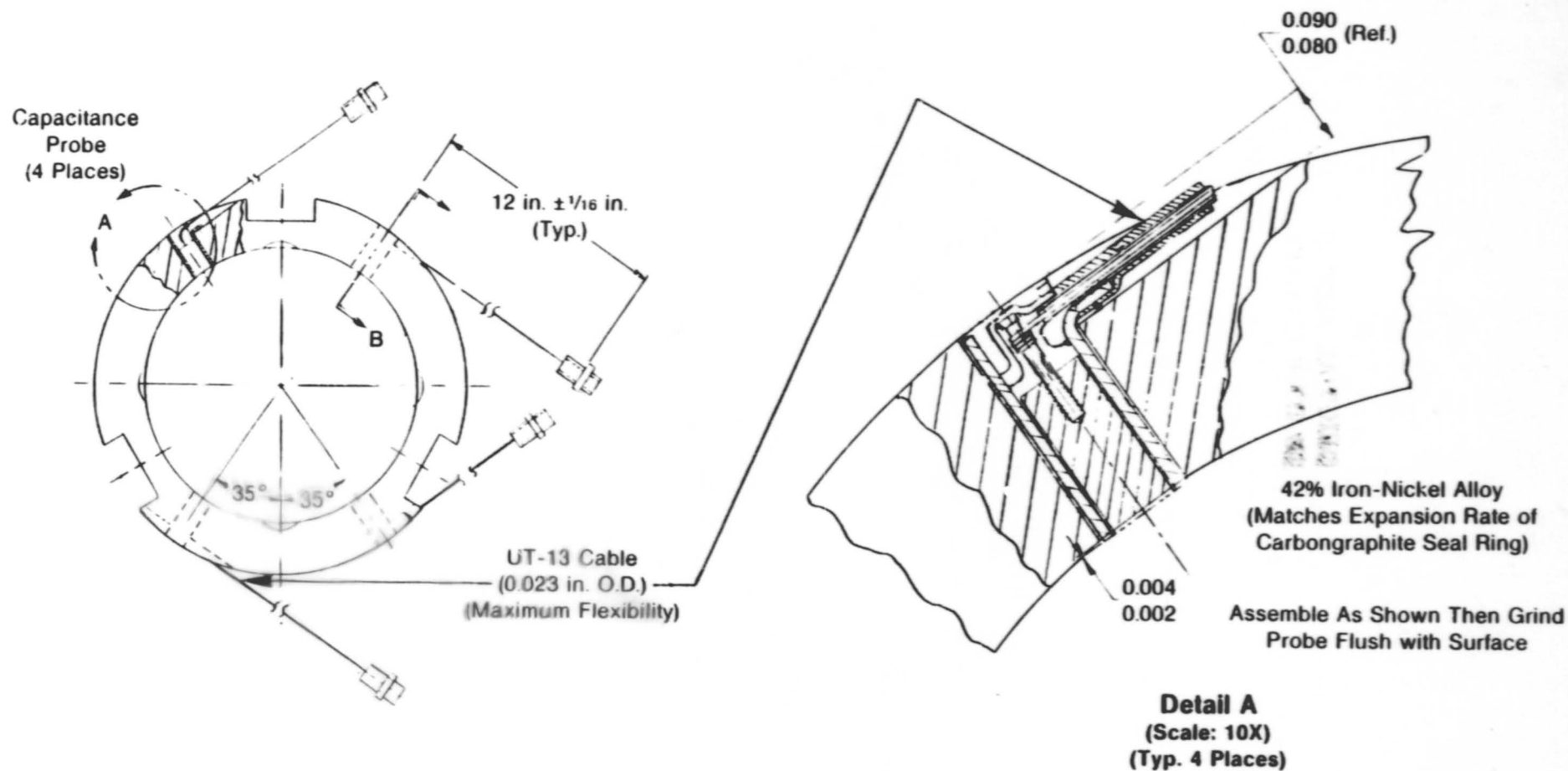


Fig. 2-23 Details of Embedded Probe Installation

ORIGINAL PAGE IS
POOR QUALITY

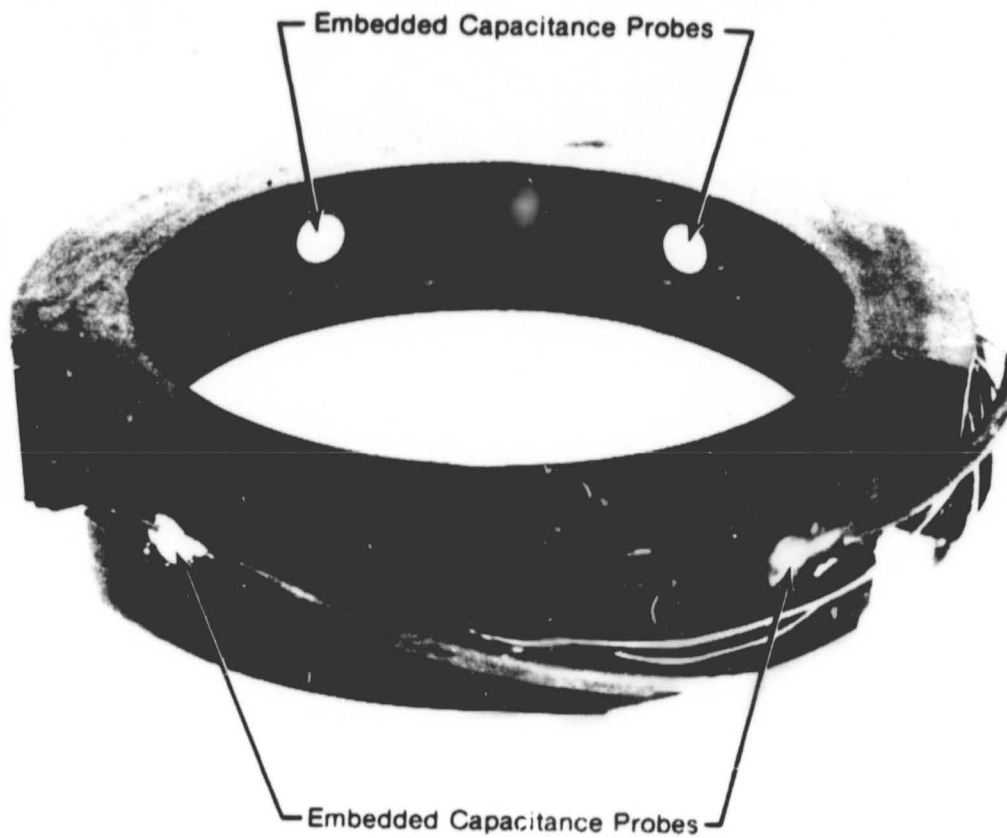


Fig. 2-24 Instrumented Seal Ring with
Embedded Capacitance Probes

TABLE 2-1

SUMMARY OF TEST RESULTS

Hardware Tested	Maximum Supply Pressure, kPa Absolute (psia)	Maximum Speed rad/s (r/min)	Cumulative Run Time (min)	No. of Fast Starts	Hardware Conditions
SEAL SET NO. 1					Outboard seal rubbed due to tester vibration.
Runner No. 1	1,179 (171)	5,895 (56,300)	96	0	Outboard seal ring worn. Runner has surface cracks.
SEAL SET NO. 2					No damage.
Runner No. 2	1,482 (215)	5,099 (48,700)	261	50	
SEAL SET NO. 3					Outboard seal rubbed due to contamination.
Runner No. 2	1,482 (215)	4,963 (47,400)	236	40	Outboard seal ring worn. Runner has surface cracks.
SEAL SET NO. 4					Inboard seal rubbed due to loss of clearance.
Runner No. 3	827 (120)	5,968 (57,000)	20	0	Inboard seal ring worn. Runner surface galled and worn.

TABLE 2-2

DIMENSIONS OF PRESSURE-BALANCED, 50-MM,
OUTWARD PUMPING, SPIRAL-GROOVE SEAL

Outside Groove Dam Radius:	40.13 mm (1.58 in.)
Inside Groove Dam Radius:	38.86 mm (1.53 in.)
Inside Groove Radius:	35.05 mm (1.38 in.)
Outside Seal Dam Radius:	32.51 mm (1.28 in.)
Inside Seal Dam Radius:	30.48 mm (1.20 in.)
Secondary Seal Radius:	30.99 mm (1.22 in.)
Inside Ring Radius:	25.4 mm (1.00 in.)
Seal Length:	20.32 mm (0.8 in.)
Secondary Seal Position (Distance from Face):	15.75 mm (0.62 in.)
Groove Depth:	0.254 mm (0.010 in.)
Groove Angle:	11°
Land Width/Groove Width:	0.45

TABLE 2-3

STEADY-STATE PERFORMANCE OF
50-MM SPIRAL-GROOVE SEAL

	Pressure Balanced <u>-Cooled-</u>	Pressure Balanced <u>Uncooled</u>
Film Thickness, mm (in.)	0.0236 (0.0009)	0.0236 (0.0009)
Axial Stiffness, N/mm x 10 ⁻³ (lb/in. x 10 ⁻³)	81.1 (463)	81.1 (463)
Leakage, m ³ /s x 10 ⁻⁵ (in. ³ /s)	29.8 (18.18)	29.8 (18.18)
Power Loss, kW (hp)	9.47 (12.69)	9.47 (12.69)
T Groove, °C (°F)	-118 (-180.4)	-104 (-155.2)
ΔT Grooves, °C (°F)	21.44 (38.6)	35.56 (64)
ΔT Seal, °C (°F)	2.83 (5.09)	17.22 (31)
Load, N (lb)	10,608 (2,385)	10,608 (2,385)
N, rad/s (r/min)	5,864 (56,000)	5,864 (56,000)

P = 5.17 MPa (750 psig)

TABLE 2-4

DIMENSIONS OF PRESSURE-BALANCED, 20-MM,
OUTWARD PUMPING, SPIRAL-GROOVE SEAL

Outside Groove Dam Radius:	25.91 mm (1.02 in.)
Inside Groove Dam Radius:	24.64 mm (0.97 in.)
Inside Groove Radius:	20.83 mm (0.82 in.)
Outside Seal Dam Radius:	18.29 mm (0.72 in.)
Inside Seal Dam Radius:	16.26 mm (0.64 in.)
Secondary Seal Radius:	17.53 mm (0.69 in.)
Inside Ring Radius:	11.18 mm (0.44 in.)
Seal Length:	20.32 mm (0.80 in.)
Secondary Seal Position (Distance from Face):	15.75 mm (0.62 in.)
Groove Depth:	0.203 mm (0.008 in.)
Groove Angle:	11°
Land Width/Groove Width:	0.45

TABLE 2-5

STEADY-STATE PERFORMANCE OF 20-MM
SPIRAL-GROOVE SEAL

	<u>Pressure Balanced Cooled</u>
Film Thickness, mm (mils)	25.9 (1.02)
Axial Stiffness, N/m x 10 ⁻⁷ (lb/in. x 10 ⁻⁵)	4.85 (2.77)
Leakage, m ³ /s x 10 ⁴ (in. ³ /s)	1.9 (11.6)
Power Loss, kW (hp)	7.1 (9.5)
ΔT Grooves, °C (°F)	25 (45)
ΔT Seal, °C (°F)	2.22 (4)
Load, N (lb)	6383 (1435)

$$P = 5.17 \text{ MPa (750 psi)}$$

$$N = 10,472 \text{ rad/s (100,000 r/min)}$$

3.0 TEST RESULTS

3.1 Introduction

Four helium seal sets and three runners were tested during the course of the program. All were subjected to steady-state tests while two sets additionally underwent high acceleration rate tests. The tests resulted in 618 min of cumulative running time and 90 high acceleration rate starts. (Refer to Table 2-1 for a brief summary of the tests performed.)

The following sections provide a detailed report of the results of the four seal tests and their correlation with theoretical predictions.

The test rig configuration for the first three seal tests followed the original design (see Figure 2-19). A 50-mm seal runner is secured to the left side of the rotor. The two seal rings fit back-to-back over the runner and are held apart by a spring. They are restrained on the right side by the seal housing and on the left side by a ring bolted to the housing. The seal rings are made of carbon graphite while the seal runner consists of Inconel 718 with a tungsten carbide coating on the outside diameter.

Helium gas is supplied through two radial ports to the annular space between the seal rings. Part of the flow passes between the runner and left seal ring (outboard) exiting into the large drain cavity on the left side of the tester and from there into a separate drain line. The remainder of the helium flow passes between the runner and the right-hand seal ring (inboard) into a chamber between the seal housing and adjacent bearing housing. From the nearby journal bearing, LN₂ also flows into the chamber and mixes with the helium. The mixture then flows through a passage under the journal bearing and out through one of several radial ports. The LN₂ has a substantial cooling effect on the end of the runner and acts to increase the operating clearance of the inboard seal.

Six capacitance probes were installed to measure the seal film thickness. Three of the probes are oriented horizontally while the other three are directed vertically. In the vertical group, two probes observe the back of the two seal rings. (Refer to Figure 2-19.) A third probe, not shown,

observes the surface of the runner between the rings. The vertical film thickness is derived by electronically subtracting the output of the respective seal probe from the common runner probe. The horizontal components are similarly measured.

Because of problems uncovered during the first three tests, three modifications were made prior to the fourth seal test. Perhaps the most significant was the addition of a small labyrinth seal between the inboard helium seal ring and the nearby journal bearing as was shown in Figure 2-22. Helium leaking from the seal and an additional flow of helium entering through a new external port were maintained at a slightly higher pressure than the bearing drain pressure. This prevented LN₂ from flowing through the new labyrinth seal and bathing the inboard end of the runner. It also was done to reduce the heat generation from windage losses that was causing vaporization in the adjacent bearing film, reducing bearing effective stiffness and damping and resulting in unacceptable rotor response. The insertion of the labyrinth seal insured that only gaseous helium would contact the seal runner with significantly lower windage losses than that produced by LN₂.

In place of the six-probe differential array, an outboard seal ring containing four embedded probes was installed permitting a direct measurement of film thickness during the fourth test. Figure 2-23 showed the instrumented ring. The two original probes observing the seal runner were kept and used to monitor runner motion. The embedded probes were not subject to error due to thermal distortions of the seal housings.

A final change consisted of a new runner with an electrolyzed surface to replace the tungsten carbide coating used in the original design. The rubs which occurred during the first and third seal tests resulted in partial delamination of the coating which contributed to the failures. It was hoped the electrolyzed runner would provide a better surface in the event of a rub.

The pretest seal clearances are given in Table 3-1*. The overall accuracy of the measurements is approximately ± 0.005 mm (± 0.0002 in.). For the most part,

*Tables are presented consecutively, beginning on page 3-44.

the pretest clearances of the first three seal sets conform to the design requirements. The maximum discrepancy, found on the No. 1 outboard seal, was 0.002 mm (0.00008 in.), certainly within the range of measurement accuracy. The pretest clearances for the fourth seal set are slightly larger than the original design requirements. This was considered desirable because of the higher runner temperatures that were expected due to the installation of the new labyrinth seal.

3.2 Steady-State Test Results

3.2.1 Seal Set No. 1

Principal data was taken during three runs conducted over an 82-min period. Figures 3-1* and 3-2 provide time history plots of the test showing tester speed and helium supply pressure. Figure 3-3 gives an operating map with the actual test points superimposed. Three additional starts were made which are not documented in the figures. The total cumulative running time was 96 min.

Prior to rig rotation, helium pressures ranging from 662 to 1827 kPa absolute (96 to 265 psia) were applied to check the integrity of the seal installations and provide zero speed data.

During operation, steady-state data were sequentially taken at 3665 rad/s (35,000 r/min), 4188 rad/s (40,000 r/min), 4712 rad/s (45,000 r/min), and 5235 rad/s (50,000 r/min) with helium supply pressures ranging from approximately 552 to 1172 kPa absolute (80 to 170 psia). Drain pressures downstream of both seals were maintained between 448 to 552 kPa absolute (65 to 80 psia). The helium supply temperature varied between 38 and 43°C (100 and 110°F).

As indicated on Figure 3-3, virtually all of the test points were in the high friction region of the operating map. At lower speeds of 3665 rad/s (35,000 r/min) and 4188 rad/s (45,000 r/min), this was necessary to maintain a positive pressure drop across the seals. At the higher speeds of 4712 to

*Figures are presented consecutively, beginning on page 3-48.

5759 rad/s (45,000 to 55,000 r/min), proportionally higher pressures were maintained in an effort to add damping to the rotor system to combat the vibration problem.

Despite these attempts, vibrations were encountered at approximately 5235 rad/s (50,000 r/min) and became worse as speed increased to 5759 rad/s (55,000 r/min). While several data points were taken at the latter speed, the tester was tripped out when the outboard seal temperature abruptly increased signifying a rub. Figure 3-4 is a strip chart recording of the temperature excursion. A torque check revealed that the shaft was tight. Consequently, no additional running was attempted. An analysis of the failed hardware is given in Section 3.5.1.

In general, the facility and instrumentation worked well; however, several problems did develop. The two capacitance probes observing the seal runner rubbed briefly and shorted out due to rotor vibration and a greater than anticipated loss of gap during initial chill-down. The failures occurred shortly after the first start. Consequently, no usable probe data was logged. Secondly, the Venturi flowmeter, set to measure the leakage from the outboard seal was sized anticipating larger flows and resulted in pressure drops too low to measure. Both problems were corrected before the second seal test.

Figure 3-5 shows both measured and predicted flow as a function of pressure drop across a single seal ring. The data is for the zero speed case with the tester chilled down. The theoretical predictions are based on the latest model incorporating both viscous and inertial pressure drops. (See Appendix A.) The four theoretical curves cover the range of anticipated radial clearances and were calculated using the data given in the block insert in the figure. Because of the flowmeter problem, the flow through the individual seal could not be separated. The experimental flow plotted equals one-half the total measured supply flow. The data in the block insert also applies to the experimental flow curve except for the eccentricity ratio and discharge coefficient which could not be measured.

Because the film thickness was not measured, no correlation between measured flow and clearance was possible. However, correlating the measured flow with the theoretical flows showed that the experimental data follows the predicted curve for a radial film thickness of 0.020 mm (0.0008 in.) at low flows and 0.023 mm (0.0009 in.) at higher flow conditions. Given the room temperature clearances of 0.015 mm (0.0006 in.) for the outboard seal and 0.008 mm (0.0003 in.) for the inboard seal, the measured flow seems reasonable.

Figure 3-6 shows the surface temperature of the seal rings during the same test. The temperatures increase between 65 and 85°C and (117 and 153°F) from low flow to high flow conditions. This demonstrates the strong warming effect that the helium flow has on the seal rings. It is somewhat surprising that the inboard ring registers slightly higher temperatures than the outboard ring.

Figure 3-7 contains a series of experimental flow curves at different tester speeds. Again, these represent one half the total measured flow. Theoretical curves are also depicted covering four seal clearances. The maximum flow rate occurred at 5759 rad/s (55,000 r/min) at a pressure drop of approximately 650 kPa (94 psi) and is equal to 0.0017 kg/s (21 scfm).

The experimental curves show a definite decrease in flow as speed is increased. This is probably due to a decrease in clearance caused by centrifugal and thermal growth of the runner. The anticipated decrease in clearance due to centrifugal runner growth is about 0.001 mm (0.00004 in.) for each speed increment of 524 rad/s (5000 r/min). Thus, if the flow at 3665 rad/s (35,000 r/min) corresponds to a clearance of 0.026 mm (0.00106 in.), the curve at 5235 rad/s (50,000 r/min) should match up with a curve at 0.023 mm (0.0009 in.). The actual data at 5235 rad/s (50,000 r/min) follows a clearance line of 0.021 mm (0.00083 in.), indicating a slightly greater than expected clearance decrease. Also, the data at 5759 rad/s (55,000 r/min) does not follow the trend at all.

Figures 3-8 and 3-9 present the corresponding seal ring temperatures for the inboard and outboard seal rings respectively. Again, there is a very significant warming effect as flow increases at higher pressures. It is also readily apparent that the rate of change of temperature with pressure is much

higher at lower flows and tends to level off at higher rates. At constant pressure, both figures tend to show slight decreases in temperature as speed is increased. This goes along with the decreased clearance, and thus decreased flow, due to centrifugal and thermal growth of the runner. The data at 5759 rad/s (55,000 r/min) deviates from the trend.

Figure 3-10 compares inboard and outboard seal temperatures at 4188 rad/s (40,000 r/min) and shows that the inboard tends to be about 5 to 10°C (9 to 18°F) colder than the outboard at constant pressure. This is also typical of the data at other speeds.

Since neither the individual seal flow rates nor the actual operating clearances were measured for seal set No. 1, it was difficult to make any more definitive correlation.

3.2.2 Seal Set No. 2

Figures 3-11 through 3-16 give a time history covering the three days over which the seals were tested. The curves depict tester speed and helium supply pressure. Figure 3-17 provides an operating map covering the entire test. As mentioned in Section 2.0, the seal principally operated in the high friction range.

Steady-state data were accrued over five runs resulting in data at 3665 rad/s (35,000 r/min), 4188 rad/s (40,000 r/min), 4712 rad/s (45,000 r/min), and 5026 rad/s (48,000 r/min). Speed was limited to 5026 rad/s (48,000 r/min) due to sharply increasing rotor vibrations. Seal set No. 2 completed all subjected tests without evidence of failure of any kind.

The first four runs covered a range of supply pressures from 586 to 1069 kPa absolute (85 to 155 psia). The fifth run conducted after a series of high acceleration rate runs included additional data points at 4712 rad/s (45,000 r/min) and reached a helium supply pressure of 1482 kPa absolute (215 psia).

In addition to varying the helium supply pressure at each speed, the outboard seal drain pressure was also varied including values of 517, 310, and 103 kPa absolute (75, 45, and 15 psia). The inboard drain pressure was maintained between 517 and 551 kPa absolute (75 and 80 psia). The upstream helium supply temperature was between 38 and 43°C (100 and 110°F).

A zero speed run was also made varying helium supply pressures from 648 to 1820 kPa absolute (94 to 264 psia). Both seal drain pressures were maintained at approximately 517 kPa absolute (75 psia) during this particular test.

Not counting the high acceleration rate runs which are discussed in Section 3.5, a total of eight runs were made resulting in a total accumulated test time of 261 min. No problems were encountered and the seals were removed intact and undamaged. Also, no problems developed in the instrumentation which yielded good supply and drain flow data. While the capacitance probes functioned properly, later analyses revealed potential inaccuracies in the readings due to thermal distortions of the seal housing.

Zero speed flows are given for the inboard and outboard seals in Figures 3-18 and 3-19, respectively. Both predicted and measured data are given. The total flow through the seals is approximately 0.0068 kg/s (85 scfm) at a pressure drop of 1250 to 1300 kPa (181 to 189 psi). This is slightly less than the 0.0077 kg/s (97 scfm) passed by seal set No. 1 at the same pressure. However, seal set No. 2 has slightly lower clearances (see Table 3-1).

The flow from the inboard seal dominates by a factor of two to one and closely follows the predicted flow curve corresponding to radial clearances of 0.024 to 0.027 mm (0.0009 to 0.0011 in.). This represents an increase in clearance of 0.018 mm (0.0007 in.) from ambient to test conditions due to contraction of the runner from LN₂ at the inboard end. The outboard seal flow runs along the 0.020 mm (0.0008 in.) predicted flow curve at lower pressures and falls to 0.017 mm (0.0007 in.) at higher pressures. It shows a more modest clearance increase of 0.007 to 0.010 mm (0.0003 to 0.0004 in.) from ambient to test conditions.

Figure 3-20 shows the seal surface temperatures for the zero speed test. As in the previous test, a substantial temperature increase is registered as the pressure drop is increased. Although of a slightly lower magnitude, 40 to 50°C (72 to 90°F), as opposed to the 65 to 85°C (117 to 153°F) in seal set No. 1, the inboard seal again shows the higher temperature. The reason in this case is the larger flow passed by the inboard seal. This may also be the case with seal set No. 1.

The flow curves for the inboard seal at the different test speeds are given in Figure 3-21. The first four runs comprise the data at 3665, 4186, 5026 rad/s (35,000, 40,000, 48,000 r/min), and the lower pressure data at 4712 rad/s (45,000 r/min). These runs produced the maximum flow rate of 0.0018 kg/s (23 scfm) at a pressure drop of approximately 430 kPa (62 psi) and show the expected trend of decreasing clearance as speed increases. Again, the magnitude of the decrease is more than can be explained by centrifugal growth alone. The actual decrease between 3665 and 5026 rad/s (35,000 and 48,000 r/min) appears to be approximately 0.010 mm (0.0004 in.) while the predicted amount is 0.0025 mm (0.0001 in.). Clearly, additional effects (thermal growths) are taking place.

A fifth run was made at a speed of 4712 rad/s (45,000 r/min) during which a pressure drop of 940 kPa (136 psi) was applied to the seals. Given the prevailing drain pressure of 544 kPa absolute (79 psia), the absolute pressure slightly exceeded the design point of 1379 kPa absolute (200 psia). The resulting flows are much lower and bear little correspondence with the first four runs.

Figure 3-22 presents the inboard seal temperature variations corresponding to the flow curves in Figure 3-21. A high temperature gradient with pressure drop exists at low pressures that gradually decrease as pressure increases. However, no clear-cut trend exists among the first four runs at different speeds. The high-pressure run at 4712 rad/s (45,000 r/min) shows quite a bit lower temperature than the earlier run at the same speed.

Outboard seal leakage flows are plotted in Figures 3-23, 3-24, and 3-25. Four speeds are represented in each figure with two runs at different pressure

ranges at 4712 rad/s (45,000 r/min). Figure 3-23 corresponds to an outboard drain pressure of 517 kPa absolute (75 psia). Figure 3-24 corresponds to a drain pressure of 310 kPa absolute (45 psia) and Figure 2-5 to a drain pressure of 103 kPa absolute (15 psia). The results here are quite different than those shown for the inboard seal and yield the following observations:

1. The flows are lower than those of the inboard seal indicating smaller clearances.
2. The flows increase only slightly with pressure. This indicates that the clearances are closing as the supply pressure increases.
3. There is no discernable trend among flow lines at different speeds. The loss of clearance due to centrifugal growth is most likely overshadowed by the flow-related temperature effects.

Outboard seal temperature plots are given in Figures 3-25, 3-26, and 3-27 corresponding to the data given in the flow plots. Previously established trends continue to prevail with higher temperatures, lower gradients at higher pressure drops, and the lack of a definite trend as speed is increased.

Figure 3-28 is a plot of the outboard seal temperature and flow during the first run at 41887 rad/s (40,000 r/min) at each of the three drain pressures versus pressure drop across the seal. Figure 3-29 plots the same temperature versus the supply pressure. Referring to Figure 3-28, the flow follows a straight line as a function of pressure drop across the seal and appears to be independent of drain pressure. The corresponding seal temperatures, on the other hand, all cover about the same range of -40 to -25°C (-40 to -15°F) and seem to be independent of the increased pressure drop permitted by the incremented decreases in drain pressure. Figure 3-29 shows a different relationship. The flow curves appear as parallel lines as expected. The temperature curves are much more closely grouped together and, in fact, coincide at -34°C (-30°F) indicating that the outboard seal temperatures have a stronger dependency on the total seal supply pressure than the pressure drop across the outboard seal. This tends to indicate a strong thermal interaction between the outboard seal and the inboard seal with the larger, more dominant flow.

Figures 3-30, 3-31, and 3-32 are plots of seal film thickness versus time for the five test runs being analyzed. As mentioned previously, evidence of substantial thermal distortion of the seal housing was observed during the chill-down process which appears to have caused inaccuracies in the absolute measurement of the film thickness. This is particularly evident in the vertical outboard seal curve which shows nearly three times the expected film thickness.

3.2.3 Seal Set No. 3

Figures 3-33 and 3-34 give time history plots of supply pressure and test rig speed, while Figure 3-35 gives an operating map. Principal data was acquired during three runs taken over a 240-min period. Two additional starts were made. The total cumulative running time was 236 min.

Steady-state data were taken at 3665, 4188, and 4712 rad/s (35,000, 40,000, and 45,000 r/min). Attempts were again made to reach higher speeds but vibrations were encountered at approximately 5026 rad/s (48,000 r/min). It was decided to limit operation to 4712 rad/s (45,000 r/min).

A broad range of supply pressures were achieved from 654 to 1482 kPa absolute (95 to 215 psia). Outboard seal drain pressures were incremented at each speed covering values of 517, 310, and 103 kPa absolute (75, 45, and 15 psia). No zero speed data was taken with this seal set.

The steady-state tests were completed without problems and were followed by high acceleration rate tests. After 40 fast starts and during a short steady-state run to check operation, a rub was encountered on the outboard seal. Figure 3-36 shows the strip chart data documenting the increase in seal ring temperature and the subsequent shutdown. Two attempts to restart resulted in immediate increases in temperature indicating that significant damage had taken place during the first occurrence. The rig was then torn down and inspected. A fair amount of contamination had entered the supply cavity and probably initiated the rub. Subsection 3.6 provides additional details of the inspection and an analysis of the failed parts.

Figure 3-37 provides the inboard seal flow data at the three test speeds; predicted flows are superimposed. The maximum flow is approximately 0.0026 kg/s (33 scfm) and occurred at 3665 rad/s (35,000 r/min) at a pressure drop of 630 kPa (92 psi). The measured flows show a decrease with speed, although the amount is more than expected based on centrifugal growth of the runner.

Figure 3-38 shows the corresponding inboard seal temperatures. The data shows a definite decrease in temperature as speed increases and presents a clear trend unlike the corresponding plot (Figure 3-22) from seal set No. 2.

Flow data from the outboard seal at different drain pressures are shown in Figures 3-39, 3-40, and 3-41. The flows range between 0.0008 and 0.0012 kg/s (10 and 15 scfm) going from low to high pressure drops. Speed appears to have no appreciable effect. The small variation with pressure seems to indicate a decrease in operating clearance as observed in previous tests.

The temperature plots for the outboard seal are given in Figures 3-42, 3-43, and 3-44. As with the inboard seal, the temperatures are generally lower at higher speeds.

3.2.4 Seal Set No. 4

This test was comparatively short due to a rub on the inboard seal. One start was made and the cumulative test time was about 20 min. Figure 3-45 is an operating map while Figures 3-46 and 3-47 present time history plots showing seal supply pressures and tester speeds. The time history plots are expanded to include about 2 hours of data prior to and after the running portion of the test.

The strategy for this test was somewhat different than for the first three tests because of the test rig modifications. The most important was the labyrinth seal. With this in place, it was hoped that the vibration problem would be solved and the tester would be able to run at the full speed of 7329 rad/s (70,000 r/min). Because of the importance of this achievement, testing at

multiple pressures at low speeds that had been done in previous tests was postponed.

The test run consisted of an initial ascent to 3141 rad/s (30,000 r/min) followed by incremental increases of 524 rad/s (5,000 r/min) to about 5759 rad/s (55,000 r/min). The supply pressure was held constant at 827 kPa absolute (120 psia). The relatively low value was chosen to minimize the risk of friction lock-up. The inboard seal drain pressure was held at approximately 637 kPa absolute (92 psia) while the outboard seal drain pressure went from 483 to 310 kPa absolute (70 to 45 psia) as the test proceeded.

Operation at 5235 and 5759 rad/s (50,000 and 55,000 r/min) showed that the vibrations were lower than in previous tests. However, the outboard seal clearances which were being measured using the embedded probes also revealed low film thicknesses of approximately 0.008 mm (0.0003 in.) and a slight vertical eccentricity reducing the distance between the seal ring and the runner. To provide the best chance for the seal to center itself, the supply pressure was dropped slightly to 724 kPa absolute (105 psia) prior to increasing speed above 5759 rad/s (55,000 r/min). Speed was increased to 5968 rad/s (57,000 r/min). Shortly after, a rub occurred on the noninstrumented inboard seal ring and the tester was tripped out. Figure 3-48 shows a strip chart of the failure. A torque check on the unit revealed that damage had taken place and the test was ended.

Despite the narrow span of operating conditions and the seal failure, a fair amount of good data was recorded including a running measurement of seal film thickness and eccentricity from the embedded capacitance probes. The film thickness measurements were very important because they provided one of the crucial links between the theoretical model and the actual seal performance. Previous tests fell short in achieving the necessary accuracy in film thickness measurements.

To maximize the data yielded by the test, the analysis was expanded to include not only the actual run which essentially consisted of a very slow speed sweep at constant supply pressure, but also a pretest and post-test period each consisting of about 2 hours. Full data scans including measurements of pres-

tures, flows, temperatures, and film thicknesses were taken during both intervals. The pretest period showed the seals in the final stages of chill-down, prior to introducing a significant flow of helium and the subsequent effects on ring temperature and clearances as the pressures were increased to the levels applied during the run. While a high-pressure zero speed run was not made, as had been done for seal sets Nos. 1 and 2, sufficient data points were covered to establish a zero speed flow-pressure curve. This also provided a zero speed datum at the run pressure to help characterize the effects of speed on film thickness. The post-test data is a little less revealing because the helium was shut off shortly after the test rig was tripped out. However, several data points were taken before this occurred. These consisted of a repeat of several flow-pressure points which permitted a comparison with prerun data. The results clearly demonstrated the increase in clearance of the inboard seal caused by the rub.

Because the test consisted essentially of one run rather than a number of runs, as was the case in previous tests, the data is most easily reviewed and is hence presented in a chronological or time history format. Specific plots of one variable against another are presented as required to illustrate key parametric relationships. The two independent variables are speed and pressure. Time history plots of these were presented in Figures 3-46 and 3-47. Because the seal drain pressures were different than the previous tests and the outboard drain pressure tended to vary somewhat, differential pressures across both seal rings are plotted along with the absolute supply pressure. Leakage flows are plotted in Figures 3-48 and 3-49.

During the initial part of the pretest period (-100 to -60 min) the supply pressure was held at the relatively low value of 310 kPa absolute (45 psia) to maintain a small but positive flow through both seal rings while the tester was undergoing final chill-down. Subsequent to this, the seal supply pressure was increased to 827 kPa absolute (120 psia) in preparation for starting. During the entire period, the outboard seal flow was quite a bit larger than the inboard flow.

Figure 2-6 presents a plot of the measured pretest zero speed flows versus the predicted flows at various clearances. Most of the data from the outboard

seal follows the 0.0305 mm (0.0012 in.) clearance line while that from the inboard seal tended toward even higher indicated clearances. Both measured flows are higher than the corresponding data from seal set No. 2 (see Figures 3-18 and 3-19). A direct comparison, however, is difficult because of the various differences between the seals and instrumentation. One of the big differences which supports the existing data is that seal set No. 4 had room temperature clearances which were nearly twice those of seal set No. 2. A difference which drives the argument in the opposite direction is the difference in boundary temperatures and their effect on the seals and runners.

Seal set No. 4 and runners were relatively warm because of the labyrinth seal (see Figure 2-18) which prevented LN₂ from flowing into the inboard seal drain cavity. Seal temperatures were in the -10 to +10°C (14 to 50°F) range. Seal set No. 2 was much colder because in that installation the inboard end of the runner was in direct contact with the LN₂ flow (see Figure 2-15). For the same pressure range, their temperature varied between about -55 and -30°C (-67 and -22°F). Thus, because seal set No. 2 and the runner were colder, their increase in clearance from room temperature to the test condition would be greater.

During the actual test run the outboard seal differential pressure rose initially from approximately 350 to 450 kPa (51 to 68 psi) due to decreases in the drain pressure. It later dropped back to about 400 kPa (58 psi) when the supply pressure was lowered. The inboard seal pressure drop stayed constant at 200 kPa (29 psi) until the supply was lowered when it dropped to about 90 kPa (13 psi).

Both flows dropped significantly during the run as speed increased. The outboard seal went from about 0.0013 to 0.0005 kg/s (16 to 6 scfm). The inboard seal went from 0.0006 kg/s (8 scfm) to zero flow which coincides with the occurrence of the rub and indicates a complete loss of clearance in the seal.

While there is some variation of flow with the changes in outboard seal pressure drop, and there may be some effect on both seals due to temperature changes, the principal cause of the changing flows is the decrease in clear-

ance as speed increased. Figure 2-7 presents a plot of flow versus pressure drop for the test run illustrating the effect.

Both seal flows increased after the tester was shut down. The flow through the outboard seal returned to ~80% of the level recorded prior to the run at the same differential pressure. The flow through the inboard seal, however, went up dramatically reaching twice the level achieved before operation. The net increase through the inboard seal clearly reflects the increase in clearance due to the material worn away during the rub.

Refocusing on the flow curves for the outboard seal in Figures 2-6 and 2-7, another anomaly is observed. The actual measured (average) film thicknesses are noted for many of the data points and are considerably smaller than the radial clearances corresponding to the predicted flows. The ratio of measured-to-predicted seal clearance is approximately 0.64 with the theory tending to overstate the clearance required to achieve a given flow. A possible explanation is that the "extra" flow is bypassing the normal path and leaking out between the axial sealing surfaces. Unfortunately, the data does not allow a more definitive explanation.

Figure 3-50 plots the surface temperatures of both seal rings. While the outboard seal is slightly warmer, both seals follow a parallel path with a difference of about 7 to 8°C (13 to 14°F). Both are observed to decrease in the early portion of the pretest period due to steadily declining temperatures in the test rig. After the helium flow is increased (~60 min to start-up time), the temperature increased and attained values slightly greater than they had at the beginning of the pretest period. This resulted from the warming effect of the helium flow. Previous discussions pointed out the substantial differences between the temperatures of these seals and those of seal set No. 2 (also seal sets Nos. 1 and 3) with the higher temperatures being achieved by better isolation of the seals and runner from the cryogenic bearing fluid.

Both the gradual chill-down and the subsequent warming effect can be observed in the behavior of the outboard seal film thickness during the pretest period. This is shown in Figure 3-51. The corresponding eccentricities are shown in

Figure 3-52. Initially, when the seal temperature was decreasing the average film thickness increased slightly. Inversely, during the later pretest period (-60 min and start-up) the clearance closed up again as the temperature increased.

The change in seal clearance is directly due to the temperature change in the seal ring and runner. If the temperature changes in both parts are the same, the rate of change of the radial seal clearance is about 2.1×10^{-4} mm/°C (4.6×10^{-6} in./°F). This is based on expansion coefficients of 12.6×10^{-6} m/m-°C (7.0×10^{-6} in./in.-°F) and 4.3×10^{-6} m/m-°C (2.4×10^{-6} in./in.-°F) for Inconel 718 and P-5N carbon graphite respectively. Ignoring the discontinuity at -50 min, the outboard seal temperature changes about 14°C (57.2°F) during the pretest period. Assuming equal changes in the runner temperature, the outboard seal clearance should have changed about 0.0029 mm (0.00011 in.). This compares well with the measured change which is ~ 0.004 mm.

Referring again to Figures 3-48 and 3-49, both seal temperature and clearance decrease substantially as speed is increased during the test run. The principal effect is the centrifugal growth of the seal runner which causes the seal clearance to decrease accordingly. This, in turn, causes the leakage flow to go down and, hence, the seal ring temperatures go down.

Figure 3-53 plots the measured average film thicknesses of the outboard seal as a function of speed. Also plotted is the predicted film thickness based on a zero speed film thickness equal to 0.016 mm (0.0006 in.) and a full speed 7329 rad/s (70,000 r/min) radial growth of 0.011 mm (0.00045 in.). Again, the data shows very strong correlation between measured and predicted values.

While the decrease in temperature is due to the decrease in flow, the effect is not as easy to substantiate by calculation. However, a comparison of data points during the test run with data points recorded during the pretest period which show equal flows, also reveal data points with nearly equal temperatures. For example, the flow through the outboard seal at 5 min after start-up is about 0.001 kg/s (8 scfm). This is the same as the flow at

40 min. The outboard seal temperature is approximately 5°C (41°F) at both times.

What does not appear, or at least is not obvious, is the effect of the temperature decrease during the run on the film thickness. The simple calculation contained in the previous discussions would predict an increase of approximately 0.003 mm (0.00013 in.) based on the measured temperature drop of 10°C (18°F). However, since this change is about one third of the change due to centrifugal growth, its effect could be easily overlooked.

Toward the end of the test run the inboard seal temperature began to increase, showing a 4°C (7°F) change over about 1 min. This corresponds with the time at which the seal dropped to near zero clearance and signifies the start of the seal failure.

Immediately after the tester was shut down, both seal temperatures and the outboard seal film thickness returned to virtually the same values as they had immediately before the run. After the helium supply was shut off at about 30 min, the temperatures dropped nearly 70°C (126°F) as the seal components were chilled by the cryogenic section of the test rig. This, in turn, resulted in a 0.016 mm (0.0006 in.) increase in film thickness which is the expected amount based on previous rates.

3.3 Dynamic Behavior During Seal Testing

While the tests were not structured to examine the dynamic behavior of the seals, it is an aspect of considerable importance. Dynamic data was thus monitored, recorded, and later analyzed. Basic characteristics such as the size of the runner orbit and whether the seal rings remain locked or tended to whirl were disclosed.

For the first three seal tests, the instrumentation consisted of six capacitance probes observing the seals and the runner. During the first test, no data were gathered because two of the probes failed and several others were forced out of their usable operating range. The problems were corrected and, despite thermally induced offsets which caused bothersome errors in static

position measurements, the second and third seal tests proved more successful and yielded good dynamic data. The fourth seal test also resulted in good dynamic information from the outboard seal containing the four embedded probes and the two probes retained to observe the runner. No measurements were made on the inboard seal ring.

3.3.1 Seal Set No. 2

With only a few exceptions which will be noted, the seal rings were motionless during steady-state operation. The runner orbit varied in size between 0.004 and 0.010 mm (0.00015 and 0.0004 in.) reaching the larger size at higher speeds. The orbit consisted only of the synchronous and its harmonic frequencies.

Figure 3-54 shows one of the cases where seal motion was detected. This occurred at 3665 rad/s (35,000 r/min) when the outboard seal drain pressure was lowered to 103 kPa absolute (15 psia). The supply pressure was 655 kPa absolute (95 psia). Both seals show approximately 0.013 mm (0.0005 in.) of straight-line motion, the inboard seal moving vertically while the outboard seal vibrated horizontally. The seal amplitudes grew worse with supply pressure and the condition shown was the highest supply pressure attempted.

While the seal probe settings seemed to check out, the unusual nature of the indicated motion (i.e., absolutely straight-line) casts some doubt on the validity of the data.

Figure 3-55 shows seal and runner orbits at 4188 rad/s (40,000 r/min) with a supply pressure of 862 kPa absolute (125 psia) and equal drain pressures of 517 kPa absolute (75 psia). This data point was taken immediately following the one illustrated in Figure 3-52. A small amount of the straight-line seal motion remains. The seals were motionless at all other flow conditions at this speed.

Figure 3-56 depicts the seal runner orbits during the first data point of run No. 3. Speed was 4712 rad/s (45,000 r/min), supply pressure 938 kPa absolute (136 psia), and drain pressure 517 kPa absolute (75 psia). Some seal motion

is observed. At succeeding data points, the rings again locked and remained motionless.

3.3.2 Seal Set No. 3

The runner from the No. 2 test was reused and resulted in similar runner orbits. The seal ring motion, however, was quite different. While the outboard seal was motionless, the inboard seal exhibited an orbit with amplitudes at times reaching 0.030 mm (0.0012 in.).

Figures 3-57, 3-58, 3-59, and 3-60 show four data points at 3665 rad/s (35,000 r/min). The scales in the figures are the same as those in Figure 3-54. The first two represent supply pressures of 655 and 1206 kPa absolute (95 and 175 psia), respectively. Both drain pressures were 517 kPa absolute (75 psia). The second of these shows a narrow elliptical orbit on the inboard seal which grew in a uniform manner as the pressure was increased.

Figures 3-59 and 3-60 represent the data runs where the outboard drain pressure was reduced to 310 and 103 kPa absolute (45 and 15 psia), respectively, and the supply pressure was raised to the maximum value of 1206 kPa absolute (175 psia). In each case the inboard seal orbit progressed from small amplitudes to the sizes shown as the supply pressure was increased.

Figures 3-61 and 3-62 show similar occurrences at 4188 and 4712 rad/s (40,000 and 45,000 r/min). In these cases, amplitudes at low supply pressure grow from about one-half the amount shown in the photo, to full size. In these cases the amplitudes are very large and could easily have resulted in a seal rub. They are clearly unacceptable.

While the mechanism causing the whirl is unknown, the following summarizes its salient aspects:

1. The whirl is synchronous although some harmonic activity is present. It must therefore be a result of runner excitation.

2. The seal amplitude is much larger than the runner motion indicating an amplification and a system resonance having to do with the seal ring may be involved.
3. The whirl is obviously very sensitive to the surrounding fluid conditions, e.g., supply and drain pressures and also to speed since the amplitudes become much worse when speed increases from 3665 to 4188 rad/s (35,000 to 40,000 r/min).
4. The whirl did not occur on the outboard ring operating under virtually identical conditions, nor did it occur on either of seal set No. 2 rings. This suggests that there is something unique about the seal set No. 3 inboard ring.
5. The operating map showed that the seal operates in the high friction region and the frictional forces (based on a friction coefficient of 0.20) should exceed the hydrodynamic forces and prevent the seal from moving. There was concern that problems may develop due to the inability of the seal rings to move. Clearly this was not the case for the seal in question. Its actual behavior suggests that the frictional forces are not being developed and that the seal may be lifting off enough, at least, to result in the development of a partial lubricating film under the radial sealing land to lower the prevailing friction coefficient.

3.3.3 Seal Set No. 4

No unusual motions were noted during the test. However, with the exception of speed, the range of operating conditions was very narrow. Supply pressure was held constant at 827 kPa absolute (120 psia). Hence, the conditions under which seal set No. 3 showed, large whirl amplitudes were not encountered. Speeds covered the range from 3141 to 5968 rad/s (30,000 and 57,000 r/min).

Figures 3-63 through 3-67 each show displays of the runner orbit and the embedded probe output superimposed on the same photo. Speeds range between 3665 and 5759 rad/s (35,000 and 55,000 r/min). The runner display shows a

normal orbit using vertical and horizontal probes. Over the speed range it indicates a modest growth from an orbital diameter of approximately 0.004 to 0.008 mm (0.00015 to 0.0003 in.)

The displays resulting from the embedded probes do not show seal orbits. Each one was generated by a pair of embedded probes. The probes are not 90° to each other, rather, they are 180° apart. Thus, one display represents the vertical components of the ring motion while the other shows the horizontal motion. The arrangement is illustrated in Figure 3-68. The display format provides several pieces of information. Measurements 'a' and 'b' represent the average film thickness at each probe; 'c' is the arithmetic average of 'a' and 'b', and represents the average radial film thickness in the direction of the probes; 'd' is half the difference between 'a' and 'b', and represents the eccentricity in the direction of the probes. The x- and y-axes of the scope display represent the zero gap values and the point at which the seal rubs the runner. They are shown by the heavy white lines in the photos and are the same for both pairs of probes in Figures 3-63, 3-64, and 3-65. For Figures 3-66 and 3-67, the y-axis for the vertical probe display is moved to the right to prevent the displays from overlapping. All other aspects are the same. The position of the runner orbit on the photo is completely arbitrary and has no bearing on the other displays. If the ring remains rigid, a relative orbit between seal and runner registers a straight line with a slope of -1. The whirl amplitude in the given direction is equal to 'e'.

Referring again to Figures 3-63 through 3-67, it is observed that the horizontal seal probe display shows as a straight line with x and y components which are equal to themselves and to the horizontal diameter of the runner orbit. This indicates that all of the relative motion measured by the embedded probes is actually seal runner motion and the seal ring is essentially stationary.

The vertical seal probe displays are not very straight. This is because of harmonic distortion in the horizontal component of the scope display. Figure 3-69 shows the relative seal motion versus time for the four embedded probes. The fourth trace shows the distortion. The distorted waveform should be equal but out of phase with the third trace which shows the output from the

probe installed 180° away. Note the mirror image relationship between the top two traces representing the other opposed pair of probes.

Literally interpreted, the distortion indicates that the seal ring is flexing; however, because there is no evidence of harmonic activity in the other traces it is discounted as an instrumentation anomaly.

Observing the nondistorted component of the vertical display, it can be seen that the relative seal motion is again equal to the runner motion, indicating that the ring is, in fact, stationary. The net result is that the outboard seal ring stayed motionless at all test conditions.

3.4 Acceleration Testing

High acceleration rate tests were performed on seal set Nos. 2 and 3. Each test consisted of starting the tester from zero speed and accelerating it to maximum speed at an average rate of 152 m/s^2 (500 ft/s^2). Due to the dynamic problems, the maximum speed was set at 4188 rad/s ($40,000 \text{ r/min}$) for seal set No. 2 and approximately 4712 rad/s ($45,000 \text{ r/min}$) for seal set No. 3. This resulted in an acceleration time of approximately 0.7 to 0.8 s. Supply and drain pressures were set prior to the run. The starts were achieved by opening the turbine solenoid trip valve, allowing the unit to accelerate and closing the valve using an overspeed trip signal. Figure 3-70 depicts a speed and time curve typical of these tests.

Because each fast start was followed immediately by a shutdown, there was no way to check steady-state operation during the run to assess any potential damage. Therefore, after every five fast starts performed in the manner described, a slow start was made using manual controls. These runs allowed the unit to run at steady-state conditions to permit a cursory performance check.

3.4.1 Seal Set No. 2

A total of 50 fast starts were performed with average acceleration rates varying from approximately 149 to 198 m/s^2 (490 to 650 ft/s^2). The helium supply

pressure was held at 931 kPa absolute (135 psia) and both inboard and outboard drain pressures maintained at 517 kPa absolute (75 psia).

The first 30 acceleration runs were done in groups of 5 with slow start steady-state runs in between. The remaining 20 were performed in two groups of 10, again with a periodic steady-state check before and after.

Table 3-2 gives the test conditions and provides steady-state performance data between each group of acceleration runs. While the flow rates do show some variation, there is no obvious sign of deterioration. Also, the post-test inspection revealed no wear or other signs of distress.

3.4.2 Seal Set No. 3

Forty acceleration runs were conducted on these seals with average rates varying between 119 and 171 m/s² (390 and 560 ft/s²). Helium supply pressures started at 1069 kPa absolute (155 psia) on the early runs and increased to 1482 kPa absolute (215 psia) on the latter runs. Both drain pressures were held at 517 kPa absolute (75 psia). The acceleration runs were done in groups of five.

The runs proceeded in a normal fashion with no sign of problems through run No. 48. Table 3-3 documents steady-state performance between groups of acceleration runs; no obvious deterioration was noted. A second slow start, run No. 48a, was then made. The conditions were 1482 kPa (215 psia) and 4712 rad/s (45,000 r/min). About 15 s into the run, the tester was manually tripped when its noise level increased abruptly. The strip charts revealed a subsequent increase in the outboard seal ring temperature signifying a rub (see Figure 3-36). Two attempts to restart the tester resulted in additional rubbing with attendant temperature increases. The test was terminated at that point.

3.5 Post-Test Hardware Inspections and Failure Analysis

Tables 3-1 and 3-4 summarize the condition of the seals and runners before and after testing. The former provides key dimensional data while the latter is a

qualitative description.

An overall evaluation of the post-test condition of the seal rings and runners reveal that they fall into essentially one of two categories: those with significant damage and those with no damage at all.

Three seal rings fall into the first group. All were damaged due to rubs between the ring and runner. In all cases the rubs happened suddenly and unexpectedly. Fortunately, the rubbing was very obvious in the data and permitted quick shutdowns. In fact, in all three cases, the turbine was tripped within 5 s of the start of the rub. While the damage was confined for the most part to surface effects, it is obvious by the rate at which it took place that the rubs were very destructive and had they been allowed to progress for even 10 to 20 s, much more serious damage would have resulted.

The remaining five seal rings constitute the undamaged group. These went through the same battery of tests as the failed seal rings. Additionally, three rings were subjected to a failure of the adjacent seal ring. None of the rings showed signs of wear or other distress on the mating surfaces with the possible exception of some slight polishing over short arcs.

3.5.1 Seal Set No. 1

The outboard seal ring rubbed due to high runner vibration at a speed of approximately 5759 rad/s (55,000 r/min). Removal of the end cap revealed the outboard seal drain cavity had a film of black soot on all surfaces. The damaged outboard seal ring was tight on the runner due both to wear debris and surface damage. It had to be worked loose. Figure 3-71 gives a partial view of the seal ring showing heavy rub marks over all surfaces of the bore. Before and after bore measurements which are shown in Table 3-1 indicate that 0.023 to 0.028 mm (0.0009 to 0.0011 in.) of carbon graphite had worn away. This can be observed in Figure 3-71 by noting that the machined depths of the pockets was also approximately 0.023 to 0.026 mm (0.0009 to 0.0011 in.) and that the lands had worn down and blended with the bottom of the pockets. The seal ring showed no other signs of damage although a slight bit of polishing was noted on the axial sealing land.

The inboard seal ring was loose on the runner in its normal position, however, was tight when it was pulled over the area damaged by the outboard seal. To prevent additional damage, LN₂ was poured onto the runner to decrease its size and alleviate the bind. The inboard seal was successfully removed and is partially shown in Figure 3-72. While there is some evidence of slight polishing over a 10 to 20° arc (shown as the darker areas in Figure 3-72), there is no real wear. The few scratches which show in the photo most notably, those in the axial direction, are thought to have happened during the disassembly. Very slight polishing of the axial sealing land was noted.

Figure 3-73 shows the seal runner illustrating several aspects of the damage. First, the rubs are confined to the middle and right-hand or outboard side of the runner. The marks in the middle were caused by rubs with the capacitance probes. The marks on the right side are due to the seal. They are heaviest towards the edge. These show a continuous pattern all the way around and correspond with the axial breakdown land on the seal. The marks inboard of that land correspond with the Rayleigh-step portion of the seal. These appear as discontinuous skip marks and indicate lighter contact in this area. The periodicity is probably attributable to slight high spots built in during the grinding of the runner. Numerous longitudinal heat cracks are in evidence in all rub areas. Also, several small pieces of the tungsten carbide coating came off in the cracked areas. The latter is illustrated by the magnified view shown in Figure 3-74 (11.4X). The other end of the runner is free of rub marks.

3.5.2 Seal Set No. 2

Both seal rings went through the testing with no rubbing. The post-test disassembly showed no sign of soot or other wear debris. Both rings were loose and easily disassembled. Except for a slight bit of polishing over a 90° band on the downstream edge of the inboard seal ring and in spots on the axial sealing land of both seal rings, neither ring shows evidence of having run at all. Figure 3-75 shows a partial view of the outboard ring. Likewise, an inspection of the runner revealed no evidence of any marks.

3.5.3 Seal Set No. 3

The outboard seal ring rubbed unexpectedly while running at steady-state conditions at 4712 rad/s (45,000 r/min).

Removal of the tester end cap and seals revealed that in addition to small amounts of black soot in both the seal supply chamber and the outboard seal drain cavity, there was several small pieces of leaf material. It was also found that one of the two helium supply ports was partially plugged with the same leaf material. The failure was thus attributed to the presence of the contamination.

Both rings were removed by chilling the runner with LN₂. This was done to prevent additional damage. The outboard seal showed substantially less damage than the failure of the first seal. In this case, the wear was concentrated on the breakdown land and adjacent bearing land on the downstream end of the ring. Figure 3-76 shows a typical partial view. While the upstream land areas were not heavily worn, a number of heavy scratches were in evidence. Figure 3-77 shows the undamaged inboard ring.

As with the two previous seal sets, the axial sealing face of seal set No. 3 rings showed some evidence of slight polishing. Likewise, the mating land areas on the seal housing showed areas of contact where minute deposits of carbon graphite had rubbed off.

The damage to the runner was less than the first failure, however, it followed a similar pattern as shown in Figure 3-78. The rub marks are heaviest in the area of the breakdown land and less severe under the adjacent bearing land areas. The only other marks under the outboard seal are at extreme upstream end and are very slight. A pattern of skip marks appear and predominantly longitudinal heat cracks abound. Figure 3-79 shows a magnified view (11.5X) of where several small pieces of the tungsten carbide coating came off.

3.5.4 Seal Set No. 4

The inboard seal rubbed due to insufficient radial clearance at 5968 rad/s (57,000 r/min). The outboard drain cavity was clean and the outboard seal was loose on the runner and easily taken out. The inboard ring was tight to the runner and had to be pulled off.

The damaged inboard ring is shown in Figure 3-80. In addition to signs of moderate rubbing across most of the width of the seal and all the way around its circumference, a single radial crack extended through a cross section of the ring. This can be seen in the photo between the feed groove and the end of the adjacent pocket.

The outboard seal ring which has the embedded capacitance probes is shown in Figure 2-24. It is completely undamaged and shows no sign of having rubbed.

A photo of the runner is shown in Figure 3-81. Heavy rub marks appear in the areas under the pressure breakdown land and the adjacent bearing land. Next to the latter there is some evidence of the "skip marks" noted on the other runners and narrow streak-like rub marks under the other bearing land. The entire area under the seal ring shows evidence of polishing. The middle and other end of the runner show no marks at all.

3.6 Discussion Of The Results

The testing addressed a number of important aspects of the design of the 50-mm Rayleigh-step helium buffer seal. These include:

- Steady-state operation
- Fast-start capability
- Seal life
- Leakage rates
- Parametric effects
 - Seal flow path
 - Environmental interaction
 - Supply pressure

- Shaft speed
- Seal clearance
- Seal temperature
- Dynamic performance of the seal rings
- Material considerations.

3.6.1 Steady-State Operation

The seals proved themselves capable of operating over a wide range of supply pressures and speeds. Supply pressures of up to 1482 kPa absolute (215 psia) were applied to three of the four test seal sets at various shaft speeds with very satisfactory operation resulting. Testing at maximum pressure included slow ascents from low to high speeds with maximum pressure applied and application of increasing pressures up to the maximum value at various constant speeds. The only indication of a problem which may have been connected with high supply pressures, occurred during the testing of seal set No. 3 when the inboard seal ring developed a sizable orbit that appeared to get larger as pressure was increased.

Despite the whirl, the seal ring ran satisfactorily at 1482 kPa absolute (215 psia) at the maximum allowable tester speed. The dynamic consideration of this instance is discussed in Subsection 3.4.2. A great deal of running was also done at fairly low supply pressures with no evidence of problems.

Satisfactory seal operation was achieved up to speeds of 5759 rad/s (55,000 r/min). Operation at higher speeds was precluded because of the dynamics problem in the tester which resulted in large whirl orbits at the seal runner. The whirl which had an estimated double amplitude of 0.038 to 0.051 mm (0.0015 to 0.002 in.) occurred during seal set No. 1 testing and caused the failure of the outboard seal ring. Seal set Nos. 2 and 3 were arbitrarily limited to lower speeds to avoid repeating the failure. Seal set No. 4 inboard also failed at about the same speed as seal set No. 1; however, its problem occurred for a different reason and under different circumstances. The failure was due to a total loss of clearance. This was well substantiated by the data recorded and presented in Subsection 3.3.4. The clearance loss was due to two factors which were:

1. Increasing centrifugal growth of the runner
2. Higher film temperature due to a higher temperature environment.

To avoid test rig problems, seal set No. 4 and the runner were not exposed to LN₂ (see Subsection 3.1). There was no question that larger machined clearances would have prevented the seal from closing up and allowed operation to continue.

In summary, despite the tester-imposed speed limitation, all indications were that the seals would have operated successfully at the full speed of 7329 rad/s (70,000 r/min) with up to maximum supply pressure applied. Therefore, it is concluded that the design meets the basic speed pressure performance requirements and should receive continued consideration as a viable design.

3.6.2 Start-Up Performance

This appears to be one of the lesser demands imposed on the seals. Both seal sets that were subjected to the high acceleration rate tests showed no problems during or immediately after any of the fast starts. This is not unexpected given the conditions which apply during a start-up. Helium supply pressure is applied to the seals prior to rotation. During the testing, this included various pressures up to a maximum of 1482 kPa absolute (215 psia). In actual turbopump operation the full design pressure is applied. The pressure seats the seal rings and establishes flow, although the rings are probably not concentric with the runner. During the initial start, rubbing will occur if the seal is in contact with the runner. As the speed increases, a hydrodynamic film develops which results in forces tending to center the seal. These forces increase as speed goes up until they are sufficient to overcome the frictional forces, at which point the seal ring moves to a concentric position and the rubbing stops. The required acceleration rates resulted in start-up times of approximately 0.77 s from 0 to 4712 rad/s (0 to 45,000 r/min), the maximum test speed, and 1.20 s for acceleration to 7329 rad/s (70,000 r/min). Therefore, the time during which rubbing would occur is very short. Moreover, because it occurs during the initial part of the run, the speeds are lower. This results in less heat and lower temper-

atures at the rubbing surfaces. All of these factors combine to actually favor the high acceleration rate starts.

While no operational problems resulted from the fast starts, neither was there a buildup of significant wear on the seal rings. Seal set No. 2 underwent 50 fast starts while seal set No. 3 was subjected to 40 starts. Excluding the No. 3 outboard seal which failed due to contamination, the post-test inspection (see Subsection 3.6.3) found very little wear on the seal rings. In fact, the only real evidence of wear were several short arcs in the bore area which showed some polishing. This is slightly evident on the left side of the photo showing seal set No. 3 ring (Figure 3-77). The tests show that the seal design is capable of undergoing multiple high acceleration rate starts without damage or significant wear.

3.6.3 Seal Life

This readdresses the topics of steady-state operation and fast start capability but from a slightly different viewpoint. Evaluating seal life potential based on the tests that were conducted is a matter of:

1. Reviewing the life that was achieved in the seals
2. Evaluating the failures that occurred
3. Identifying any mechanisms that were present and could have caused a failure.

Table 2-1 presents the cumulative test time and number of fast starts for each of the test seals. Seal sets Nos. 2 and 3 were operated for the longest periods of time, each one achieving approximately 4 h of running. This in itself is significant because it represents about 40% of the design life. What is more important is that the 4 h logged by each seal set is not really indicative of their useful life which could have been much longer. This is easy to see for seal set No. 2. These seals went through the most extensive battery of tests of the four sets including acceleration testing. At the end of tests, both the seals and the runner looked as good as before they were tested. By all indications they could have been reinstalled and run for an indefinite period. Seal set No. 3 falls into a similar category. It also went

through a substantial schedule of tests which although not quite as long, routinely achieved higher supply pressures than seal set No. 2. It operated successfully right up to the point at which the outboard seal rubbed and the test was terminated, yet the inboard seal was removed and like seal set No. 2 showed almost no signs of having run.

Seal set Nos. 1 and 4 logged considerably less time than seal set Nos. 2 and 3, the former achieving about 1-1/2 h and the latter approximately 20 min. Both tests were terminated by failures of one of the rings. However, the rings that did not rub showed no signs of deterioration and, like seal set No. 2, would probably have run for a much longer period of time.

While the three failures that did occur certainly ended the lives of both the seals and runners involved, they need to be carefully evaluated to determine what they really revealed about the life potential of the seal design.

As discussed in Subsection 3.6, all three failures share several common characteristics. The major manifestation of the failures were radial rubs between the runner and one of the seal rings. All happened very suddenly and unexpectedly. Despite quick shutdowns, significant damage resulted in each case. Thus, there is no question that the seal design is very sensitive in this area and with existing materials, even the briefest of rubs are to be avoided.

While damaging rubs were common to all the failures, the triggering mechanism was different in each case. Furthermore, each of the mechanisms could have been avoided by changes in the design or more careful control of the system in which the seals were installed.

The failures of seal set Nos. 1 and 3 were caused by outside influences, the former being triggered by runner whirl diameters which were estimated to be between 0.038 and 0.051 mm (0.0015 and 0.002 in.) peak to peak and the latter apparently caused by fairly substantial amounts of contamination in the seal area. While the exact levels of vibration the seals should be capable of handling can be argued, the levels to which seal set No. 1 was exposed were clearly excessive. The amount of contamination was much greater than should

have occurred. Both problems can be avoided in future application. Seal set No. 4 failed because of insufficient clearance. This also is easily remedied.

The only other mechanisms which were observed to have potential for limiting seal life involved wear in the bore of the seal due to brief rubbing during start-ups and wear on the axial sealing faces of the seal rings. Both appear to be minor problems and would not be expected to limit seal life to less than the 10-h, 300-start requirement.

In summary, despite being highly sensitive to rubs between the seal rings and runner as are most high-speed radial seals, the current design appears capable of meeting the NASA life requirement of 10 h and 300 starts.

3.6.4 Leakage Rates

Low helium leakage rates are a very important aspect of the seal design. The leakage rates of the 50-mm Rayleigh-step design were found to be very low and represent a significant improvement over currently used designs. Figure 2-8 provides an overview showing a maximum flow envelope for each seal set as a function of pressure drop. Each flow curve represents the higher of the two seal (inboard or outboard) flows at a given operating point. All speeds and pressure conditions included in the testing are covered except for zero speed. The highest flow recorded during steady-state testing was 0.0026 kg/s (33 scfm). Typically, the flows ranged between 0.001 and 0.002 kg/s (13 and 25 scfm). While the leakage flows were quite low, the governing relationships proved to be very complex. Thus, given the number of test conditions represented, the reader is cautioned not to draw any conclusions beyond simply establishing the general range of flows.

Figure 2-9 shows a slightly more simplified overview. Again, the maximum flow is given for each seal set. However, in this case, only test points at shaft speeds of 4712 rad/s (45,000 r/min) are given. While it is not the highest speed tested, it is the highest speed at which a wide range of supply pressures were applied to each seal set. Most of the flows were in the 0.0010 to 0.0016 kg/s (13 to 20 scfm) range. Seal set Nos. 2 and 3 had maximum pressure drops of 1365 and 1250 kPa (198 and 181 psi). Extrapolating to a pressure

drop of 100 kPa (200 psi) results in expected flows of 0.0019 and 0.0012 kg/s (24 and 15 scfm). Because the radial flow clearances will go down as speed increases due to centrifugal growth of the runner the extrapolated flows could also be regarded as conservative estimates of the flows that would have occurred at the full design conditions.

3.6.5 Parametric Effects

The testing uncovered a number of relationships among the various system parameters. Some of these were very logical and supportive of the design analysis, while others pointed out new insights that need to be included or more heavily weighted in the design. Because the system proved to be very complex, primarily because of strong parametric interaction both from within the system and with the surrounding environment, the measurements though fully adequate to verify the main performance variables (supply pressure, speed, leakage, etc.) were not sufficient to explain all aspects of the system behavior. With these considerations in mind, the following sections discuss the principal system variables in terms of: 1) how they affected or were affected by system performance, particularly leakage flow, 2) how their behavior correlates with the design analyses, and 3) what emphasis, both experimental and theoretical, should be placed on them in future designs and studies. The discussion includes:

- Seal flow path
- Environmental interaction
- Seal pressure
- Shaft speed
- Seal clearance
- Seal temperature.

3.6.5.1 Seal Flowpath. Most of the discussions of seal flow so far have assumed that all of the helium flow goes through the annular space between the seal ring and the runner. This is not necessarily the case. A second flow path exists across the radial sealing land of the ring and the mating surface on the seal housing. If either surface is not flat or becomes distorted, a flow area will exist and flow will take place. Likewise, if for any reason the

ring lifts off slightly, a flow will take place. In either case, the flow instrumentation would not have been able to distinguish between the normal flow through the radial clearance and an axial bypass flow. Any bypass flow would have been combined with the normal flow.

Bypass flows, if they occur, are likely to be fairly small and therefore probably do not have a large effect on overall performance. However, at conditions of low flow between the seal and runner, bypass flows may cause substantial errors in the measurements and result in poor correlation with predicted results. Future work should give consideration both to predicting and measuring bypass flow.

3.6.5.2 Environment Interactions. The system surrounding the seal rings and runner had a very strong effect on the leakage rates. Moreover, effects were not the same for all of the seals even though the principal test conditions (supply pressure, speed, etc.) may have been the same. Differences occurred in two areas: 1) between the inboard and outboard seal rings, and 2) between seal set No. 4 and the first three seal sets. Subsection 3.2 describes the mechanical differences of both.

The principal differences between the inboard and outboard seals were the temperatures of the seal rings and the corresponding sections of the runner. The main effect was on the runner for the first three seal sets. The inboard face was directly exposed to the LN₂ in the inboard drain cavity whereas the outboard face was exposed to the outboard drain cavity containing only helium. This resulted in the runner taking on the shape of a truncated cone due to a net contraction of the inboard end. The effect on the rings was somewhat less. Heat was conducted out of both rings through the axial sealing lands into the adjacent housing. Because of the temperature difference across the housing, the inboard ring was slightly colder and therefore contracted more than the outboard ring. This was predicted by the thermal analyses and verified by measurements of the seal ring temperatures. Typical data is shown in Figure 3-10. Measurements were not possible on the runner. The net effect of the differences in thermal contraction between the inboard and outboard seals (and runner) was that the inboard clearances tended to increase more than

those on the outboard as the unit cooled down to operating temperature. This permitted generally larger flows through the inboard seal ring.

The physical changes between the fourth seal and the previous three are described in Subsection 3.2. The major effect was that the labyrinth seal prevented the draining of LN₂ from the adjacent bearing from contacting the end of the runner and the inboard side of the seal housing. This resulted in two changes: 1) the thermal contraction of the runner was less on both ends, and 2) the coning effect was greatly diminished. Similar effects occurred with the seal rings. With the seal housing better isolated, its temperature also went up resulting in less heat transferred from the seal rings and higher ring temperatures. The overall result of the addition of the labyrinth seal was higher and more uniform seal ring and runner temperatures, e.g., less difference between the inboard and outboard seals and less change in radial clearance due to tester chill-down. The latter is illustrated by comparing the temperatures in Figure 3-10 and those in Figure 3-50. The latter accounts for the comparatively low flows measured on seal set No. 4, despite its larger room temperature clearances. Overall, the changes were beneficial because they reduced the effects of the surrounding system allowing better control over seal operating parameters. Future developmental tests should give careful consideration to achieving good isolation. Tests designed to evaluate the seal's design in a specific application, e.g. the LOX turbopump, must simulate the environmental interaction as closely as possible.

3.6.5.3 Seal Pressure. Both supply and drain pressures were key independent variables controlled during the testing and of obvious importance in determining helium flow rates. While various supply pressures were applied, the inboard drain pressure was held fairly constant. Thus, for the inboard seal, the supply pressure also determined the pressure drop. The outboard drain was set at several different values resulting in different pressure drops and, therefore, flow rates at the same supply pressures.

Experimentally evaluating the effects of supply pressure or pressure drop was very difficult for the first three seal tests because the operating clearances were not accurately known. Since substantial changes in the clearance were known to have taken place, it was impossible to experimentally separate the

effects of the pressure and clearance, at least for the bulk of the testing. To provide a rational (if only first order approach), a comparative analysis was conducted which consisted of computing theoretical flow-pressure curves at different clearances and comparing them with the measured flow-pressure curves. This automatically provided an estimate of the actual operating clearances. The data taken during seal set test No. 4 included good measurements of clearance on the outboard seal and thus a much better basis for analysis.

At low speeds most of the experimental flows from the inboard seals of seal set Nos. 2 and 3 were found to increase in the same manner as theoretical flow at constant clearance. For these data, the flow increased solely as a function of supply pressure. At high speeds, the flow was found to be flatter with higher pressure points corresponding with smaller theoretical clearances than lower pressure points.

Generally as the speed increased, the indicated theoretical clearance decreased. While some of this was clearly due to the effect of centrifugal growth causing the runner to increase in diameter, the indicated decrease was more than was expected due to growth alone. This suggested that other effects are also taking place. The three effects are illustrated in Figure 3-82a.

The outboard seals of set Nos. 2 and 3 showed a quite different flow behavior as illustrated in Figure 3-82b. Generally, the flows were considerably less than the inboard seals. This was most pronounced at low speed where the inboard flows followed fairly high theoretical clearance lines. At constant speeds, the outboard seal flow curve stayed flat as pressure increased indicating that the clearances were decreasing. This may have been due to the increase in total seal flow (due to increased inboard seal flow) which would have a warming effect on the runner and thus cause a net decrease in the already small outboard seal clearance. The second strong effect was no discernable change of flow or indicated clearance as speed was increased. The speed effect was almost the reverse of what occurred on the inboard seal. For the inboard seal, the decrease in indicated clearance was much greater than the centrifugal growth would permit; for the outboard seals there was no decrease. Some of the effects are baffling and strong thermal interactions

are suspected. The flow data from seal set No. 1 was excluded from the discussion because only total flows were measured.

During the testing of seal set No. 4 only one pressure was applied at each speed, therefore, no experimental flow-pressure curves were generated. However, the flow decreased substantially on both seals as a function of speed, permitting a comparison of measured clearance with indicated clearance over a range of values. This showed that the actual clearances were considerably less than those indicated by the theoretical flow relationship (see Figure 2-7). This further indicates that actual flows are greater than predicted flows at the same clearance. Two possibilities arise to explain the discrepancy: 1) the flow model needs to be modified to fully account for the conditions in the seal, or 2) the difference between actual and predicted flows occurred as a bypass flow. Unfortunately, the shortness of the test precluded exploring the behavior to any greater extent. It is important to note that the anomaly found with the fourth seal more than likely applies to the three previous tests and must be considered in evaluating their behavior

Future work needs to concentrate both experimentally and analytically to better characterize the pressure-flow relationship and its interaction with seal and runner temperatures and speeds. The strong thermal effects underscore the recommendation of the previous section. Other items should include:

1. Measuring seal film thickness of both seal rings using embedded probes. This is clearly the most satisfactory approach.
2. Measuring the bypass flow. Even a rough measurement would be useful.
3. Measuring the drain flow from both seals. This would provide a check on the overall accuracy of the flow measurements.

3.6.5.4 Shaft Speed. Shaft speed was another carefully controlled independent system variable. Speed has a major effect on the stiffness and damping properties of the Rayleigh-step part of the seal ring and hence the ability of the seal ring to maintain a centered position and good dynamic behavior. Its effect on seal leakage flows, however, is entirely indirect and theoretically

consists only of causing the runner to grow in diameter because of centrifugal forces which cause a decrease in seal clearance and leakage flow.

The effect of decreasing clearance with increasing shaft speed was more or less borne out during the testing. Data from seal set No. 1 (combined flows) and the inboard seals from seal sets Nos. 2 and 3 clearly showed decreases in indicated clearances as speed increases. The outboard seals of seal set Nos. 2 and 3 did not show the clearance decrease which indicates the presence of an opposite influence.

The testing of the fourth seal also showed the effect and since the outboard seal clearance was accurately measured permitted a direct comparison with the predicted behavior. Figure 3-53 showed the measured decrease in clearance matched the predicted change.

3.6.5.5 Seal Clearance. This proved to be one of the most elusive parameters with an accurate measurement not being achieved until the fourth seal test. Clearance is important both in determination of the stiffness and damping properties of the seal rig and the leakage flow rates.

Operating clearances were found to be very sensitive to several factors including speed, environment effect, and flow effects. The second and third are entirely thermal effects and more difficult to fully characterize. The environmental influence from the nearby cryogenic tested section, cause the clearances to increase by decreasing the temperature of both the seal ring and runner. The clearance increase results from the larger expansion rate of the runner material. The helium flow, being much warmer than either seal parts, has the opposite effect causing the temperatures to increase and the clearance to decrease.

Since leakage flow and seal clearance are so closely related, the discussions of the pressure-flow characteristics given in Subsection 3.6.5.3 also provide direct insights into the clearance behavior. In summary, these arrangements indicated that the inboard seal clearances of seal set Nos. 2 and 3 were insensitive to pressure and flow and decreased as speed increased. The outboard seal clearances of seal set Nos. 2 and 3 decreased as pressure

increased and were insensitive to speed changes. Both of these effects were actually caused by the concurrent thermal changes. The seal data of seal set No. 4 were too limited to establish clearance sensitivity to pressure, however, did disclose that both seals showed the predicted clearance (based on actual clearances) as speed increased.

One additional consideration worth noting is the effect of the manufactured clearances and the initial chill-down. For seal set Nos. 2 and 3, the manufactured clearances of the inboard seals were smaller than the outboard seals by 30% (see Table 3-1). However, due to initial chill-down, the inboard seal clearances become larger than the outboard seals. This condition resulted in the inboard flows being generally larger than those of the outboard seals. The larger flow of the inboard seal was thus likely to have a stronger thermal effect both on its own clearance and the clearance of the outboard seal than the much smaller flow from the outboard seal. Along the same lines, the smaller clearance of the outboard seal makes its flow more sensitive to a given change in its clearance. Both effects tend to enhance the likelihood of the inboard seal flow having a strong effect on both the clearance and flow of the outboard seal.

The manufactured clearances of the No. 4 seals were larger than most of the previous seals. However, after the initial chill-down, its indicated clearances dropped below those of seal set Nos. 2 and 3. This showed the diminished environmental effect resulting from the addition of the labyrinth seal, and the better thermal isolation it caused. Because supply pressures were held constant during the run, the tendency for the inboard seal flow to strongly affect the outboard seal could not be established.

The arguments again underscore the need for good clearance and flow measurements. Also, given the strong system interactions which effect clearance, future efforts should incorporate an extensive thermal analyses.

3.6.5.6 Seal Temperature. The importance of both seal and runner temperatures in determining clearance and leakage flows has already been established. Runner temperatures are probably more important because of the higher

expansion rate of Inconel. However, because the runner rotates temperature measurements are virtually impossible and were not attempted during the program. At best, seal ring temperatures provide only part of the desired relationship and help to establish trends.

One effect common to all of the seals was the extremely low seal temperature that resulted at very low helium flow rates. Temperatures of -70 to -90°C (-94 to -130°F) were recorded. This is not unreasonable because the only source of heat is that transmitted through the seal housing from the outside air. For the first three seal sets, the rate of change of seal temperature with supply pressure was very high at low pressures and gradually tapered off at intermediate and high pressures.

The No. 4 seal data did not permit a parallel assessment. The temperature data given in Figure 3-50 did show, however, that with no flow (which was the case after the tester shut down), the seal temperatures did reach -70°C (-94°F). However, when a small flow was present, the temperatures quickly rose to -10 to $+10^{\circ}\text{C}$ (14 to 50°F). (See the -100 to -60 min period on Figure 3-50.) Figure 3-82c illustrates the effects. The effects of speed on seal temperatures were significant in most cases. Seal set Nos. 1 and 3 showed a roughly parallel downward shift of the temperature supply pressure curves as speed increased (see Figure 3-82d). The temperature data of seal set No. 2 did not show a clean trend. Seal set No. 4 also exhibited a temperature decrease as speed increased.

A last observation worthy of mention is the effect illustrated in Figures 3-82e and 3-82f. This was described in the latter part of Subsection 3.2.2. Figure 3-82d shows several curves of flow and temperature versus pressure drop across the outboard seal of seal set No. 2. The curves represent high, medium, and low outboard drain pressures and show that while as outboard seal flow increased steadily as the pressure drop increased, the corresponding seal temperature curves showed major discontinuities. Figure 3-82f plots the same flow and temperature data plus the total flow from both seals versus supply pressure. The figure also shows the temperature curves falling much closer together. Since the inboard seal drain pressure was the same for all the runs, its flow, and hence the total flow from both seals,

function of supply pressure. Therefore, total flow appeared to be a much greater factor in determining the outboard seal temperature than was the outboard seal flow.

3.6.6 Dynamic Performance

The dynamic performance of the seals tested proved to be very good. However, the testing was not designed to evaluate this aspect in any particular fashion, therefore, no controlled excitations were applied. Neither were the operating conditions intentionally changed to require the seals to run in a region where self-excited motions were predicted to take place; i.e., the low friction region. In fact, quite the contrary, drain pressure requirements resulted in the seals operating almost totally in the high friction region of the operating map where dynamic motions are heavily retarded by substantial friction forces.

Seal runner whirl orbit diameters were generally in the 0.005 to 0.008 mm (0.0002 to 0.0003 in.) range except for some of the high speed runs where orbit diameters reached 0.010 to 0.013 mm (0.0004 to 0.0005 in.). For most of these runs, the seals remained motionless which is the predicted response considering the operating region. It is also the preferred response since the whirl orbits of the sizes described are small in relation to the operating clearances generally observed.

Seal motions did arise on several occasions. The principal occurrence was with the inboard seal of seal set No. 3. The seal ring developed an in-phase, generally elliptical orbit. The orbit was observed at all three test speeds, 3665, 4188, and 4712 rad/s (35,000, 40,000, and 45,000 r/min) and became larger in amplitude as the supply pressure was increased. The maximum orbit diameter was approximately 0.025 to 0.030 mm (0.001 to 0.0012 in.). Since the supply pressures and shaft speed placed seal operation clearly in the high friction region, the motions are baffling. Details of the occurrence are provided in Subsection 3.3.2.

In summary, the tests did show that the seals were generally well behaved dynamically, but in view of the lack of specific dynamic testing and the

occurrence of large whirl, it is suggested that future studies give particular attention to this area. Analytical studies should consider how a seal ring might respond in the presence of a significant bypass flow.

3.6.7 Material Considerations

All three seal failures were due to rubs between one of the seal rings and the runner. While each of these was precipitated by a different mechanism, the end result was unacceptable damage to both parts. Two combinations of materials were tried. The first consisted of P5-N formulation of carbon graphite by Purebond for the seal ring against a tungsten carbide coating using a silicon carbide binder on an Inconel 718 runner. This was used for the first three seal tests. Two failures occurred with this combination resulting in substantial wear of both the seal ring and runner. Also, numerous surface cracks and some delamination of the carbide coating occurred on the runner. Very high temperatures had been generated at the rubbing interface and were responsible for the cracking and rapid deterioration. The second combination which was used for the fourth seal set did not work any better. It consisted of the same seal ring material, however the runner had an electrolyzed surface with Inconel 718 again as the base material. The failed parts again showed evidence of rapid wear and high temperatures. While no cracks were observed on the runner surface, the grooving and wear were no more acceptable than the damage of the previous runners.

Given these results, it is clear that additional work needs to be done to identify or develop material combinations that are more suitable. While good strength properties are necessary and important, good rubbing properties at both low and high temperatures are key. Low coefficients of friction and high thermal diffusivity are very important. Other necessary properties need to be identified.

Another aspect that needs to be considered is the match-up of coefficients of expansion of the seal ring and runner materials. The base materials used in the testing have substantially different rates, $10.8 \mu\text{m/m-}^{\circ}\text{C}$ ($6.0 \mu\text{in./in.-}^{\circ}\text{F}$) for the Inconel 718 runner and $4.3 \mu\text{m/m-}^{\circ}\text{C}$ ($2.4 \mu\text{in./in.-}^{\circ}\text{F}$) for the P5-N carbon graphite seal rings. The much higher

rate for the runner results in a tendency for the runner to rapidly grow into the seal due to the heat generated during the initial stages of a rub. This would aggravate a partial rub and, because the operating clearances are very small, would quickly result in a progression to a full rub. Material combinations with closer expansion rates or in which the seal ring material has higher rates than the runner material would help to alleviate the problem.

TABLE 3-1

SEAL DIMENSION SUMMARY

Seal Set Number		Serial Number	Mating Surface Diameter (mm)	Radial Clearance (mm)	Mating Surface Diameter (mm)	Radial Clearance (mm)
Design Dimensions:	Outboard Ring	--	50.028-50.033	0.009-0.015	---	---
	Inboard Ring	--	50.020-50.025	0.015-0.011	---	---
	Runner	--	50.002-50.010	---	---	---
1	Outboard Ring	108302	50.030-50.033	0.013-0.017	50.079-50.086	0.025-0.047
	Inboard Ring	108306	50.020-50.024	0.008-0.012	---	---
	Runner	078303	---	---	---	---
	Otb. Sur.	--	50.000-50.004	---	49.992-50.028	---
	Inb. Sur.	--	50.000-50.004	---	49.995-50.002	---
2	Outboard Ring	108304	50.029-50.033	0.009-0.012	50.038-50.041	---
	Inboard Ring	108308	50.023-50.025	0.006-0.008	50.033-50.035	---
	Runner	078302	---	---	---	---
	Otb. Sur.	--	50.009-50.011	---	50.009-50.011	---
	Inb. Sur.	--	50.009-50.011	---	50.009-50.011	---
3	Outboard Ring	108305	50.029-50.030	0.009-0.011	50.038-50.089	0.001-0.044
	Inboard Ring	108301	50.020-50.025	0.004-0.008	50.030-50.033	---
	Runner	078302	---	---	---	---
	Otb. Sur.	--	50.009-50.011	---	50.000-50.025	---
	Inb. Sur.	--	50.009-50.011	---	50.005-50.008	---
4	Outboard Ring	108301	50.029-50.033	0.016-0.018	---	---
	Inboard Ring	108302	50.020-50.025	0.013-0.016	---	---
	Runner	078304*	---	---	---	---
	Otb. Sur.	--	49.997-	---	---	---
	Inb. Sur.	--	49.992-49.995	---	---	---

*MTI

TABLE 3-2
ACCELERATION RUN PERFORMANCE DATA - SEAL SET NO. 2

Run No.	Acceleration Rate H - High/L - Low	Maximum Shaft Speed (rad/s)	Helium Supply Pressure (P12) (kPa, Abs.)	Outboard Drain Pressure (P2) (kPa, Abs.)	Outboard Seal Flow (kg/s x 10 ⁴)	Inboard Seal Flow (kg/s x 10 ⁴)
1-5	H	4,188	931	517	-	-
6	L	↓	↓	↓	8.1	9.1
7-11	H	↓	↓	↓	-	-
12	L	↓	↓	↓	8.5	7.8
13-17	H	↓	↓	↓	-	-
18	L	↓	↓	↓	8.9	7.4
19-23	H	↓	↓	↓	-	-
24	L	↓	↓	↓	9.2	6.3
25-29	H	↓	↓	↓	-	-
30	L	↓	↓	↓	9.3	6.2
30a*	L	↓	↓	↓	6.7	17.2
31-35	H	↓	↓	↓	-	-
36	L	↓	↓	↓	6.5	15.4
37-46	H	↓	↓	↓	-	-
47	L	↓	↓	↓	7.6	11.7
48-57	H	↓	↓	↓	-	-
58	L	↓	↓	↓	8.8	8.8

*Run 30a was a repeat of Run 30, after a brief shutdown to change chart paper.

TABLE 3-3

ACCELERATION RUN PERFORMANCE DATA - SEAL SET NO. 3

Run No.	Acceleration Rate H - High/L - Low	Maximum Shaft Speed (rad/s)	Helium Supply Pressure (P12) (kPa, Abs.)	Outboard Drain Pressure (P2) (kPa, Abs.)	Outboard Seal Flow (kg/s x 10 ⁴)	Inboard Seal Flow (kg/s x 10 ⁴)
1-5	H	4,712	1,069	517	-	-
6	L		↓		10.4	11.5
7-11	H				-	-
12	L		↓		9.6	13.1
-			1,206		10.8	14.1
13-17	H		↓		-	-
18	L				9.6	17.3
19-23	H		↓		-	-
24	L				9.2	25.6
-			1,344		9.2	27.9
25-29	H		↓		-	-
30	L				8.8	28.3
31-35	H		↓		-	-
36	L				8.8	27.5
-			1,482		9.8	31.2
37-41	H		↓		-	-
42	L				8.8	31.1
43-47	H		↓		-	-
48	L				8.9	31.3
48a*	L		↓		-	-

*Run 48a was a repeat of Run 48, after a brief shutdown to change reels of magnetic tape.

TABLE 3-4

SEAL INSPECTION SUMMARY

Seal Set Number	Outboard Ring S/N	Inboard Ring S/N	Runner S/N Material	Pre-Test Condition	Post-Test Condition
1	108302	108306	078303 Inconel 718 with tungsten carbide coating.	All new parts.	Both seal rings intact. Outboard ring had moderate surface wear. Inboard had no wear. Runner had numerous heat cracks and some delamination of coating.
2	108304	108308	078302 Inconel 718 with tungsten carbide coating.	All new parts.	No wear on seal rings nor runner. Very slight deposit of carbon graphite on axial seal lands of seal housing.
3	108305	108301	078302 Inconel 718 with tungsten carbide coating.	New seal rings; runner from previous test; no evidence of wear.	Seal rings intact. Outboard ring had moderate wear while inboard ring showed none. Heat cracks and some delamination on runner.
4	108301 Integral Probes	108302	078304 (MTI) Inconel 718 with electrolyzed surface.	All new parts.	Outboard ring intact. Inboard ring had radial crack and showed moderate wear. Runner surface galled and worn.

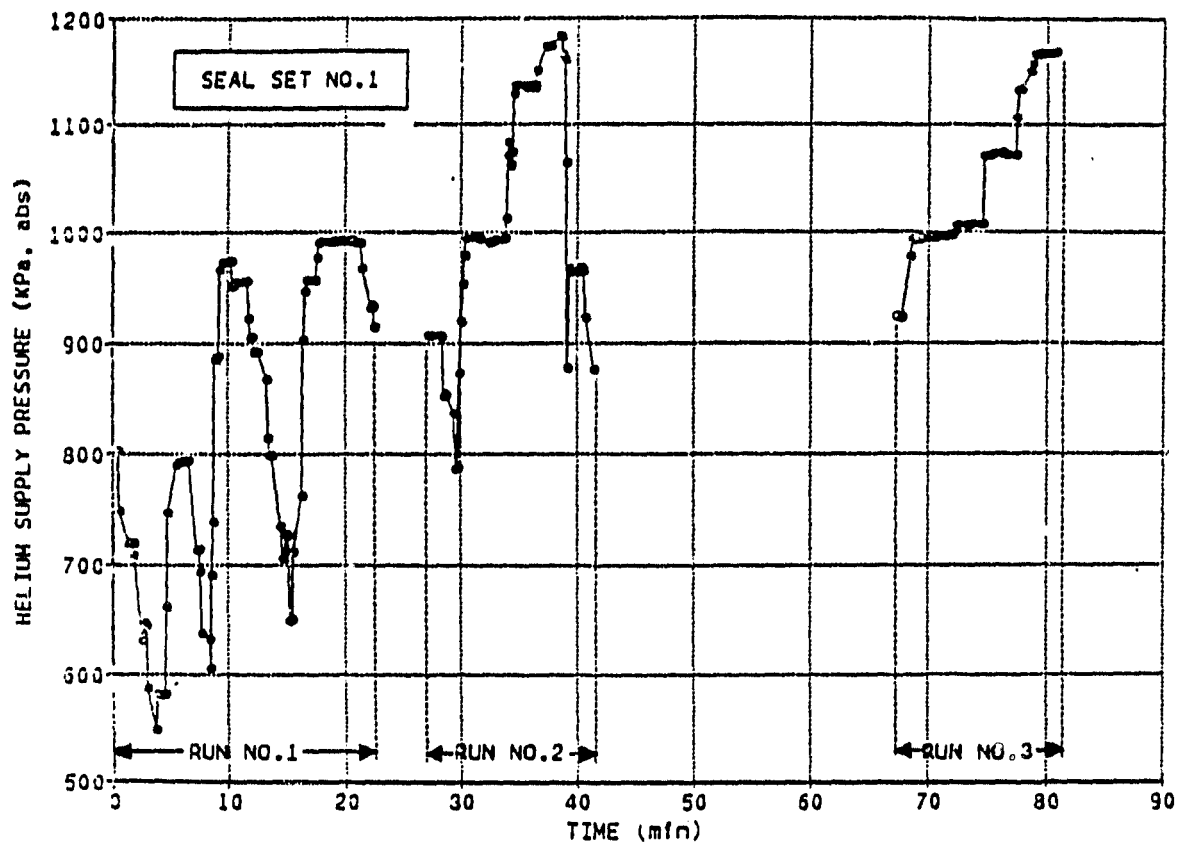


Fig. 3-1 Pressure History - Seal Set No. 1

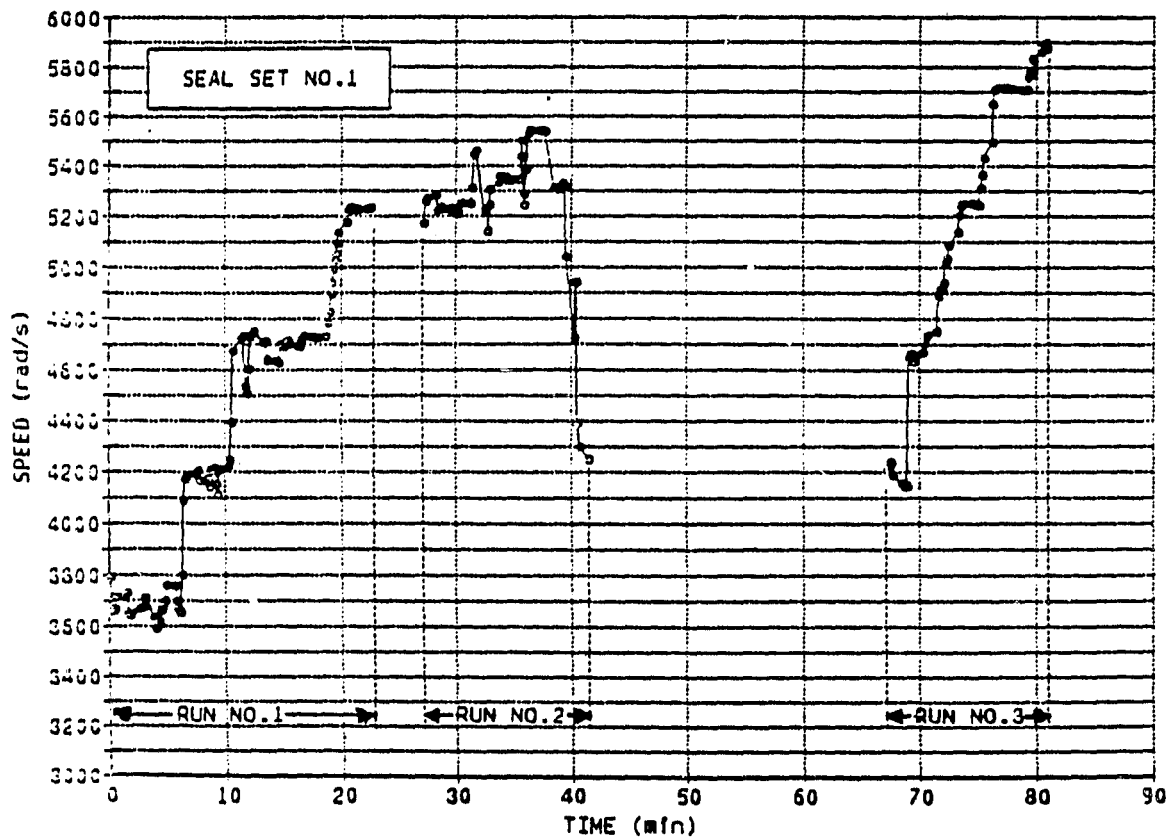


Fig. 3-2 Speed History - Seal Set No. 1

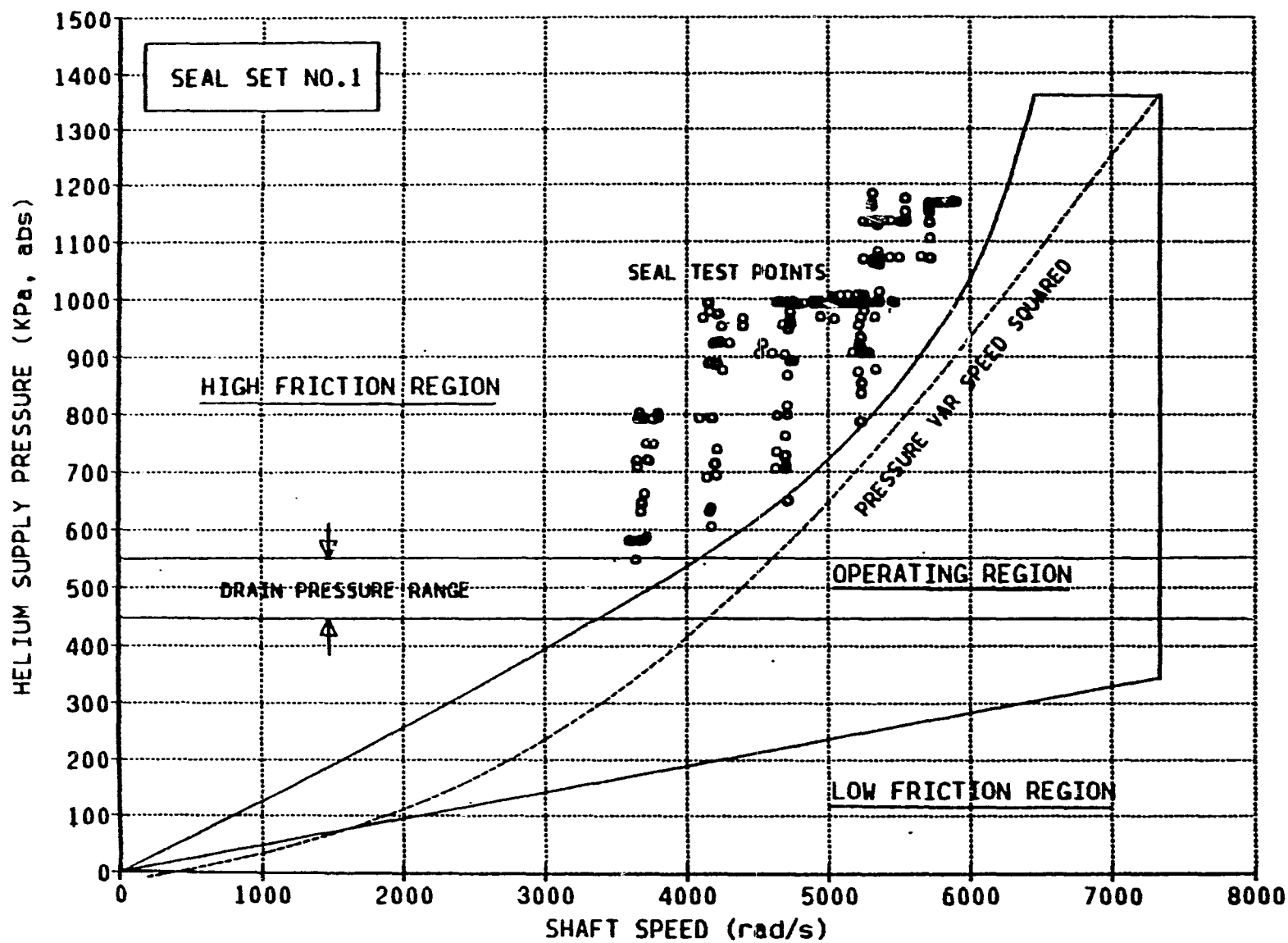


Fig. 3-3 Operating Map for Seal Set No. 1

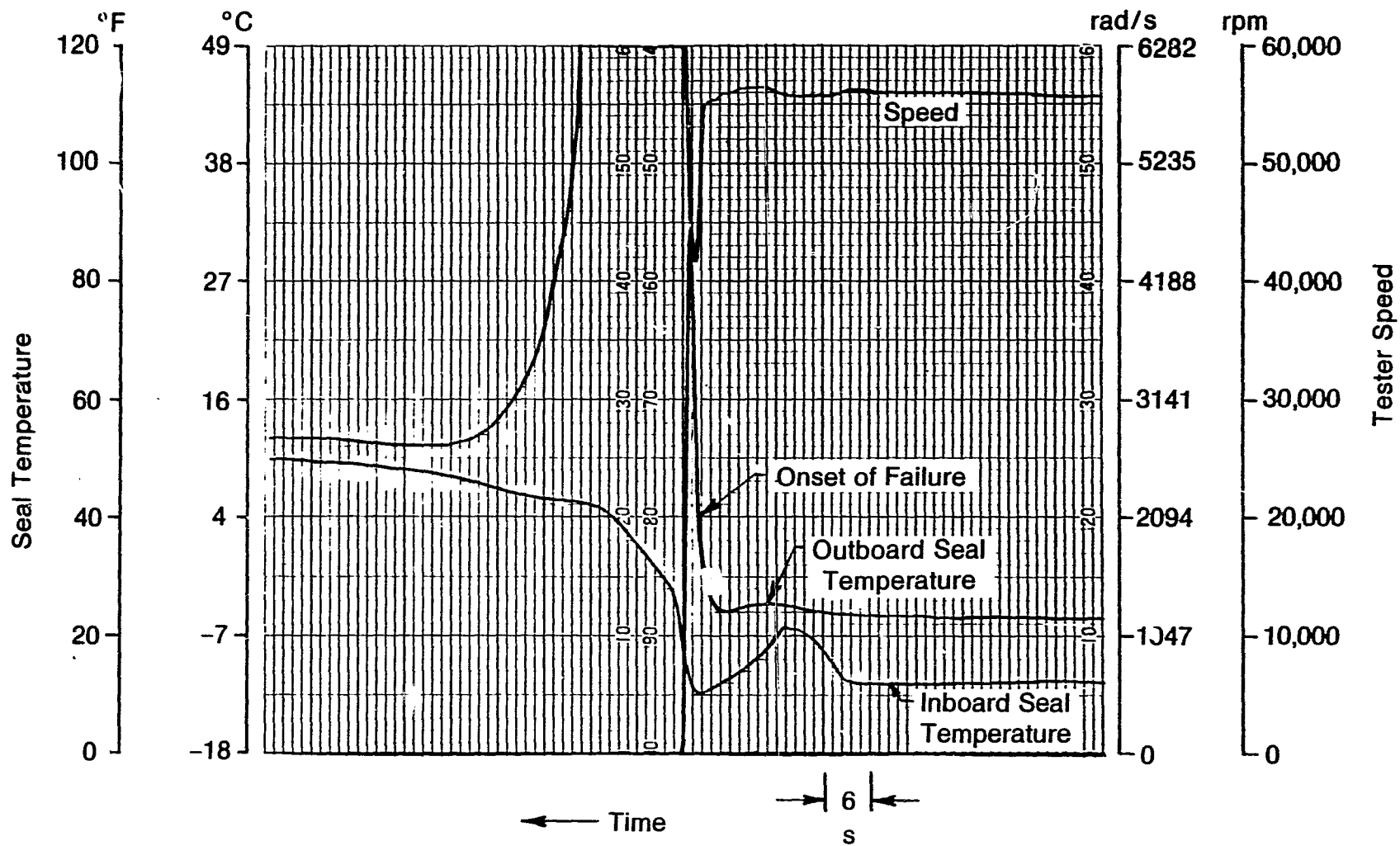


Fig. 3-4 Failure of No. 1 Outboard Seal Ring

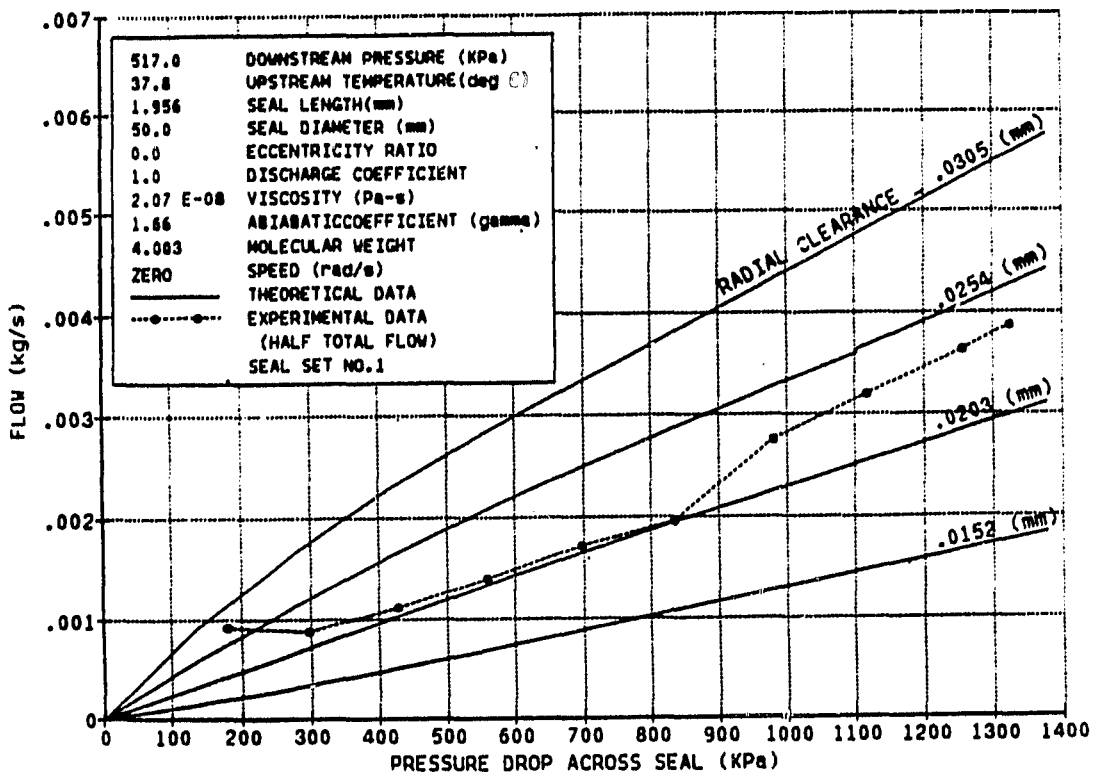


Fig. 3-5 Zero Speed Flow versus Pressure Drop - Seal Set No. 1

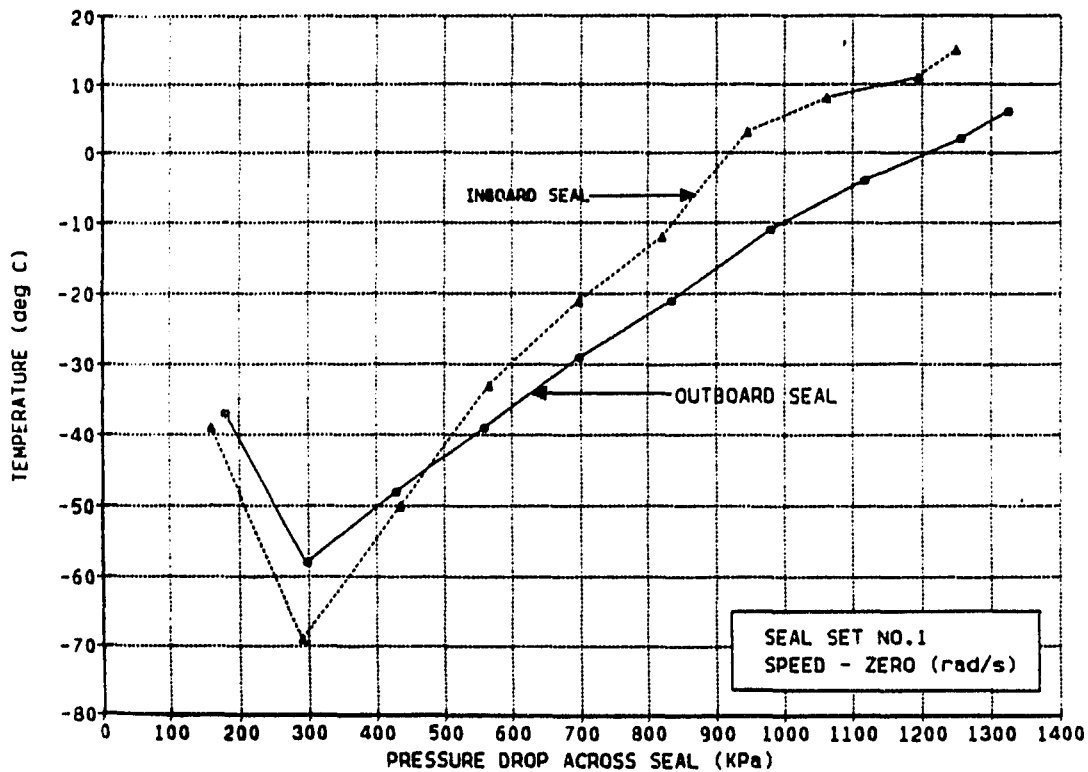


Fig. 3-6 Zero Speed Seal Temperatures versus Pressure Drop - Seal Set No. 1

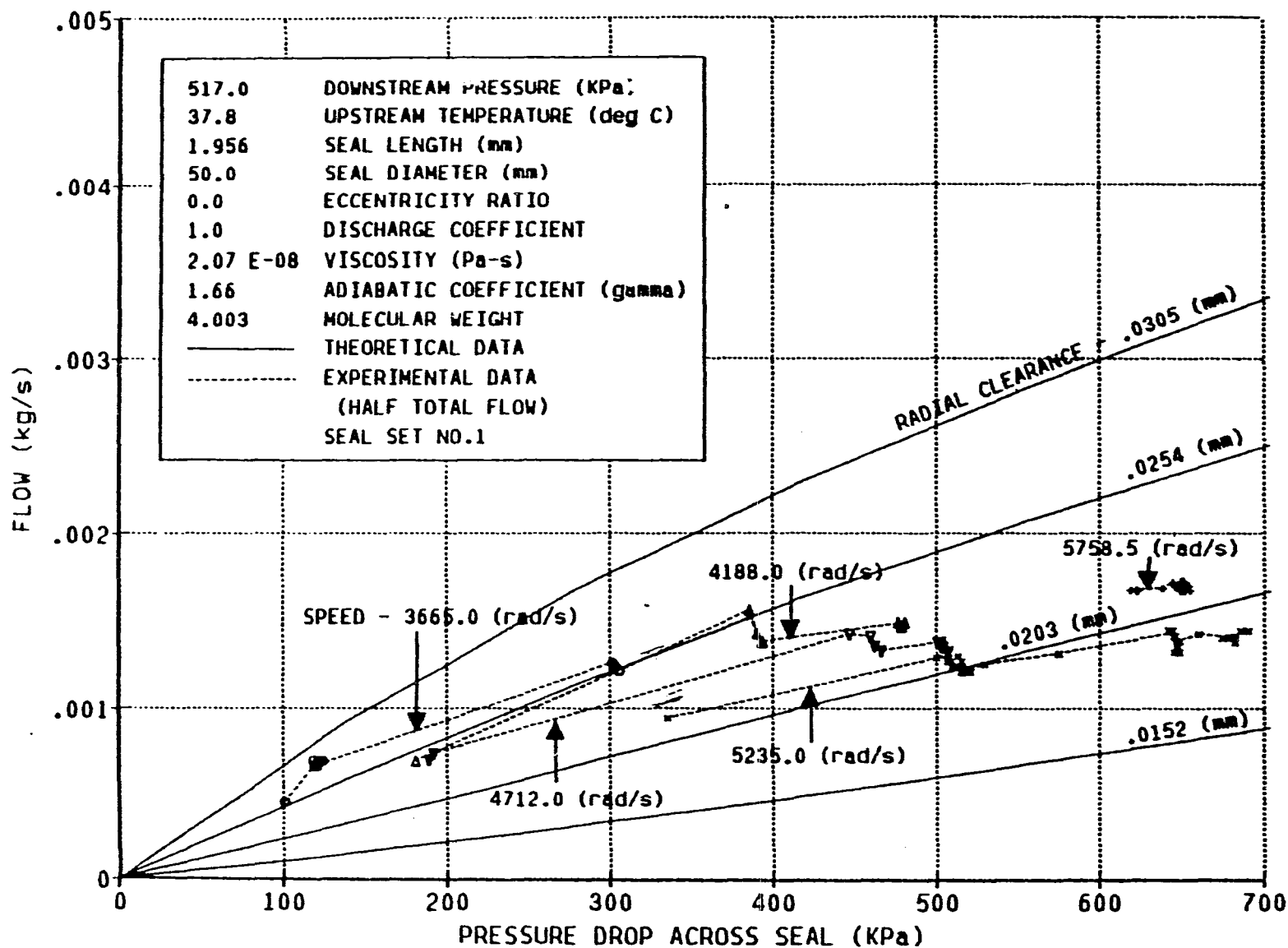


Fig. 3-7 Flow versus Pressure Drop - Seal Set No. 1

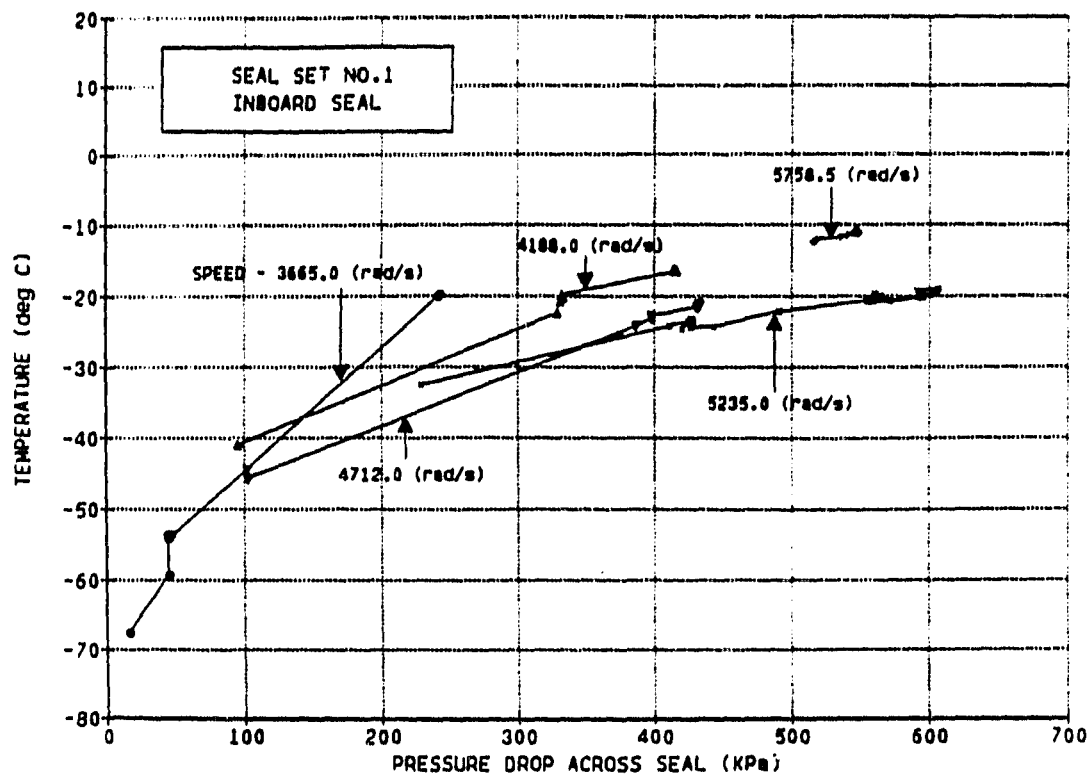


Fig. 3-8 Inboard Seal Temperature versus Pressure Drop - Seal Set No. 1

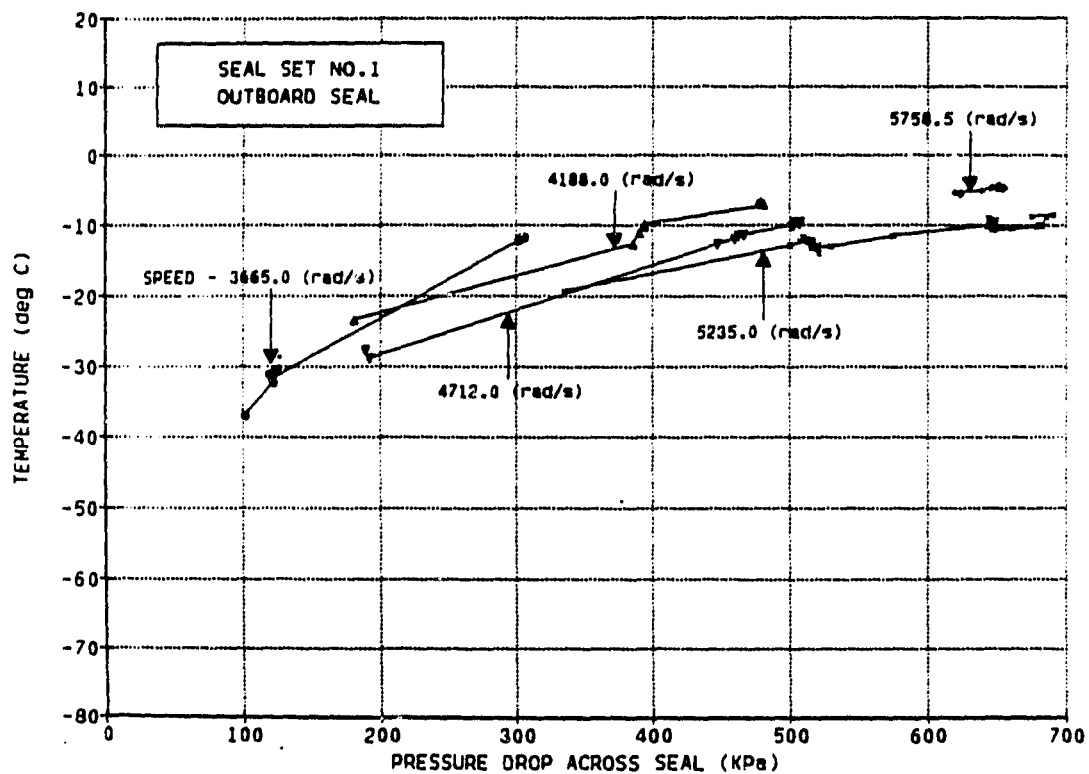


Fig. 3-9 Outboard Seal Temperature versus Pressure Drop - Seal Set No. 1

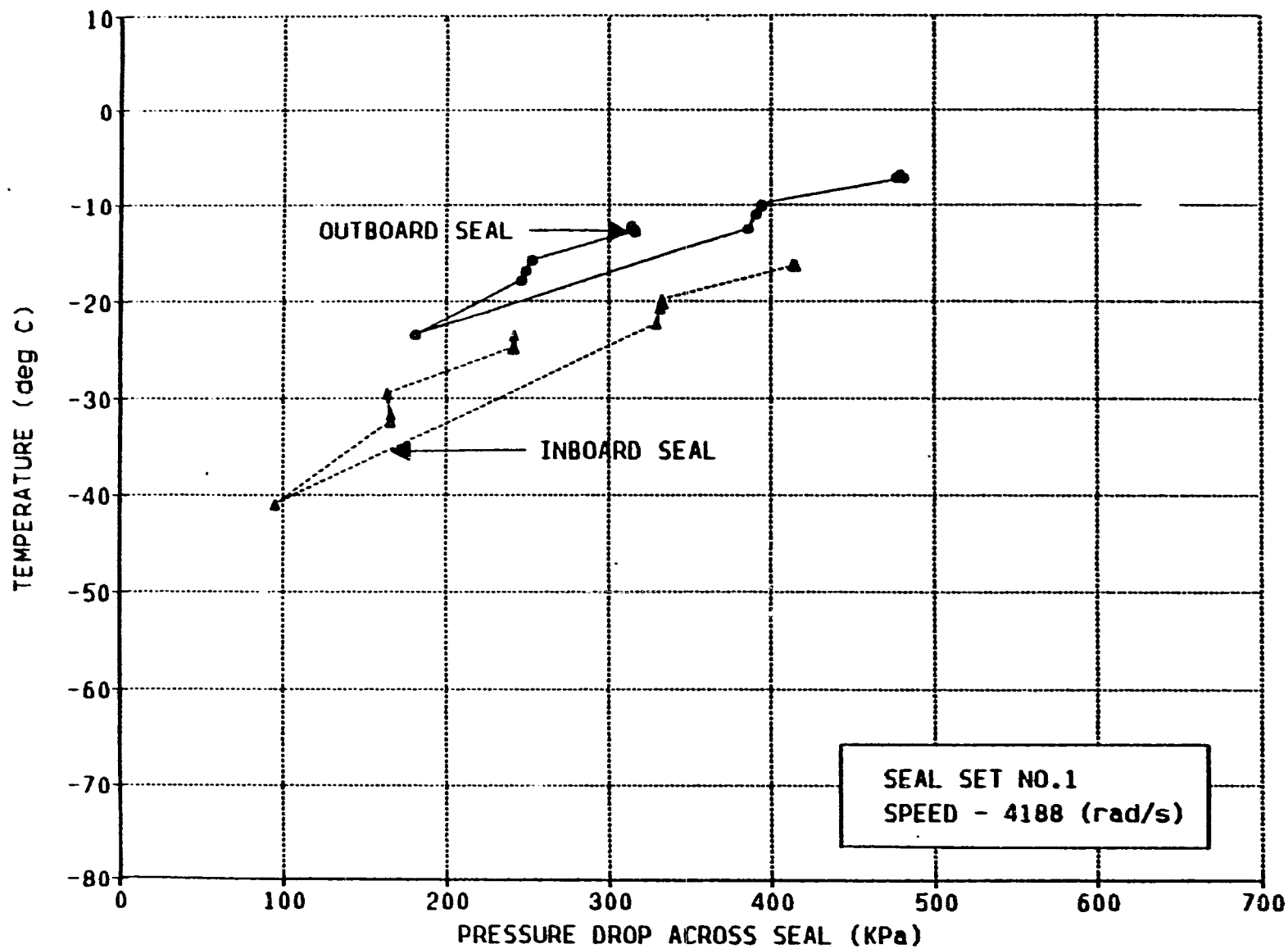


Fig. 3-10 Inboard and Outboard Seal Temperature versus Pressure Drop - Seal Set No. 1

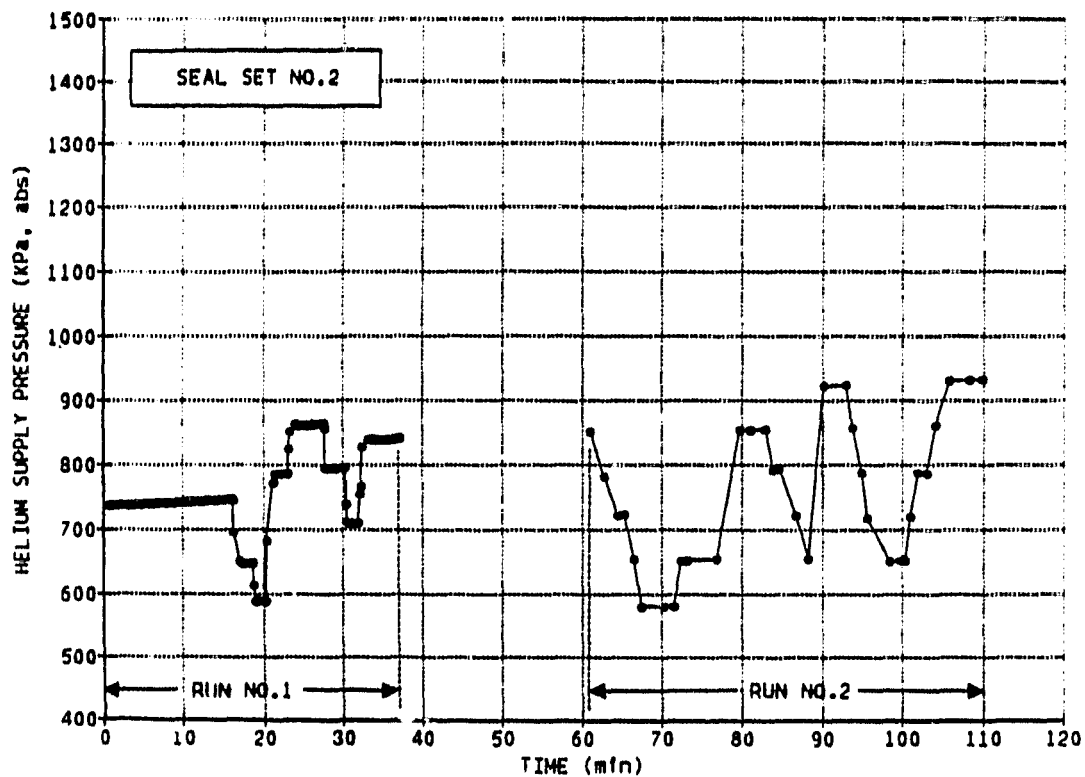


Fig. 3-11 First Day Pressure History - Seal Set No. 2

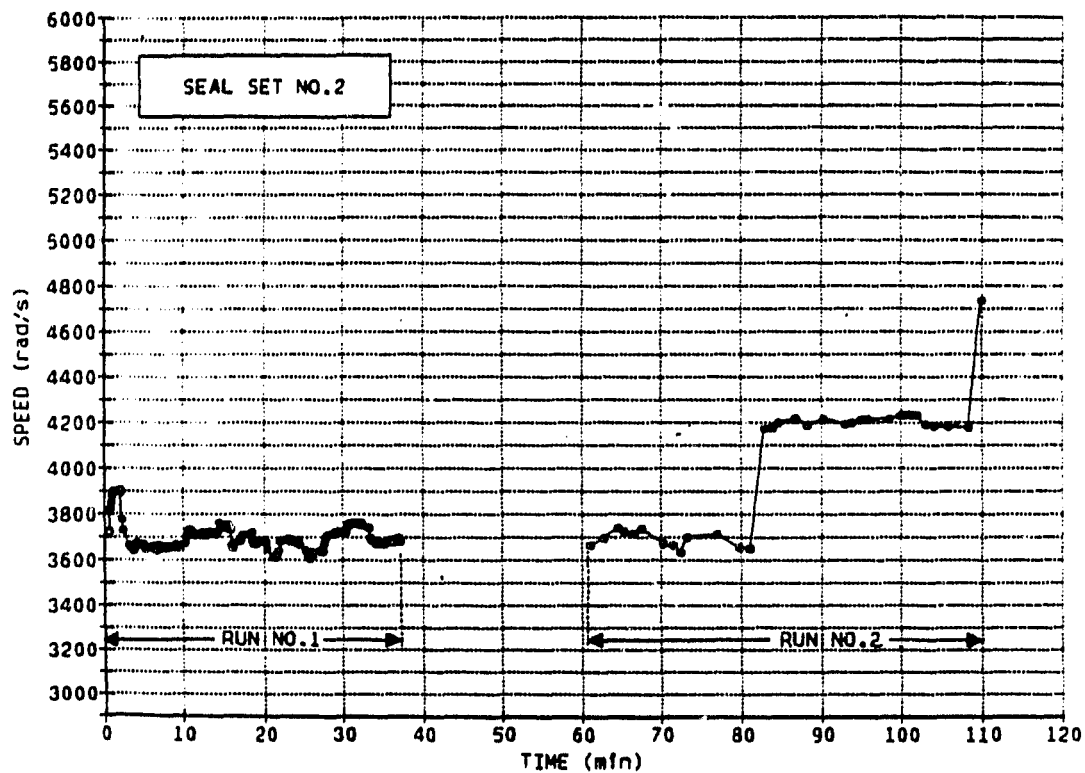


Fig. 3-12 First Day Speed History - Seal Set No. 2

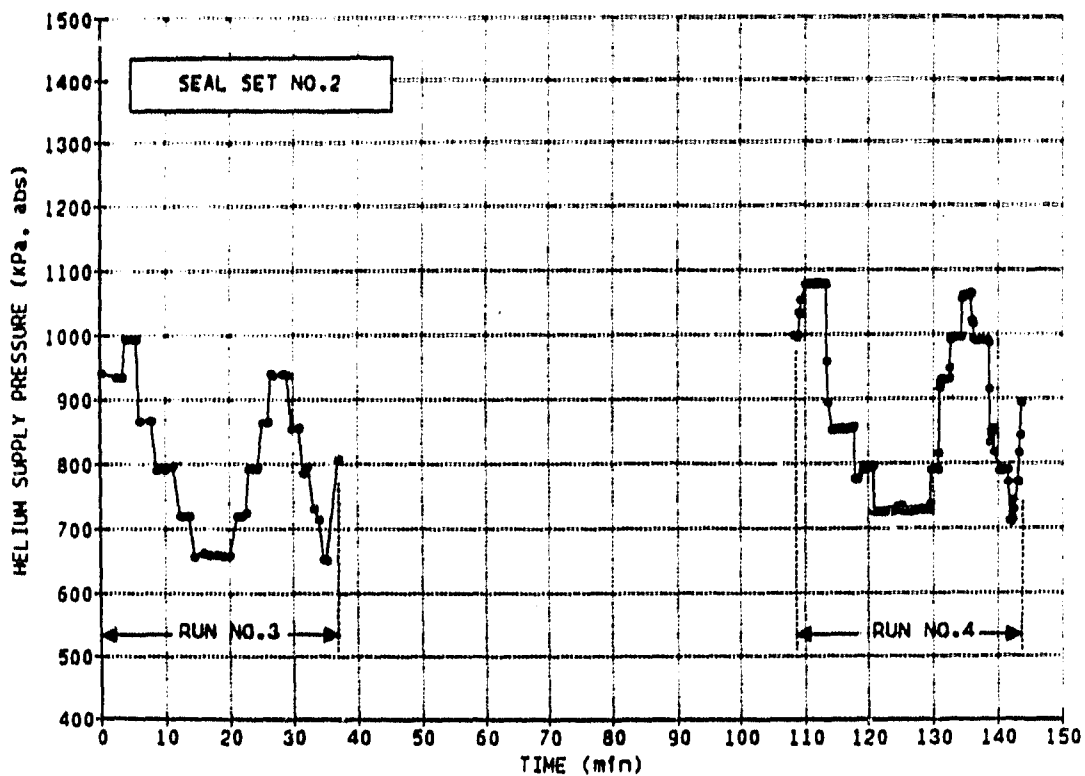


Fig. 3-13 Second Day Pressure History - Seal Set No. 2

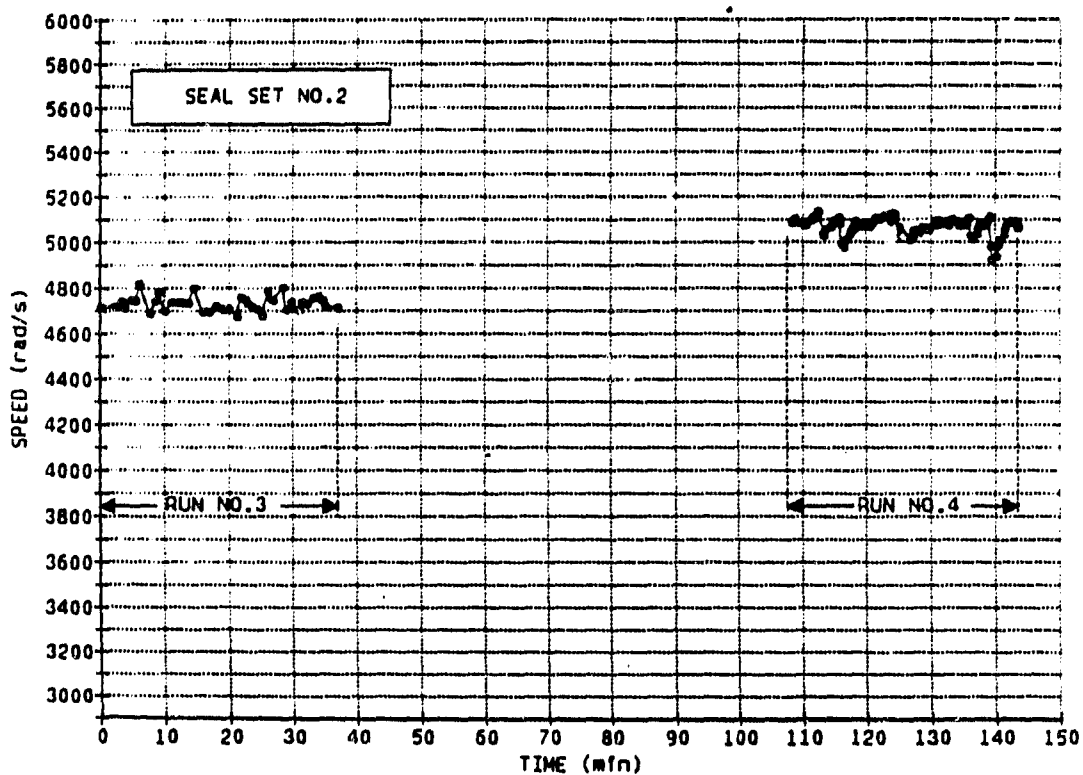


Fig. 3-14 Second Day Speed History - Seal Set No. 2

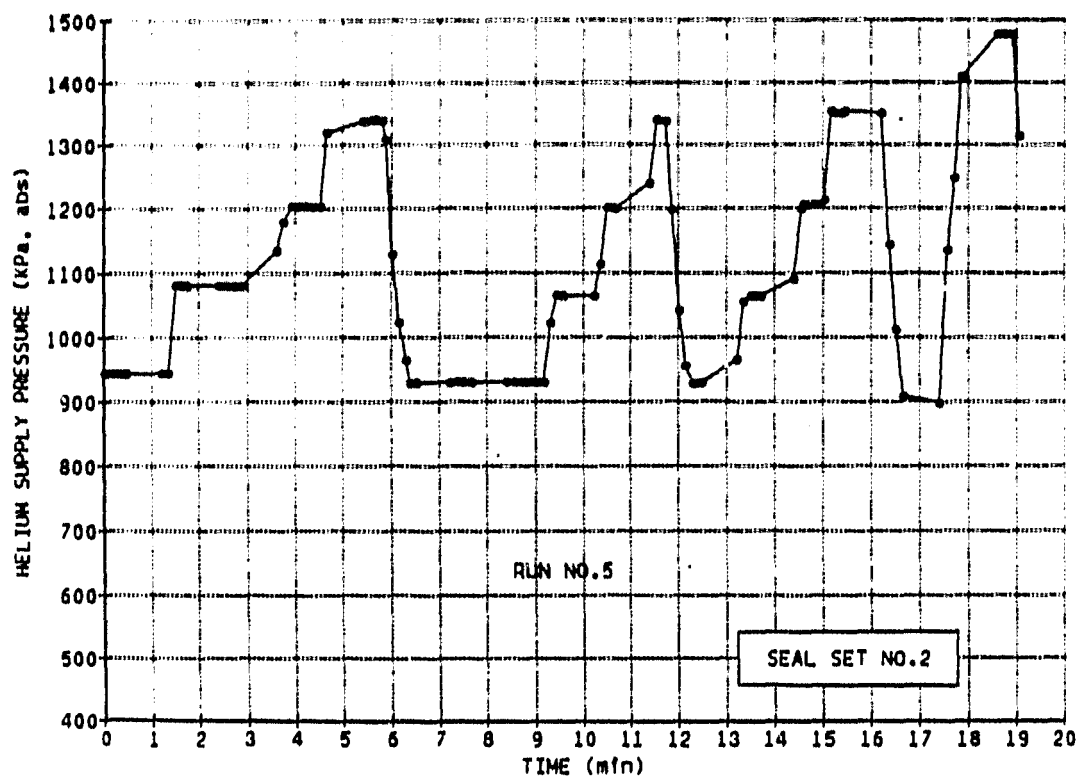


Fig. 3-15 Third Day Pressure History - Seal Set No. 2

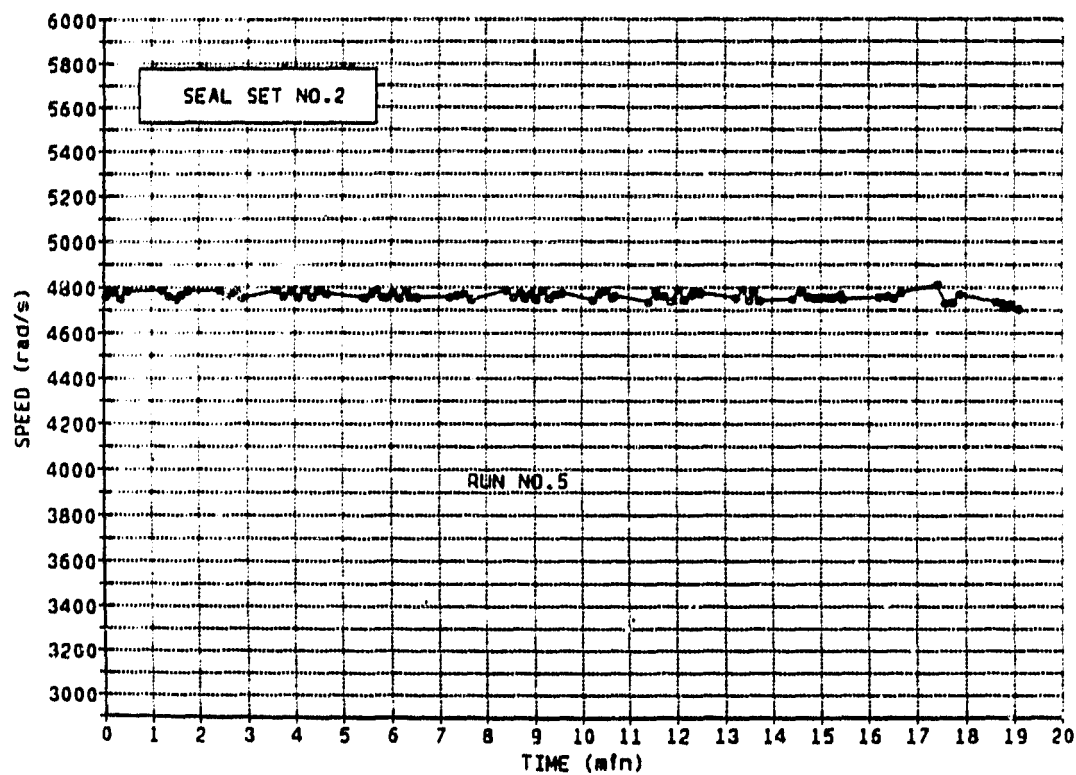


Fig. 3-16 Third Day Speed History - Seal Set No. 2

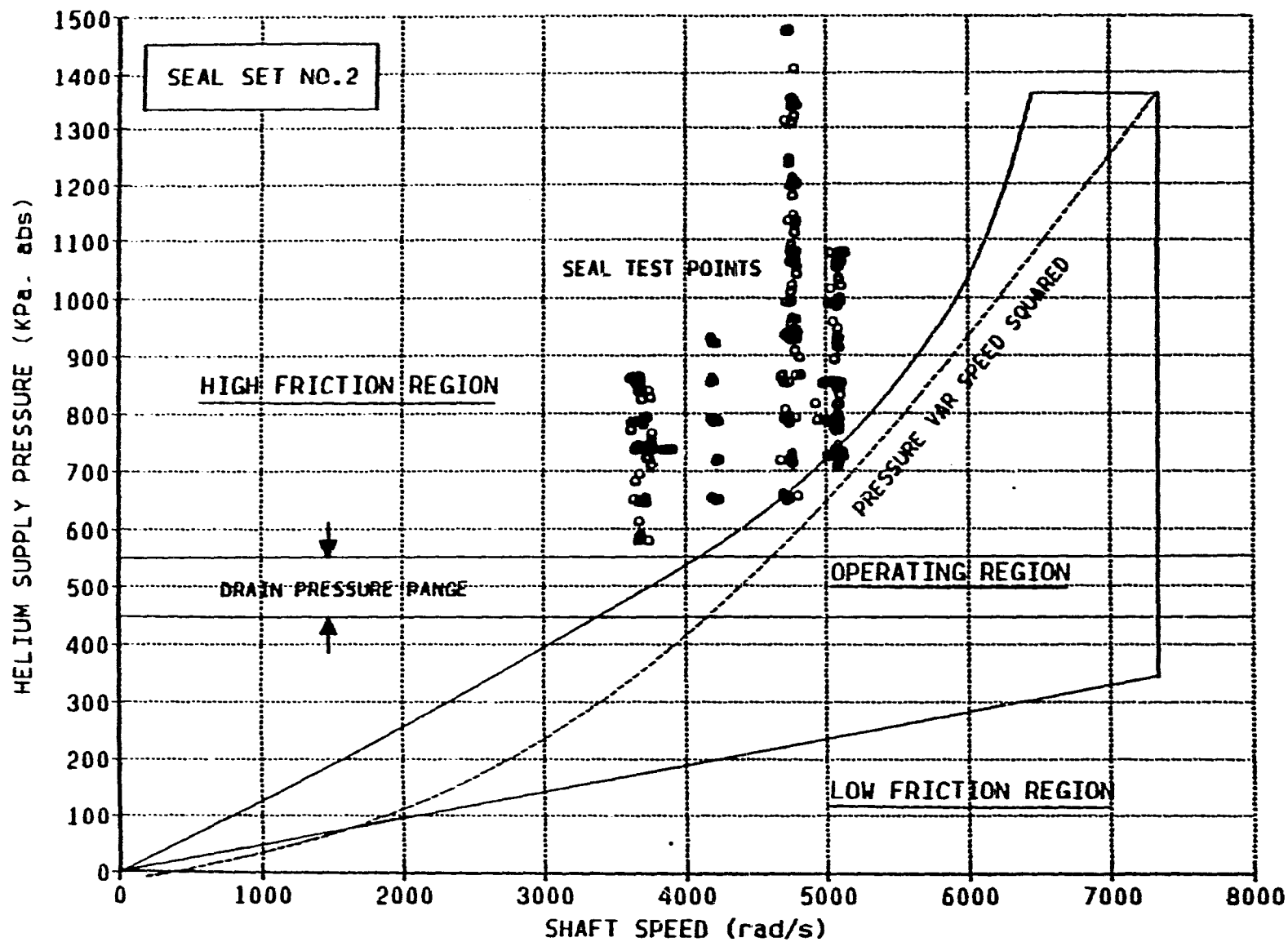


Fig. 3-17 Operating Map for Seal Set No. 2

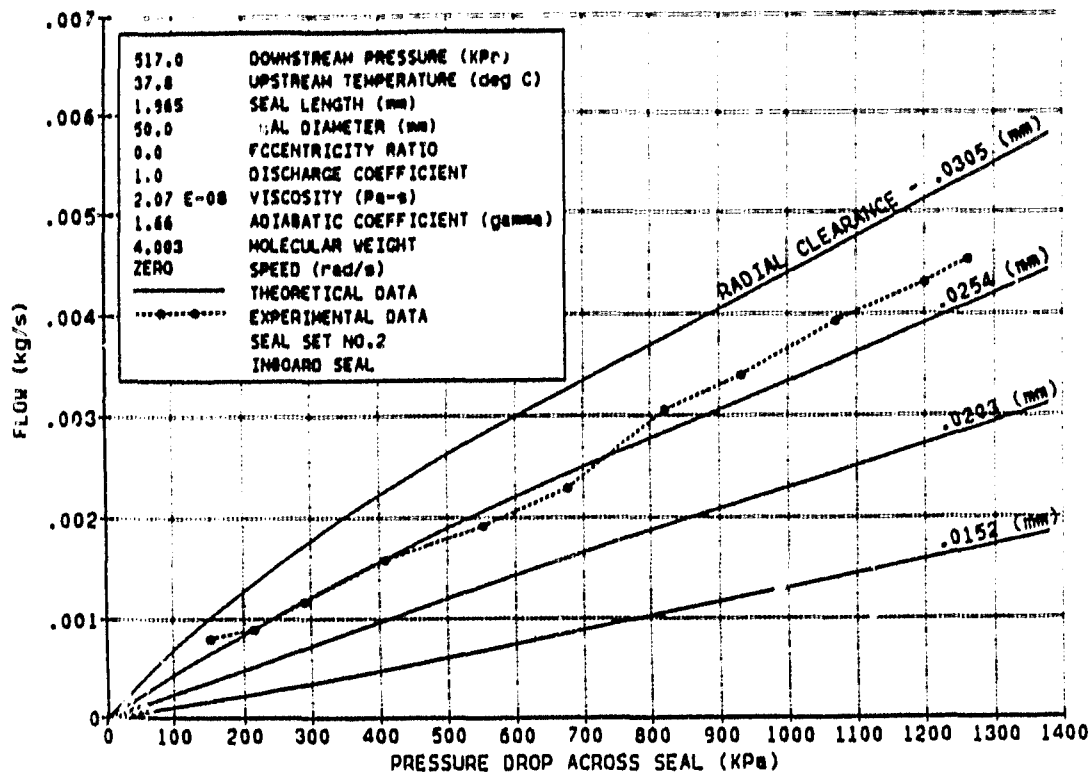


Fig. 3-18 Inboard Seal Flow versus Pressure Drop, Zero Speed - Seal Set No. 2

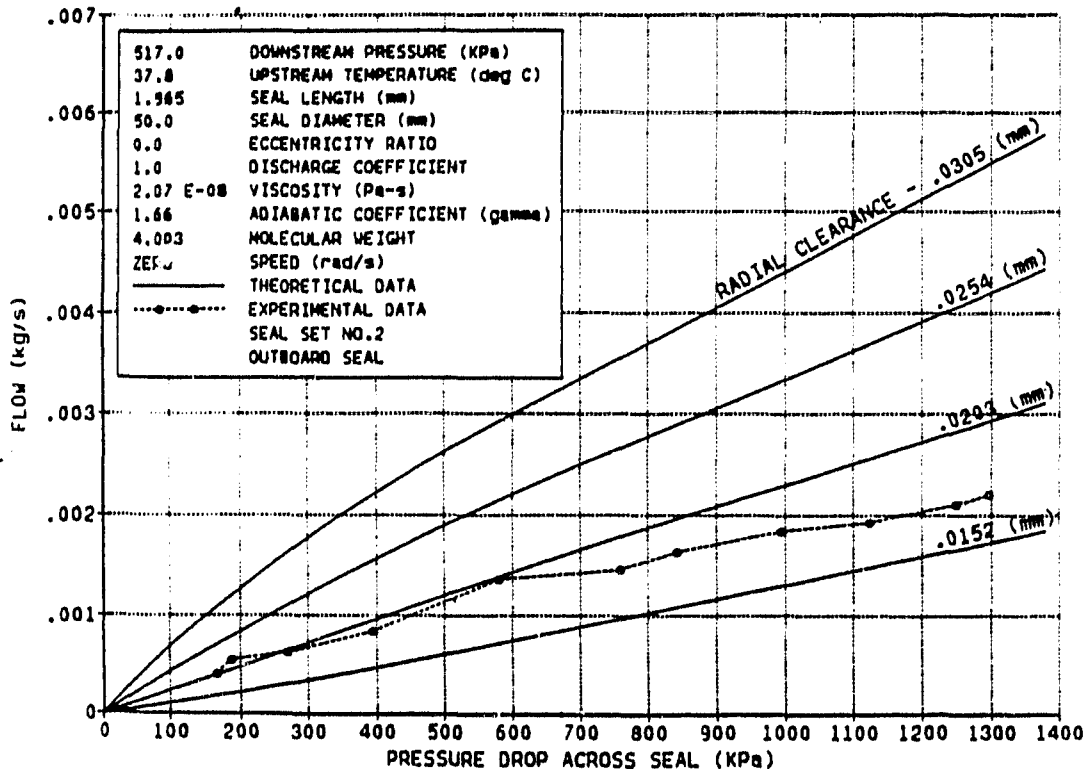


Fig. 3-19 Outboard Seal Flow versus Pressure Drop, Zero Speed - Seal Set No. 2

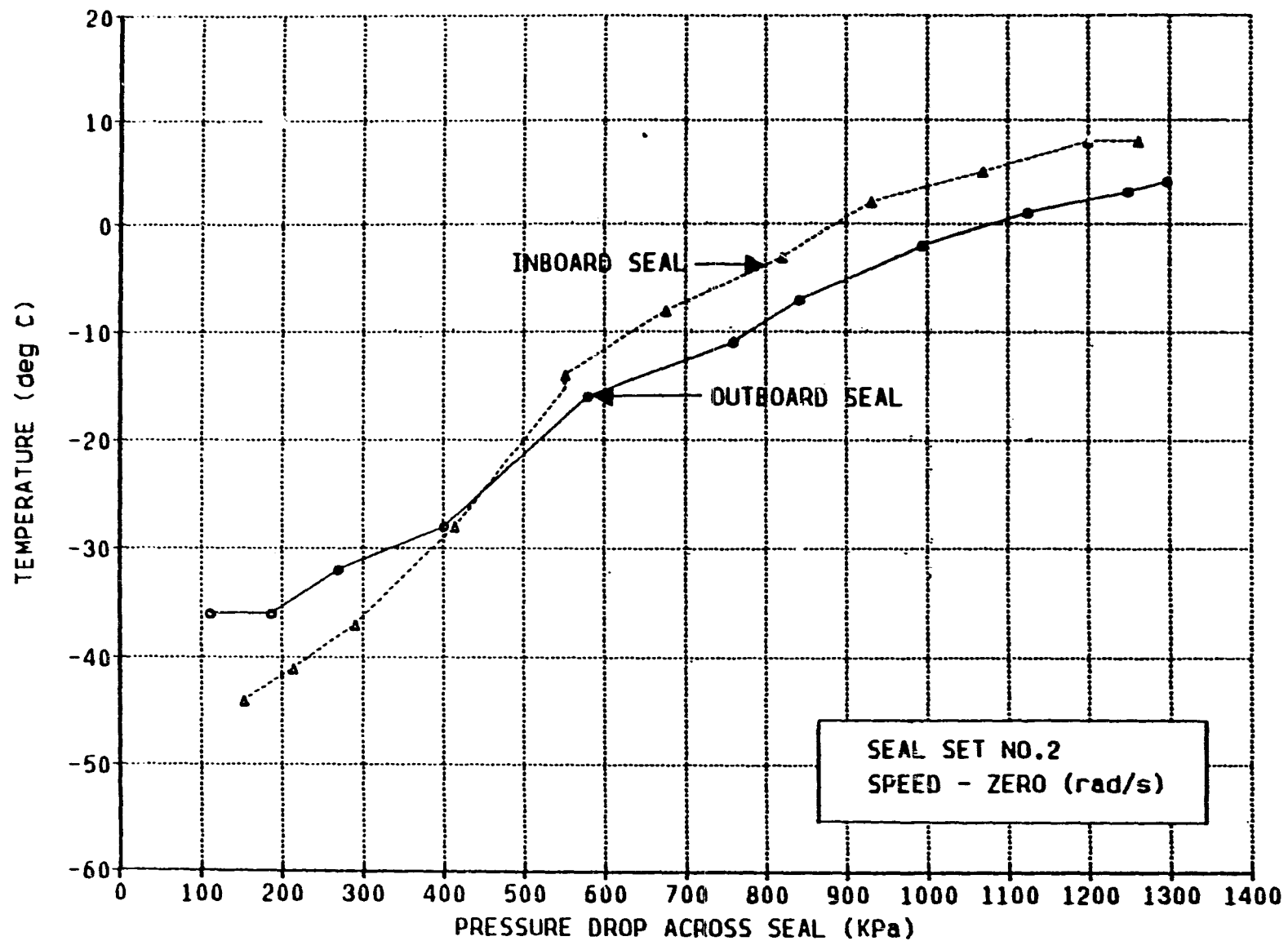


Fig. 3-20 Zero Speed Seal Temperatures versus Pressure Drop - Seal Set No. 2

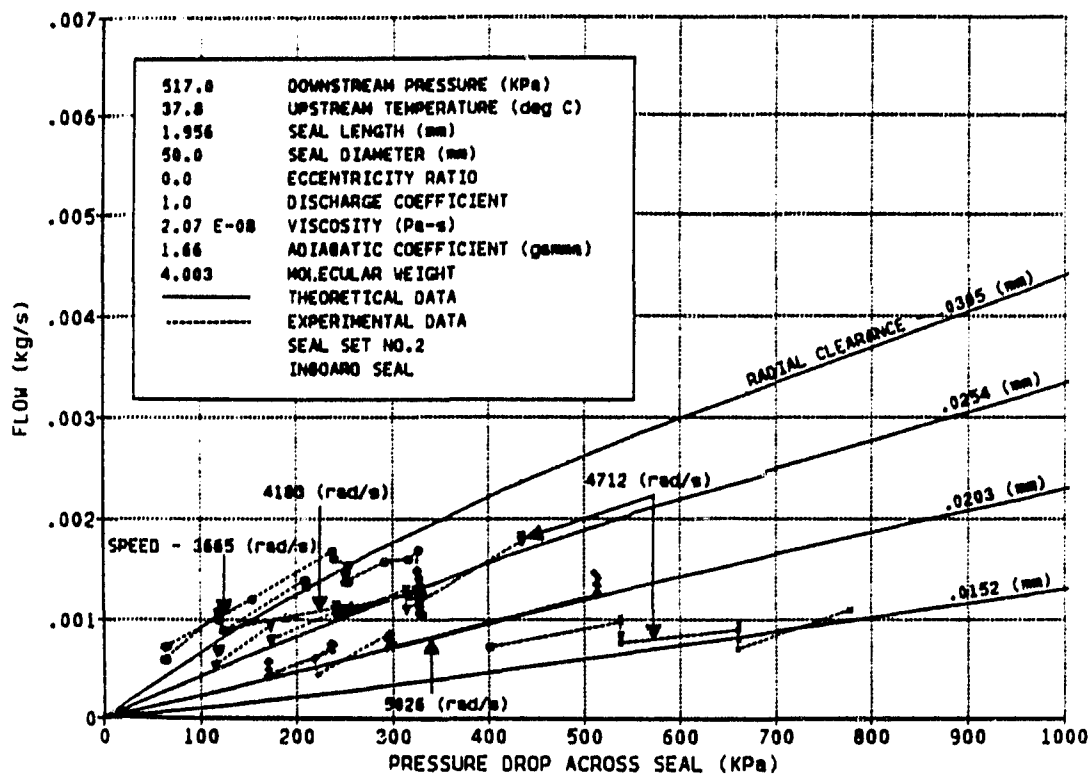


Fig. 3-21 Inboard Seal Flow versus Pressure Drop - Seal Set No. 2

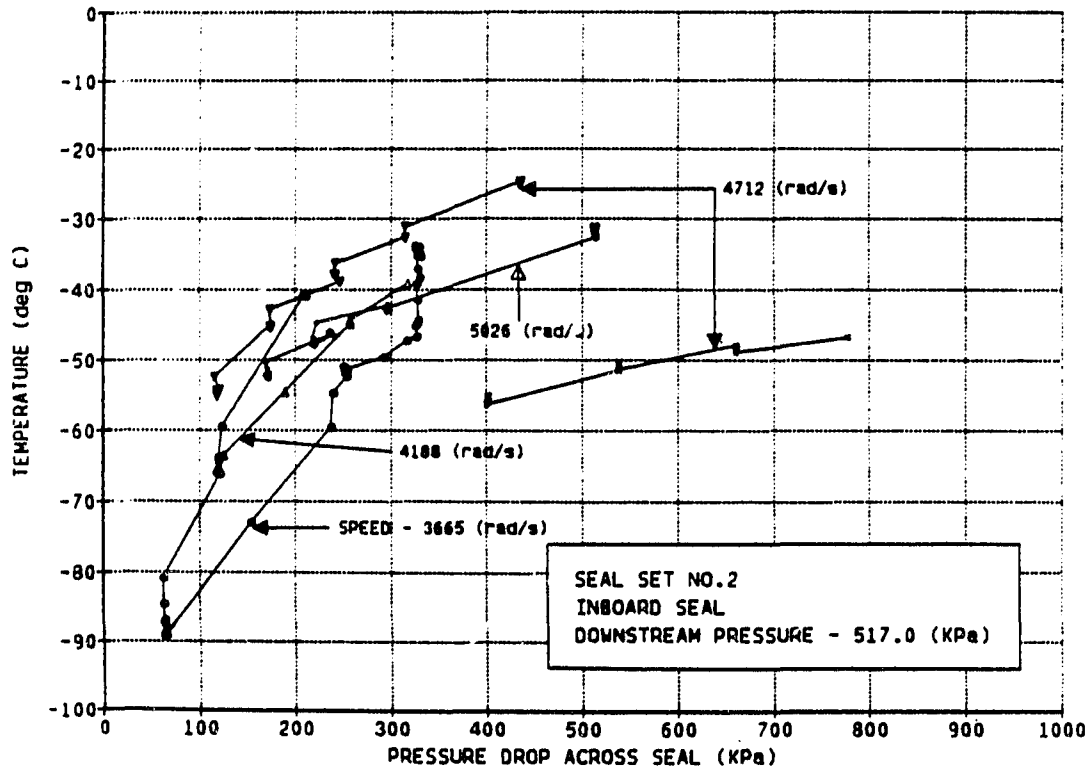


Fig. 3-22 Inboard Seal Temperature versus Pressure Drop - Seal Set No. 2

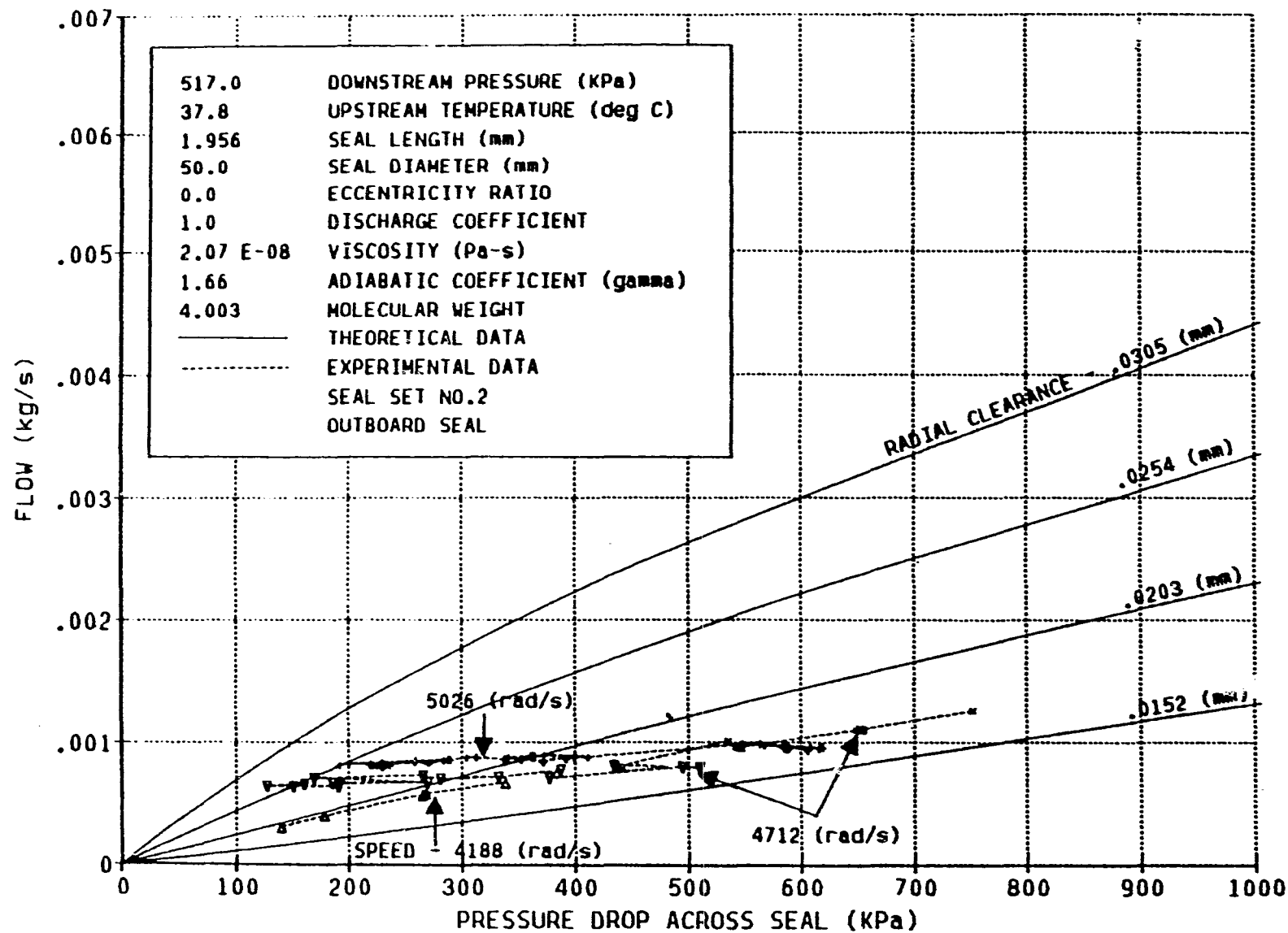


Fig. 3-23 Outboard Seal Flow, 517 kPa Drain Pressure - Seal Set No. 2

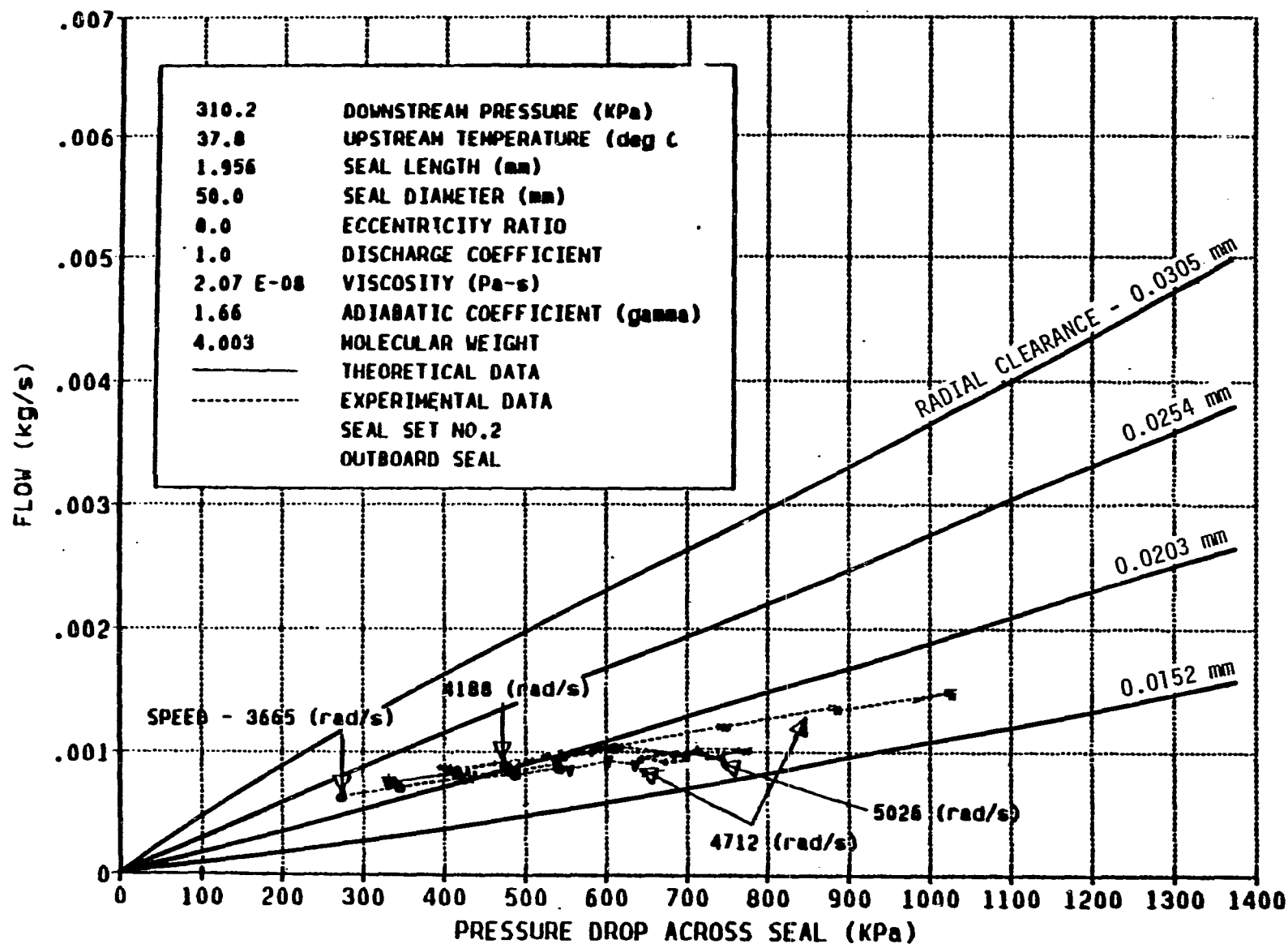


Fig. 3-24 Outboard Seal Flow, 310 kPa Drain Pressure - Seal Set No. 2

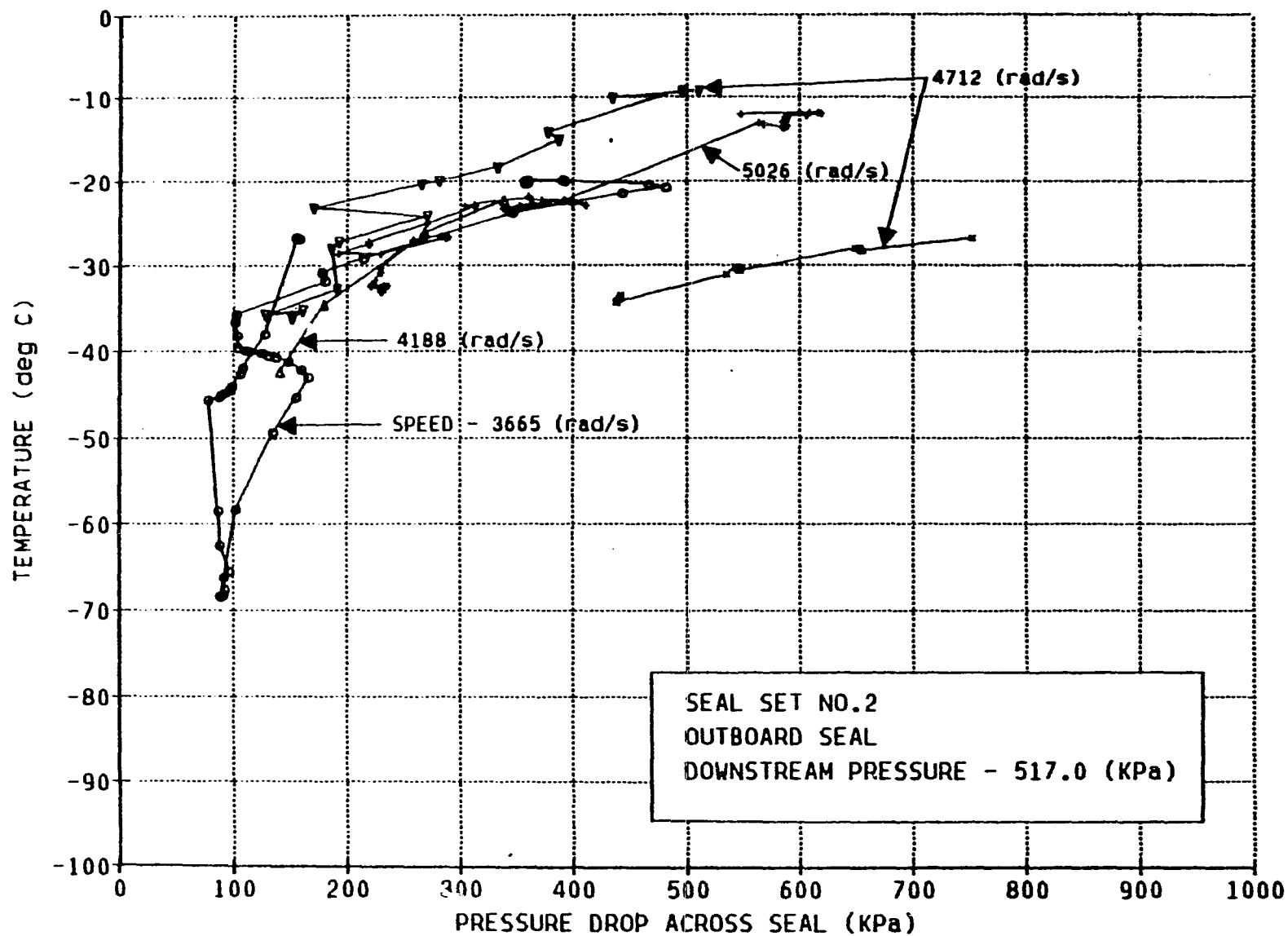


Fig. 3-25 Outboard Seal Temperature, 517 kPa Drain Pressure - Seal Set No. 2

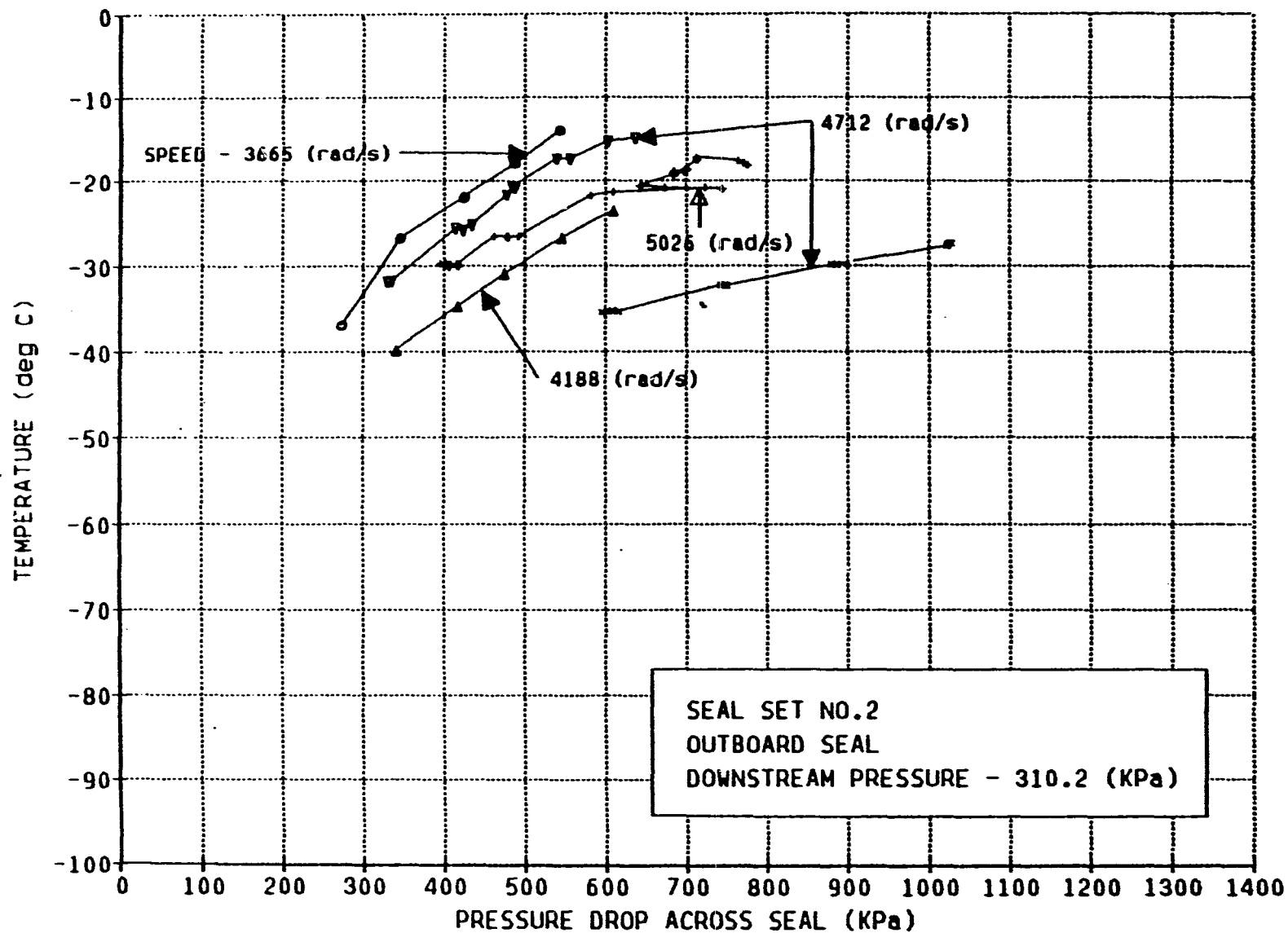


Fig. 3-26 Outboard Seal Temperature, 310 kPa Drain Pressure - Seal Set No. 2

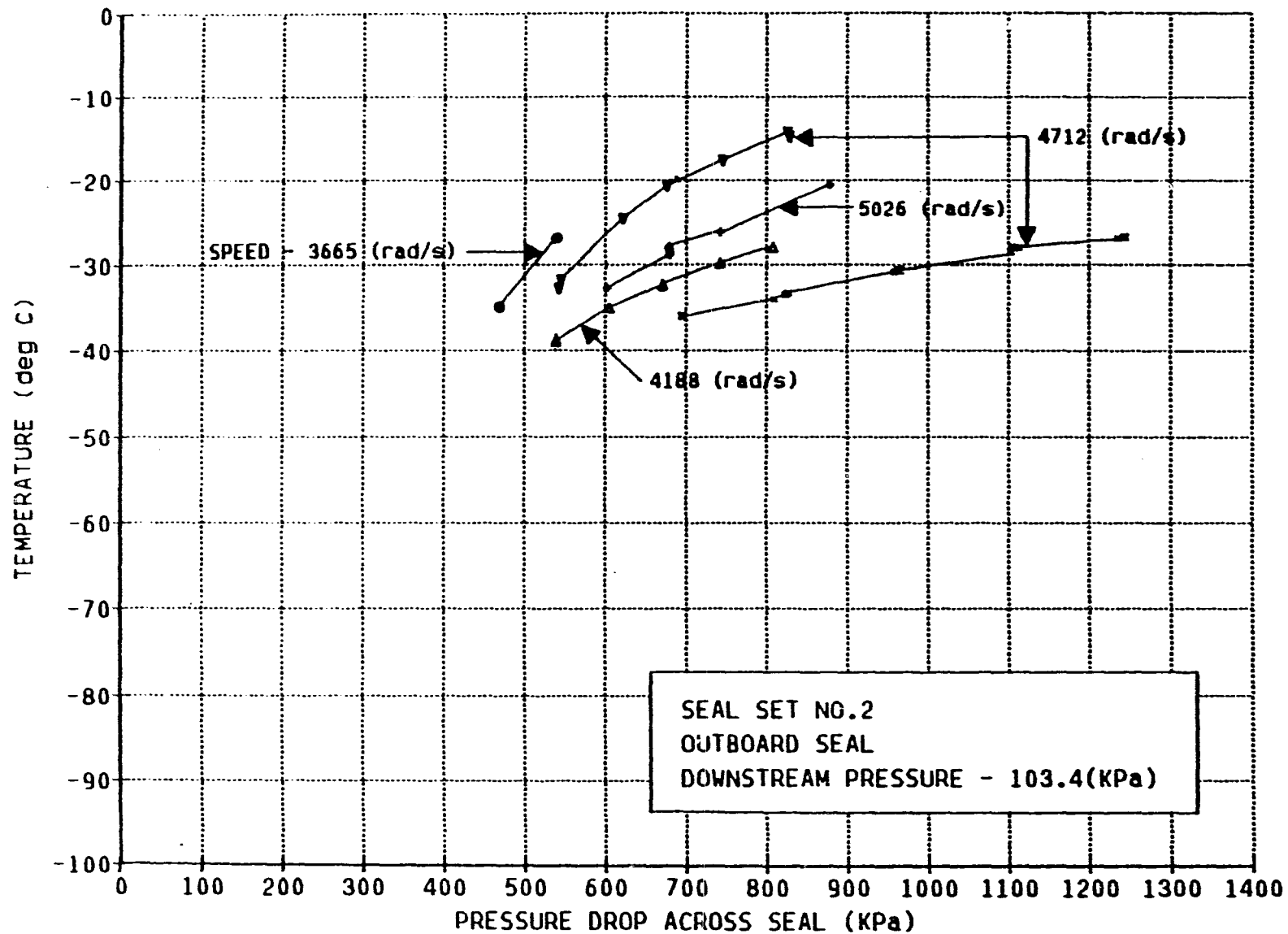


Fig. 3-27 Outboard Seal Temperature, 103 kPa Drain Pressure - Seal Set No. 2

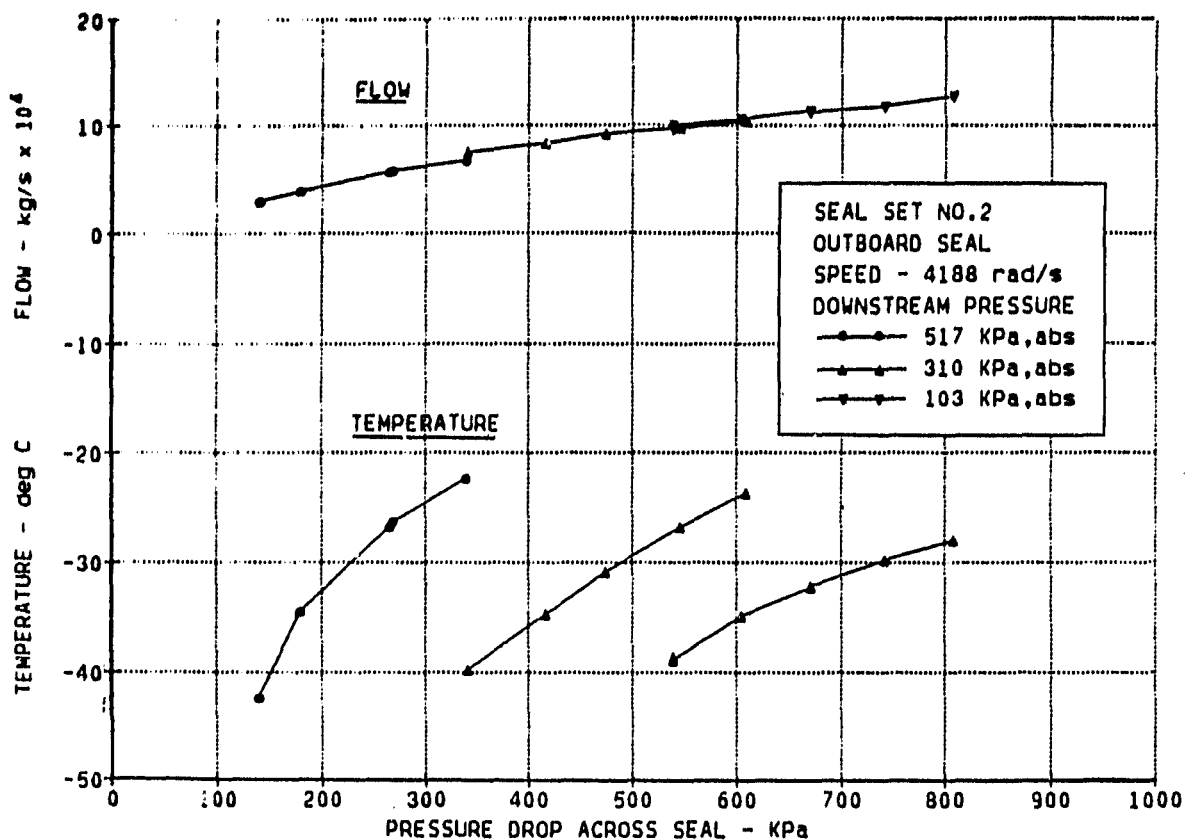


Fig. 3-28 Outboard Seal Temperature and Flow versus Pressure Drop - Seal Set No. 2

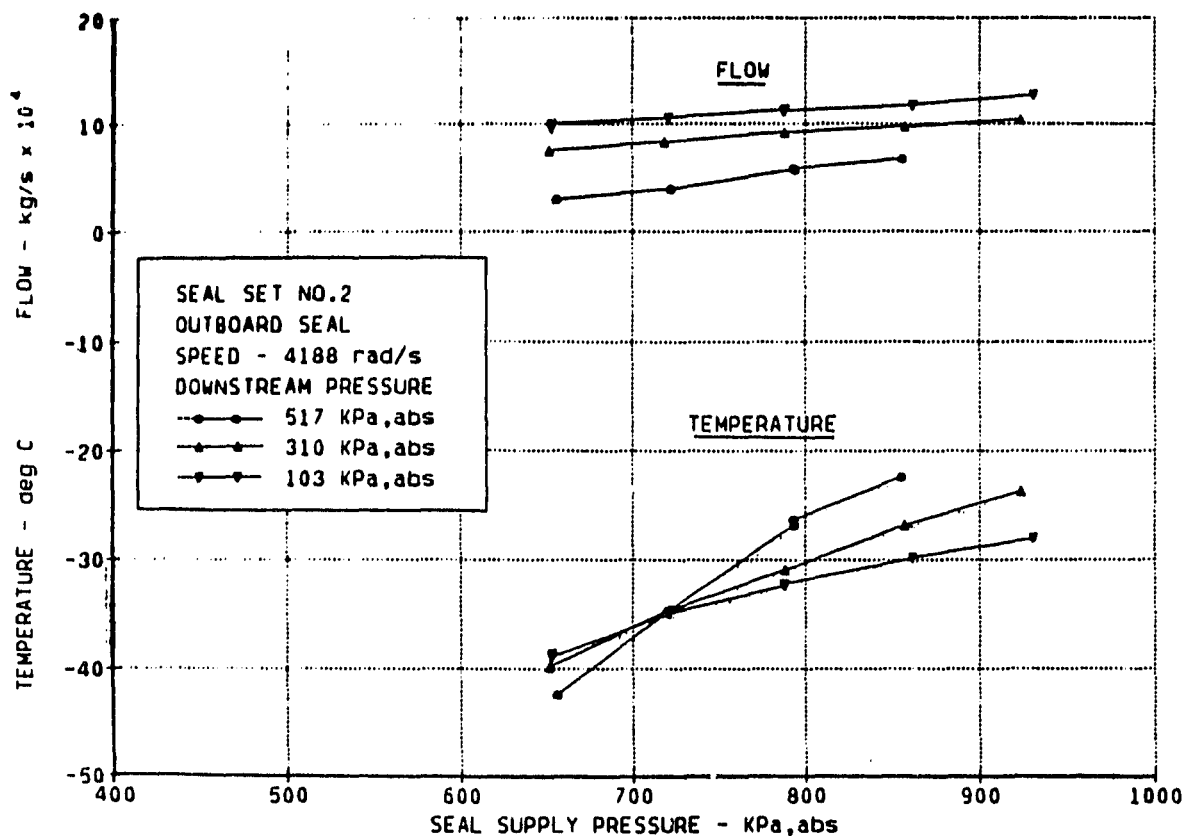


Fig. 3-29 Outboard Seal Temperature and Flow versus Supply Pressure - Seal Set No. 2

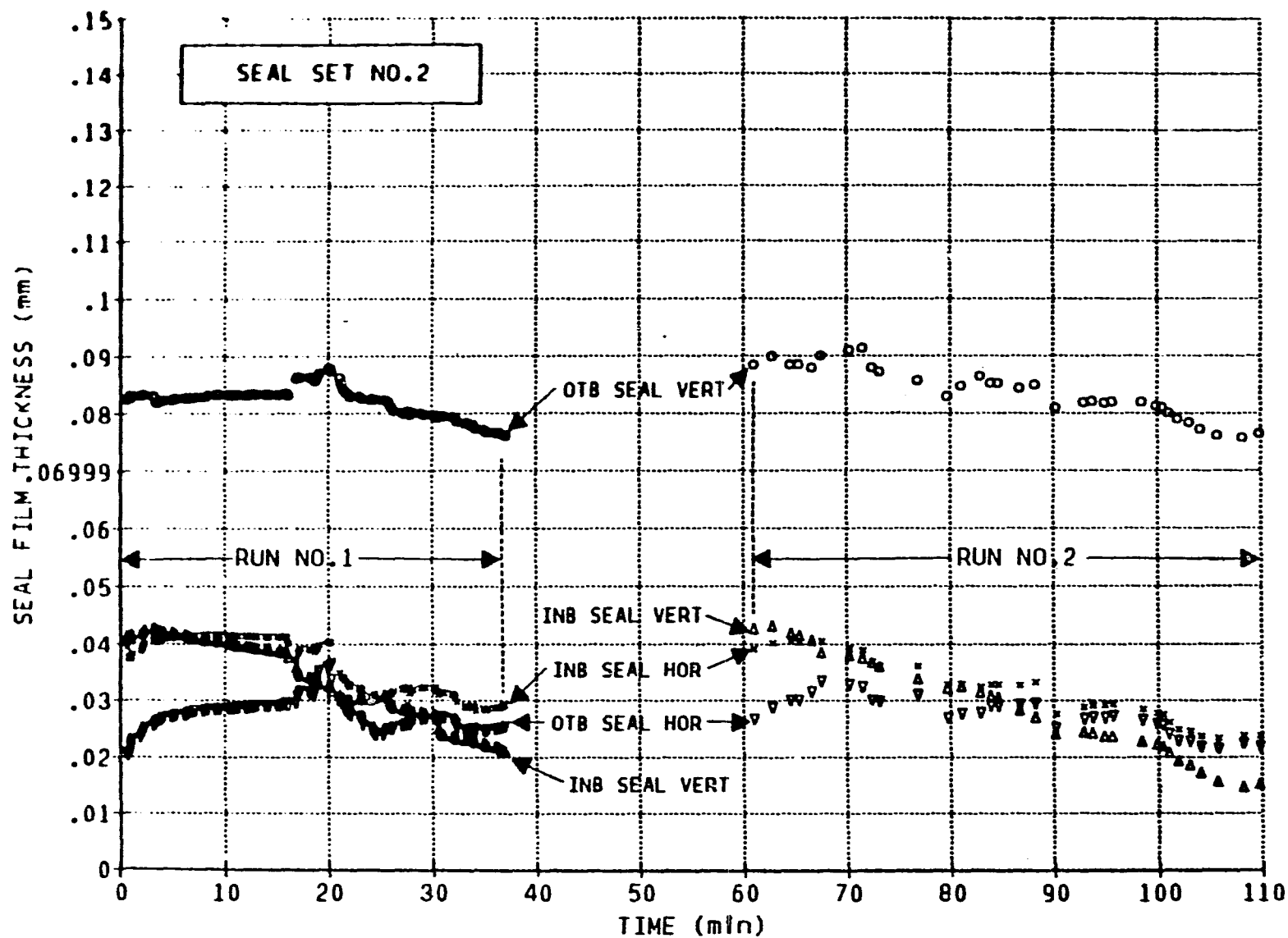


Fig. 3-30 First Day Seal Film Thickness History - Seal Set No. 2

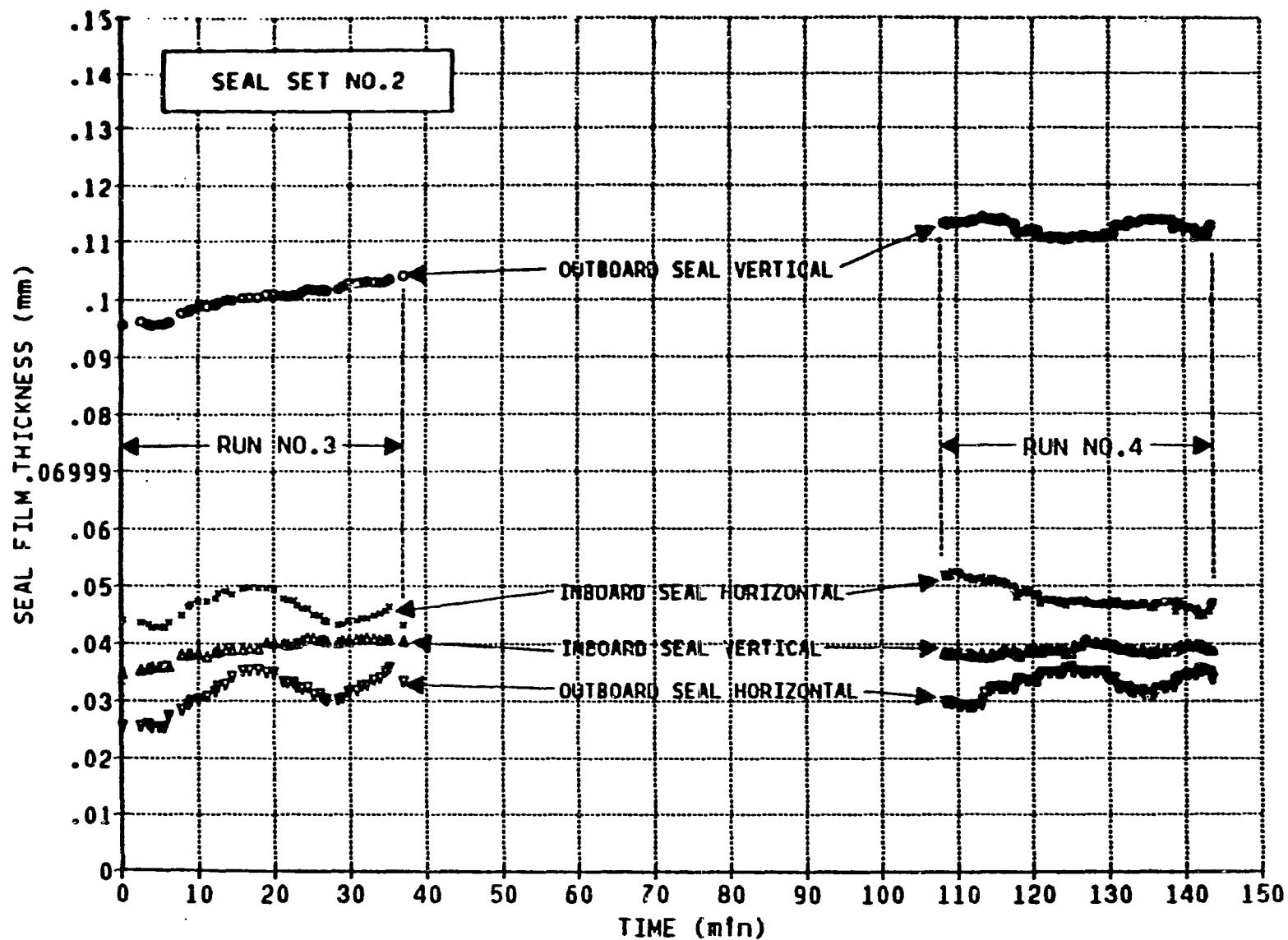


Fig. 3-31 Second Day Film Thickness History - Seal Set No. 2

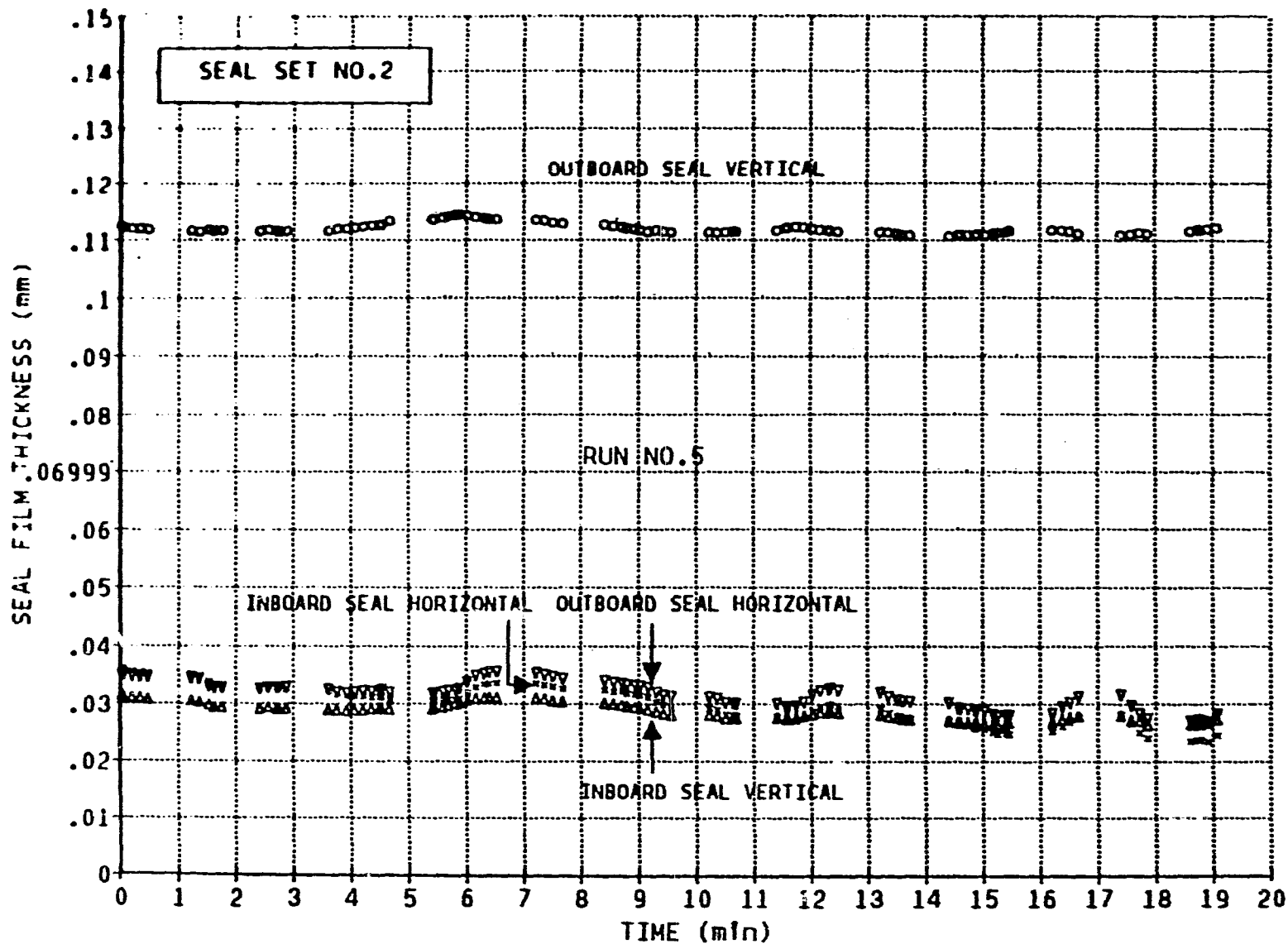


Fig. 3-32 Third Day Film Thickness History - Seal Set No. 2

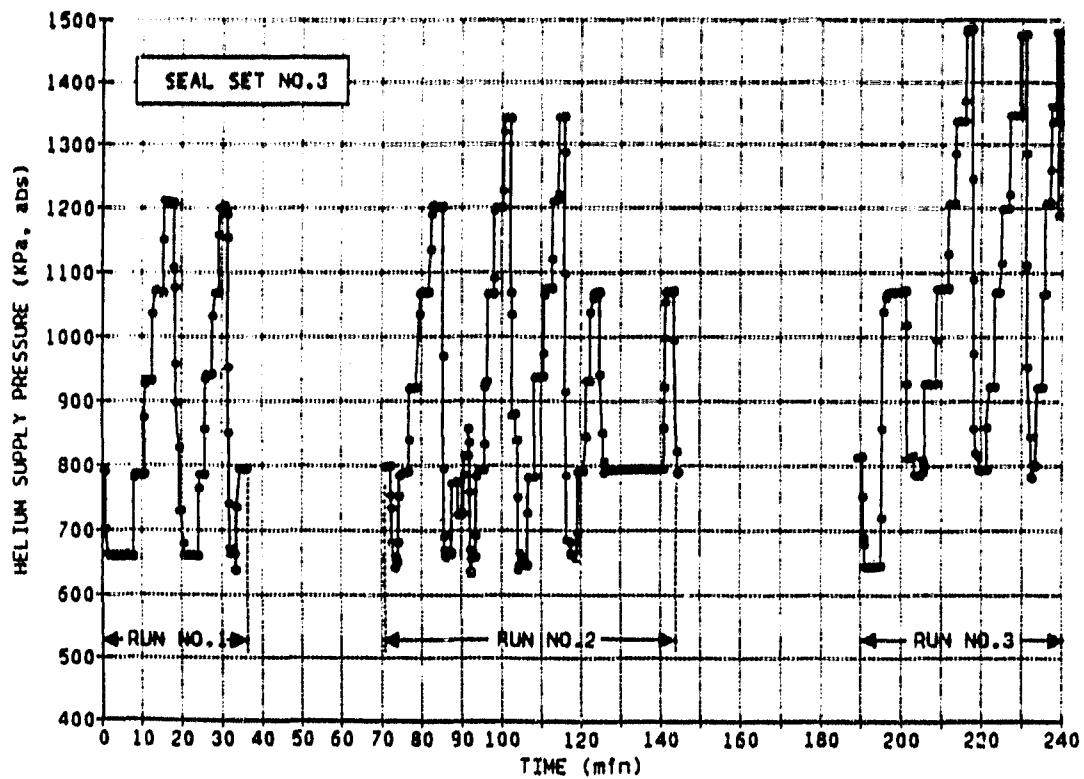


Fig. 3-33 Pressure History - Seal Set No. 3

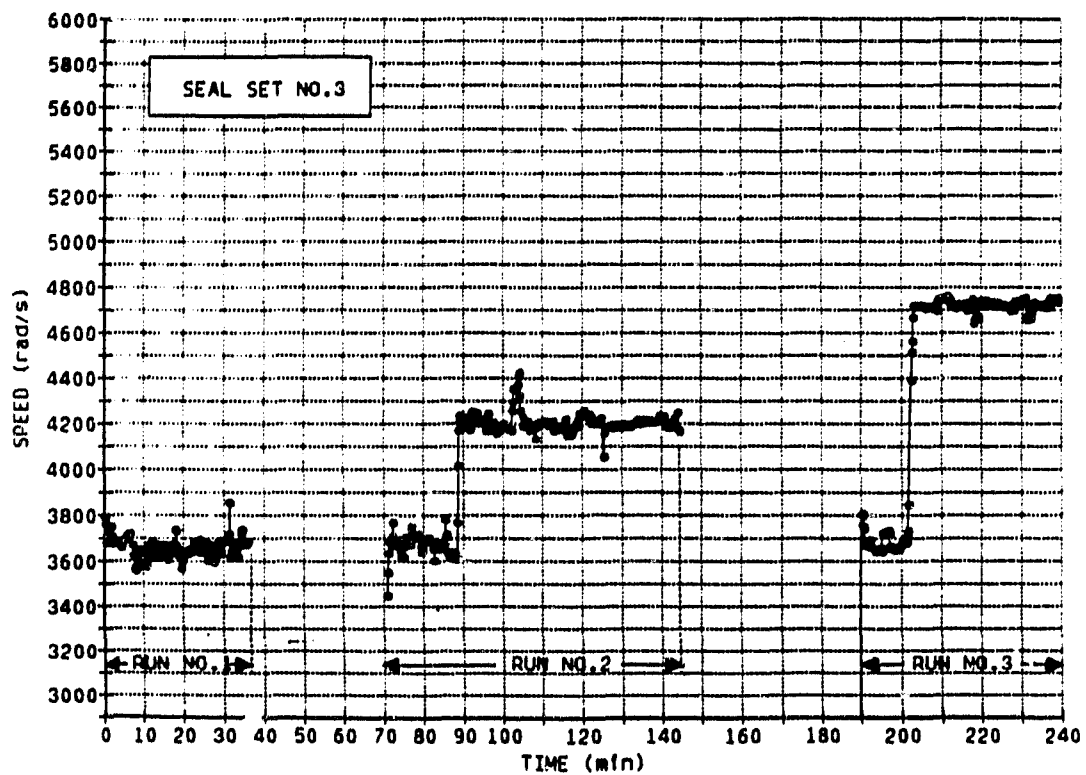


Fig. 3-34 Speed History - Seal Set No. 3

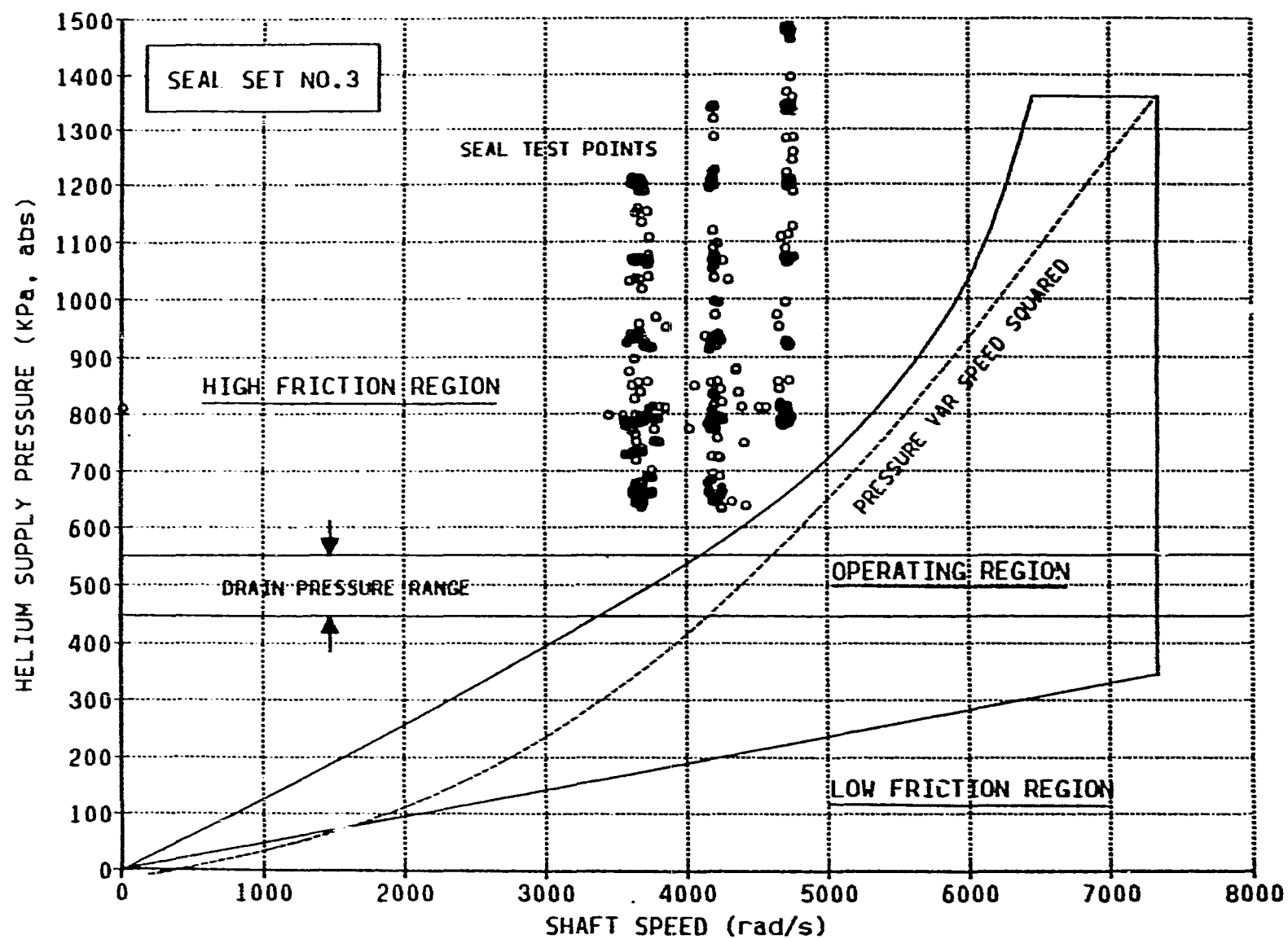


Fig. 3-35 Operating Map - Seal Set No. 3

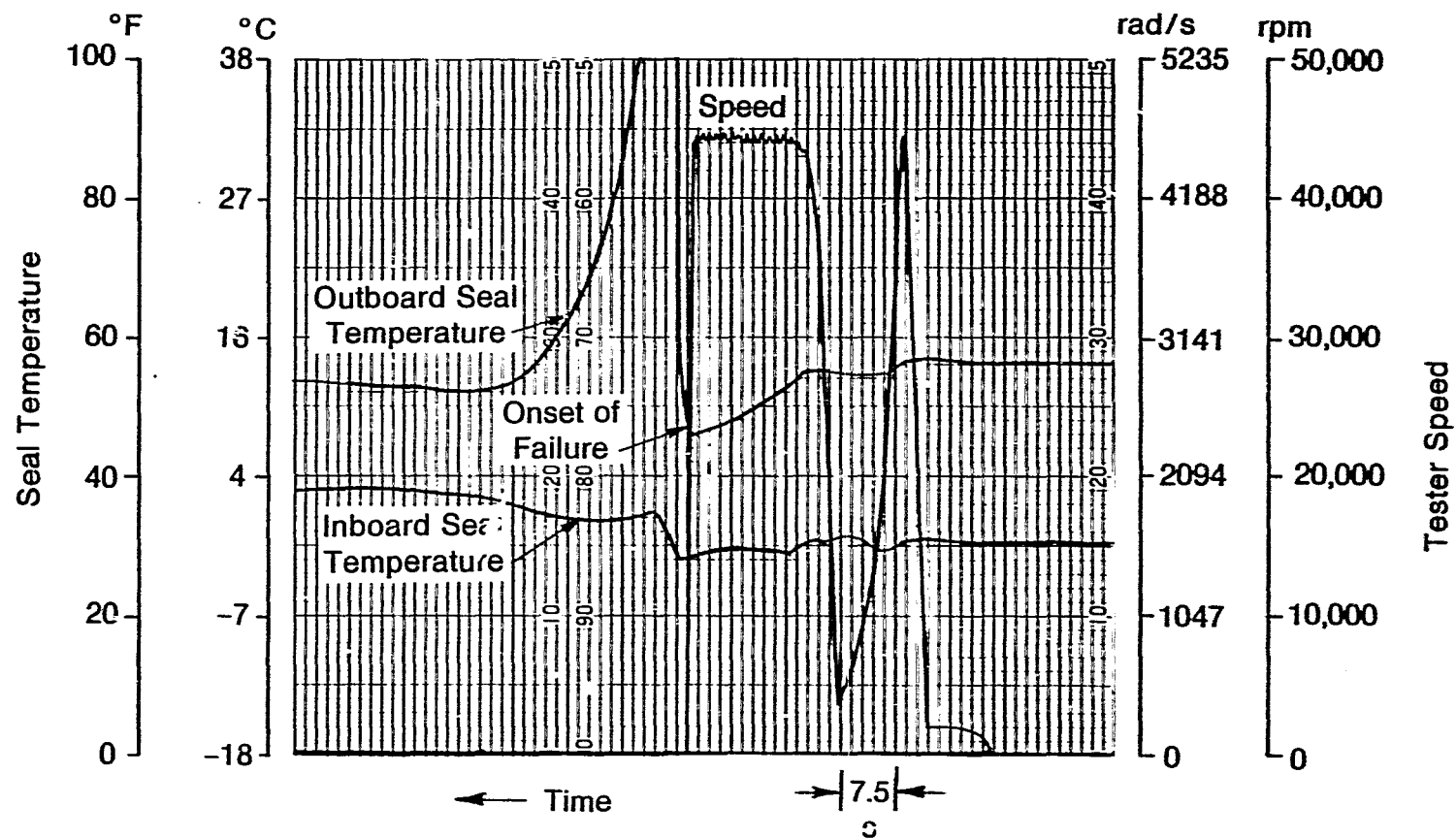


Fig. 3-36 Failure of No. 3 Inboard Seal Ring

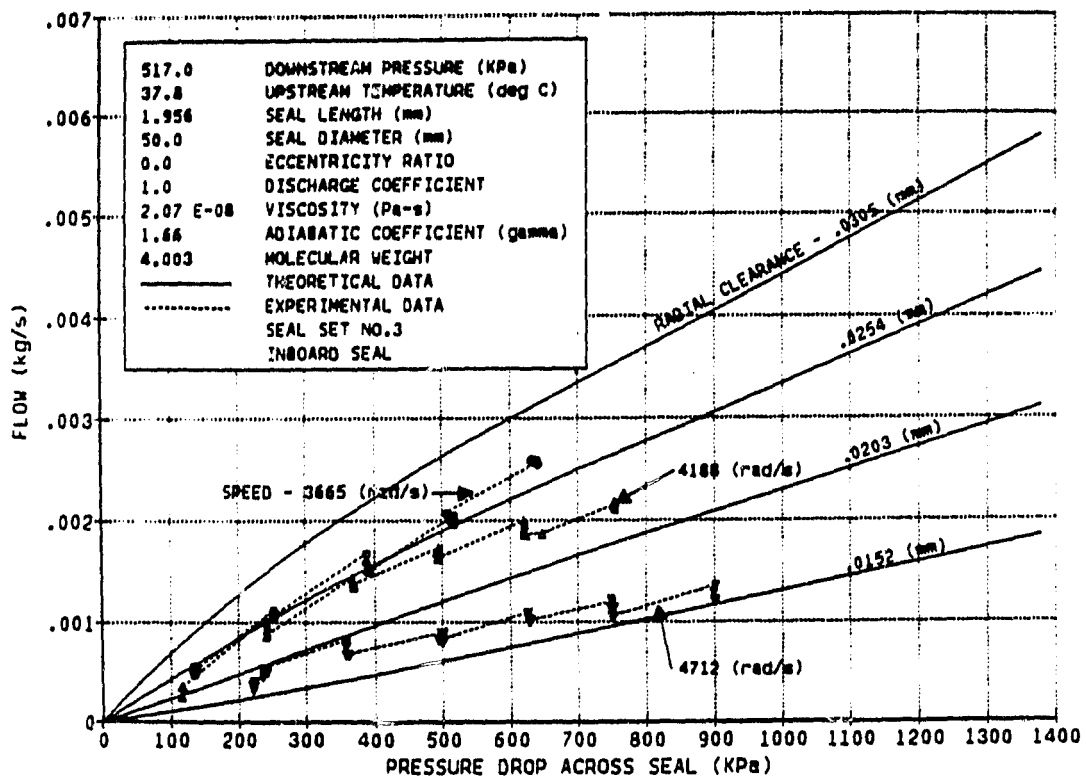


Fig. 3-37 Inboard Seal Flow versus Pressure Drop - Seal Set No. 3

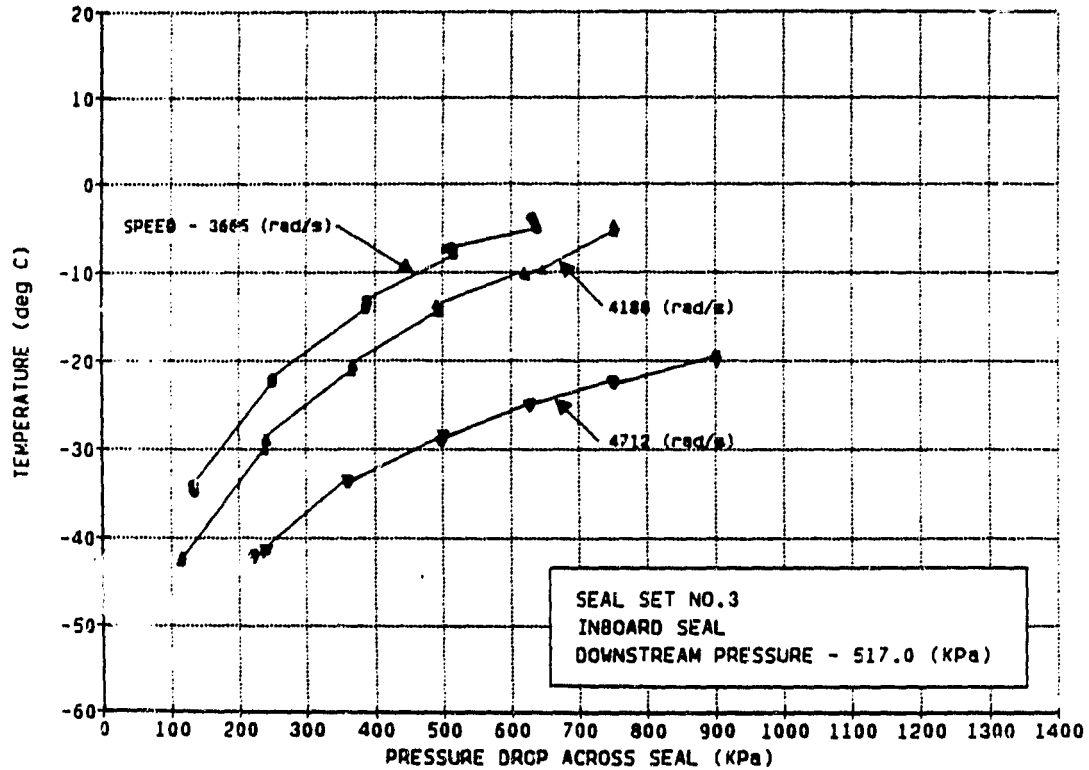


Fig. 3-38 Inboard Seal Temperature versus Pressure Drop - Seal Set No. 3

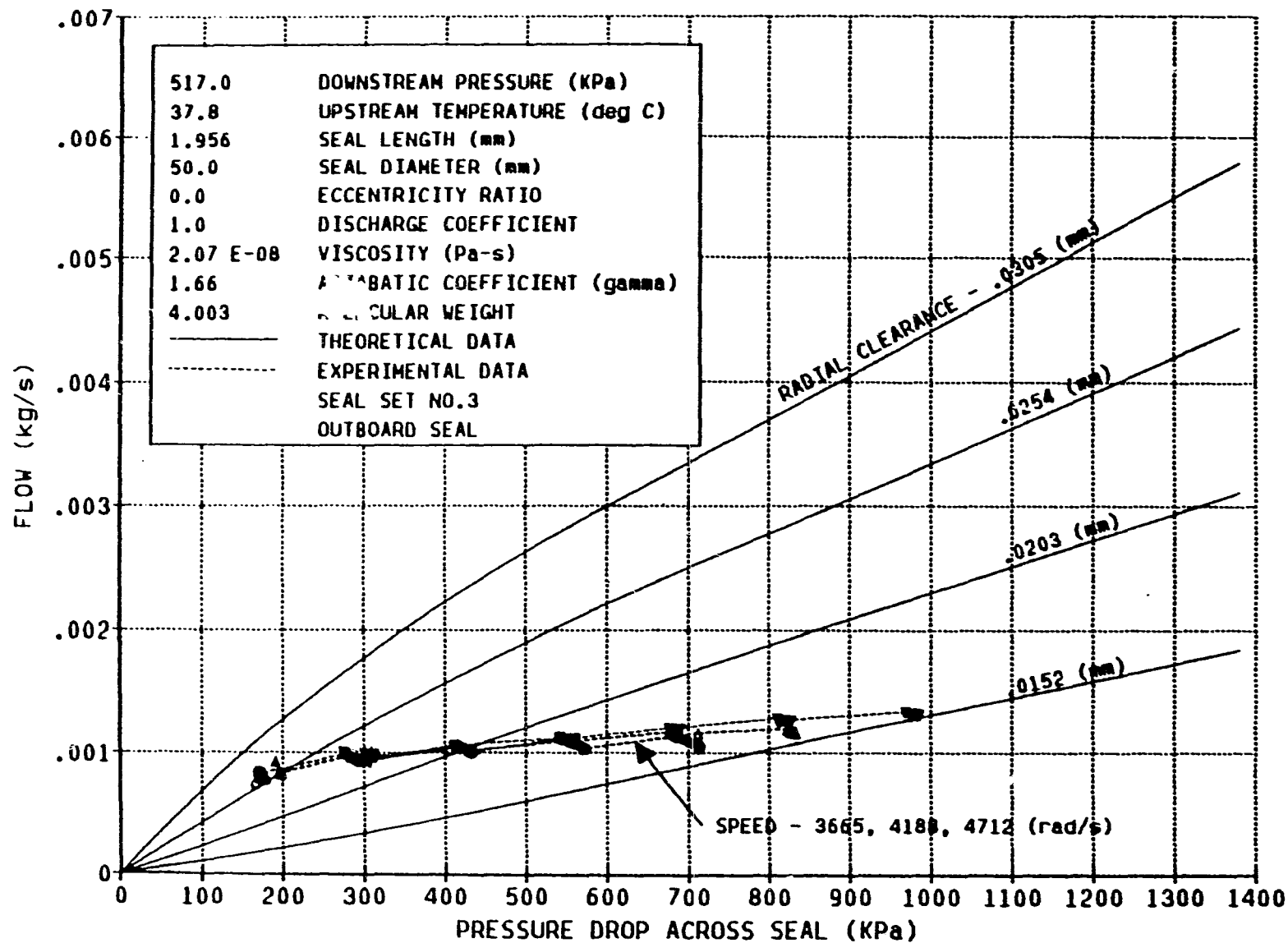


Fig. 3-39 Outboard Seal Flow, 517 kPa Drain Pressure - Seal Set No. 3

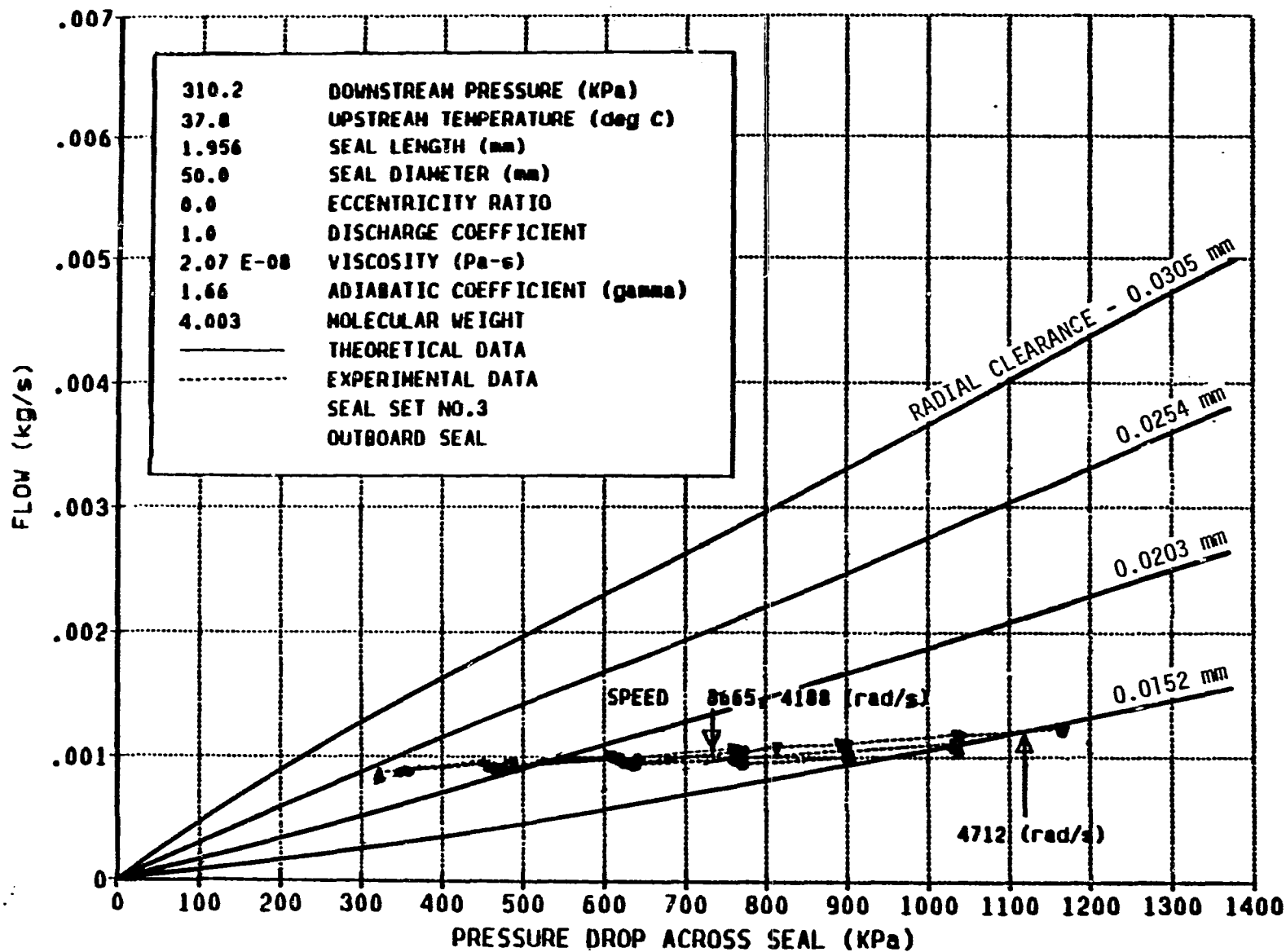


Fig. 3-40 Outboard Seal Flow, 310 kPa Drain Pressure - Seal Set No. 3

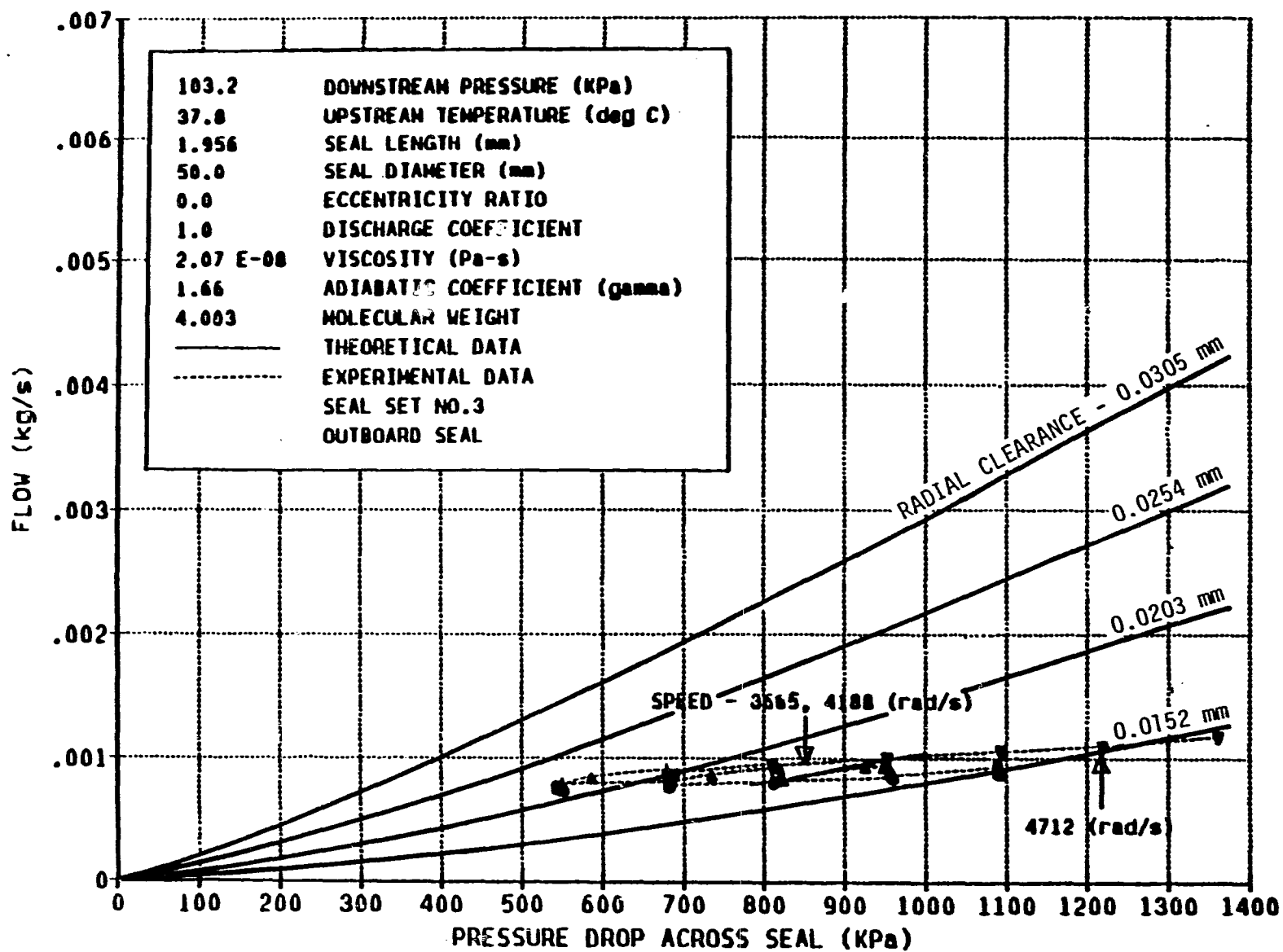


Fig. 3-41 Outboard Seal Flow, 103 kPa Drain Pressure - Seal Set No. 3

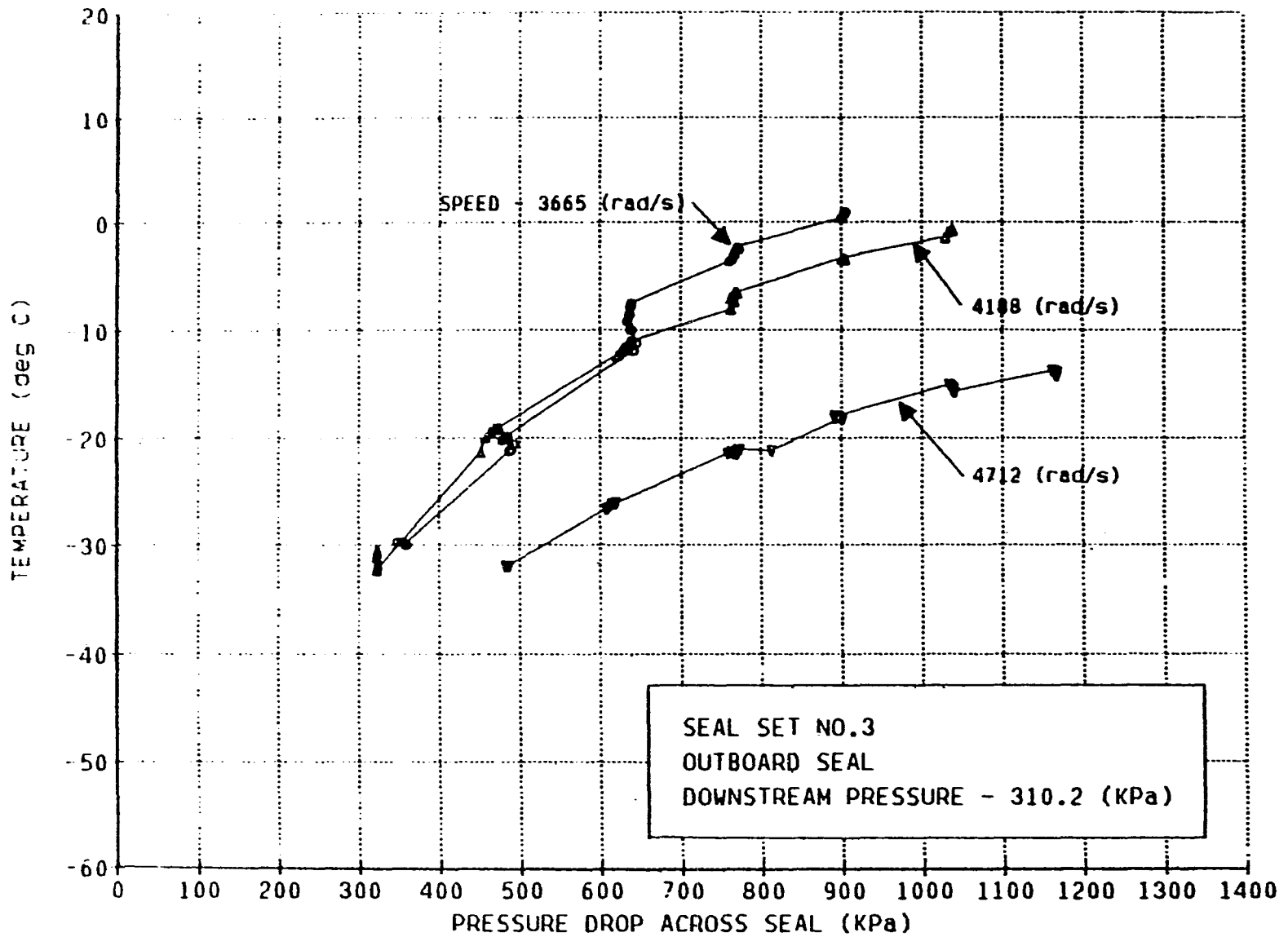


Fig. 3-42 Outboard Seal Temperature, 517 kPa Drain Pressure - Seal Set No. 3

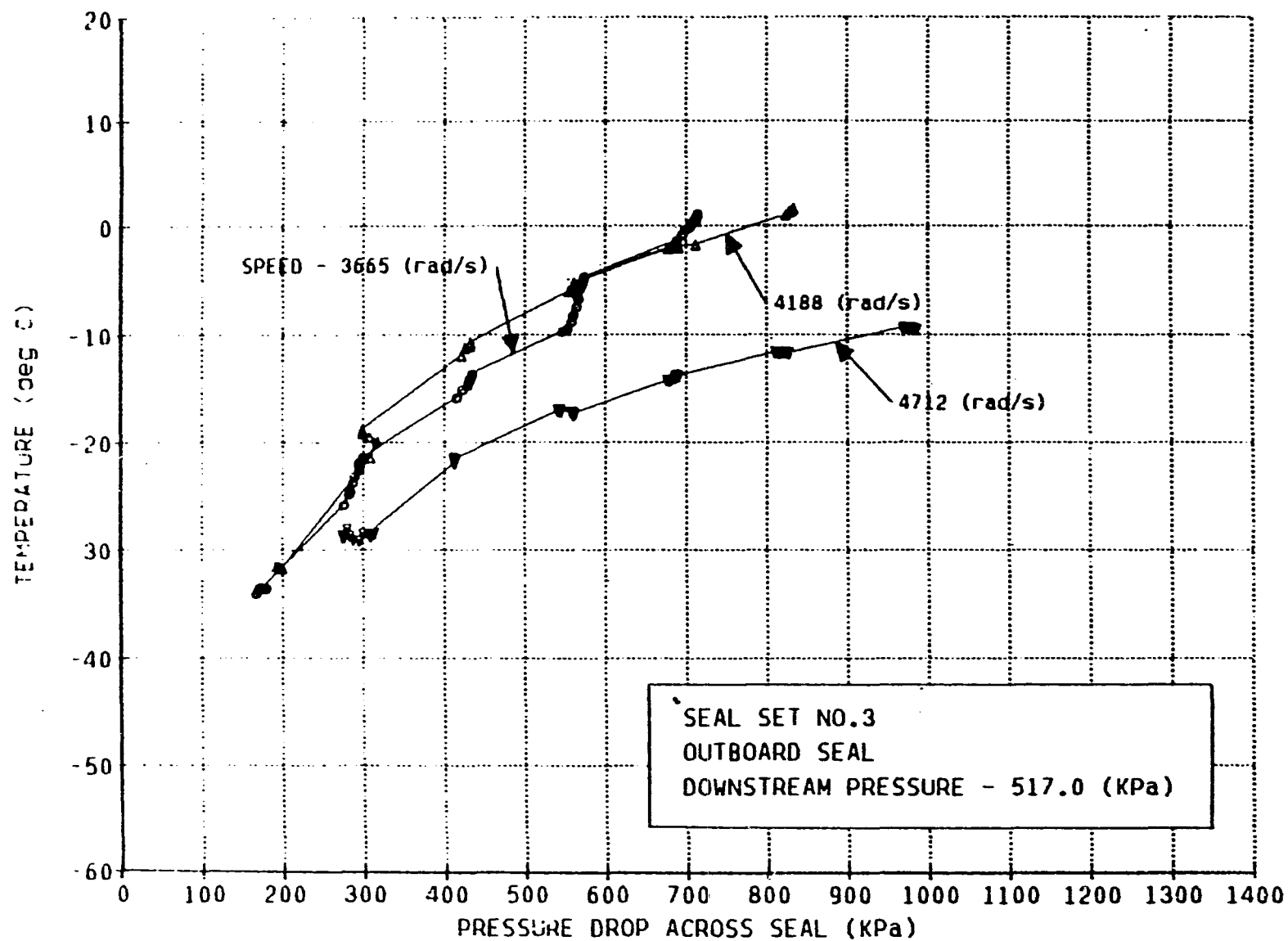


Fig. 3-43 Outboard Seal Temperature, 310 kPa Drain Pressure - Seal Set No. 3

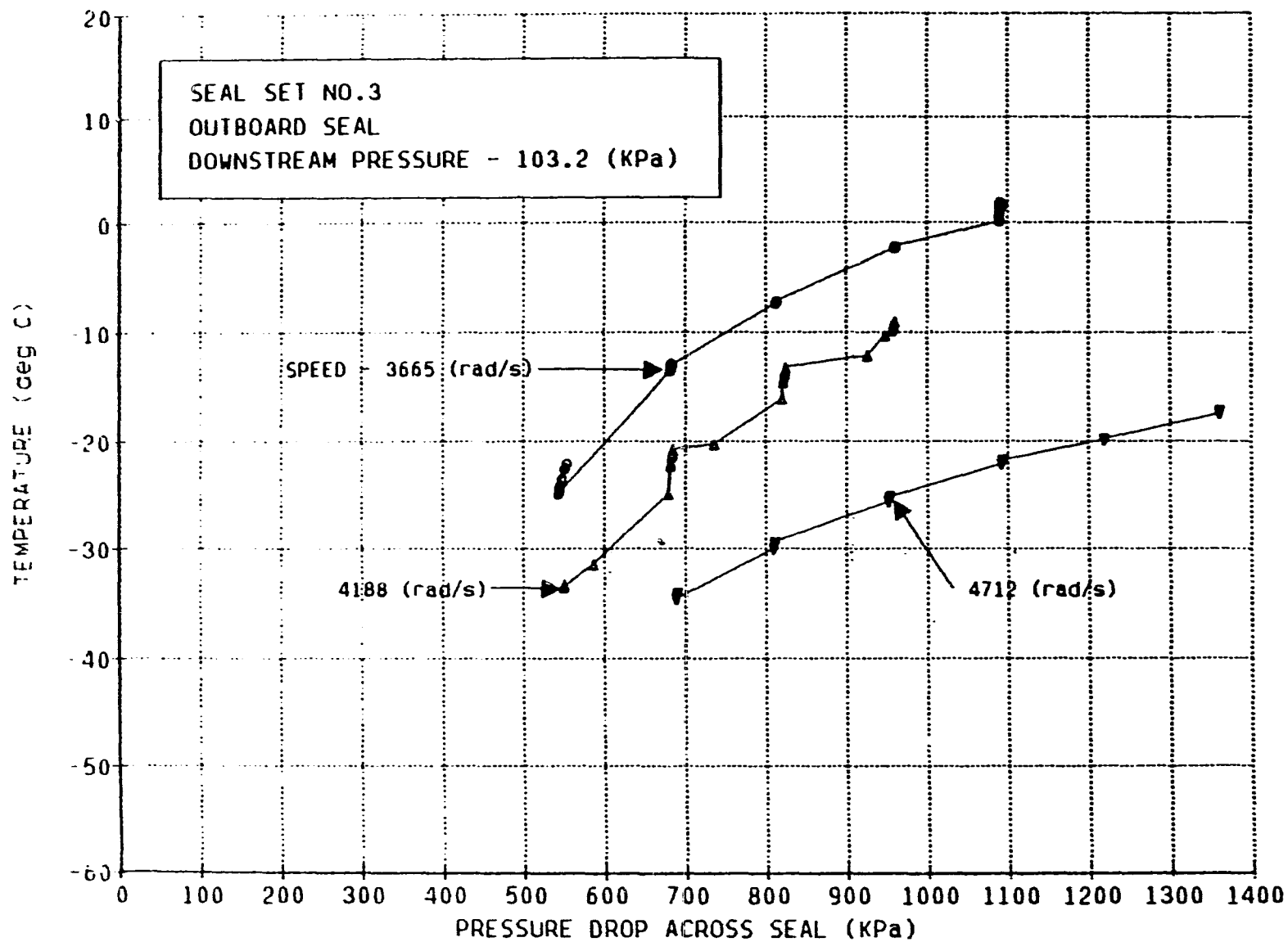


Fig. 3-44 Outboard Seal Temperature, 103 kPa Drain Pressure - Seal Set No. 3

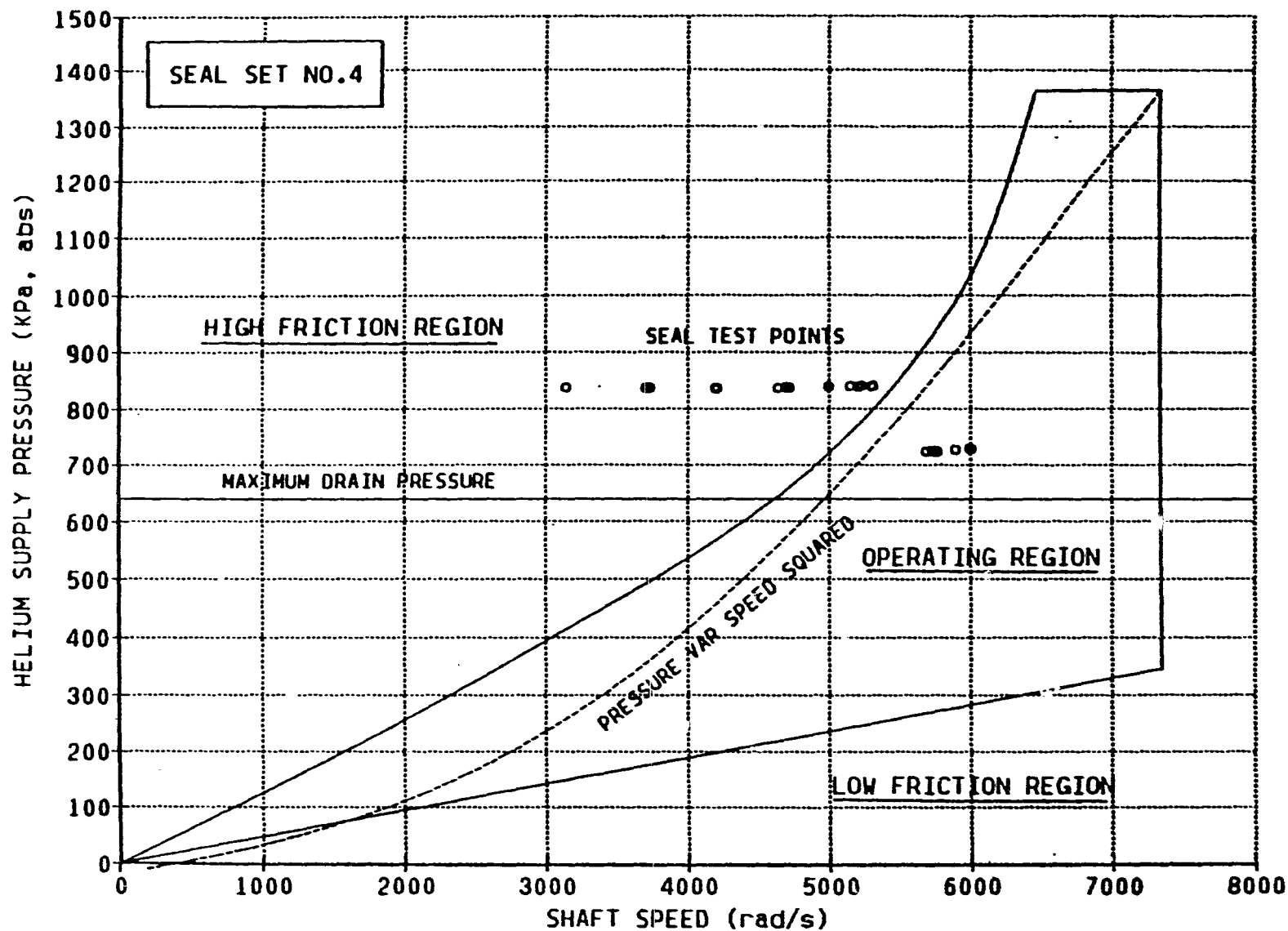


Fig. 3-45 Operating Map of Seal Set No. 4

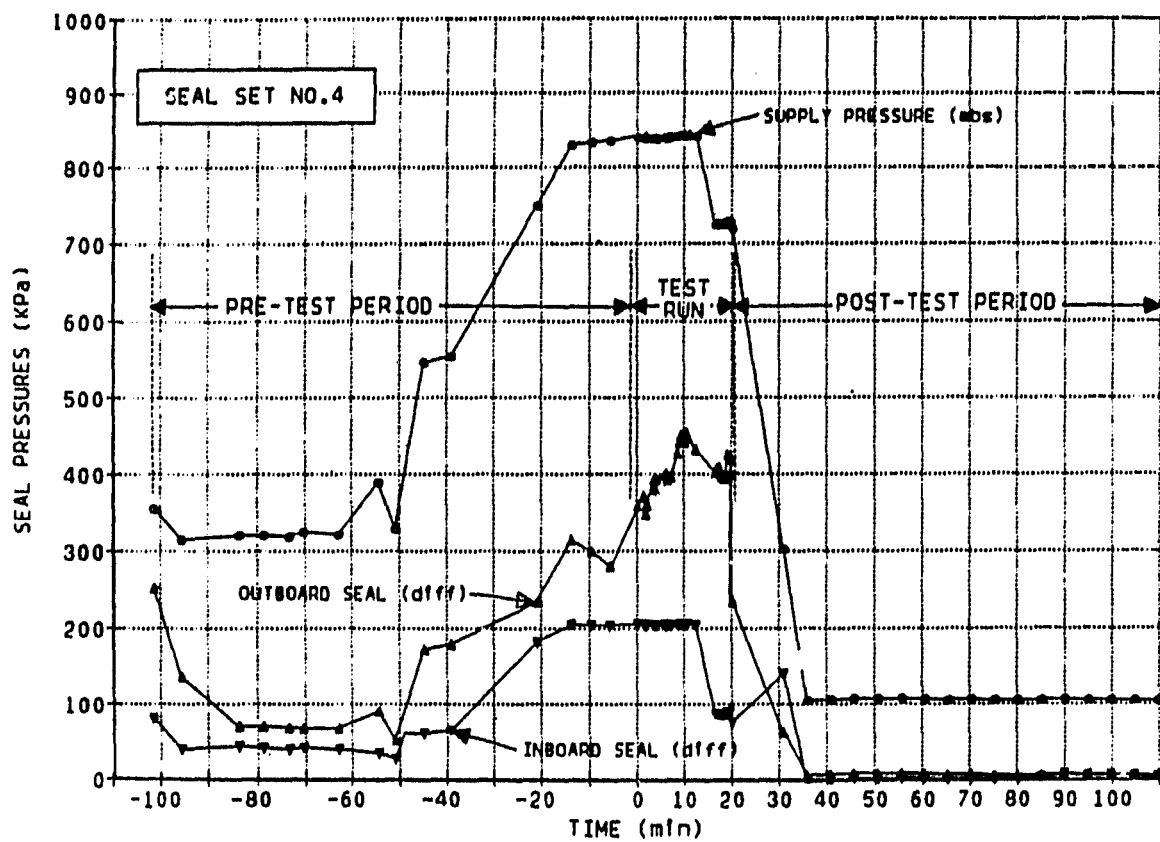


Fig. 3-46 Pressure History - Seal Set No. 4

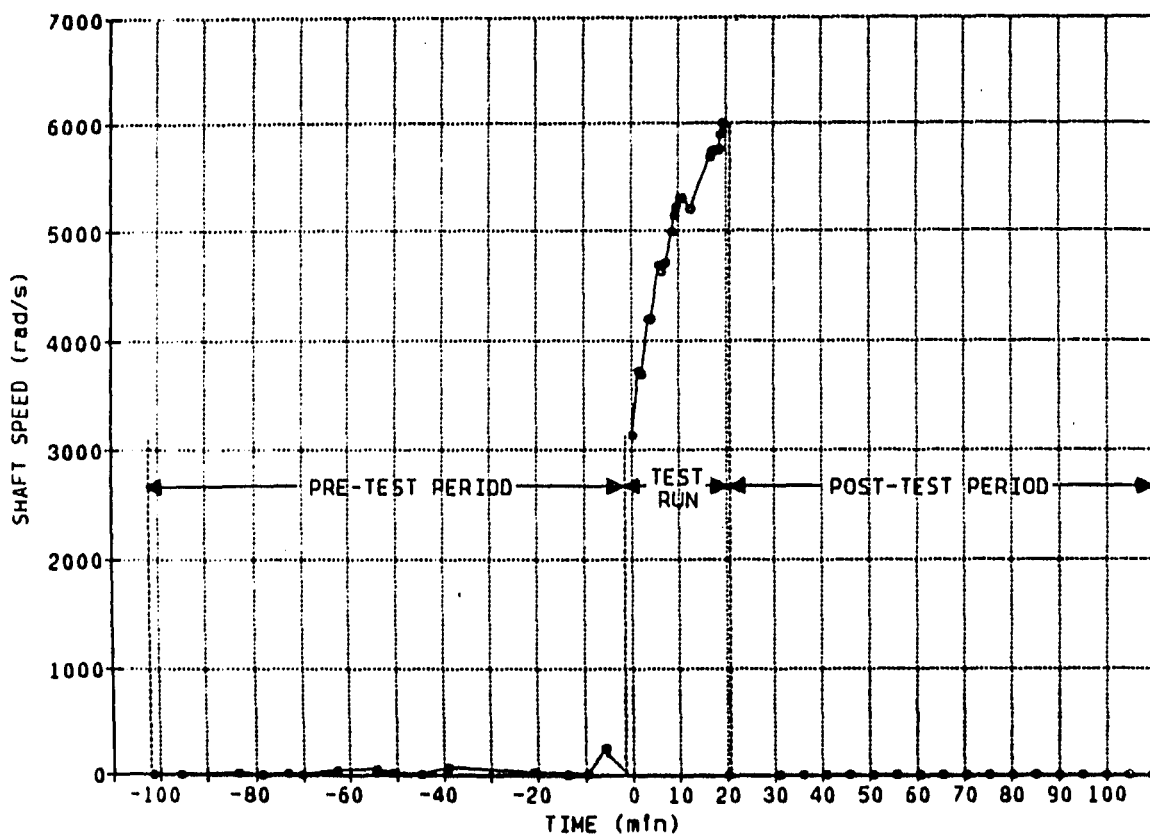


Fig. 3-47 Speed History - Seal Set No. 4

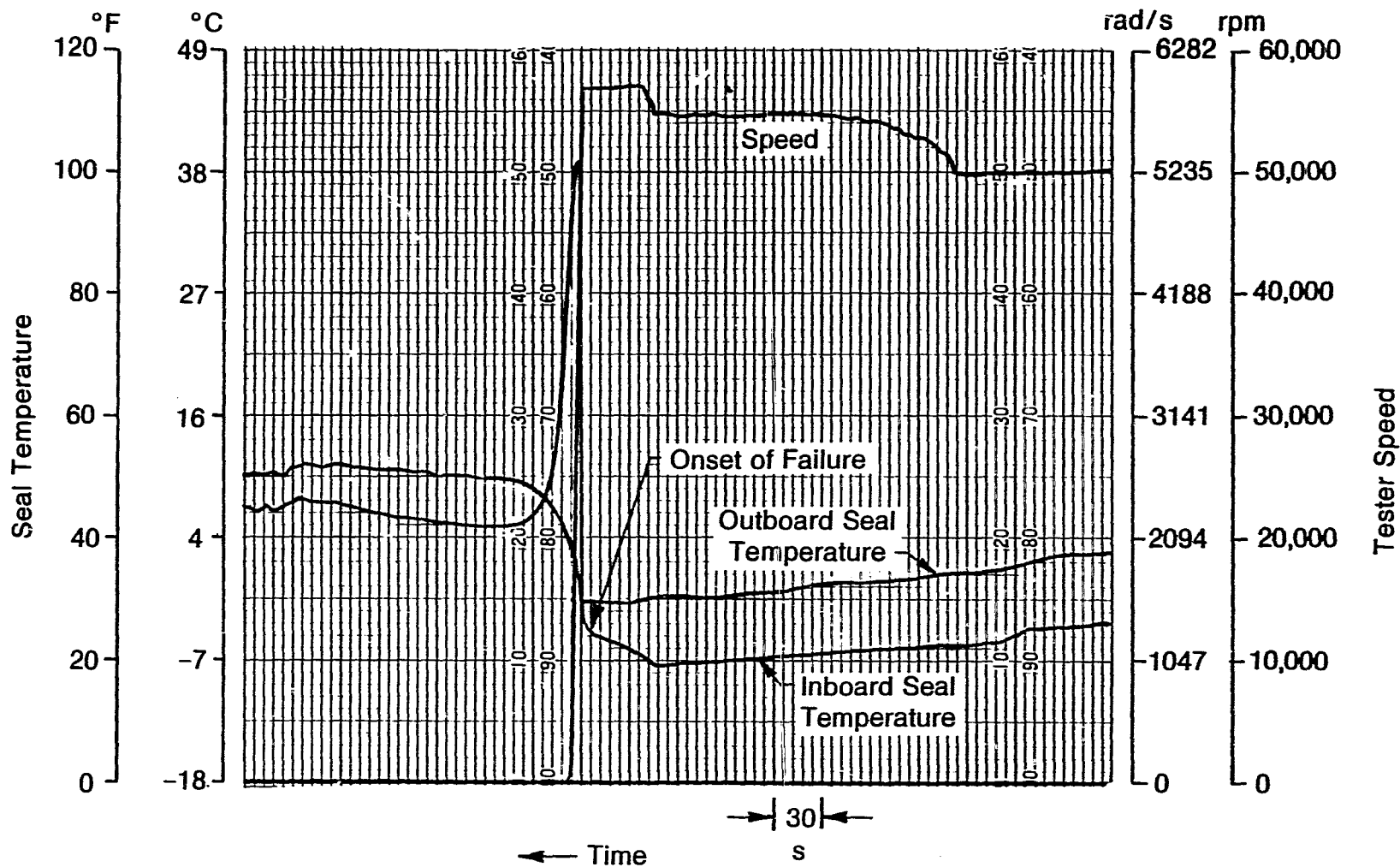


Fig. 3-48 Failure of No. 4 Inboard Seal Ring

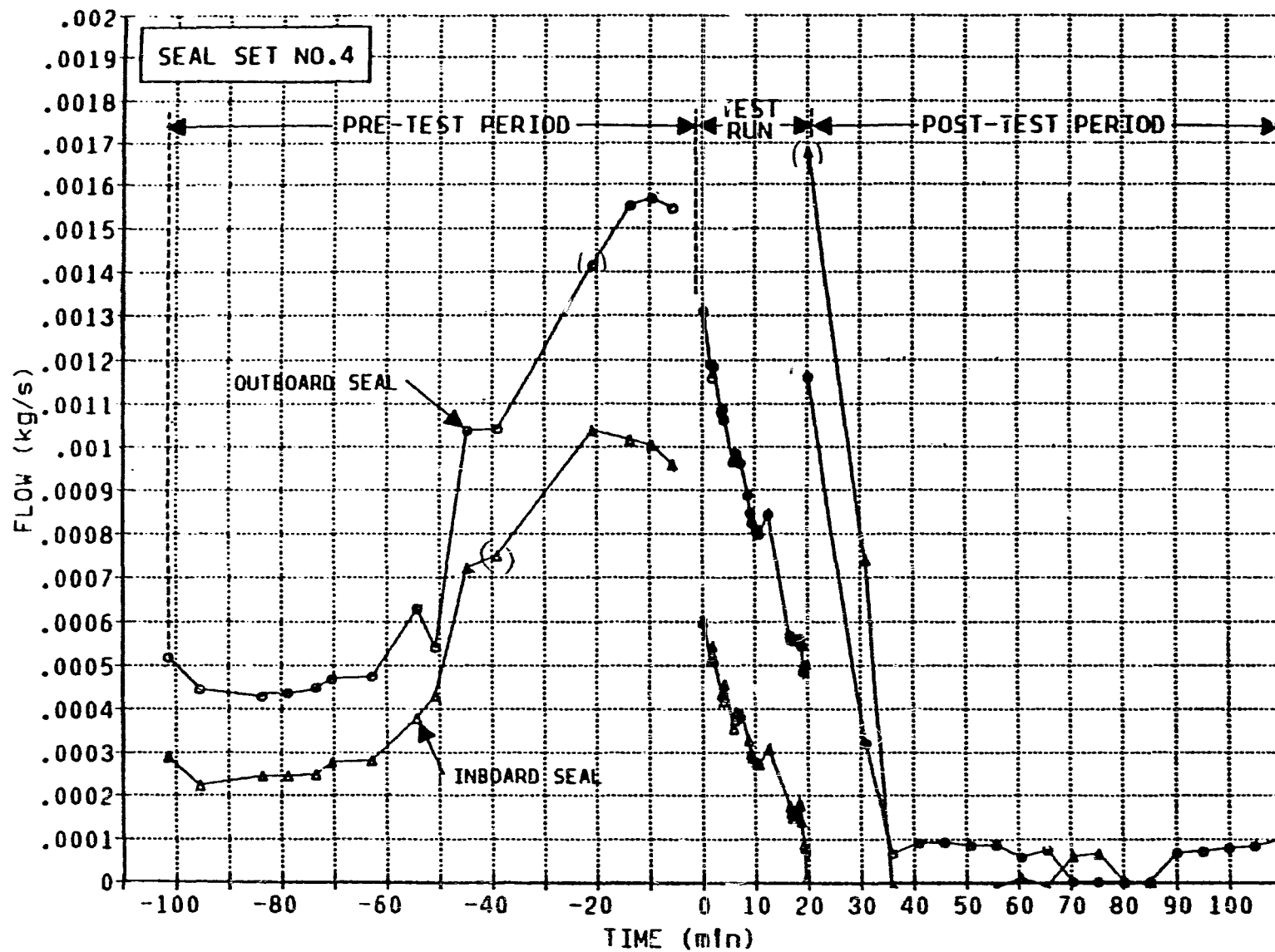


Fig. 3-49 Flow History - Seal Set No. 4

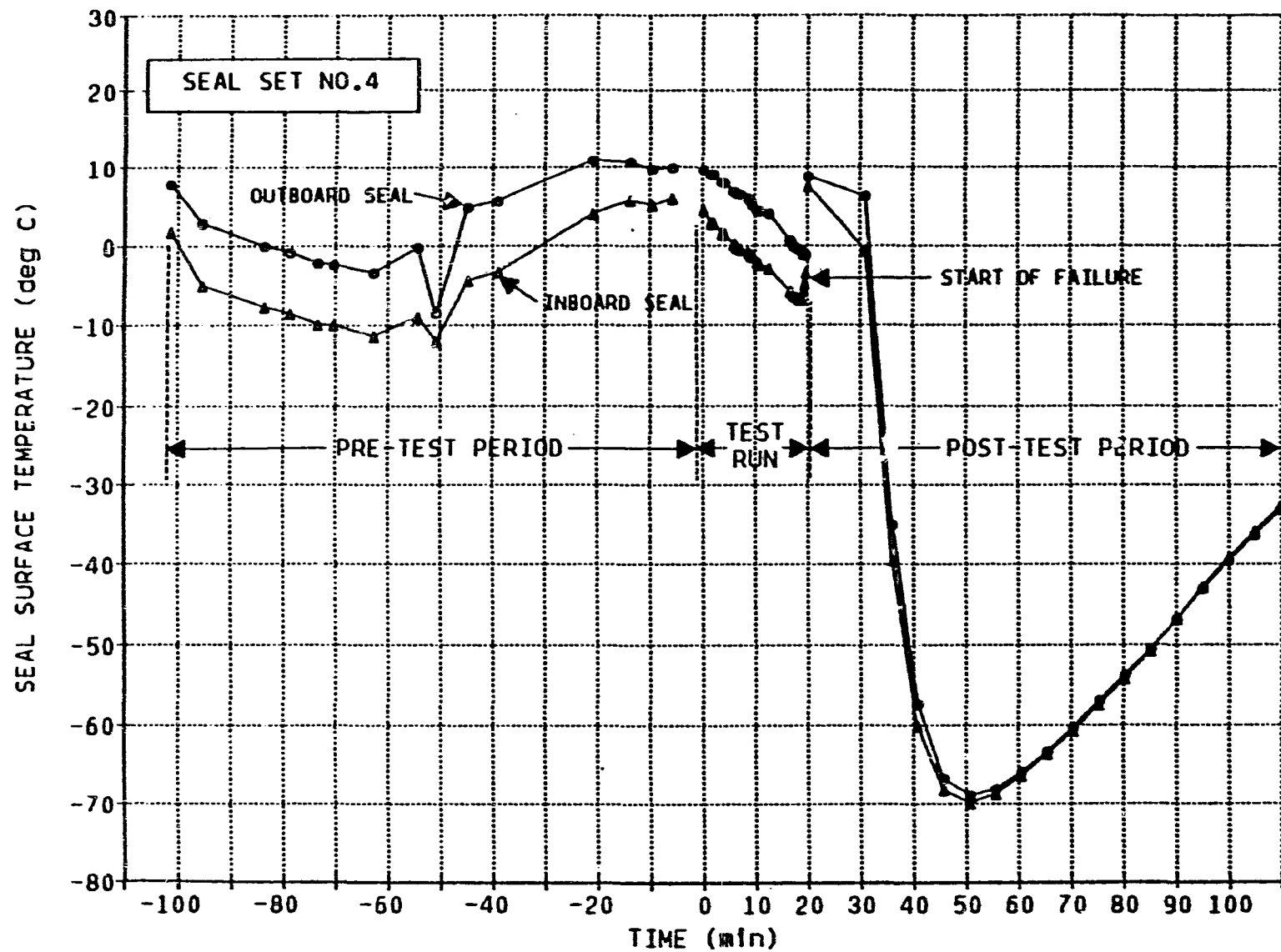


Fig. 3-50 Seal Temperature History - Seal Set No. 4

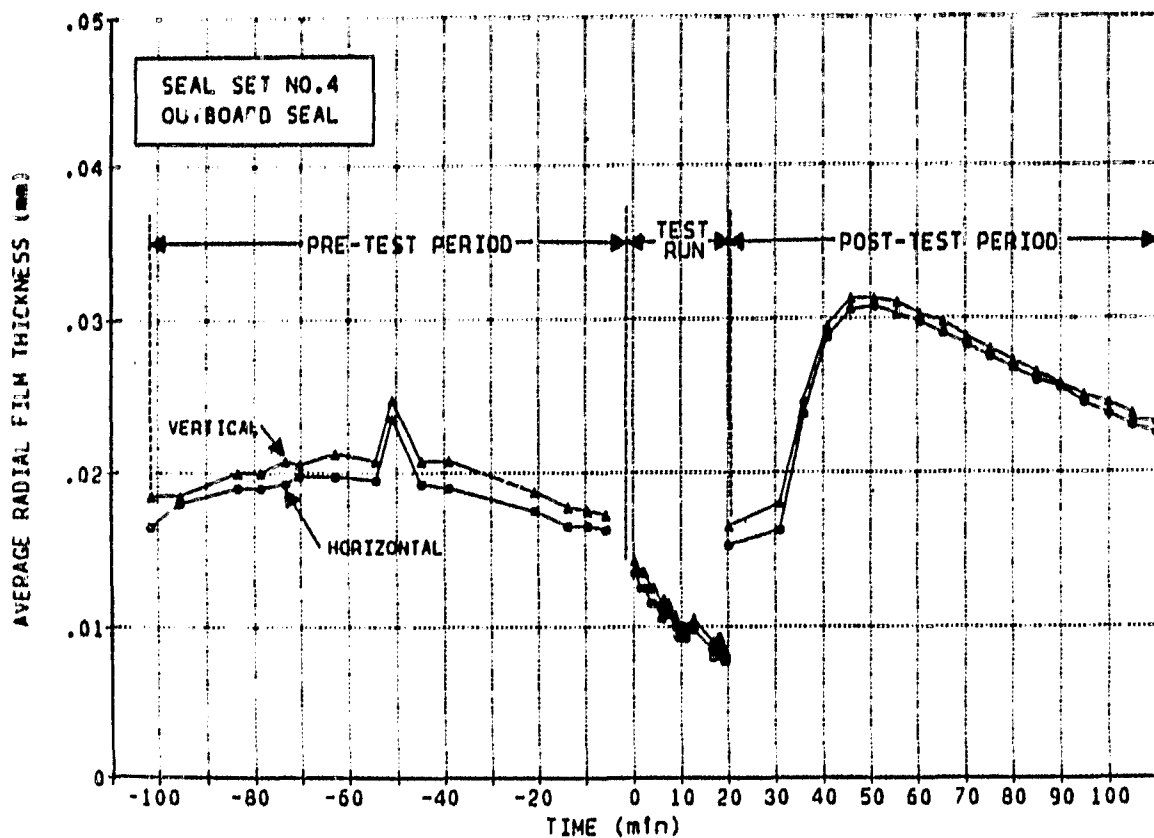


Fig. 3-51 Outboard Seal Film Thickness History - Seal Set No. 4

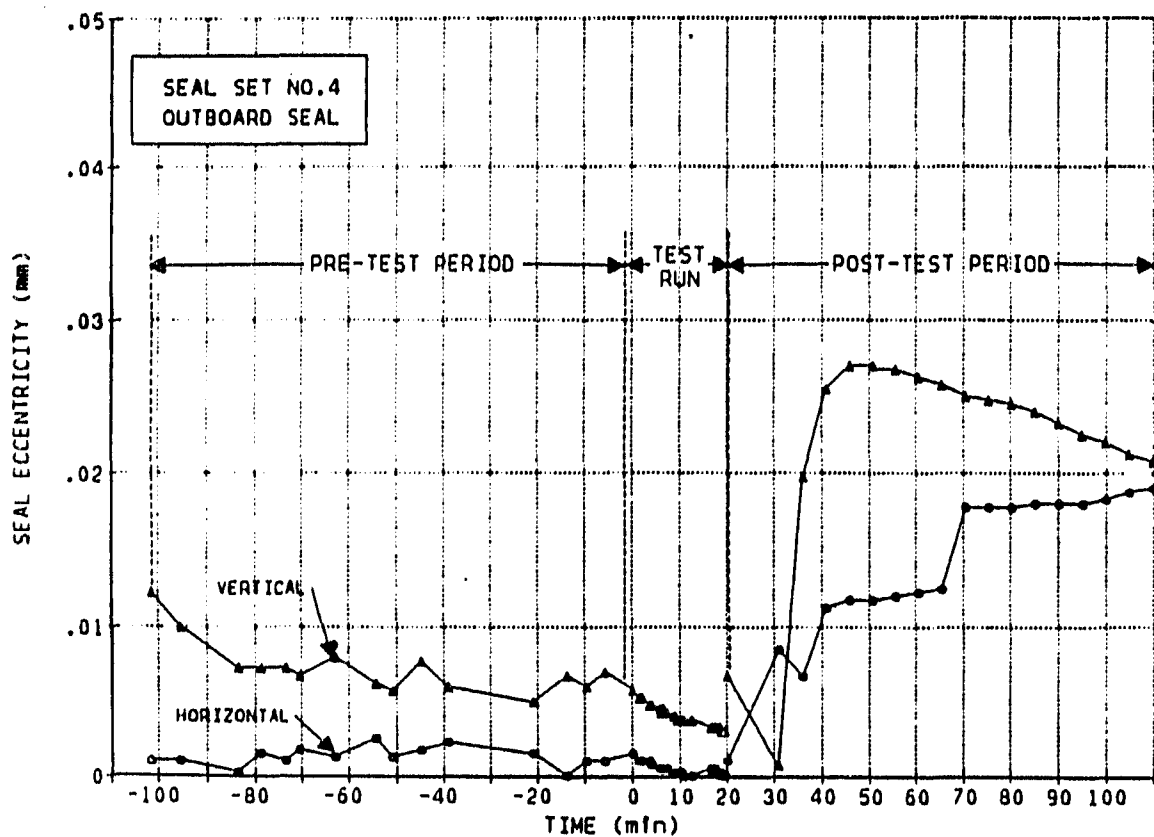


Fig. 3-52 Outboard Seal Eccentricity History - Seal Set No. 4

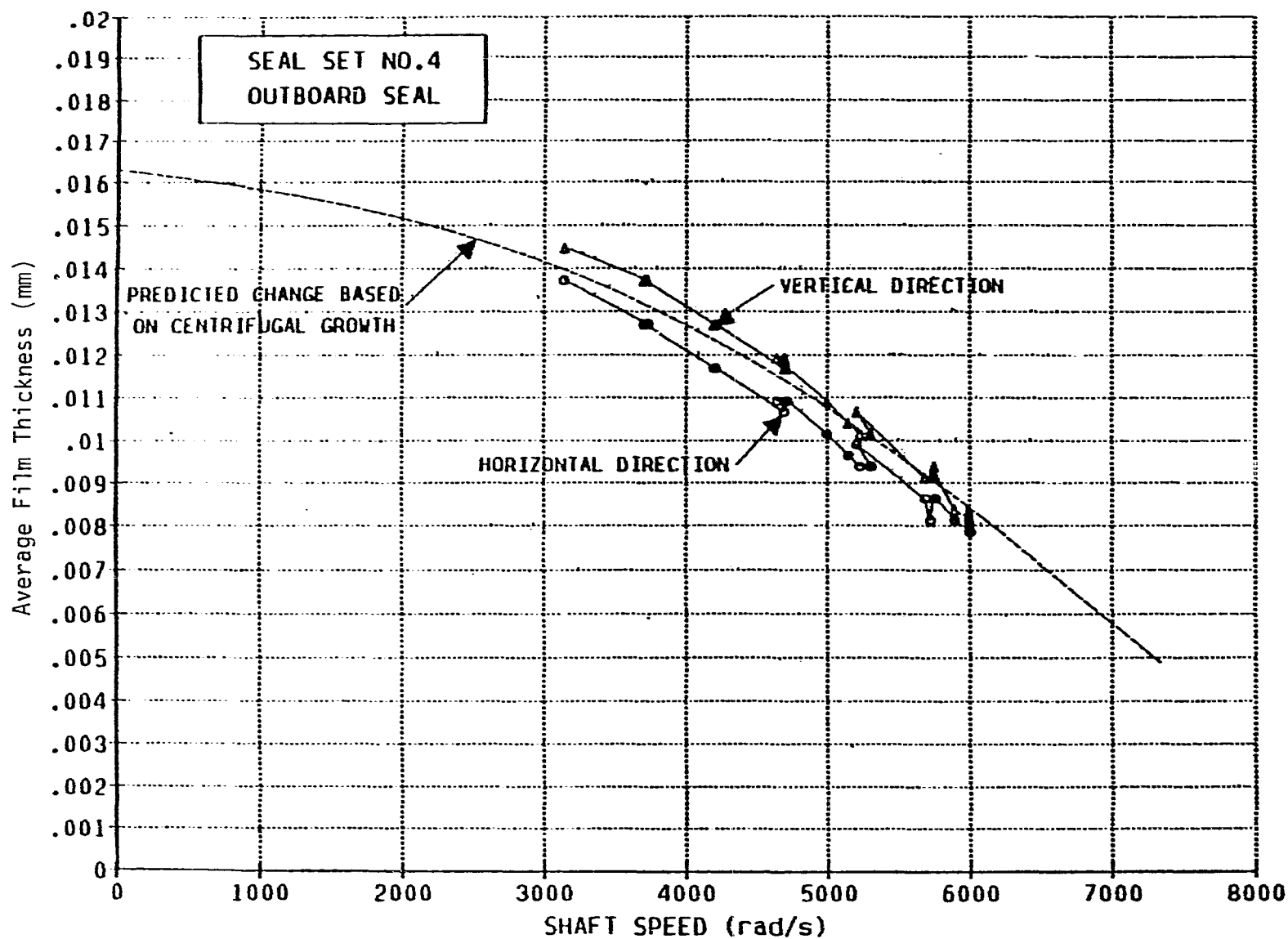
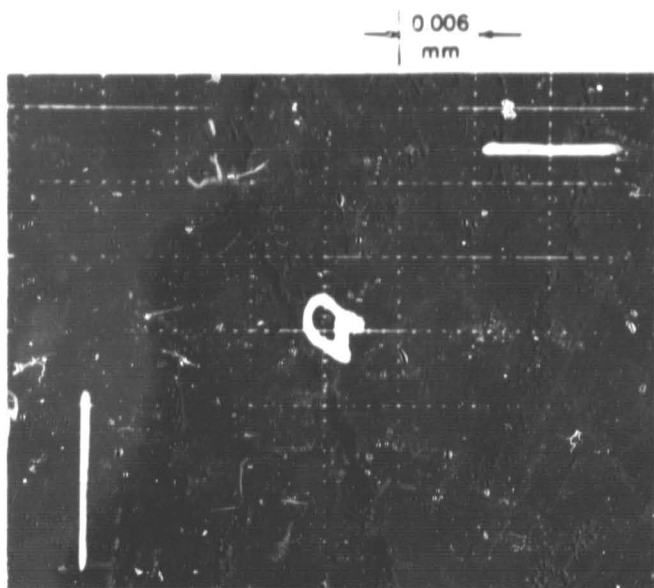


Fig. 3-53 Outboard Seal Film Thickness versus Shaft Speed - Seal Set No. 4



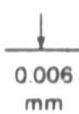
Otb
Seal

Fig. 3-54

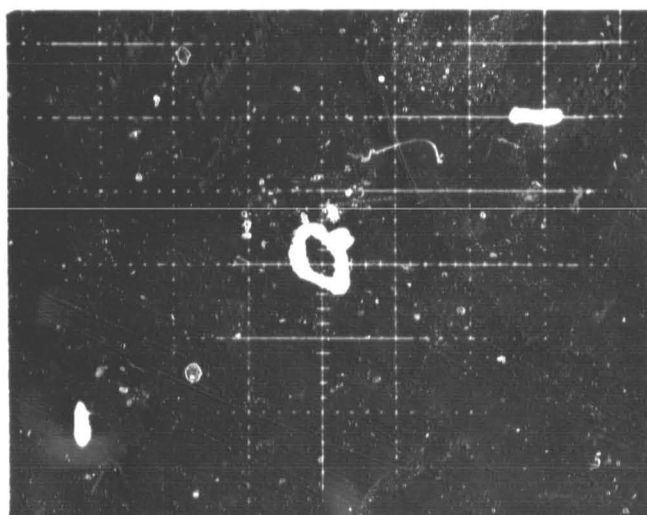
Seal and Runner Motion
Seal Set No. 2 at 3665 rad/s

- 655 kPa Supply Pressure
- 103 kPa Otb Drain Pressure

Runner



Inb
Seal



Otb
Seal

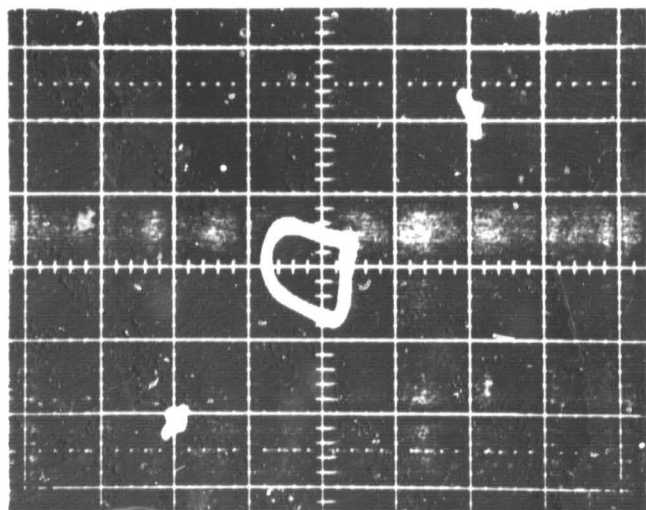
Fig. 3-55

Seal and Runner Motion
Seal Set No. 2 at 4188 rad/s

- 862 kPa Supply Pressure
- 517 kPa Otb Drain Pressure

Runner

Inb
Seal



Inb
Seal

Fig. 3-56

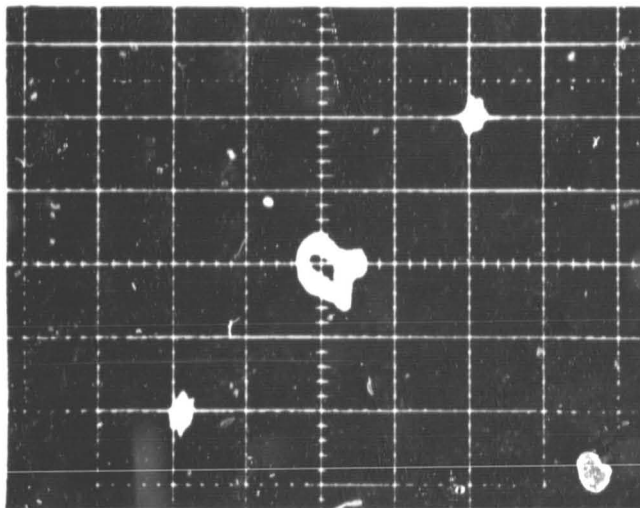
Seal and Runner Motion
Seal Set No. 2 at 4712 rad/s

- 938 kPa Supply Pressure
- 517 kPa Otb Drain Pressure

Runner

Otb
Seal

ORIGINAL PAGE IS
OF POOR QUALITY



Otb
Seal

Runner

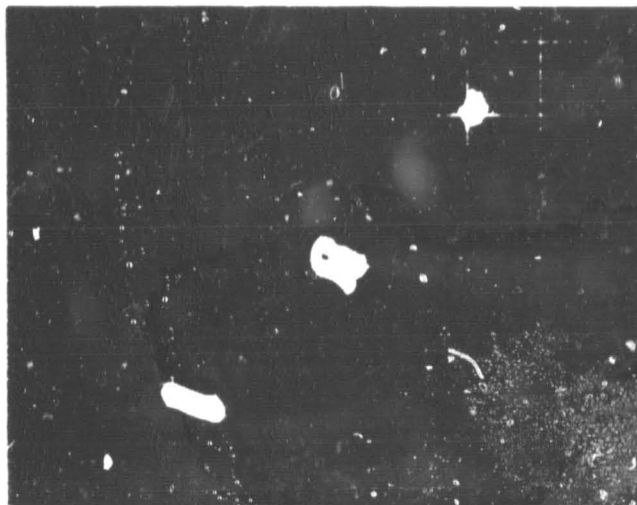
Inb
Seal

Fig. 3-57

Seal and Runner Motion

Seal Set No. 3 at 3665 rad/s

- 655 kPa Supply Pressure
- 517 kPa Otb Drain Pressure



Otb
Seal

Runner

Inb
Seal

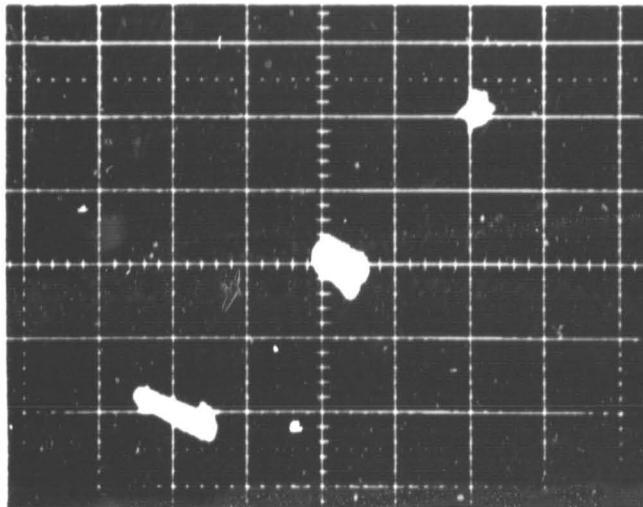
Fig. 3-58

Seal and Runner Motion

Seal Set No. 3 at 3665 rad/s

- 1206 kPa Supply Pressure
- 517 kPa Otb Drain Pressure

ORIGINAL PAGE IS
OF POOR QUALITY



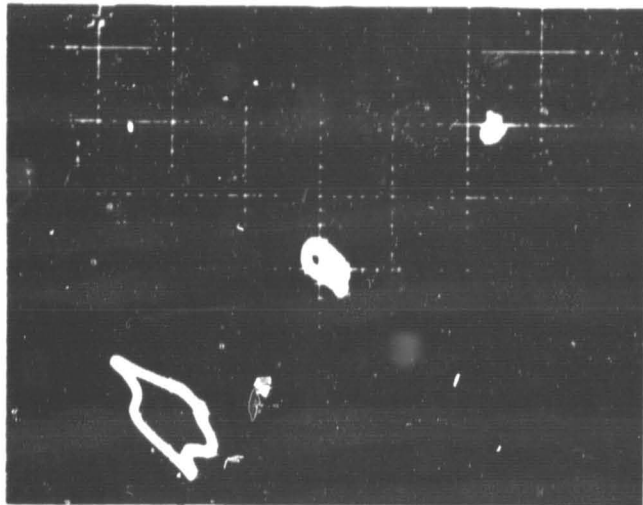
Oth
Seal

Runner

Inb
Seal

Fig. 3-59

Seal and Runner Motion
Seal Set No. 3 at 3665 rad/s
• 1206 kPa Supply Pressure
• 310 kPa Otb Drain Pressure



Otb
Seal

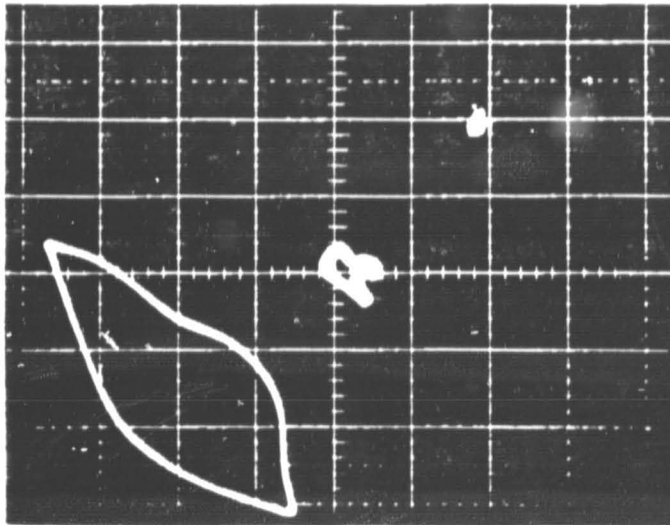
Runner

Inb
Seal

Fig. 3-60

Seal and Runner Motion
Seal Set No. 3 at 3665 rad/s
• 1206 kPa Supply Pressure
• 103 kPa Otb Drain Pressure

ORIGINAL PAGE IS
OF POOR QUALITY



Otb
Seal

Runner

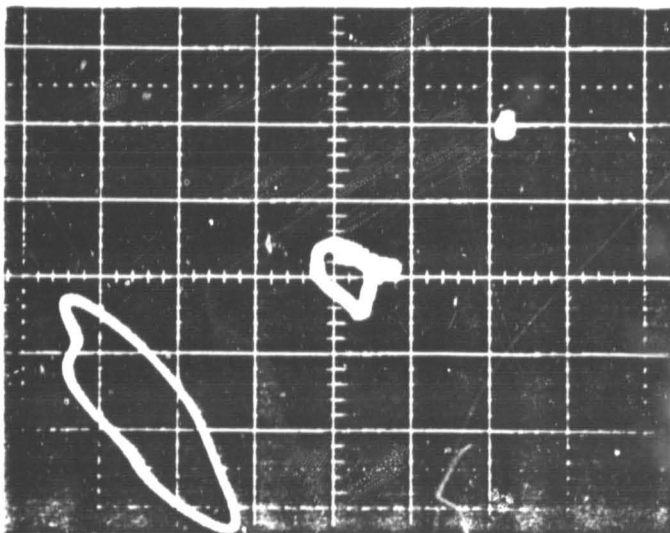
Inb
Seal

Fig. 3-61

Seal and Runner Motion

Seal Set No. 3 at 4188 rad/s

- 1069 kPa Supply Pressure
- 103 kPa Otb Drain Pressure



Otb
Seal

Runner

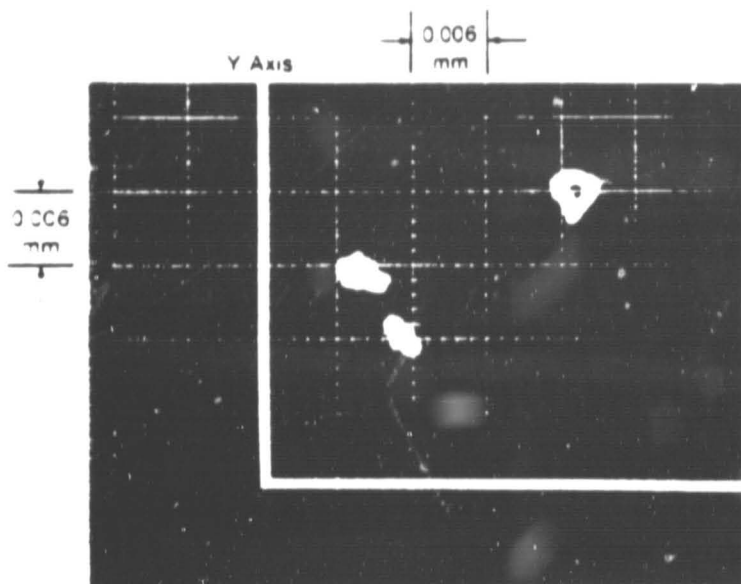
Inb
Seal

Fig. 3-62

Seal and Runner Motion

Seal Set No. 3 at 4712 rad/s

- 1482 kPa Supply Pressure
- 517 kPa Otb Drain Pressure



ORIGINAL PAGE IS
OF POOR QUALITY

Runner

Vertical
Probes

Horizontal
Probes

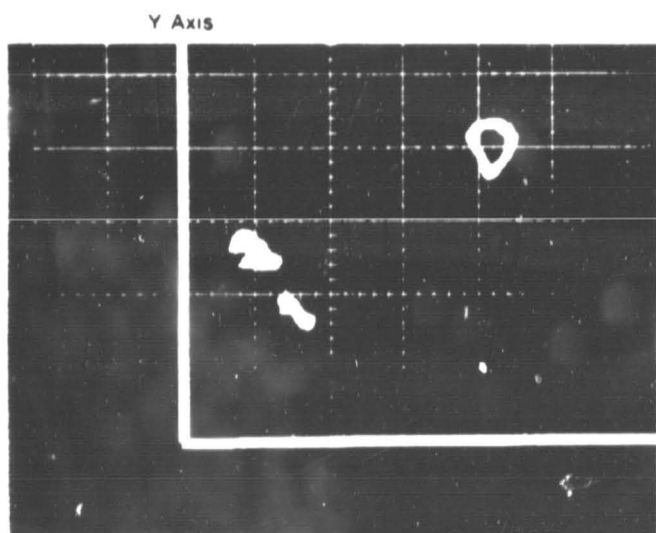
X Axis

Fig. 3-63

Seal and Runner Motion

Seal Set No. 4 at 3665 rad/s

- 827 kPa Supply Pressure
- 517 kPa Otb Drain Pressure



Runner

Vertical
Probes

Horizontal
Probes

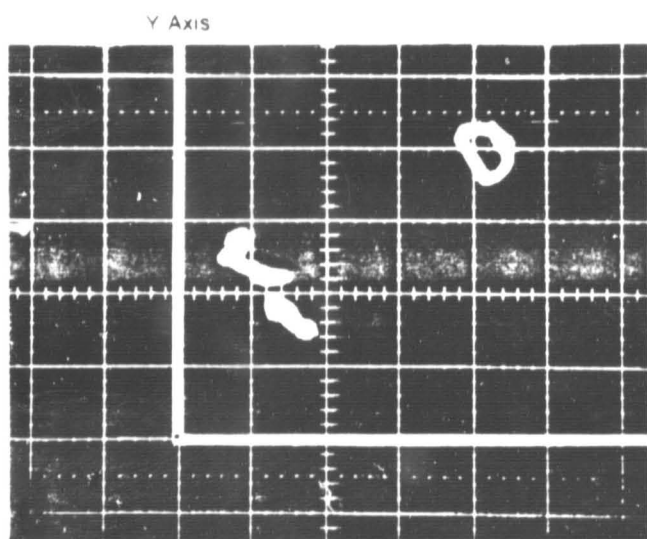
X Axis

Fig. 3-64

Seal and Runner Motion

Seal Set No. 4 at 4188 rad/s

- 827 kPa Supply Pressure
- 517 kPa Otb Drain Pressure



Runner

Vertical
Probes

Horizontal
Probes

X Axis

Fig. 3-65

Seal and Runner Motion

Seal Set No. 4 at 4712 rad/s

- 827 kPa Supply Pressure
- 517 kPa Otb Drain Pressure

ORIGINAL PAGE IS
OF POOR QUALITY

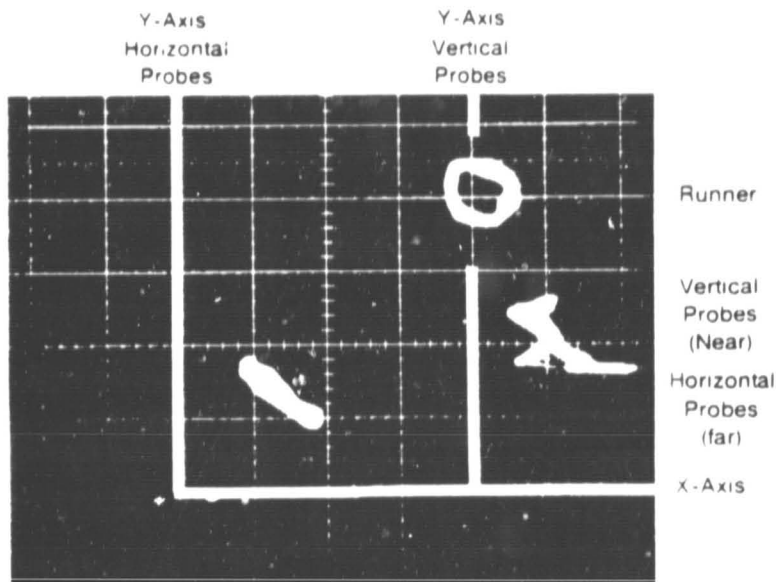


Fig. 3-66

Seal and Runner Motion

Seal Set No. 4 at 5235 rad/s

- 827 kPa Supply Pressure
- 517 kPa Otb Drain Pressure

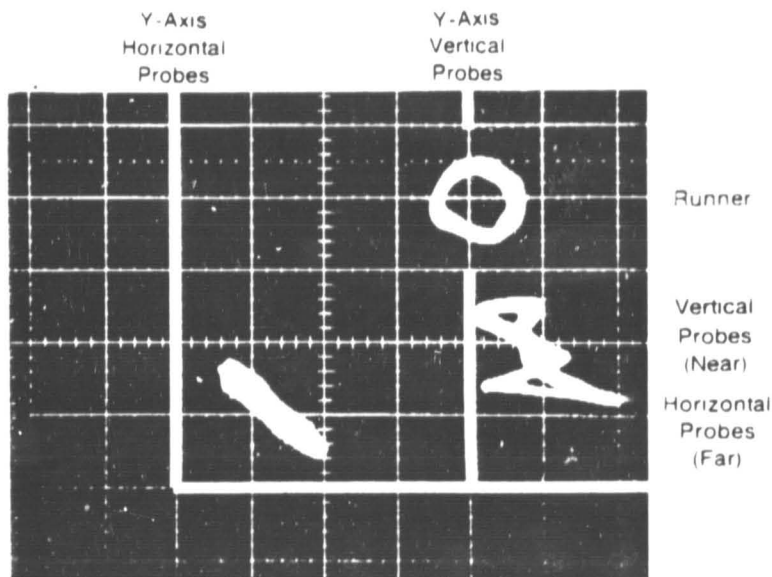


Fig. 3-67

Seal and Runner Motion

Seal Set No. 4 at 5759 rad/s

- 724 kPa Supply Pressure
- 517 kPa Otb Drain Pressure

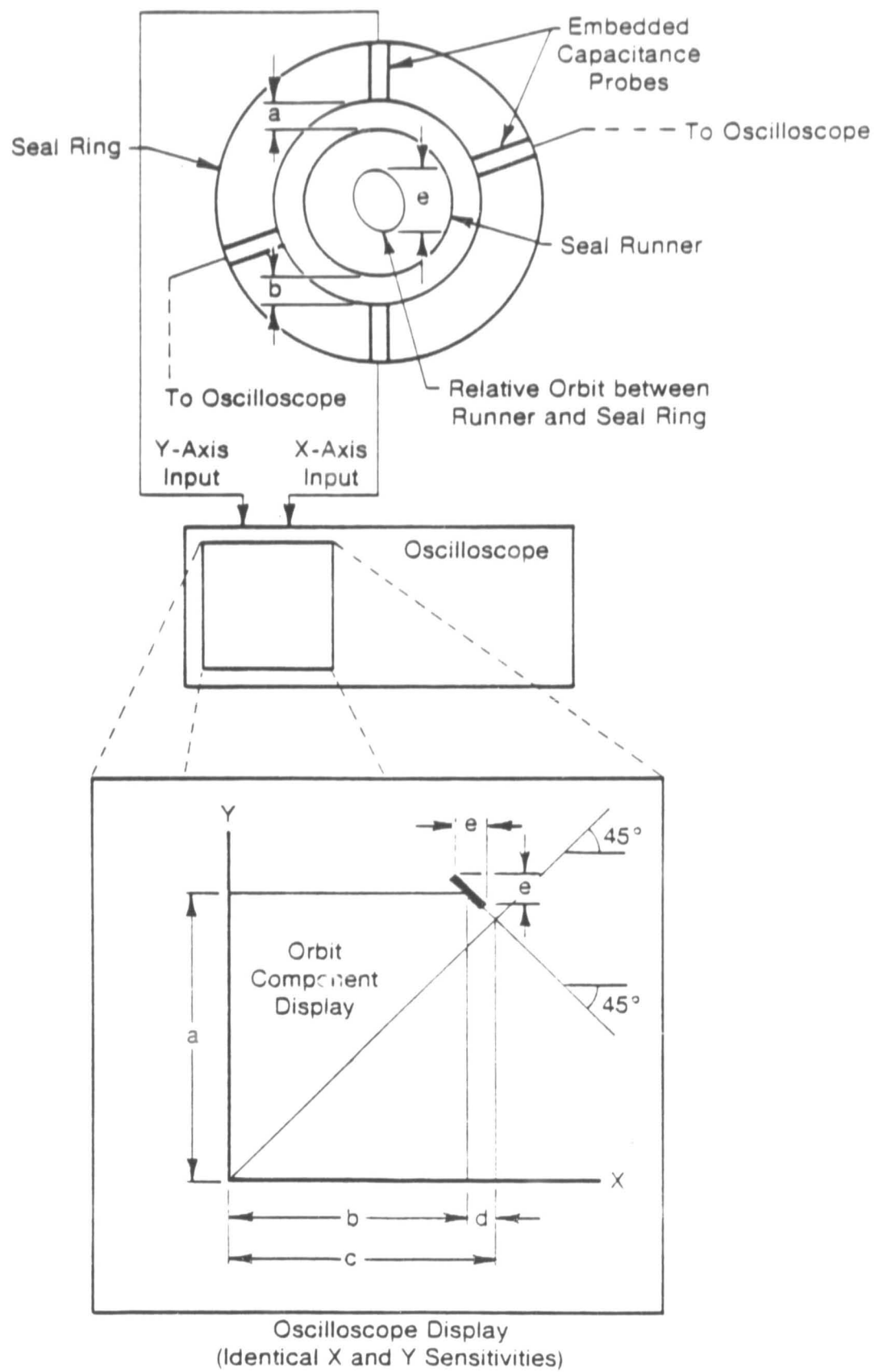
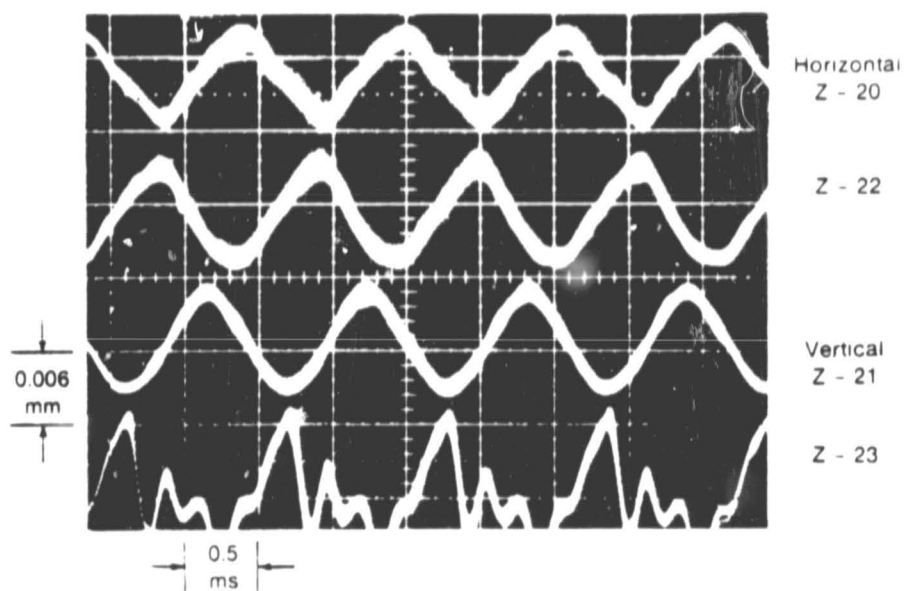


Fig. 3-68 Embedded Probe Oscilloscope Display Format

851144

ORIGINAL PAGE IS
OF POOR QUALITY



Seal Probe Time Trace

Seal Set No. 4 at 5759 rad/s

- 724 kPa Supply Pressure
- 517 kPa Otb Drain Pressure

Fig. 3-69

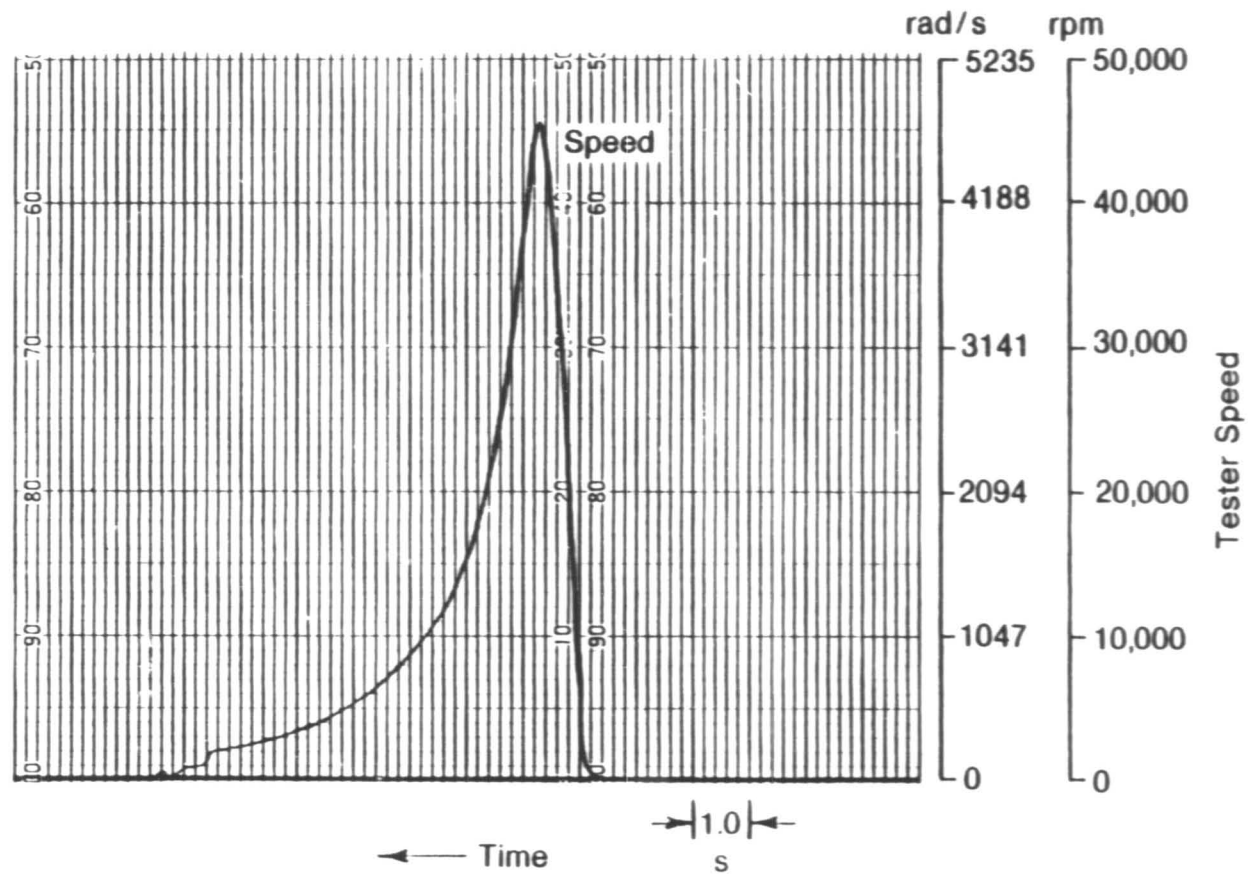


Fig. 3-70 Speed-Time Curve for Typical Acceleration Run



Fig. 3-71 Damaged Seal; Outboard Ring - Seal Set No. 1

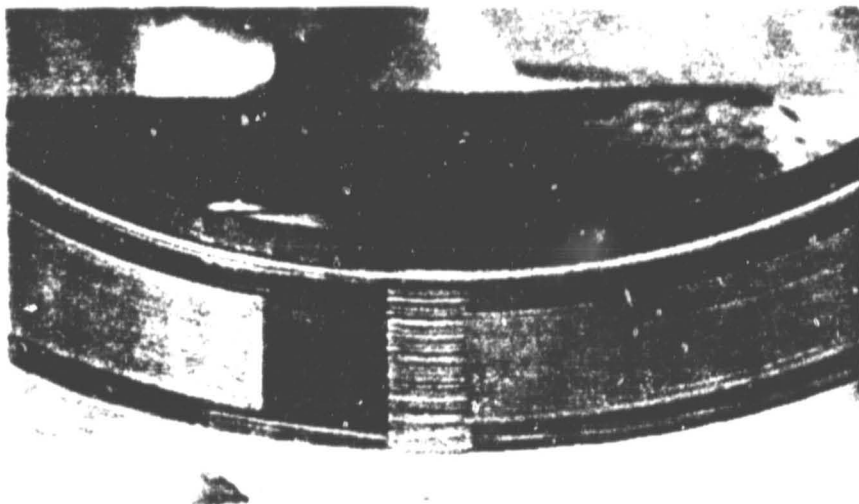


Fig. 3-72 Undamaged Seal; Inboard Ring - Seal Set No. 1

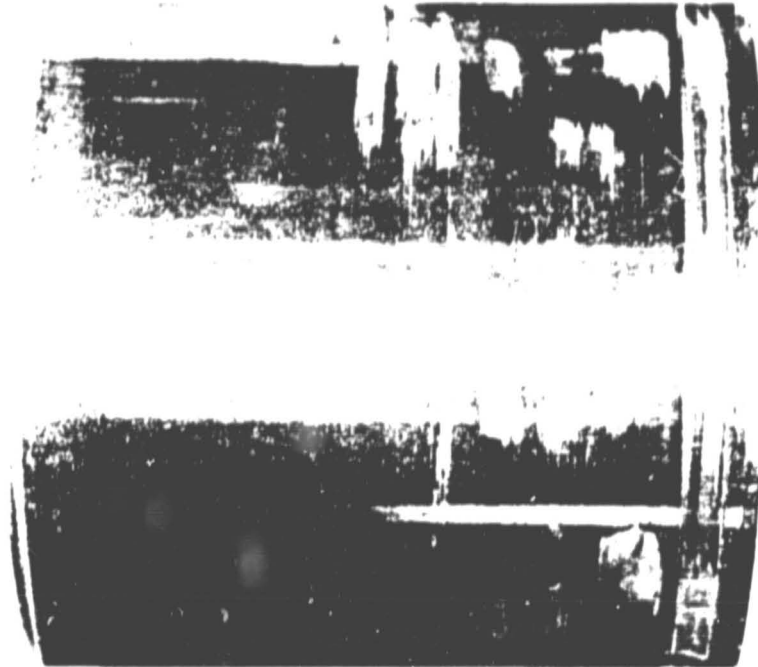
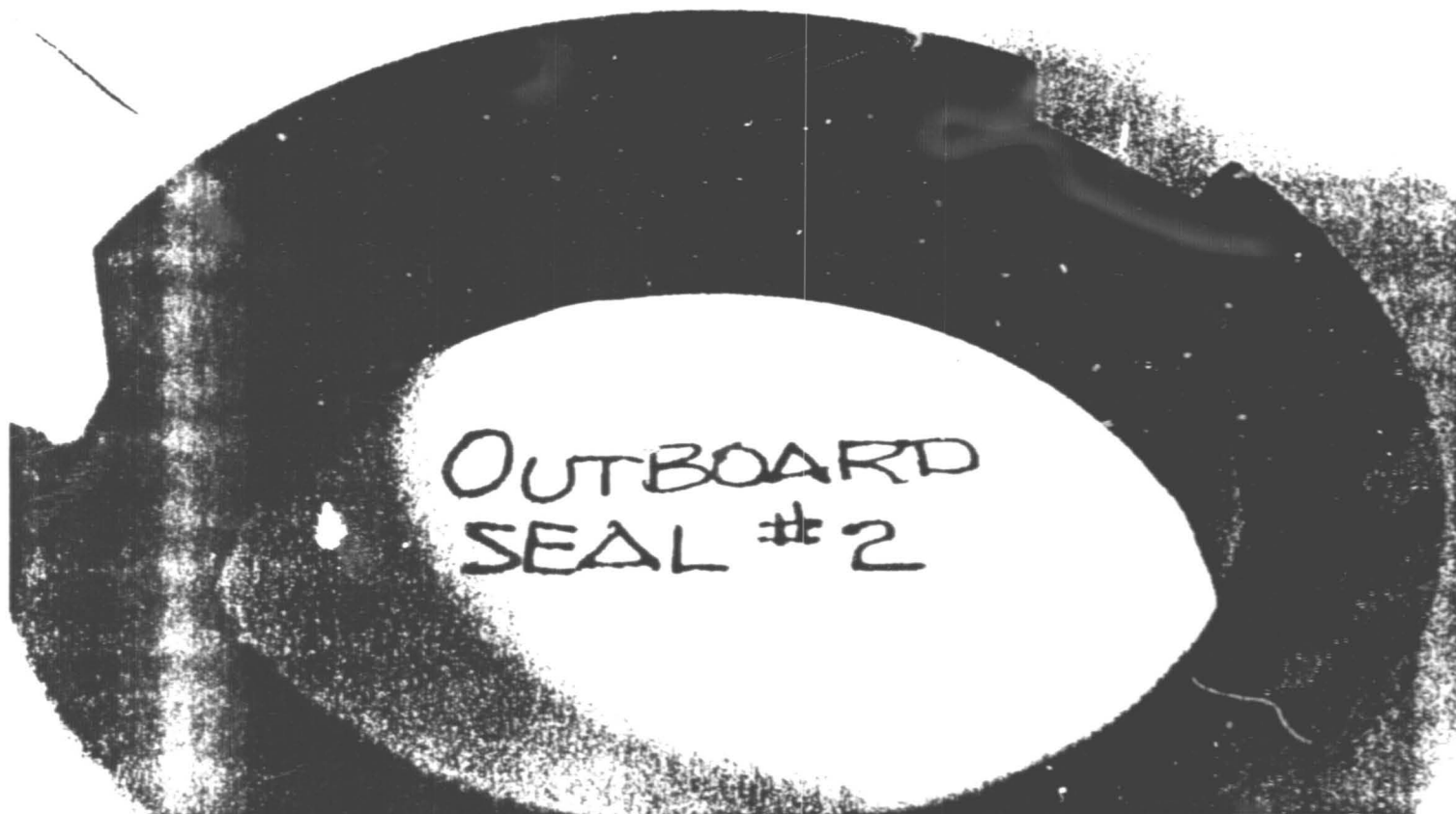


Fig. 3-73 Damaged Runner; Inboard Left, Outboard Right -
Seal Set No. 1



Fig. 3-74 Magnified View (X11.4) of Damaged Runner -
Seal Set No. 1



ORIGINAL PAGE IS
OF POOR QUALITY

Fig. 3-75 Undamaged Seal; Outboard Ring - Seal Set No. 2

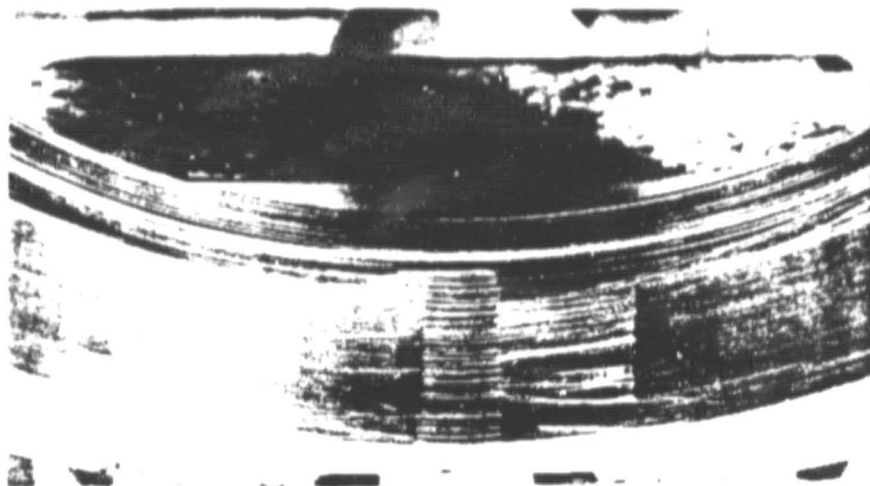


Fig. 3-76 Damaged Seal; Outboard Ring - Seal Set No. 3

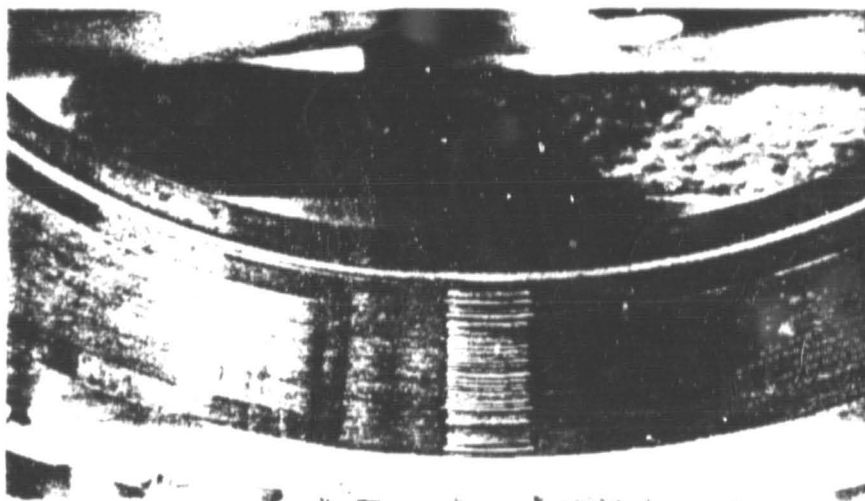


Fig. 3-77 Undamaged Seal; Inboard Ring - Seal Set No. 3

ORIGINAL PAGE IS
OF POOR QUALITY

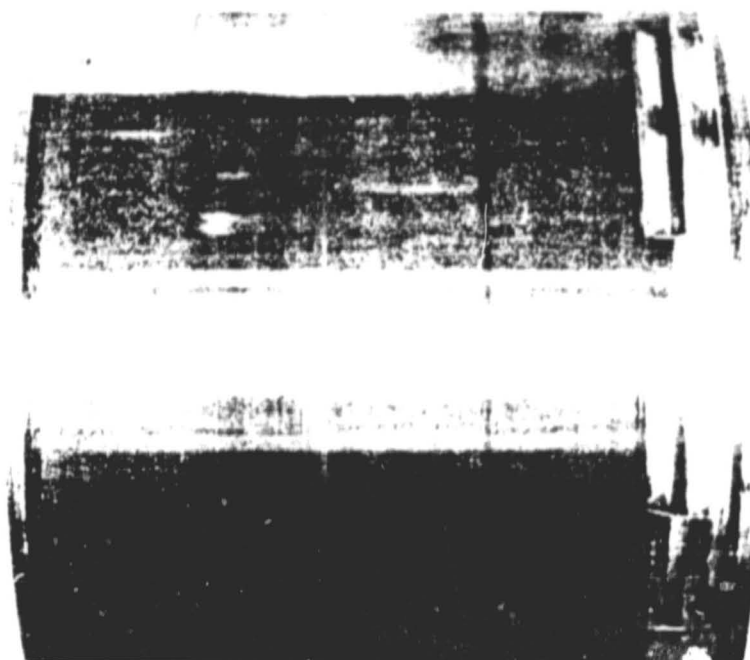


Fig. 3-78 Damaged No. 2 Runner; Inboard Left, Outboard
Right - Seal Set No. 3

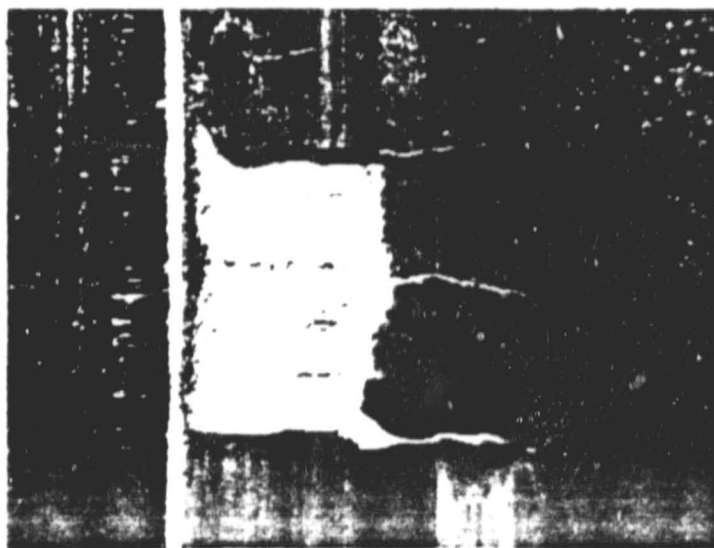


Fig. 3-79 Magnified View (X11.5) of Damaged No. 2 Runner

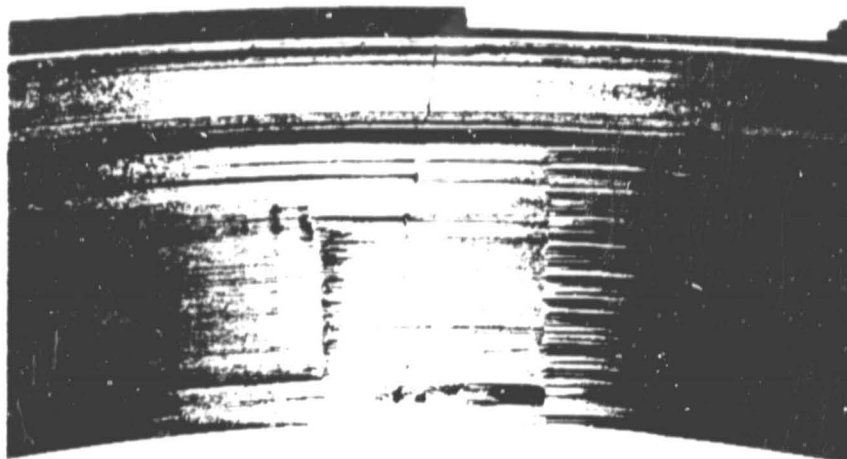


Fig. 3-80 Damaged Seal; Inboard Ring - Seal Set No. 4

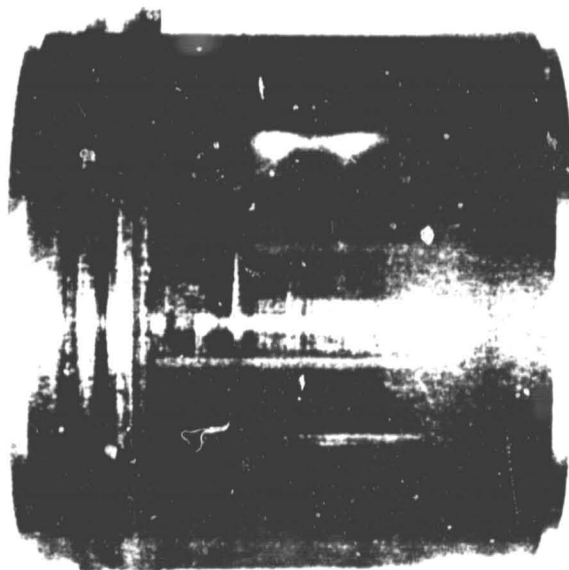


Fig. 3-81 Damaged No. 3 Runner; Inboard Left, Outboard Right - Seal Set No. 4

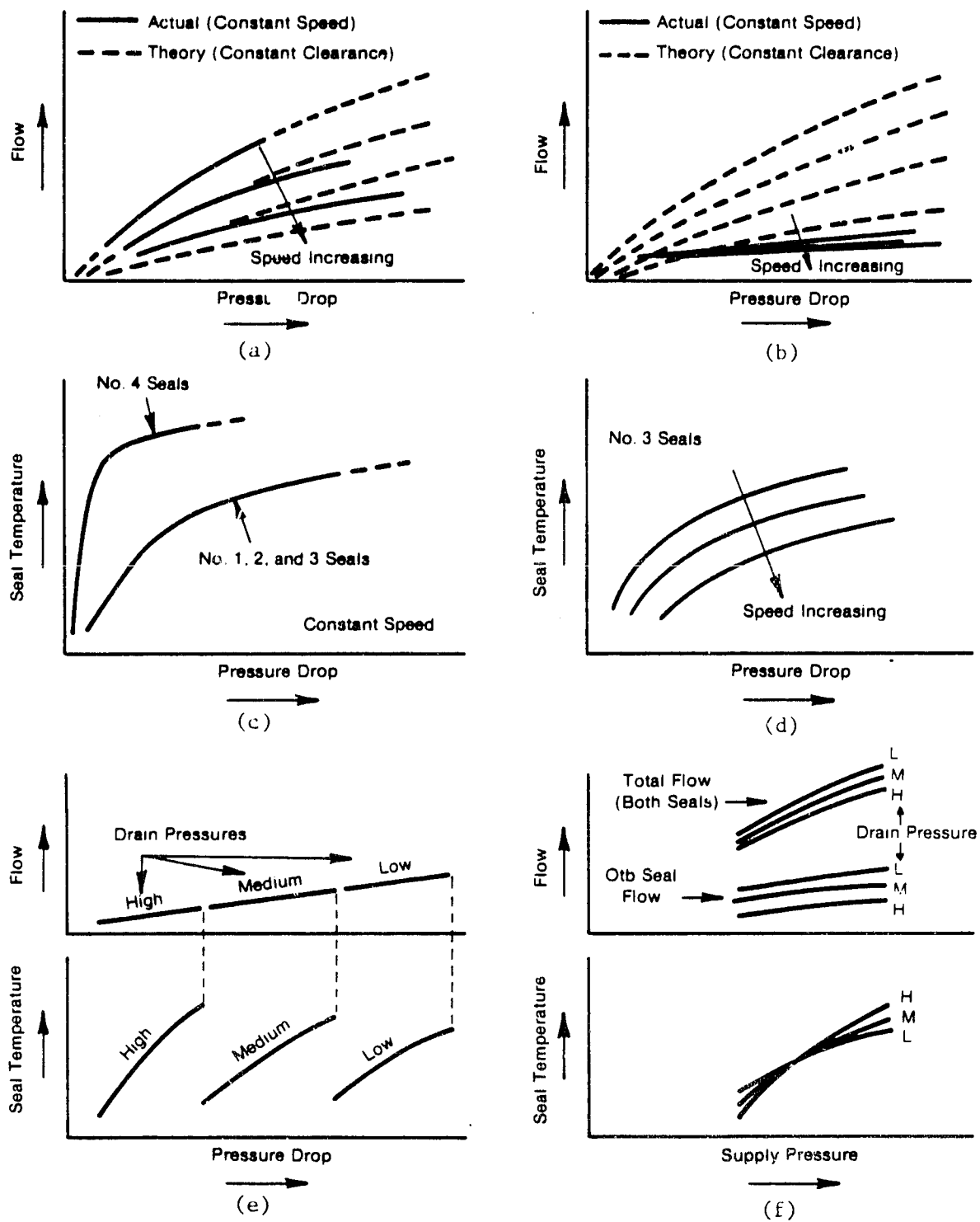


Fig. 3-82 Parametric Variations as a Function of Pressure Drop and Supply Pressure

4.0 ANALYSIS AND DESIGN OF RAYLEIGH-STEP, HELIUM BUFFER SEALS

4.1 Operating Conditions

The principles of operation and general geometry were presented in Section 2.0. Additional details concerning performance and theoretical development are included in References [2], [6], and [7].

Refer to Table 1-1 for the geometric and operational parameters. The surface speed of 183 m/s (600 fps) and the buffer fluid pressure of 1379 kPa (200 psia) are two conditions that extend the state of the art.

The properties of helium as a function of pressure and temperature are indicated on Table 4-1*. The analysis used the helium viscosity and density at 37.8°C (100°F) and at pressures of 1379, 689, and 344 kPa (200, 100, and 50 psia), with ambient (101 kPa/14.7 psia) downstream pressures. As indicated on Table 4-1, helium gas viscosity varies only $\pm 6\%$ from the value of 37.8°C (100°F) and is independent of pressure. Also the density varies only $\pm 10\%$ from the value of 37.8°C (100°F) and is proportional to pressure.

4.2 Design Considerations

When designing hydrodynamic gas-lubricated floating-ring seals, there are several important considerations. First, the hydrodynamic forces that are generated when the rings go eccentric with the shaft must be sufficient to overcome the friction forces between the rings and the stationary walls. This is necessary to maintain the rings concentric with the shaft.

To minimize leakage, the operating film thicknesses must be relatively small. Small film thicknesses are also necessary to provide high fluid-film stiffness which is desirable for causing the rings to follow shaft excursions.

*Tables are presented consecutively, beginning on page 4-17.

The clearances involved are generally smaller than centrifugal growth and thermal variations in clearance. Therefore, it is important to account for both centrifugal growth and thermal distortions in designing the seal.

Finally, the seal rings must respond to shaft excursions and runouts without contact between the shaft and the rings. This requires that dynamic analyses be conducted and dynamic response be carefully investigated.

The analytical process that was used in designing the seals was to:

1. Optimize the Rayleigh-step geometry principally on the basis of fluid-film stiffness using steady-state fluid-film gas bearing theory.
2. Include the effects of centrifugal and thermal variations in shaft and ring geometries in establishing predicted performance. These effects change the operating film thickness which is a sensitive parameter with respect to performance.
3. Conduct dynamic response analyses to ensure that the rings follow shaft excursions without contact.

A constraint imposed upon the design of these type seals is to keep the axial length as small as possible to minimize shaft length and not compromise rotor-dynamics of the shaft bearing system. In considering both the 50- and 20-mm seals, it was necessary to maintain the axial length of each ring within approximately 12.7 mm (0.5 in.). This was considered a practical number for incorporation into actual pump machinery.

4.3 Analysis and Design of the 50-mm Floating-Ring Helium Purge Seal

4.3.1 Rayleigh Step Optimization Studies

Initially, studies were made to determine the optimum Rayleigh-step geometry. The parameter optimized was the fluid-film stiffness, which is most important

to prevent shaft/ring contact. Figure 4-1* shows dimensionless stiffness as a function of the step clearance/land clearance ratio. The step clearance includes the step height plus the film thickness above the step. The curve indicates that the step clearance should be 2.65 x the land clearance. The seal was designed for an operating land film thickness of 0.0127 mm (0.0005 in.), so the step height should have a nominal value of 0.0210 mm. The stiffness values are fairly symmetrical about the optimum point so that the tolerance range could be on either side of the optimum value. The actual step height selected was 0.0229 to 0.0254 mm (0.0009 to 0.001 in.) to allow for variations in actual operating clearances. These step dimensions provide good stiffness over a wide clearance range.

Figure 4-2 shows the effects of the axial length ratio which is the step length/pad length ratio = L_1/L , as a function of dimensionless stiffness. This parameter is quite insensitive, although the optimum length ratio is 0.66.

Figure 4-3 shows the effect of the circumferential length of the Rayleigh step. Over the range shown, it is an insensitive parameter, but the optimum ratio of step length/pad length is 0.82, which indicates that long steps are desirable.

The step dimensions were optimized for concentric bearing stiffness. The dimensionless length, width, and depth of the step have the following optimum values:

- Depth of step, step clearance/land clearance = 2.65
- Axial extent of step, $L_{\text{step}}/L_{\text{pad}} = 0.66$
- Circumferential extent of step, $\theta_{\text{step}}/\theta_{\text{pad}} = 0.82$

Studies were also made varying the total numbers of pads. Increasing the number of pads from 4 to 5 (while maintaining the same ratio of groove width to circumferential pad extent and the same step geometry) decreased the centered

*Figures are presented consecutively, beginning on page 4-22.

stiffness by only 1%, indicating that four pads yield fairly optimum fluid film performance. The four-pad geometry was selected. Figures 2-1 and 2-2 indicate the nominal dimensions used.

4.3.2 General Configuration and Design

Figure 4-4 indicates a developed view of the inner surface, including the hydrodynamic geometry and also shows the end wall contact surface region in larger scale. The contact surface was maintained as small as practical (0.762 mm) (0.030 in.) and as close to the shaft as possible to reduce the maximum thrust loading on the seal rings.

Figure 4-5 shows the installation of the rings in the seal tester. What is to be particularly noted is the diameter of the seal runner which is considerably larger than the shaft diameter used in the experimental rig. The shaft size is approximately 30 mm (1.18 in.) in diameter while the runner size is required to be 50 mm (1.97 in.) in diameter. Examination of this figure indicates that centrifugal growth of the seal runner will be significant. The seal runner configuration was designed to provide equal distribution of the centrifugal growth without causing closure at the ends of the runner.

Figure 4-6 indicates what centrifugal growths will do to the runner at the maximum operating speed of 7330 rad/s (70,000 r/min). It will expand radially, approximately 11.43 μ m, with slight variations at the end (1.88 μ m). The end closures are inconsequential and confirm the advantage of the taper, T, configuration employed. The total radial expansion, however, is of the same order of magnitude as the film thickness, thus manufacturing and installation dimensions must be large enough to accommodate the runner growth or clearance closure. The runner was shrunk over a flexure which could compensate for increase in the inside diameter of the runner due to centrifugal expansion.

The dimensions of shaft and ring indicated on Figure 4-5 were selected to provide near optimum clearance at the operating condition considering the effects of both thermal contraction and centrifugal growth, respectively.

The seal rings were made entirely of carbon (i.e., no metallic bands) to enhance dynamic response characteristics (Pure Carbon P5N). The runner was made of Inconel 718 for strength purposes and coated with a layer of tungsten carbide with a chromium binder. The ring mating housings were Inconel 600.

The final seal detail drawings were completed by the seal manufacturer, Stein Seal Company of Philadelphia, Pa. Figure 4-7 shows the assembly drawing of the seal and housings. Figure 4-8 shows a detail drawing of the outboard seal ring. A photograph of one set of seal rings was previously shown on Figure 2-3.

4.3.3 Fluid-Film Performance

Fluid-film performance was initially established using a nominal radial clearance of $12.7\text{ }\mu\text{m}$ and correcting for centrifugal growth of the shaft sleeve. Subsequently, larger clearances were examined to allow for variations in clearance due to tolerances and to thermal contractions of the sleeve. Figure 4-9 shows the variation in concentric seal clearance due to centrifugal expansion of the sleeve as a function of shaft speed, presuming a $12.7\text{ }\mu\text{m}$ operating clearance at the maximum speed (7330 rad/s) ($70,000\text{ r/min}$) condition. The assembled radial clearance is approximately $29\text{ }\mu\text{m}$ to attain a $12.7\text{ }\mu\text{m}$ clearance at operating speed. This assembled clearance does not account for thermal contractions. It was subsequently found that the installed clearance should be as small as possible, to achieve an operating clearance of approximately $12.7\text{ }\mu\text{m}$, because thermal contractions of the runner had a stronger influence than centrifugal growth.

Figure 4-10 shows the fluid-film force developed in a seal ring versus eccentricity ratio at three different helium pressure levels, 344, 689, and 1379 kPa (50, 100, and 200 psia). Superimposed on these curves, are frictional resistance forces between the floating rings and the stationary housing. The radial clearance was $12.7\text{ }\mu\text{m}$. The results indicate that maximum frictional resistance can be overcome by hydrodynamic forces at high-speed operation. It also indicates that at 1379 kPa (200 psia) buffer pressure, low-speed hydrodynamic forces will not overcome frictional resistance. At maximum speed of

7330 rad/s (70,000 r/min) and maximum buffer pressure of 1379 kPa (200 psia), an eccentricity ratio of approximately 0.65 is necessary to overcome the maximum frictional resistance of approximately 42.3 N (9.5 lb). Table 4-2 shows the effects of radial clearance on the seal's ability to overcome frictional resistance.

The tabulated values of eccentricity ratio and minimum film thickness are necessary to produce sufficient hydrodynamic forces to overcome the maximum friction forces at each of the buffer fluid pressures indicated. The results clearly indicate the superior performance at the low clearance condition of 12.7 μm . At the high buffer fluid pressures, the low clearance installation produces the higher minimum film thickness. At a 25.4 μm radial clearance, the seal would not adequately overcome frictional resistance at a buffer pressure of 1379 kPa (200 psia).

Viscous power loss for a single ring as a function of speed and pressure is indicated on Figure 4-11. At maximum speed and pressure the total power loss is approximately 85 W.

Seal leakage, on the basis of laminar flow without inertia drop losses, is shown on Figure 4-12. A reduction in leakage with speed occurs because the centrifugal runner growth causes closure of the clearance as the speed increases. At 7330 rad/s (70,000 r/min) with an operating clearance of 12.7 μm , the seal leakage (single ring) is 0.908×10^{-3} kg/s (11.5 scfm). The leakage values on Figure 4-12 assume concentric operating clearance (i.e., the rings are centered with respect to the shaft). The leakage increases approximately 40% from concentric to full eccentric operation.

Testing indicated that seal leakage was lower than predicted. Modifications were made to the analysis to include inertia effect at the seal dam inlet and in the film itself. The analysis to accomplish this is described in Appendix A. Correlation between experiment and theory was then significantly improved.

Figure 4-13 shows fluid temperature rise as a function of speed and pressure. These curves assume all heat generated by viscous friction is absorbed by the flow leaking through the clearance annulus; heat transferred to the shaft is

not accounted for. Therefore, the temperature rises indicated on Figure 4-13 are exaggerated. Since flow increases with buffer pressure, the temperature rise is an inverse function of buffer pressure and will be lower as the pressure increases. The results indicate that high-speed, low-pressure operation is to be avoided. Table 4-3 indicates maximum operating speed as a function of buffer pressure to limit the temperature rise to 22°C (39.6°F), which can be considered a maximum safe value. The values of flow used in the temperature rise computations were based on viscous laminar theory without inertia. When inertia effects are included, there is a flow reduction which would result in a proportional increase in temperature rise. This increase in temperature rise was one of the contributing factors to clearance closure that was experienced by the inboard ring of seal No. 4.

4.3.4 Thermal Analysis

The model for the thermal analysis is shown on Figure 4-14. The four significant modes are 6 and 7 for the two rings and 9 and 10 for the runner. Relatively hot helium enters the space between the two rings and flows inboard and outboard through the annular clearance between the rings and rotating collar. On the inboard side near node 9, the collar is cooled by the LOX escaping from the bearing, while on the outboard side near node 10, helium at much higher temperature escapes. The analysis considered 0.0018 kg/s (22.74 scfm) of helium entered the buffer chamber at an inlet temperature of 21°C (69.8°F) and that approximately 90 W of heat was generated at the fluid-film interface. Studies were made to establish the sensitivity of varying parameters. Table 4-4 lists the cases that were run on the computer and the results obtained.

The table indicates that the resulting temperatures are not very sensitive to the values of the heat transfer coefficients used.

Seal operating film thicknesses have been calculated using various values of installed clearance and accounting for centrifugal growth and thermal effects. Recommended dimensions are indicated on Table 4-5. The following nomenclature applies:

D_{ring} = ID of the seal ring
 D_{shaft} = OD of the shaft runner
 C_0 = Assembled radial clearance
 C_0' = Radial clearance including centrifugal growth of shaft
 C_0'' = Running radial clearance including centrifugal and thermal growth

Each set of three consecutive lines in the table corresponds to the maximum, average, and minimum clearance of the tolerance range. These calculations of running clearance used the following data:

- Radial growth of shaft runner at 7330 rad/s (70,000 r/min):
11.43 μm
- Mean coefficient of thermal expansion of carbon graphite:
 $5.58 \times 10^{-6}/^{\circ}\text{C}$ ($3.1 \times 10^{-6}/^{\circ}\text{F}$)
- Mean coefficient of thermal expansion of Inconel 718:
 $12.78 \times 10^{-6}/^{\circ}\text{C}$ ($7.1 \times 10^{-6}/^{\circ}\text{F}$) at 21°C (69.8°F)
 $10.62 \times 10^{-6}/^{\circ}\text{C}$ ($5.9 \times 10^{-6}/^{\circ}\text{F}$) at -196°C (-320.8°F)

The difference in operating clearances on Table 4-5 are due to differences in nominal ring and shaft dimensions. The middle line corresponds to nominal size with tolerance variation indicated above and below. Table 4-5 also indicates recommended final dimensions to account for both centrifugal and thermal growths.

The results clearly indicate that the assembly clearance be 5 to 8 μm (as small as possible for assembly without requiring an interference fit). That is, the dimension of the ring ID should be 50.02022/50.0253 mm (1.9693/1.9695 in.), while that of the shaft runner OD should be 50.00598/50.01006 mm (1.9693/1.9689 in.). The running seal clearances are then reduced to 11.176 and 25.4 μm on the air and LOX sides, respectively. In the final design, it was necessary to compromise further for manufacturing purposes. The outboard seal ring was designed for higher clearance than the inboard seal ring, since thermal effects would cause increased clearance on the inboard ring. The final clearances employed are discussed in Section 2.0.

4.3.5 Seal Ring Dynamic Response

Because of high surface speeds and low operating film thickness, it was important to investigate dynamic response and to design a system that avoids rubbing contact. A time-transient analysis was employed, whereby time is discretized into small increments. At each increment fluid-film and friction forces are examined to determine net forces on the ring. These forces can then be inserted into the equations of motion to establish ring motion for that time increment. Thus, a time history of ring movement is provided as a function of shaft excursions. If frictional forces exceed fluid-film forces at any instant of time, ring motion is curtailed.

Studies indicated that for any particular eccentricity ratio, the fluid-film force did not vary strongly with angular position and using a constant value would produce accurate results. This was done in the computer analysis, but the conservative or the lowest values of film forces were used for each eccentricity ratio. Figure 4-15 shows typical fluid-film force curves that were applied in the program. Shown are the radial component (along the line of centers) and the tangential component (normal to the line of centers) as a function of eccentricity ratio at the 1379 kPa (200 psia), 7330 rad/s (70,000 r/min) operating condition. Note the tangential component is small.

Force information was interpolated in the computer code, so that knowing the shaft location produced the normal and tangential forces required. Similar information was produced at other pressures and speeds.

A shaft orbital radius of 2.5 μm simulates anticipated test conditions. However, much larger orbital amplitudes were also examined to establish an adequate "factor of safety" with respect to dynamic response.

Figure 4-16 shows a typical orbital response case when the shaft runout is 7.62 μm , operating at 7330 rad/s (70,000 r/min) and 1379 kPa (200 psia) buffer fluid pressure. The starting position was with the seal ring concentric with the shaft. The ring settles into a rectangular shaped orbit with a maximum eccentricity ratio of 0.625. The eccentricity and orbit indicated are rela-

tive to the shaft, and the clearance circle, between the outside circle and the orbit is the clearance seen by an observer riding on the shaft.

Figure 4-17 shows a case at 345 kPa absolute (50 psia) buffer pressure at a shaft speed of 2094 rad/s (20,000 r/min). At the lower speed condition hydrodynamic forces and stiffness are relatively low, so that the ring can be expected to respond rather sluggishly to shaft motions. This is demonstrated by the case shown on Figure 4-17. In this instance, the shaft radial runout is 0.0102 mm (0.0004 in.). The starting position was at a shaft eccentricity ratio of 0.95. The ring moved slightly more concentric, and then maintained its position without further motion. The shaft is moved eccentrically within the clearance circle at its prescribed eccentricity ratio of 0.8. Basically, at these conditions film stiffness was insufficient to center the ring and permit it to follow shaft motions in a nearly concentric position. For this case, the 345 kPa absolute (50 psia) buffer pressure will not produce high friction forces; therefore, at higher pressure levels the seal ring will continue to remain stationary.

Figures 4-18 and 4-19 show response at low speed and relatively high pressure conditions so that friction forces dominate. The orbital relationship between the shaft and ring is erratic and complex with reverse loops involved with each cycle.

Studies were also made of composite rings where an Inconel ring was shrunk around the outer periphery of the carbon ring. This was done to produce more uniform thermal distortions between the rings and shaft. The added mass of the composite rings, however, caused contact failure due to excessive inertial accelerations that would not permit the rings to move in unison with the shaft. A typical case is shown on Figure 4-20. Contact occurs before an orbit can be completed. Thus, it is important to keep the ring mass as low as possible, and integral carbon rings without metal shrouds are necessary for adequate dynamic response.

Table 4-6 summarizes the operating conditions and results of the dynamic response computer runs. The variables included shaft eccentricity or runout, operating clearance, buffer fluid pressure and speed. The orbit eccentricity

is the maximum eccentricity of the resulting steady-state orbit of the ring. The minimum film thickness, h_m , was the minimum value experienced during the orbital response. Potential problem areas, where minimum films are becoming dangerously small or are negative, are underlined. The 1379 kPa (200 psia), 7330 rad/s (70,000 r/min) condition is considered acceptable; it might be a marginal problem at very high shaft runouts, which were not anticipated to occur. In fact, they did occur and caused failure of Seal Set No. 1.

Figure 4-21 shows the effects of varying the shaft runout. Note that at a 2094 rad/s (20,000 r/min) and 344 kPa (50 psia) buffer pressure, the eccentricity ratio is becoming very high and is an operating condition that should be avoided. In this instance, inertia-dominated motions of the ring are overcoming the friction retardation forces and the fluid-film stiffness capacity. At 70,000 rad/s (7330 r/min) and 1379 kPa (200 psia), the limit cycle is well controlled even with a high shaft eccentricity of 12.7 μm . An overall summary plot is shown on Figure 4-22. It is a plot of maximum transient orbital eccentricity ratio versus shaft vibration or runout orbit for varying types of rings (solid carbon or composite carbon and metal) at different pressure conditions. Composite rings are sometimes used to more nearly equalize thermal expansions between the rings and shaft. The operating speed is 7330 rad/s (70,000 r/min).

Note that the composite carbon/Inconel rings have significantly less tolerance to shaft orbit than do the solid carbon rings. Note also that higher pressure and consequently higher frictional forces are beneficial (at high operating speeds) because the friction forces prevent excessive inertial response of the rings. Thus, there are really two limiting conditions concerned with ring design. First, the fluid-film forces should be great enough to overcome frictional resistance to ensure against contact, and second, there should be sufficient friction to prevent inertia dominated motion of the ring that could cause contact under high-speed conditions.

All of the dynamic discussion thus far has presumed an operating radial clearance of 12.7 μm . Because of the difficulty of obtaining this clearance precisely, due to manufacturing tolerances, centrifugal growth and thermal contractions, studies were also made at varying clearances. The dominating

influence is the thermal effects which causes a reduction in shaft diameter and an opening of the clearance. Thus, several computer runs were made at 25.4 μm radial clearance or twice the designed clearance.

The principal result was that the rings are forced into a concentric position without contact, and they remain fairly stationary in that position with shaft orbits inside the clearance volume. Operation at larger clearances is safe from a dynamic standpoint.

4.3.6 Summary of Results and Conclusions of Analytical Studies

Performance at a design clearance of 12.7 μm is very good and can satisfy all requirements. Also, performance will be satisfactory over the tolerance range specified. The two limitations on performance are as follows:

1. Insufficient hydrodynamic forces to overcome friction forces - a low-speed, high-pressure constraint
2. Insufficient friction to counteract inertia forces - a high-speed, low-pressure constraint.

Figure 2-4 showed an operating range map seal that accounts for all constraints. If the pressure follows a speed squared relationship to a maximum of 1379 kPa (200 psia) at 7330 rad/s (70,000 r/min), it is expected that seal performance will be satisfactory.

Centrifugal runner growth and thermal contractions significantly affect operating clearances and they must be considered in performing the analysis. Centrifugal forces on the runner tend to close the clearances while thermal contractions tend to open the clearances. Thermal effects have the stronger influence, requiring installation clearances to be as small as practical (10.2 - 22.9 μm diametral clearance).

Low mass rings are necessary to dynamically track runner excursions. The rings should be made of carbon without composite metallic rings on the outer circumference.

4.4 Analysis and Design of the 20-mm Floating-Ring Helium Purge Seal

4.4.1 General Configuration and Operating Conditions

The general configuration of the 20-mm helium purge seal is shown on Figure 4-23. A separate shaft would have been used for testing of the 20-mm design and the buffer rings were intended to mate directly against the shaft. In other respects, the design is very similar to the 50-mm with a proportional size reduction. The optimization parameters were the same as for the 50-mm design.

The 20-mm seal was constrained in surface speed by limitations on the maximum operating speed of the test rig. The maximum design speed of the rig is 10,472 rad/s (100,000 r/min). A 20-mm shaft rotating at 10,472 rad/s (100,000 r/min) will produce a surface speed of 105 m/s (344 ft/s) which is only 57% of the 183 m/s (600 ft/s) specified. Limitations on surface speed also limits hydrodynamic force generation, which in turn limits the buffer fluid pressure or allowable friction force at the contact interface. It appears that the absolute maximum pressure would be 689.5 kPa (100 psia) and the allowable pressure will further reduce as speed decreases.

Another factor concerned with the 20-mm seal is centrifugal growth of the runner will be negligible. This is due to the runner of the 20-mm seal being integral with the shaft, and because of limitations on the maximum shaft surface speed.

Although the 20-mm seal is significantly smaller than the 50-mm seal, the nominal operating clearance of 0.0127 mm (0.0005 in.) remains the same, because this was considered to be the smallest practical value for safe operation.

4.4.2 Fluid-Film Performance

Figure 4-24 shows the fluid-film forces as a function of the eccentricity ratio and operating speed. The effects of buffer pressure are indicated, but

variations in hydrodynamic fluid-film force due to this parameter are practically insignificant. The maximum speed examined was 10,472 rad/s (100,000 r/min), which is the limit of the test rig. Superimposed upon this curve are the contact friction forces at 689.5 kPa (100 psia) and 344.7 kPa (50 psia) buffer fluid pressure levels. At a buffer pressure of 1379 kPa (200 psia), there is insufficient hydrodynamic capability to overcome the contact friction force. Maximum load capacity at 10,472 rad/s (100,000 r/min) is approximately 13.34 N (3 lb), which occurs at an eccentricity ratio of slightly over 0.9. To provide a reasonable safety margin the maximum buffer was designed to be 689.5 kPa (100 psia) which would require an eccentricity ratio slightly below 0.8, or a minimum film thickness of approximately 0.0025 mm (0.1 mils) to move the ring into a concentric position.

Figure 4-25 indicates what occurs if the buffer fluid pressure is increased as the square of the speed, the anticipated method of bringing the test rig up to speed. Two pressure-speed curves are shown, one for a 345 kPa (50 psia) pressure at 10,472 rad/s (100,000 r/min) and one for a 689 kPa (100 psia) pressure at 10,472 rad/s (100,000 r/min). For the 345 kPa (50 psia) situation, the eccentricity ratio remains safely between 0.5 and 0.55. For the 689 kPa (100 psia) case, the eccentricity ratio will exceed 0.75 at approximately 6597 rad/s (63,000 r/min), and as indicated on Figure 4-25 will approach 0.8 before it overcomes the anticipated friction force. This will probably be an acceptable situation, because the ring moves to a concentric position after the friction force is overcome.

Figures 4-26 and 4-27 show the effects of clearance variations on ring load capacity. Figure 4-26 is for a constant operating speed of 10,472 rad/s (100,000 r/min). Note the significant decrease in load capacity as the clearance is increased. At a clearance of 0.0191 mm (0.00075 in.), the maximum allowable pressure is more like 345 kPa (50 psia) rather than 689 kPa (100 psia). At a clearance of 0.0254 mm (0.001 in.), a maximum pressure of 206.8 kPa (30 psia) appears to be appropriate. Figure 4-27 indicates fluid film load capacity as a function of speed and eccentricity at a clearance of 0.0254 mm (1 mil). This curve demonstrates that it is necessary to operate at low pressure levels to overcome friction at high clearance conditions.

Anticipated leakage flow through one ring is shown on Figure 4-28. This curve applies to an eccentricity ratio of 0.5. At the helium pressure levels that the rig will operate at 689 kPa (100 psia), the leakage is only 0.000118 kg/s (0.00026 lb/s). At a maximum pressure level of 889.6 kPa (200 psia), the leakage is 0.000363 kg/s (0.0008 lb/s). If the clearance is double, the flow will increase by a factor of 8, so that it will increase to approximately 0.000908 kg/s (0.002 lb/s) at 689 kPa (100 psia). This assumes laminar viscous flow. The actual flow will be less when account is taken of inertia effects at entrance and in the film, as was done for the case of the 50-mm seal. Leakage as a function of eccentricity ratio is shown on Figure 4-29. From fully eccentric to fully eccentric, the leakage increases by a factor of 1.7.

Figure 4-30 shows power loss as a function of speed at an eccentricity ratio of 0.5. The power loss is approximately 12 W at 10,472 rad/s (100,000 r/min). Fluid temperature rise is shown on Figure 4-31. As with the 50-mm design, this curve was based on the assumption that all the heat goes into the flowing fluid, while in reality a good deal of it will be transferred into the cool shaft. High temperatures are predicted for the low-pressure, high-speed conditions where there is high heat generation and low flow.

4.4.3 Dynamic Response

Rotor dynamic studies indicate maximum shaft amplitudes will probably be less than 0.00254 mm (0.0001 in.).

Figure 4-32 shows the radial and tangential force magnitudes of the fluid film obtained from the steady-state computer code, as a function of eccentricity ratio. These values were interpolated for use in the dynamic computer code.

A spectrum of response computer runs were made over a range of varying pressures, speeds and ring clearances. They are summarized on Table 4-7. Examination of the table indicates acceptable response except at high shaft runouts, E_s , low pressures, P_0 , and relatively high operating speeds and at high runouts, low speed, and high pressures. Problem situations are under-

lined. At high-speed, low-pressure conditions, ring inertia forces predominate over the retarding friction force so that the seal ring runs away around the shaft and ultimately contacts. These are operating conditions which are to be avoided.

Figures 4-33 and 4-34 graphically display the summary results with a shaft runout of 0.00254 mm (0.0001 in.). Figure 4-33 shows that the limit cycles become larger as speed reduces and as pressure increases. This indicates a degradation of the hydrodynamic capacity to permit low amplitude or concentric response with the rotating shaft. In all cases, however, there was sufficient capacity to prevent contact between the ring and shaft. Figure 4-34 shows a cross-plot with pressure as the abscissa. Again the plot clearly shows the higher amplitudes at the lower speeds and higher pressure conditions.

TABLE 4-1
PROPERTIES OF HELIUM

<u>Temperature</u> <u>(°C)</u>	<u>Pressure</u> <u>(kPa)</u>	<u>Mass Density</u> <u>(kg/m³)</u>	<u>Viscosity</u> <u>(MPa-s)</u>
10	1379	2.34	19.4
10	689	1.17	19.4
10	344	0.58	19.4
37.8	1379	2.13	20.7
37.8	689	1.07	20.7
37.8	344	0.53	20.7
65.6	1379	1.96	21.9
65.6	689	0.98	21.9
65.6	344	0.49	21.9

TABLE 4-2

REQUIRED ECCENTRICITY AND FILM THICKNESS
TO OVERCOME FRICTIONAL RESISTANCE

<u>Buffer Pressure (kPa)</u>	<u>Maximum Frictional* Force (N)</u>	<u>Radial Clearance C_0 (μm)</u>	<u>Eccentricity Ratio (ϵ)</u>	<u>Minimum Film Thickness h_{\min} (μm)</u>
1379	42.26	12.7	0.6	5.08
689	21.13	12.7	0.35	8.26
344	10.59	12.7	0.17	10.54
1379	42.26	19.05	0.87	2.49
689	21.13	19.05	0.60	7.62
344	10.59	19.05	0.32	12.95
1379	42.26	25.4	0.99	0.254
689	21.13	25.4	0.76	6.10
344	10.59	25.4	0.48	13.21

*Coefficient of Friction = 0.2

TABLE 4-3

MAXIMUM OPERATING SPEED FOR $\Delta T = 22^\circ\text{C}$

<u>Buffer Pressure (kPa)</u>	<u>Speed (rad/s)</u>
344	5,131
689	6,283
1379	7,330

TABLE 4-4
RESULTS OF 50-MM THERMAL ANALYSIS

Case No.	He Inlet Temperature (°C)	Node Temperature (°C)				Remarks
		6	7	9	10	
1	21	-9.8	-10.3	-41.4	-92.1	Base case
2	21	-9.8	-10.3	-40.4	-90.3	Recalculated He-Fluid veloc- ity 60% of runner speed.
3	21	-9.8	-10.3	-42.6	-95.1	Same as Case 2, but all h_c 's doubled.

TABLE 4-5
RECOMMENDED DIMENSIONS ACCOUNTING FOR
CENTRIFUGAL GROWTH AND THERMAL CONTRACTIONS

<u>D_{ring}</u> (μ m)	<u>D_{shaft}</u> (μ m)	<u>C_o</u> (μ m)	<u>T_{shaft}</u> (°C)	<u>T_{ring}</u> (°C)	<u>C_o'</u> (μ m)	<u>C_o''</u> (μ m)
<u>Air Side</u>						
50.02430	50.00498	10.16	-41.44	-9.83	-1.27	13.72
50.02276	50.00752	7.62	-41.44	-9.83	-3.81	11.20
50.02002	50.01006	5.08	-41.44	-9.83	-6.35	8.66
<u>LOX Side</u>						
50.02530	50.00498	10.16	-92.11	-10.28	-1.27	27.97
50.02276	50.00752	7.62	-92.11	-10.28	-3.81	25.45
50.02002	50.01006	5.08	-92.11	-10.28	-6.35	22.91

TABLE 4-6

50-MM SEAL TRANSIENT ANALYSIS: SUMMARY OF RESULTS

Clearance, C_0 (μm)	Shaft Eccentricity (μm)	Pressure, P_0 (kPa)	Speed, N (rad/s)	Orbit Eccentricity Ratio (ϵ)	Minimum Film Thickness (μm)
12.7	2.54	1379	2094	0.63	4.7
		1379	3142	0.64	4.6
		1379	5236	0.26	9.4
		1379	7330	0.24	9.7
		689	2094	0.46	6.9
		689	3142	0.28	9.1
		689	5236	0.25	9.5
		689	7330	0.22	9.9
		344	2094	0.26	9.4
		344	3142	0.24	9.7
		344	5236	0.22	9.9
		344	7330	0.25	9.5
		172	2094	0.22	9.9
		344	2094	0.49	6.5
	5.08	1379	7330	0.40	7.6
		1379	7330	0.63	4.7
	7.62	344	7330	0.63	4.7
		344	2094	0.62	4.8
	10.16	689	7330	0.43	7.2
		344	2094	0.85	1.9
		1379	7330	0.65	4.4
2.54	12.7	1379	7330	0.66	4.3
	10.16	517	7330	0.44	1.4
		448	7330	0.42	1.5
		344	7330	1.02	-0-
		379	7330	0.43	1.4
		344	2094	0.85	3.8
	12.7	689	7330	0.52	1.2
		1379	7330	0.60	1.0
		517	7330	0.60	1.0
		482	7330	0.58	1.1

TABLE 4-7

20-MM SEAL TRANSIENT ANALYSIS: SUMMARY OF RESULTS

Weight of Ring - 0.0146 kg (0.0322 lb)

Coefficient of Friction, $\mu = 0.2$

Clearance C_O (μm)	Shaft Eccentricity, E_S (μm)	Pressure, P_O (kPa)	Speed, N (rad/s)	Orbit Eccentricity Ratio (ϵ)	Minimum Film Thickness, h_M (μm)
12.7	2.54	345	10,472	0.231	9.65
		689		0.225	9.9
		1379		0.259	9.4
		345	7,854	0.220	9.9
		689		0.204	10.1
		1379		0.350	8.26
		345	5,236	0.221	9.91
		689		0.241	9.65
		1379		0.459	6.86
		345	2,618	0.238	9.68
		689		0.546	5.77
		1379		0.735	3.35
	7.62	345		0.639	4.57
		345	5,236	1.013	-0-
		689		0.636	4.62
		345	7,854	1.008	-0-
		517		0.615	4.83
		689		0.648	4.47
		345		1.05	-0-
		517		1.006	-0-
		689		0.635	4.51
19.1	2.54	1379		0.4113	11.2
25.4		345		0.270	13.97
		345		0.312	13.21
		1379		0.364	12.20
	7.62	1379	10,472	0.55	8.64
	5.08	1379		0.508	9.40
	7.62	345	7,854	0.459	10.4
		345	5,236	0.490	9.65
		345	2,618	0.588	7.87

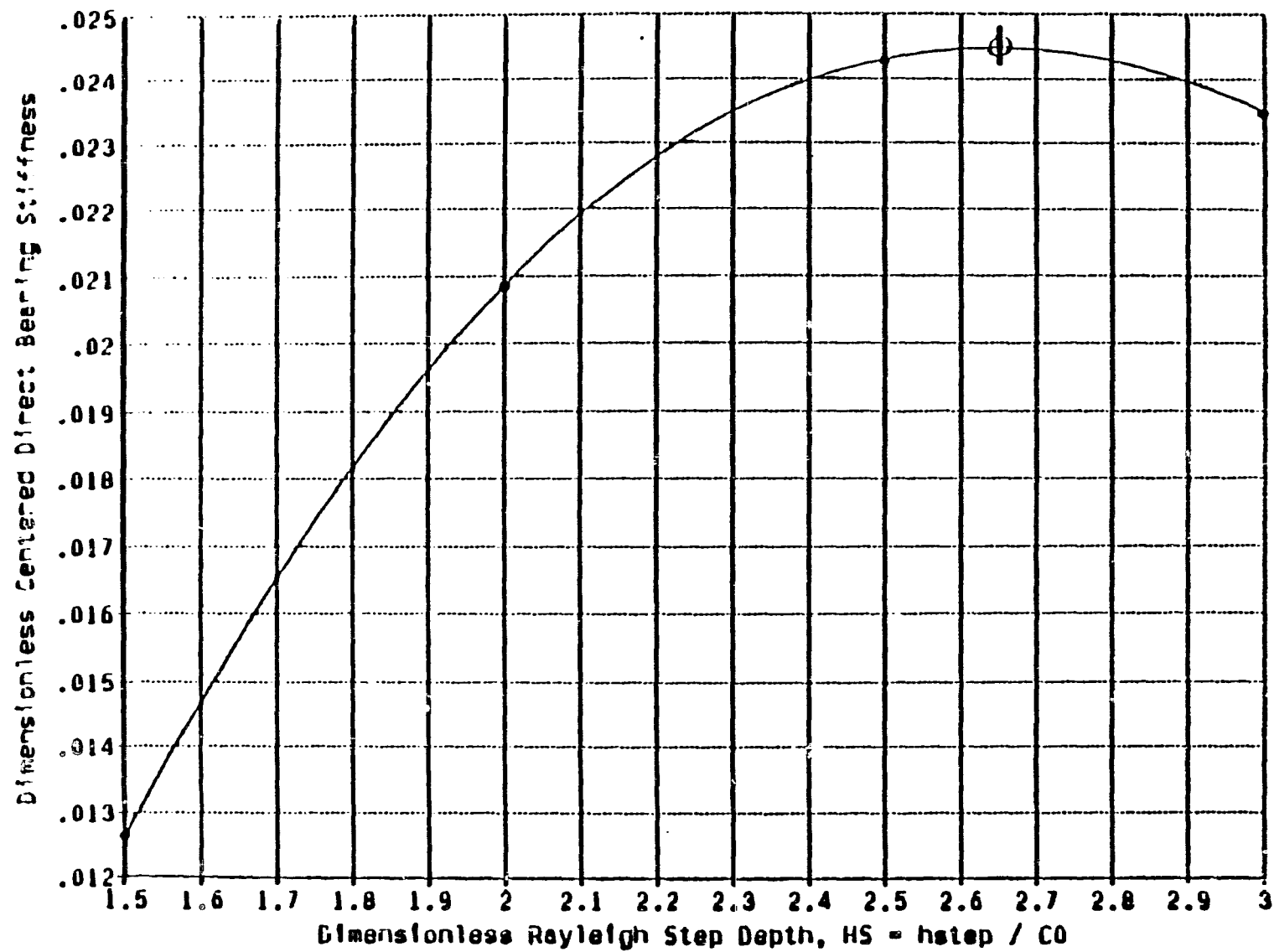


Fig. 4-1 Dimensionless Direct Stiffness Versus Step Depth

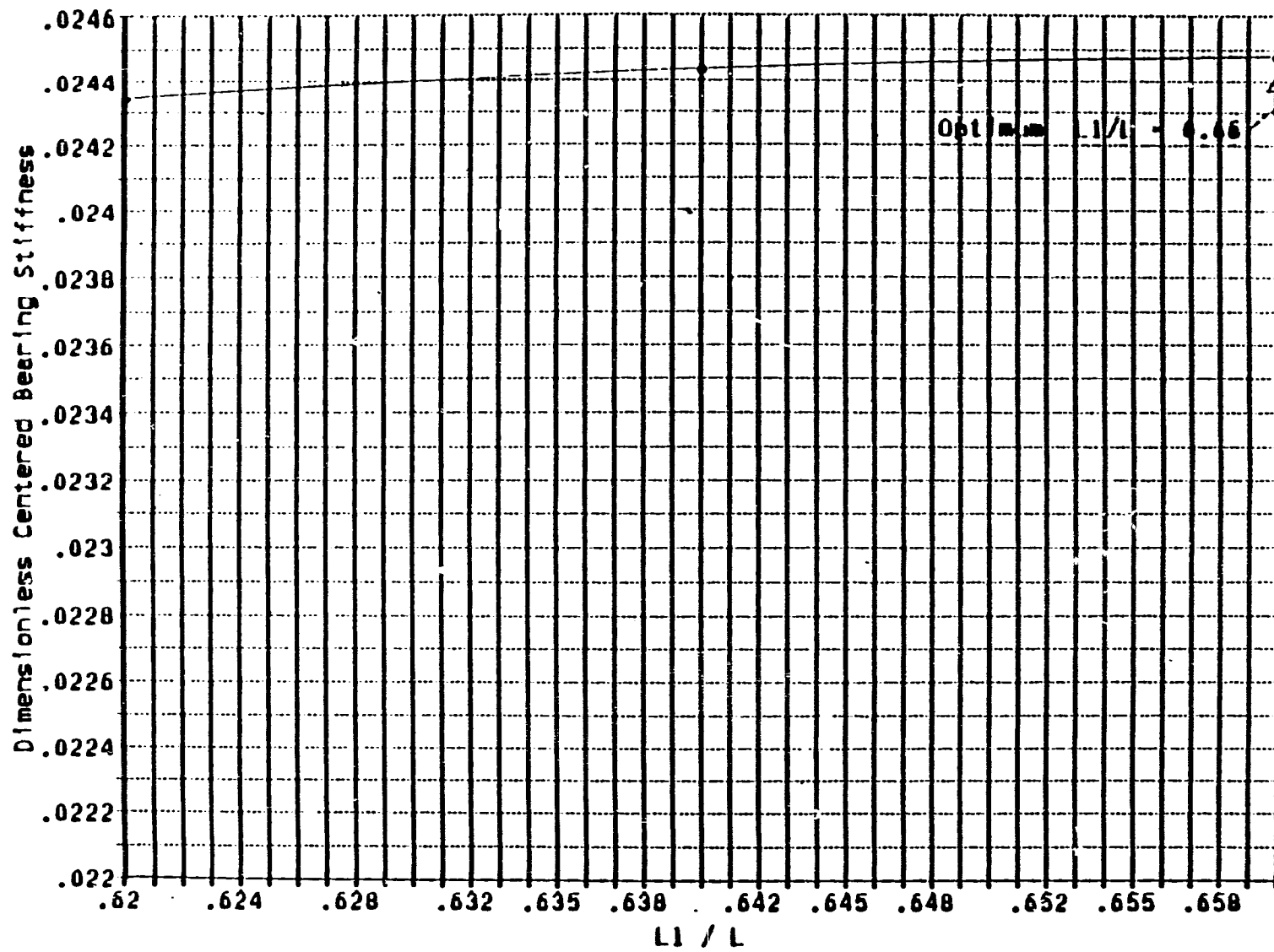


Fig. 4-2 Axial-Step-Length Optimization

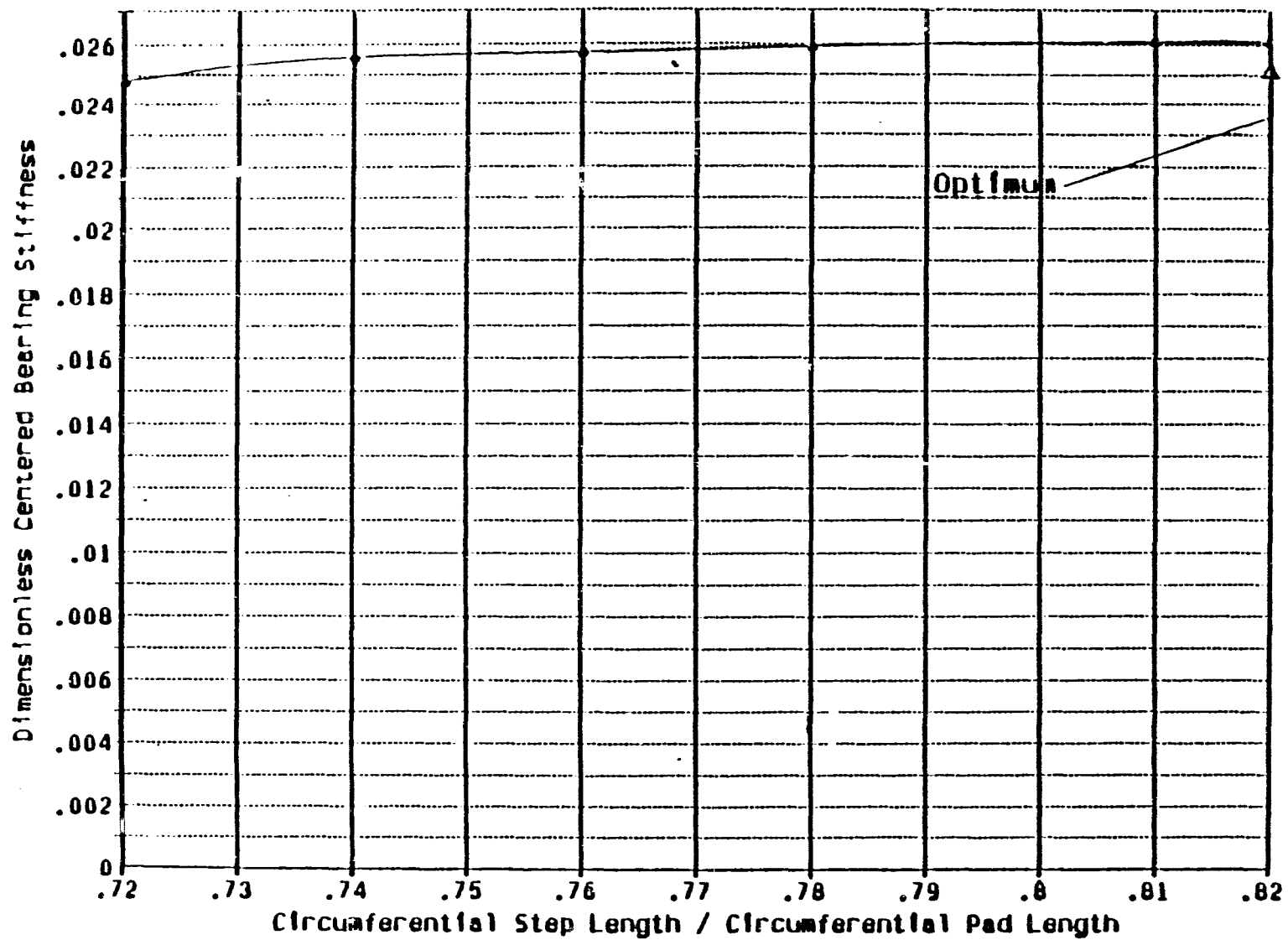
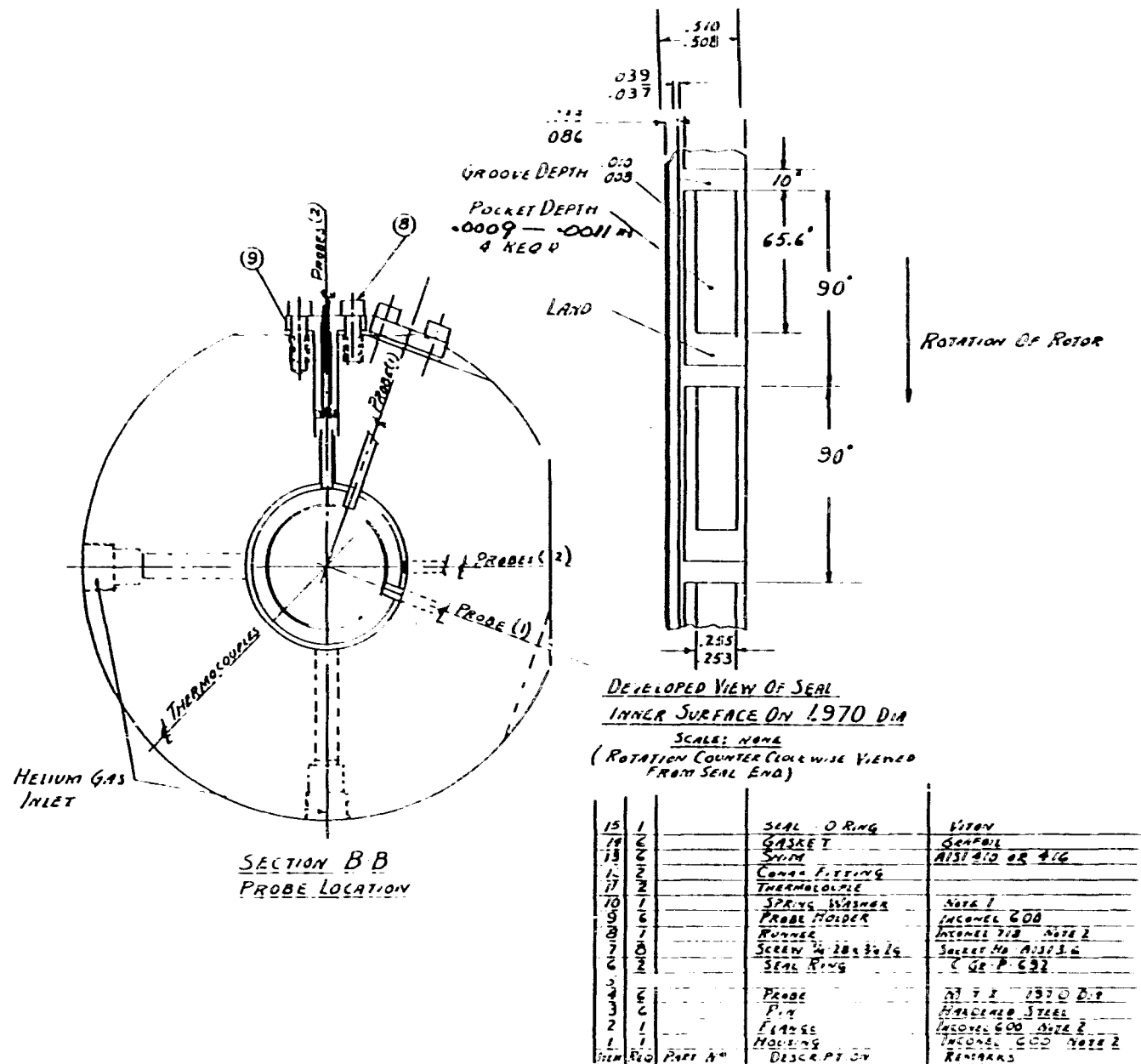


Fig. 4-3 Optimization of Circumferential Pocket Extent

ORIGINAL PAGE IS
OF POOR QUALITY

83030

Fig. 4-4 50-mm Rayleigh-Step Pad

ORIGINAL PAGE IS
OF POOR QUALITY

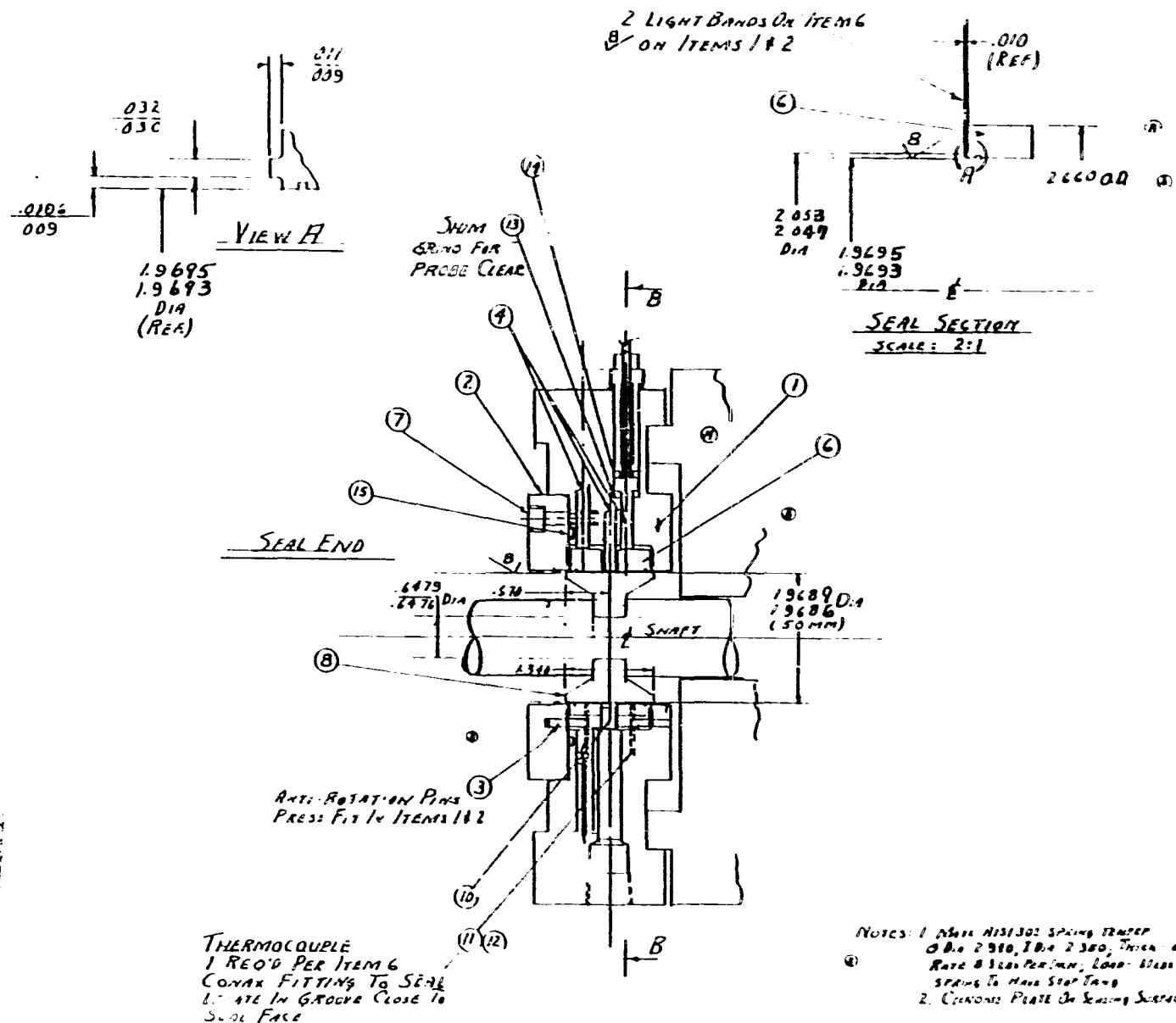
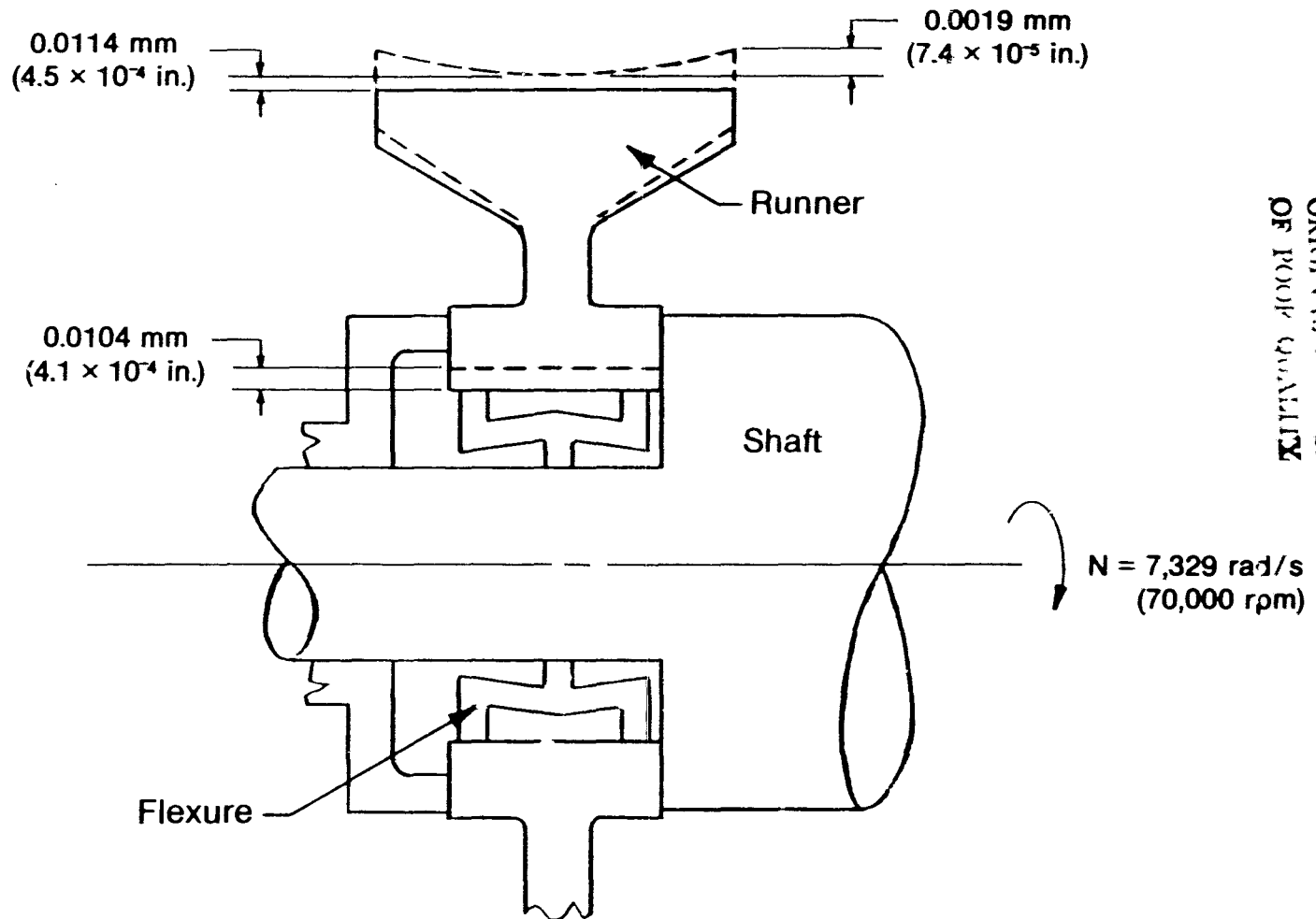


Fig. 4-5 50-mm Runner Seal Installation

Lox Seal Test Rig 50-mm HELIUM SEAL RUNNER



ORIGINAL PHOTO IS
OF POOR QUALITY

Fig. 4-6 50-mm Helium Seal Runner Centrifugal Distortions

ORIGINAL PAGE IS
OF POOR QUALITY

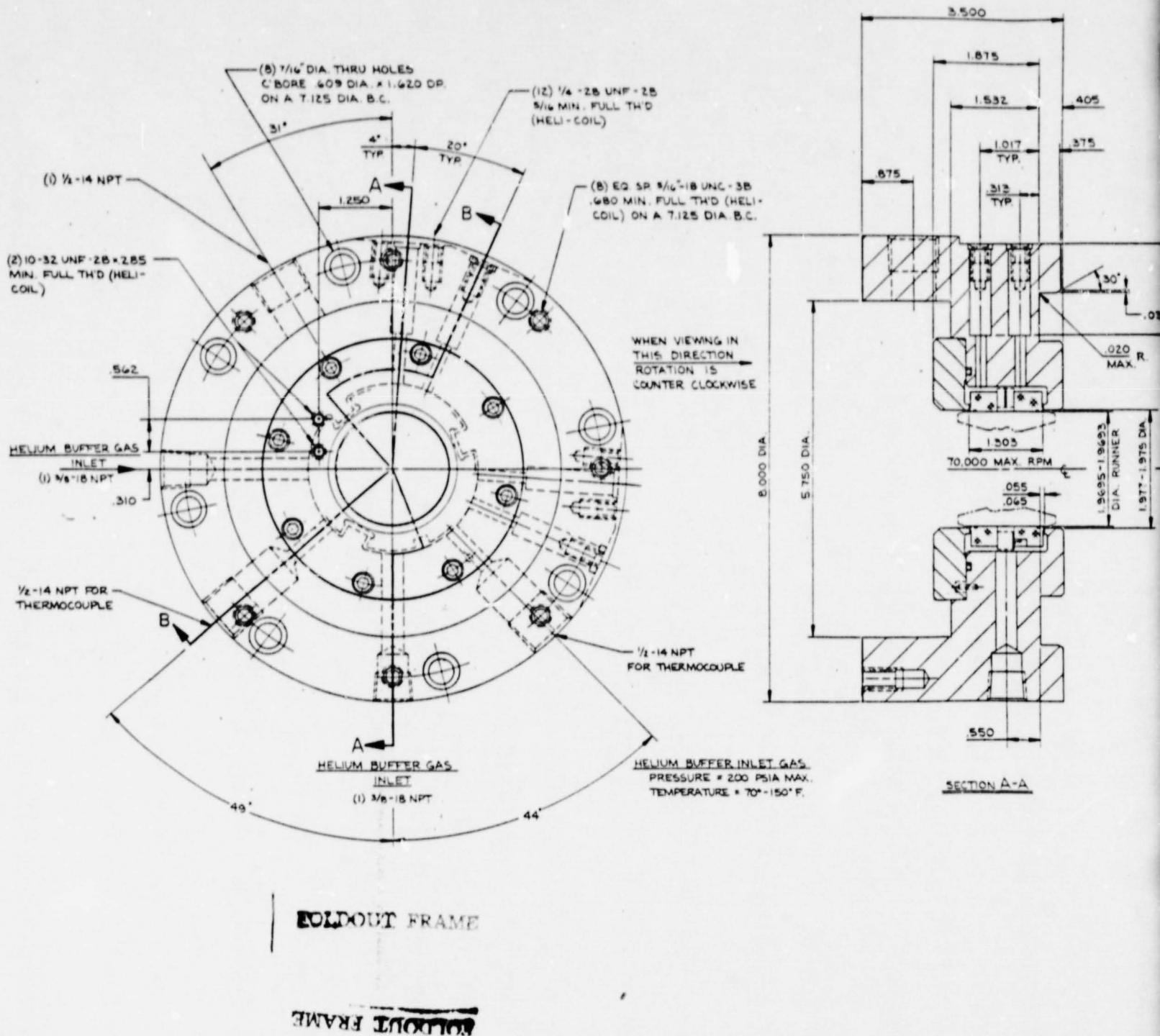
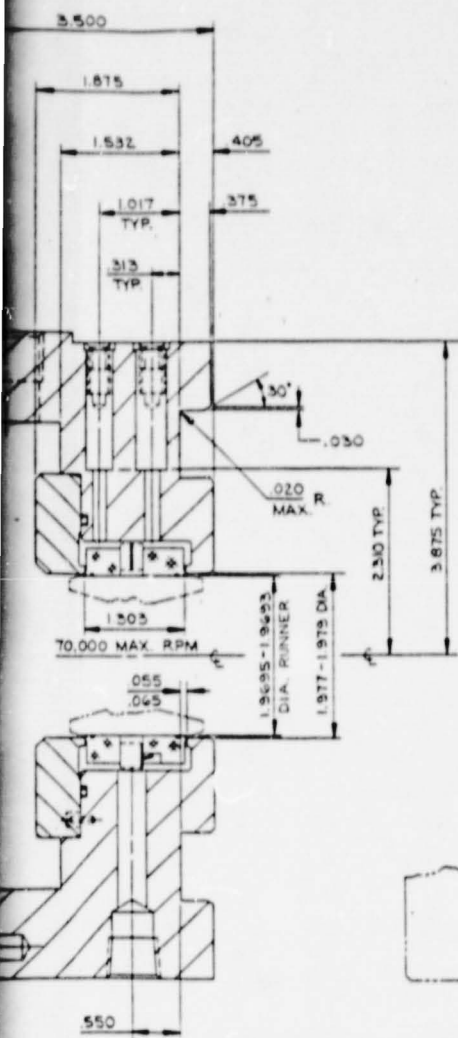
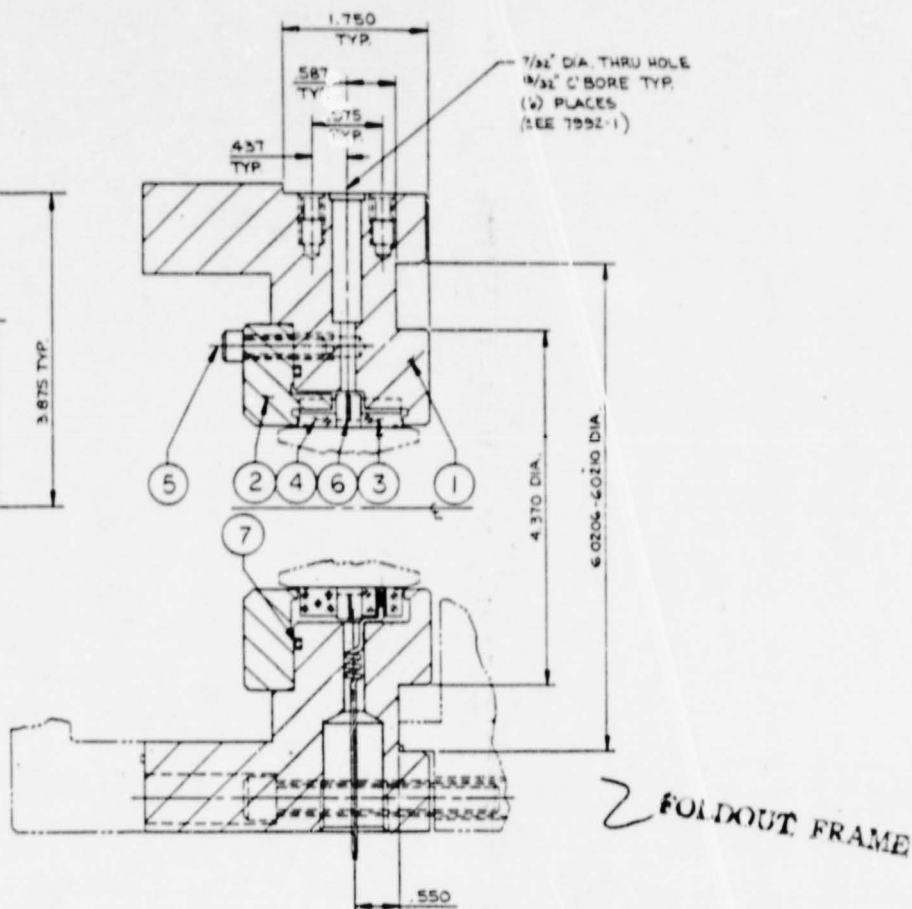


Fig. 4-7 50-mm Helium Purge Bushing Seal Ass

REVISIONS			
LTR	DESCRIPTION	DATE	APP'D
A	RELEASED	2-7-83	AF 4/1/83
B	UPDATED DESIGN	4/7/83	AF



SECTION A-A



SECTION B-B

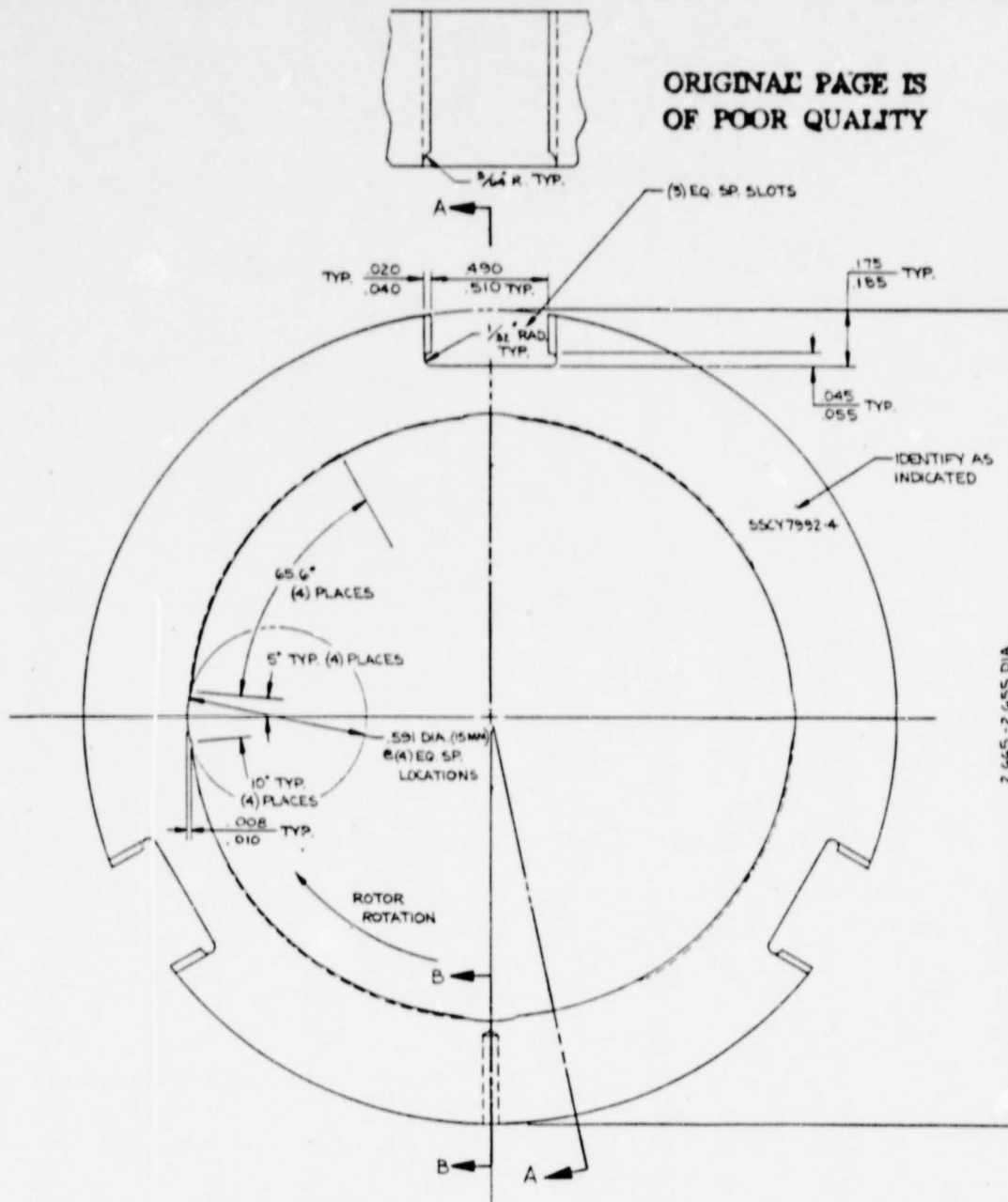
7	1	SSCY7992-7	O' RING (PARKER® 2-152)	VITON	V-147-75
6	1	SSCY7992-6	WAVE SPRING	SST	AISI 301
5	3	SSCY7992-5	1/2" X 1/2" CAP SCREW	SST	TYPE 18-B
4	1	SSCY7992-4	BUSHING SEAL (CCW)	G-6PH	P-5N
3	1	SSCY7992-3	BUSHING SEAL (CW)	G-6PH	P-5N
2	1	SSCY7992-2	FLANGE	INCONEL	
1	1	SSCY7992-1	HOUSING	INCONEL 800	
ITEM	QTY	PART NO.	DESCRIPTION	MATL.	MATL SPEC.

LIST OF MATERIAL

DO NOT SCALE FROM THIS DRAWING UNLESS OTHERWISE SHOWN		CONTRACT NO.		STEIN SEAL COMPANY 204 STREET & INDIANA AVENUE, PHILADELPHIA, PA. 19122					
MATERIAL AS SPECIFIED OTHER SPECIFICATIONS		DESIGNED BY	WCM	HELIUM PURGE BUSHING SEAL ASSEMBLY, 50 MM.					
		DRAWN BY	2-4-83						
		CHECKED BY	HF						
		DATE	4/1/83						
		DATE		S/N	03673	DRAWING NO.	SSCY 7992	REV	B
				SCALE	FULL	REFERENCE	MTI 700002		

2 FOLDOUT FRAME

ORIGINAL PAGE IS
OF POOR QUALITY

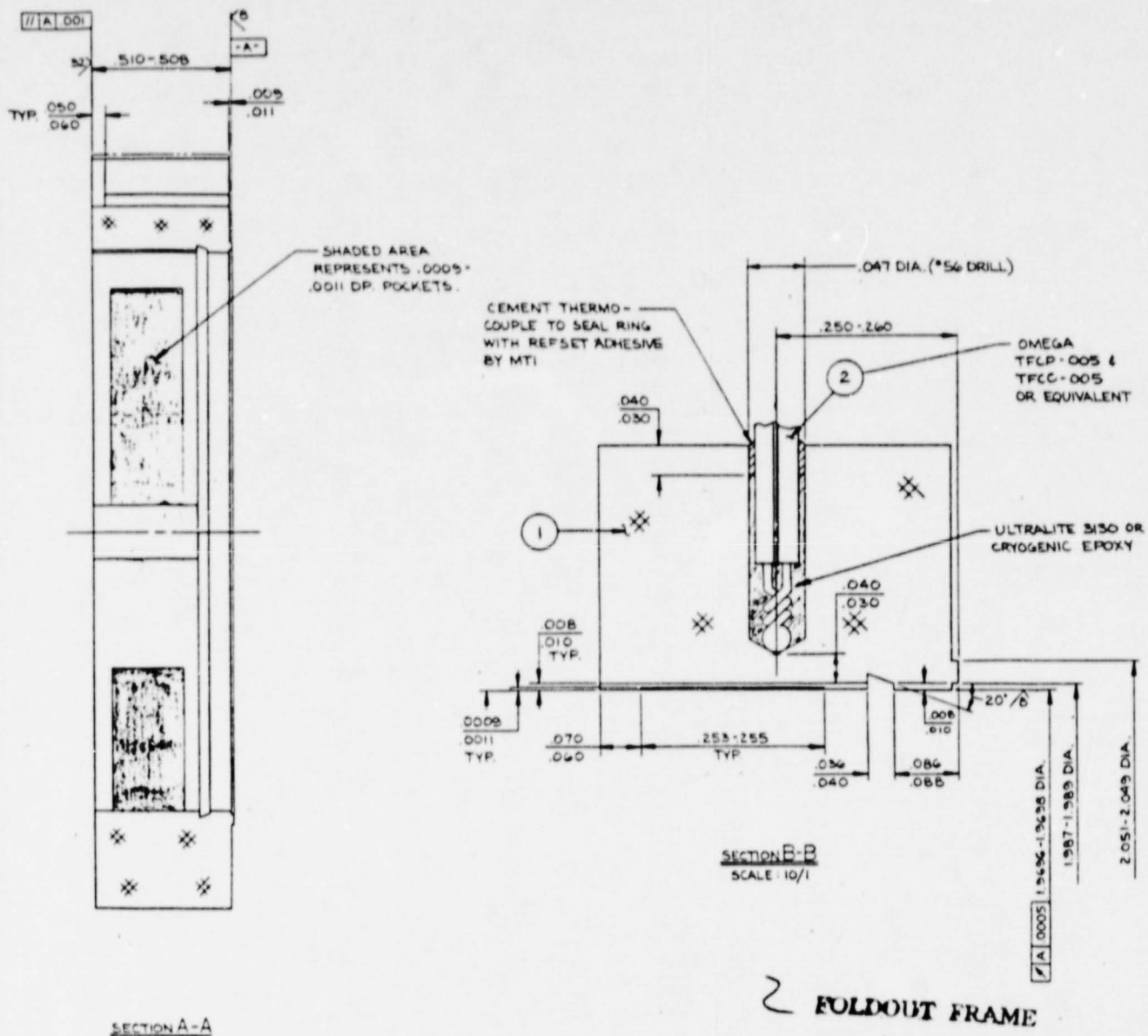


FOLDOUT FRAME

1. FACE -A- TO BE FLAT W/IN (2) MEDIUM LIGHT BINDS.
NOTES:

Fig. 4-8 Bushing Seal, CC

REVISIONS			
LTR	DESCRIPTION	DATE	APPR'D
A	RELEASED	2/22/83	HF
B	DESIGN UPDATE	3/13/83	HF

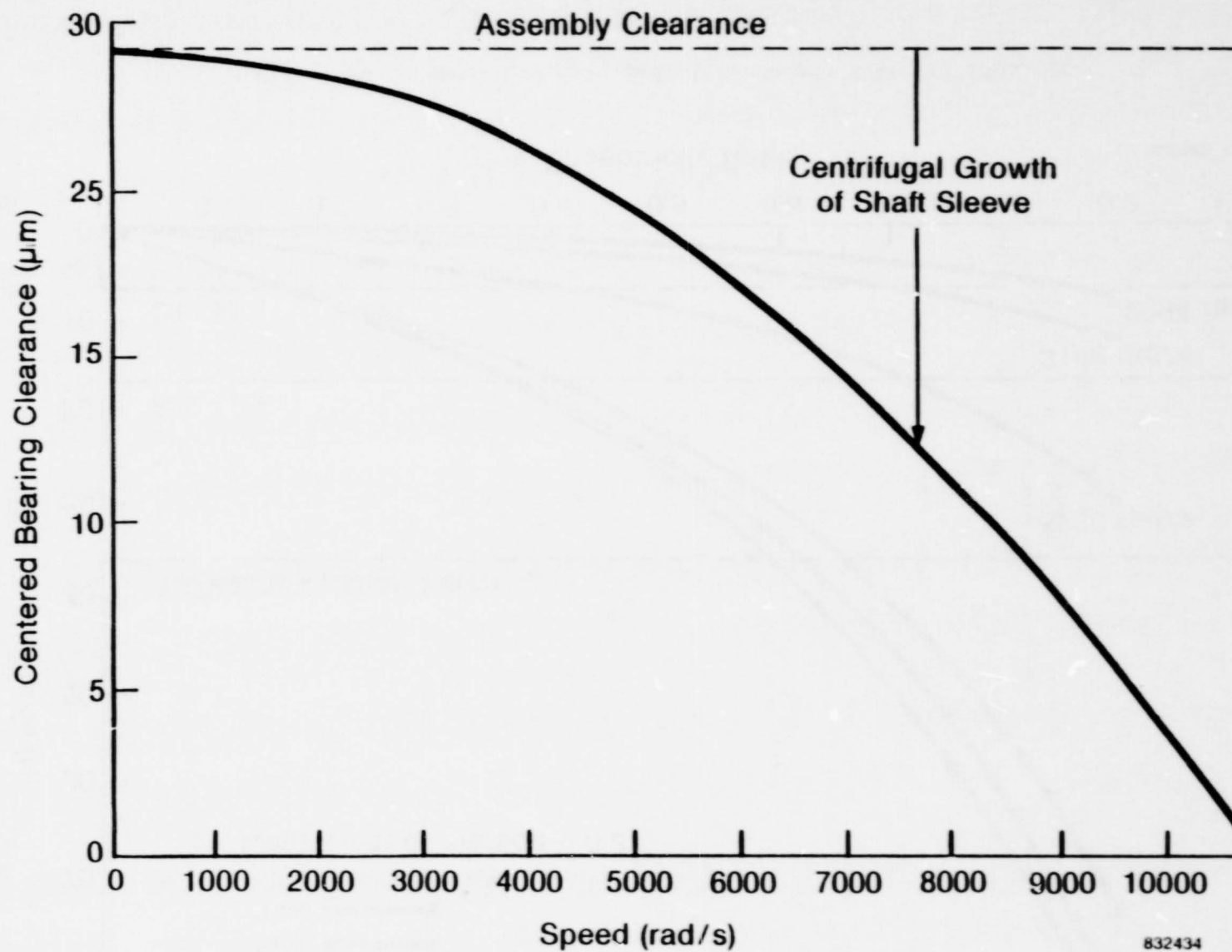


2	1	SSCY 7992-B	THERMOCOUPLE	OMEGA TFCP-005 & TFCC-005 OR EQUIVALENT
1	1	SSCY 7992-4A	BUSHING SEAL, CCW	C-GPH PURE P-SN
ITEM REQ'D	PART NO	DESCRIPTION	MAT'L	MAT'L SPEC

LIST OF MATERIAL

ALL ANGLES ±1°		WCM 2-10-83 HF 0.0005		STBIN SEAL COMPANY 200 STREET & BROADWAY, PHILADELPHIA, PA. 19106	
AS NOTED				BUSHING SEAL, CCW.	
				D 03673 SSCY 7992-4	
				B	

Fig. 4-8 Bushing Seal, CCW



832434

Fig. 4-9 Concentric Clearance Versus Speed Including Centrifugal Growth

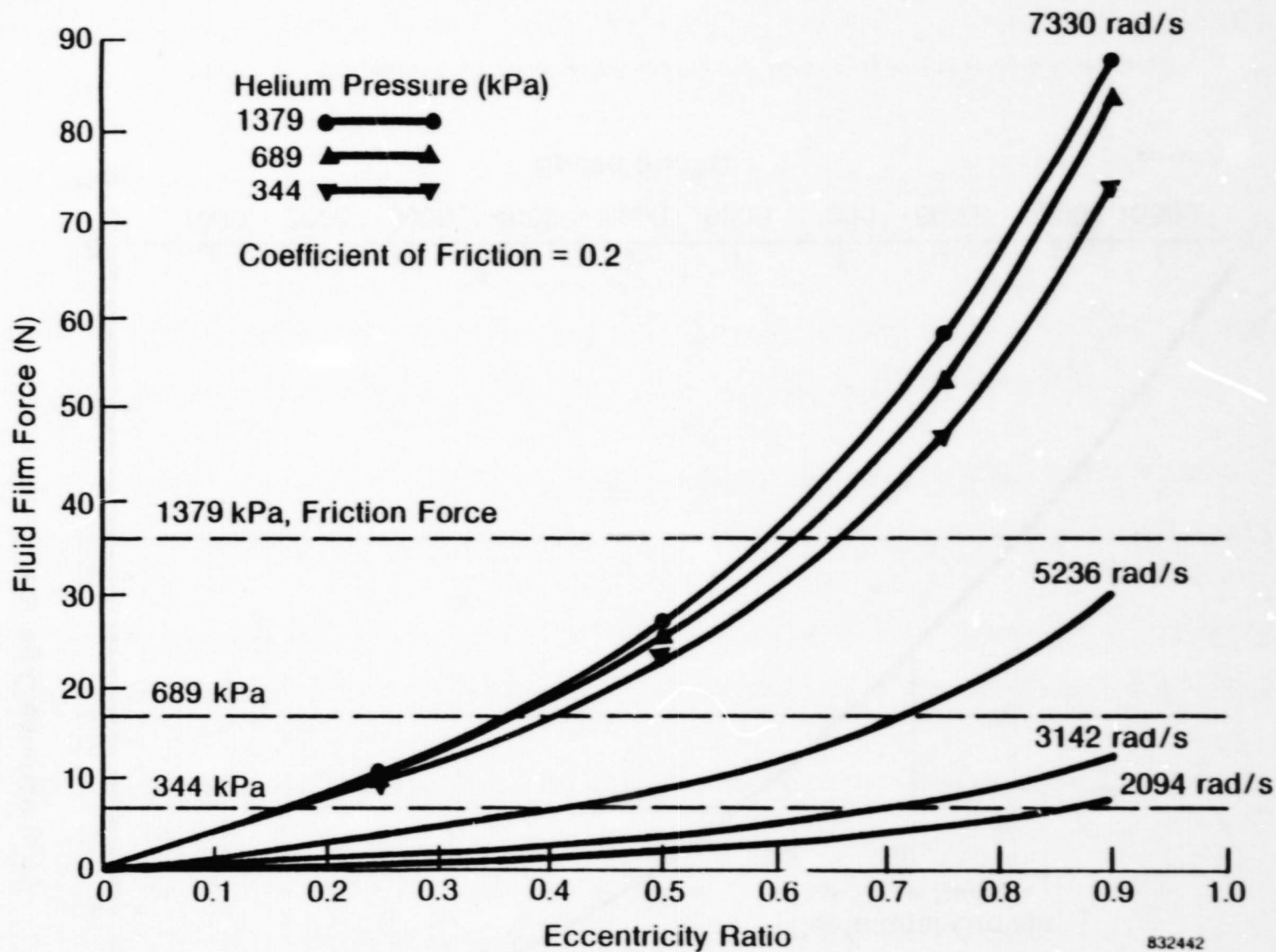


Fig. 4-10 50-mm Fluid-Film Radial Force and Seal Friction Force

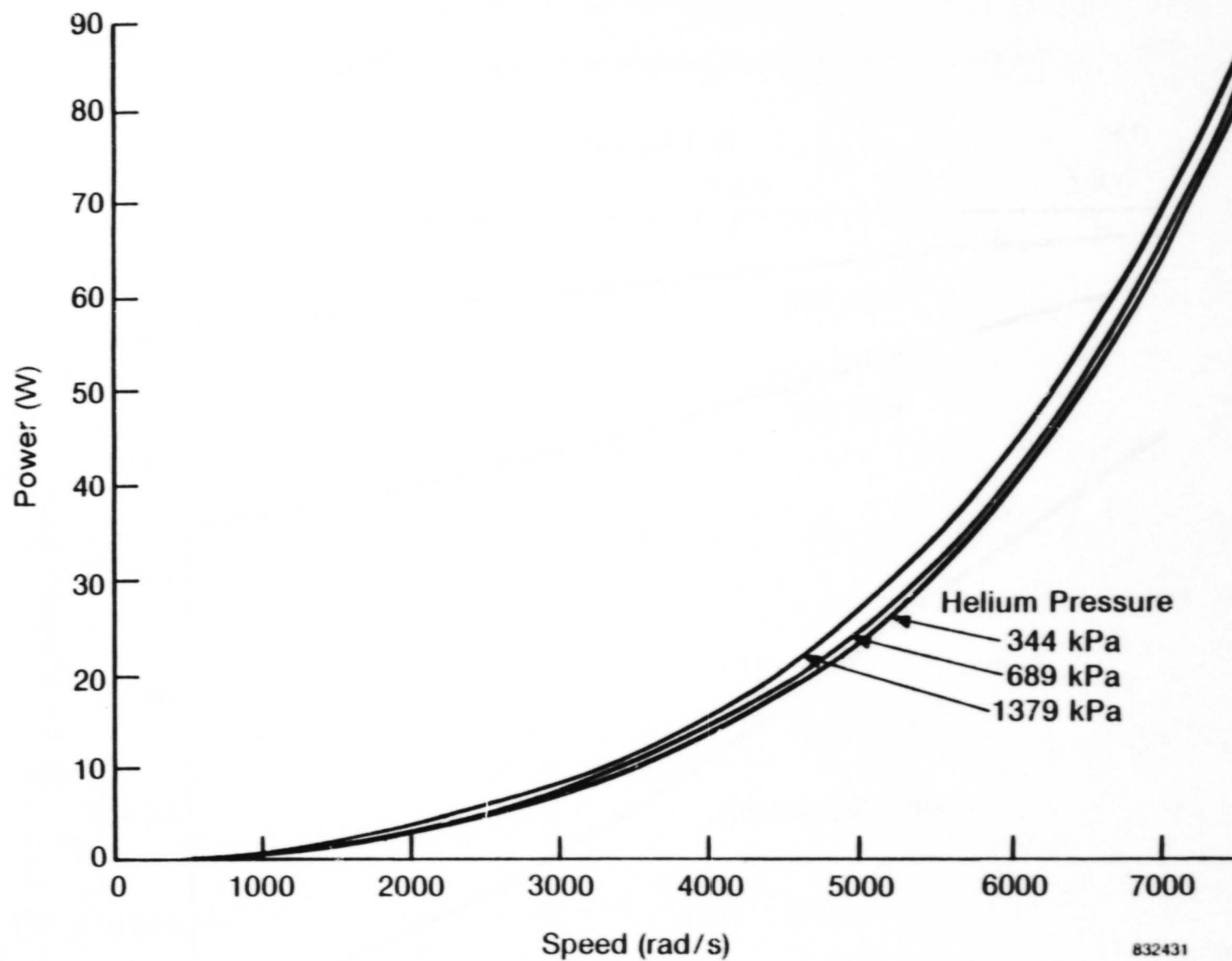


Fig. 4-11 50-mm Viscous Power Loss as a Function of Speed and Pressure, $\epsilon = 0.5$

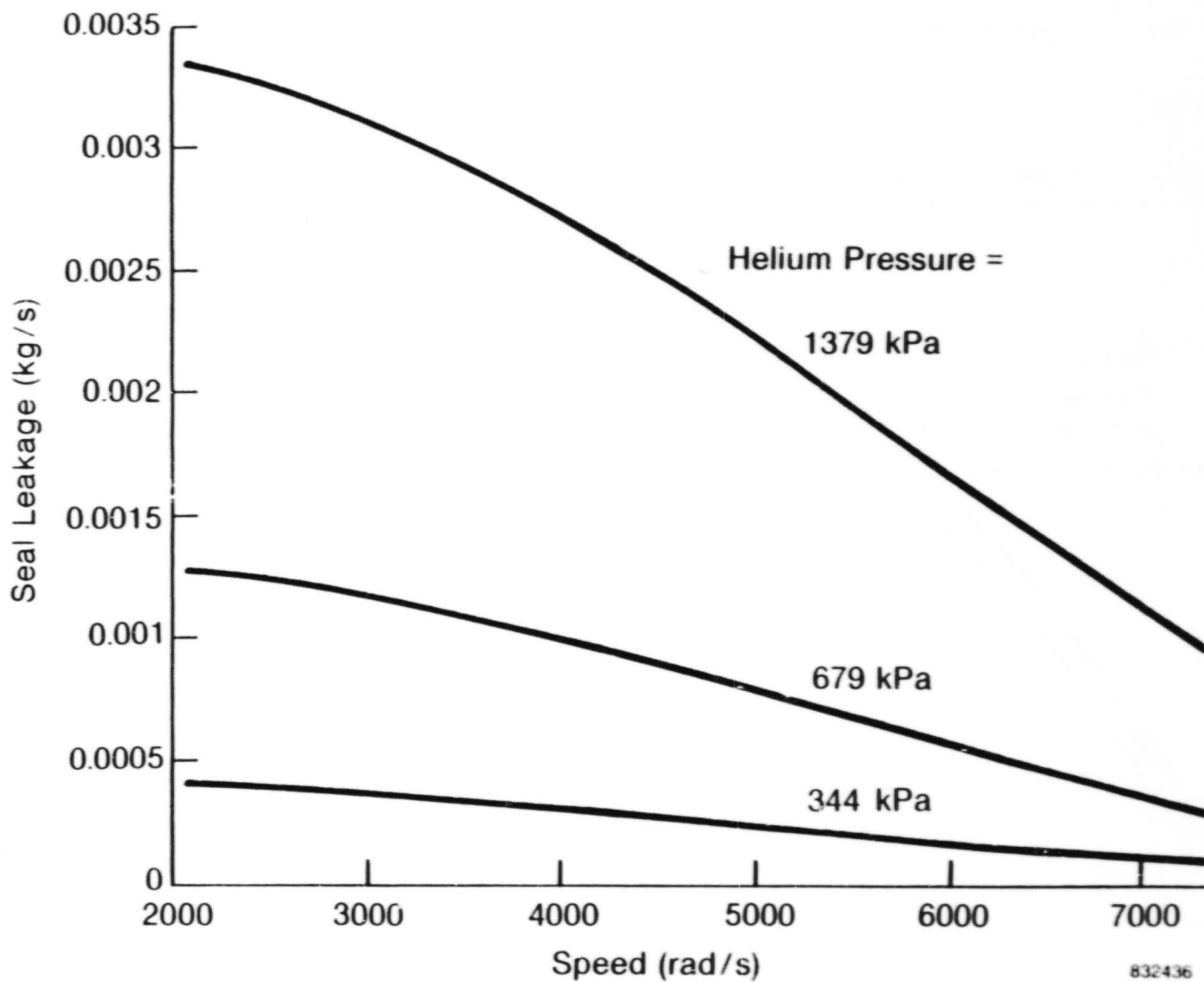


Fig. 4-12 50-mm Seal Leakage Versus Speed and Pressure

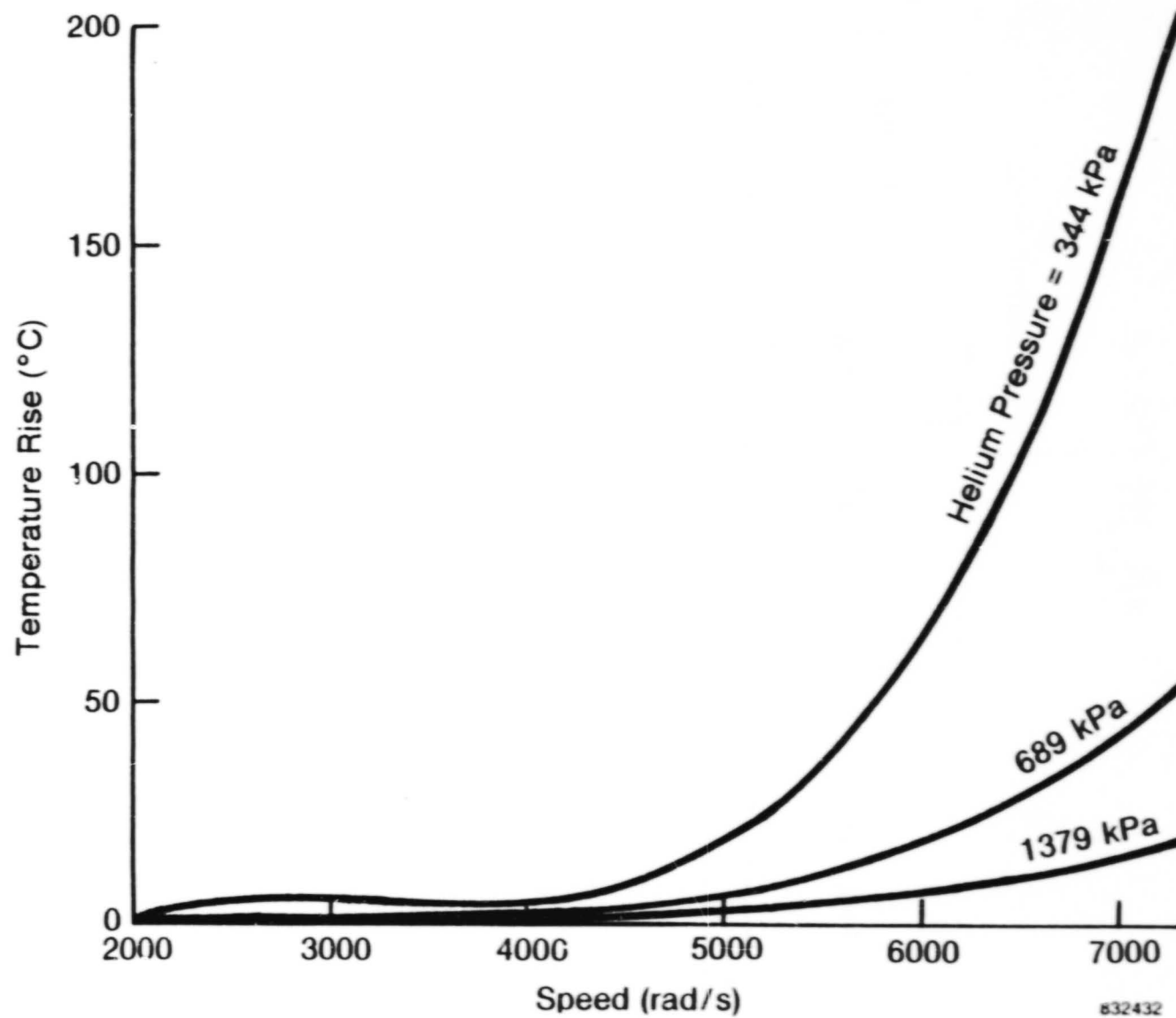


Fig. 4-13 50-mm Fluid Temperature Rise

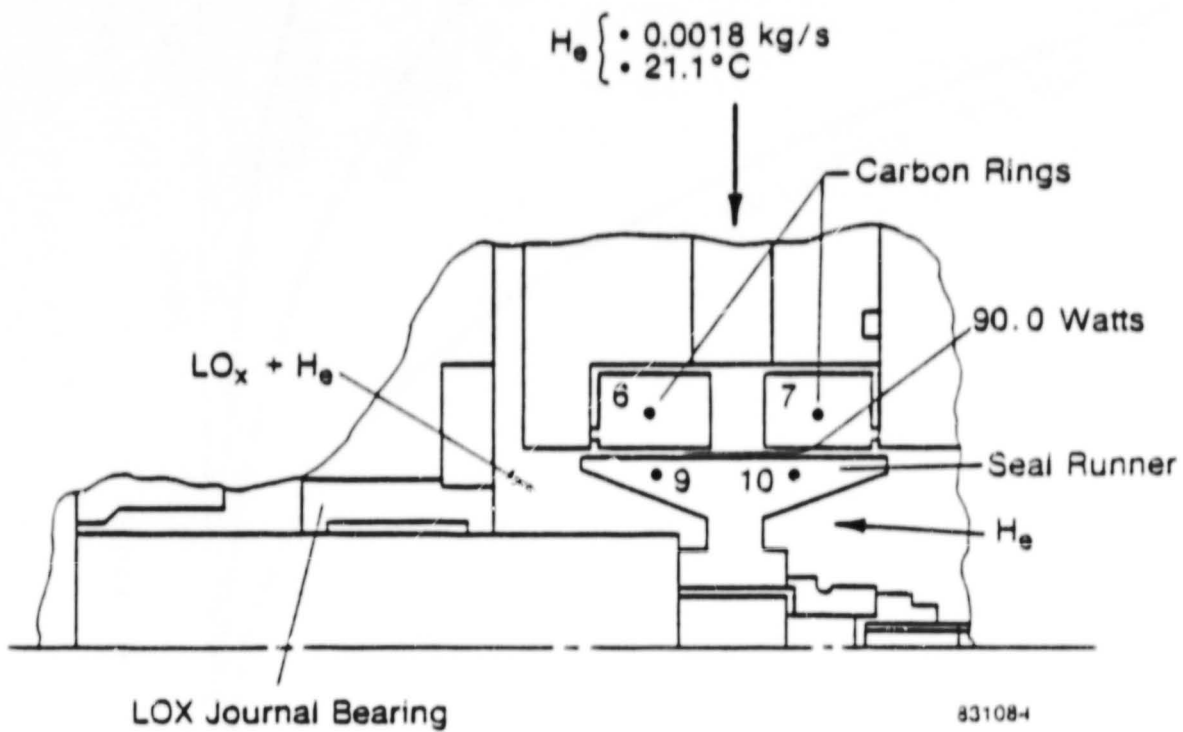


Fig. 4-14 50-mm Thermal Analysis Model

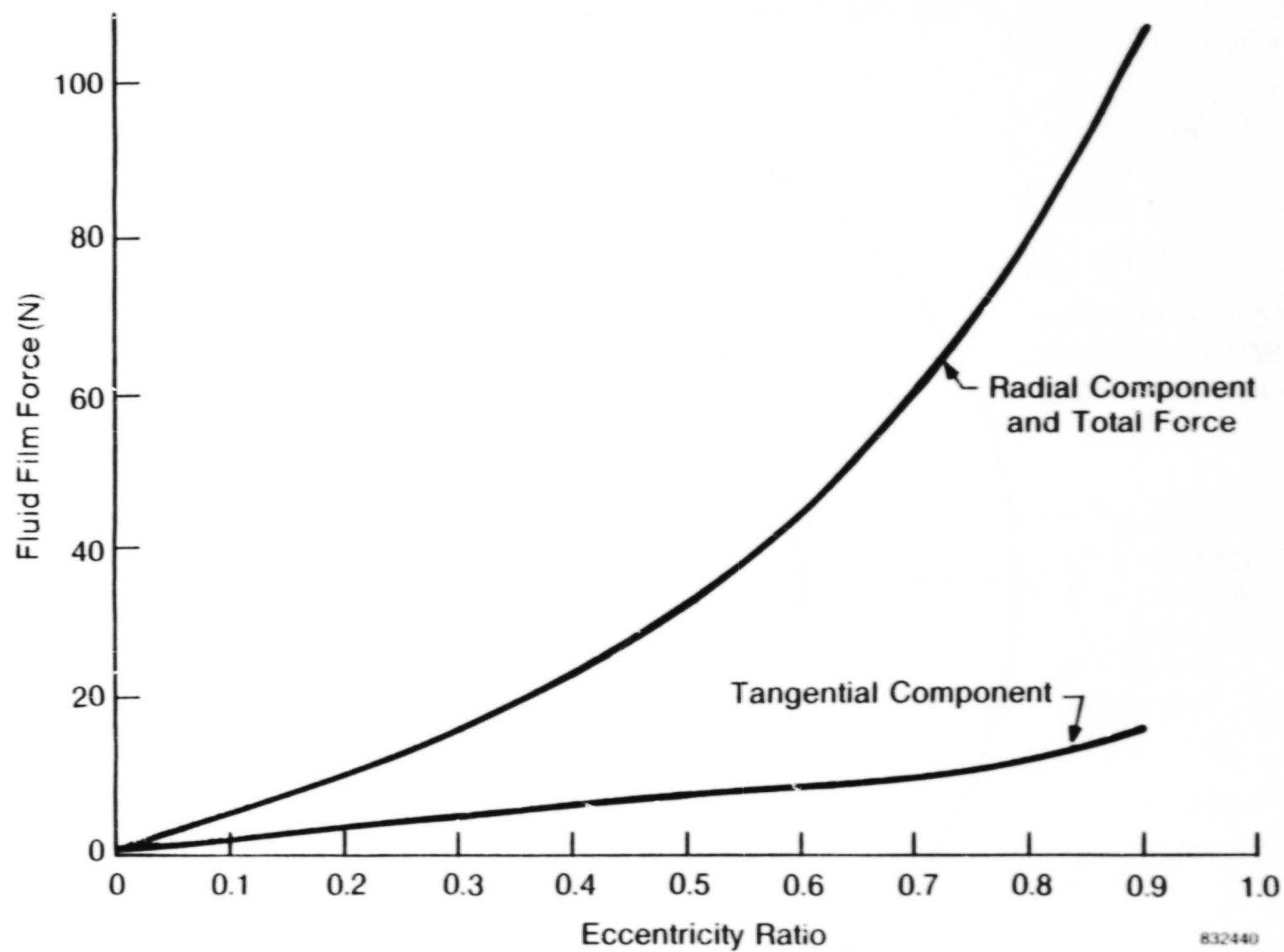


Fig. 4-15 50-mm Fluid Film Forces Versus Eccentricity Ratio;
1379 kPa Helium Pressure; 7330 rad/s

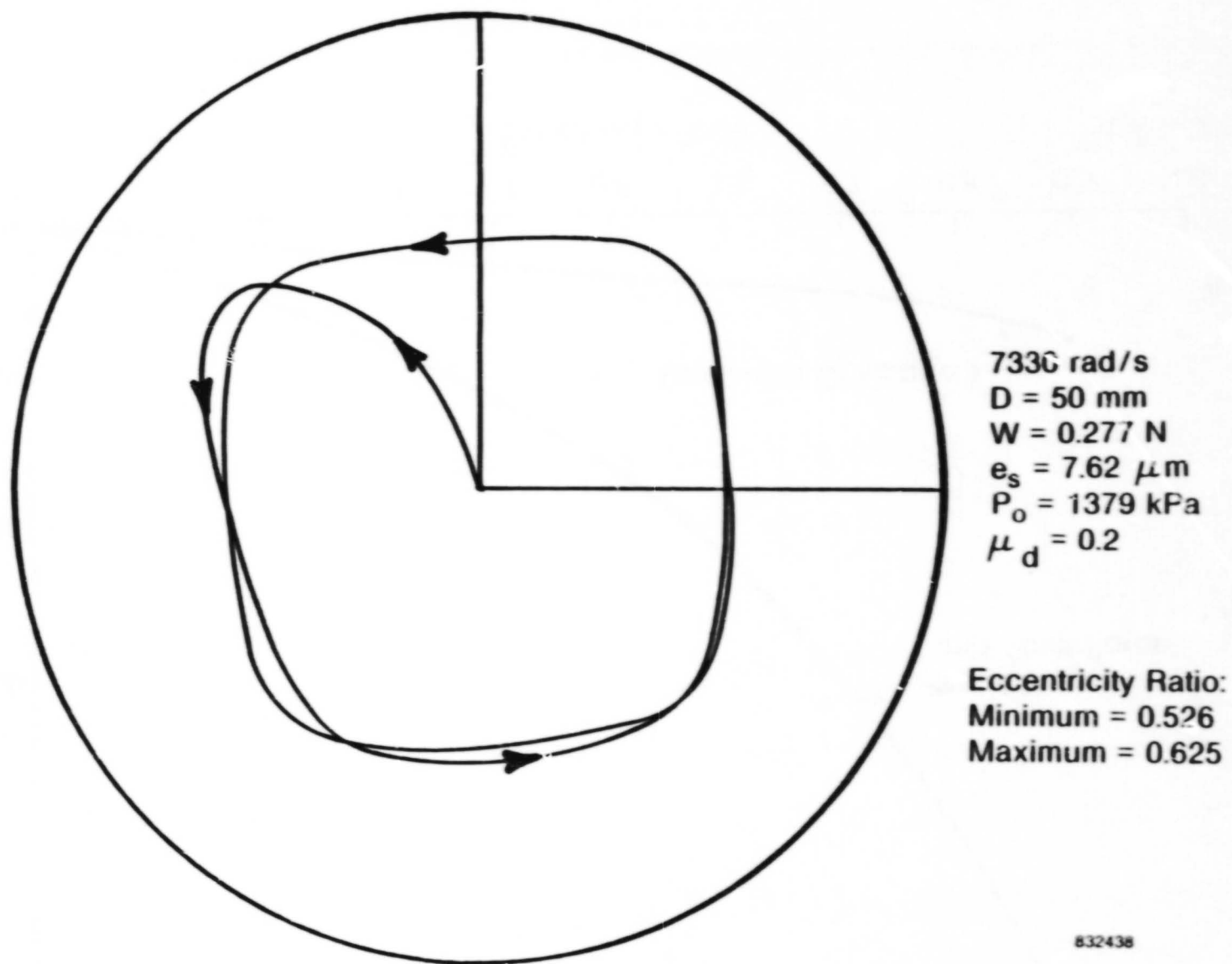
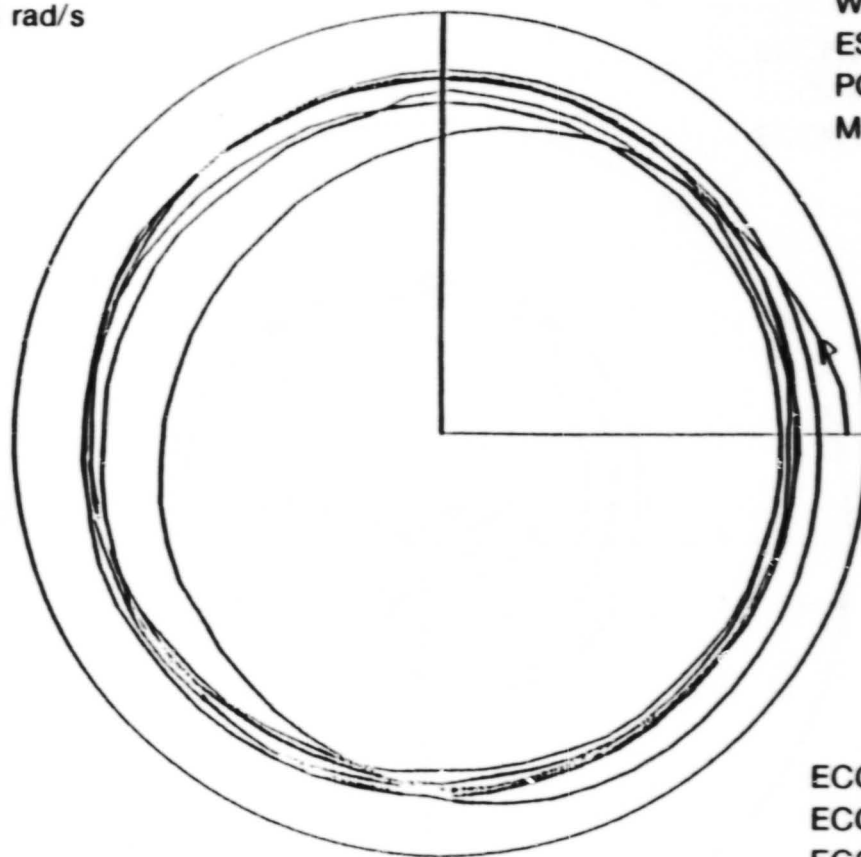


Fig. 4-16 50-mm Ring Orbital Response; 1379 kPa, 7330 rad/s,
7.62 μm Shaft Runout

2094 rad/s



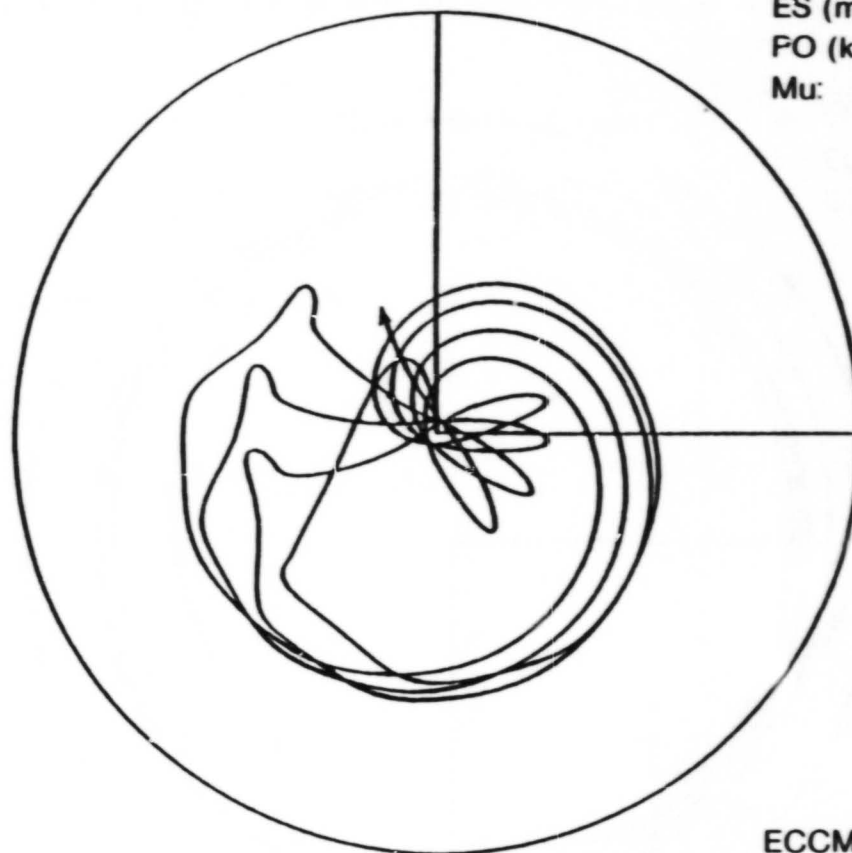
D (mm): 50.0
W (kg): 0.0282
ES (mm): 0.0102
PO (kPa, abs): 345
Mu: 0.2

ECCMAX: 0.95
ECCMN1: 0.792964
ECCMX1: 0.848226

Fig. 4-17 50-mm Ring Orbital Response, 345 kPa Absolute (50 psia),
2094 rad/s (20,000 r/min), 0.0102 mm (0.0004 in.) Shaft Runout

2094 rad/s

D (mm): 50.0
W (mm): 0.0282
ES (mm): 0.0102
PO (kPa, abs) 689
Mu: 0.2

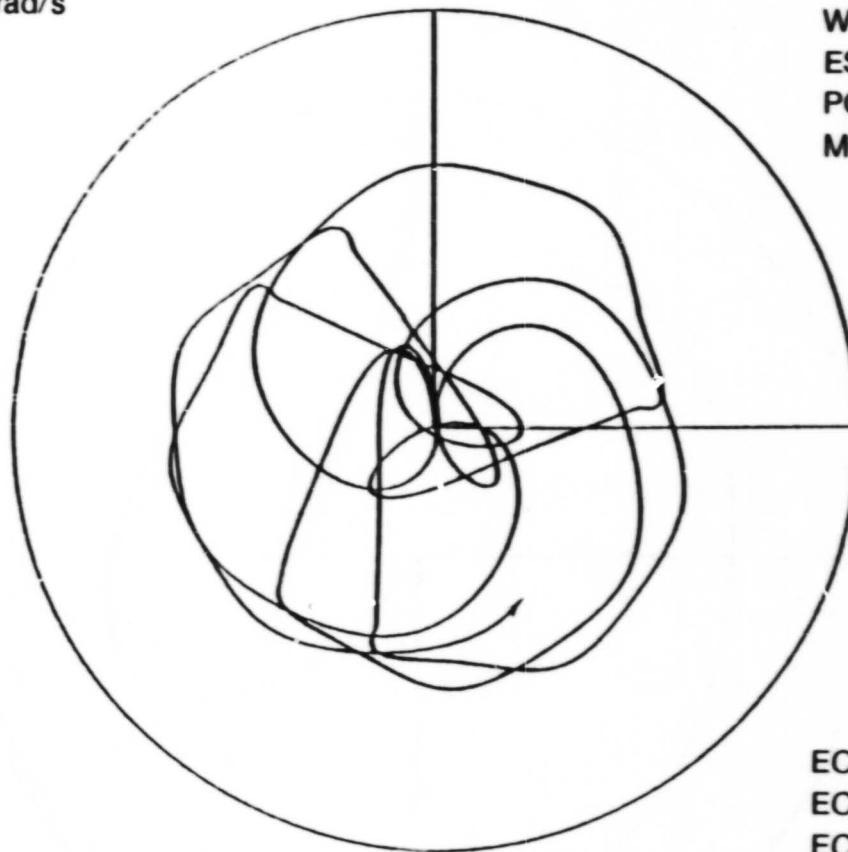


ECCMAX: 0.635413
ECCMN1: 0.0235992
ECCMX1: 0.460899

Fig. 4-18 50-mm Ring Orbital Response; 689 kPa Absolute (100 psia);
2094 rad/s (20,000 r/min); 0.0102 mm (0.0004 in.) Shaft Runout

3142 rad/s

D (mm): 50.0
W (kg): 0.0282
ES (mm): 0.0102
PO (kPa, abs) 1379
Mu: 0.2



ECCMAX: 0.637233
ECCMN1: 0.130857
ECCMX1: 0.635234

Fig. 4-19 50-mm Ring Orbital Response; 1379 kPa Absolute (200 psia);
3142 rad/s (30,000 r/min); 0.0254 mm (0.0004 in.) Shaft Runout

7330 rad/s

Carbon/Inconel Ring

ES (mm): 0.00635

PO (kPa): 1279

Mu: 0.2

Contact - 0

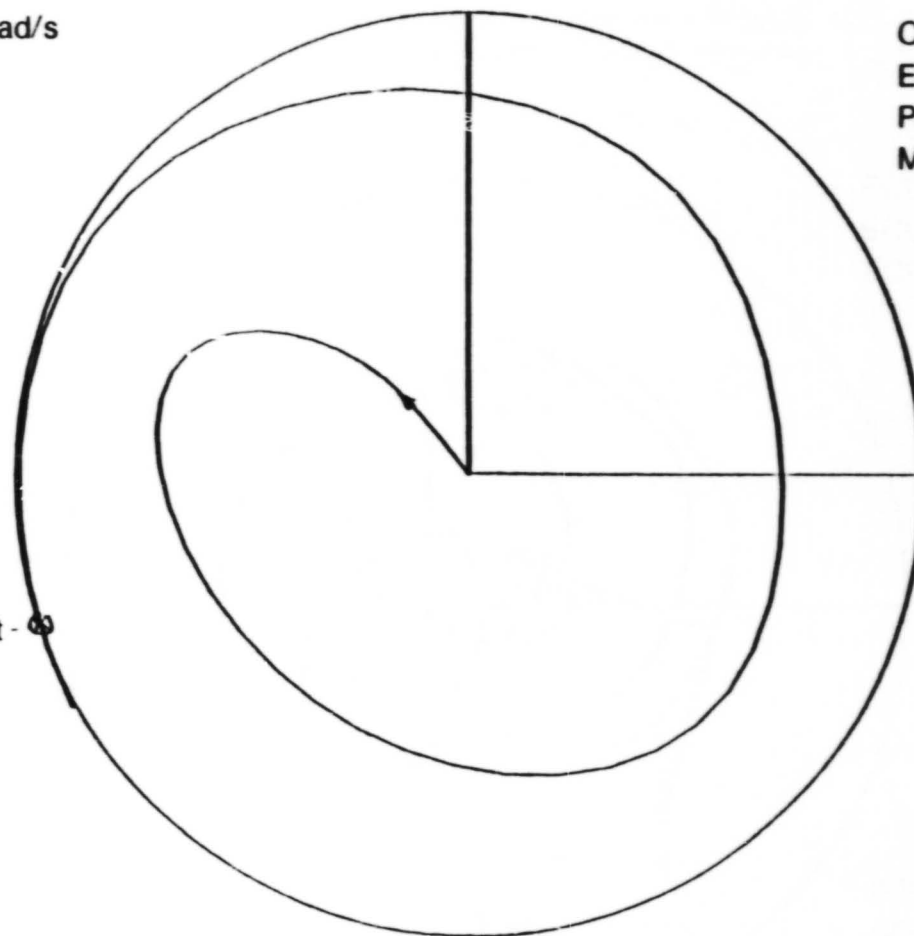


Fig. 4-20 50-mm Composite Metal Ring, Orbital Response; 1379 kPa Absolute (200 psia), 7330 rad/s (70,000 r/min); 0.00635 mm (0.00025 in.) Shaft Runout

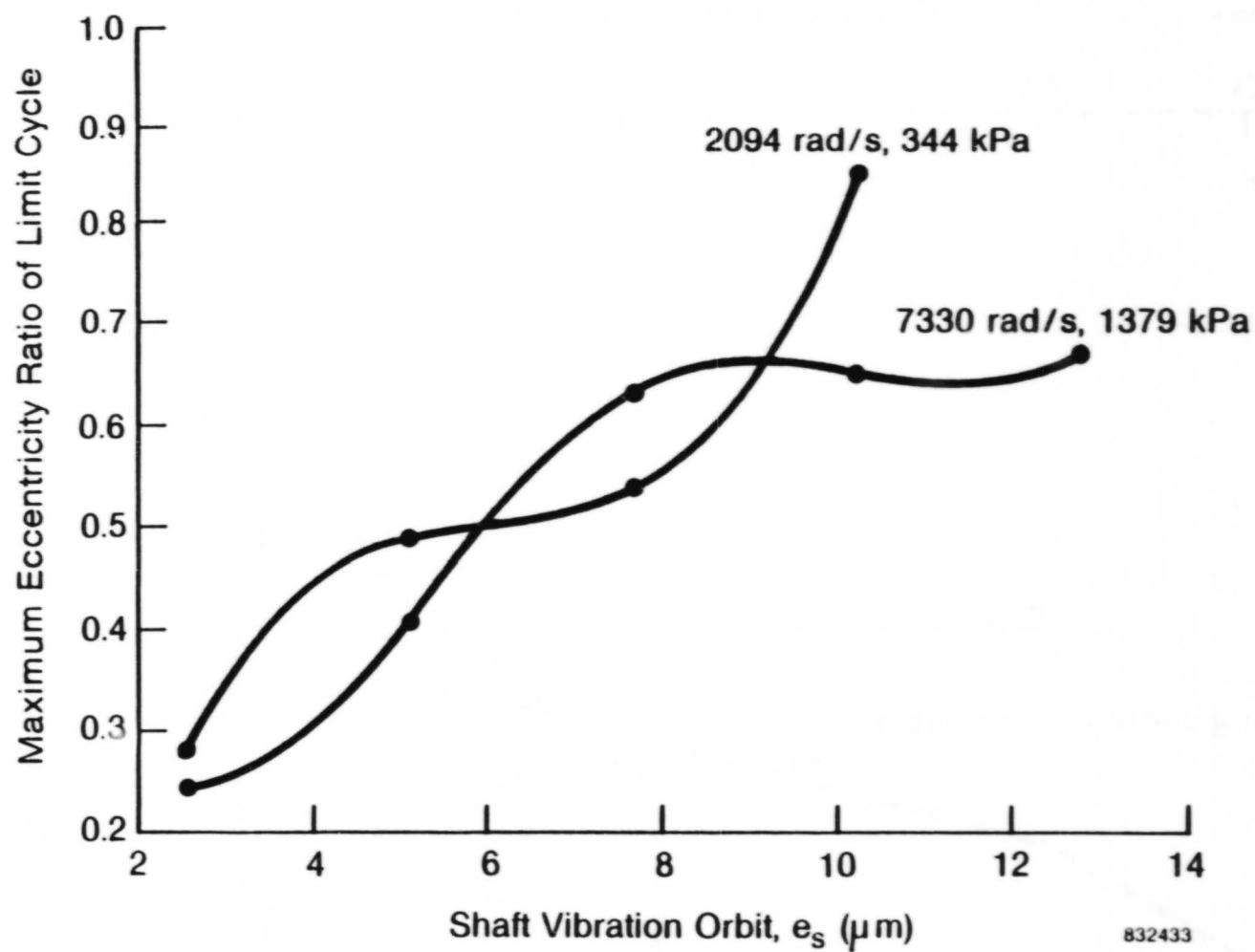


Fig. 4-21 50-mm Ring Response Versus Shaft Orbit

832433

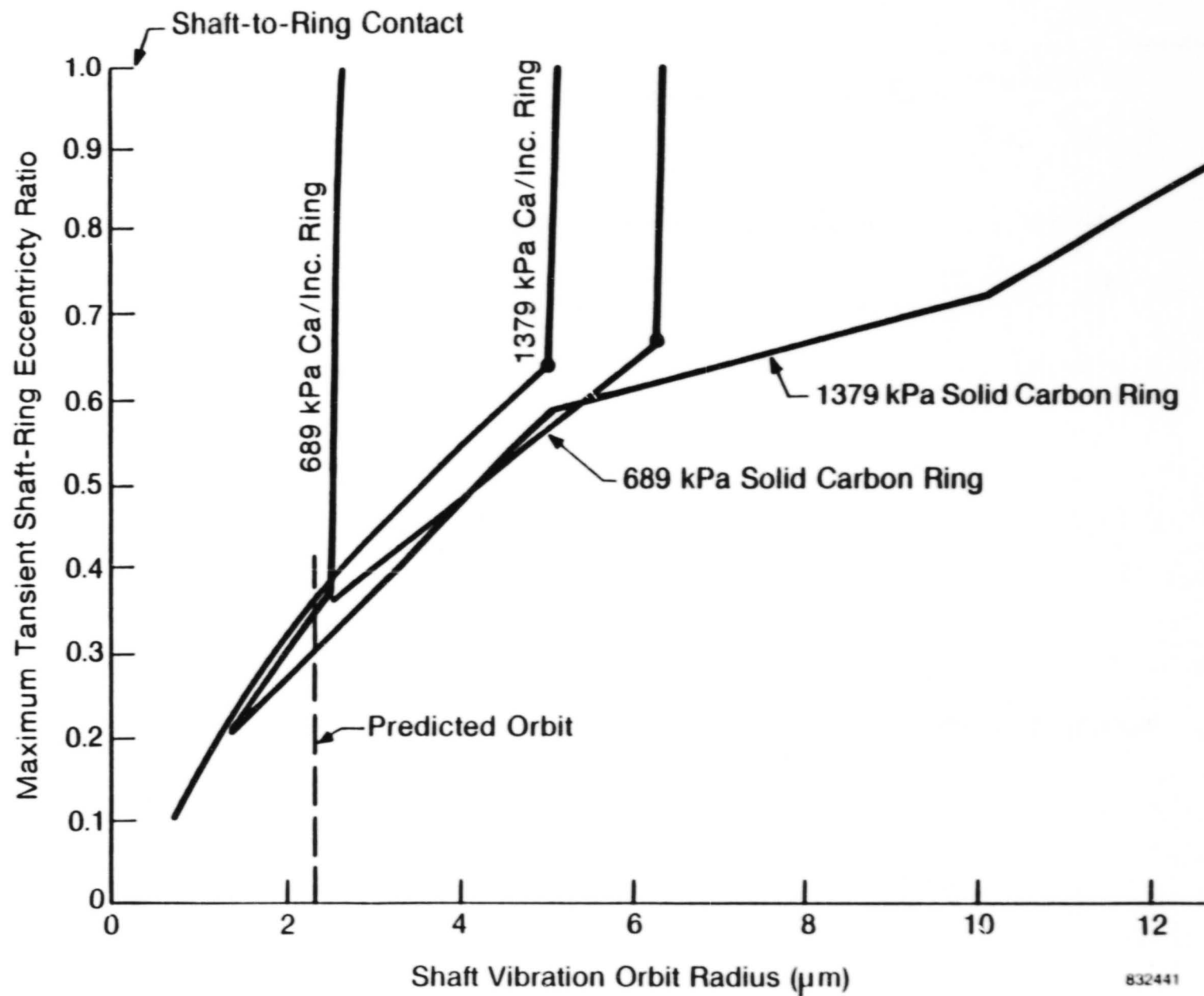


Fig. 4-22 50-mm Composite and All Carbon Ring Orbit Summary Versus Shaft Runout

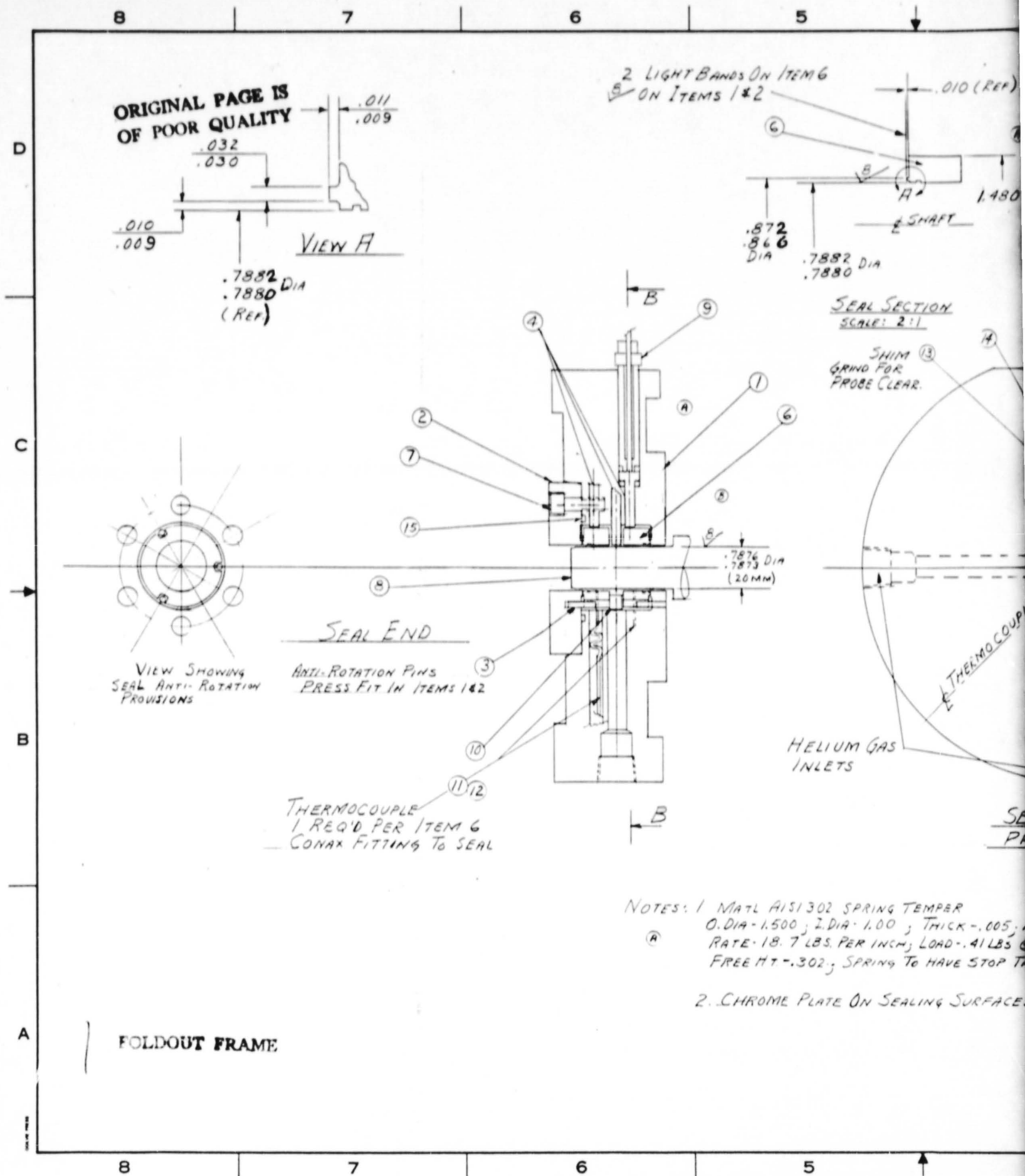


Fig. 4-23 20-mm Helium Pu

4
3
2
1

SEAL SECTION
SCALE: 2:1

SHIM GRIND FOR PROBE CLEAR.

SECTION B-B
PROBE LOCATION

ORIGINAL PAGE IS
OF POOR QUALITY

GROOVE DEPTH: .010
.008

POCKET DEPTH: .0009
.0011

4 REQ'D.

LAND

DEVELOPED VIEW OF SEAL
INNER SURFACE ON .7886 DIA
SCALE: 2:1
(ROTATION COUNTER CLOCKWISE VIEWED FROM SEAL END)

ROTATION OF ROTOR

FOLDOUT FRAME

ITEM	QTY	PART	DESCRIPTION	REMARKS
15	1		SEAL O-RING	VITON
14	6		GASKET	GRAPHITE
13	6		SHIM	AISI 410 OR 416
12	2		CONAX FITTING	
11	2		THERMOCOUPLE	
10	1		SPRING WASHER	NOTE 1
9	6		PROBE HOLDER	INCONEL 600
8	1	700D037	SHAFT	
7	6		SCREW 1/4-28 x 3/4 L9	SOCKET HD - AISI 316
6	2		SEAL RING	C-GR-F-692
5				
4	6		PROBE	M.T.I. .197 O.DIA
3	6		PIN	HARDENED STEEL
2	1		FLANGE	INCONEL 600 NOTE 2
1	1		HOUSING	INCONEL 600 NOTE 2

4
3
2
1

HELIUM GAS
LEAKS

SPRING TEMPER
DIA. 1.00; THICK. .005; NR WAVES 3;
PER INCH; LOAD .41 LBS @ .250 HT;
SPRING TO HAVE STOP TANG

TE ON SEALING SURFACES

COMPANY CLASSIFICATION

PROPRIETARY ☐ NAME-DATE

NON-PROPRIETARY ☐ TITLE

DESIGN ☒ H. JONES 8/5/92

ANALYTICAL

MATERIALS

PROJ. ENGR.

QUALITY CONTROL

ISSUED ☒ FULL

SCALE

WT. CALC.

CODE IDENT NO. 26741

SIZE D 700D030

4
3
2
1

23 20-mm Helium Purge Seal

4-47

PRECEDING PAGE BLANK NOT FILMED

Page intentionally left blank

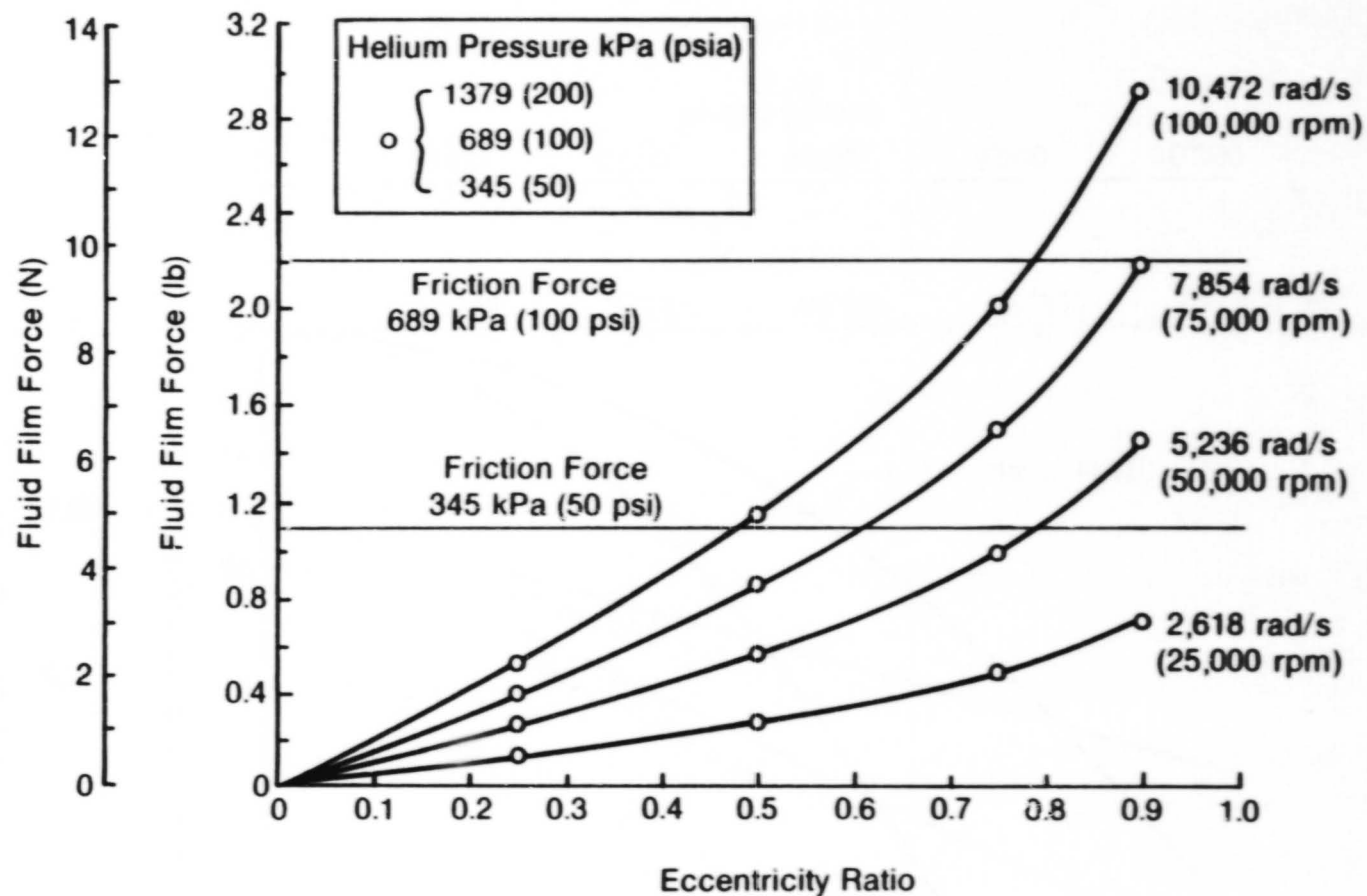


Fig. 4-24 20-mm Helium Seal; Force versus Eccentricity at Different Pressures and Speeds

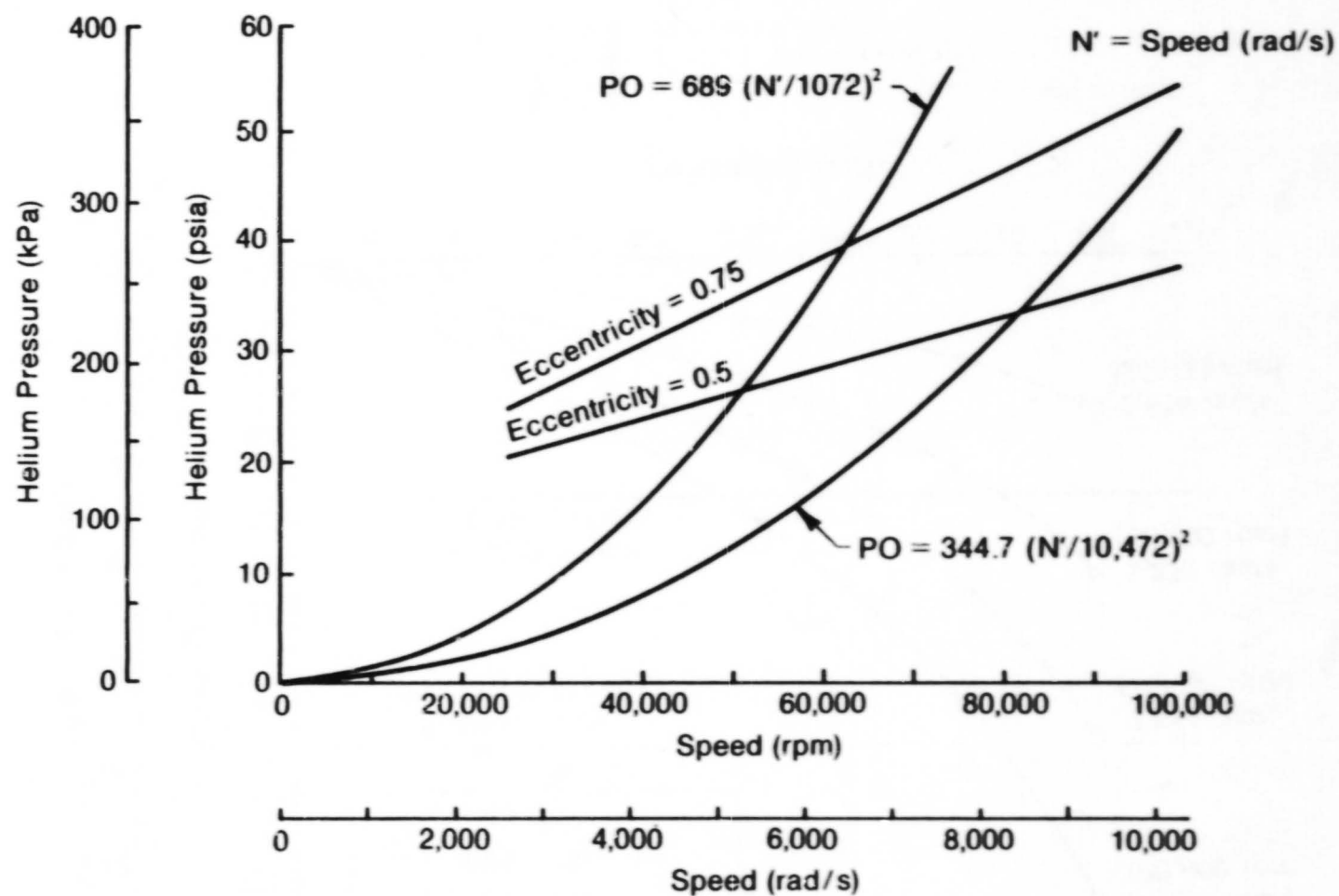


Fig. 4-25 20-mm Helium Seal; Pressure versus Eccentricity to Balance Frictional Force

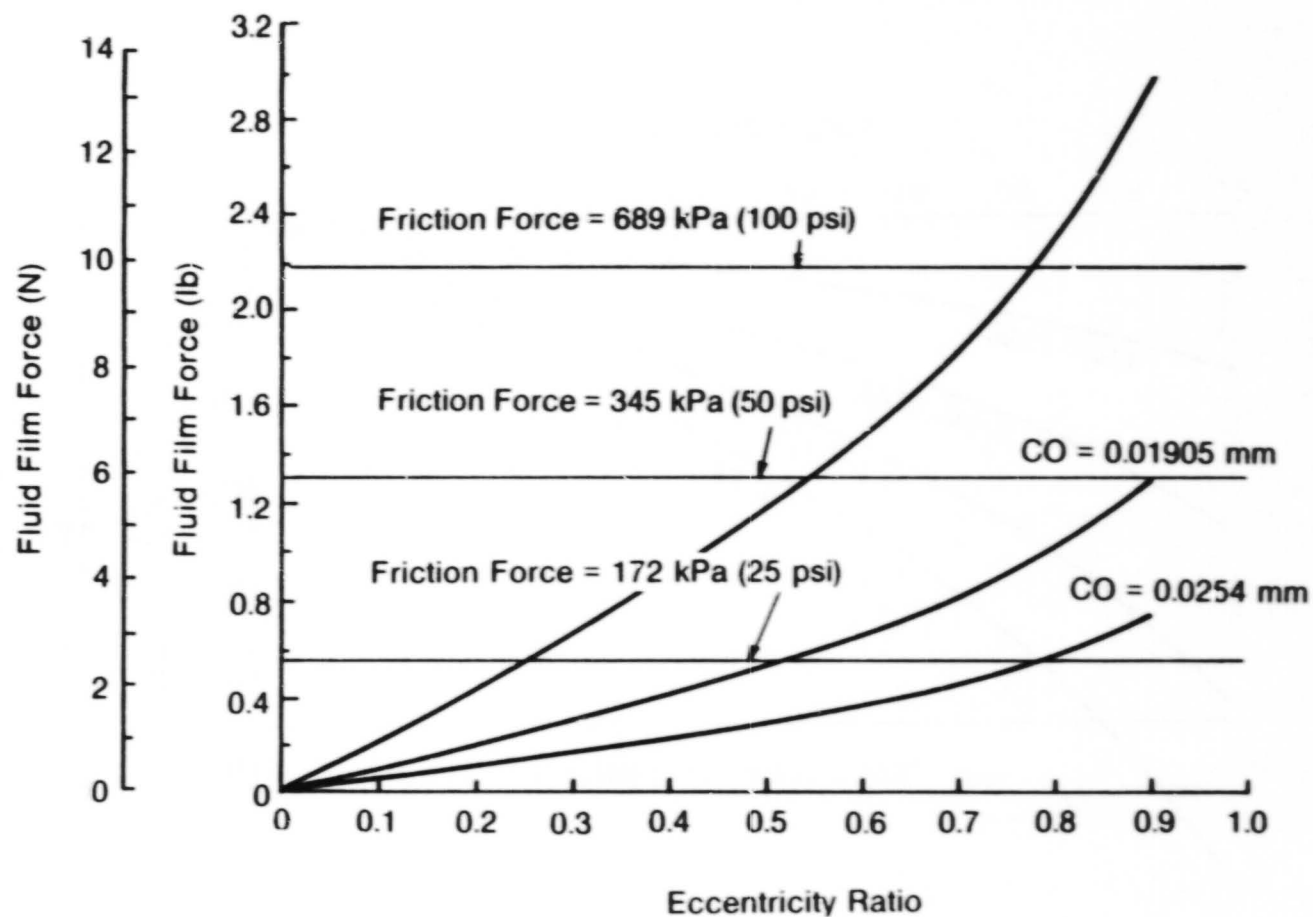


Fig. 4-26 20-mm Helium Seal; Effect of Clearance on Fluid Film Force;
10,472 rad/s (100,000 r/min); 1379 kPa Absolute (200 psia)

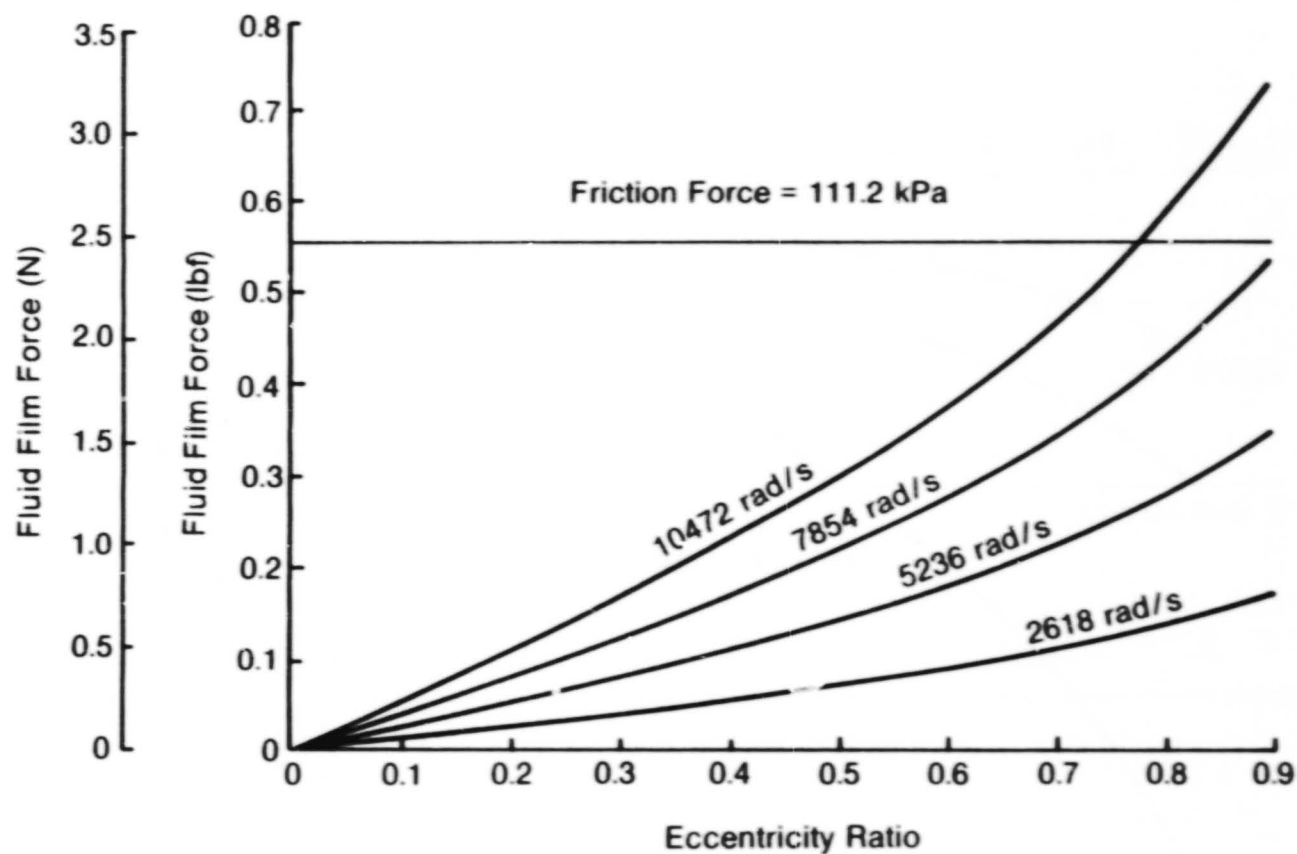


Fig. 4-27 20-mm Helium Seal, Force versus Eccentricity at Larger Clearance ($CO = 0.0254$ mm)

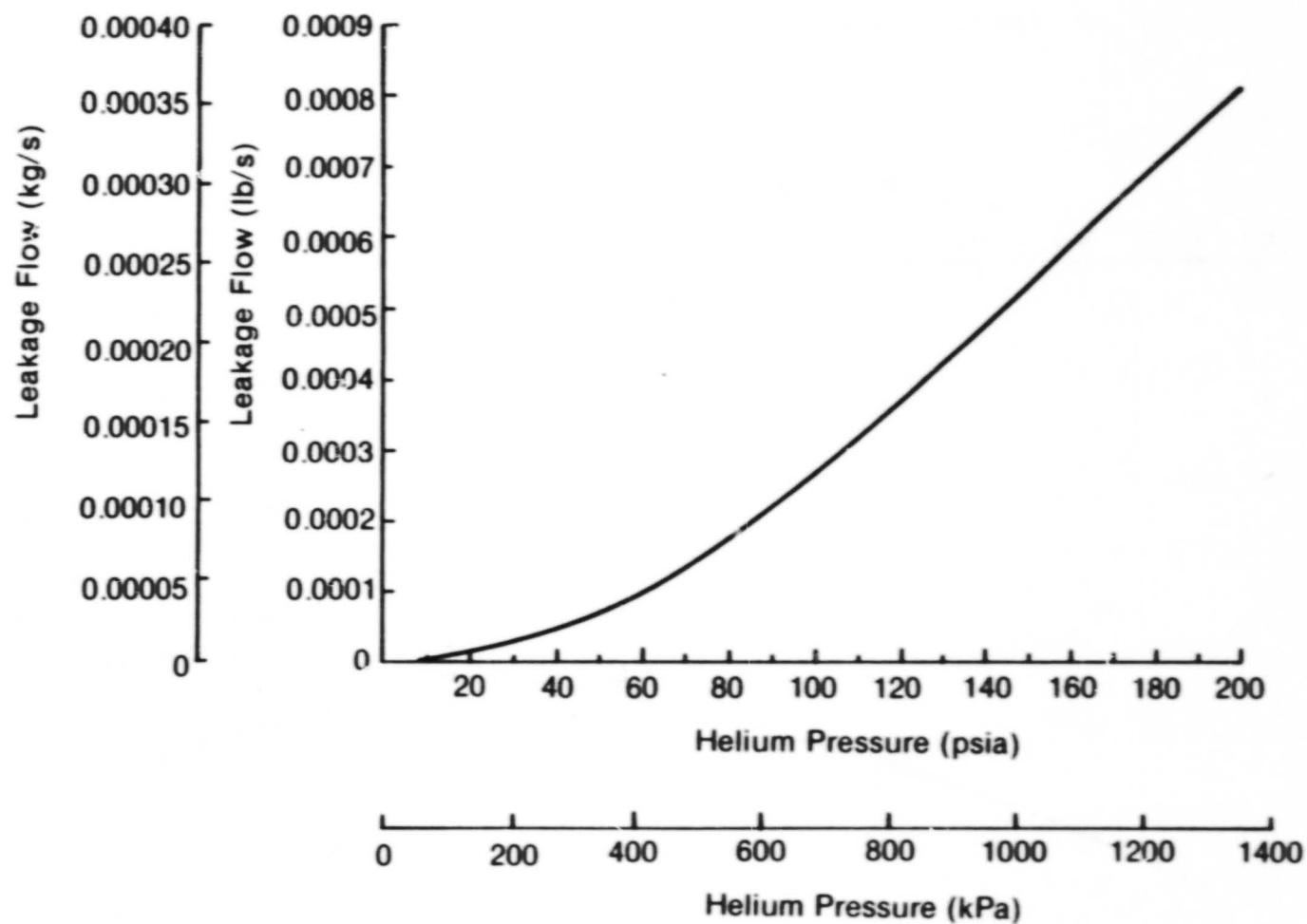


Fig. 4-28 20-mm Helium Buffer Seal at 0.5 Eccentricity Ratio;
Leakage versus Helium Pressure

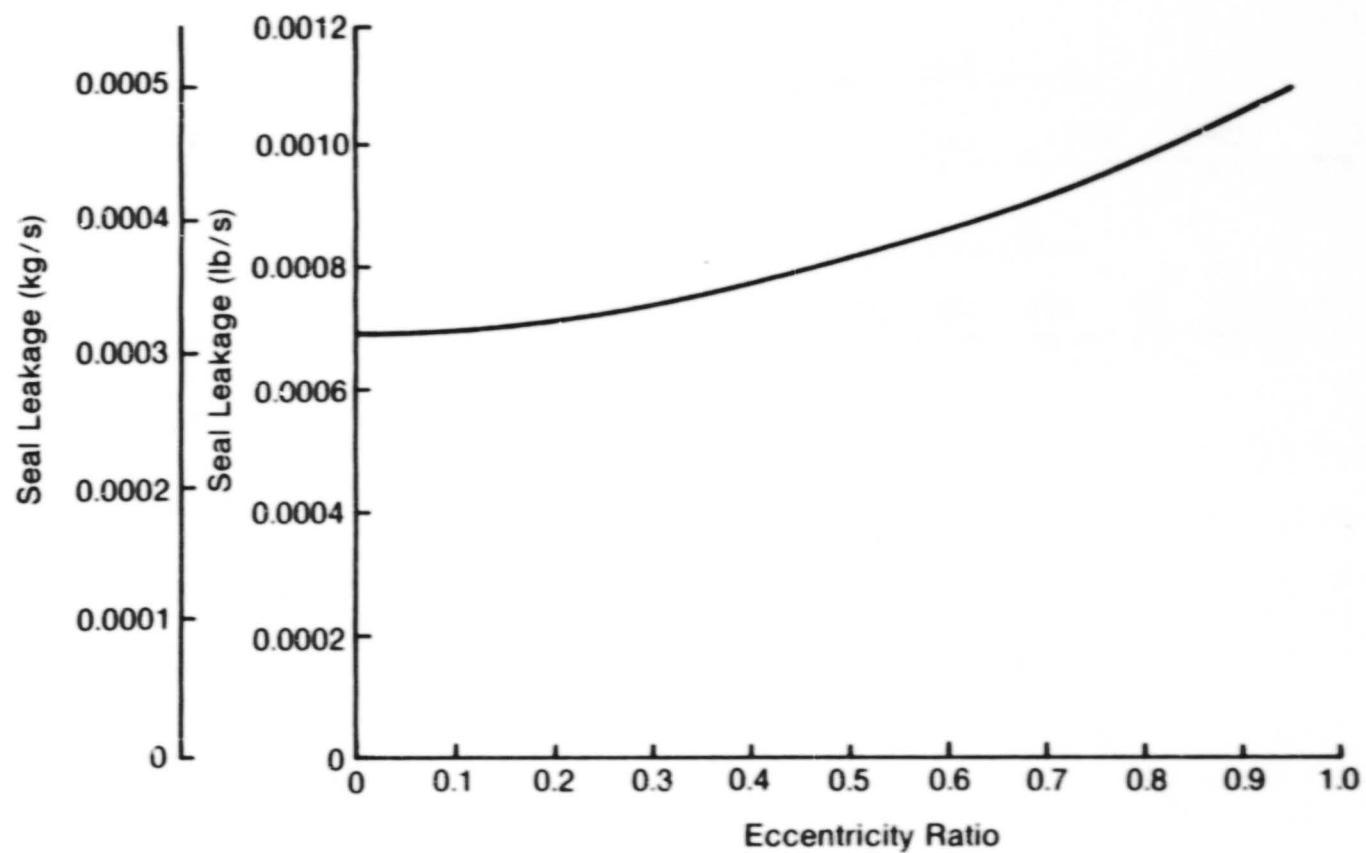


Fig. 4-29 20-mm Helium Seal; Leakage versus Eccentricity 1379 kPa (200 psia)

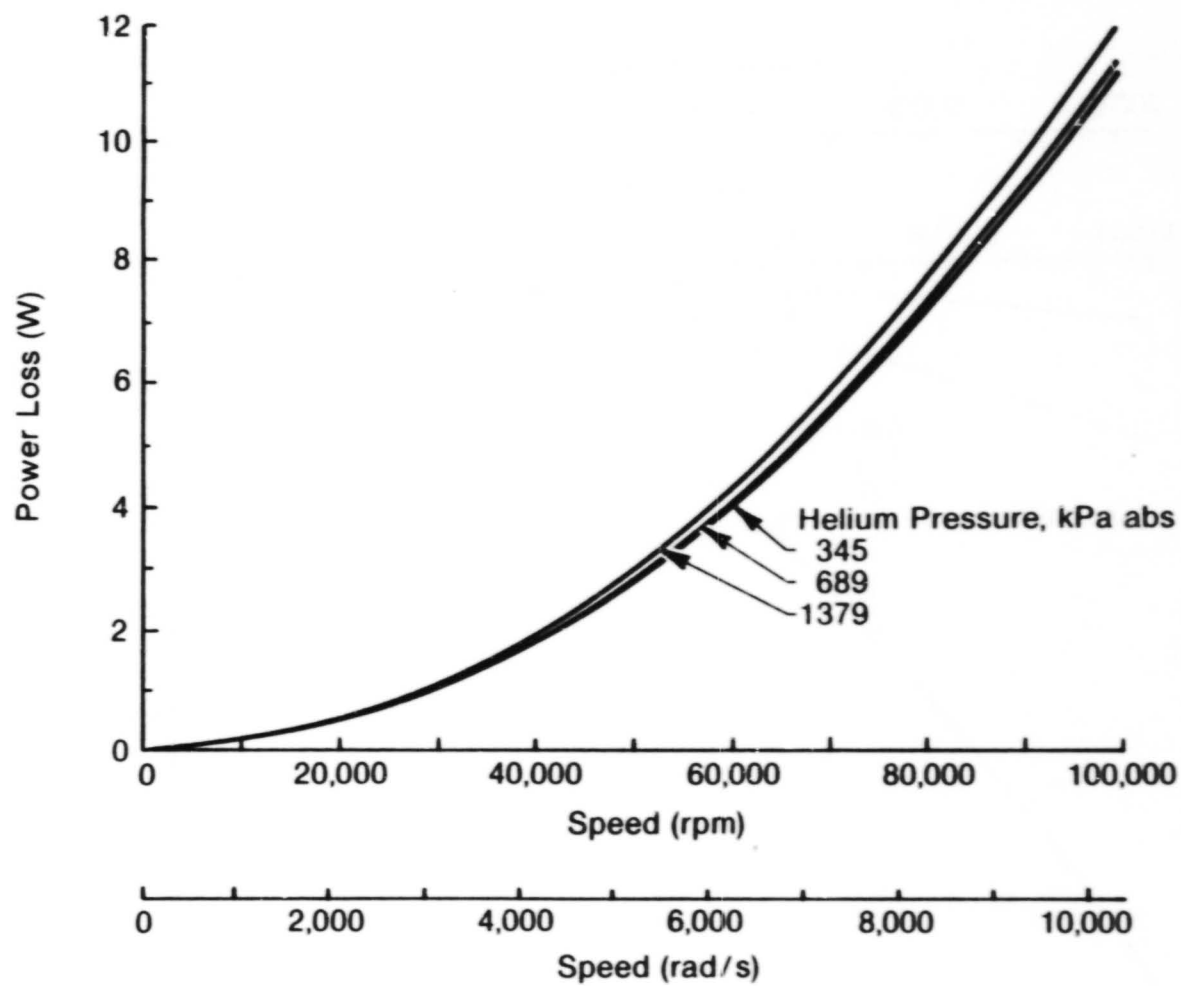


Fig. 4-30 20-mm Helium Seal, Power Loss versus Speed

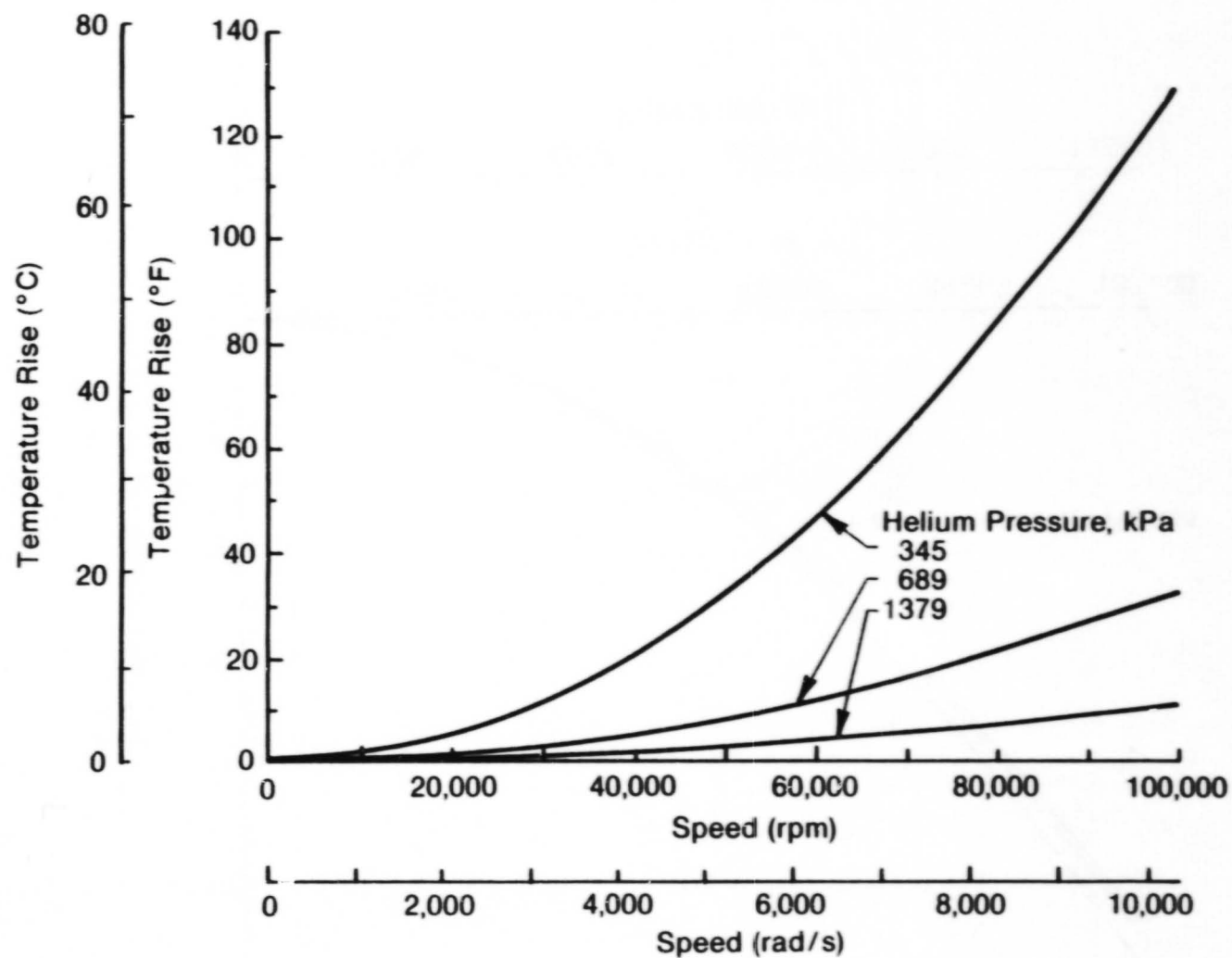


Fig. 4-31 20-mm Helium Buffer Seal at 0.5 Eccentricity Ratio;
Temperature Rise versus Speed

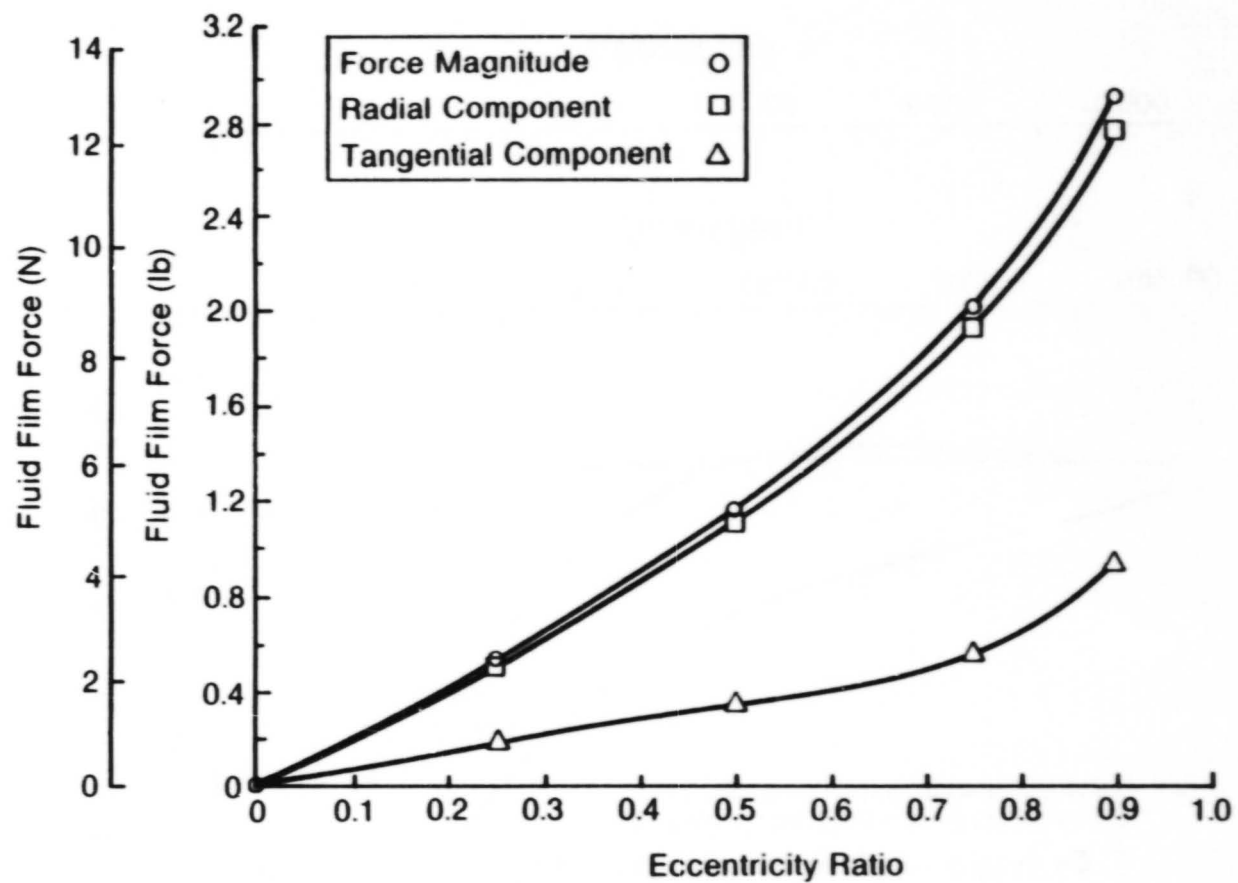


Fig. 4-32 20-mm Helium Seal, Fluid Film Force versus Eccentricity at 1379 kPa Absolute (200 psi), 10,472 rad/s (100,000 r/min)

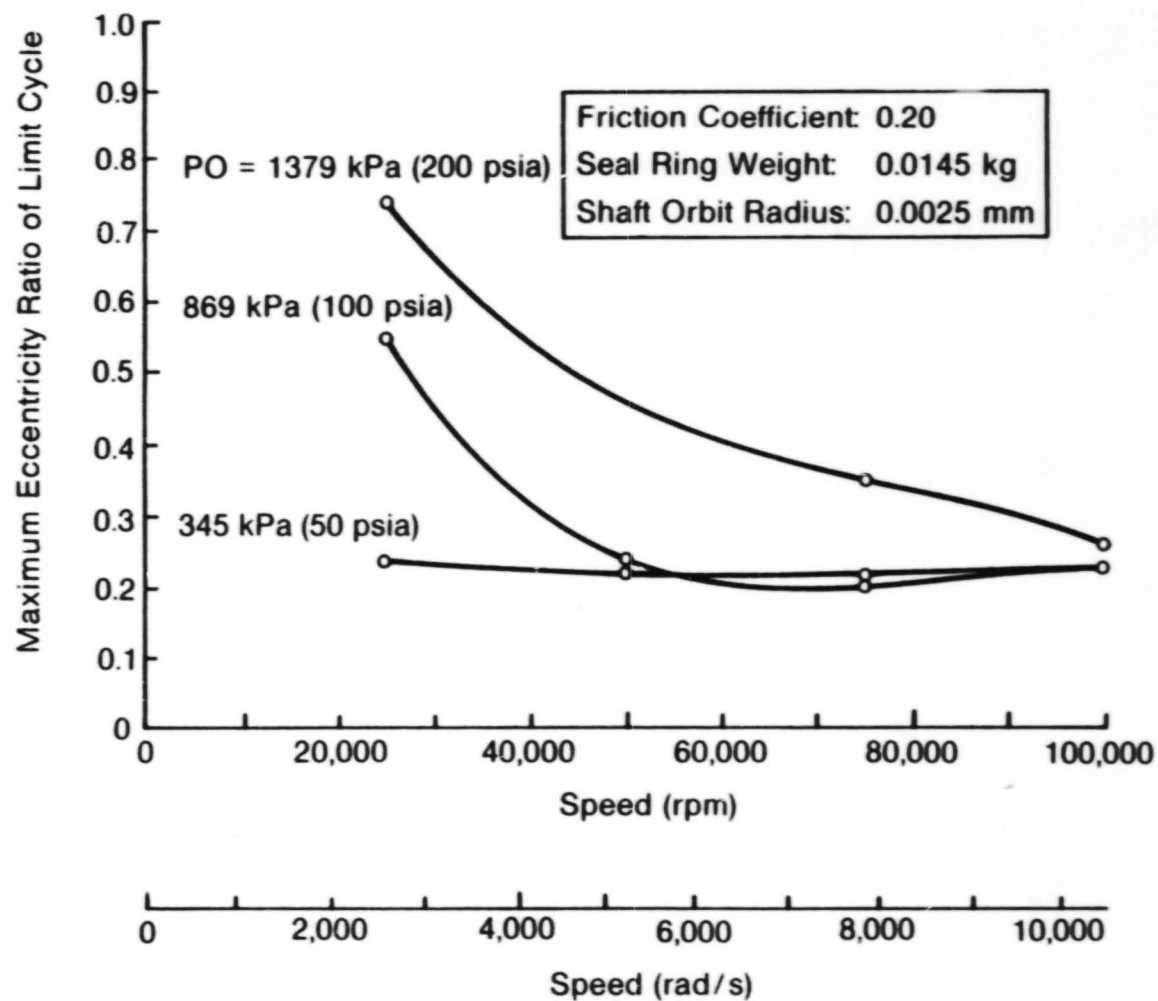


Fig. 4-33 20-mm Helium Seal; Transient Response Summary;
0.0025-mm Shaft Runout

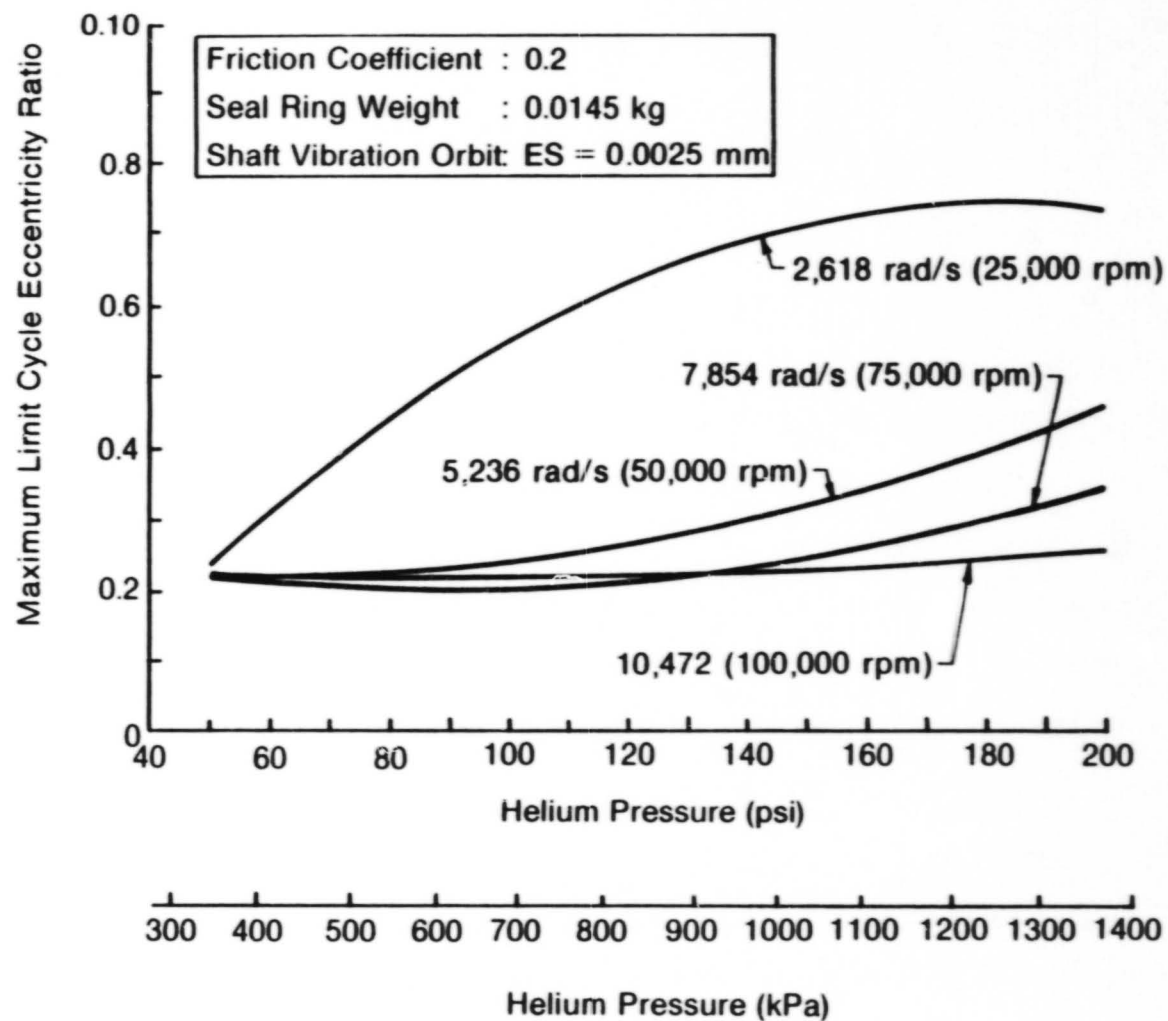


Fig. 4-34 20-mm Helium Seal; Transient Response Summary versus Buffer Pressure; 0.0025-mm Shaft Runout

5.0 ANALYSIS AND DESIGN OF SPIRAL-GROOVE LOX SEALS

5.1 General Discussion

The spiral-groove face seal is a prime candidate for application to LOX turbo-pumps. It is a fluid-film seal that can effectively inhibit leakage and avoid rubbing contact that could cause catastrophic explosion failure in a LOX environment. As described in the introduction, the function of the LOX seal is to aid in preventing leakage of LOX from the pump end of the machine. Requirements and operating conditions were presented in Section 1.0.

The most demanding requirements that extend the present state of the art include the high relative surface speed of 183 m/s (600 ft/s) and the high pressure of 5.17 MPa (750 psig) to be sealed.

Originally, MTI examined a conventional type of spiral-groove seal that was labeled the straight-through design. The spiral grooves extended to the outside diameter and the fluid was pumped inward to a dam region at the interior ID of the seal. Although excellent performance characteristics were predicted, the straight-through designs were ultimately abandoned because of the probability of vaporization in the flow path.

The pressure-balanced concept selected was conceived by NASA/LeRC and recommended for the LOX turbopump application, because it obviated vaporization problems. Additional details concerning the analysis and design are presented in References [1] and [8].

5.2 Analytical Approach

The parametric studies necessary to optimize the seal design fall into three categories:

1. Steady-state fluid-film performance
2. Minimizing any detrimental effects of thermoelastic distortions
3. Ensuring acceptable dynamic response to external excitations

In general, fluid-film geometry and performance are first optimized. Thermoelastic distortions are checked to see that they do not significantly affect the fluid-film performance. Variations in materials and exterior geometry can be applied to reduce distortions. Finally, dynamic response is checked and mass and inertia properties of the seal ring varied to assure acceptable response.

The fundamental reference for the spiral-groove analysis was the work done by E.A. Muijdermann [9]. Laminar theory was subsequently expanded to include the effects of turbulence and inertia at sudden contractions in a manner similar to that described in References [6] and [10]. Elastic distortions were determined using a theory modeled upon that described in Reference [1].

The computer code was written for spiral-groove geometry optimization and performance evaluation. The analytical procedure is summarized in Appendix A. The final computer code could:

1. Optimize geometrical variables on the basis of stiffness, flow, or fluid temperature rise.
2. Determine the operating film thickness as a function of sealed pressure and secondary seal diameter.
3. Produce film thickness, power loss, circulating flow, leakage flow, fluid temperature rise in spiral-grooves and seal dam, axial and angular stiffnesses, natural frequencies, dynamic amplitude ratios, and thermoelastic distortions and stresses.

5.3 Configuration for the 50-mm Seal

The general groove geometry is shown on Figure 2-13. Note that deep and wide grooves are necessary to pump the highly turbulent fluid, because of its high effective viscosity. Table 2-2 defines the principal nominal dimensions of the pressure-balanced design.

The original MTI design layout drawing of the 50-mm pressure-balanced seal, is shown on Figure 2-14. In the test rig, it will be installed in a back-to-back configuration as shown on the bottom left corner of the drawing. This was done to eliminate excessive thrust loading on the test rig thrust bearing. The outboard seal is the test seal, while the inboard seal is the thrust balancing seal. Using the layout (Figure 2-14), the seal vendor, Stein Seal Company of Philadelphia, Pa., produced assembly and manufacturing drawings. There are some variations between the original layouts and the final design, but the subsequent seal vendor drawings govern, and provide accurate information regarding the final product.

The nonrotating member of the spiral-groove seal is made from carbon graphite (P-5N) and contains the interior high pressure grooving and feed holes.

The seal rings do not have metal shrouds or interface pieces. The intent is to maintain the mass of the seal ring members as low as possible for improved dynamic response.

The spiral grooving is not machined into the carbon because of potential wipe-out from a high speed rub. The test seal assembly is indicated on Stein Seal Company drawing, Figure 5-1*. Details of the carbon graphite face seal are shown on Figure 5-2. There are three slots on the outer periphery that mate with antirotation pins on the housing elements. The design incorporates provisions for a thermocouple installation to measure the feed groove temperature. Figure 5-3 shows details of the mating ring or spiral-groove runner. The spiral-groove lands and dam and the seal land regions were coated with tungsten carbide containing a chrome-cobalt binder (Linde LW-15). The base material for the spiral-groove mating ring is Inconel 718 to insure structural integrity when exposed to centrifugal and pressure force fields. An interesting feature of the design which was prescribed by Stein Seal Company is the circumferential secondary seal. It is of split construction and held together by a garter spring. There are two sealing surfaces; a stationary radial surface between the secondary seal and housing and a sliding sealing surface

*Figures are presented consecutively, beginning on page 5-11.

between the inner circumference of the secondary seal and the secondary seal OD on the face seal element. The sliding seal is pressure balanced significantly to prevent excessive crush and friction when high pressure is applied. The secondary seal is made from the same carbon graphite material as the face seal (P-5N). A wavy washer spring loads the secondary seal against the housing.

Figure 5-4 is a drawing of the secondary seal and Figure 5-5 is a photograph of the secondary seal. On the left side of the picture, the secondary seal is installed in its housing; on the right, the three sectors that comprise the major seal components are shown separated from one another.

5.4 Calculated Fluid-Film Performance of the 50-mm Spiral-Groove Seal

A series of computer runs were made over a range of speeds and pressure. Principal results are tabulated on Table 5-1*. The indicator, G, stands for the spiral-groove region and S for the sealing ridge. Cooled means the inlet to the groove is at a constant prespecified temperature indicating sufficient bypass flow through the seal compartment to maintain the constant inlet temperature. On the other hand, uncooled means the inlet groove temperature is an equilibrium temperature based upon leakage flow and viscous power generation.

Performance information was computed using a constant viscosity of 1.172×10^{-4} Pa-s which corresponds to LOX at -173°C (-279.4°F) and a fluid density of 1080 kg/m^3 (0.039 lb/in.^3).

Film thickness data is shown on Figure 5-6. As expected, the film thickness reduces as the pressure goes up and as the speed goes down. The numbers indicate that rapid liftoff to approximately 3000 rad/s ($28,647 \text{ r/min}$) would be desirable to avoid excessive rubbing of this seal. The operating film thickness at 5864 rad/s ($56,000 \text{ r/min}$) which corresponds to a rubbing speed at the seal interface of 183 m/s (600 ft/s) is 0.024 mm (0.0009 in.). It is interest-

*Tables are presented consecutively, beginning on page 5-41.

ing to note that a straight-through inflow design which had been initially examined, has superior low-speed characteristics. The reason for this is that a large pressure gradient exists across the grooves of the inflow design, and there are pressure-induced hydrostatic forces between the spiral-grooves and the inside seal dam region that provide a substantial lifting force at low speed and high pressure. The straight inflow design, however, would fail because of vaporization in the interface and was thus eliminated.

Axial stiffness is shown on Figure 5-7. The stiffness increases with pressure and attains an optimum value at 3000 to 4000 rad/s (28,648 to 38,197 r/min), depending upon the pressure level. As speed increases, the stiffness falls off, probably because of the high film thickness at high speeds. Low-speed stiffness is very poor, and again reflects the need to become fluid-borne quickly and operate at speeds above 3000 rad/s (28,648 r/min). At an operating speed of 5864 rad/s (56,000 r/min), maximum pressure of 5.17 MPa (750 psig), the axial stiffness is 81.1×10^6 N/m (718×10^6 lb/in.).

Circulating groove flow is shown on Figure 5-8. This is not the leakage flow, but is the quantity of fluid that is circulated through the pumping grooves. The circulating flow varies inversely with pressure because film thickness increases as the pressure goes down. At a maximum speed and pressure of 5864 rad/s (56,000 r/min) and 5.17 MPa (750 psig) respectively, the circulating flow is 2×10^{-4} m³/s (12.2 in.³/s). Note the poor circulation at low-speed conditions, which reflects the poor pumping capability, low film thickness, and generally poor operation at the lower shaft speeds. Leakage, or flow through the sealing dam, is shown on Figure 5-9. The leakage flow is a function of pressure differential and film thickness. Film thickness effects are usually predominant. Note that the leakage curves cross one another. Not only is pressure differential and film thickness affecting flow, but there are strong effects of turbulence and inertia, especially at the higher pressure differential. These effects cause the crossover of the flow curves. Leakage at operating condition of 5.17 MPa (750 psig) and 5,864 rad/s (56,000 r/min) is 2.98×10^{-4} m³/s (18.2 in.³/s).

Power loss curves are shown on Figure 5-10. As expected, power loss increases with speed and pressure. For the pressure-balanced seal, power loss is quite

substantial because of the relatively large interface area. At the operating speed of 5864 rad/s (56,000 r/min) and 5.17 MPa (750 psig) pressure differential, the power loss is 9.47 kW (12.7 hp).

Temperature rises of the fluid being circulated through the spiral grooves and leaking through the sealing dam are indicated on Figures 5-11 and 5-12, respectively. These temperature rises assume that there is external cooling flow entering the seal cavity, thus maintaining a constant inlet temperature. It also presumes that all heat transfer occurs between fluids and not to the outside ambient. Exorbitant temperature rises occur at the lower speed (<3,000 rad/s) (28,648 r/min) conditions because of the very low flow to carry away the heat generated. At operating conditions of 5.17 MPa (750 psig) and 5864 rad/s (56,000 r/min) the groove fluid temperature rise is approximately 21.4°C (38.5°F), and 2.83°C (5.1°F) through the seal land. Both of these temperature rises are acceptable. For a noncooled inlet condition, the equilibrium temperatures become much higher. These have been calculated. The results are a 35.6°C (64.1°F) rise through the spiral-grooves and a 17.2°C (31°F) rise through the seal land. In addition, the equilibrium groove temperature increases from -118°C to -104°C (-180°F to -155°F).

5.5 Dynamic Analysis of the 50-mm Spiral-Groove Seal

Initially, three types of dynamic analyses were considered. The analyses started from a simplified approach and then graduated toward real-time response analyses including Coulomb friction in the secondary seal. In each analysis, the fluid film was approximated by fluid-film stiffnesses obtained from the spiral-groove fluid-film analysis. Cross-coupling between axial and angular stiffness was neglected and only principal angular stiffnesses applied. Cross-coupling only occurs in the seal land regions and not in the spiral-groove region. Since the spiral-groove interface is dominant, cross-coupling can be safely neglected. In the analyses considered, the angular stiffness was computed on the basis of the computed axial stiffness at the operating condition (i.e., assuming an infinite number of axial springs). The relationship between axial and angular stiffness is as follows:

$$K_{\theta} = \frac{K_a}{2} \bar{R}^2 \quad (5.1)$$

where:

K_{θ} = angular stiffness

K_a = axial stiffness

\bar{R} = mean seal radius

Fluid film damping was neglected.

Comparative results of the simplified and comprehensive dynamic studies indicated that the differences were not significant. Therefore, the simplified methods were applied to facilitate parametric evaluations.

The analytical model for the simplified approach considered two circular flat plates separated by linear springs. Fluid-film damping and secondary seal ring friction were neglected. Axial stiffness of the springs was obtained from the fluid-film analysis (see Figure 5-7) and angular stiffness obtained from Equation 5.1. One plate was vibrated in the axial and angular modes. The results could be put into a general format for both axial and angular vibrations as follows:

$$\frac{\Delta h}{a} = \frac{\tilde{\omega}^2}{1 - \tilde{\omega}^2} \quad (5.2)$$

where:

Δh = change in clearance

a = vibration amplitude

ω = ratio of operating frequency/natural frequency.

The quantity $\Delta h/a$, defined as the amplitude ratio, can be interpreted as the clearance closure at the outer radius divided by one-half of the TIR runout of the mating ring for angular vibrations. For axial vibrations it is the cyclical clearance closure divided by one-half of the total supplied amplitude. The angular amplitude ratio as a function of speed and pressure is indicated on Figure 5-13. The misalignment angle was 0.75 m rad, which gives a peak-to-peak amplitude at the OD of the seal portion of the mating ring of 0.0381 mm (0.0015 in.).

Except for low-pressure, high-speed conditions, the resulting amplitude ratios indicate very good dynamic response with less than 20% of the available clearance consumed by response lag of the seal ring. The high stiffness at relatively large clearances (due to turbulence) contribute to the good overall performance. The reason for the poor performance at the low pressure, high-speed operation is due to very high operating clearances with consequent poor stiffness. The seal should not be run at low-speed, high-pressure conditions, because of the poor start-up characteristics previously mentioned.

5.6 Elastic and Thermal Distortions of the 50-mm Spiral-Groove Seal

Combined elastic and thermal distortions of the pressure-balanced design are shown on Figure 5-14. In computing the thermal effects, it was assumed that a percentage (approximately 50%) of the fluid temperature rise previously computed by heat balance, penetrated the seal ring thickness as indicated on the figure. The thermal penetrations were taken to be rectangular to a depth of approximately 3.3 mm (0.13 in.). This temperature distribution would produce greater distortions than actually experienced. A 45-N (10.1-lb) spring force was assumed to be acting on the seal ring in the position shown. Also, the secondary seal is approximately 15.75 mm (0.61 in.) from the seal face. The distorted position of the seal ring indicates that it has moved radially approximately 0.026 mm (0.001 in.) and the face has tilted in a converging direction approximately 160 μ rad. This tilt translates into a variation in film thickness across the seal face of only 3.2×10^{-4} mm (0.126×10^{-4} in.) which is insignificant. Since the length beyond the secondary seal is not exposed to the high pressure, it will not move in as far radially as the length on the inboard side of the secondary seal that is exposed to the high pressure. The net effect is the bend in the seal ring indicated by the dashed line in Figure 5-14. At its very end, this distortion is approximately 0.015 mm (0.0006 in.). The slope of this bend must be taken into account when designing the secondary seal. The net result indicates that the distortions are not excessive and will not have a serious effect on performance of the seal.

5.7 Design of the 20-mm Spiral-Groove Seal

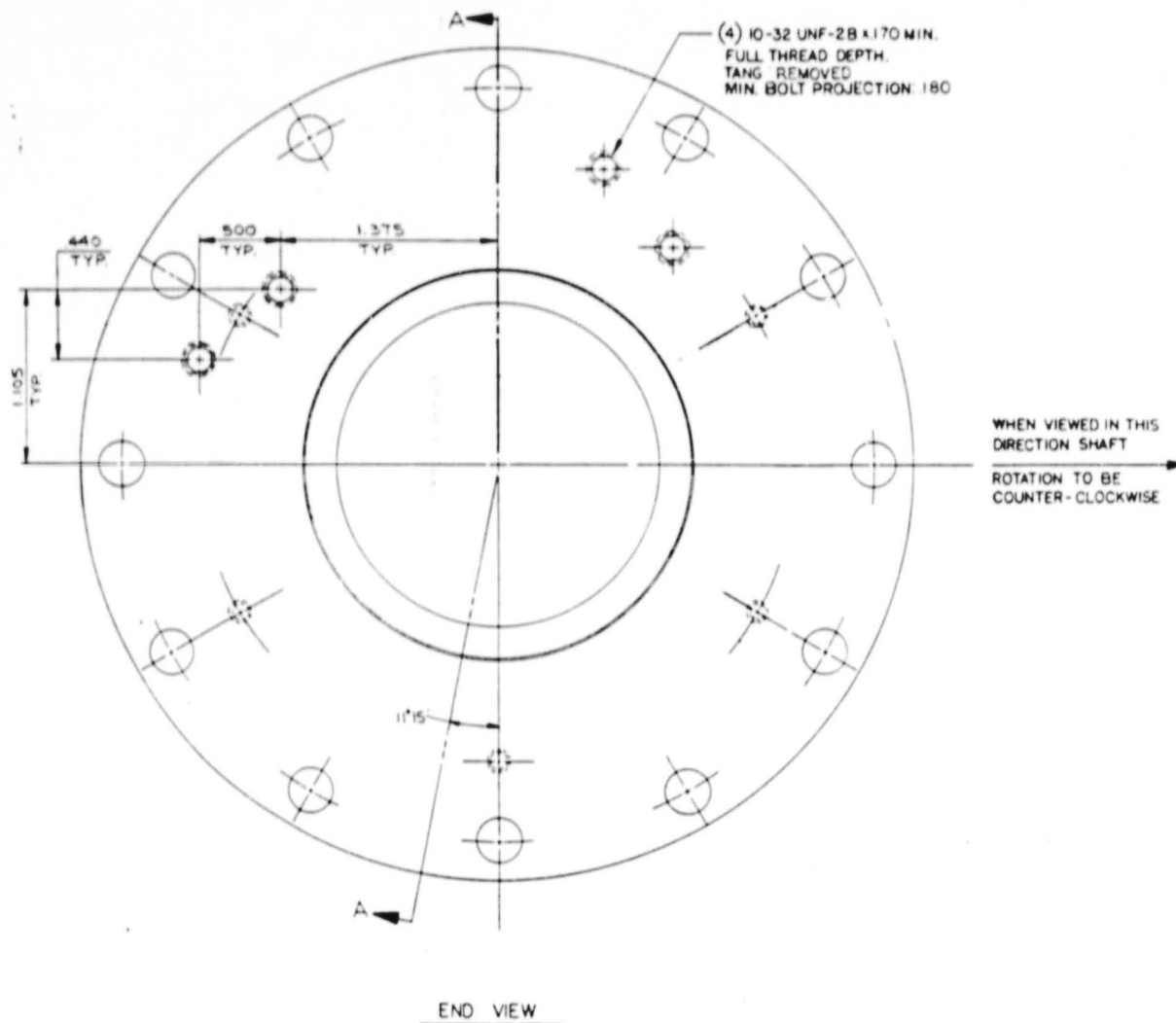
Results of computerized analysis over a speed-pressure range are indicated on Table 5-2 and on Figures 5-15 through 5-26. Results are similar to the 50-mm design so that only pertinent comments are summarized below:

- Film thickness (as shown on Figure 5-15) varies inversely with pressure as expected. At maximum pressure the speed should be above 3665 rad/s (35,000 r/min) to operate safely. As with the 50-mm design, low-speed performance is very poor.
- Axial stiffness is shown on Figure 5-16. Low-speed stiffness is poor. At maximum speed and pressure, the stiffness is 48.5×10^6 N/m (277,000 lb/in.)
- Leakage flow is indicated on Figure 5-17. At maximum speed and pressure, the leakage is 1.9×10^{-4} m/s (11.6 in.³/s).
- Circulating groove flow is shown on Figure 5-18. At maximum conditions, the flow is 1.38×10^{-4} m/s (8.4 in.³/s). The maximum circulating flow occurs at low-pressure, high-speed conditions, because of the high film thickness at this condition. The maximum flow is 1.56×10^{-4} m/s (9.5 in.³/s).
- Power loss is indicated on Figure 5-19. Maximum power is dissipated at maximum pressure and speed and is equal to 7.084 kW (9.5 hp).
- The temperature rise in the seal land is shown on Figure 5-20. The 20-mm seal was only analyzed at the cooled inlet condition since that is the anticipated operation. The maximum temperature rise through the seal is only 2.28°C (4.1°F). At the lower speeds, over-temperature would occur at sustained operation.
- The temperature rise of the circulating fluid through the grooving is shown on Figure 5-21. At maximum speed and pressure, the temperature of the circulating fluid rises approximately 25°C (45°F).

- The natural frequency of the seal ring in the axial mode is shown on Figure 5-22. It is only at the low-pressure conditions that the frequency approaches uncomfortably close to the operating speed.
- Angular natural frequency is shown on Figure 5-23. Again, the indications are that low-pressure, high-speed operation should be avoided.
- Axial amplitude ratio is shown on Figure 5-24. It clearly indicates the danger for operating below a pressure of 1.724 MPa (250 psig) at full speed.
- Angular amplitude ratio is shown on Figure 5-25. Identical comments as for the axial amplitude ratio apply.
- Figure 5-26 shows elastic distortions. These are all very moderate. Elastic distortions produce a variation in film thickness of 0.00084 cm (33 μ in.) which is negligible compared to the operating film thickness.

ORIGINAL PAGE IS
OF POOR QUALITY

(2) EQ. SP. 9/32 DIA. THRU
HOLES ON A 4.750 DIA. B.C.



5.255 - 5.245 DIA.

2.464 - 2.465 DIA.

2.441 - 2.440 DIA.

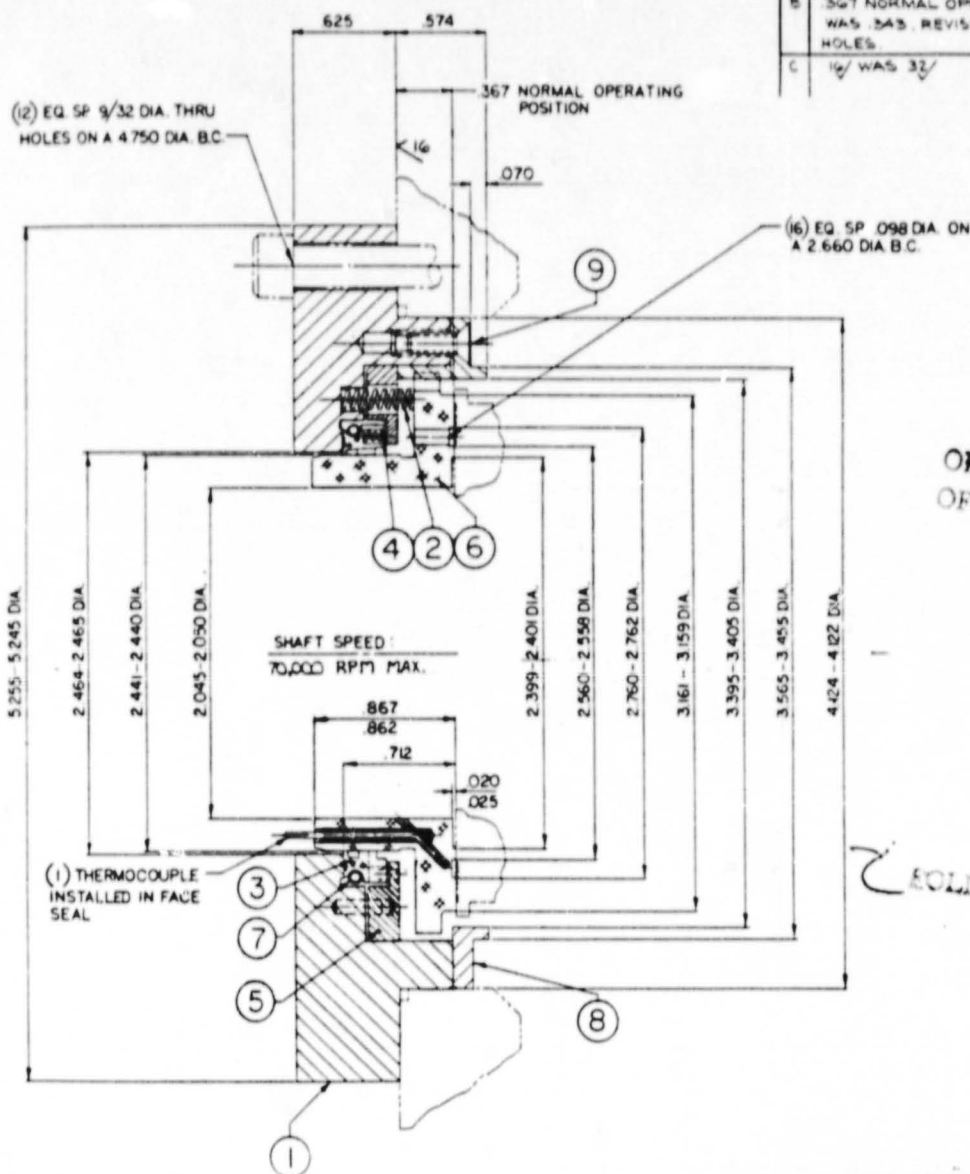
2.045 - 2.050 DIA.

(1) THERMOCOUPLE
INSTALLED IN FACE
SEAL

EXPLOSION FRAME

Fig. 5-1 50-mm LOX Spiral-Groove Seal As

IN THIS
SHAFT
BE
CLOCKWISE



SECTION A-A
SCALE: 2/1

REVISIONS			
LT#	DESCRIPTION	DATE	APPROVED
A	RELEASED	1-28-83	
B	367 NORMAL OPERATING POSITION WAS .343. REVISED PROBE BRACKET HOLES.	2-21-83	H.F.
C	16/ WAS 32/	3-18-83	H.F.

ORIGINAL PAGE IS
OF POOR QUALITY

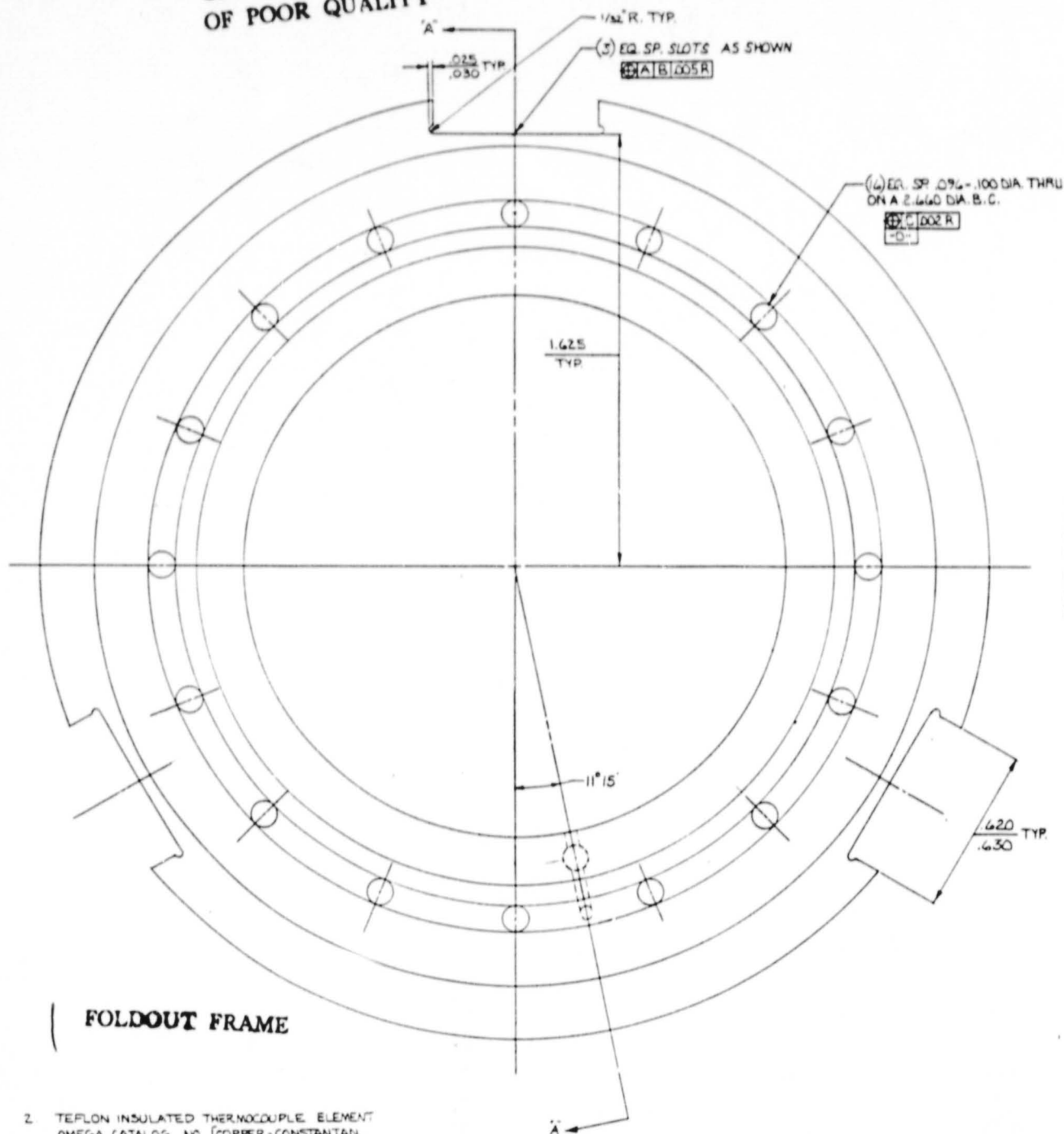
WELDOUT FRAME

9	6	SSCY7994-8	RETAINER	SSC	TYPE B-8
8	1	SSCY7994-7	EXTENSION SPRING	INCO	AMS 5043 AND 5044
7	1	SSCY7994-6	FACE SEAL	C-GPH	P-5N
6	1	SSCY7994-5	END PLATE	INCO	AMS 5043 AND 5044
5	1	SSCY7994-4	COMPRESSION SPRING	INCO	AMS 5043 AND 5044
4	9	SSCY5158-2	CIRCUM. SECONDARY SEAL	C-GPH	P-5N
3	1	SSCY7994-3	COMPRESSION SPRING	SSC	AISI 302
2	12	SSCY7994-2	FLANGE	INCO	AMS 5043 AND 5044
1	1	SSCY7994-1			

ITEM REQD PART NO DESCRIPTION MATL. MATL SPEC.

DO NOT SCALE UPON TO ONE SHOWN UNLESS OTHERWISE SHOWN		CONTACT NO.		STEIN SEAL COMPANY 704 STREET & INDIANA AVENUE, PHILADELPHIA, PA. 19132	
NATURAL AS NOTED OTHER SPECIFICATIONS		DATE: 1/18/83 BY: R.R. APPROVED: 1-28-83		TEST SEAL ASSEMBLY LOX SEAL-BALANCED 50 MM SIZE	
		DATE: 1-28-83		REV C	
		DATE: 1-28-83		D 03673 SSCY 7994	
		DATE: 1-28-83		SCALE 2/1 REFERENCE MT: 70000004	

ORIGINAL PAGE IS
OF POOR QUALITY



FOLDOUT FRAME

2. TEFLON INSULATED THERMOCOUPLE ELEMENT
OMEGA CATALOG NO. [COPPER-CONSTANTAN,
DUPLEX-ANSI TYPE T, TT-136, GAGE SOLID
WIRE .017 X .028] ALTERNATE CATALOG NO. STC-
TTT-36-36-STD. THERMOCOUPLE TO BE
CEMENTED TO FACE SEAL USING URALITE 3130 OR CRYOGENIC
EPOXY, AND RESET L-3203 G BY MTI.
1. FACE [A] TO BE FLAT W/IN (2) HELIUM LIGHT BANDS.

NOTES:

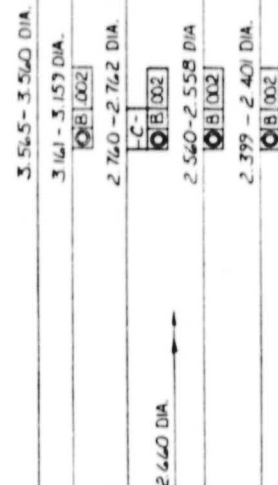
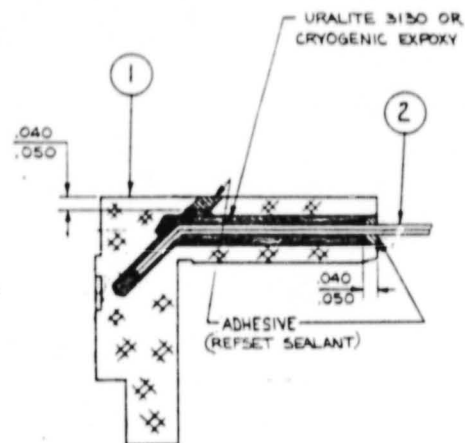


Fig. 5-2 50-mm Spiral-Groove Face

REVISIONS			
LTR	DESCRIPTION	DATE	APPROVED
A	RELEASED	1-27-83	
B	ADDED 16/	2-21-83	HF
C	MODIFIED THERMOCOUPLE LOCATION	3-10-83	HF
D	REMOVED 1/16" DIA. INTERSECTING HOLE; AND 1/16" DIA. HOLE WAS	5-18-83	HF
1/16" DIA. HOLE ON (1) 3/32" DIA. HOLE			

ORIGINAL PAGE 1

100% QUALITY



FACE SEAL SUB ASSY.
SSCY 7994-5

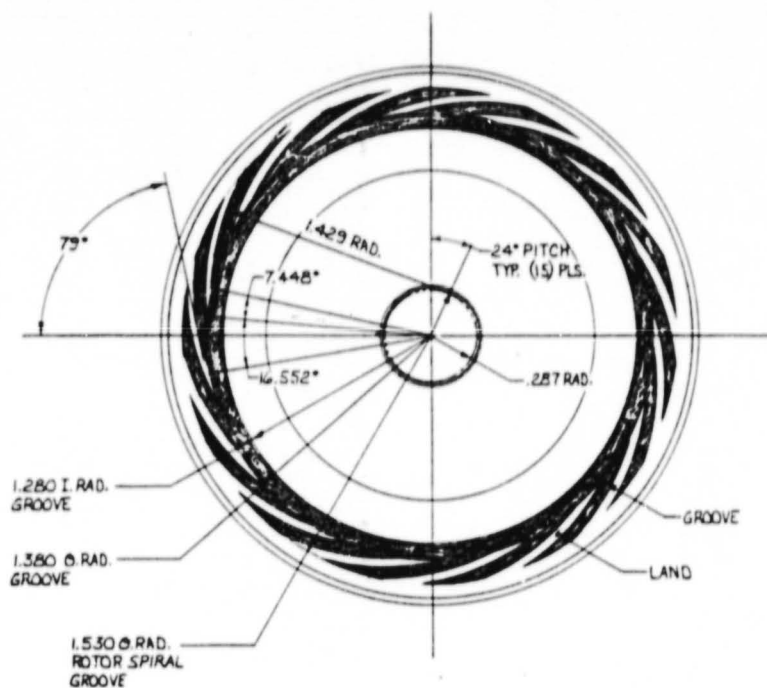
2 FOLDOUT FRAME

PRECEDING PAGE BLANK NOT FILMED

2	1	SSCY 7994-10	THERMOCOUPLE	SEE NOTE 2	
1	1	SSCY 7994-5A	FACE SEAL	C-GPH	P-5N
ITEM	QTY	PART NO.	DESCRIPTION	MATL.	MATL. SPEC.
LIST OF MATERIAL					

LIST OF MATERIAL

ALL DIM. SCALE UNLESS OTHERWISE SHOWN ALL ANGLES $\pm 2^\circ$		CONTRACT NO. DRAWN BY: M. L. LANE DATE: 1-24-83 CHECKED BY: R. R. H. DATE: 1-27-83 APPROVED BY: DATE:		STEIN SEAL COMPANY 20th STREET & INDIANA AVENUE, PHILADELPHIA, PA. 19122	
MATERIALS: AS NOTED OTHER SPECIFICATIONS:		FACE SEAL		DRAWING NO.: D 03673 SSCY 7994-5	
SCALE: 4/1		REV. 4/1		REV. D	

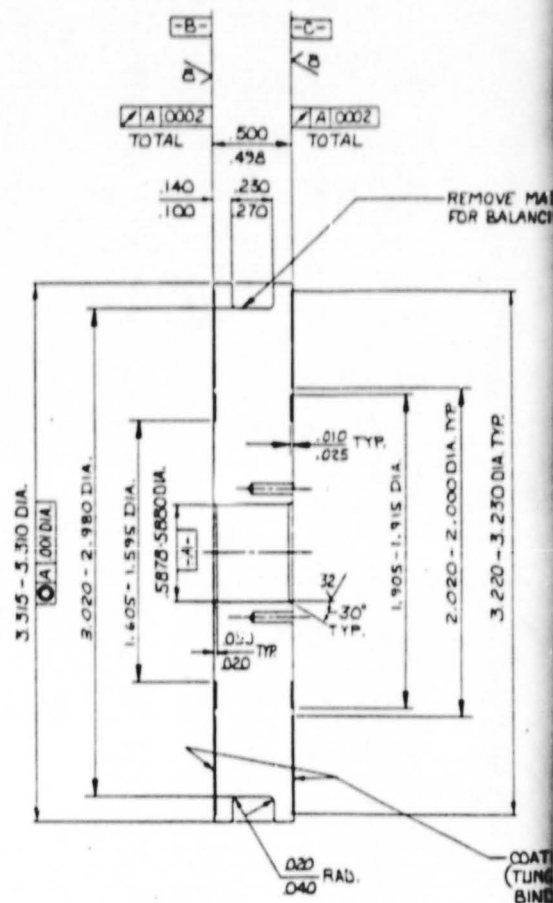


NO. OF GROOVES = 15
 GROOVE DEPTH = .008 - .010
 LAND WIDTH = .450
 GROOVE WIDTH

EOLDOUT FRAME

- 5) UNLESS OTHERWISE SPECIFIED ALL GROOVE DIMENSIONS & LOCATION DIMENSIONS TO BE TRUE POSITION TO DATUM -A- WITHIN .005 TOTAL.
- 4) BALANCE TO .0005 OZ. IN-REMOVE MAT'L IN AREA INDICATED .060 DP MAX. BLEND SMOOTH OVER 10°.
- 3) AFTER FINAL MACHINING SPIN TEST AT 65,000 RPM. VISUALLY INSPECT COATING FOR PROPER BOND AFTER SPIN TEST. MEASURE AND RECORD I.D. AND O.D. BEFORE & AFTER SPIN TEST. NO CHANGE PERMITTED.
- 2) FACES -B- AND -C- TO BE FLAT W/IN (2) HELIUM LIGHT BANDS.
- 1) STRESS RELIEVE AFTER ROUGH MACHINING. HEAT TREAT TO 150,000 PSI MIN. TENSILE (YIELD 0.2% OFFSET)

NOTES:

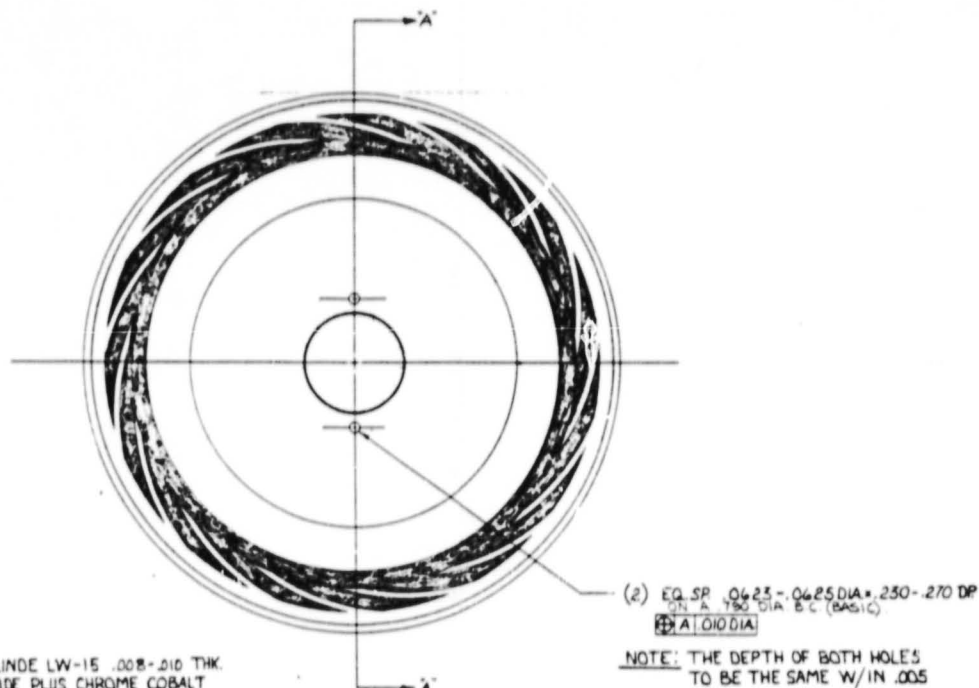
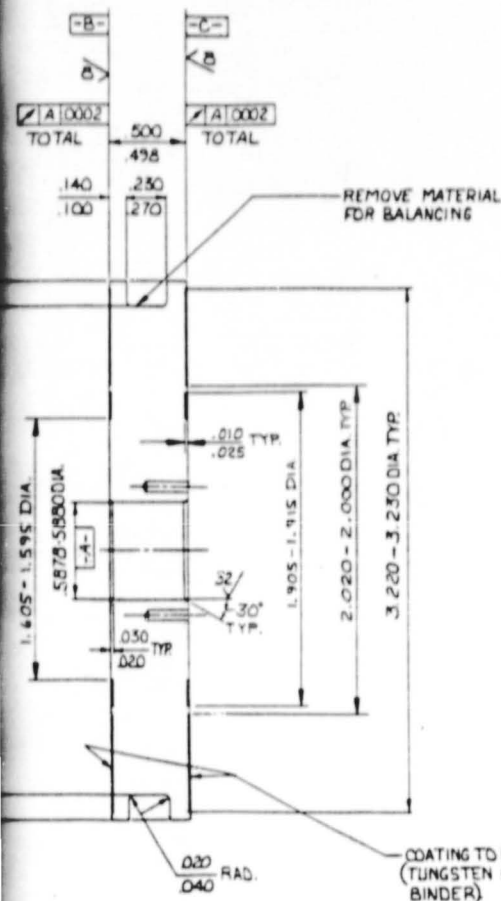


SECTION A-A

Fig. 5-3 50-mm Spiral-Groove Seal Ma

REVISIONS			
LT#	DESCRIPTION	DATE	APPROVED
A	RELEASED	1-27-83	
B	REVISED NOTE 3; 90° ALL OVER WAS 145°; ADDED NOTE 5.	2-21-83	HFF
C	ADDED: .010-.025 DEEP GROOVE (2) PLACES; .008-.010 THK. WAS .003-.007 THK.	7-1-83	ATR

ORIGINAL PAGE IS
OF POOR QUALITY



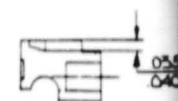
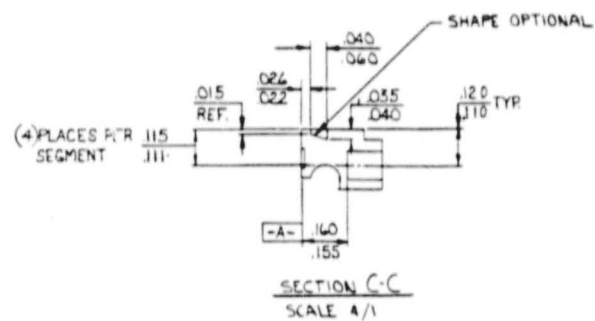
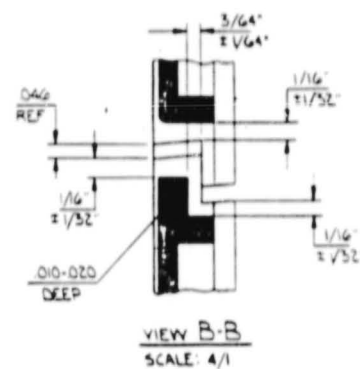
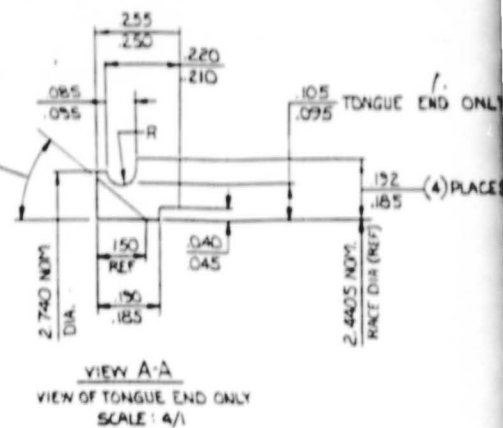
2 EOLDOUT FRAME

PRECEDING PAGE BLANK NOT FILMED

DO NOT SCALE, REFER TO DIM. SHEET		CONTRACT NO.		STEIN SEAL COMPANY 700 STREET & INDIANA AVENUE, PHILADELPHIA, PA. 19132	
UNLESS OTHERWISE SPECIFIED: G3/ ALL OVER BREAK EDGES .005-.005 ALL ANGLES 1:1 TO BE HELD W/IN .005 DIA. WITH RESPECT TO DIA. (A-A)		DATE: 1-13-83 REVIEW: 1-27-83 APPROVED: 1-27-83		MATING RING LOX SEAL-BALANCED 50MM SIZE	
MATERIAL: INCONEL 718 OTHER SPECIFICATIONS:		REF. M.T.I. DWG. NO. 7000024 FOR P2		D 03673 SSCY8133	
		SCALE: 2/1		REV: C	

FOLDOUT FRAME

MATE TONGUE & GROOVE EACH ADJOINING SEG.
MARK TO INSURE UNVARYING ASSEMBLY



SECTION E-E
SCALE: 4/1

Fig. 5-4 50-mm Spiral-Groove Secondary

ORIGINAL PAGE IS
OF POOR QUALITY

ANGULAR LOCATION
OF HOLES

FACE VIEW NOT TO SCALE

DO NOT SCALE WORK TO ONE DIMENSION UNLESS OTHERWISE SHOWN		CONTRACT NO.		STEIN SEAL COMPANY 709 STREET & BELLEVUE AVENUE PHILADELPHIA PA. 19122			
		DESIGN	N/LANE	CIRCUMFERENTIAL SEAL RING			
		DATE	1-25-83				
		CHECKED	R/R/K				
		DATE	1-28-83				
		APPROVED					
		SITE					
INTERNAL: C-GPH GR P-SN UNDER SUPERVISION				BAT D	OUR IDENT NO. 03673	DRAWING NO. SSCY7994-3	REV A
				SCALE 4"/1"	NOTES SEE T&E 709.DG.24		

ORIGINAL PAGE IS
OF POOR QUALITY

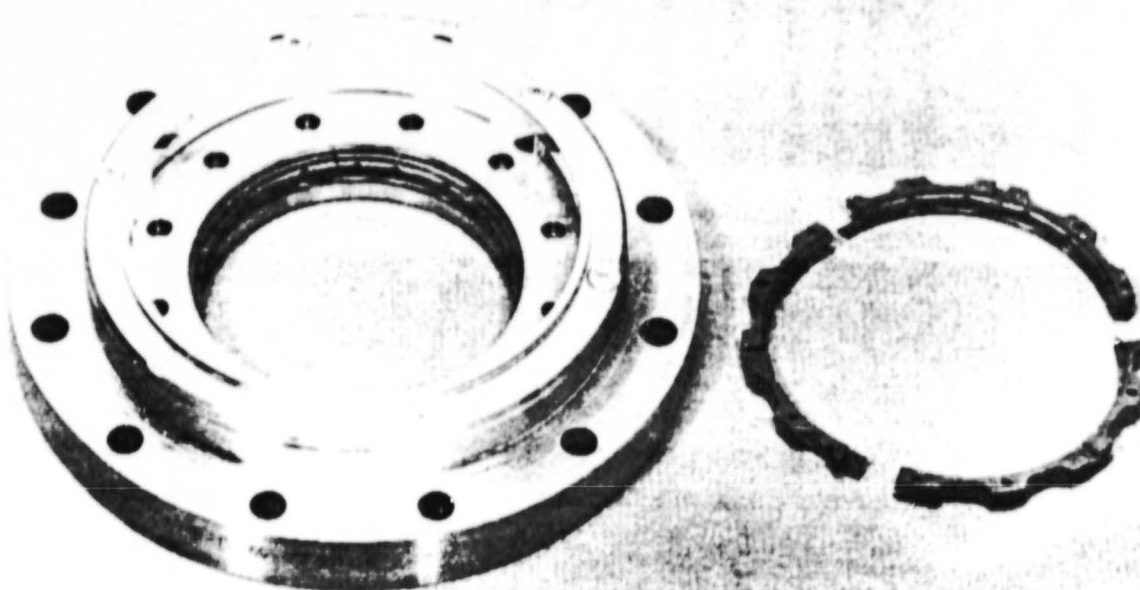


Fig. 5-5 Split Spiral-Groove Secondary Seal

PRECEDING PAGE BLANK NOT FILMED

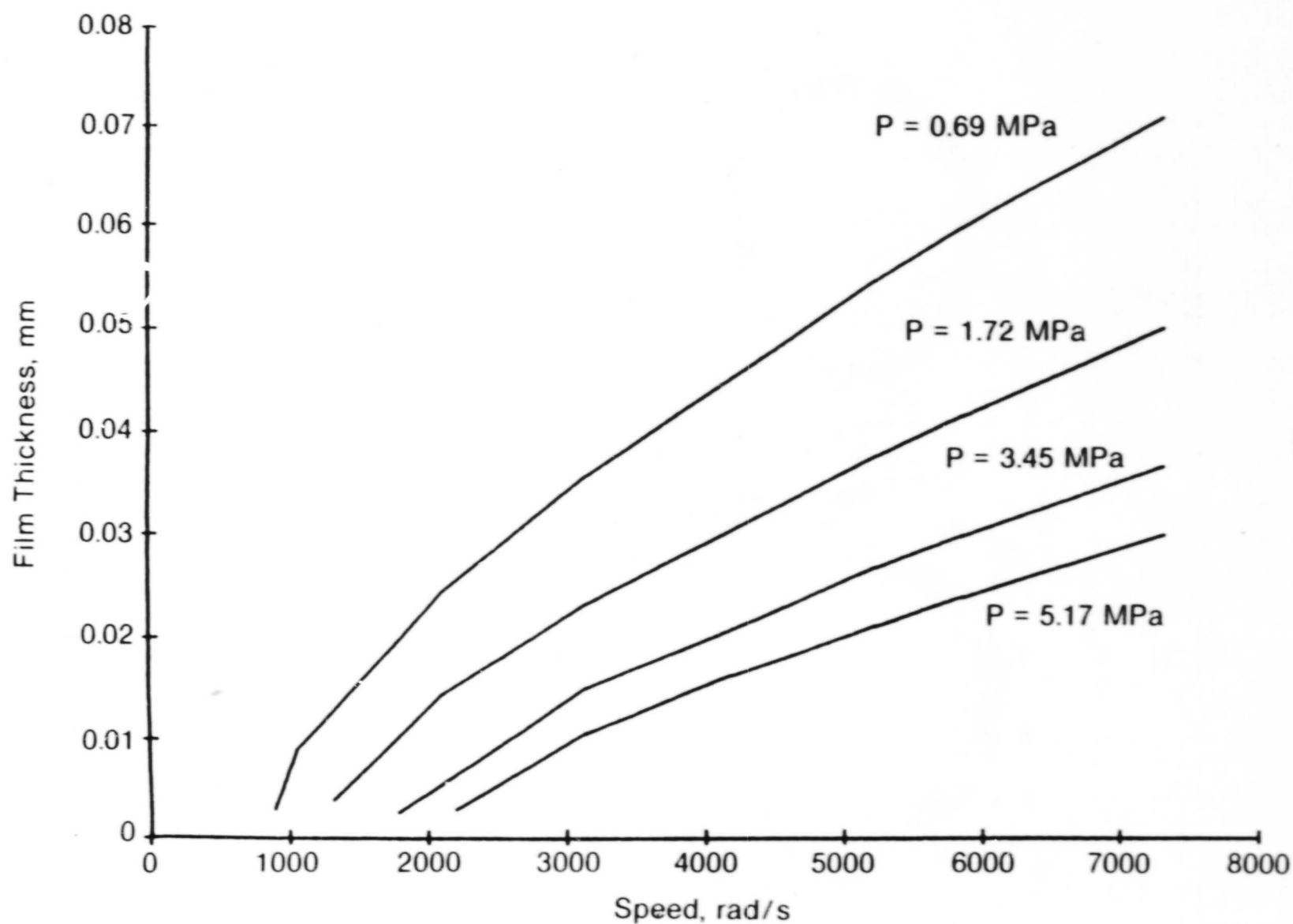


Fig. 5-6 50-mm Spiral-Groove Seal; Film Thickness Versus Speed and Pressure

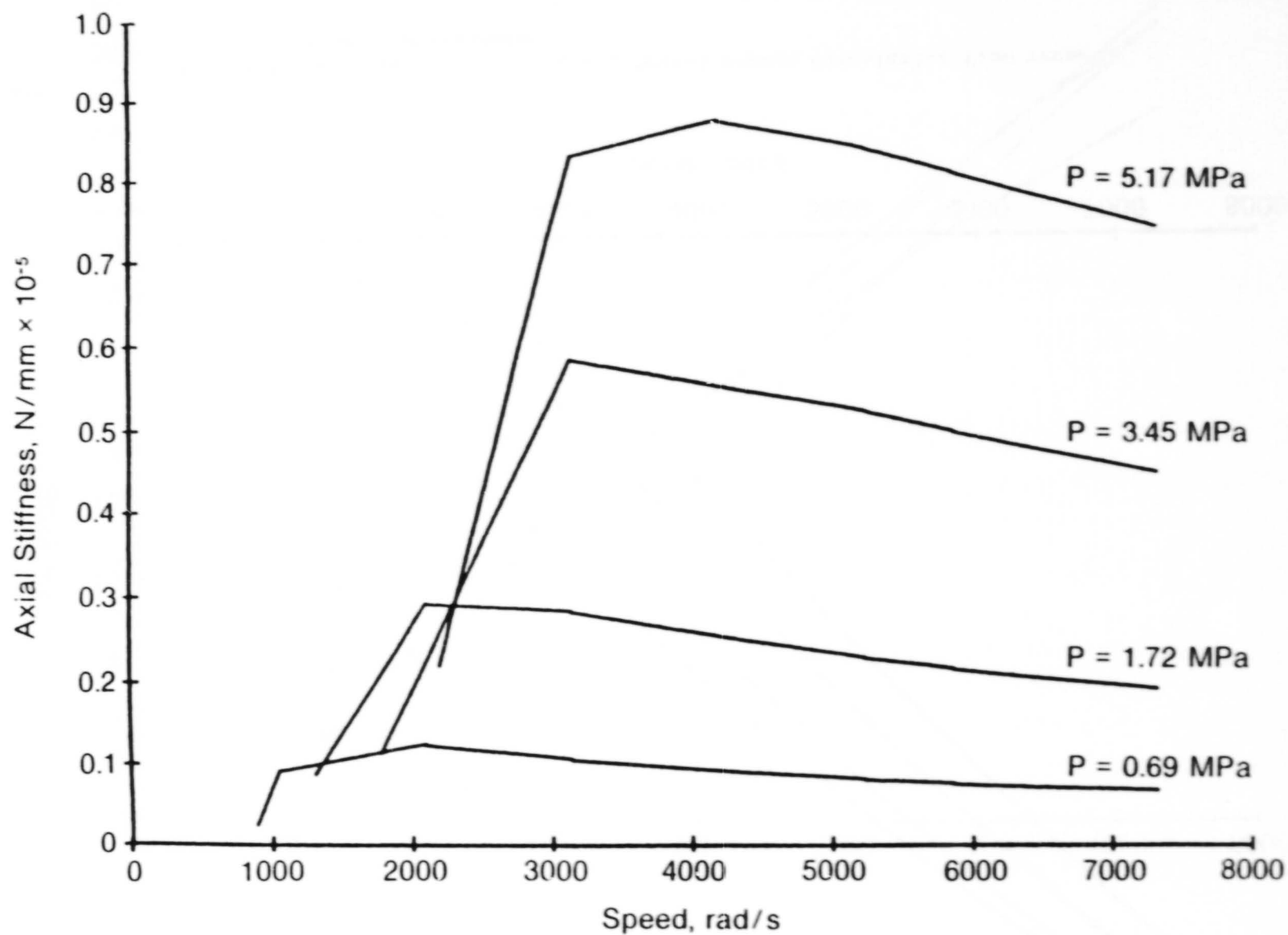
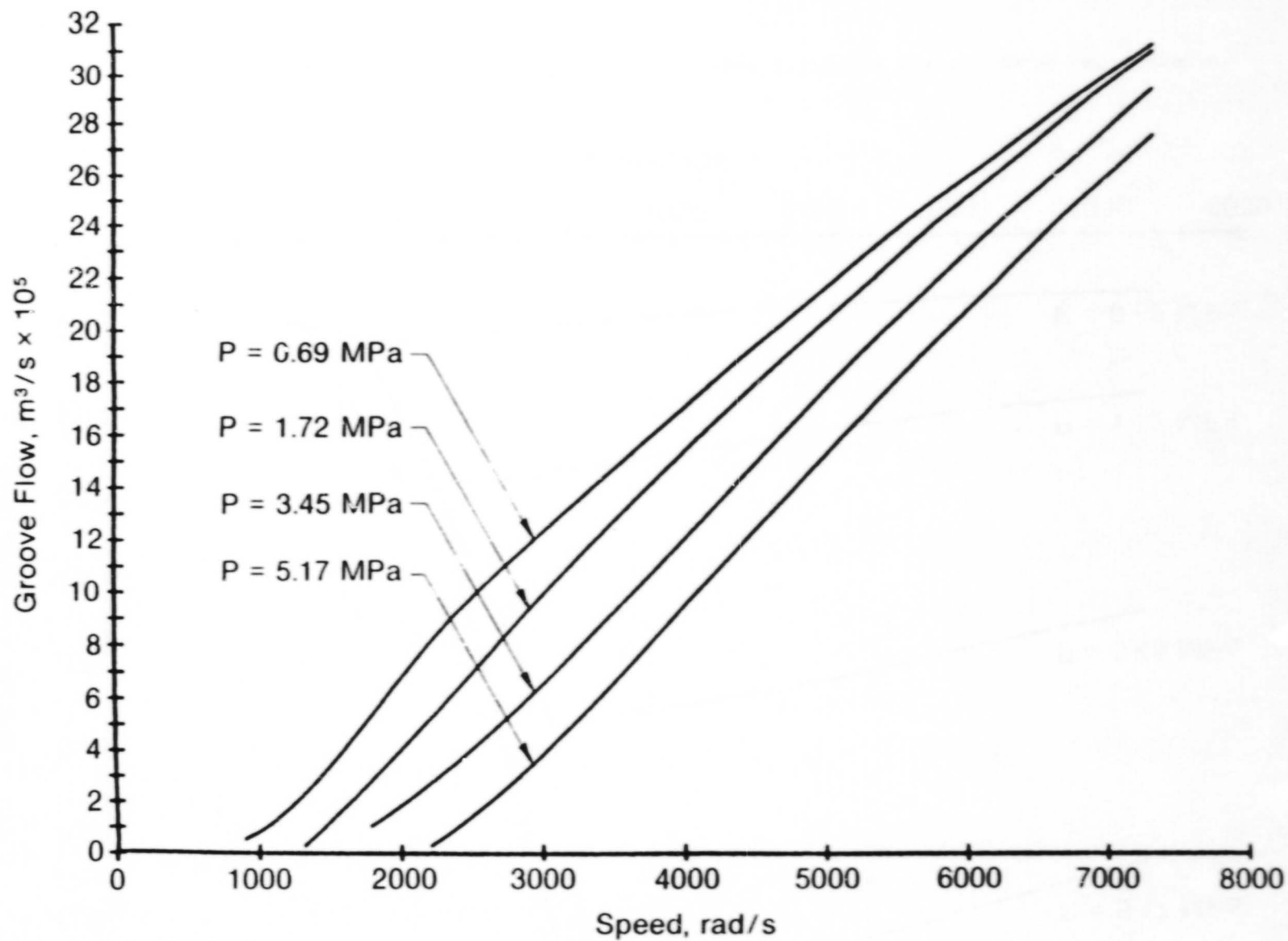


Fig. 5-7 50-mm Spiral-Groove Seal; Axial Stiffness Versus Speed and Pressure



83612

Fig. 5-8 50-mm Spiral-Groove Seal; Spiral Groove Circulating Flow Versus Speed and Pressure

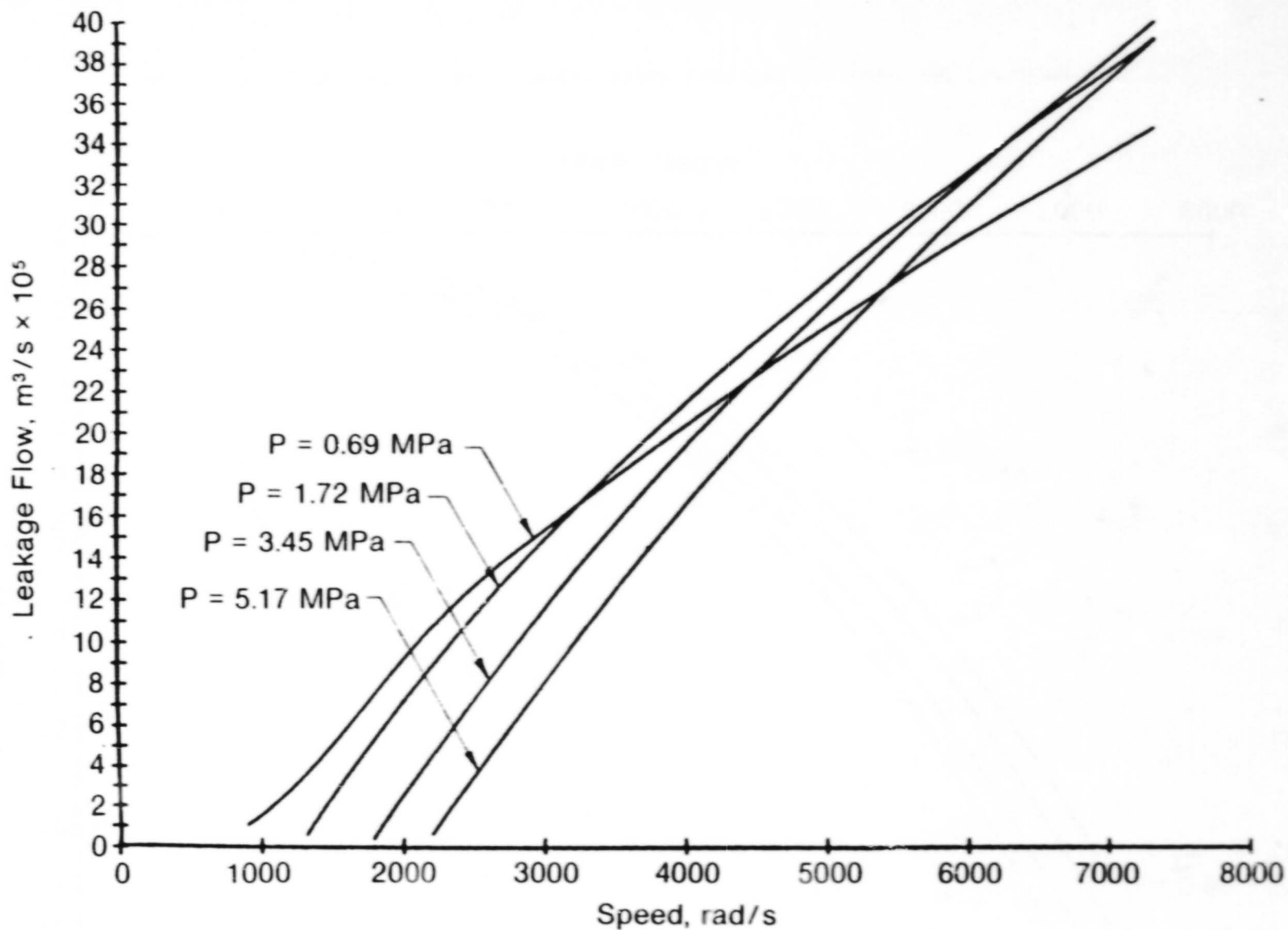


Fig. 5-9 50-mm Spiral-Groove Seal; Leakage Flow Versus Speed and Pressure

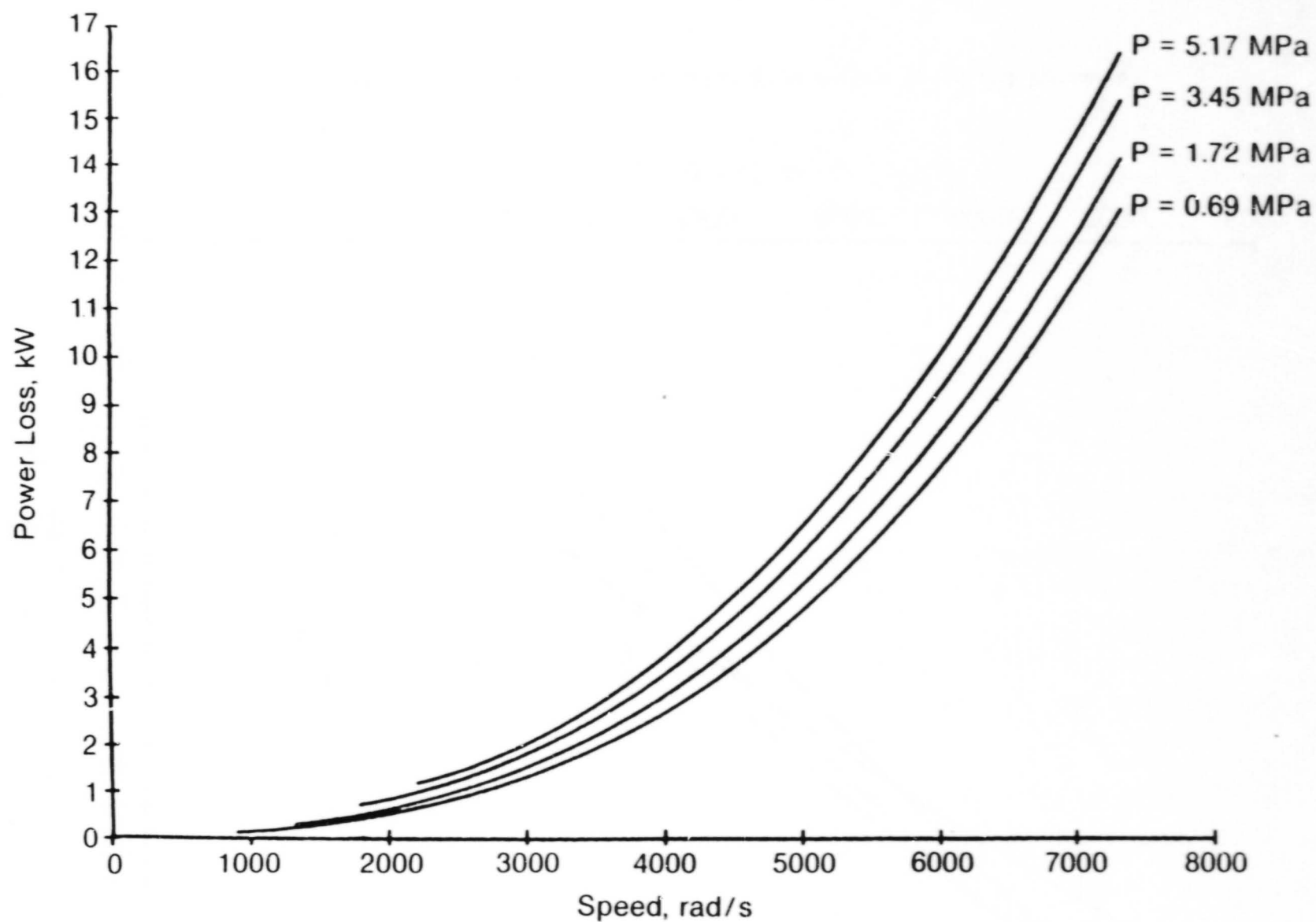
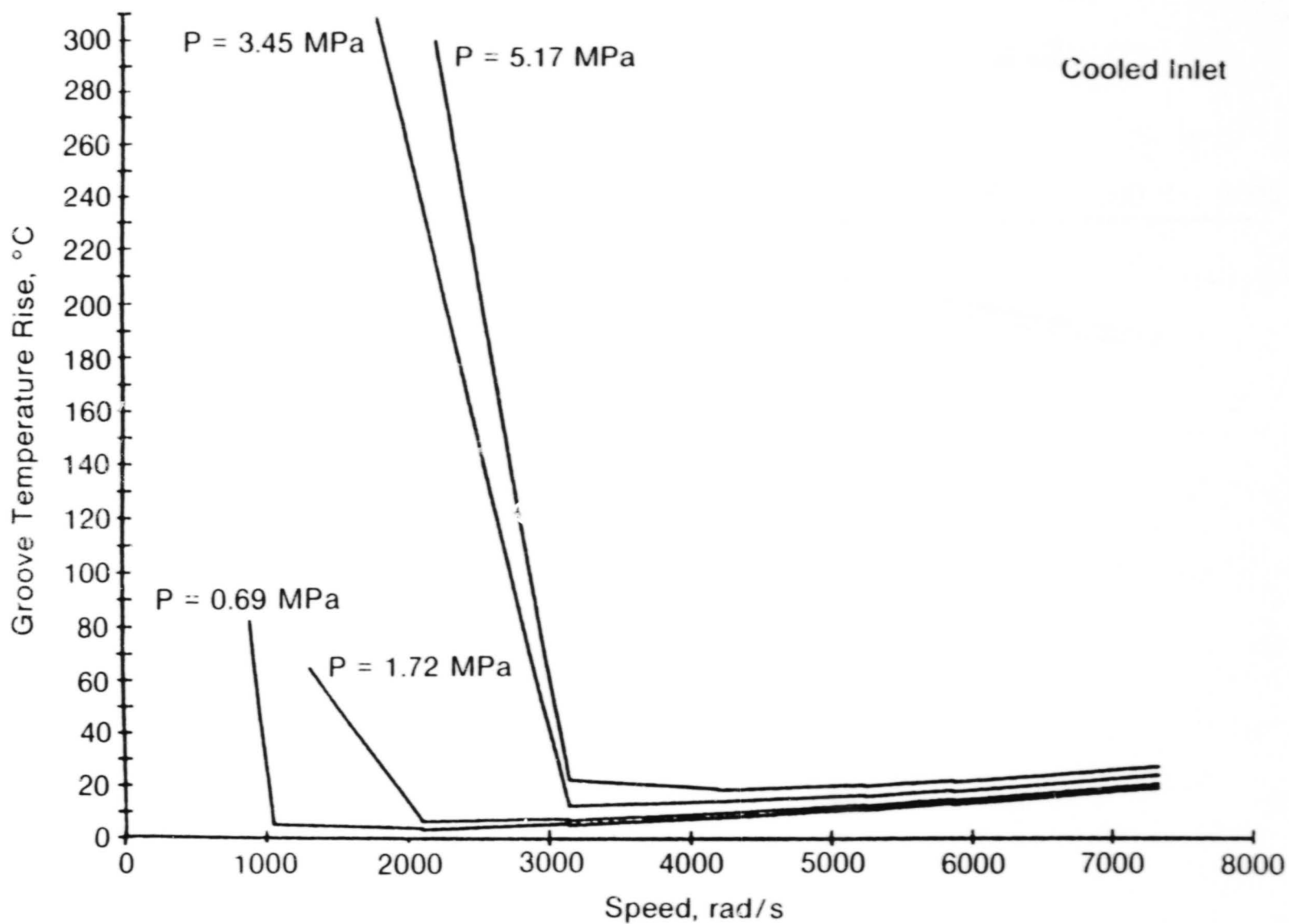


Fig. 5-10 50-mm Spiral-Groove Seal; Power Loss Versus Speed and Pressure



33615

Fig. 5-11 50-mm Spiral Groove Seal; Spiral-Groove Temperature Rise Versus Speed and Pressure

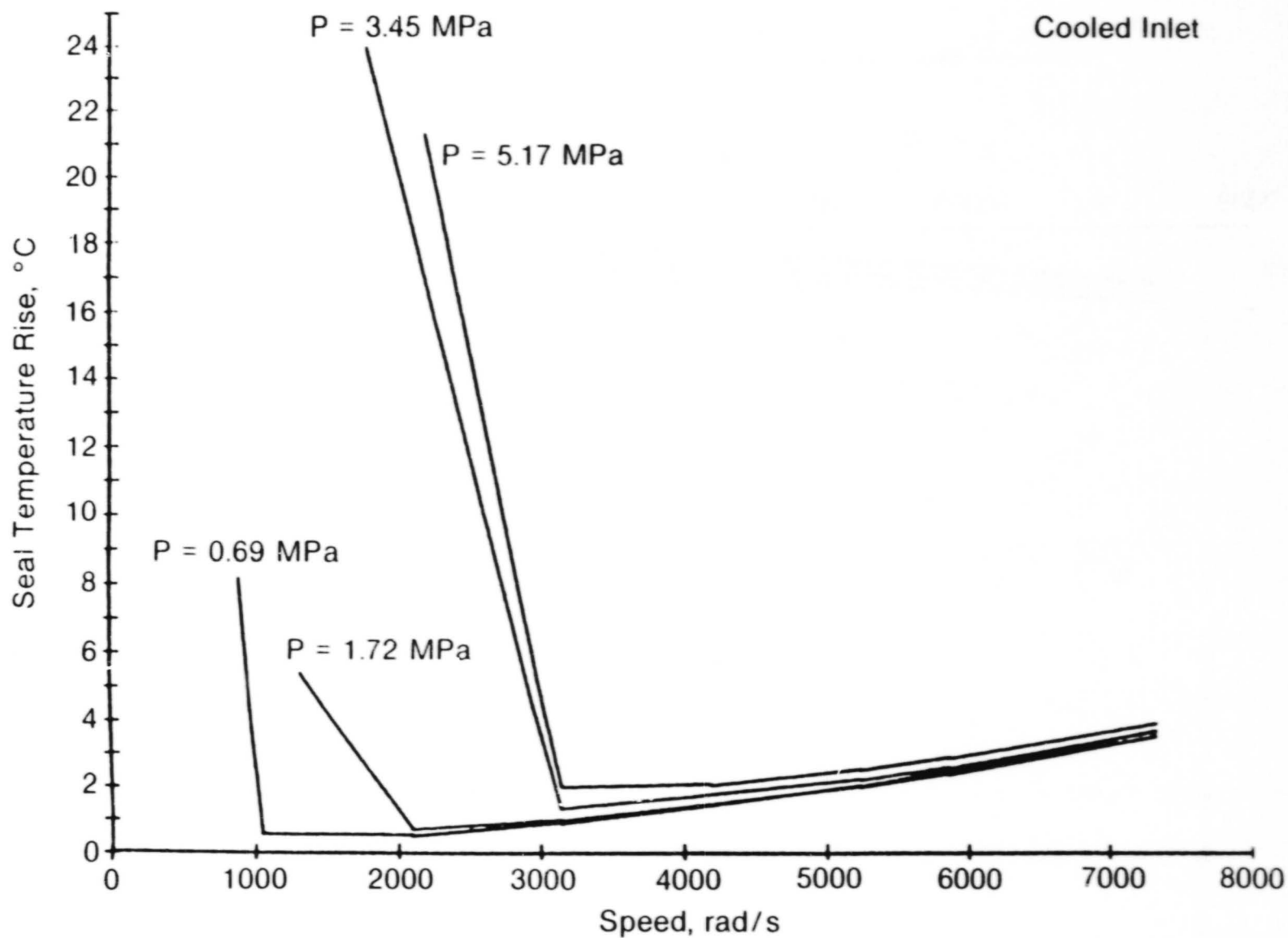
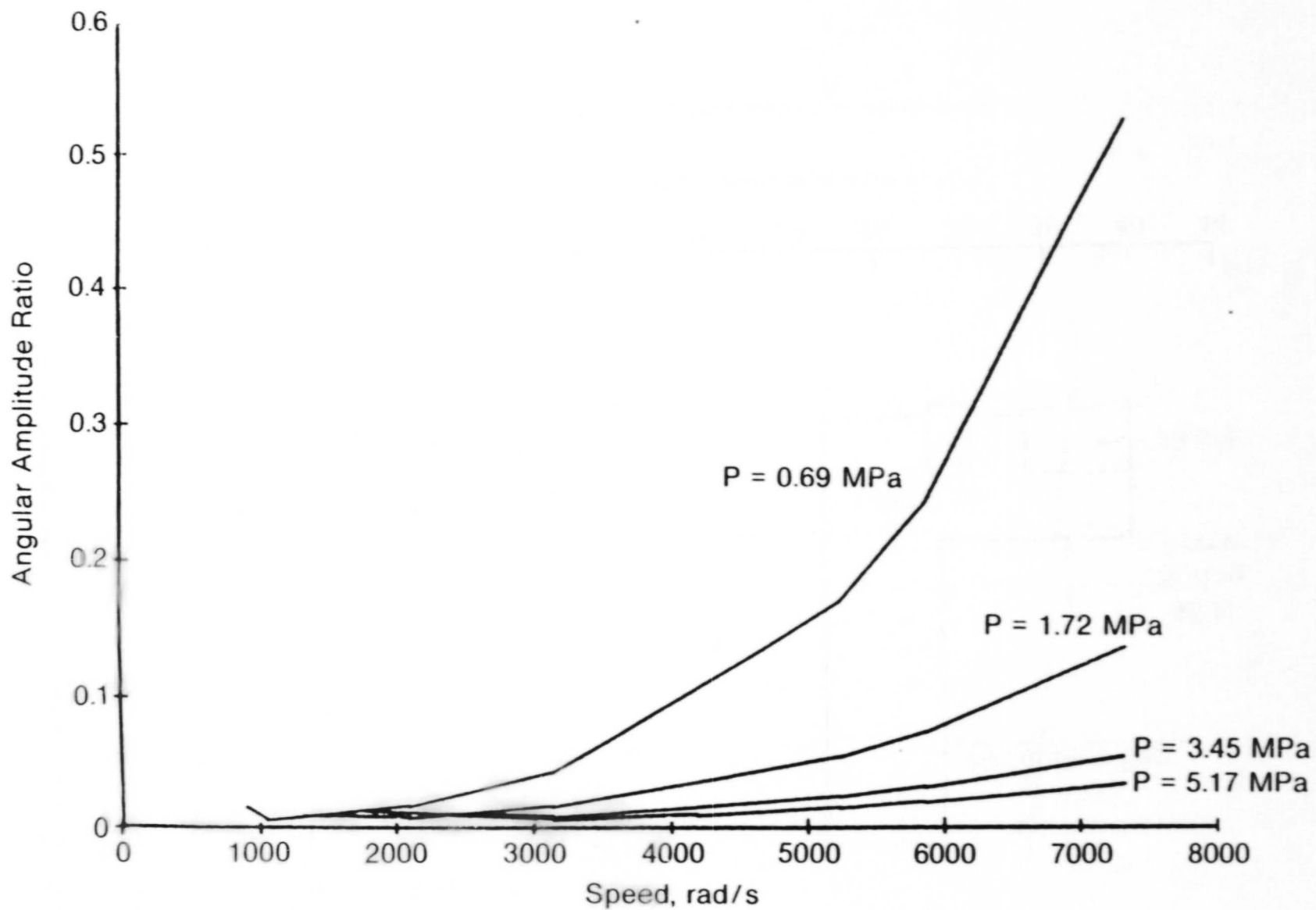
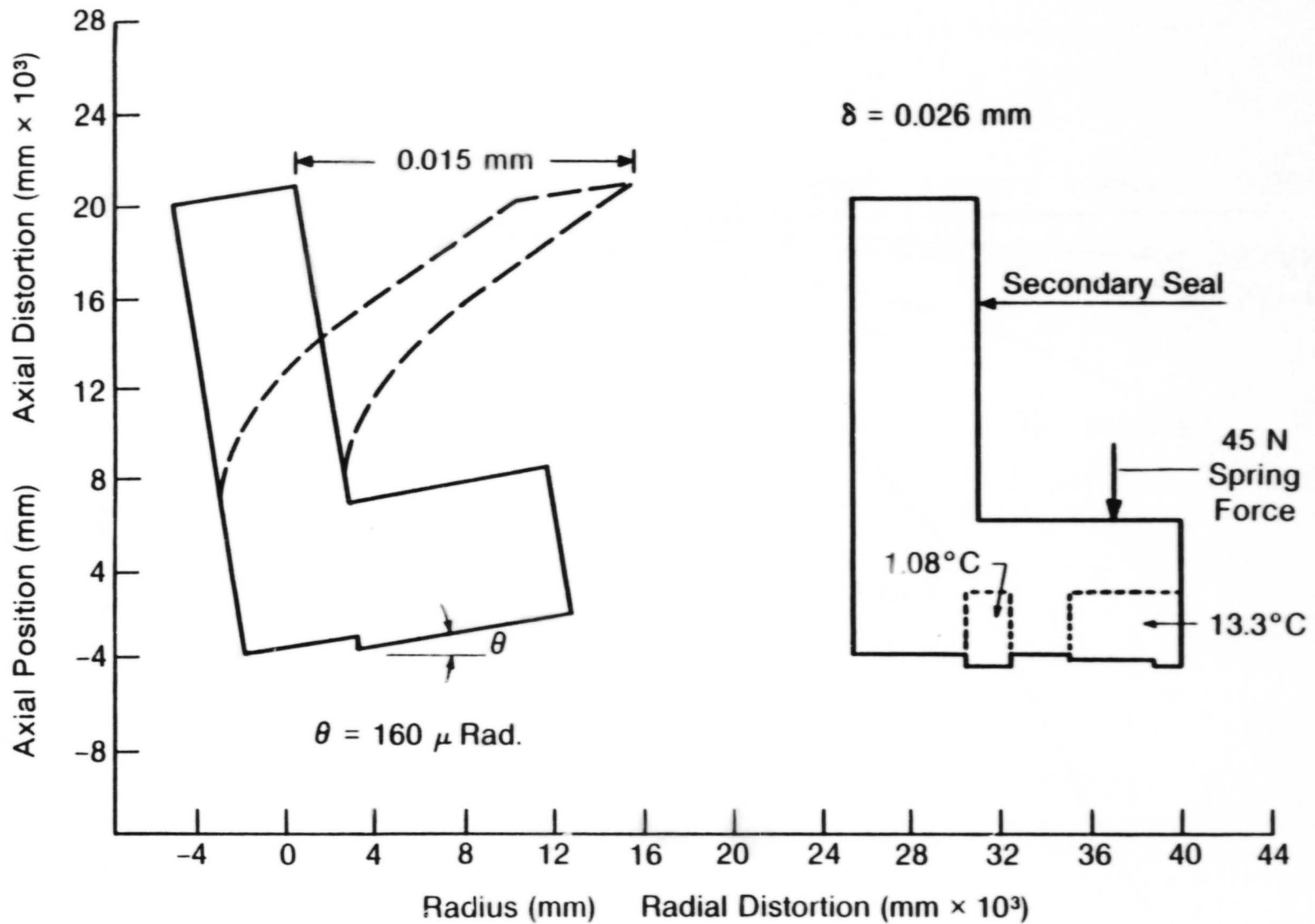


Fig. 5-12 50-mm Spiral-Groove Seal; Temperature Rise Versus Speed and Pressure



83619

Fig. 5-13 50-mm Spiral-Groove Seal; Angular Amplitude Ratio Versus Speed and Pressure



83113

Fig. 5-14 50-mm Spiral-Groove Seal; Thermoelastic Distortion

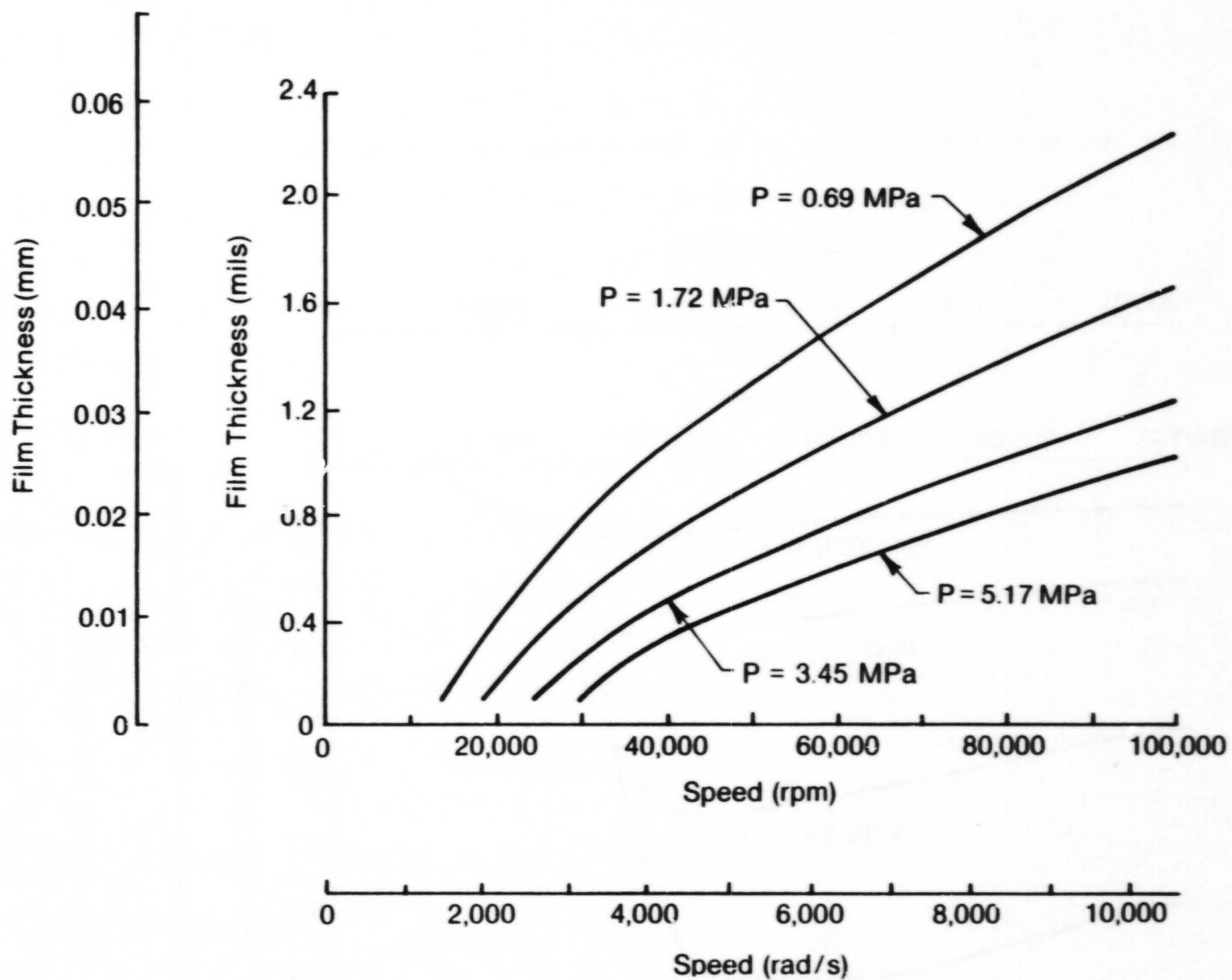


Fig. 5-15 20-mm Spiral Groove Seal; Film Thickness versus Speed

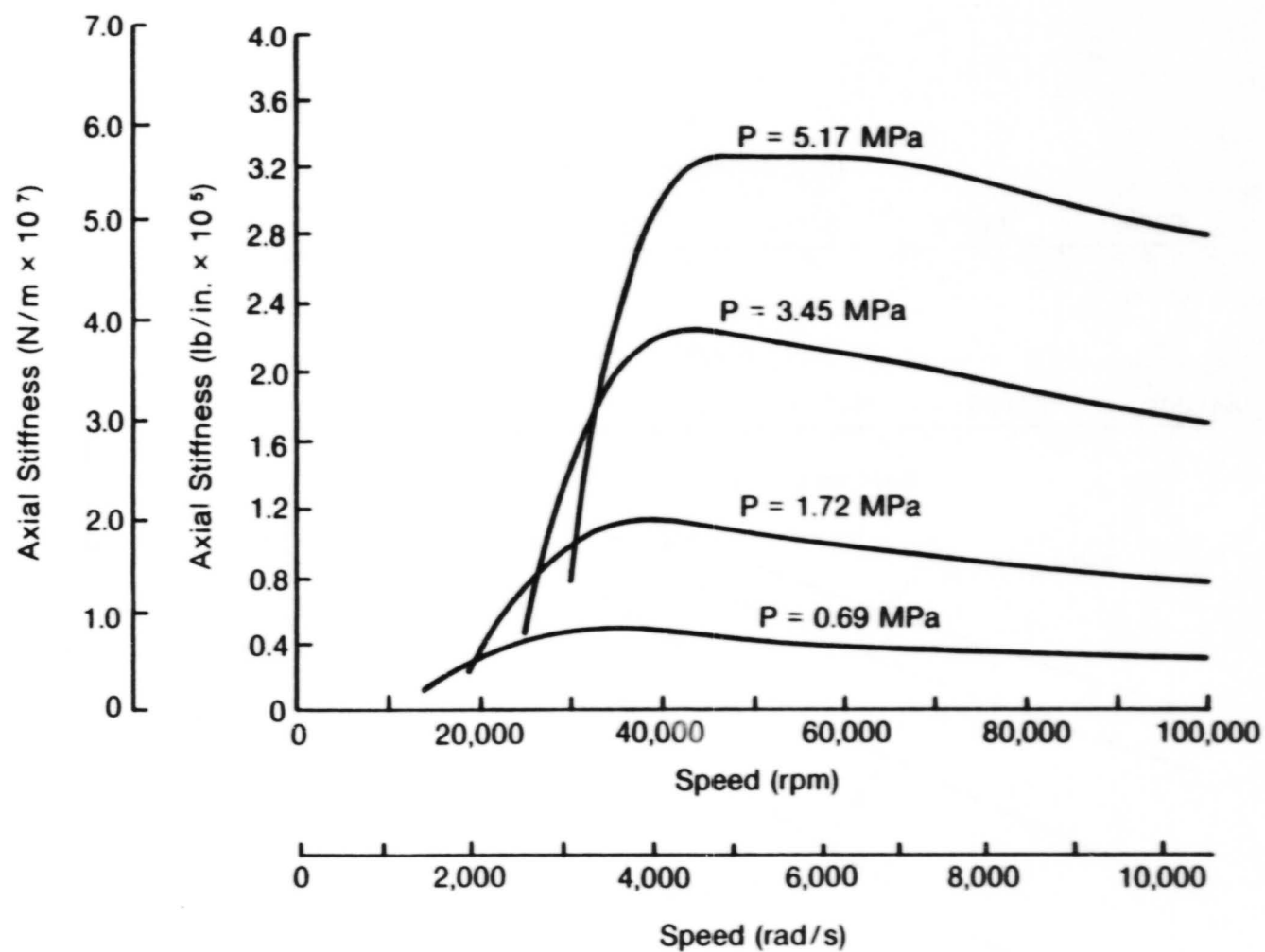


Fig. 5-16 20-mm Spiral Groove Seal; Axial Stiffness versus Speed

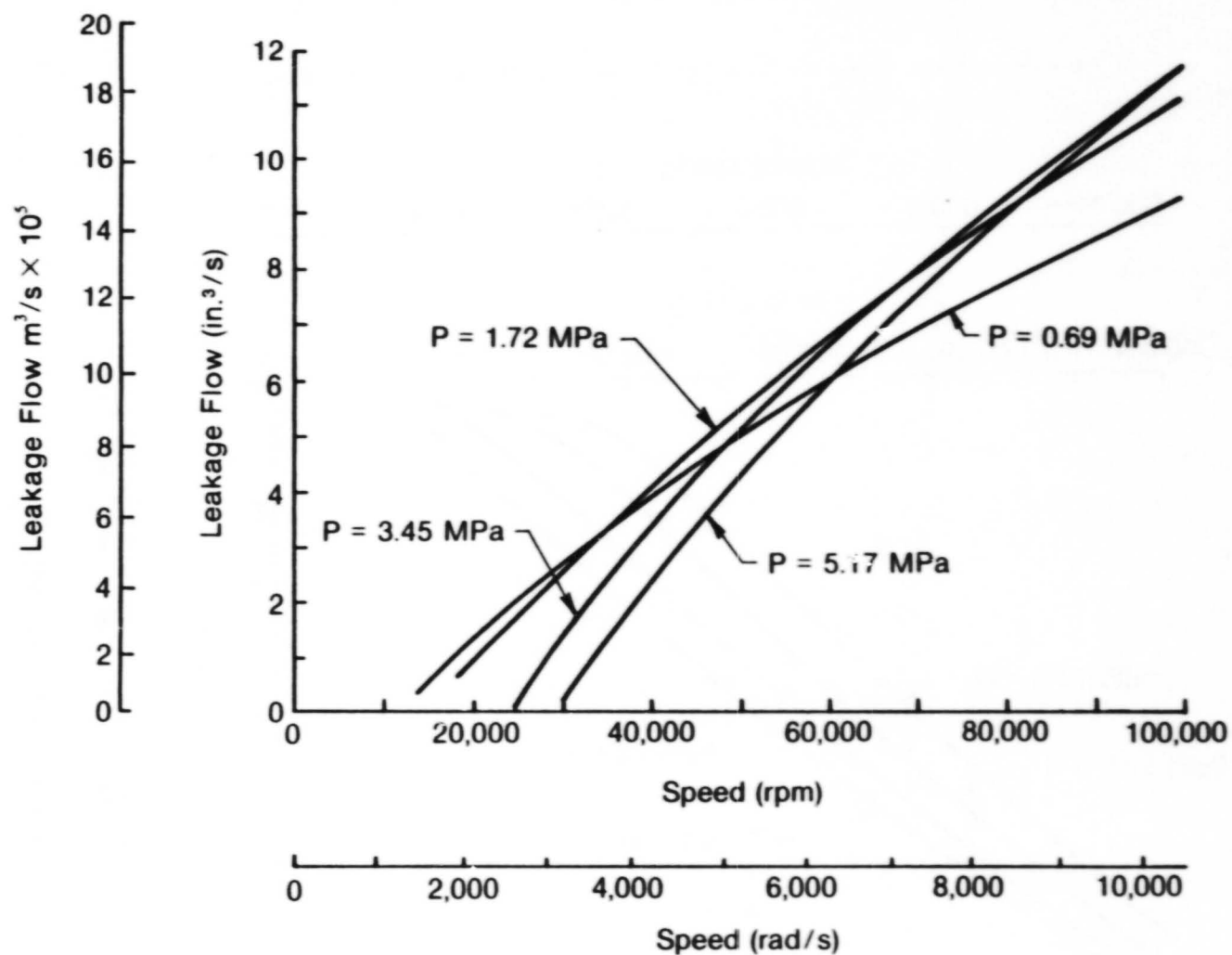


Fig. 5-17 20-mm Spiral Groove Seal; Leakage Flow versus Speed

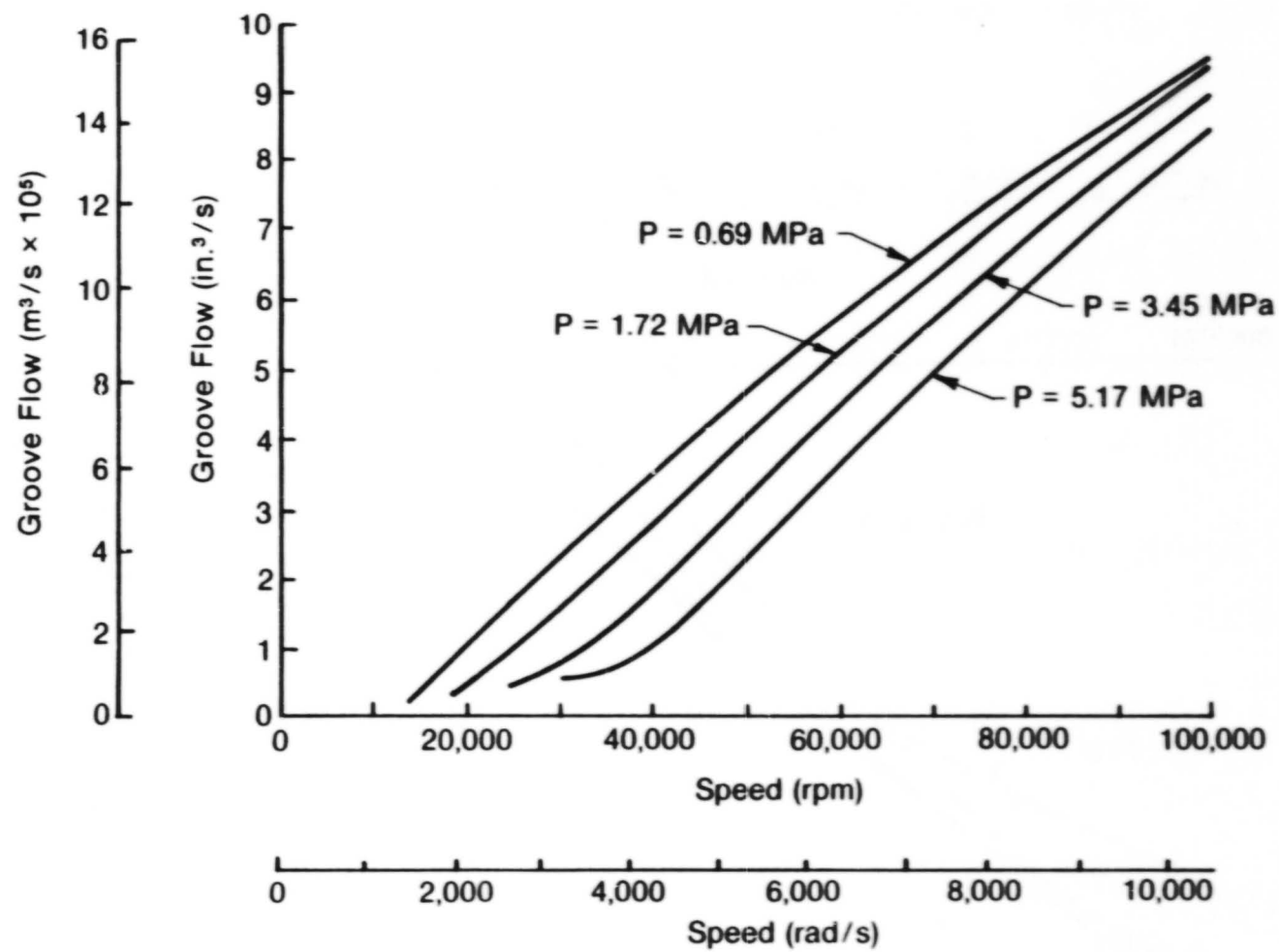


Fig. 5-18 20-mm Spiral Groove Seal, Groove Flow versus Speed

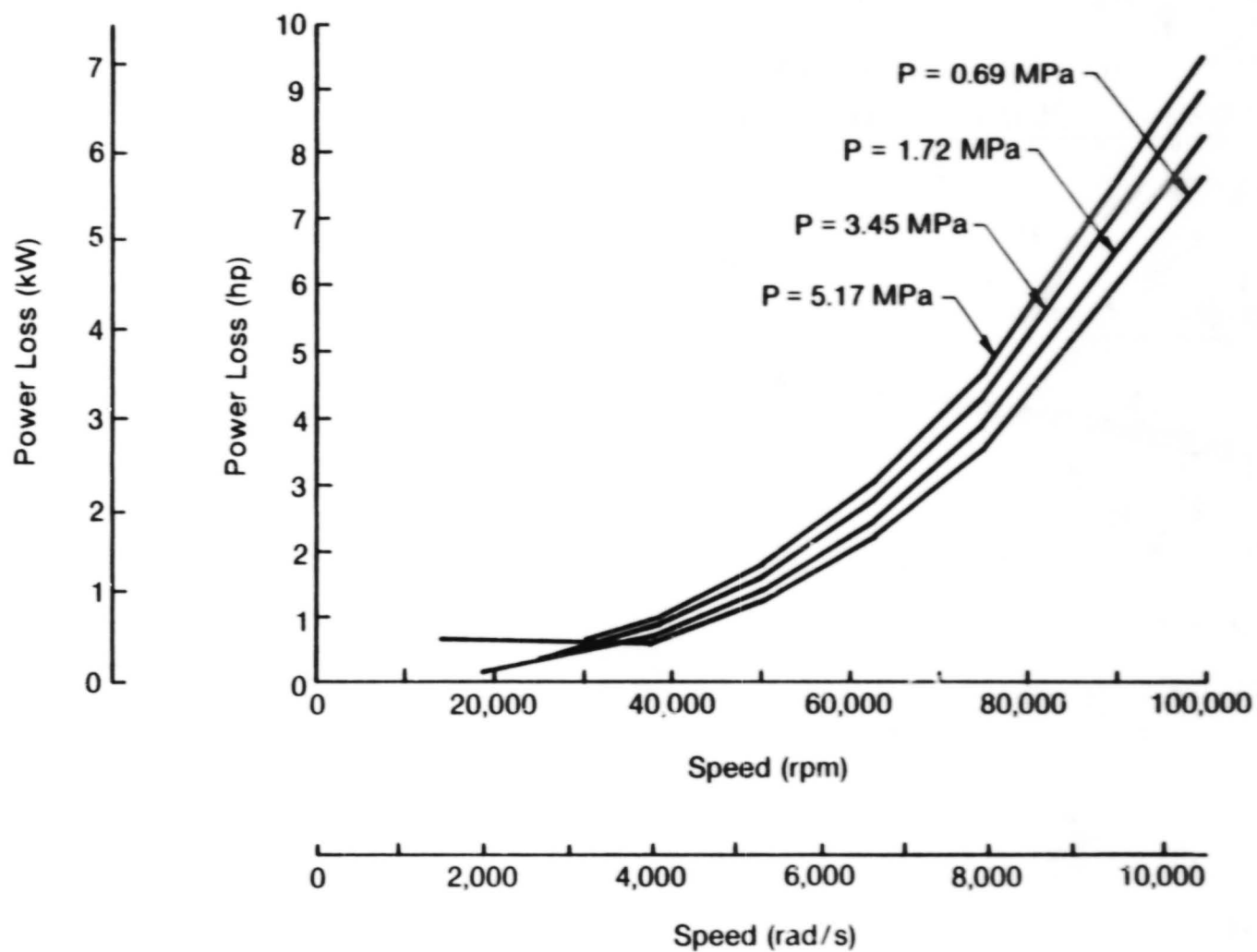


Fig. 5-19 20-mm Spiral Groove Seal; Power Loss versus Speed

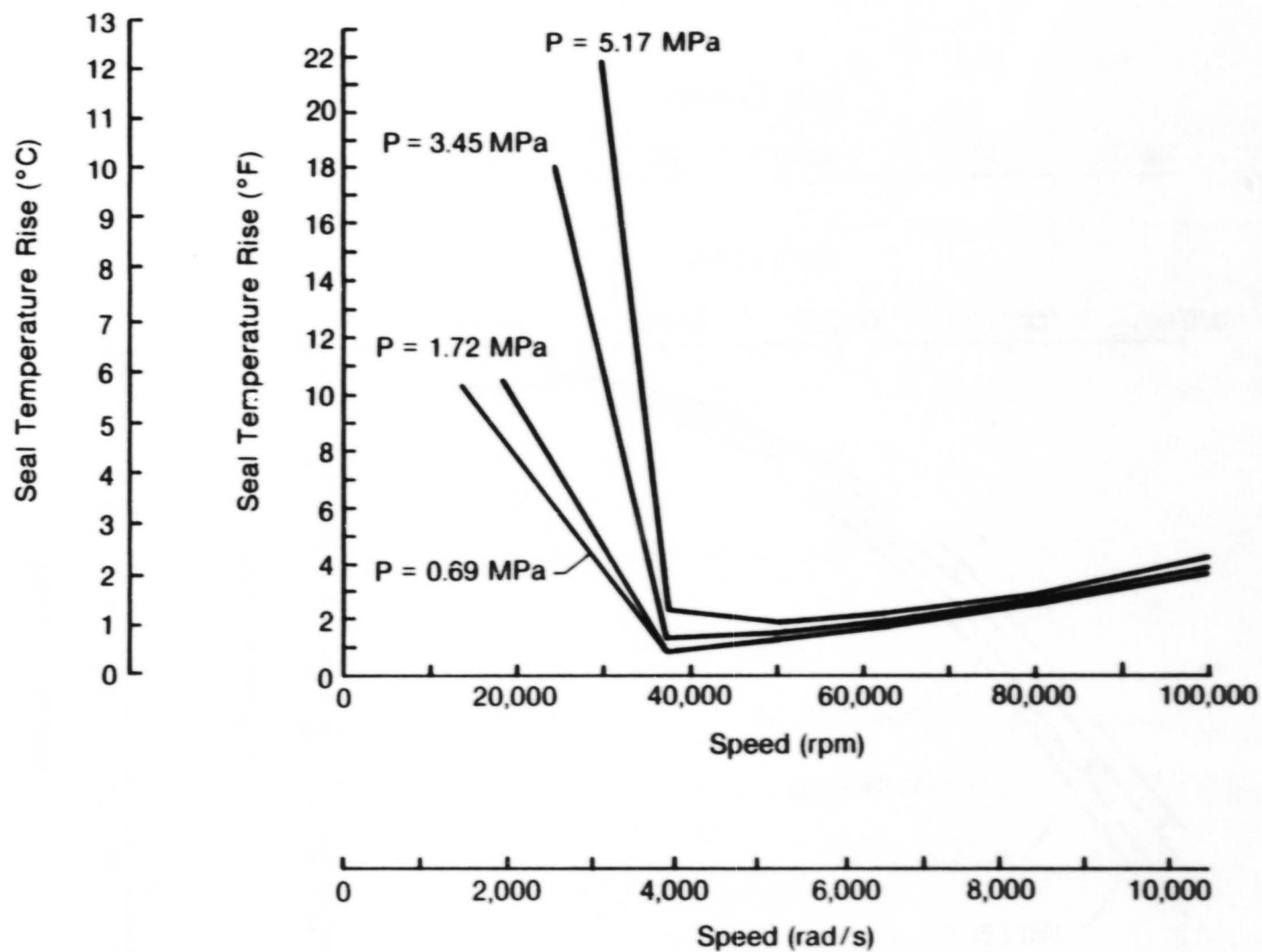


Fig. 5-20 20-mm Spiral Groove Seal; Seal Temperature Rise versus Speed

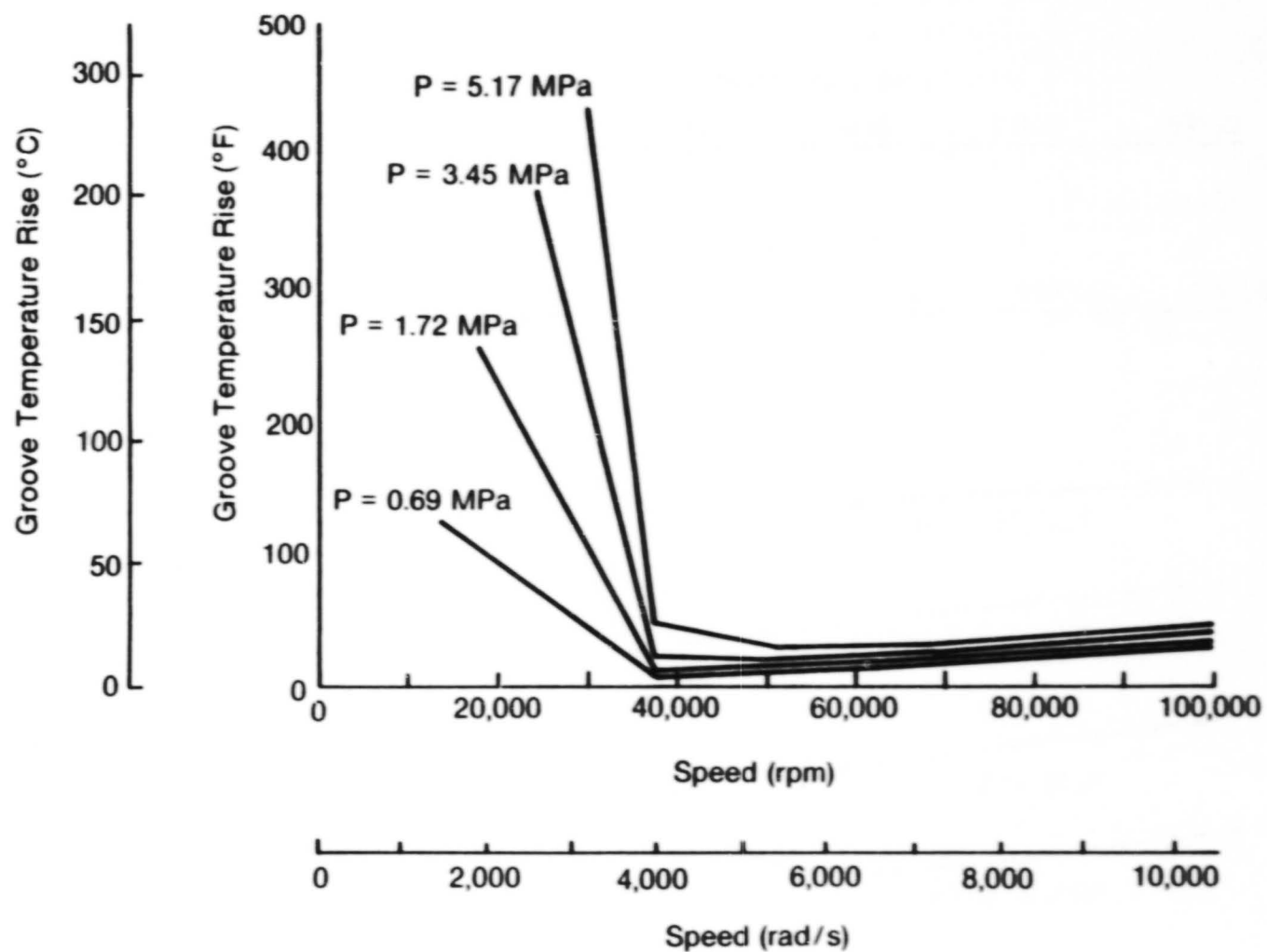


Fig. 5-21 20-mm Spiral Groove Seal; Seal Temperature Rise versus Speed

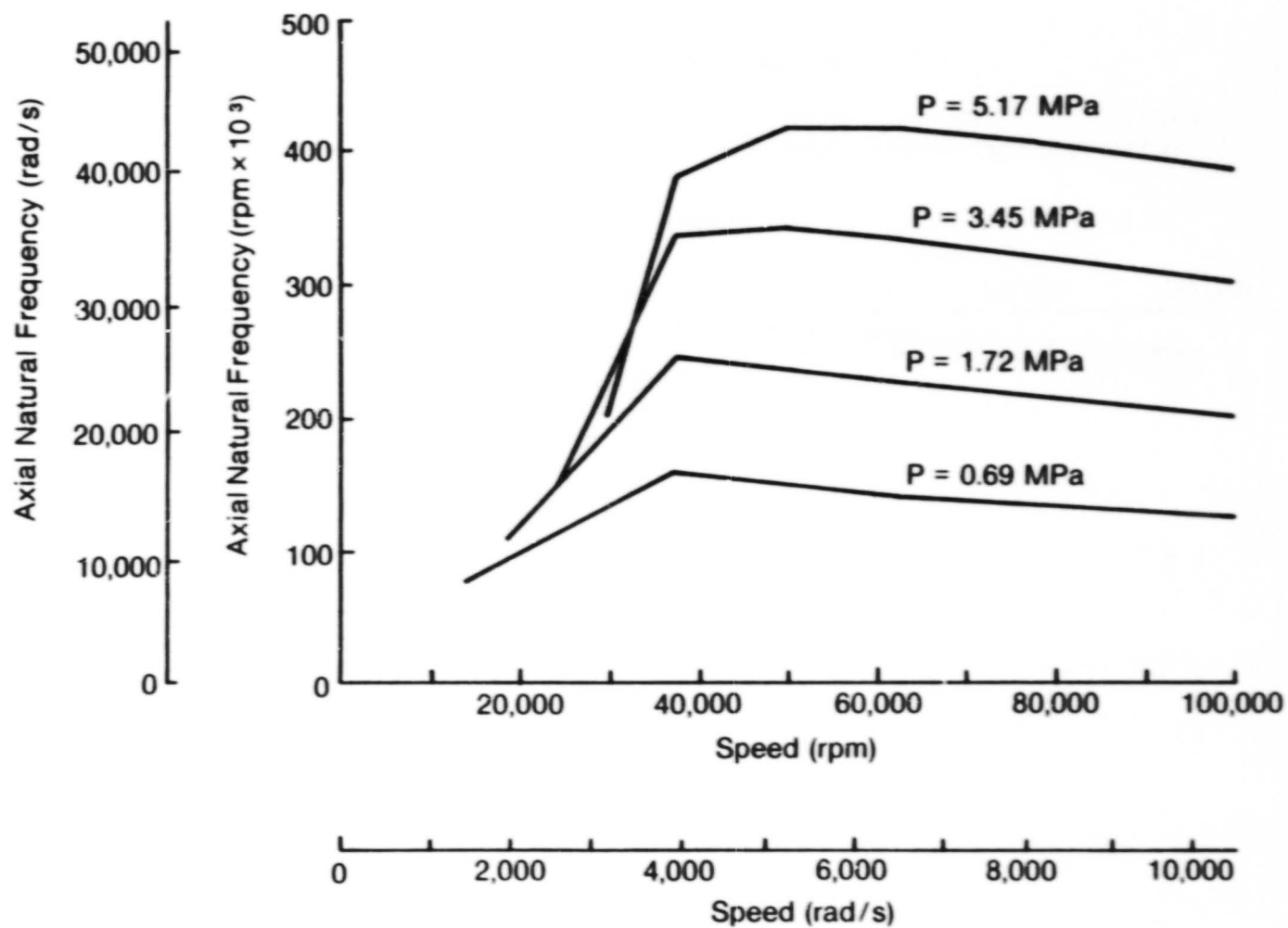


Fig. 5-22 20-mm Spiral Groove Seal; Axial Natural Frequency versus Speed

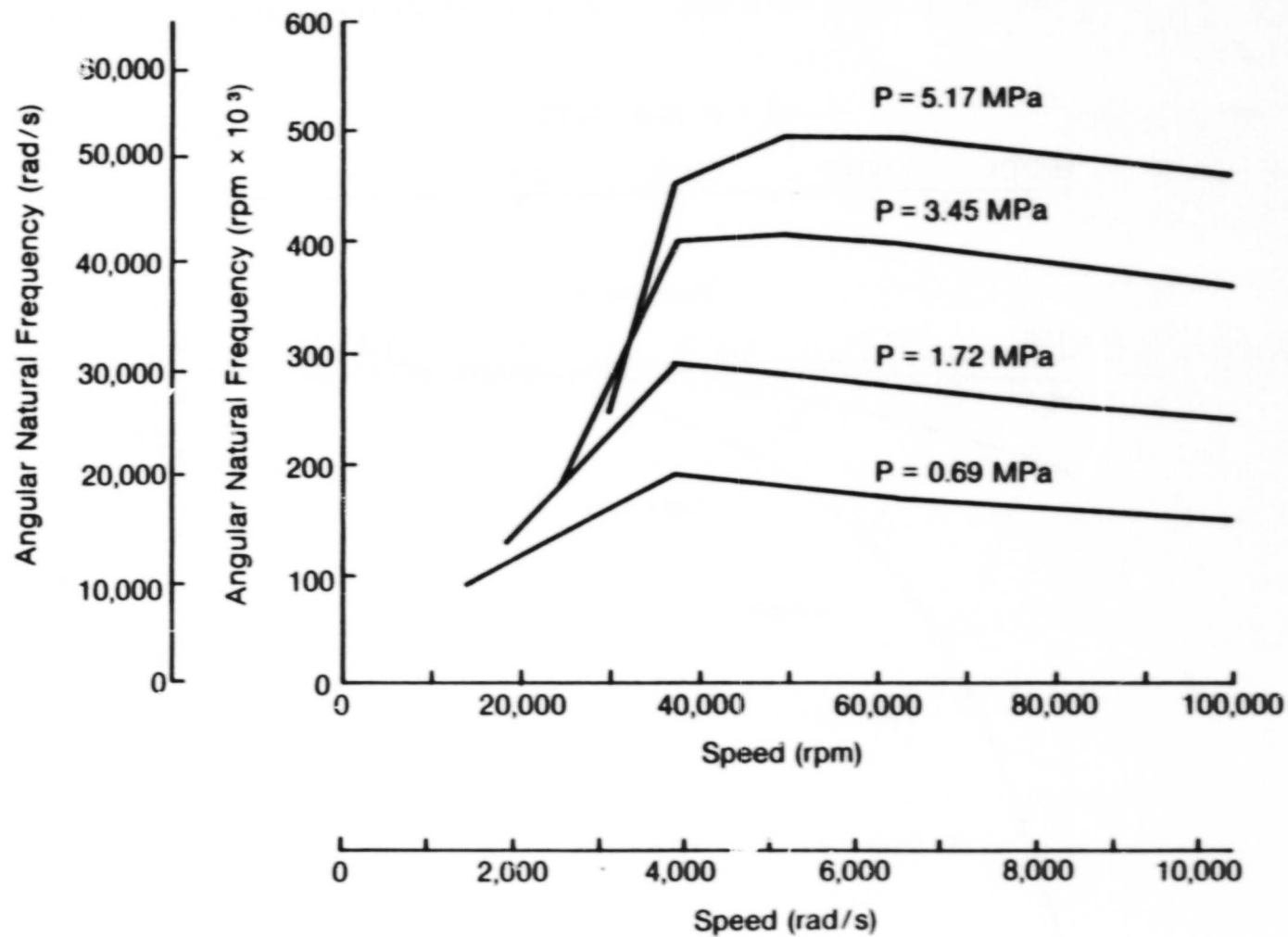


Fig. 5-23 20-mm Spiral Groove Seal; Angular Natural Frequency versus Speed

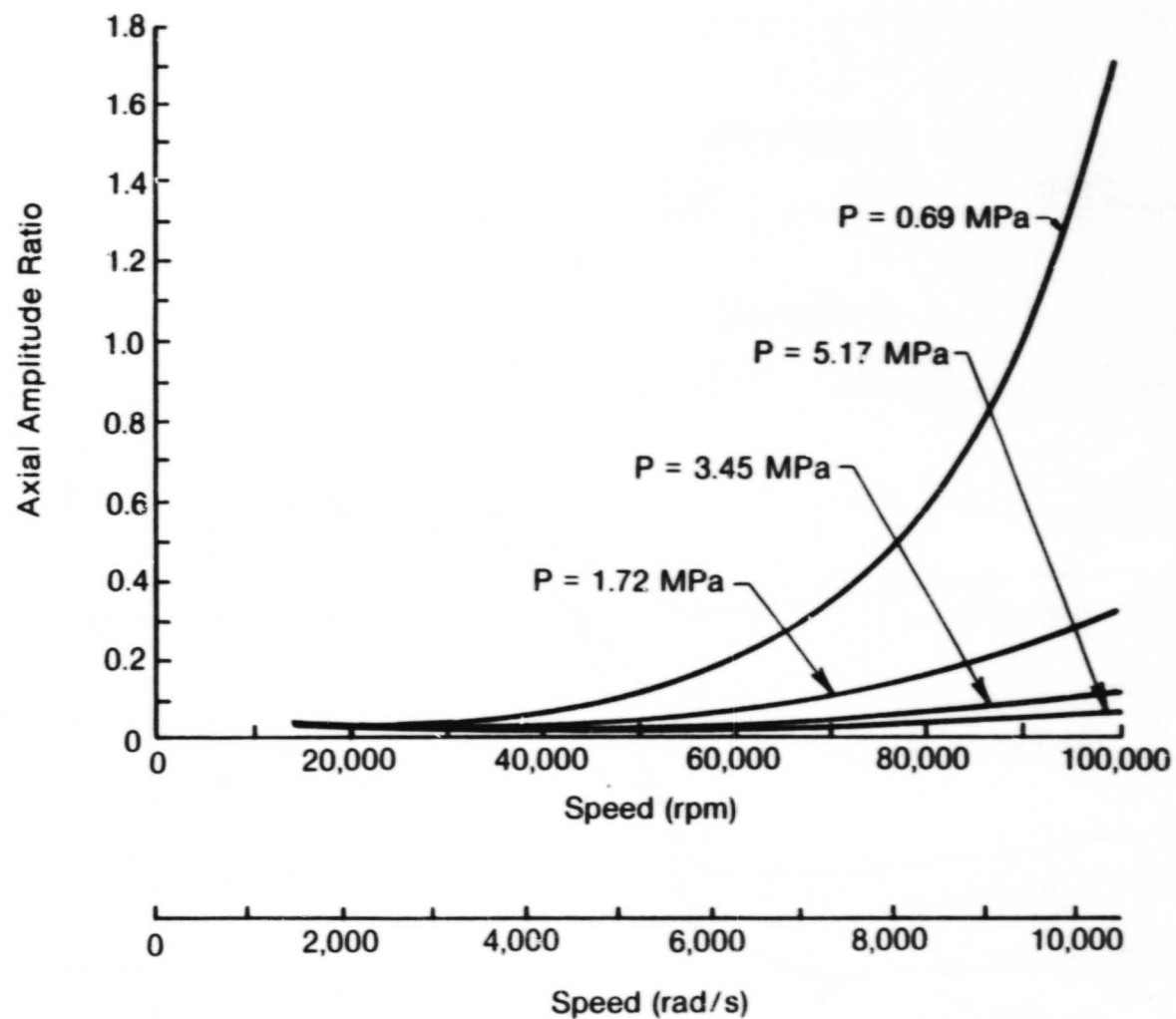


Fig. 5-24 20-mm Spiral Groove Seal; Axial Amplitude Ratio versus Speed

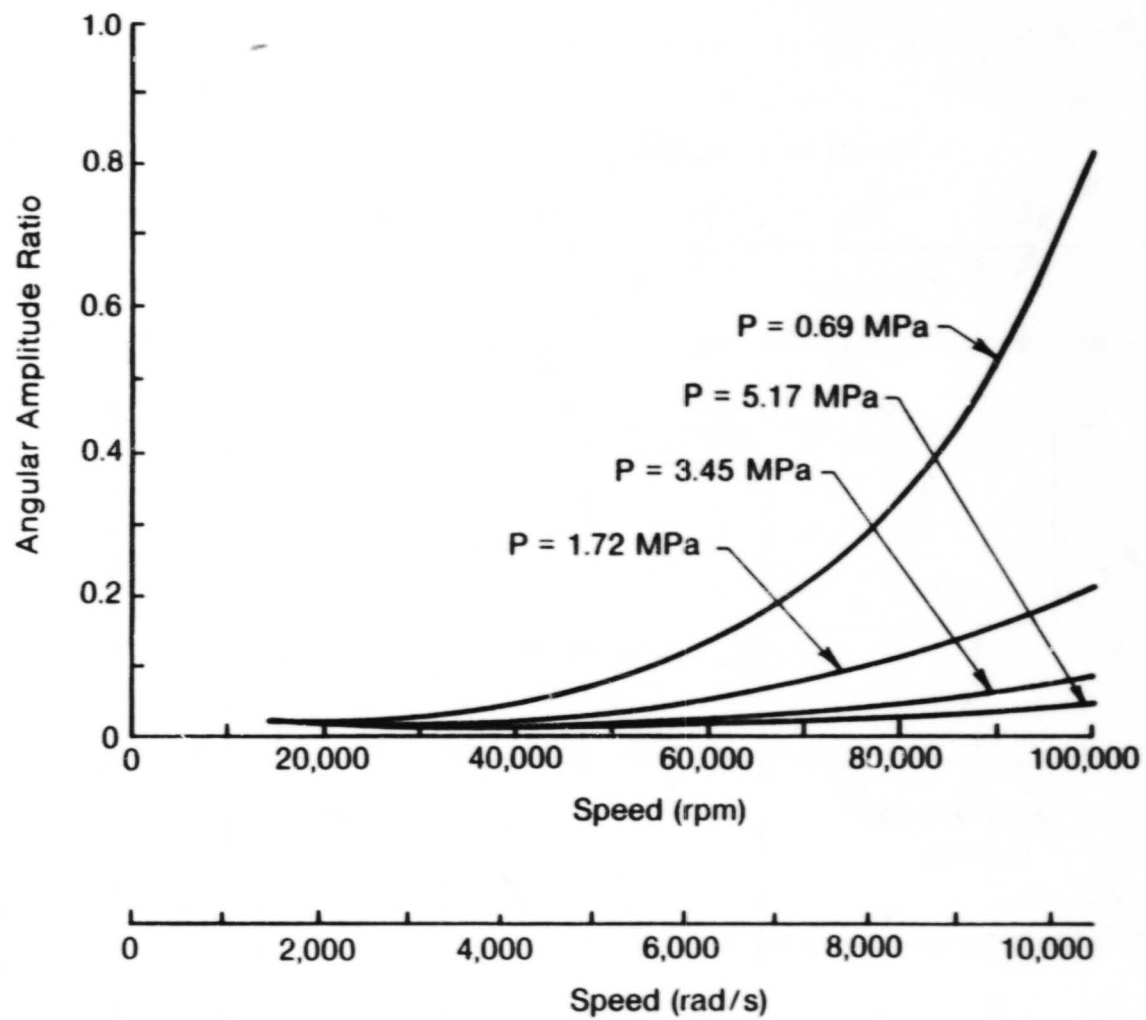


Fig. 5-25 20-mm Spiral Groove Seal; Angular Amplitude Ratio versus Speed

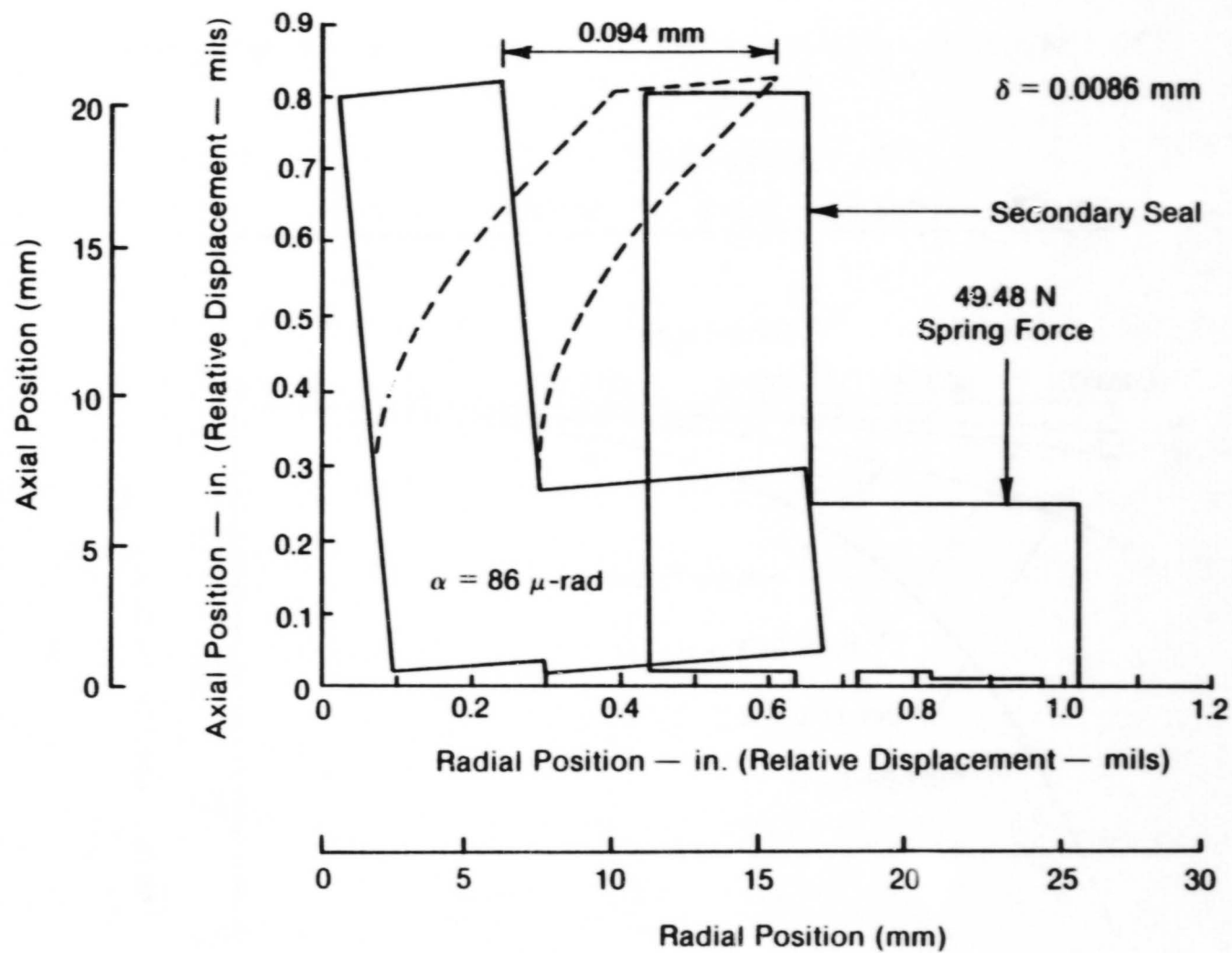


Fig. 5-26 Spiral-Groove Seal - Elastic Distortions

TABLE 5-1

50-MM PRESSURE-BALANCED SEAL

N (rad/s)	Pressure (MPa)	Film Thickness (mm)	Flow, $\text{m}^3/\text{s} \times 10^5$		Power Loss (kW)	Temperature, Cooled (-C)		Temperature, Uncooled (-C)		Axial Amplitude Ratio	Angular Amplitude Ratio	Axial Stiffness $\text{N/m} \times 10^{-4}$	Face Load (N)
			(g)	(s)		(g)	(s)	(g)	(s)				
7330	5.17	29.7	27.5	39.0	16.36	26.7	3.8	45.5	22.6	0.042	0.031	7.38	10,608
5864		23.7	20.0	29.8	9.46	21.4	2.8	35.7	17.1	0.024	0.018	8.07	
5236		20.98	16.6	25.6	7.23	19.8	2.5	32.5	15.2	0.019	0.014	8.37	
4189		16.1	10.5	17.9	4.25	18.4	2.1	29.2	12.8	0.011	0.008	8.70	
3142		10.44	4.6	9.34	2.24	22.3	2.0	33.2	12.8	0.007	0.005	8.26	
2199		2.79	0.16	0.510	1.12	300.6	21.3	401.0	122.0	0.013	0.009	2.18	
7330	3.45	36.3	29.3	39.9	15.3	23.3	3.61	40.6	20.6	0.072	0.053	4.46	7,086
5864		29.7	22.3	31.5	8.8	17.7	2.57	30.0	15.0	0.040	0.030	4.96	
5236		26.4	19.0	27.5	6.6	15.7	2.18	26.7	12.8	0.0303	0.023	5.21	
3142		14.8	7.21	12.7	1.94	12.4	1.32	19.4	8.3	0.009	0.007	5.81	
1780		2.54	0.098	0.272	0.67	308.9	24.1	417.0	132.0	0.016	0.012	1.12	
7330	1.72	49.5	30.97	39.2	14.1	20.26	3.4	36.1	19.4	0.188	0.135	1.89	3,562
5864		41.1	24.42	31.8	7.9	14.4	2.4	25.6	13.3	0.099	0.072	2.14	
5236		37.3	21.47	28.5	5.9	12.2	1.9	21.7	11.1	0.072	0.053	2.28	
4189		23.06	10.65	15.8	1.64	7.1	0.94	11.7	5.6	0.020	0.015	2.81	
2094		14.22	4.42	7.93	0.67	6.6	0.72	10.6	4.4	0.008	0.006	2.91	
1309		3.73	0.179	0.456	0.30	65.6	5.4	91.1	31.1	0.011	0.008	0.860	
7330	0.69	70.36	31.22	34.37	13.04	18.6	3.7	35.0	20.6	0.844	0.524	0.65	1,450
5864		59.18	25.25	28.84	7.23	12.7	2.4	23.9	13.3	0.347	0.240	0.75	
5236		54.10	22.58	26.06	5.36	10.5	2.0	19.4	11.1	0.238	0.169	0.79	
3142		35.31	12.95	16.06	1.42	4.9	0.83	8.9	5.0	0.055	0.041	1.05	
2094		24.13	7.37	9.87	0.52	3.3	0.47	5.6	2.8	0.020	0.015	1.22	
1047		8.89	0.97	1.74	0.15	5.4	0.57	8.3	3.3	0.007	0.005	0.912	
890		2.79	0.46	0.092	0.07	82.8	0.011	125.0	50.0	0.620	0.015	0.228	

TABLE 5-2

20-MM PRESSURE-BALANCED SEAL

N (rad/s)	Pressure (MPa)	Film Thickness (mm)	Power Loss (kW)	Flow, $m^3/s \times 10^5$		Temperature, Cooled (-C)		Axial Amplitude Ratio	Angular Amplitude Ratio	Axial Stiffness $N/m \times 10^{-4}$	Face Load (N)
				(g)	(s)	(g)	(s)				
10,472	5.17	25.91	7.08	138.0	190.0	24.8	2.3	0.073	0.051	4.85	6,383
7,854		19.56	3.51	88.5	134.0	18.9	1.6	0.035	0.025	5.42	
6,545		16.0	2.31	63.9	103.0	17.2	1.3	0.023	0.016	5.67	
5,236		11.94	1.34	37.7	68.8	17.5	1.10	0.015	0.010	5.68	
3,297		7.11	0.745	12.78	29.7	27.2	1.3	0.010	0.007	4.75	
3,126		2.54	0.522	0.98	2.62	256.0	12.1	0.021	0.015	1.40	
10,472	3.45	31.50	6.63	146.0	192.0	21.8	2.2	0.123	0.085	2.98	4,270
7,854		24.13	3.28	102.0	111.0	15.4	1.39	0.057	0.040	3.42	
6,545		20.07	2.09	77.0	113.0	13.1	1.09	0.037	0.026	3.65	
5,236		15.75	1.19	50.8	81.9	11.7	0.87	0.022	0.016	3.82	
3,927		10.92	0.671	24.6	45.9	12.7	0.77	0.013	0.009	3.72	
2,581		2.54	0.298	0.66	1.80	206.0	10.0	0.026	0.018	7.89	
10,472	1.72	41.91	6.11	154.0	183.0	19.1	2.13	0.327	0.213	1.33	2,157
7,854		33.02	2.91	112.9	134.0	12.5	1.32	0.135	0.093	1.56	
6,545		28.19	1.86	90.0	115.0	9.9	0.99	0.082	0.057	1.70	
5,236		22.86	1.04	66.2	89.5	7.8	0.72	0.046	0.033	1.86	
3,927		17.02	0.54	40.6	60.0	6.4	0.53	0.024	0.017	2.00	
1,932		2.54	0.15	0.459	1.10	139.0	5.94	0.029	0.020	0.40	
10,472	0.69	56.90	5.74	156.0	152.0	17.5	2.39	1.7	0.82	0.522	890
7,854		45.47	2.68	118.0	112.6	10.9	1.44	0.43	0.27	0.612	
6,545		39.37	1.64	97.0	100.0	8.17	1.06	0.23	0.16	0.677	
5,236		32.77	0.97	75.4	80.3	5.94	0.72	0.12	0.084	0.760	
3,927		25.15	0.45	52.0	59.0	4.22	0.49	0.057	0.040	0.861	
1,445		2.79	0.52	0.33	0.49	70.0	5.8	0.033	0.023	0.196	

6.0 TEST RIG

6.1 General Configuration

A cross section of the test rig is shown on Figure 6-1*. The right-hand portion of the rig is the drive end where the nitrogen turbine is located. The central portion is the bearing region where the journal and thrust bearings are located. The left end of the rig is the test seal section where the 50-mm helium buffer seal is shown installed.

Locating the thrust bearing in the center of the rotor avoids excessive overhang at either end and provides for a more uniform distribution of mass along the rotor. This arrangement alleviates rotordynamic difficulties due to large overhung masses. The helium buffers are installed in a back-to-back configuration and mate against a common runner.

The 30-mm (1.1811 in.) shaft journal diameter provides sufficient stiffness to be below the bending critical speed, and prevents excessive bearing and windage power losses for operation at 7330 rad/s (70,000 r/min). At the turbine end of the shaft, a heat dam is located between the turbine wheel and shaft. This dam prevents high temperature at the turbine wheel from conducting heat into the cold shaft regions. The outside periphery of the heat dam is machined with a labyrinth that provides one half of a buffer seal that prevents turbine gas from entering the bearing region. At the seal end of the shaft, the helium seal runner is secured to the shaft by a spring sleeve that is pressed onto the shaft. This compensates for bore growth of the runner.

Photographs of the seven major housing components are shown in Figures 6-2 and 6-3. At the turbine end is the nozzle box which contains the turbine inlet manifold, nozzle blades and exhaust section. The turbine blade tip clearance of 0.25 to 0.30 mm (0.010 to 0.012 in.) is established by the width of the spacer piece between the nozzle box and labyrinth seal housing (see Figure 6-1). The labyrinth seal housing is a separate member that contains inlet and

*Figures are presented consecutively, beginning on page 6-16.

exit passages for the buffer gas. The next major housing element is the turbine end bearing housing. This contains the turbine-side thrust and journal bearings with associated fluid inlets, drains and pressure tap connections. The shaft support journal and thrust bearings are externally pressurized (hydrostatic) bearings to provide stiffness and avoid whirl instabilities. The bearing housing also contains the right-hand side of the windage shroud surrounding the thrust collar. Separating the two bearing housings is a shim plate whose thickness determines the total clearance in the thrust bearing. The seal end bearing housing contains the left-hand thrust and journal bearings. The next major element is the seal housing in which the test seals are installed. Finally, the end cap is the last member and is used to contain the fluid that leaks past the test seal. (Photographs of rig components and an assembled shaft are included in Section 2.0, Figures 2-20 and 2-21.)

The assembly of the rig proceeds from inboard out. The bearing housings and shim plate are installed over the shaft and connected by cap screws torqued to their specified values. Next, the assembled buffer seal housing is installed and connected to the turbine side bearing housing. The heat dam is then shrunk onto the shaft. The turbine nozzle spacer is next inserted. The turbine wheel is chilled in LN₂ and inserted over the shaft into the bore of the heat dam. A washer and nut finish the shaft assembly. The final step at the turbine end is installation of the nozzle box. At the opposite end the helium seal housing is installed. The seal runner spring sleeve assembly is then attached to the shaft and the seal runner shrunk on and secured by the end nut. The test seals are then put in place followed by the end cap.

6.2 Fluid Systems

The various flow systems and flow paths in the rig are indicated schematically on Figure 6-4. The nitrogen gas for driving the turbine enters the nozzle box on the right-hand side, proceeds through the nozzle blading, through the radial-inflow turbine that drives the rig, and out through a central exhaust in the turbine nozzle box. Leakage at the back side of the turbine wheel passes through a labyrinth seal, mixes with the buffer seal gas, and exits from a common drain. The buffer seal consists of a central supply annulus from which

flow is directed axially through labyrinths towards the turbine wheel and in the opposite direction towards the bearing compartment.

Initially, nitrogen gas was used for the buffer fluid in the labyrinth seals. The check-out test showed, however, that the temperature of the surrounding parts was low enough to permit some of the nitrogen to liquefy. This ran back into the turbine posing a problem. Helium gas with its much lower liquefaction temperature was substituted for the nitrogen and solved the problem.

The journal and thrust bearings are externally pressurized by liquid nitrogen. There are four recesses in each bearing, each fed through an external passage via an orifice restrictor located at the outer periphery of the rig. The drain from the turbine end of the turbine side journal bearing mixes with the labyrinth seal drain. The inboard drain from the turbine side journal bearing combines with the thrust bearing drain located around the outer periphery of the central section of the thrust bearing. The inboard drain from the seal side journal bearing flows through a separate drain outlet and combines with the leakage from the thrust bearing seal drain.

Two different arrangements were used to drain the outboard side of the seal end journal bearing and the inboard helium buffer seal. The original design (shown in Figures 6-1 and 6-4) uses a common drain cavity. The helium-nitrogen mixture exited through radial drain holes directly under the journal bearing. This arrangement, used during the testing of the first three seal sets, allowed the inboard end of the seal runner to be bathed in LN₂ resulting in large windage losses. The heat generated caused the adjacent journal bearing case to warm up and partial vaporization to occur in the bearing. The vaporization of the bearing fluid caused deterioration of its stiffness and damping properties and resulted in serious dynamic problems at speeds of approximately 50,000 r/min or greater.

The second arrangement designed to prevent the vaporization problem uses a labyrinth seal to keep the LN₂ bearing flow away from the end of the seal runner. The configuration was shown in Figure 2-22. The helium side of the labyrinth is kept at a higher pressure than the LN₂ side, thus preventing any LN₂ from flowing in and contacting the end of the runner. This eliminates the

windage loss altogether. The helium is supplied by the leakage from the inboard test seal and flow from an additional supply part machined into the seal housing. A constant buffer flow is maintained across the labyrinth by keeping the externally supplied helium at a pressure slightly higher than the bearing drain.

The various fluid supply and drain systems require a large number of passages. These are shown on Figures 6-5 through 6-7. Section numbers are referred to in Figure 6-1. Figure 6-5 shows the turbine side bearing housing inlets and outlets. Section D-7 is in the journal bearing region and shows the inlet ports to each of the recesses (Connection A). The restrictor elements are located at the outer periphery of each entrance connection so that they are readily accessible for change, if desired. The two bottom recesses also have pressure tap Connections B. Inboard of the bearing, at its drainage manifold, are capacitance probe Connections C, for monitoring shaft motion. Although only one probe is shown, there are actually two, located 90 degrees apart. Section D-4 is in the right-hand bearing housing in the vicinity of the thrust bearing. Each of the four thrust bearing recesses are separately fed through Connection A. The two top recesses have pressure taps B, for measuring the thrust bearing recess pressures. There are also four separate Connections C, for inlets to the vibration pistons [3]. These were not used during the helium seal test. The several drain holes shown communicate the inboard journal bearing drain with the thrust bearing drain.

Figure 6-6 shows supply and drain connections for the seal end bearing housing. Note that the left and right-hand bearing housings are not antisymmetric because of the different drainage systems at the outboard end of the journal bearings. Section A-7 (thrust bearing housing) shows the orthogonal capacitance probes axially positioned on the inboard side of the journal bearing. Figure 6-7 shows the connections for the turbine end labyrinth seal and shim plate housings. The labyrinth seal housing, Section D-10, contains one inlet Connection A. It is at the bottom and feeds the central region of the double labyrinth seal (see Figure 6-1). At the top of the housing, Connection B, is the combination drain for the LN₂ from the outboard end of the turbine-side journal bearing and the buffer gas leaking past the inboard labyrinth. Connections C exhausts combined leakage from the turbine and outboard

labyrinth seal. The shim plate, Section A-9, has four drain connections at the bottom which are outlets for the thrust bearing and the inboard leakage from both journal bearings.

6.3 Test Seal Arrangement

The helium seal arrangement is shown in Figure 6-1. The inboard seal contacts the mating surface of the seal housing. The outboard seal contacts a similar mating surface and is retained by the end flange which is internally bolted to the seal housing. The seal rings are prevented from rotating by three equally spaced, key-like protrusions machined into the bore of the seal housing and end flange. The seals are pushed apart providing a small, but positive, axial sealing force by a wavy washer installed between the rings.

The helium seal runner attachment to the shaft was previously shown on Figure 4-6. A flexure sleeve is pressed in the bore of the seal runner. The assembly is then pressed over the shaft end. The purpose of the flexure is to compensate for centrifugal growth of the runner. As was indicated on Figure 4-6, the growth at the ID of the runner is approximately 0.0104 mm (0.0004 in). As the runner expands, it allows the flexure to release and maintain contact with the runner.

6.4 Turbine Design and Performance

The turbine used to drive the rig is a radial-inflow turbine designed for a maximum of 74 kW (100 hp). The principal losses in the rig are due to windage, bearings, and seals viscous losses. Computed total power loss for the test rig with helium seals installed and the original inboard seal drain arrangement is approximately 31 kW (41 hp) at 7329 rad/s (70,000 r/min). With the labyrinth seal installed between the helium seal and journal bearing, the total computed loss drops to about 17 kW (23 hp). Figure 6-8 shows the locations of the various losses.

Figure 6-9 presents the turbine configuration; Figure 6-10 provides a photo. Design and performance data are given below:

Basic Turbine Design

Type:	Unshrouded, cantilevered, radial-inflow
OD, mm (in.):	71.9 (2.83)
Speed, rad/s (r/min):	7,329 (70,000)
Tip Speed, m/s (ft/s):	284 (865)
Nozzle Angle, rad (deg):	1.29 (74)
Blade Angle, rad (deg):	1.05 (60)
Reaction (%):	30
U/Co:	0.5

Estimated Performance

Gas:	N ₂ at 21°C (70°F, 360°R)
Power, kW (hp):	37 (50)
Inlet Pressure, kPa absolute (psia):	1034 (150)
Exhaust Pressure, kPa absolute (psia):	103.4 (15)
Isen. Enthalpy Drop, Btu/kg (Btu/lb):	27.2 (60)
Efficiency, %:	70%
N ₂ Flow Rate kg/s (scfm):	0.40 (700)

Off-design performance data are provided by Figures 6-11 and 6-12 showing output power versus inlet pressure and turbine efficiency versus speed, respectively.

6.4.1 Acceleration

The specification calls for an acceleration rate of 152 m/s^2 (500 ft/s^2). This is equivalent to 15.5 g. The turbine design speed torque is:

$$T = (50)(63,000)/70,000 = 45 \text{ in.-lb} = 5.08 \text{ N/m}$$

The stalled torque for this type of turbine is two times the design torque, 10.2 N/m or (90 in./lb). The 2.15 kg (4.75 lb) rotor has a mass moment of inertia of 0.00068 N/m-s^2 ($6 \times 10^{-3} \text{ lb/in.-s}^2$). The average acceleration is then:

$$g = (90 + 45)/(2 \times 0.006 \times 386) = 29$$

Therefore, there is ample torque available to meet the specification acceleration rate.

6.4.2 Stress

At the design conditions of 37 kW (50 hp) at 7329 rad/s (70,000 r/min), the maximum stress is 137.9 MPa (20,000 psi) which occurs at the blade ID from both the centrifugal forces and torque load. Aluminum alloy 2024-T3 has a yield strength of 413.6 MPa (60 psi), hence the maximum safe operating speed is about 10,470 rad/s (100,000 r/min).

6.4.3 Design

The design drawing of the turbine wheel is shown in Figure 6-13.

6.5 Bearing Design and Performance

6.5.1 Journal Bearings

The journal bearing is a four-pad hydrostatic bearing with a pocket or recess geometry as shown in Figure 6-14. The recess angular extent is 1.26 rad (72°) and approximately 16.4 mm (0.644 in.) wide. The bearing width is 22.0 mm (0.866 in.) and the L/D ratio is approximately 0.73. The design radial clearance is 0.0191 to 0.0254 mm (0.00075 to 0.00100 in.). The actual measured radial clearance was 0.0188 mm (0.00074 in.).

Bearing performance is summarized in Table 6-1*. Since the program originally called for the use of LOX (for spiral groove seal testing) and test speeds of 10,470 rad/s (100,000 r/min) for testing 20-mm seals, bearing performance for those conditions is also given. The data applies to the concentric shaft position which, given the low rotor weight, is the expected mode of operation.

*Tables are presented consecutively, beginning on page 6-49.

The bearing flow is very sensitive to clearance and only slightly affected by speed. The flow is used to size the orifice to produce a pressure drop between the supply and bearing recess equal to about one half the total drop between the supply and drain. The original orifices installed were 0.940 mm (0.037 in.) in diameter. These were changed during check-out operations to 0.813 mm (0.032 in.) in diameter, yielding a recess pressure 0.45 to 0.50 times the supply pressure.

Both stiffness and damping are also sensitive to clearance. The bearing land areas are silver plated from 0.05 to 0.10 mm (0.002 to 0.004 in.) to reduce rubbing friction with the shaft. The bearings are energized prior to start-up of the shaft and after it has stopped rotating during shutdown. Thus, there should not be rubbing contact between the shaft and bearings.

6.5.2 Thrust Bearings

The general configuration of the thrust bearing is shown in Figure 6-15. It is a four-pad bearing with each pad being of 1.22 rad (70°) angular extent. A single pocket is incorporated in each pad. The pocket angular extent is 0.98 rad (56°). Each pocket is individually fed through an orifice restrictor and two of the pockets have pressure taps for measuring pocket pressure. The design clearance of the thrust bearing (per side) is 0.038 mm to 0.0432 mm (0.0015 to 0.0017 in.). The actual clearance is also 0.038 mm to 0.0432 mm (0.0015 to 0.0017 in.).

The thrust loads imposed on the seal test rig are shown in Figure 6-16. They are dependent on the pressure maintained in the outboard seal drain cavity, the bearing drain pressure and the turbine pressures. At design turbine conditions, the net thrust pushes the rotor toward the seal end and can go from 369 N (83 lb) with an outboard seal drain pressure of 517 kPa absolute (75 psia) to approximately 1432 N (322 lb) as the outboard drain pressure is lowered to 103 kPa absolute (15 psia). At low turbine power conditions, when its thrust is very low, the net thrust would go from 309 N (69 lb) toward the turbine end to a net 529 N (119 lb) to the seal end as the outboard drain pressure is decreased from 517 kPa absolute to 103 kPa absolute (75 psia to

15 psia). In either case the net loads are well within the capability of the thrust bearing.

Table 6-2 and 6-3 show thrust bearing performance at 7329 rad/s (70,000 r/min) and 10,470 rad/s (100,000 r/min) for both liquid nitrogen and LOX. The tabulations show single side properties of the bearing and indicate variations in performance as a function of clearance.

Load versus displacement for the total bearing is indicated in Figure 6-17. Because of light loading, the bearing will remain essentially centered with runner axial displacements less than 0.0025 mm (0.1 mils). At full displacement, the load capacity is approximately 5115 N (1150 lb). Bearing flow for the double-acting thrust bearing is shown in Figure 6-18. In the centered position, the flow is 1.17 kg/s (16.2 gal/min at 70,000 r/min). Viscous power losses for a single-sided thrust surface are indicated in Figure 6-19. Pocket or recess pressure versus film thickness is shown in Figure 6-20. In the centered position, the recess pressure is 2585 kPa (375 psia), or half of the supply pressure. This pressure ratio provides near optimum stiffness. The double-sided stiffness is approximately 175 m-N/m (1,000,000 lb/in.). Figure 6-21 is a plot of fluid-film temperature rise versus film thickness, for a single side. It is based on the assumption that all heat generated by viscous friction is added to the fluid as it flows through the bearing and no heat is transferred through the bearing surfaces. In the centered position, the temperature rise is 1.3°C (2.3°F) at 7329 rad/s (70,000 r/min). When the bearing clearance approaches 0.013 mm (0.0005 in.) the temperature rises dramatically and represents a failed condition. It is important to keep the temperature rise as low as possible to assure against vaporization in the bearing film.

6.6 Rotor Dynamics

The following three major analyses were performed on the 50-mm test seal rotor:

1. Undamped critical speeds as a function of bearing stiffness
2. Synchronous unbalance response

3. Stability analysis to establish system stability, natural frequencies, and mode shapes.

Because of the early emphasis on the spiral-groove LOX seals, the rotordynamic studies modeled the tester rotor as outfitted for the LOX seal tests. The differences between the LOX seal rotor and the helium seal rotor are the mass and the polar and transverse moments of inertia of the seal runners. The LOX runner is greater in all three properties. Critical speeds or natural frequencies are higher and system stability is greater for the helium seal runner. Thus, if the analysis is not entirely accurate, it is at least conservative.

In summary, the analyses show that seal tests should operate satisfactorily over its entire speed range. The most troublesome natural frequency, the first bending mode, resides at approximately 13,611 rad/s, (130,000 r/min) and is well above the speed range. The lowest natural frequency, a rigid body conical mode, should occur at about 7329 rad/s (70,000 r/min) for the LOX rotor (higher for the helium rotor). The resulting vibrations should be well damped. Response analyses at 7329 rad/s (70,000 r/min) show acceptable amplitudes for expected levels of residual unbalance. The stability parameters or growth factors of all natural frequencies calculated are all negative and large, indicating good system stability.

In practice, the dynamic characteristics of the tester proved considerably more troublesome than expected. Despite careful balancing and assembly, large shaft vibrations developed during both the rig checkout and the first three seal tests. Vibration amplitudes started to grow around 4397 rad/s (42,000 r/min) and reached unacceptably high shaft levels 0.025 to 0.038 mm peak to peak, (1.0 to 1.5 mils peak to peak) between 4816 and 5444 rad/s (46,000 and 52,000 r/min).

A brief experimental analysis revealed the following observations:

1. Varying the bearing supply pressures between 3.79 and 6.20 MPa (550 and 900 psig) did not eliminate the vibrations.

2. The orbits while operating at pressures of 4.82, 5.51, and 6.20 MPa (700, 800, and 900 psig) were close to (but not locked to) shaft speed. Orbits at pressures of 3.79 and 4.14 MPa (550 and 600 psig) were exactly synchronous.
3. The speeds at which the vibration became large decreased somewhat as bearing supply pressure was increased. Also, the occurrence of noticeable bubbling around the seal end probe showed the same trend. Both effects are noted below:

Supply Pressure (MPa)	Vibration Threshold (rad/s)	Bubbling Threshold (rad/s)
6.20	4837	-
5.51	4837	3769
4.82	5026	>3769
4.14	5403	5151
3.79	5407	5151

4. Both the vibration and bubbling were most severe on the seal end of the tester.
5. Lower speed operation revealed small but noticeable synchronous vibration peaks at 3141 rad/s (30,000 r/min) and second harmonic peaks at 2450 rad/s (23,400 r/min). The latter may correspond with a natural frequency of 4900 rad/s (46,800 r/min).
6. Because of the bubbling occurring around the shaft probes and the nonsynchronous behavior at the higher pressures, the mode shapes could not be determined.

From these analyses, it was concluded that the design stiffness and damping properties of the seal end journal bearing were not being achieved. This would have the general effect of lowering the natural frequencies and decreasing the damping. The following comparisons provide additional evidence of weakened bearing properties. The first and second undamped critical speeds are predicted to occur at 7329 and 9423 rad/s (70,000 and 90,000 r/min),

respectively based on bearing stiffnesses of 117.3 m-N/m (6.7×10^5 lb/in.). If, however, the stiffness degraded to about 17.5 m-N/m (1.0×10^5 lb/in.) the same analysis would predict 3141 rad/s (30,000 r/min) for the first critical speed and 4816 rad/s (46,000 r/min) for the second. Both speeds coincide with measured peaks in vibration.

The occurrence of self-excited vibration of frequencies very close to the synchronous frequency is very unusual. However, additional analyses of the tester revealed that such an instability can occur with sufficiently degraded damping.

The most likely cause of poor stiffness and damping in the seal end bearing is vaporization in the bearing film. Experimental observations provided ample evidence of gas bubbles when the vibration occurred. Previously completed design studies indicated that the LN₂ bearing fluid is near saturation condition as it exits the bearing. An additional factor is the windage loss resulting from the LN₂ contacting the end of the seal runner. This generates a substantial amount of heat which would transmit to the surrounding parts and increase the tendency for vaporization. To eliminate the windage loss and hopefully the vaporization, the second labyrinth seal was installed (see Section 2.0) prior to the fourth seal test.

6.6.1 Rotor Model for the 50-mm LOX Seal Shaft

The rotordynamic models used for both the 50- and 20-mm LOX shafts are shown in Figure 6-22. Table 6-4 indicates pertinent information relative to the various mass stations and shaft elements for the 50-mm LOX seal rotor. The model contained 20 mass stations with disk elements located at Stations 5, 9, and 16 representing the seal runner, thrust runner, and turbine wheel, respectively.

6.6.2 Undamped Critical Speeds for the 50-mm LOX Seal Rotor

The undamped critical speed map for the 50-mm seal rotor is shown in Figure 6-23. The bearing stiffness variable is the diagonal stiffnesses along the x-

or y-axes. For the 50-mm LOX seal shaft, the bearing support stiffness was taken to be 117.9 m-N/m (6.73×10^5 lb/in.), representative of a radial clearance of 0.019 mm (0.00075 in.). At an operating speed of 5863 rad/s (56,000 r/min), the rotor speed is below the first critical, which is a rigid body mode. The first bending critical, which is the third critical speed, occurs at approximately 13,611 rad/s (130,000 r/min) which is more than two times the operating speed.

6.6.3 Synchronous Unbalance Response of the 50-mm LOX Seal Rotor

In computing the unbalance for synchronous response studies, API balance specifications were employed. This specification indicates what normal acceptable and attainable unbalance levels are.

The formula for computing the unbalance is:

$$U_x = 5 (56,347)(W_t)/N_2 \quad (6.1)$$

at 7329 rad/s (70,000 r/min). For the 50-mm LOX seal rotor:

$$U_x = 0.197 \text{ g-mm } (2.73 \times 10^{-4} \text{ oz-in.}) \quad (6.2)$$

at 10,470 rad/s (100,000 r/min). For the 20-mm LOX seal rotor:

$$U_x = 0.082 \text{ g-mm } (1.145 \times 10^{-4} \text{ oz-in.}) \quad (6.3)$$

$W_t = \text{Rotor weight (lb)}$

The above numbers are low levels and difficult to obtain. Therefore, MTI designed for an unbalance level of:

$$U_x = 0.36 \text{ g-mm } (5.0 \times 10^{-4} \text{ oz-in.})$$

The unbalances of this magnitude were applied at each of the Stations 5 and 16, representing the seal runner and turbine wheel, respectively. Two sets of runs were made; one in which the unbalances were in-phase and one in which the unbalances were 180° out-of-phase. In-phase unbalance excites the lateral

rigid body modes. Out-of-phase unbalance excites the conical rigid body modes.

Figure 6-24 shows half amplitude synchronous response at Stations 8, 10, and 11 which are the seal end journal bearing, the turbine end journal bearing, and thrust bearing, respectively with in-phase unbalance. At the operating speed of 5863 to 6073 rad/s (56,000 to 58,000 r/min), displacements are very well controlled; amplitudes are approximately 0.000254 mm (0.01 mils). The maximum speed of the rotor is 7329 rad/s (70,000 r/min) and will be run at this speed with the helium seals. Amplitudes at these stations at 7329 rad/s (70,000 r/min) are still very small and pose no problems. Figure 6-25 shows half amplitude response at Stations 9, 10, and 15 which are the thrust bearing (Stations 9, 10) and in the vicinity of the turbine wheel. Response at maximum speed is less than 0.00127 mm (0.05 in.). Figure 6-26 shows response at 1, 16, and 20. Station 1 is at the seal end extremity of the rotor; Station 16 is at the turbine wheel and Station 20 is at the extreme turbine end of the rotor. At the operating speeds, amplitudes are approximately 0.00127 mm (0.05 mils) at 5863 rad/s (56,000 r/min) and 0.00254 mm (0.1 mils) at 7329 rad/s (70,000 r/min). Figures 6-27, 6-28, and 6-29 show similar plots for out-of-phase unbalance. For the out-of-phase unbalance conditions, the maximum amplitude is 0.00381 mm (0.15 mils) at Station 1 (see Figure 6-29).

6.6.4 Stability Analysis for the 50-mm LOX Seal Rotor

As mentioned in the introductory paragraph, the stability analysis produces three significant items of information. These are a stability parameter or growth factor, natural frequencies, and mode shapes associated with the natural frequencies. Negative growth factors imply a stable system.

A tabulation of modal growth factors, natural frequencies and mode shapes is indicated in Table 6-5. The first mode is a rigid body mode. The natural frequency is 6384 rad/s (60,983 r/min) and the growth factor is -1139.2. The mode is very well damped. It coincides with the bottom line of the undamped critical speed map shown in Figure 6-23. Note that there is significant motion at the bearing stations, so that bearing characteristics influence this particular mode. Mode 2 is again very well damped. The natural frequency of

this mode is beyond the range of the maximum rotor speed. The third and fifth modes show significant bending. Mode 4 is predominantly a lateral rigid body mode.

6.7 Thermal Analysis

Using computer codes available at MTI, in-depth studies were made to establish the temperature distribution in the test rig. The original study was performed for the 50-mm LOX seal configuration using LOX as the working fluid for both the bearings and seals. The results are shown in Figure 6-30. It was assumed that the LOX entered the bearings and seal compartment at -173°C (-280°F), and that the nitrogen supply to the turbine and buffer seal was at 21°C ($+70^{\circ}\text{F}$). Fluid temperatures are indicated in bold numbers. The principal item of concern with respect to the fluid temperatures is that the LOX remain in a liquid state in and near the bearings to prevent bearing problems and erroneous capacitance probe readings. Figure 6-31 indicates drain pressure requirements versus fluid temperature rise to keep the LOX completely liquid.

The liquid at the journal bearing drains and the capacitance probes which are at the inboard drain locations is relatively cool, -173°C (-279°F). The temperature rise above the normal boiling point is 10°C (18°F). Thus a total backpressure of two to three atmospheres should be sufficient to maintain the LOX discharges in the liquid state. The housing and shaft temperatures are all quite reasonable. The largest temperature differences occur in the heat dam and buffer seal region, as would be expected. The heat dam is calculated to be effective in preventing transfer of heat from the turbine end down the shaft.

Test Seals
and Runner
(See Figs. 2-1
and 2-2 Details)

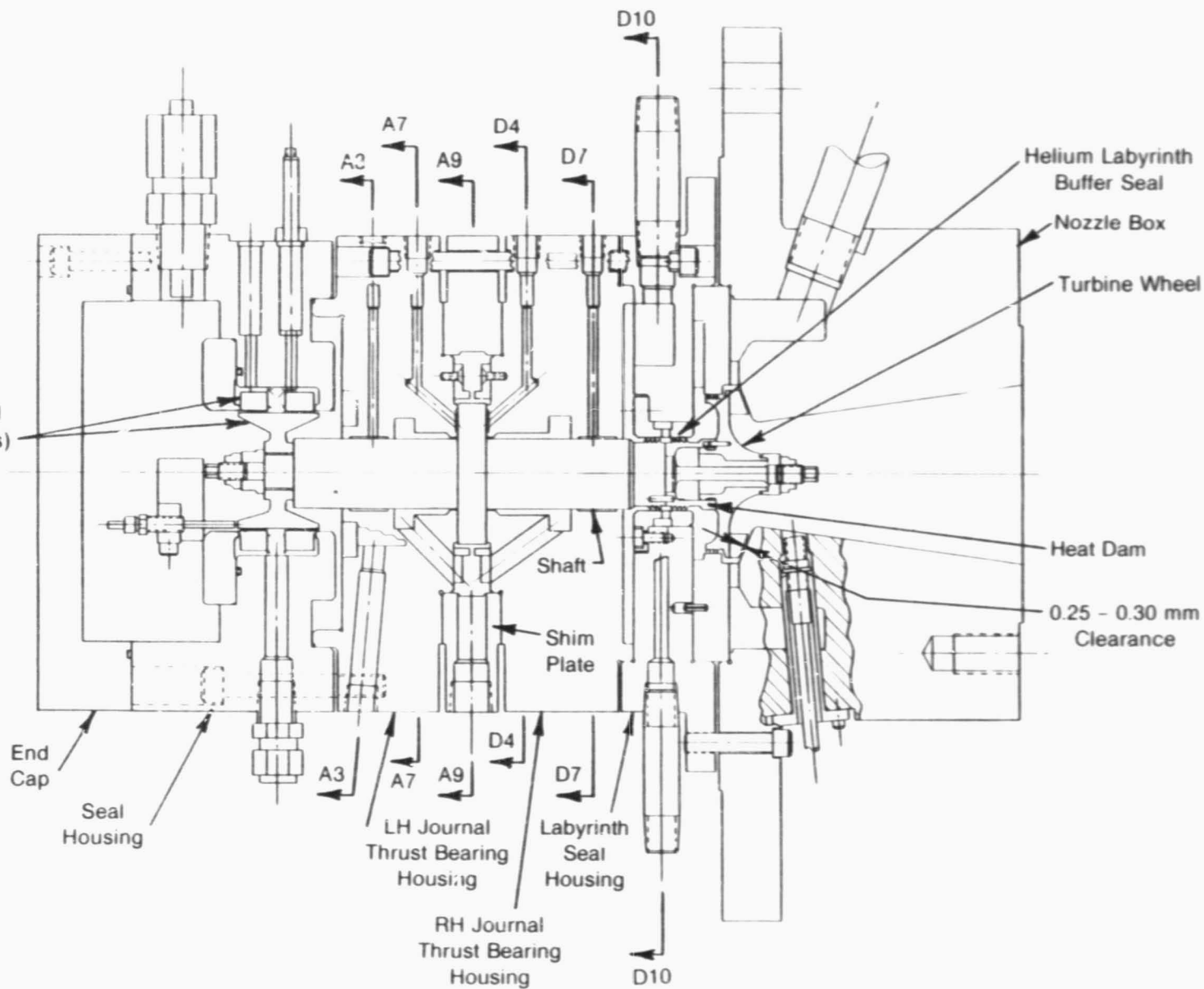


Fig. 6-1 Cross Section of Test Rig; Housing Sections Identified

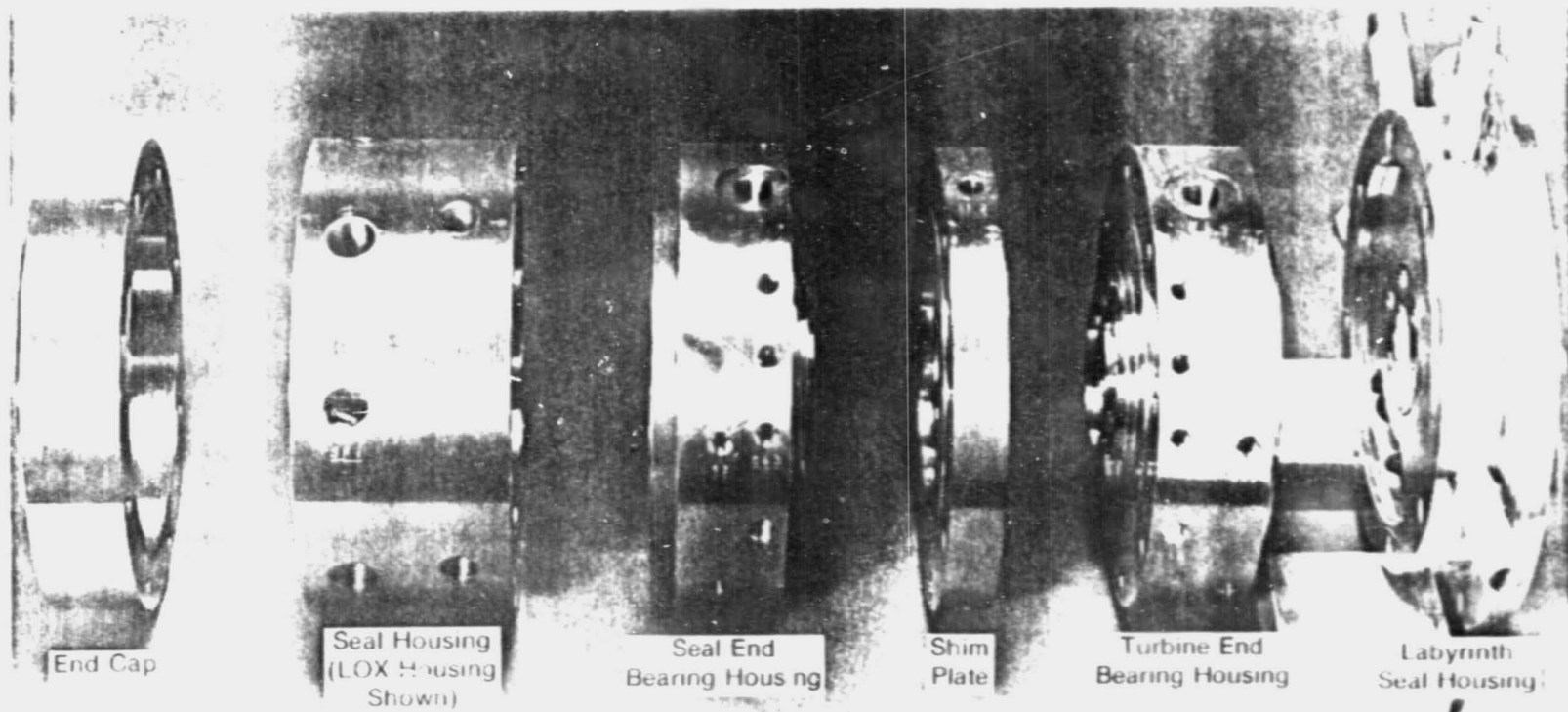


Fig. 6-2 Test Rig Housings

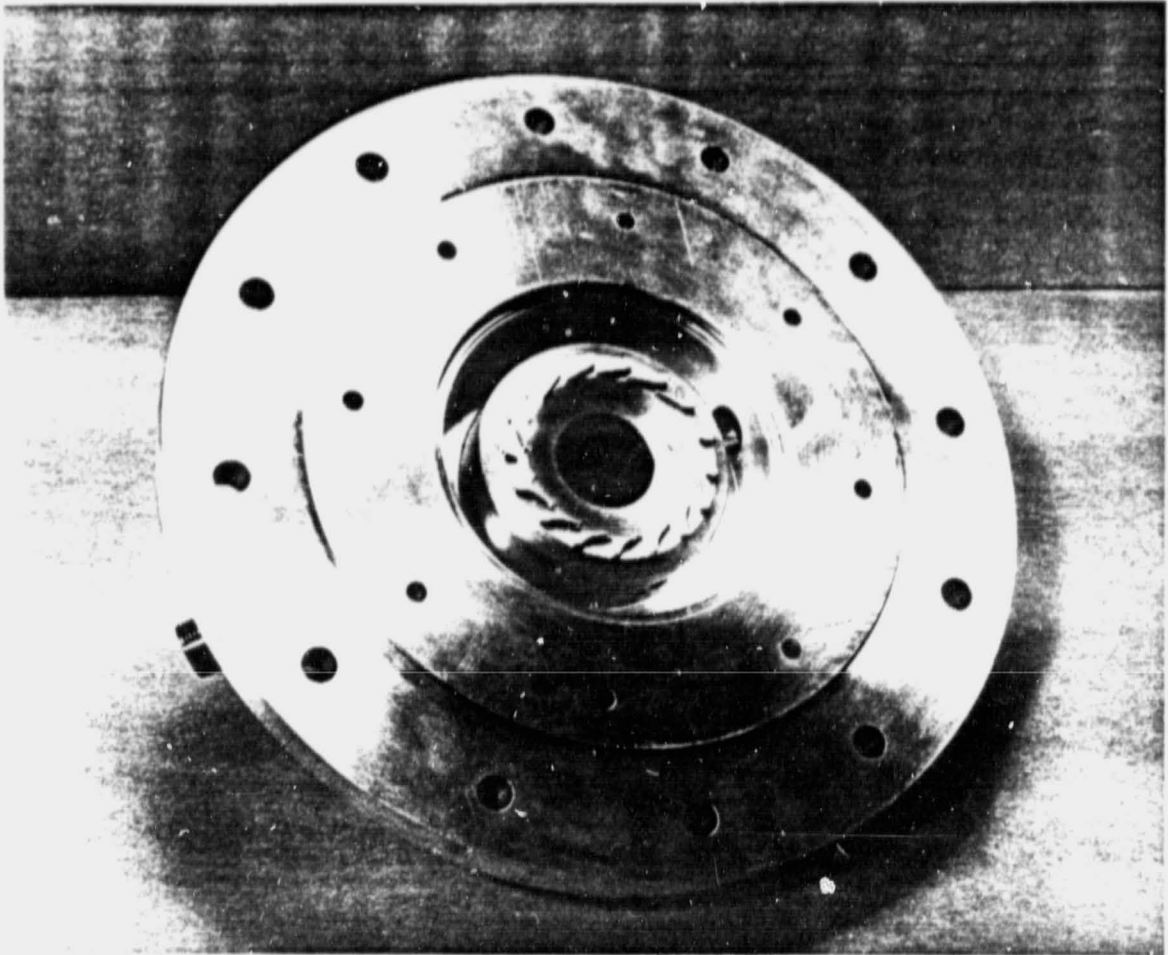


Fig. 6-3 Test Rig Nozzle Box

ORIGINAL PAGE IS
OF POOR QUALITY

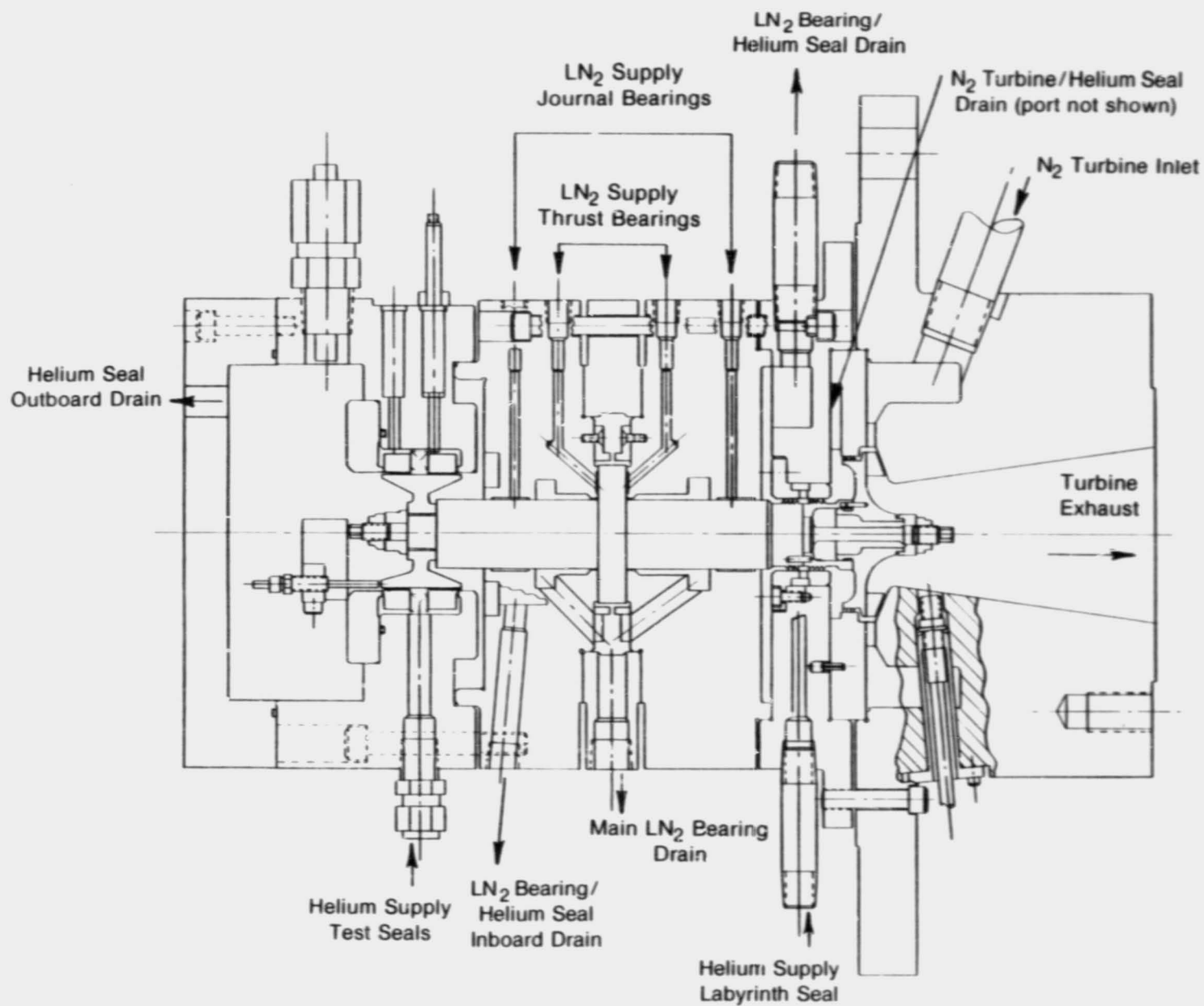
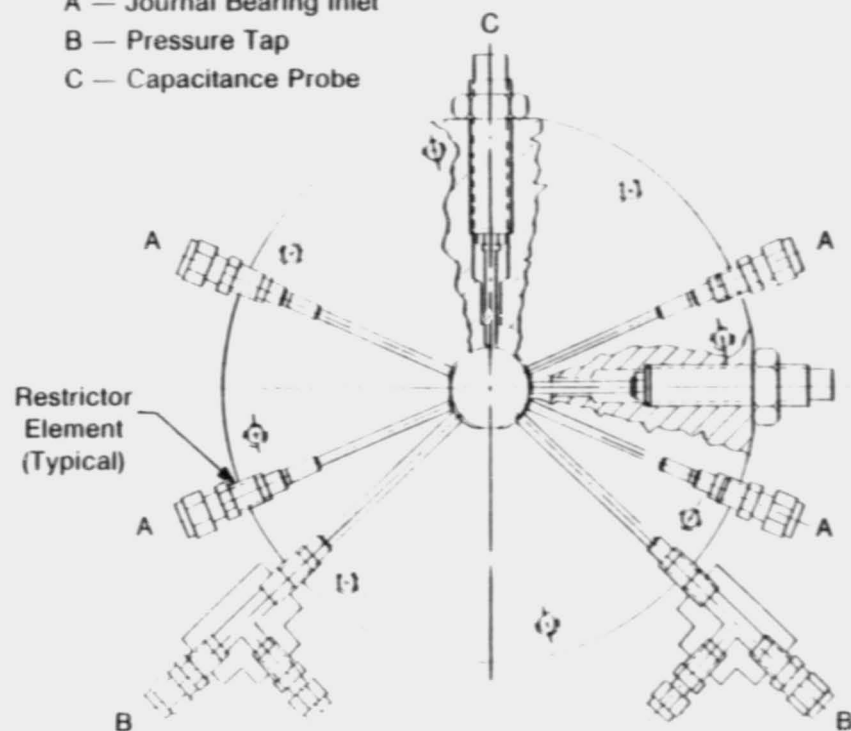
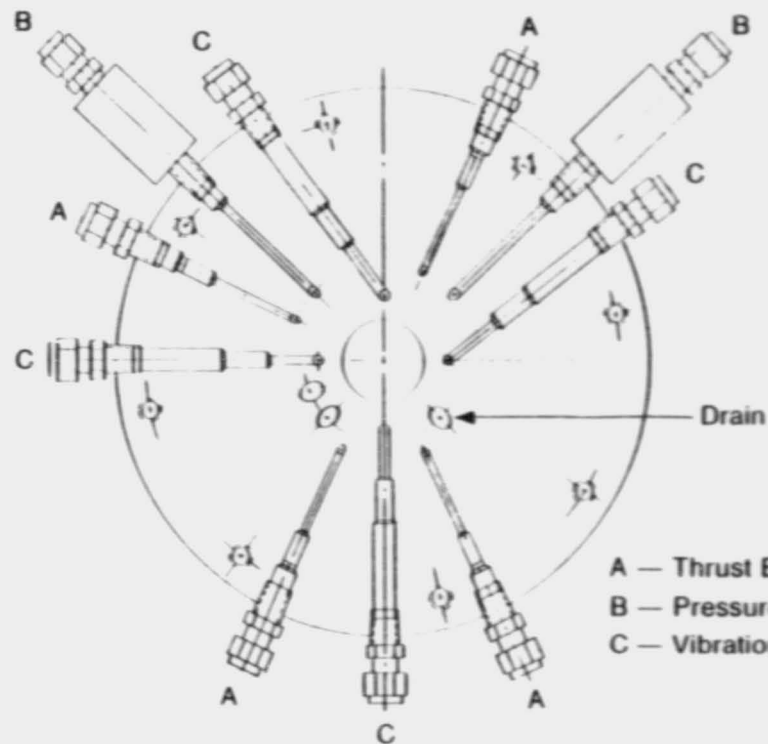


Fig. 6-4 Test Rig Fluid Systems

- A — Journal Bearing Inlet
- B — Pressure Tap
- C — Capacitance Probe



SECTION D-7
Right-Hand Bearing Housing

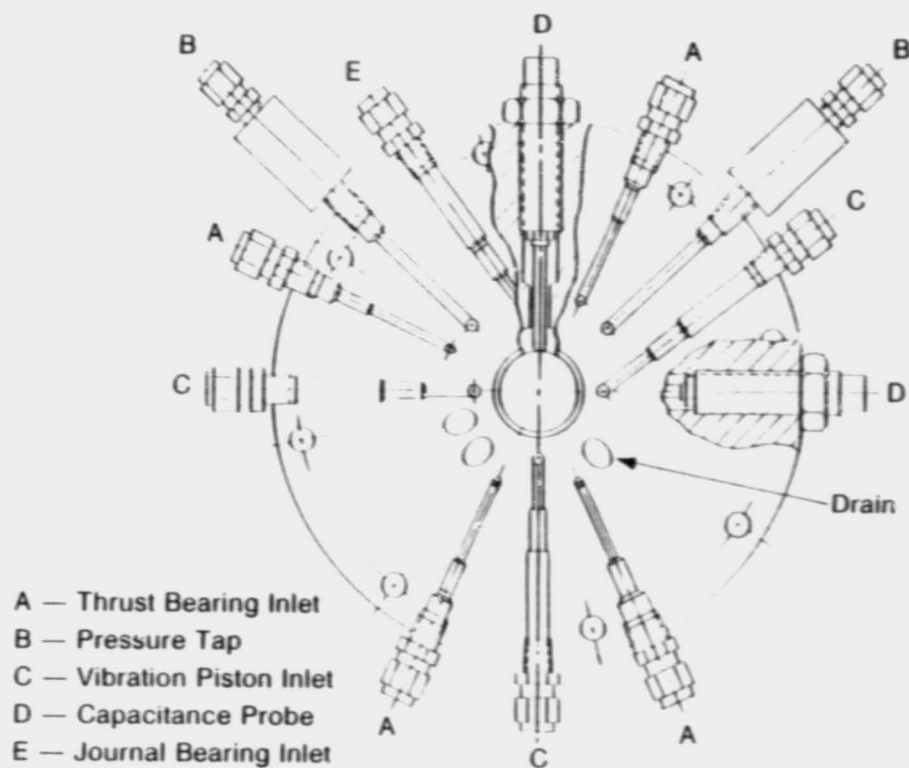


SECTION D-4
Right-Hand Bearing Housing

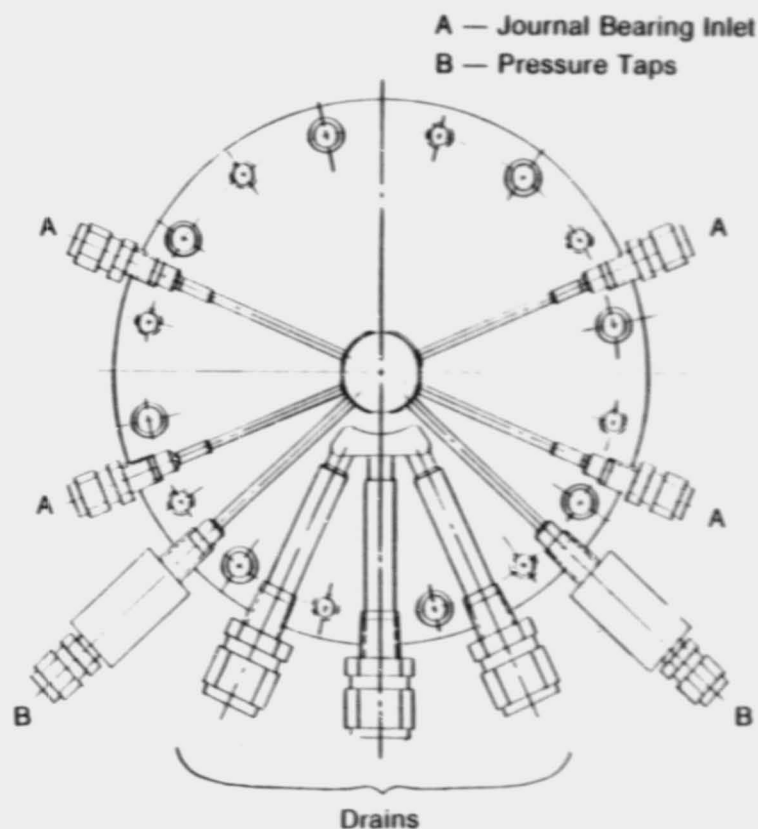
- A — Thrust Bearing Inlet
- B — Pressure Tap
- C — Vibration Piston Inlet

Fig. 6-5 Supply and Drainage - Turbine-Side Bearing Housing

ORIGINAL PAGE IS
OF POOR QUALITY

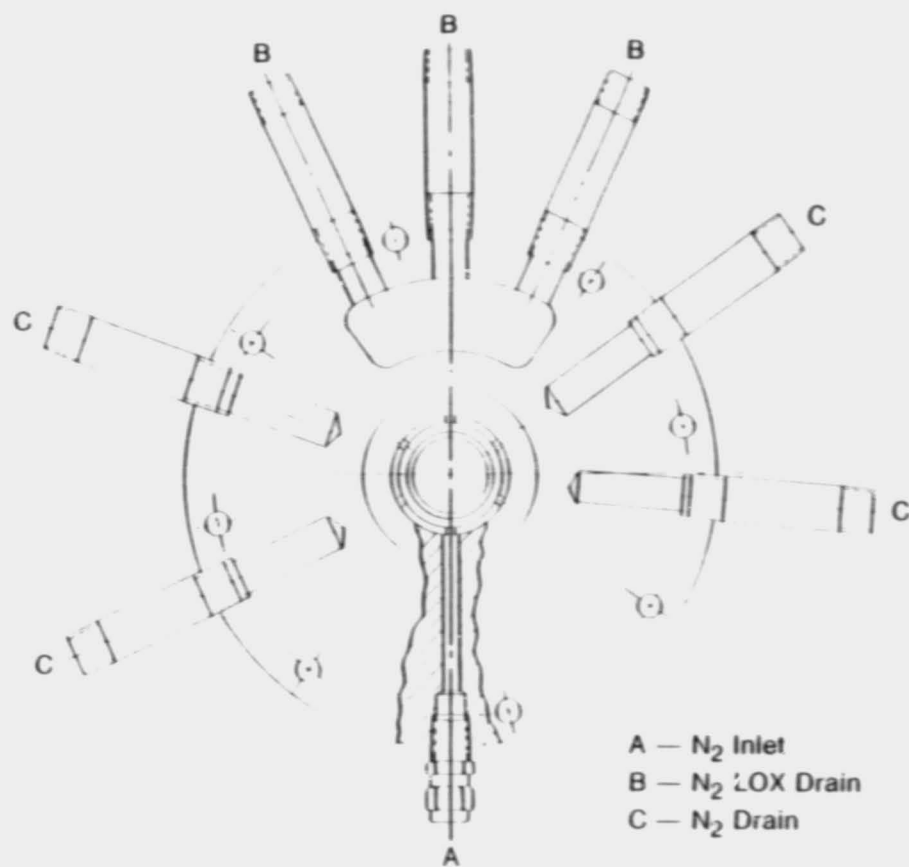


SECTION A-7
Left-Hand Bearing Housing

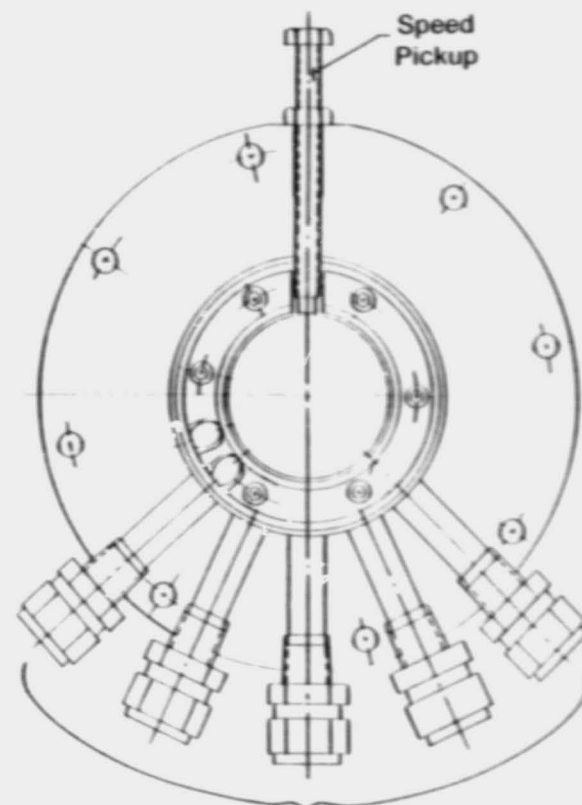


SECTION A-3
Left-Hand Bearing Housing

Fig. 6-6 Supply and Drainage - Seal-Side Bearing Housing



SECTION D-10
Helium Labyrinth Seal Housing



Thrust and Journal Bearing Drains

SECTION A-9
Shim Plate

Figure 6-7 Supply and Drainage - Labyrinth Seal and Shim Plate Housings

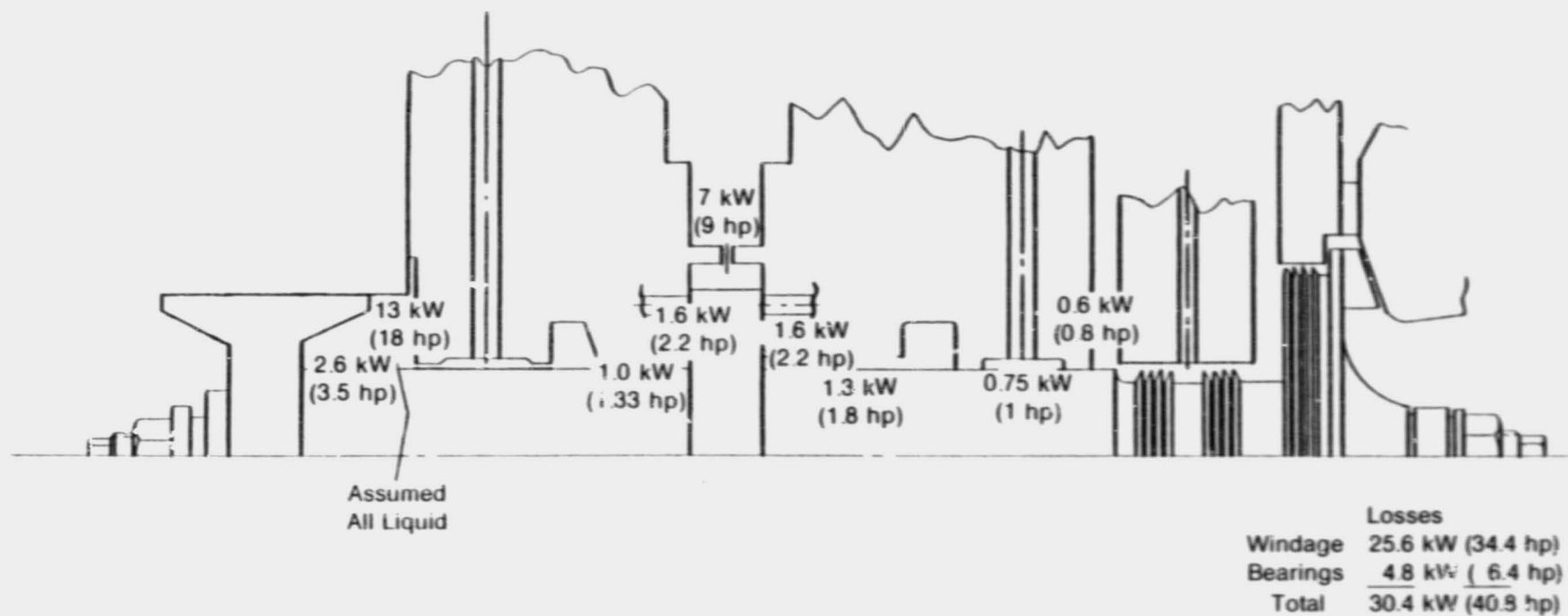
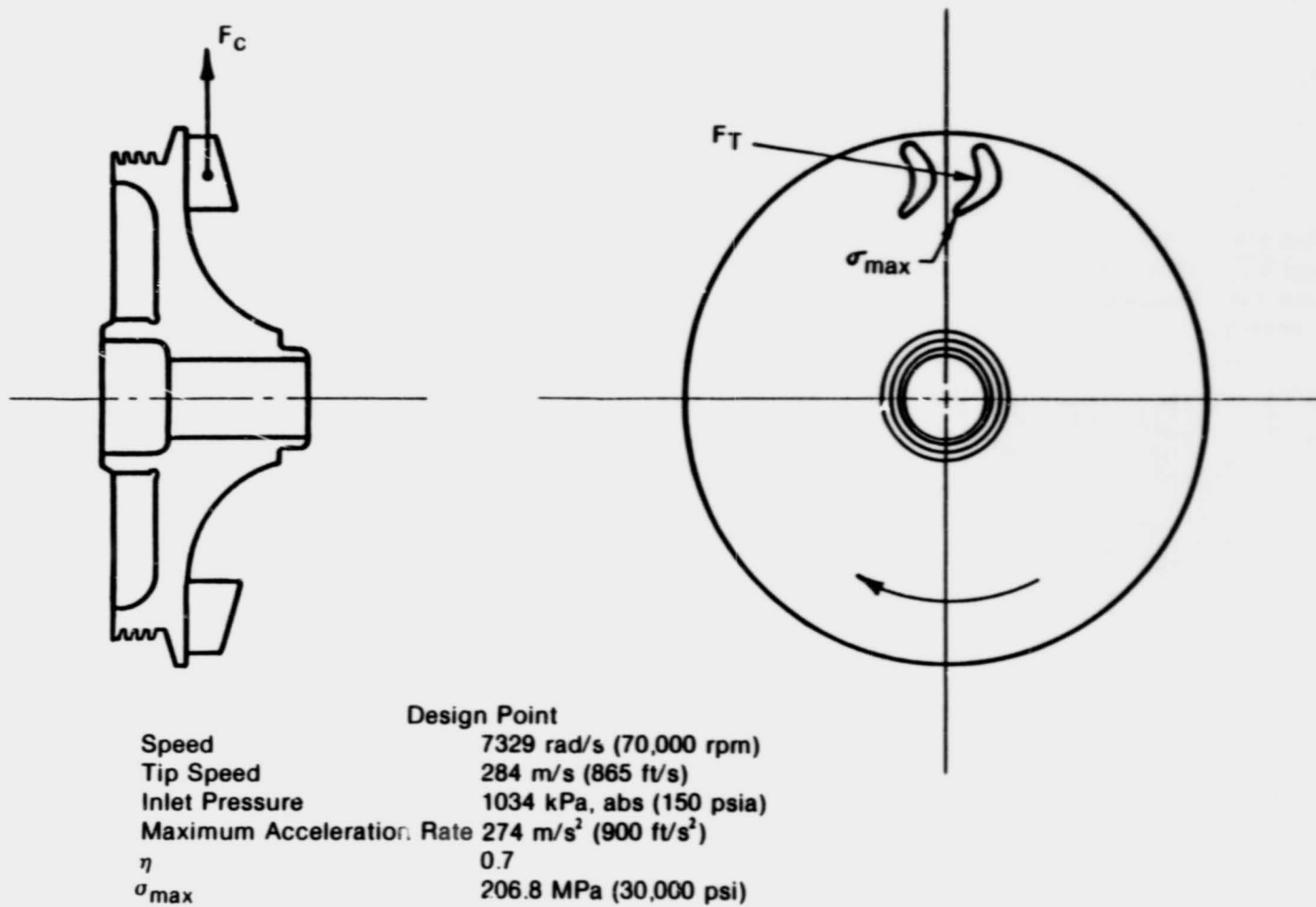


Fig. 6-8 Test Rig Power Losses



822830-1

Fig. 6-9 Turbine Design Schematic

ORIGINAL PAGE IS
OF POOR QUALITY

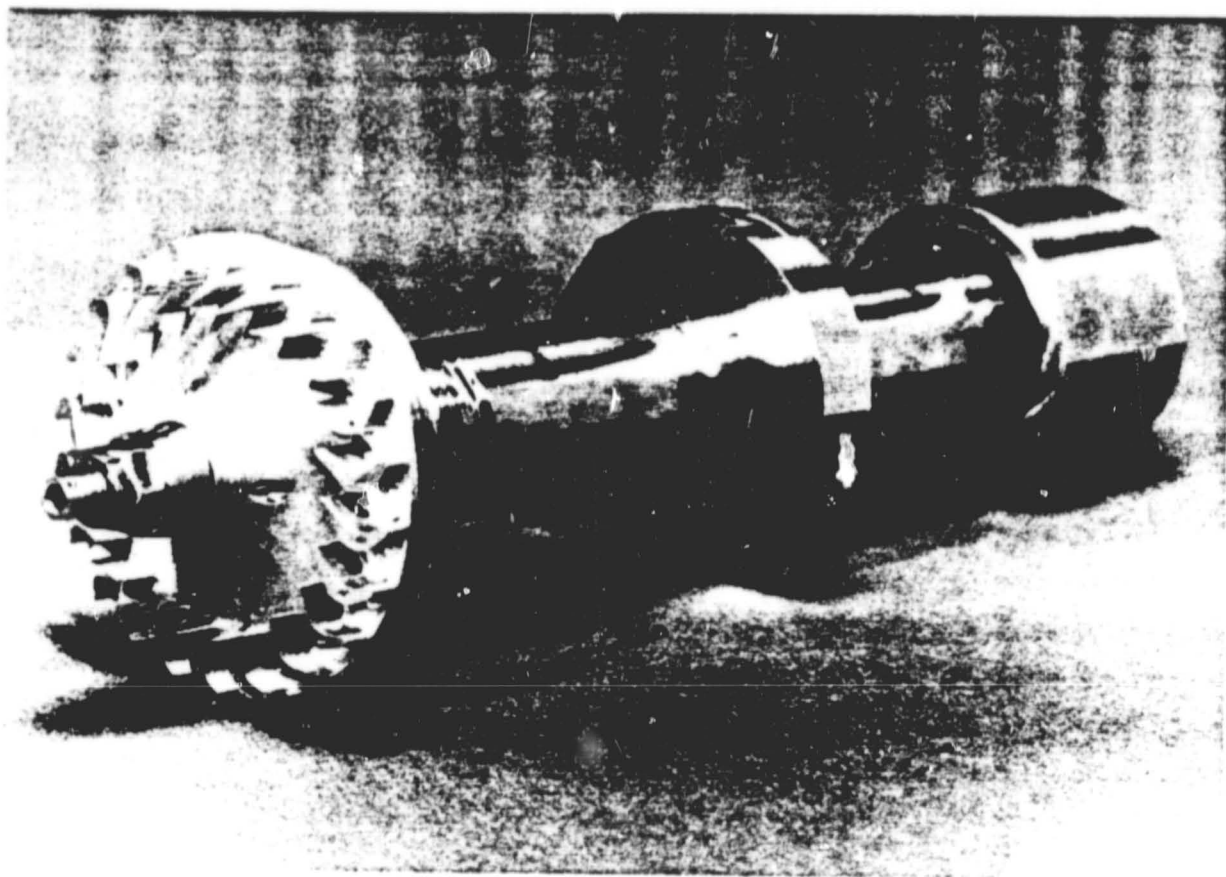
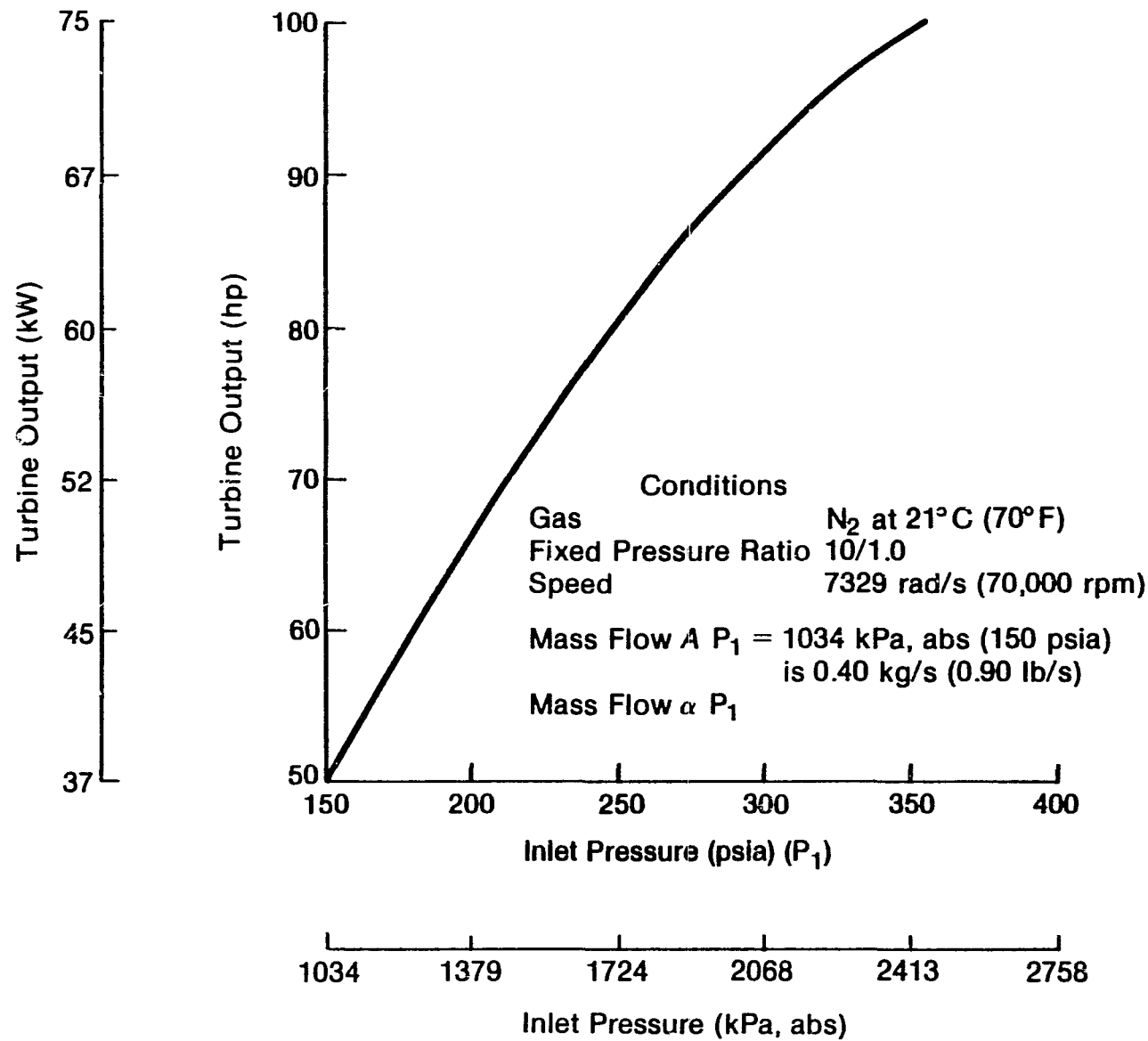


Fig. 6-10 Assembled Test Rig Shaft



83793-1

Fig. 6-11 Turbine Output Power versus Inlet Pressure

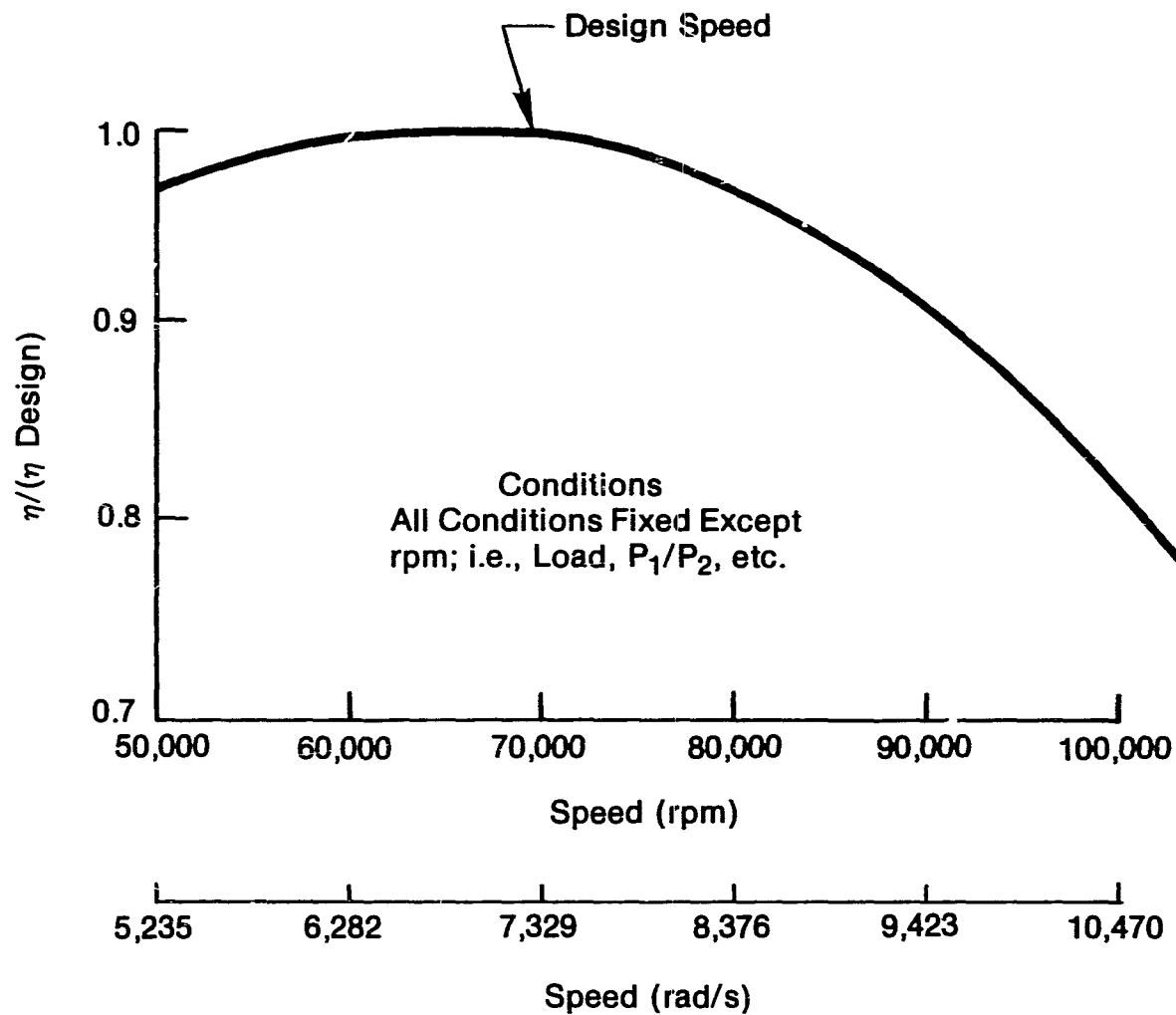
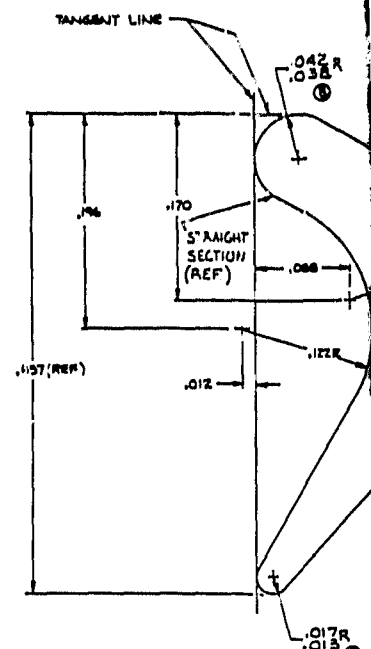
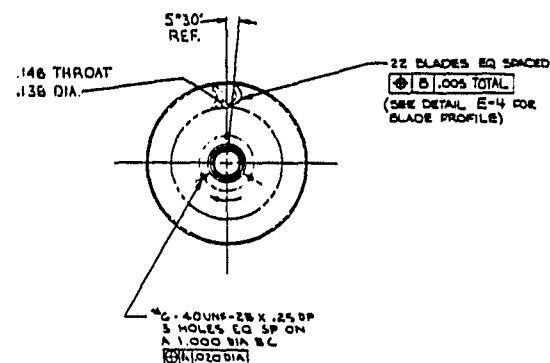


Fig. 6-12 Turbine Efficiency Ratio versus Speed



DETAIL E-4 (C)
GLAZE PROFILE
SCALE: 20/1

[illegible]

1.250 DIA.

.030R

.06R

.130
.120

30°

.080R

.14

.8757 DIA.
.8755 (REF.)

.825 DIA

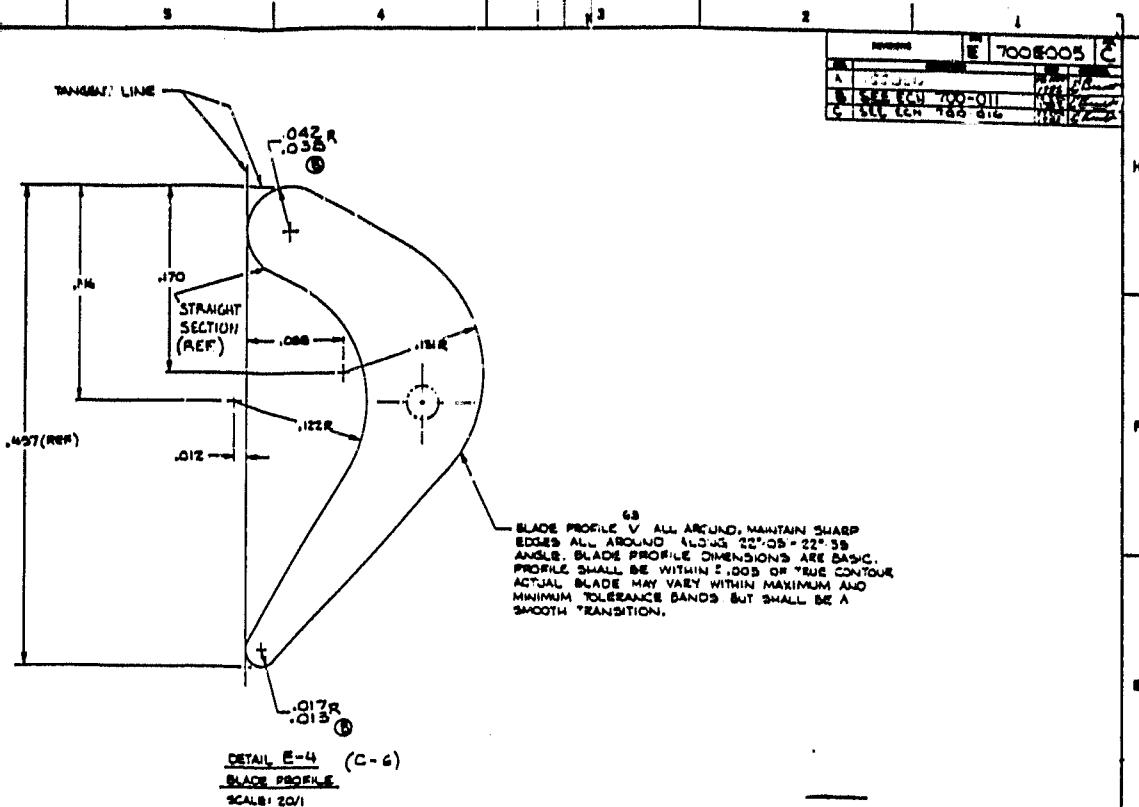
.490 DIA
.480

.840 DIA
.830

DETAIL A-7 (C-9)

SCALE: 2/1

Fig. 6-13 Turbine Wheel



ORIGINAL PAGE IS
OF POOR QUALITY

22 BLADES EQ SPACED
± .005 TOTAL
(SEE DETAIL E-4 FOR
BLADE PROFILE)

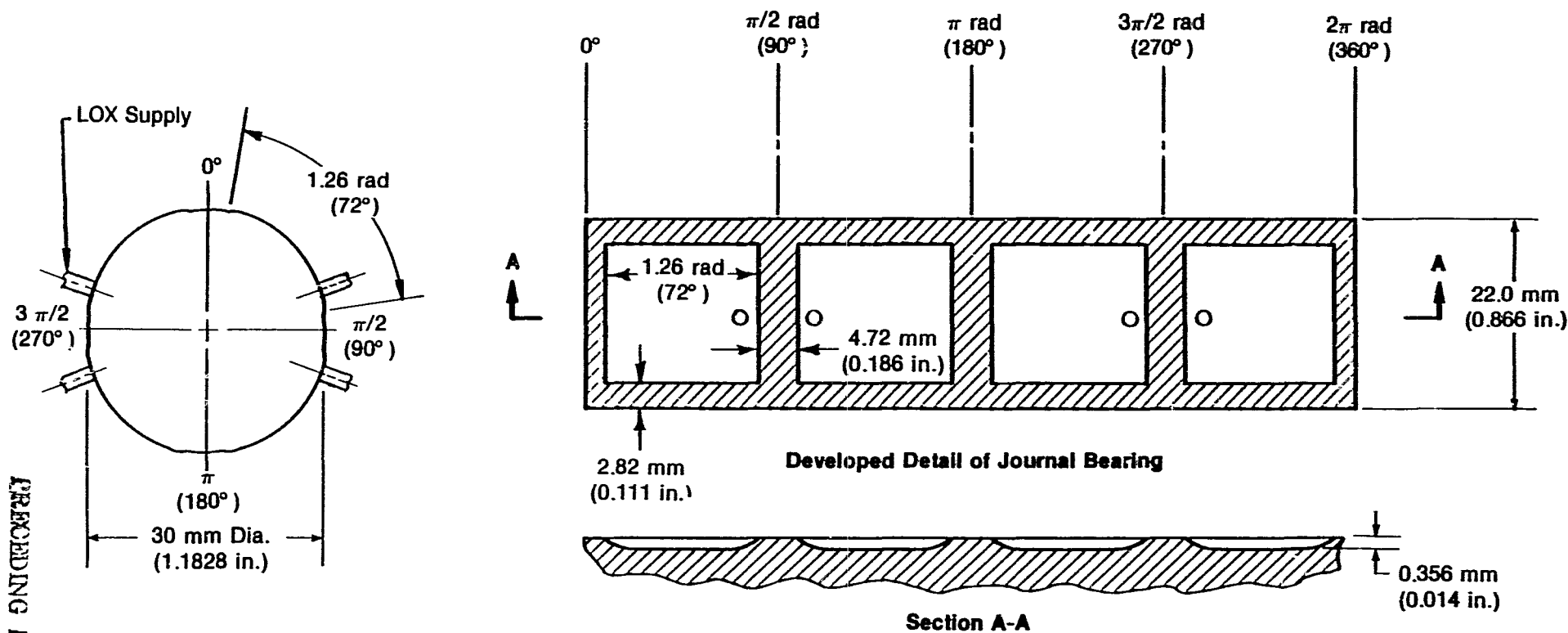
NOTES:

1. MATERIAL: ALUMINUM ALLOY 2014-T6 - PANCAKE FORGING, FORGING TO BE MADE FROM BAR STOCK HAVING A MINIMUM LENGTH OF THREE (3) TIMES FORGING THICKNESS AND SUFFICIENT DIAMETER TO ACHIEVE REQUIRED VOLUME
2. ULTRASONIC INSPECT ROUGH MACHINING PER MTI SPEC 38
3. UNLESS OTHERWISE SPECIFIED CONCENTRICITY TO BE HELD WITHIN .003 DIA TO .5"
4. WHEEL TO BE SPIN TESTED AT 110,000 RPM, MEASURE AND RECORD WHEEL OUTSIDE DIAMETER AND DIAMETERS A-A, A-B - BEFORE AND AFTER TEST, NO CHANGE PERMISSIBLE. SEE NOTE-8
5. DYNAMICALLY BALANCE WHEEL IN PLANES A-B WITHIN .0005 IN. REMOVE MATERIAL AT AREAS INDICATED.
6. ANODIZE IN ACCORDANCE WITH AMS 2471 AFTER BALANCING AND SPIN TEST
7. DATUM C-C IS DEFINED BY THE AVERAGE OF POINTS MIDWAY BETWEEN BLADES AT 2.375 DIA. BASIC.
8. BEFORE & AFTER SPIN TEST FLOURESCANT PENETRANT INSPECT PER AMS 2645, 100% SURFACE AREA, NO INDICATIONS PERMISSIBLE.
9. INSPECTION REPORTS AND MATERIAL CERTIFICATION REQUIRED.

PRECEDING PAGE BLANK NOT FILMED

2 FOLDOUT FRAME

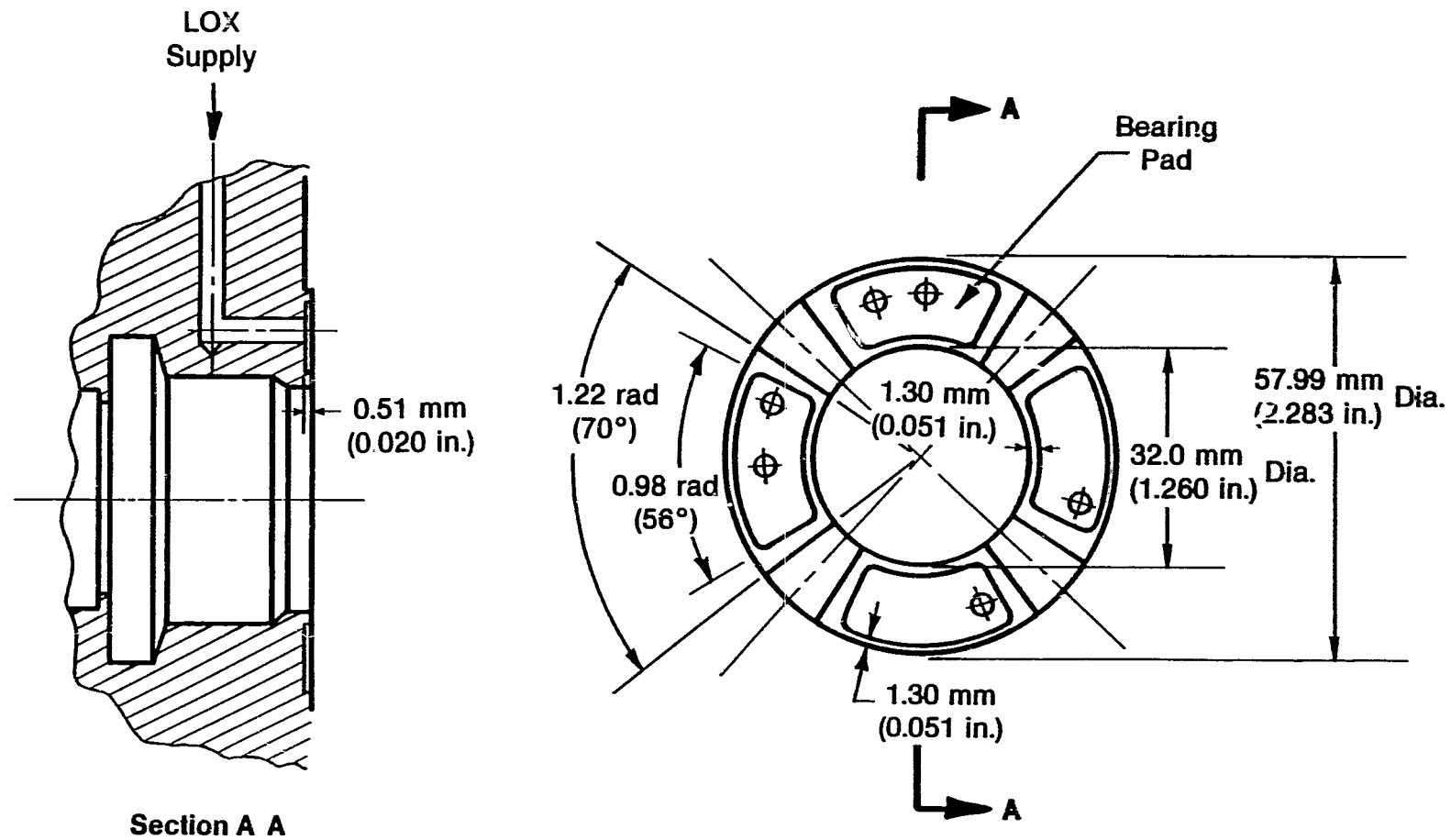
VALUE ENGINEERING ENGINEERING DATE: 11-10-61 BY: J. J. L. / J. J. L. CHECKED: J. J. L. / J. J. L. APPROVED: J. J. L. / J. J. L. SEE NOTES SEE NOTES		PROPRIETARY NON-PROPRIETARY NAME: DATE: 30 Oct 1961 TITLE: Mechanical Technology TURBINE WHEEL (2.85 DIA) 26741 E 700E005 26741 E 700E005	
--	--	--	--



Final Clearance = 0.0191 – 0.0254 mm (0.00075 – 0.0010 in.)

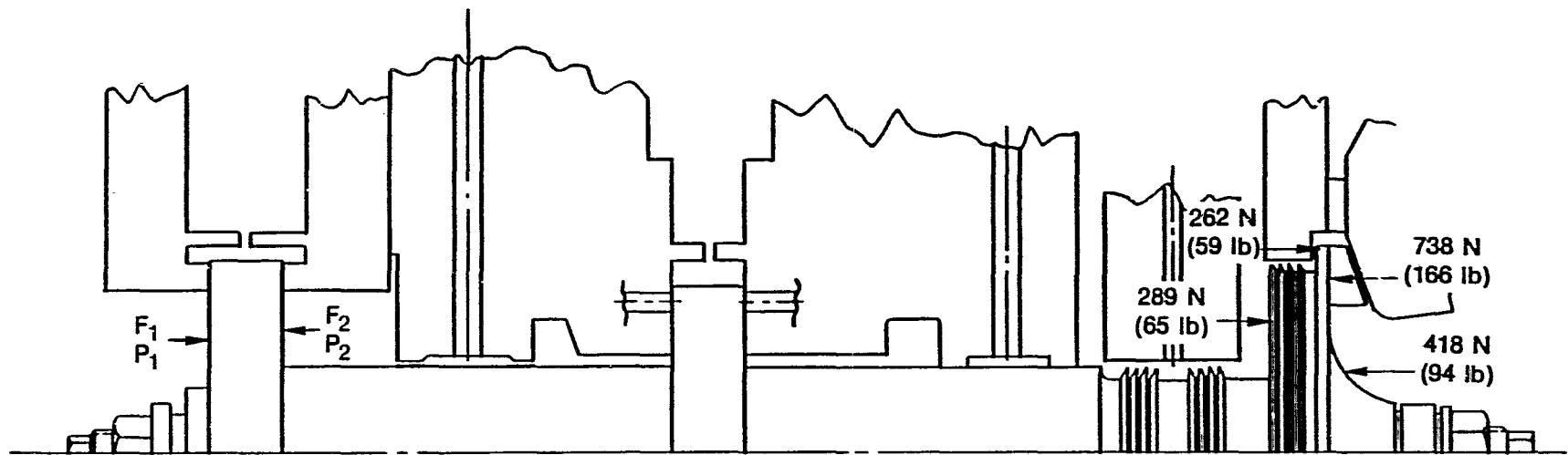
Fig. 6-14 Test Rig Journal Bearing Recess Geometry

822812-1



822762

Fig. 6-15 Test Rig Thrust Bearing Recess Geometry



$P_1 = 517 \text{ kPa, abs (75 psia)}$ $F_1 = 1490 \text{ N (335 lb)}$
 $P_2 = 517 \text{ kPa, abs (75 psia)}$ $F_2 = 1125 \text{ N (253 lb)}$
 Net Thrust = 236 N (53 lb)

$P_1 = 103 \text{ kPa, abs (15 psia)}$ $F_1 = 552 \text{ N (124 lb)}$
 $P_2 = 517 \text{ kPa, abs (75 psia)}$ $F_2 = 1156 \text{ N (260 lb)}$
 Net Thrust = 605 N (136 lb)

Fig. 6-16 Test Rig Thrust Loading

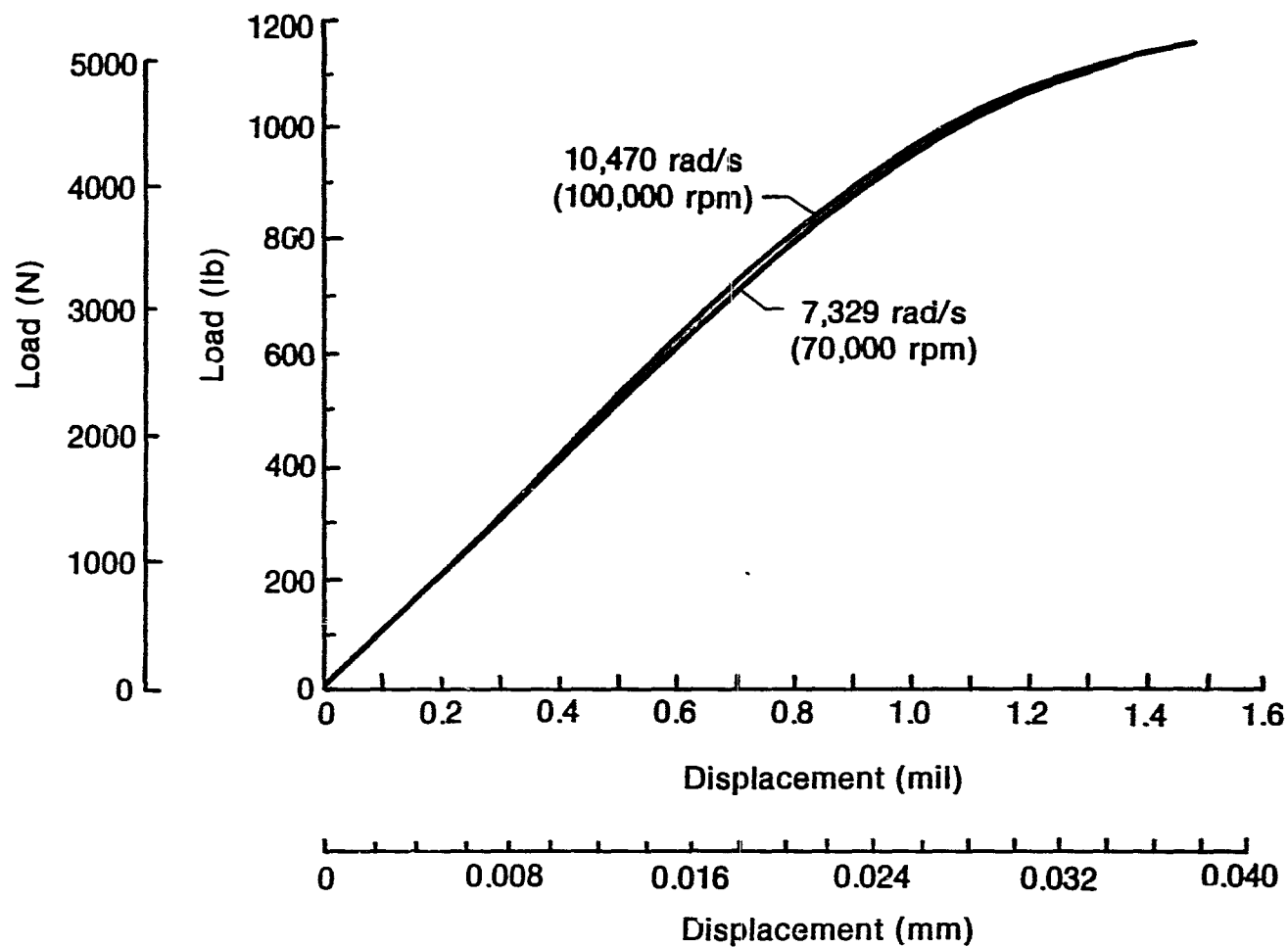


Fig. 6-17 Thrust Bearing Load Capacity versus Displacement

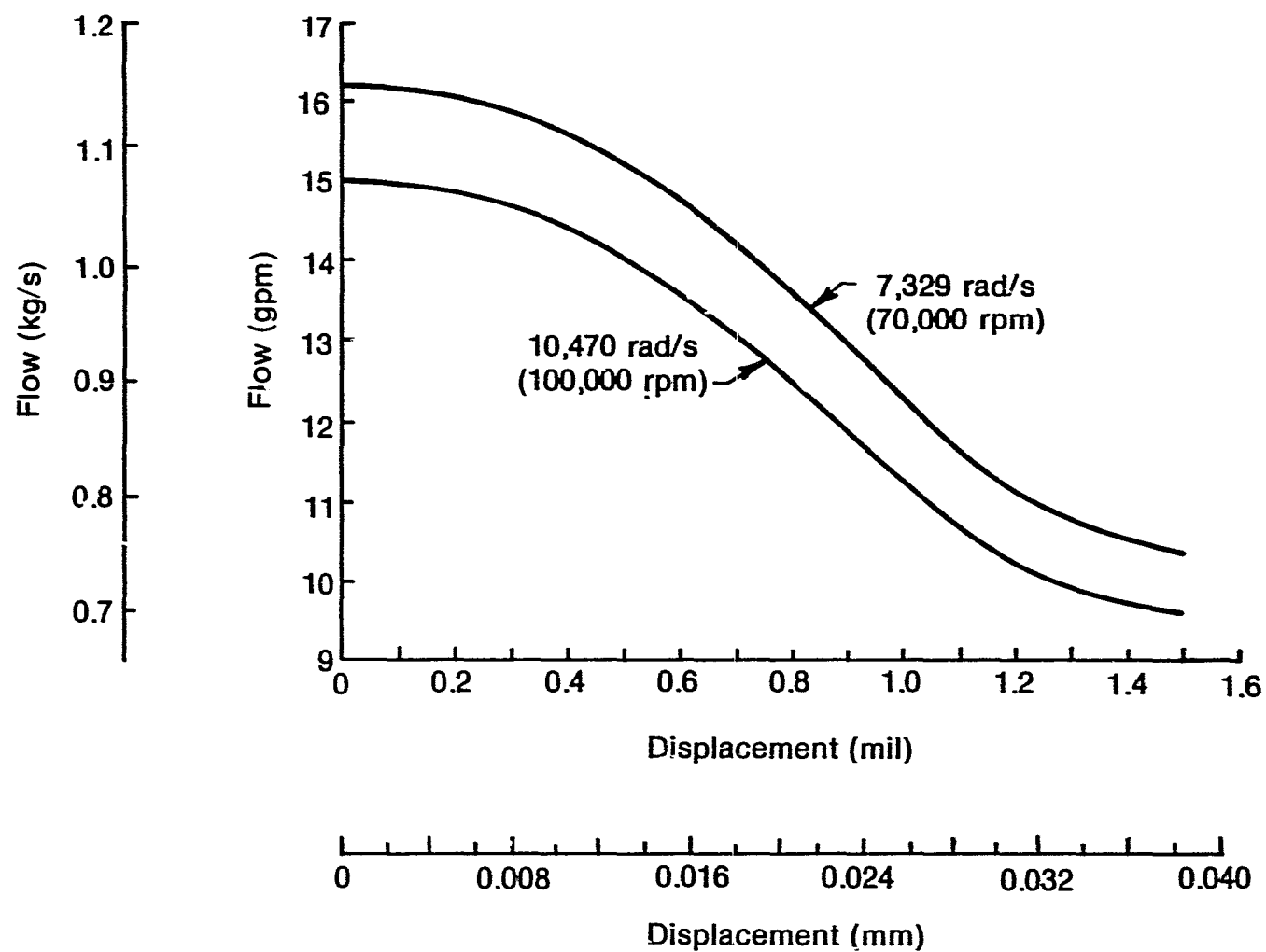


Fig. 6-18 Thrust Bearing Flow versus Displacement

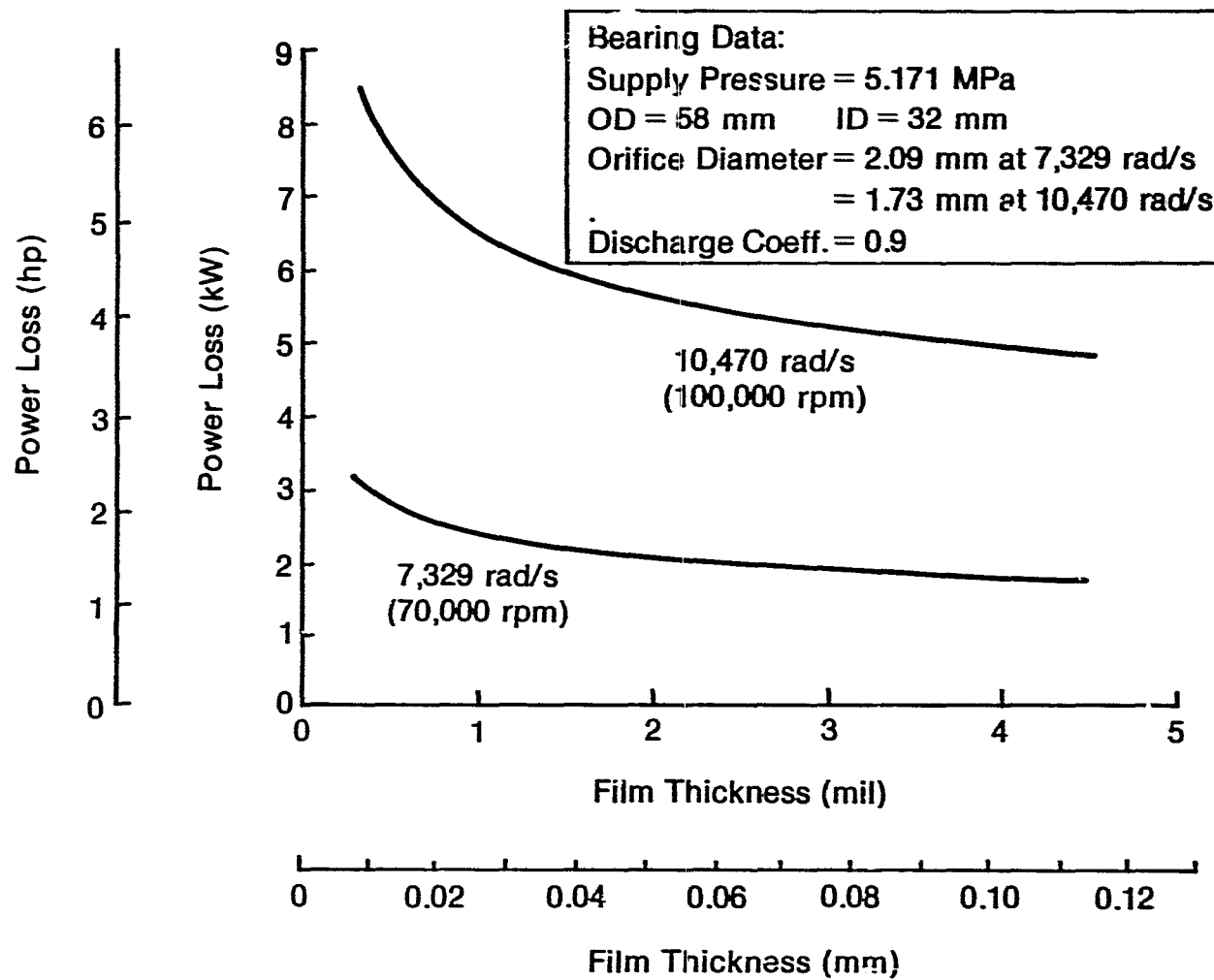


Fig. 6-19 Thrust Bearing Power Loss - Single Side

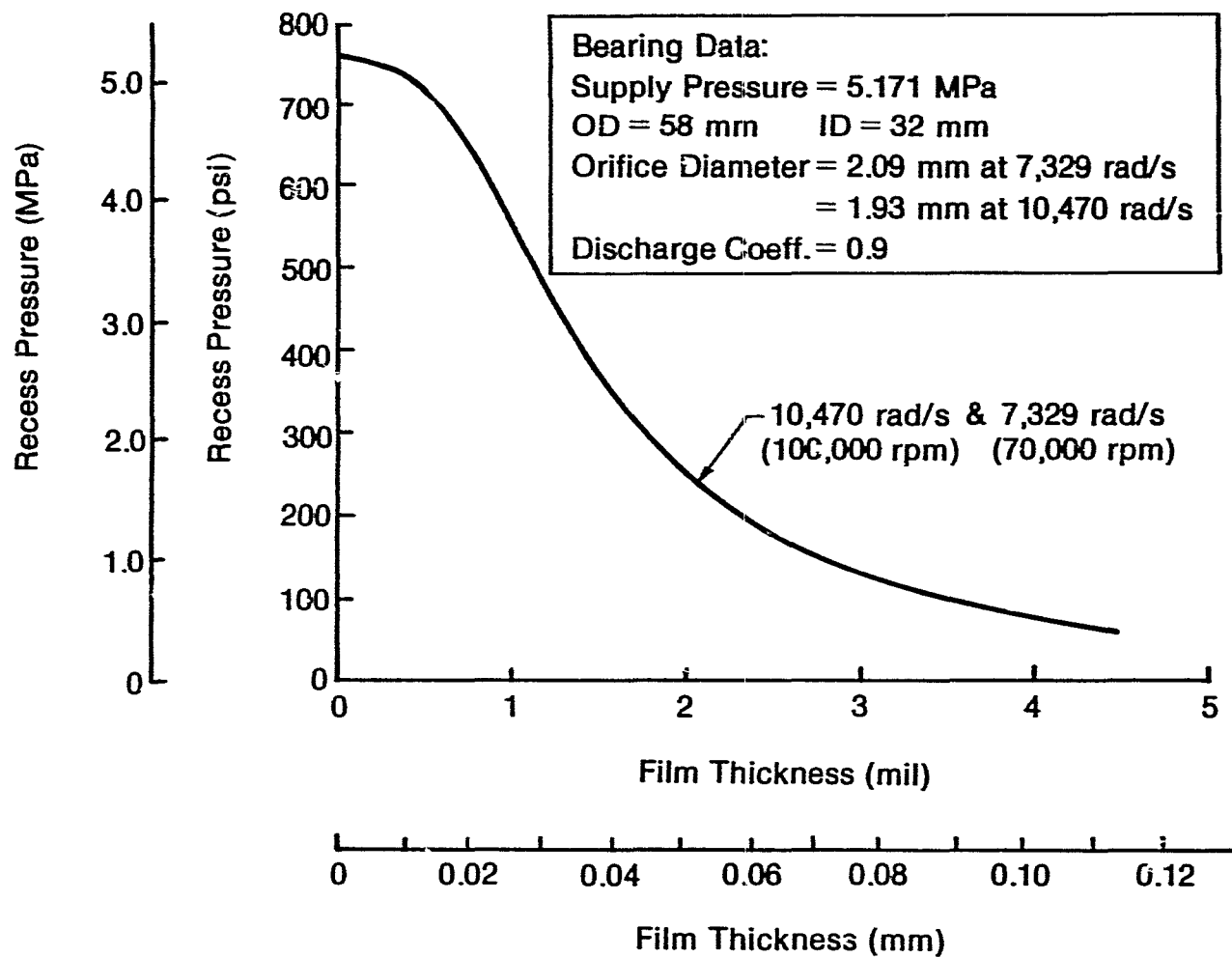


Fig. 6-20 Thrust Bearing Recess Pressure

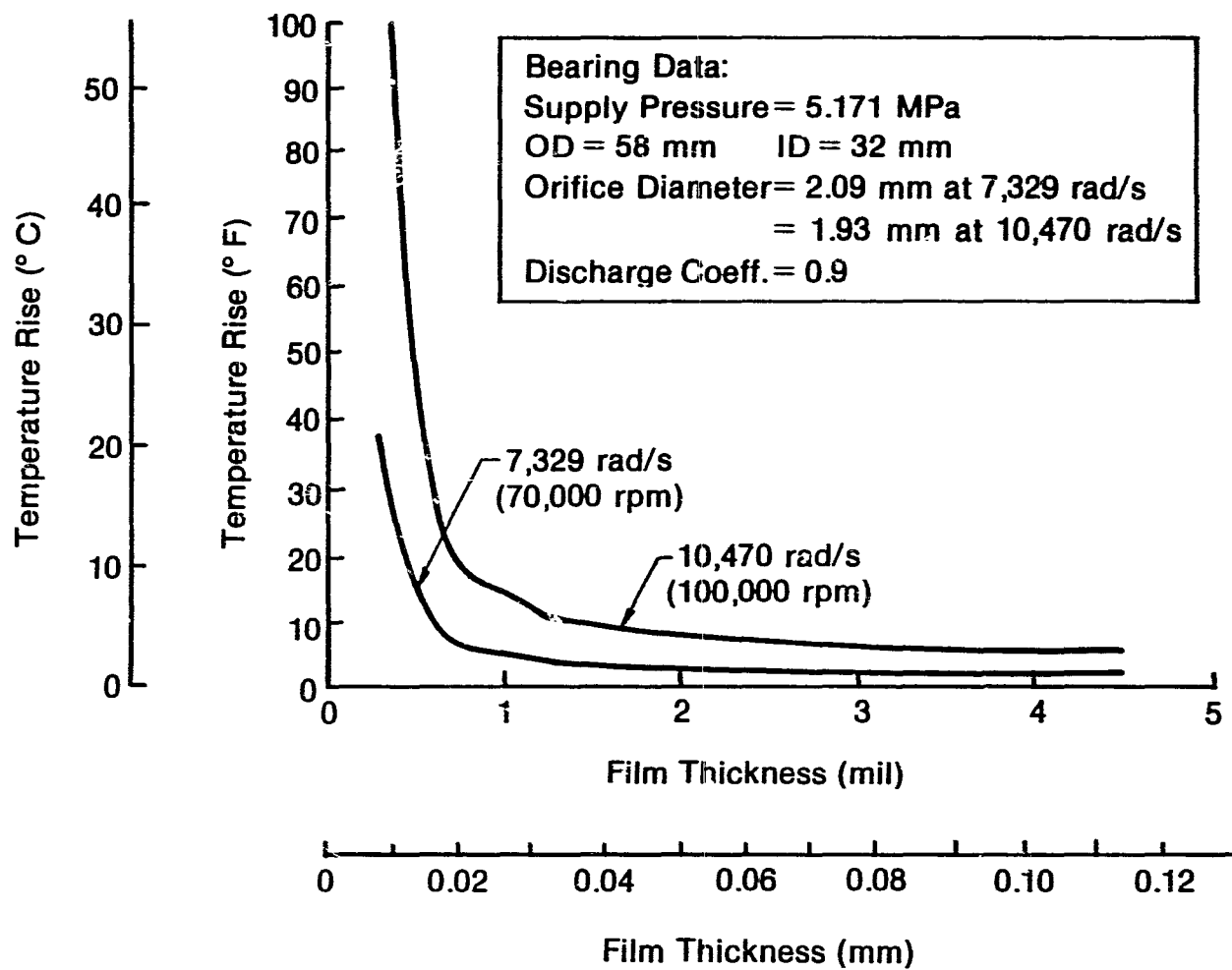


Fig. 6-21 Thrust Bearing Temperature Rise versus Film Thickness

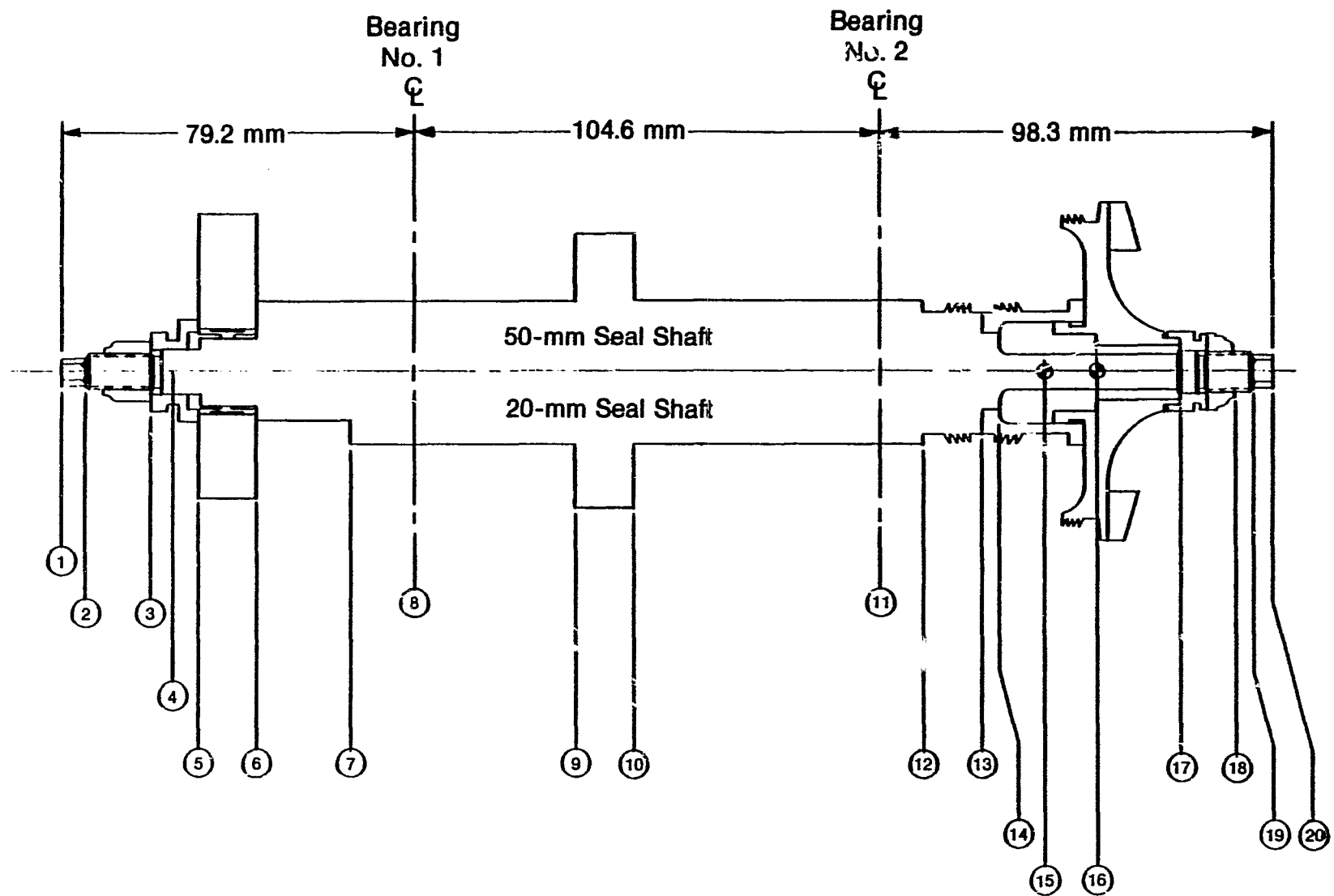


Fig. 6-22 Rotordynamics Model of Test Rig

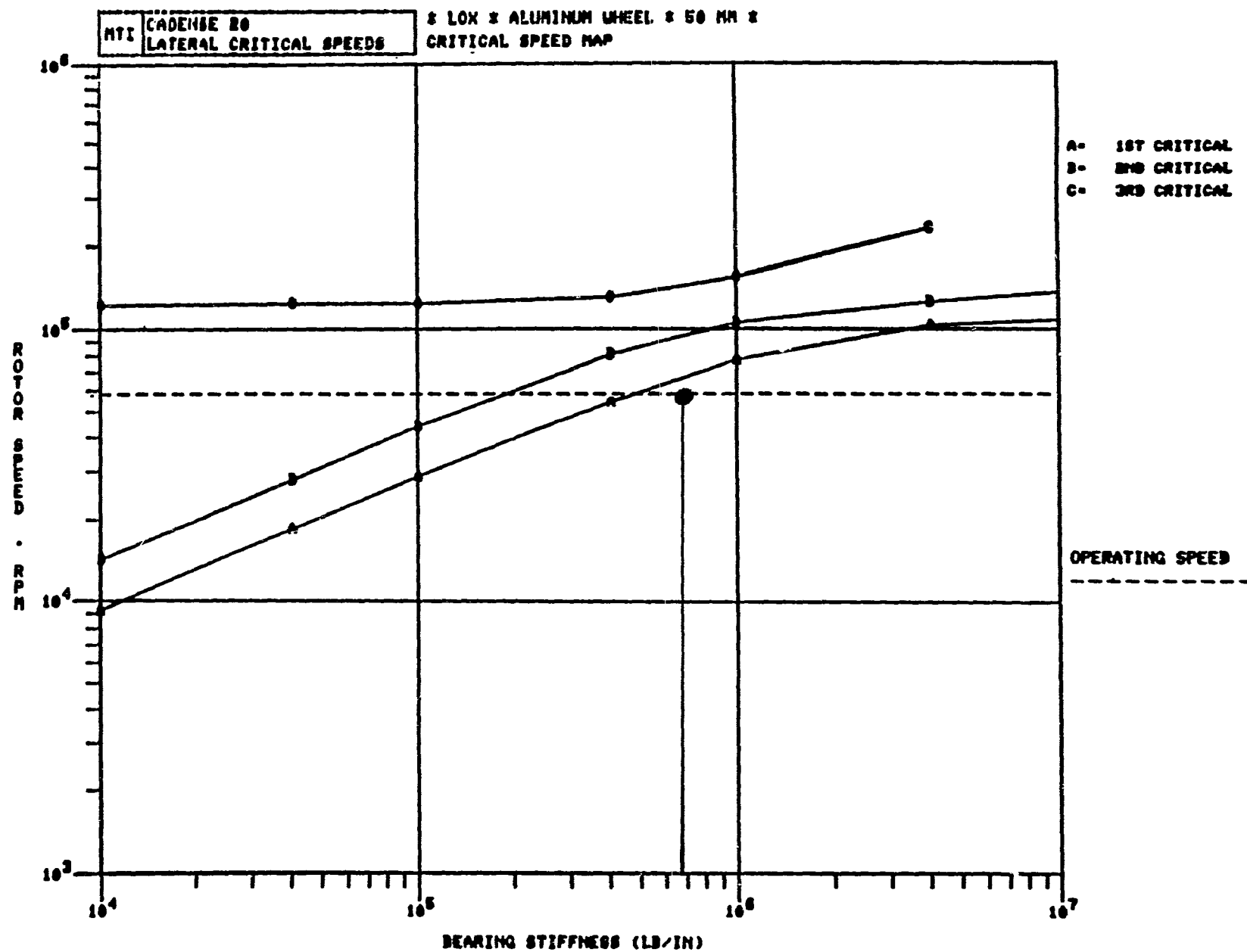


Fig. 6-23 Undamped Critical Speed Map - 50-mm LOX Seal Shaft

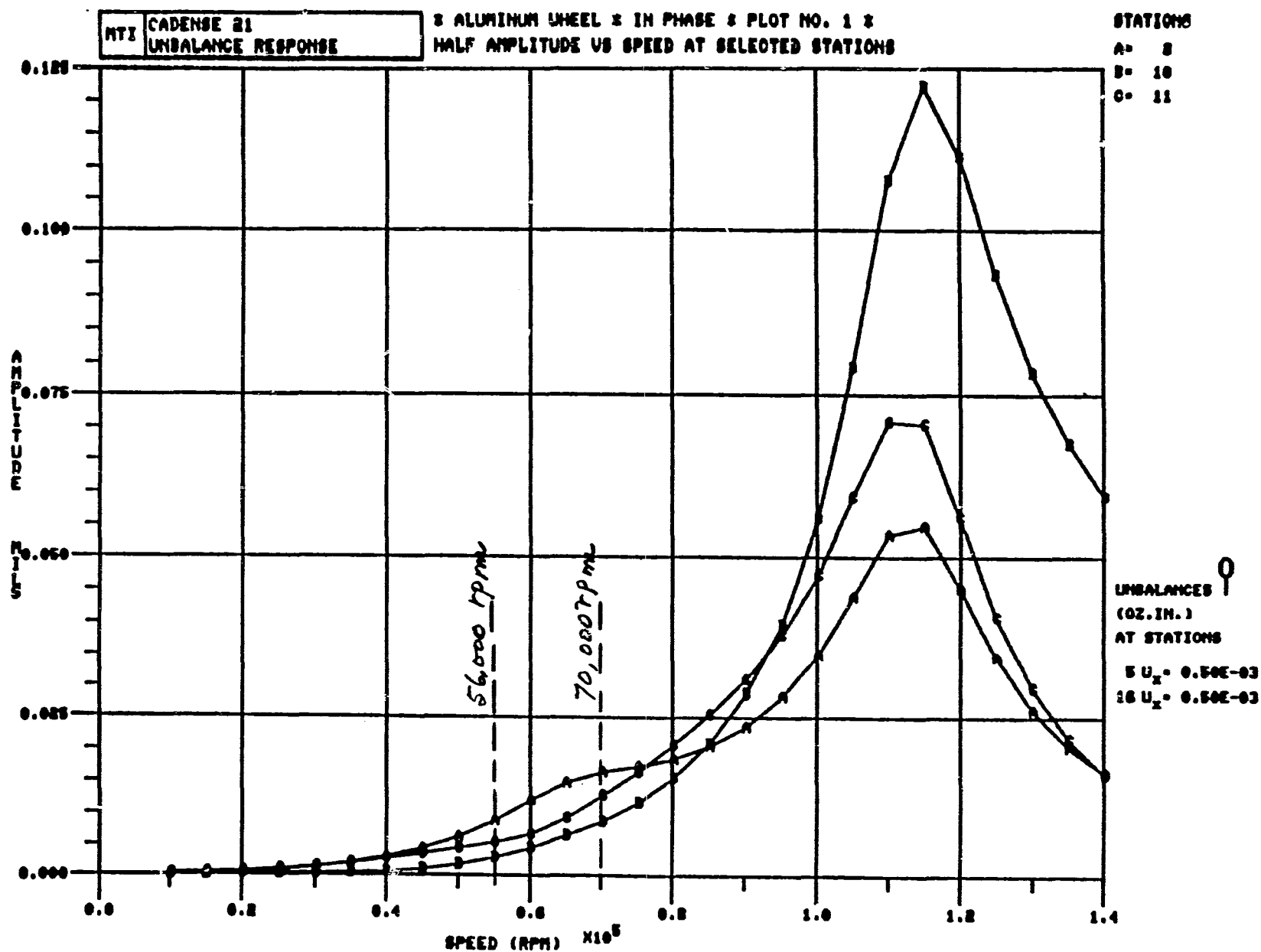


Fig. 6-24 Half Amplitude Response, Stations 8, 10, 11; In-Phase Unbalance, $C = 0.0191$ mm

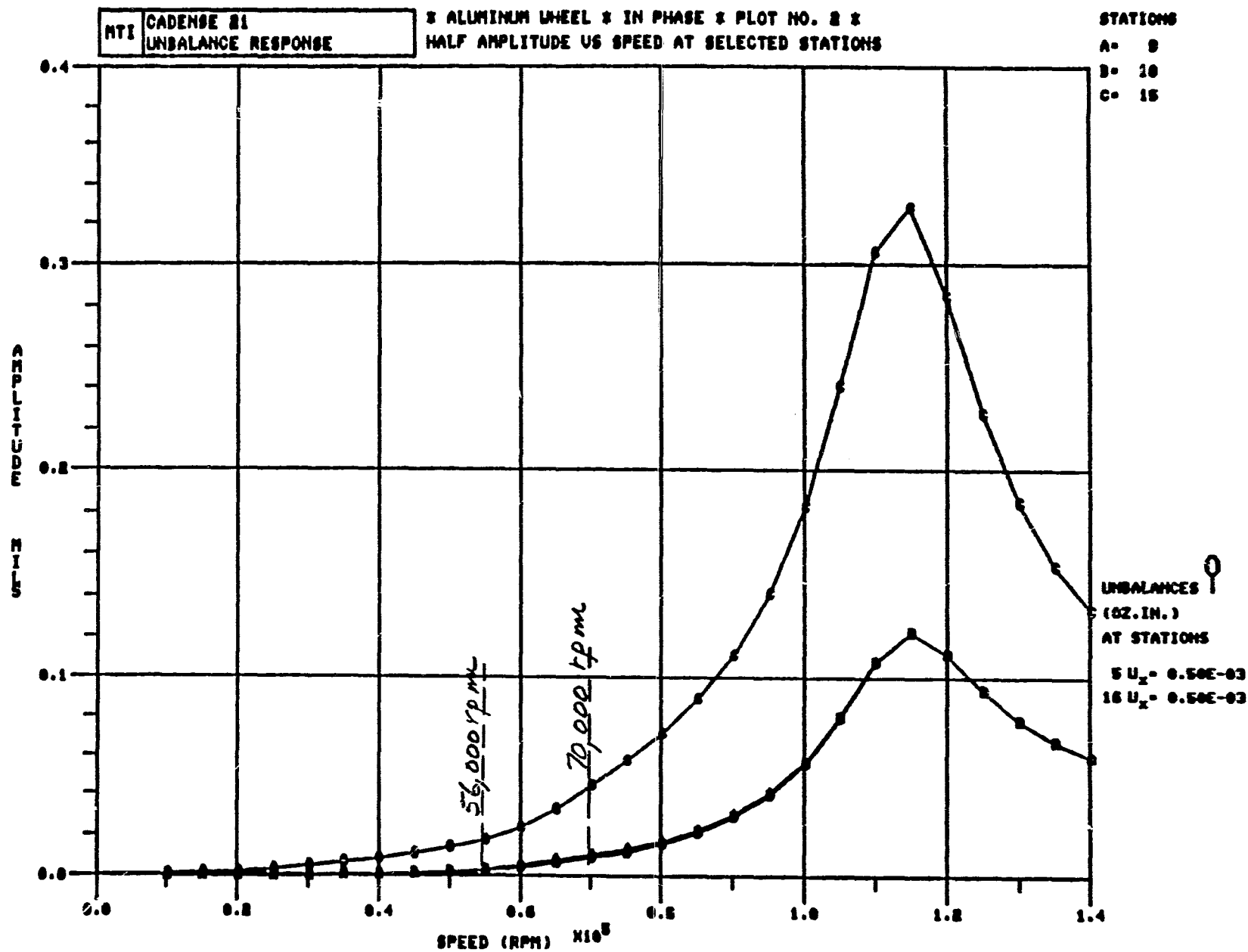


Fig. 6-25 50-mm Seal Half-Amplitude Response, Stations 9, 10, 15; In-Phase Unbalance, $C = 0.0191$ mm

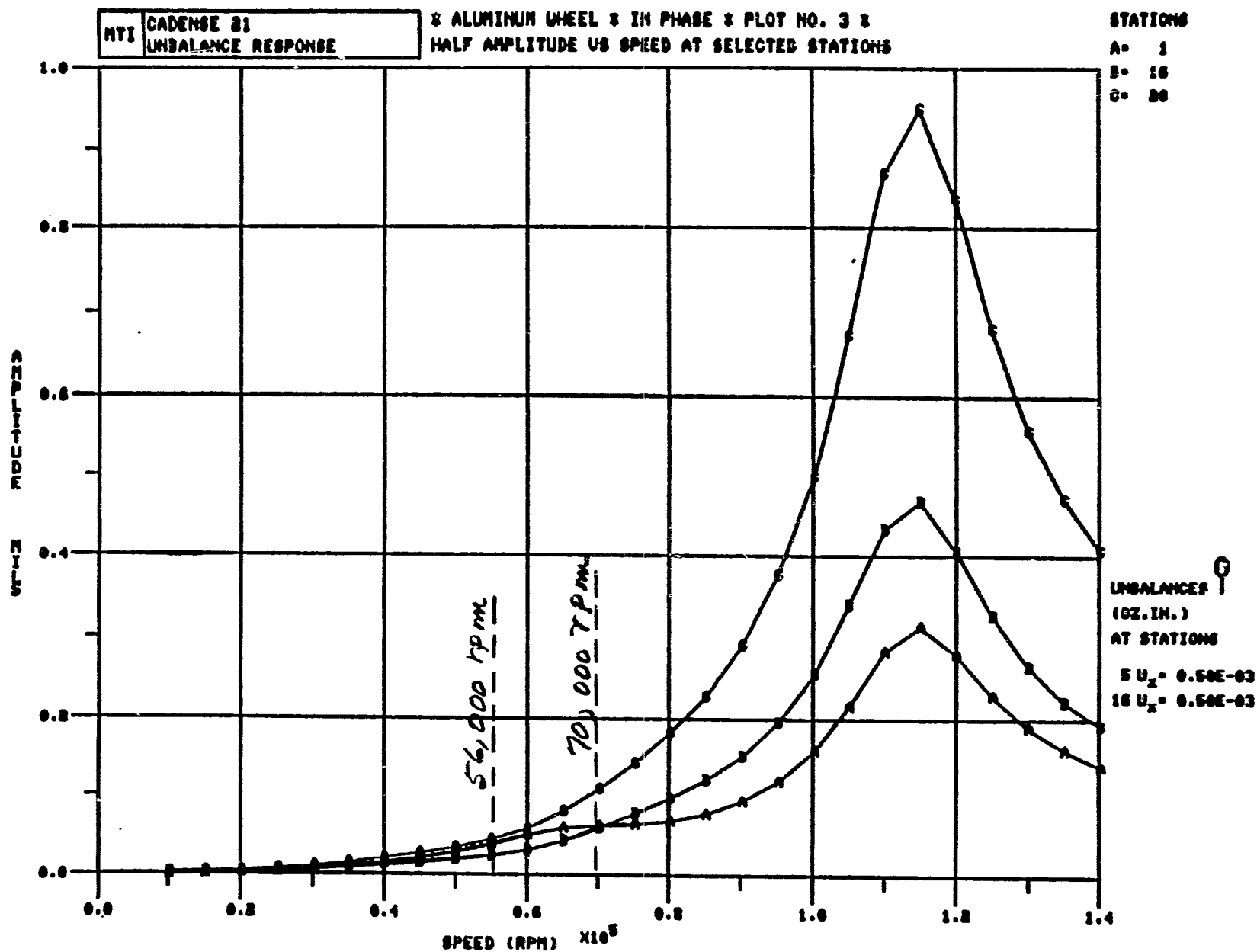


Fig. 6-26 50-mm Seal Half-Amplitude Response, Stations 1, 16, 20; In-Phase Unbalance, $C = 0.0191$ mm

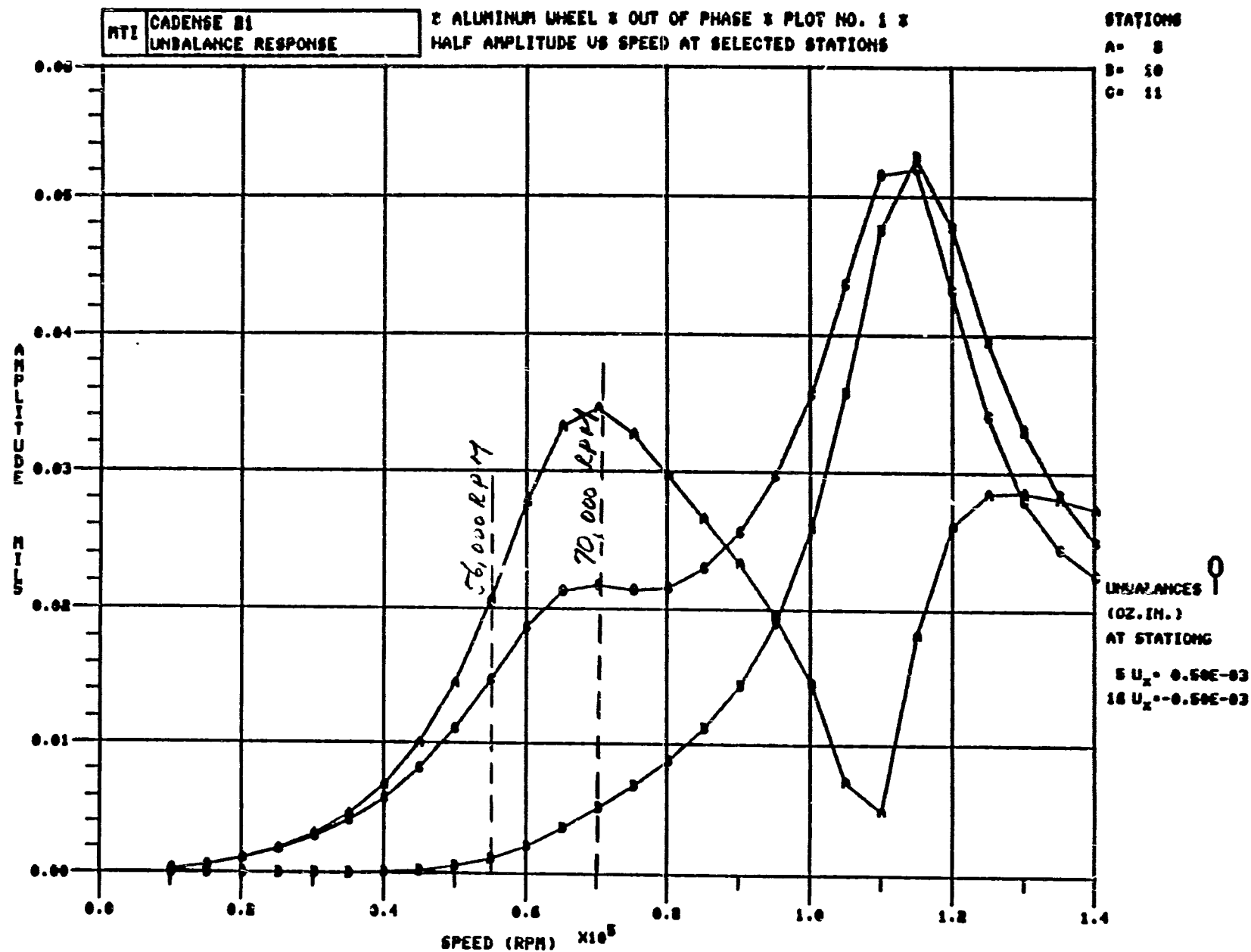


Fig. 6-27 50-mm Seal Half-Amplitude Response, Stations 8, 10, 11; Out-of-Phase Unbalance, $C = 0.0191$ mm

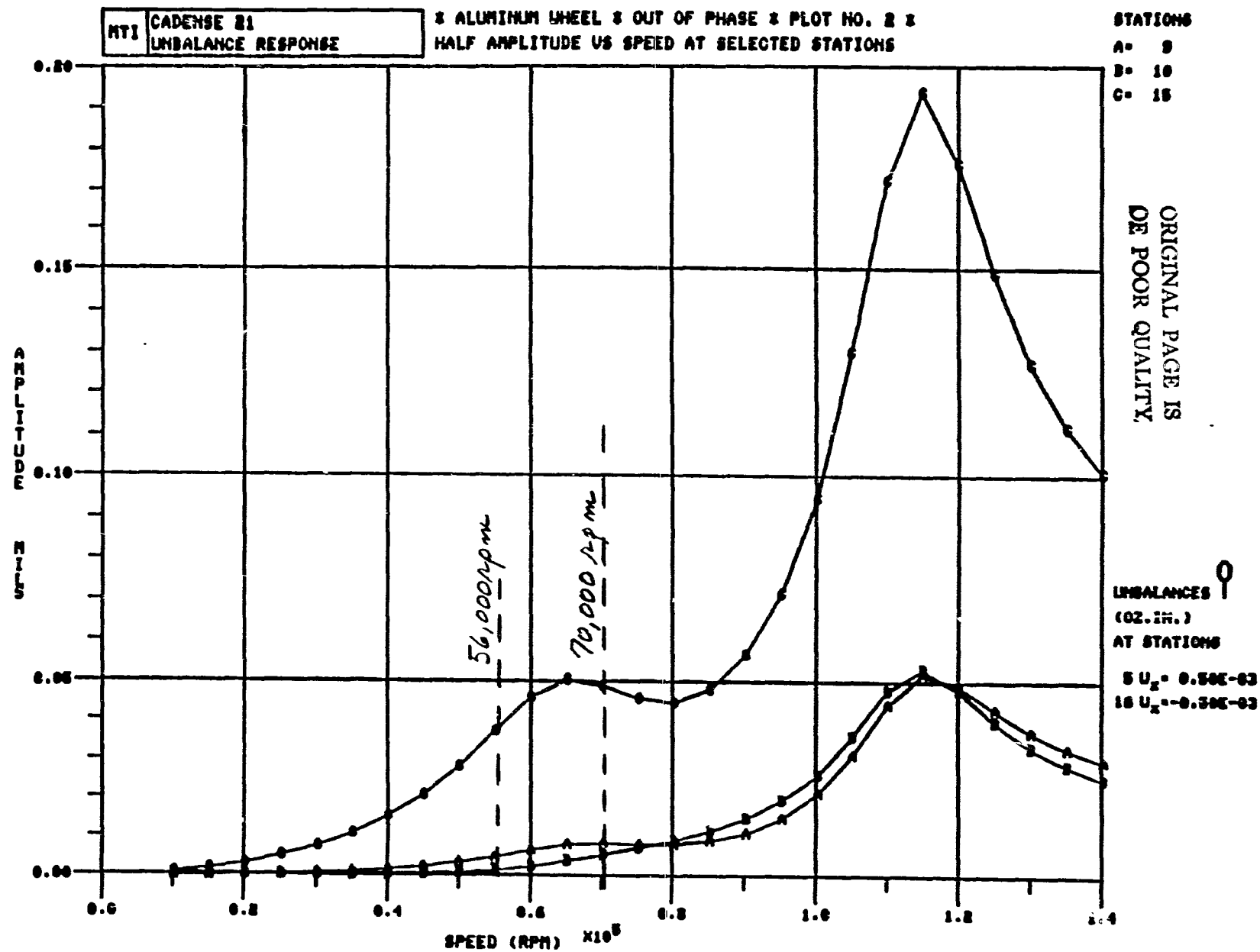


Fig. 6-28 50-mm Seal Half-Amplitude Response, Stations 9, 10, 15; Out-of-Phase Unbalance, $C = 0.019i$ mm

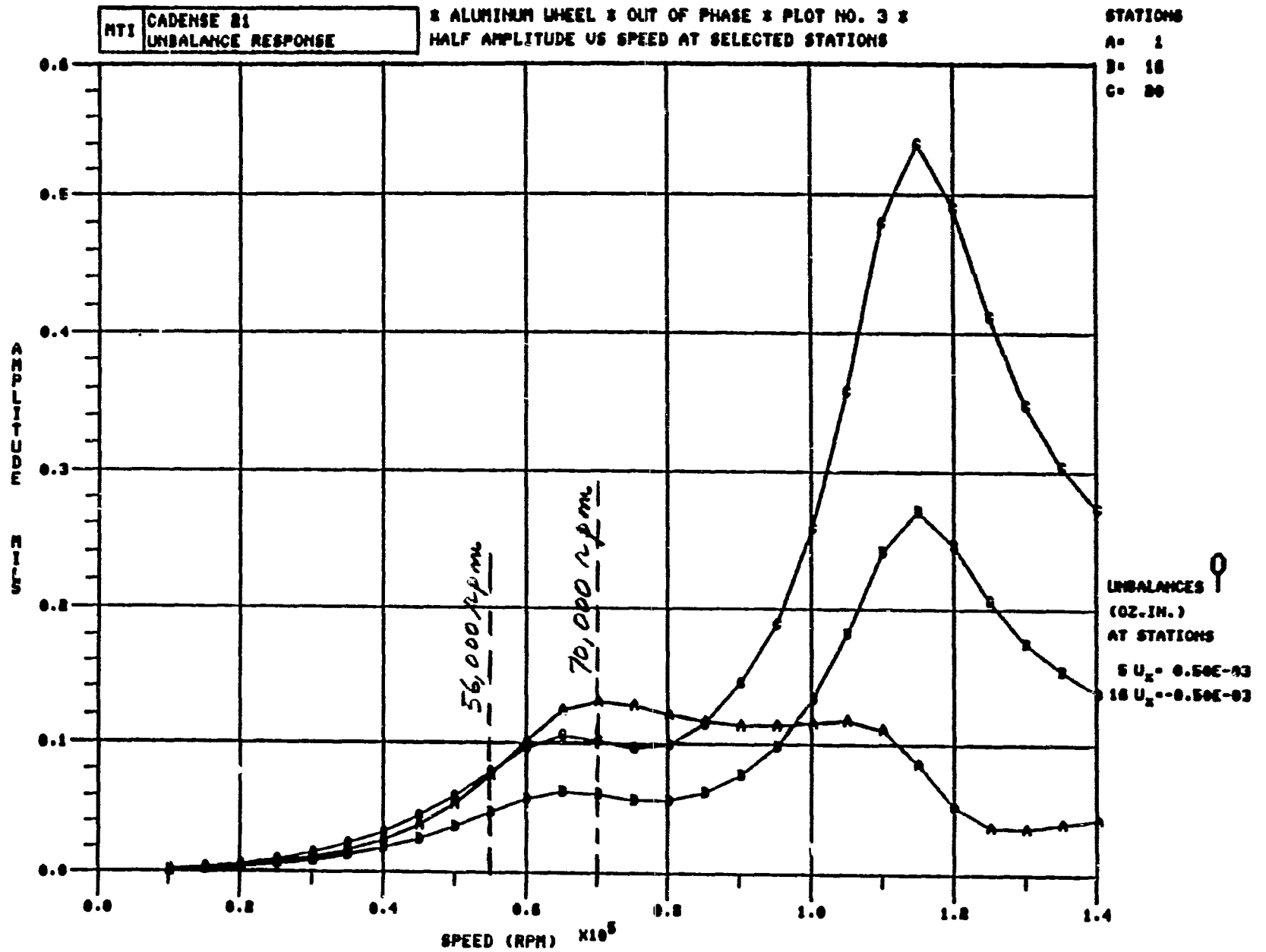


Fig. 6-29 50-mm Seal Half-Amplitude Response, Stations 1, 16, 20; Out-of-Phase Unbalance, $C = 0.0191$ mm

TEMPERATURE DISTRIBUTION (° C) **6,280 rad/s, 50-mm SPIRAL GROOVE SEAL**

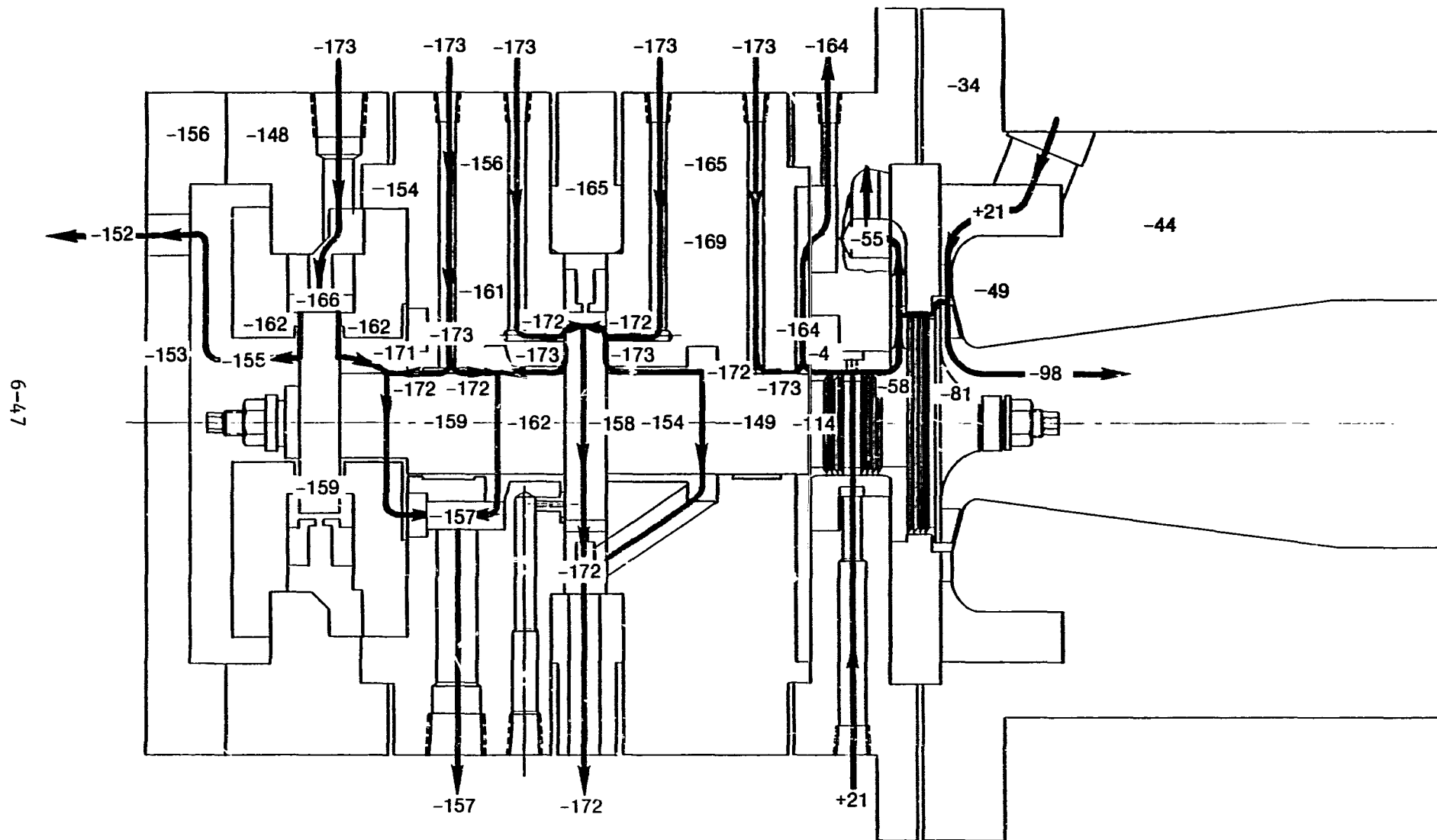


Fig. 6-30 LOX Seal Test Rig

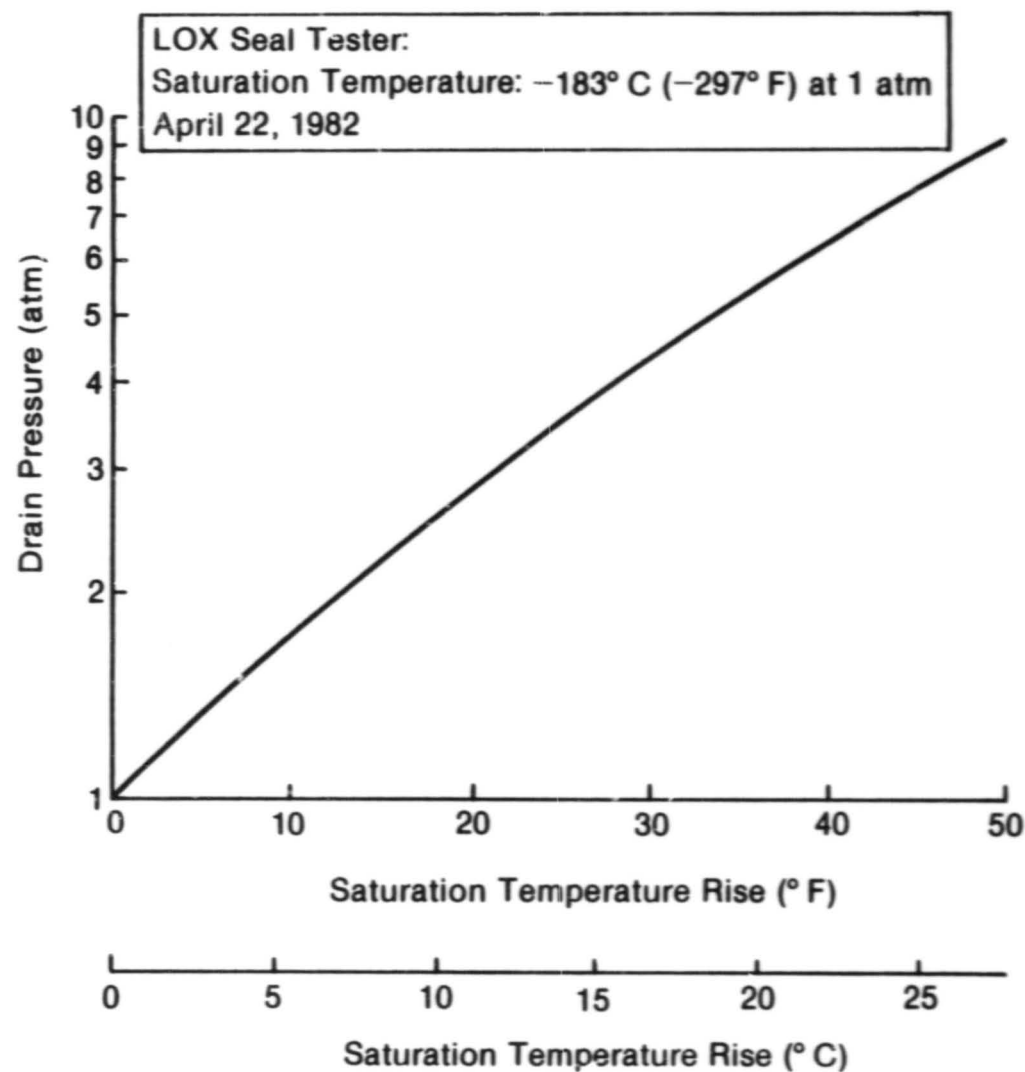


Fig. 6-31 Test Rig Drain Pressure versus Saturation Temperature

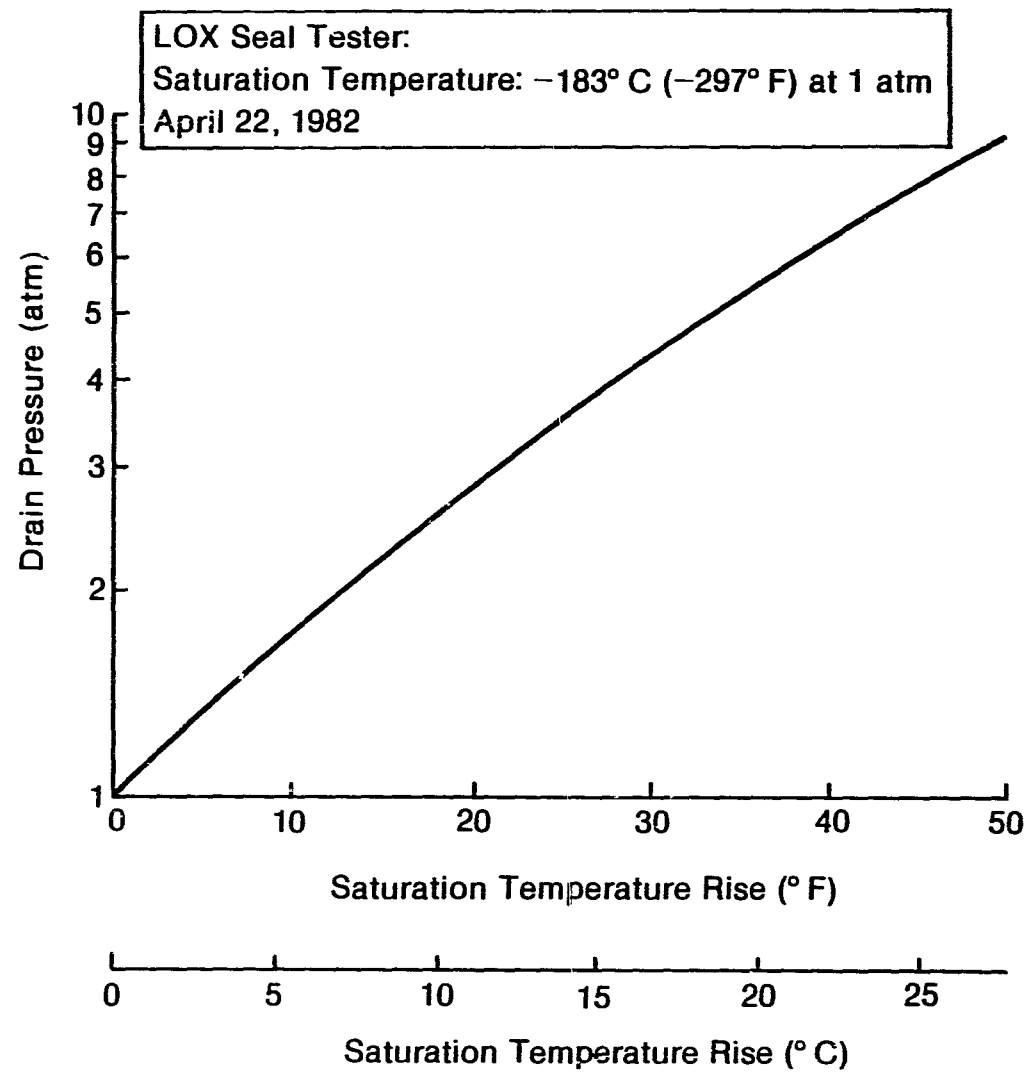


Fig. 6-31 Test Rig Drain Pressure versus Saturation Temperature

TABLE 6-1

SUMMARY OF CONCENTRIC JOURNAL BEARING PERFORMANCE

Liquid	LOX	LOX	LOX	LOX	LN ₂	LN ₂
N, Speed, rad/s	10,470	7,329	7,329	10,470	7,329	10,470
P _s , Supply Pressure, kPa	5,171	5,171	5,171	5,171	5,171	5,171
C, Radial Clearance, mm	0.0191	0.0191	0.0254	0.0254	0.0254	0.0254
d _o , Orifice Diameter, mm	0.711	0.762	0.965	0.965	0.965	0.965
P _R , Recess Pressure, kPa	2,620	2,592	2,613	2,627	2,551	2,813
Q, Flow, kg/s	0.111	0.132	0.222	0.191	0.190	0.180
hp, Power Loss, kW	2.20	0.82	0.77	2.07	0.58	1.56
K _{xx} , Stiffness, mN/m	121.9	117.9	82.7	86.3	83.7	87.0
K _{yy} ,						
K _{xy} , Cross-Coupled Stiffness, mN/m	111.4	64.6	38.0	64.1	35.4	48.5
K _{yx} ,						
D _{xx} , Damping, mN-s/m	21.2	17.7	10.3	12.1	9.6	9.3
D _{yy} ,						
ΔT, Temperature Rise, °C	12.53	3.93	2.18	6.82	1.35	3.82
M _c , Critical Mass, kg	4.45	8.78	6.17	3.15	9.98	3.17

TABLE 6-2

SUMMARY OF THRUST BEARING PERFORMANCE(7329 rad/s; Orifice (d_o) = 1.61 mm)

<u>Clearance</u> (mm)	<u>Force</u> (N)	<u>Flow</u> (kg/s)	<u>Losses</u> (kW)	<u>Temperature</u> (°C)	<u>Pocket</u> <u>Pressure</u> (kPa)
<u>LOX</u>					
0.114	429.6	0.786	1.32	1.03	430
0.0762	915.0	0.744	1.43	1.18	910
0.0666	1155.1	0.724	1.46	1.24	1144
0.0572	1490.1	0.694	1.51	1.34	1472
0.0476	1968.2	0.650	1.57	1.48	1932
0.0381	2659.2	0.580	1.64	1.73	2585
0.0305	3405.3	0.497	1.72	2.12	3272
0.0229	4301.2	0.381	1.83	2.95	4059
0.0152	5200.9	0.228	2.00	5.39	4772
0.0076	5821.8	0.069	2.36	21.0	5134
<u>LN₂</u>					
0.114	414.9	0.665	0.98	0.75	418
0.0762	884.6	0.632	1.06	0.85	891
0.0666	1117.5	0.614	1.09	0.90	1114
0.0572	1444.5	0.590	1.12	0.97	1434
0.0476	1919.23	0.552	1.17	1.07	1893
0.0381	2603.7	0.495	1.22	1.26	2543
0.0305	3344.8	0.425	1.28	1.53	3228
0.0229	4245.5	0.327	1.37	2.13	4023
0.0152	5166.7	0.197	1.51	3.88	4754
0.0076	5808.0	0.061	1.79	14.99	5131

TABLE 6-3

SUMMARY OF THRUST BEARING PERFORMANCE(10,470 rad/s; Orifice ($d_o = 1.55$ mm)

<u>Clearance</u> (mm)	<u>Force</u> (N)	<u>Flow</u> (kg/s)	<u>Losses</u> (kW)	<u>Temperature</u> (°C)	<u>Pocket</u> <u>Pressure</u> (kPa)
<u>LOX</u>					
0.114	425.2	0.727	3.61	3.04	417
0.0762	914.2	0.690	3.89	3.46	891
0.0666	1158.7	0.671	3.99	3.65	1126
0.0572	1502.8	0.642	4.10	3.92	1455
0.0476	1996.6	0.601	4.25	4.35	1922
0.0381	2709.2	0.536	4.44	5.09	2585
0.0305	3479.2	0.458	4.65	6.24	3285
0.0229	4404.0	0.347	4.93	8.74	4090
0.0152	5307.6	0.202	5.38	16.40	4805
0.0076	5868.9	0.057	6.30	68.25	5142
<u>LN₂</u>					
0.114	406.3	0.615	2.67	2.20	402
0.0762	875.9	0.585	2.88	2.50	859
0.0666	1111.3	0.569	2.96	2.64	1087
0.0572	1443.5	0.547	3.05	2.83	1406
0.0476	1922.6	0.512	3.16	3.13	1862
0.0381	2619.2	0.455	3.31	3.66	2514
0.0305	3380.9	0.394	3.47	4.46	3211
0.0229	4312.1	0.301	3.69	6.20	4026
0.0152	5248.9	0.178	4.04	11.52	4773
0.0076	5855.8	0.051	4.77	47.81	5138

TABLE 6-4

50-MM LOX SEAL ROTOR PARAMETERS

NMAT NGYRO JOFF IUNITS ISCAL IPREC
 1 1 50 0 0 0

MAT YOUNGS MOD. DENSITY SHEAR MOD.
 NG. (LB/IN**2) (LB/IN**3) (LB/IN**2)
 1 3.1300D+07 2.960D-01 9.4000D+06

ROTOR DATA

STAT NO.	MASS (LBS)	IP (LB-IN**2)	IT (LB-IN**2)	LENGTH (IN)	STIFF. DIA.	MASS DIA.	INNER DIA.	YOUNGS (LB/IN**2)	MOD. DENSITY (LB/IN**3)	SHEAR MOD. (LB/IN**2)
1	0.0	0.0	0.0	0.200	0.314	0.313	0.0	3.1300D+07	2.960D-01	9.400D+06
2	0.0	0.0	0.0	0.570	0.343	0.650	0.0	3.1300D+07	2.960D-01	9.400D+06
3	0.0	0.0	0.0	0.250	0.500	0.500	0.0	3.1300D+07	2.960D-01	9.400D+06
4	5.200D-02	9.9000D-03	5.5000D-03	0.190	0.500	0.500	0.0	3.1300D+07	2.960D-01	9.400D+06
5	0.0	0.0	0.0	0.500	0.590	3.150	0.0	3.1300D+07	2.960D-01	9.400D+06
6	0.0	0.0	0.0	0.875	1.180	1.180	0.0	3.1300D+07	2.960D-01	9.400D+06
7	0.0	0.0	0.0	0.437	1.180	1.180	0.0	3.1300D+07	2.960D-01	9.400D+06
8	0.0	0.0	0.0	1.650	1.180	1.180	0.0	3.1300D+07	2.960D-01	9.400D+06
9	0.0	0.0	0.0	0.640	1.180	2.400	0.0	3.1300D+07	2.960D-01	9.400D+06
10	0.0	0.0	0.0	1.875	1.180	1.180	0.0	3.1300D+07	2.960D-01	9.400D+06
11	0.0	0.0	0.0	0.640	1.180	1.180	0.0	3.1300D+07	2.960D-01	9.400D+06
12	0.0	0.0	0.0	0.500	1.060	1.060	0.0	3.1300D+07	2.960D-01	9.400D+06
13	0.0	0.0	0.0	0.110	0.670	0.670	0.0	3.1300D+07	2.960D-01	9.400D+06
14	0.0	0.0	0.0	0.380	0.670	0.670	0.0	3.1300D+07	2.960D-01	9.400D+06
15	1.020D-01	2.2000D-02	1.8000D-02	0.490	0.670	0.300	0.0	3.1300D+07	2.960D-01	9.400D+06
16	1.870D-01	1.6100D-01	8.6000D-02	0.750	0.670	0.300	0.0	3.1300D+07	2.960D-01	9.400D+06
17	0.0	0.0	0.0	0.450	0.670	0.670	0.0	3.1300D+07	2.960D-01	9.400D+06
18	0.0	0.0	0.0	0.150	0.375	0.375	0.0	3.1300D+07	2.960D-01	9.400D+06
19	0.0	0.0	0.0	0.190	0.281	0.281	0.0	3.1300D+07	2.960D-01	9.400D+06
20	0.0	0.0	0.0	0.0	0.0	0.0	0.0	3.1300D+07	2.960D-01	9.400D+06

BEARING STATIONS

8 11

30 MM SHAFT, 70000 RPM, C = .75 MILS, ALUMINUM TURBINE WHEEL

* ROTOR PARAMETERS *

WEIGHT OF SHAFT.....	2.97644
WEIGHT OF DISCS.....	1.77200
WEIGHT OF ROTOR.....	4.74844
SHAFT LENGTH.....	10.62500
LOCATION OF C.G.....	4.37356

Seal Runner

$$I_p = 1.488 \text{ lb-in}^2$$


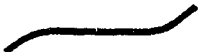



$$I_t = 2.125 \text{ lb-in}^2$$

Thrust Runner

$$I_p = 0.401 \text{ lb-in}^2$$

$$I_t = 0.201 \text{ lb-in}^2$$

TABLE 6-5
50-MM LOX SEAL STABILITY ANALYSIS

<u>Mode</u>	<u>Growth Factor</u>	<u>Frequency rad/s (RPM)</u>	<u>Shape</u>	<u>Comments</u>
1	-1139	6,385 (60,983)		Conical Rigid Body
2	-2247	7,966 (76,082)		
3	- 980	8,472 (80,921)		Some Bending
4	-4863	8,978 (85,748)		Lateral Rigid Body
5	-1028	9,995 (95,459)		Bending Mode

7.0 TEST FACILITY

The helium seal testing was performed at Wyle Laboratory in Norco, California. Figures 7-1*, 7-2, and 7-3, provide several views of the test facility while Figures 7-4 and 7-5 are close-ups showing the tester installation. An overall view of the control room is shown in Figure 7-6. The system control panel is depicted in Figure 7-7.

The sections that follow provide a detailed description of the test facility including:

- Fluid Supply Systems
- Facility Controls
- Instrumentation.

7.1 Fluid Supply Systems

Figure 7-8 is a simplified piping schematic of the fluid supply systems. The three major fluid systems supply gaseous helium to the buffer seals, liquid nitrogen to the tester bearings, and gaseous nitrogen to the tester drive turbine. Two additional systems supply gaseous helium to labyrinth buffer seals and gaseous nitrogen purges to the major fluid systems at various points.

7.1.1 Helium Seal Supply System

Gaseous helium is supplied to the facility from a 1550 m³ (55,000 scfm) tank trailer at pressures ranging from 3.45 to 17.24 MPa (500 to 2500 psig). A line from the tank trailer connects to a tank located near the tester.

The helium flow to the tester then passes through a 10 micron (nominal) line filter and then through a dome loader regulator valve (40). This reduces and controls the pressure of the helium to the range of 0 to 1724 kPa absolute (0

*Figures are presented consecutively, beginning on page 7-15.

to 250 psia). Control pressure to the dome loader is adjusted using a motorized regulator remotely operated from the control room.

The flow then passes through a calibrated Venturi flowmeter. Pressure (P5) and temperature (T5) are measured at the inlet to the Venturi as is the pressure drop from the inlet to the throat of the Venturi (P20). These allow accurate measurement of the helium supply flow. The helium then goes to a manifold near the tester where the seal supply pressure (P12) is measured.

The flow then splits into two lines and enters the tester (C9 A & B). In the tester, the flow again splits with some of the helium passing through the inboard seal ring and some through the outboard seal ring. The former joins with the bearing drain flow. The latter enters the outboard seal drain cavity and passes out through drain ports (C10 A, B, C).

Pressure (P2) and temperature (T2) are measured in the drain line providing both seal drain conditions and inlet conditions for a second Venturi flowmeter located immediately downstream. The pressure drop across the Venturi (P18) is measured providing a record of the flow through the outboard seal. The inboard seal flow is derived and is equal to the supply flow minus the outboard seal flow.

The helium drain flow then passes through a pneumatically actuated pressure control valve (8) and is vented to atmosphere through a standpipe. The control valve is used to set the drain pressure between 0 and 517 kPa absolute (75 psia), the latter being the nominal pressure of the bearing drain and hence the inboard helium seal. The valve is controlled either by a differential controller using the bearing drain pressure (P3) as a reference or by directly controlling the pneumatic actuator with a remotely located hand regulator. The latter proved to be a more convenient method of incrementally reducing drain pressure during steady-state runs.

7.1.2 LN₂ Bearing Supply System

The LN₂ originates at an 41.6 m³ (11,000 gal) storage tank near the test site. Transfer pumps at the storage tank supply LN₂ through a vacuum jacketed line

to a 1.67 m^3 (440 gal) elevated run tank at the test site. The tank is equipped with an automatic level controller which operates the tank fill valve (17) and keeps the tank about 3/4 full during operation. A 76-mm (3-in.) vent maintains the run tank at near atmospheric pressure.

A line from the bottom of the tank goes to the pump fill valve (15) which connects to the suction of a single stage boost pump. The discharge of the boost pump connects both to the suction of the high pressure vari-drive pump and a motorized bypass valve (16) leading back to the run tank.

The vari-drive pump provides the high pressure LN_2 needed for operation of the hydrostatic thrust and journal bearings in the tester. It is motor driven through a variable speed mechanical transmission capable of operation from 314 to 1152 rad/s (3,000 to 11,000r/min). The pump is a two-stage centrifugal type capable of delivering 3.0 kg/s (60 gal/min) of LN_2 at pressures up to 6.894 MPa (1000 psig).

The output of the vari-drive pump flows through a check valve and a 10 micron (nominal) filter into the LN_2 manifold. The line is equipped with a burst disk designed to rupture at a pressure of 7.58 MPa (1100 psig) to prevent accidental overpressuring of the manifold.

Two air-actuated control valves (5 and 6) connect to the manifold and supply LN_2 to the hydrostatic thrust and journal bearings, respectively. These are shown in Figure 7-2. Each valve is equipped with a controller which automatically maintains a bearing supply pressure of 4.14 MPa (600 psig). A third air-actuated control valve (2) is installed in the LN_2 supply manifold and provides a bypass back to the run tank. It is controlled by a remotely operated, motorized regulator and set in conjunction with the speed of the vari-drive pump to provide a flow sufficient for the bearings.

Each of the two bearing supply valves is connected to a supply manifold next to the tester. These are shown in Figures 7-4 and 7-5. Eight lines connect each manifold with the corresponding supply ports on the tester: C3 A, B, C, D and C8 A, B, C, D for the journal bearings and C5 A, B, C, D and C6 A, B, C, D

for the thrust bearings. Each of the 16 lines is equipped with a 60-micron line filter to prevent bearing contamination.

The tester is equipped with three groups of bearing drains. These are shown in Figure 7-3. Lines from five thrust bearing drain ports (C13 A, B, C, D, E) and three seal end journal bearing drain ports (C14 A, B, C) connect to a common manifold. Drain pressure (P3) and temperature (T3) are then measured in the line which is connected to an air-actuated drain valve (10). The valve connects to a common return line to the run tank. The pressure upstream of the valve is automatically controlled to about 68.9 kPa (10 psi) above the saturation pressure of the fluid to prevent vaporization in the tester.

The third drain (C15 A, B, C) collects a mixture of LN₂ from the turbine-side journal bearing and the helium from the adjacent labyrinth buffer seal. The line is instrumented for pressure (P4) and temperature (T4) and connected to an air-actuated drain valve (11). As with the other drain line, pressure is maintained at about 68.9 kPa (10 psi) above saturation pressure.

7.1.3 GN₂ Turbine Supply System

High-pressure GN₂ is stored in a battery of tank trailers near the test site. A line from the trailers goes to a dome loader regulator (39) which reduces the GN₂ pressure to the range of 1724 to 2068 kPa (250 to 300 psig). A run tank downstream of the regulator provides a local capacity. This is followed by a 10-micron filter. The GN₂ flow then passes through two control valves (12 and 14), splits and enters the turbine through two diametrically opposed ports (C1 A, B). The turbine exhausts to atmosphere through a short tail piece.

The first valve (12) throttles the flow to maintain desired speed. It is pneumatically actuated and can be controlled in manual or automatic mode. The second valve (14) is an emergency shutdown valve. It is a fast-acting air solenoid type requiring air pressure to open. It is equipped with a spring which closes the valve on loss of air. Air pressure is supplied by a remotely operated electric solenoid valve designed to close on loss of power.

The emergency shutdown valve (14) is used to perform the high acceleration rate testing. To make a fast start, the speed control is switched to the manual mode and the diaphragm pressure of the speed control valve (12) adjusted to provide the correct start-up flow. The actual setting is determined by trial and error. Both tester overspeed trips are then lowered to slightly under the maximum speed desired for the acceleration run. The emergency shutdown valve is then manually energized. The valve quickly opens and the in-rush of gas rapidly accelerates the turbine. Upon reaching the maximum speed, the valve is closed by the overspeed trip and the tester coasts down.

7.1.4 Helium Supply to Labyrinth Seal

The labyrinth seals are supplied by the same tank trailer that supplies the helium seals. A separate line connects to the tank located near the tester. The line goes to a 10-micron filter, then to dome loader regulator (41). The downstream pressure is set to provide a 69 to 138 kPa (10 to 20 psi) pressure difference between the labyrinth supply and the adjacent journal bearing drain. This results in a typical labyrinth supply pressure of 517 to 586 kPa absolute (75 to 85 psia). A pressure sensor (P11) is installed in the line which connects to the tester at C16. Inside the tester, part of the flow goes toward the adjacent journal bearing and mixes with the LN₂ bearing flow. The combined fluids drain out through ports C15 A, B, C. (See Section 7.1.2.) The other part goes toward the turbine, joins with a small leakage flow from the turbine and exits the tester at ports C17 A, B, C, D. The connecting drain lines join at a manifold and vent to atmosphere.

The original design of the tester used GN₂ as the buffer gas for the labyrinth seal. It was found during checkout, however, that some of the GN₂ was condensing and forming puddles of LN₂ which ran into the turbine. The problem was solved by changing the buffer gas to helium which has a much lower condensation temperature.

7.1.5 GN₂ Purge

The facility contains four GN₂ purge lines. These were used before and after all tests to prevent moisture contamination. Purge gas is supplied by a

862 kPa (125 psia) GN₂ instrument manifold supplied by the high-pressure GN₂ tank trailers through a reducing regulator. The manifold is filtered with a 10-micron (nominal) filter. Each purge line is equipped with a regulator followed by a remotely operated electric solenoid valve and a check valve. This allows individual flow rates to be set and independent operation of each line. One purge line goes to the helium seal drain cavity and a second to the labyrinth seal supply line. A third line is connected to the LN₂ supply manifold while a fourth goes to the turbine inlet. The latter proved to be very important because of the open exhaust on the turbine.

7.2 Controls

Due to the hazardous nature of the testing (especially in the LOX mode), all fluid components requiring on/off operation or adjustment during operation of the facility are designed for remote or automatic control. In addition, various automatic shutdowns are incorporated in the controls.

Remote control is accomplished by on/off operation of a series of 12-V dc relays. The switches which energize the relays are in a panel in the control room which is shown in Figure 7-7. The relays reside in a terminal box at the test site and energize 110-V ac circuits.

All four purge valves (19, 20, 21, 22) and the drain controls air supply valve (18) are electric solenoid valves directly controlled by 110-V ac circuits. The pump fill (15), tank fill (17) and turbine trip (14) valves are air-operated solenoid valves. The air to operate the air solenoids is controlled by electric solenoid valves energized by the 110-V ac relays. For the boost pump and vari-drive pump, the 110-V ac relays operate 440-V ac motor starting circuits.

Control of the adjustable position valves and vari-drive speed control is accomplished using double-throw, momentary-contact, center-off switches. With the switch thrown in one direction, one of a pair of 12-V dc relays is energized. Thrown in the opposite direction the other relay is energized. One relay causes a gear motor to slowly rotate in one direction increasing a valve or motor speed setting while the other relay causes reverse rotation of

the same gear motor, decreasing the setting. For the vari-drive pump speed control is implemented by the gear motor changing belt pulley ratio in the transmission. The pump bypass valve (16) is adjusted by direct rotation of a ball valve. The LN₂ manifold bypass valve (2), helium seal supply regulator (25), labyrinth seal supply regulator (24), and turbine speed control (manual mode only) valve (12) are air-actuated devices whose settings are controlled indirectly by motorized regulators, themselves operated in the manner described.

Several emergency shutdowns are incorporated. Emergency shutdown of the tester is achieved by de-energizing the turbine trip solenoid. This can be done manually by a switch on the control panel or automatically by alarm modules operating on selected parameters. These include:

- Overspeed (S1)
- Overspeed (S2)
- High outboard seal surface temperature (T12)
- High inboard seal surface temperature (T13)
- High tester housing vibration - axial (X1)
- High tester housing vibration - radial (X2)
- Low thrust bearing supply pressure (P14)
- Low journal bearing supply pressure (P13)

Each alarm contains a normally closed contact in series with the 12-V dc relay controlling the turbine trip valve (14). If any limit is exceeded, the turbine is tripped. All alarms operate in a latching mode requiring a manual reset before the trip valve can be re-energized.

An emergency facility shutdown circuit and LN₂ deluge system are also built in. They are controlled by separate switches on the control panel and are designed as safeguards to be used in the event of a fire or similar catastrophe during LOX testing. Opening the emergency shutdown switch shuts off the power to many of the 12-V dc relay circuits. This trips the turbine; shuts down both pumps; closes both the LN₂ tank fill and pump fill valves; and opens all LN₂ drain valves. Opening the LN₂ deluge switch opens an air solenoid valve admitting 172 to 207 kPa (25 to 30 psig) LN₂ to a perforated manifold

adjacent to the tester. A massive flow of LN₂ inundates the tester area and would help to smother an oxygen fire.

Three automatic control systems are incorporated in the test facility. One controls turbine speed while the other two are identical and control the pressure in each of two bearing drain lines.

The turbine speed control system allows either manual or automatic operation. In the manual mode, the pressure in the diaphragm of the speed control valve (12) and, hence, the GH₂ flow and turbine speed, is set using a motorized regulator operated from the control panel. This mode was used for all slow speed starts and was found to be quite satisfactory at high speeds.

In the automatic mode, the valve is controlled by Woodward Model 2301 electronic governor operating in conjunction with a valve positioner. The desired speed is set using a potentiometer connected to the governor. A speed signal (S1) from the tester is electronically compared with the speed setting. The difference or error signal is then amplified and sent to the positioner which changes the diaphragm pressure to raise or lower the tester speed to equal the desired setting.

The LN₂ drain pressure control system is used to automatically control the pressure upstream of the drain valve to about 69 kPa (10 psia) greater than the saturation pressure. A vapor bulb in the drain line is charged with nitrogen gas prior to cold testing. The charge pressure is calculated such that the fluid in the bulb is a mixture of gas and liquid throughout the entire range of drain temperatures during cold operation. Since the bulb and the drain fluids are at a common temperature and the bulb fluid is two-phase, the bulb pressure is also the saturation pressure of the drain fluid. The bulb pressure and the actual drain pressures are then measured by a differential transducer. The output signal of the transducer is fed back to the differential controller which compares it with the desired 69 kPa (10 psia) pressure difference and adjusts the setting of the drain control valve to raise or lower the drain pressure accordingly.

7.3 Instrumentation

Instrumentation was installed to measure film thickness, shaft displacement, shaft speed, tester vibration and various temperatures, pressures, and flows. Table 7-1* provides measurement and sensor details. The identification code indicates the type of sensor and its number; e.g., P5 is Pressure Number 5. The location code indicates whether the sensor is in the test rig (T) or installed externally (E). Those installed in the test rig are shown in Figure 7-9 while the external sensors are depicted in the piping schematic shown in Figure 7-8. The test code indicates the tests during which the sensors were used; e.g., A - all, 1 - seal test No. 1, etc. The following sections discuss the measurement and sensor types.

7.3.1 Film Thickness and Shaft Displacement

Special design capacitance probes supported by MTI's Accumeasure™ System 1000 amplifying and conditioning components were used for these measurements. Specifications for the Accumeasure System 1000 are given in Table 7-2.

The basic construction features of the capacitance probes are shown in Figure 7-10. Due to the large temperature range and anticipated future use in liquid oxygen, special materials are used in their construction. The seal film thickness probes are constructed using 42% iron-nickel. This was chosen because its expansion rate is very close to that of the carbon-graphite now used in the helium seal rings. The shaft displacement probes are fabricated from 304 stainless steel which provides good low temperature properties and a suitable expansion rate.

Eccobond 104 epoxy manufactured by Emerson Cummings is used to bond the internal parts together. The proper choice of adhesives was of great concern because of the need for good dimensional stability and high bond strength when subjected to repeated thermal cycling. Eccobond 104 proved to be considerably stronger and harder than several other epoxies and polyurethane adhesives that

*Tables are presented consecutively, beginning on page 7-30.

were screened during the design stage. Additionally, it was found to retain most of its bond strength when used in a typical probe construction and repeatedly cycled between 21°C and -196°C (70°F and -321°F).

While no LOX was used during the helium seal testing, the probes were designed with its use in mind for future work. The principal hazard is material ignition. The metal parts are quite safe due to their high ignition temperatures and high thermal conductivity. The epoxy, however, is highly combustible and definitely an area of vulnerability. To minimize this hazard, Refset™, a special fluoroelastomer compounded by Raybestos Manhattan Corporation, is used as a protective overcoating, both in the interelectrode grooves at the top of the probes and near the connector on the other end. The material was developed specifically to be used as a protective barrier and will not burn in an oxygen atmosphere.

7.3.2 Seal Film Thickness Probes

Two methods were used to measure seal film thickness during the testing. One uses a differential approach while the other provides a direct measurement. The former employs two probes for each measurement, one observing the back of the seal ring and the other the surface of the seal runner. The film thickness is derived by measuring the difference between the outputs. Both vertical and horizontal measurements are taken on both the inboard and outboard seal rings. Two common seal runner probes are used, one serving both the inboard and outboard seal probes in the vertical direction and the other providing a similar arrangement in the horizontal orientation. Figure 7-11 shows the differential probe installation.

The probe has an outer tip diameter of 5.0 mm (0.197 in.) and an interelectrode diameter of 2.67 mm (0.105 in.). It is calibrated to have a range of 0.127 mm (0.005 in.) in air or helium. Figure 7-12 shows the detailed construction which followed MTI's standard practice and used the materials previously discussed.

The differential method, which was employed during the first three seal tests, proved troublesome and yielded poorer results than we had hoped for. Several of the problems encountered are described as follows:

1. Thermal Distortion of the Runner. With LN₂ surrounding the inboard face and gaseous helium on the outboard side, the runner assumes the shape of a truncated cone. Thus with the reference probe measuring at the center rather than under the seal rings, the inboard seal film thickness would be understated while the outboard seal film thickness would be overstated. In either case, the amount is estimated to be about 0.0056 to 0.0085 mm (0.0002 to 0.0003 in.).
2. Thermal Distortion of the Seal Housing. This is due to the temperature gradient across the seal housing resulting in the probes which are located closer to the bearings; i.e., the cold section of the tester, moving closer to their target than the more outboard probes. This has an opposite effect to that caused by the runner and tends to overstate the inboard film thickness and understate the outboard film thickness. The amount is a direct function of the temperature difference between probes (seal probes and runner probes) and is about 0.00183 mm/°C (0.00004 in./°F).

A direct measurement of seal film thickness using embedded probes in the outer seal ring was made during the last seal test. Refer to Figure 2-23 for the arrangement and to Figure 2-24 for a photo of the actual ring. The tip geometry provides for a range of 0.076 mm (0.003 in.) The lead-off cables consist of 0.33 mm (0.013 in) diameter copper-clad cable chosen to minimize the mechanical impedance imposed on the seal ring. The diametrically opposed probe pairs allow measurement not only of the instantaneous film thickness but also the mean film thickness and the ring eccentricity. The 1.22 to 1.92 rad (70° to 110°) angular spacing of the probes is needed to avoid drilling through one of the three antirotation slots in the seal ring and to place the probe tips in the bearing pockets. The metal parts of the probe are constructed of 42% iron-nickel alloy to match the expansion rate of the seal ring.

7.3.3 Shaft Displacement Probes

Five probes are installed to observe the shaft, four radial and one axial. The radial shaft probes are installed in x-y pairs slightly inboard of the hydrostatic journal bearings. The probes are mounted in extension tubes and secured to and adjustable from the outside of the tester. The axial probe is installed in the seal cavity and observes the edge of the helium seal runner as shown in Figure 7-11.

The radial probes have an outer diameter of 5.00 mm (0.197 in.) while the axial probe has a diameter of 3.18 mm (0.125 in.). The latter is constructed without a grounded outer shield and has a smaller inner electrode to accommodate a space restriction. Both sizes of probes are calibrated to have a range of 0.127 mm (0.005 in.) in air and 0.191 mm (0.0075 in.) in LN₂. Figure 7-12 shows the detailed construction of each probe.

7.3.4 Shaft Speed

Shaft speed is measured using two separate probes. A Bently-Nevada Model 300 eddy-current probe is mounted through a radial hole to observe a notch machined into the outer diameter of the thrust collar. The second probe consists of a Spectral Dynamics Model SD43-GPT-1 fiber optic probe mounted through the turbine casing to observe a single bright mark on the turbine nose cone. Both speed measurements are independently connected to readouts and automated shutdowns.

7.3.5 Vibration

Two Endevco piezoelectric accelerometers are stud-mounted to the seal end of the test rig. One sensor is fixed in the vertical direction and the other in the axial direction. The accelerometers are connected to oscilloscope readouts and automatic shutdown devices.

7.3.6 Pressures

Validyne Model DP-15 variable reluctance pressure transducers are used to measure fluid pressures. Meter readouts or strip chart recordings are provided. Bearing supply pressures are additionally connected to low pressure automatic shutdowns.

7.3.7 Flows

Both the helium seal supply flow and the outboard seal leakage flow are measured using calibrated Venturi flow meters. The flow meter pressure drops are sensed with variable reluctance pressure transducers operating in a differential mode. The inboard seal flow is derived as the difference between the supply and the outboard drain flows.

7.3.8 Temperatures

Copper constantan thermocouples are employed. Fluid temperatures are measured using sheath-type sensors inserted in the flow stream through pressure-tight fittings. Seal ring surface temperatures are sensed using small diameter embedded thermocouples.

7.3.9 Data Acquisition Equipment

Figures 7-6 and 7-13 provide an overall view of the control room and a simplified schematic of the data acquisition equipment, respectively. Detailed schematics of the instrumentation system are provided in Appendix B.

Oscilloscopes are the principal means for monitoring the dynamic data from the test rig. They provide x-y displays of the radial capacitance probes to show rotor orbital motion and position with respect to the bearing at each end of the rotor and vertical and horizontal seal film thickness at both inboard and outboard seals. Dual trace swept oscilloscope displays are provided for test rig housing vibration. One speed signal is displayed on a panel meter, while the other is recorded on a strip chart recorder.

A Honeywell Model 101 28-channel FM magnetic tape recorder is used to record all dynamic test data. A time code is also recorded to permit synchronizing the tape recorder with the data logger.

Static data consisting of pressures, temperatures, and flows are individually displayed in the control room using panel meters and a strip chart recorder. Some of the panel meters are equipped with alarms to provide automatic shut-down in selected parameters.

A Fluke Model 2280 data logger is used as the principal means of recording test data. All test parameters excepting test rig vibration are included. Data signals are serially recorded with a full scan cycle of 2 to 3 s. The value of each test parameter along with the time at which the data scan is initiated is transmitted through an RS-232 digital output to a Columbia Data Products Model 300D digital cassette recorder tape storage system. Digital cassette recordings of test runs are played back and entered into MTI's IBM 4341 mainframe computer system for analysis.

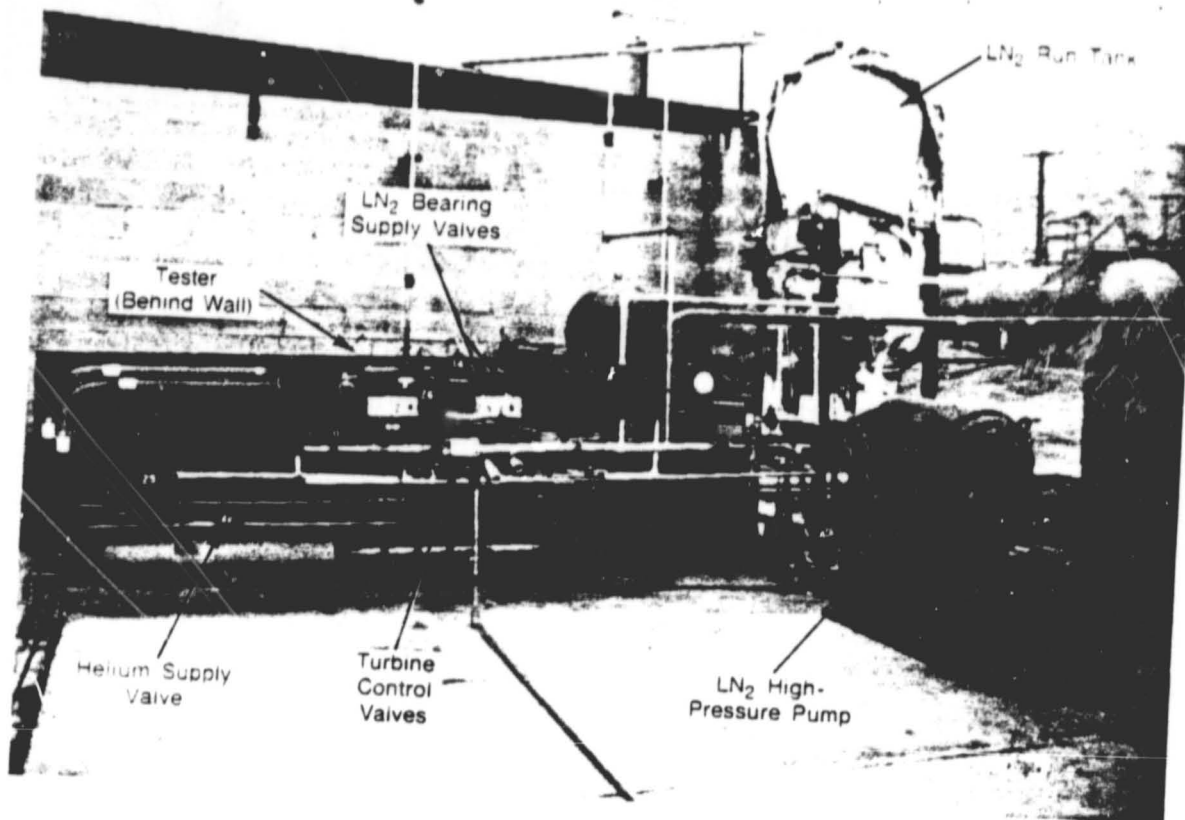


Fig. 7-1 Overall View of Helium Seal Test Facility

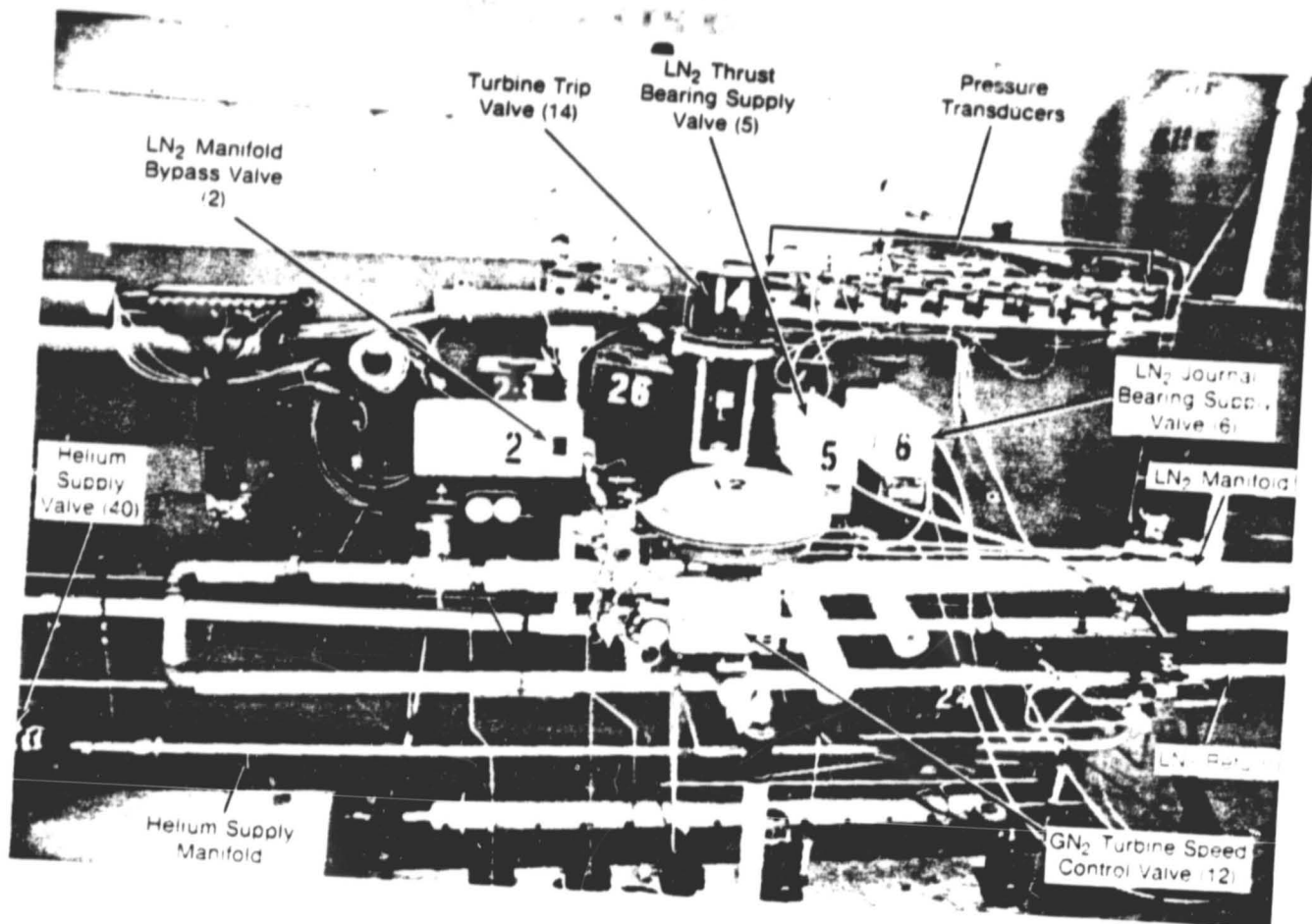


Fig. 7-2 Close-Up View of LN₂ Manifold and Bearing Supply Valves

ORIGINAL PAGE IS
OF POOR QUALITY

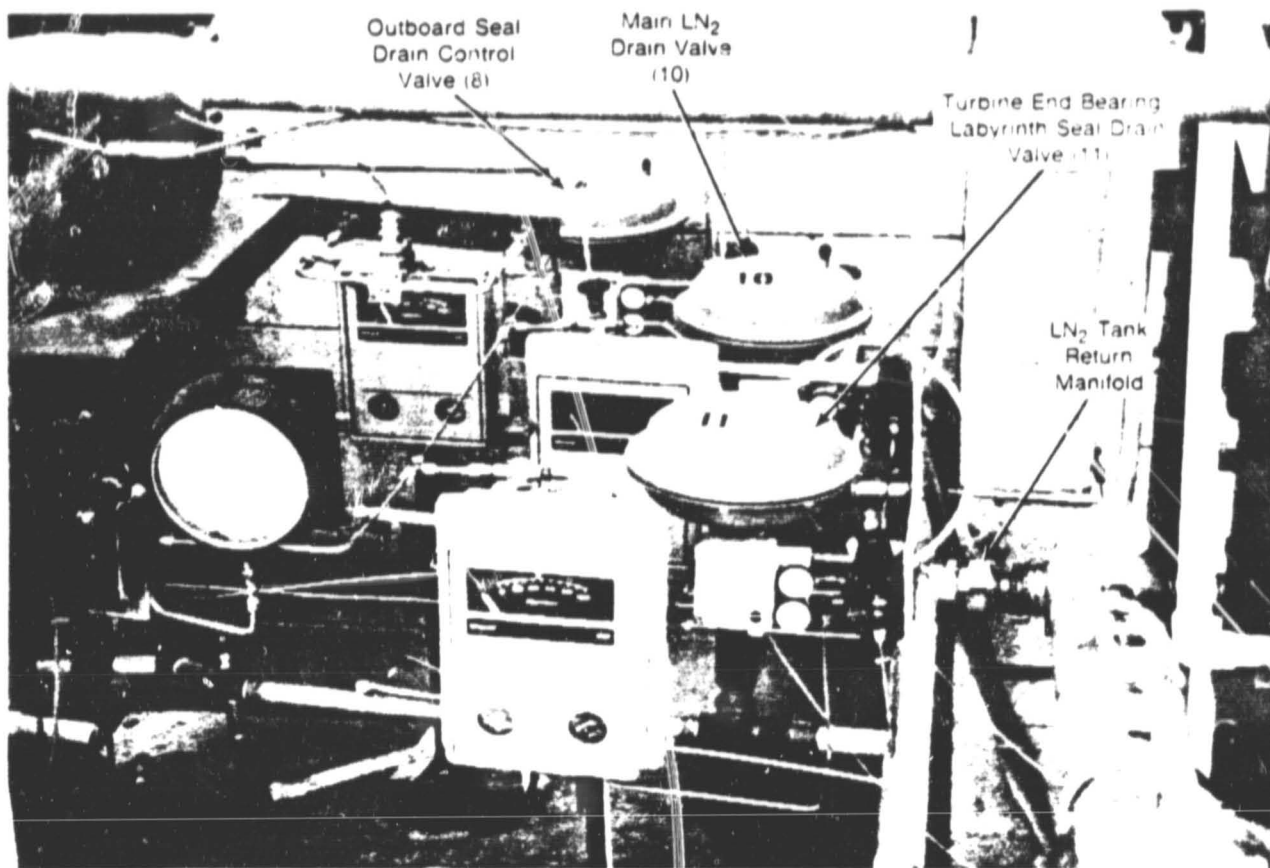


Fig. 7-3 Close-Up View of Test Rig Drain Valves

ORIGINAL PAGE IS
OF POOR QUALITY

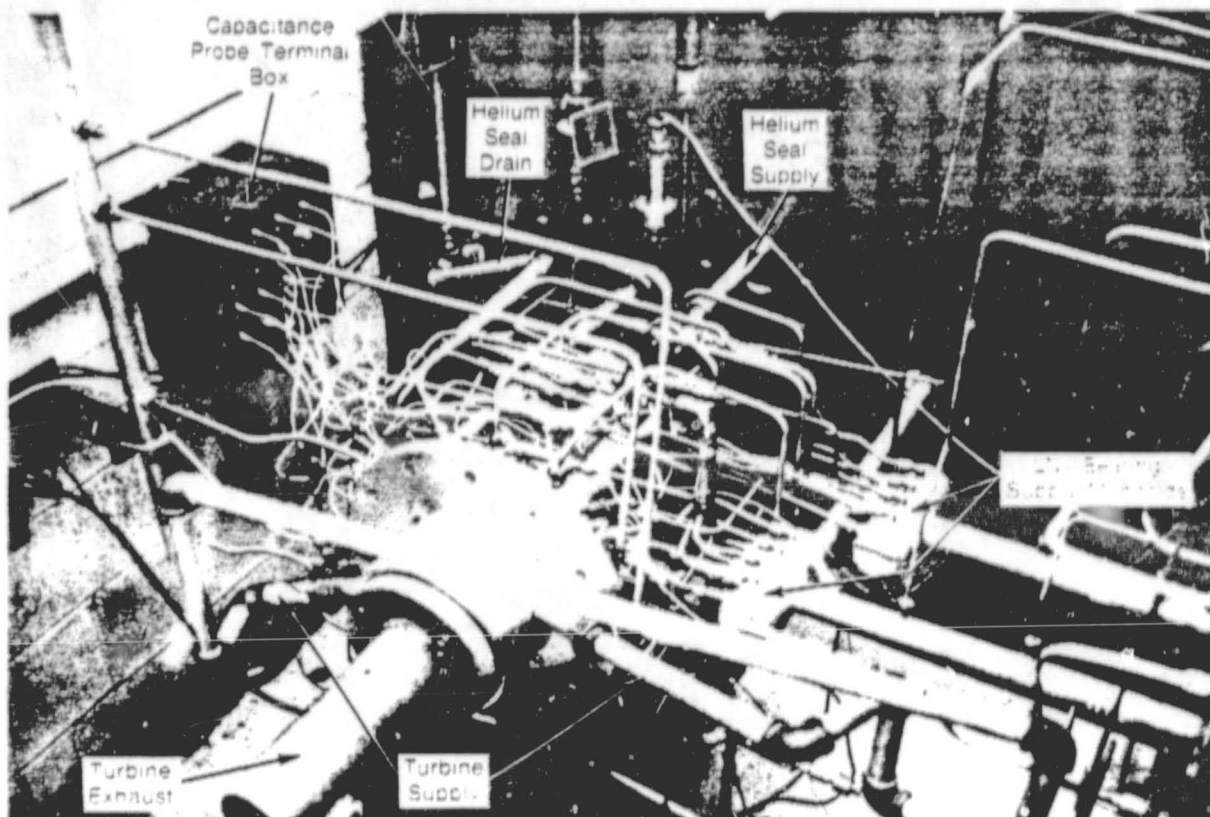


Fig. 7-4 Close-Up View of Helium Seal Test Rig

ORIGINAL PAGE IS
OF POOR QUALITY

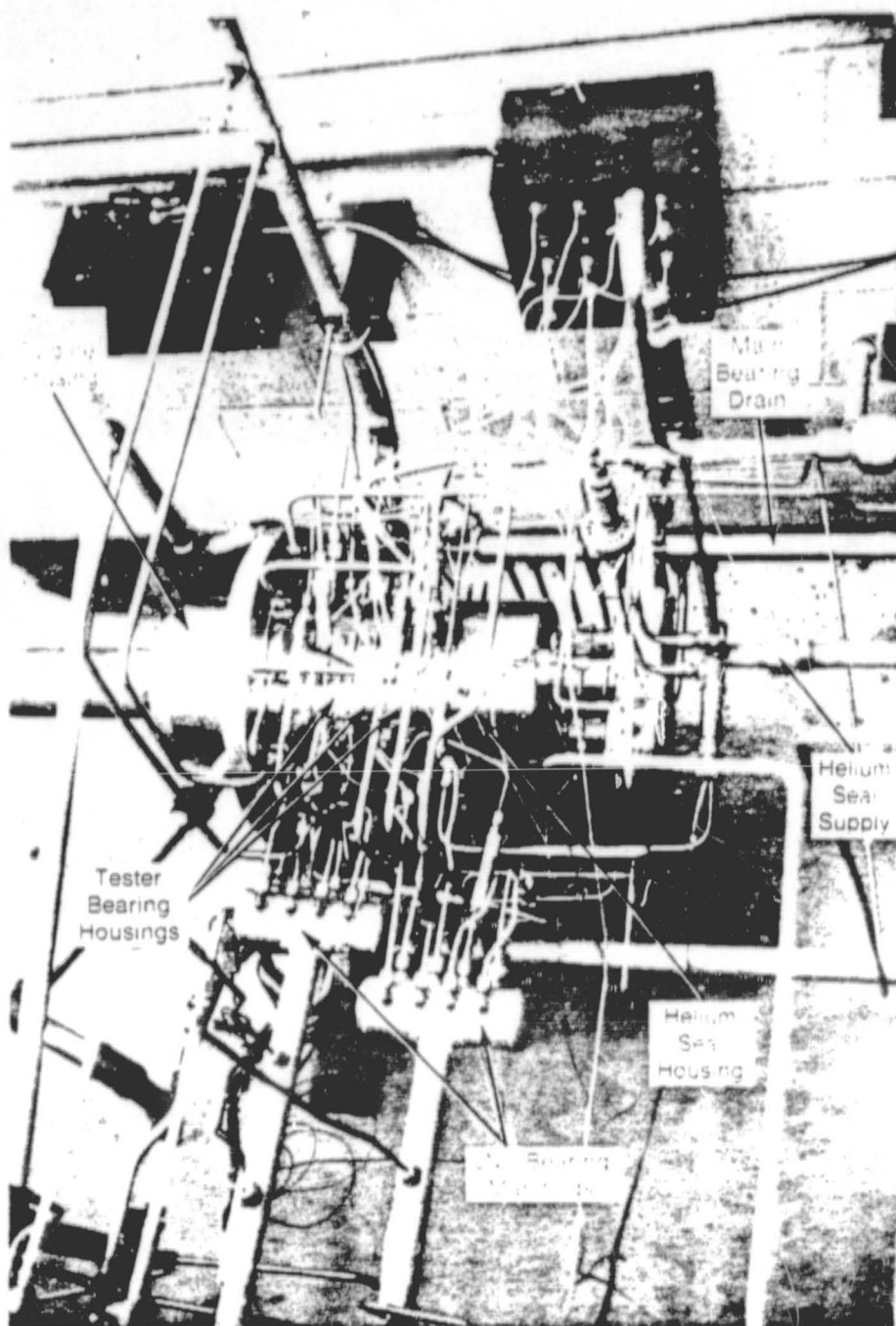


Fig. 7-5 Overhead View of Helium Seal Test Rig

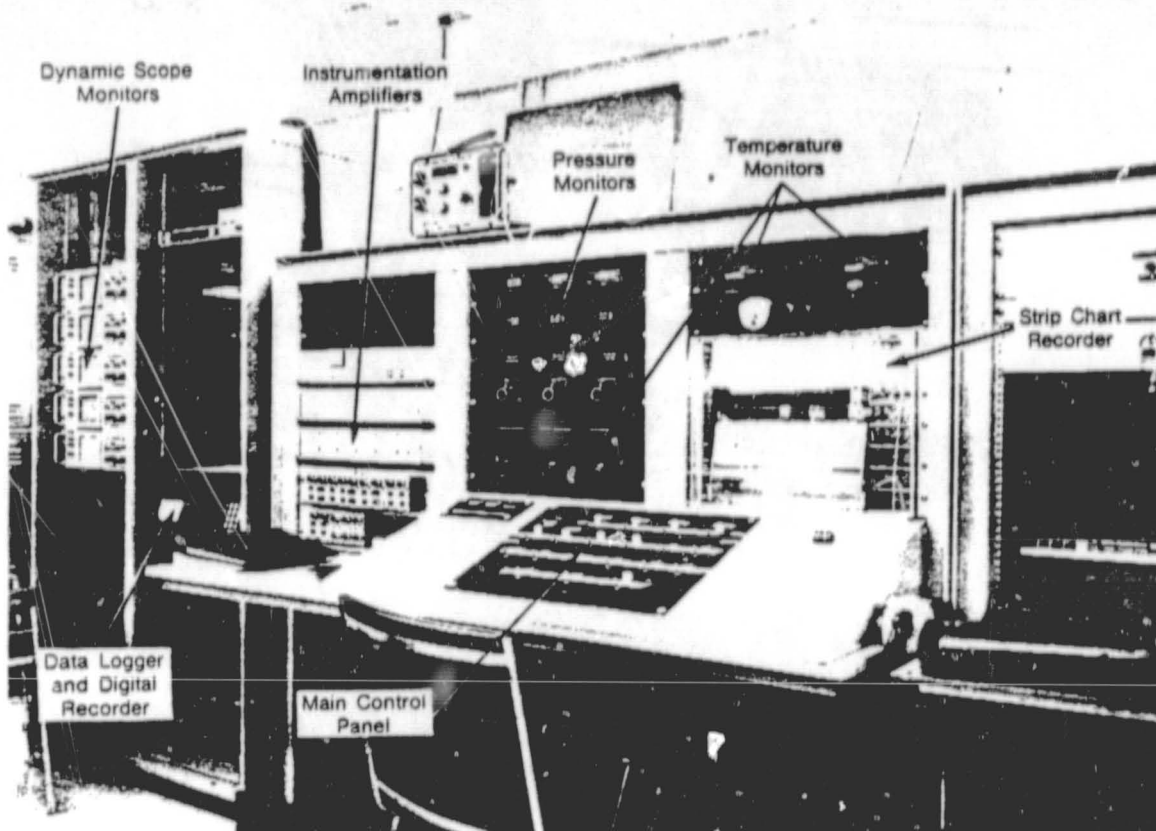


Fig. 7-6 Overall View of Control Room

ORIGINAL PAGE IS
OF POOR QUALITY

ORIGINAL PAGE IS
OF POOR QUALITY

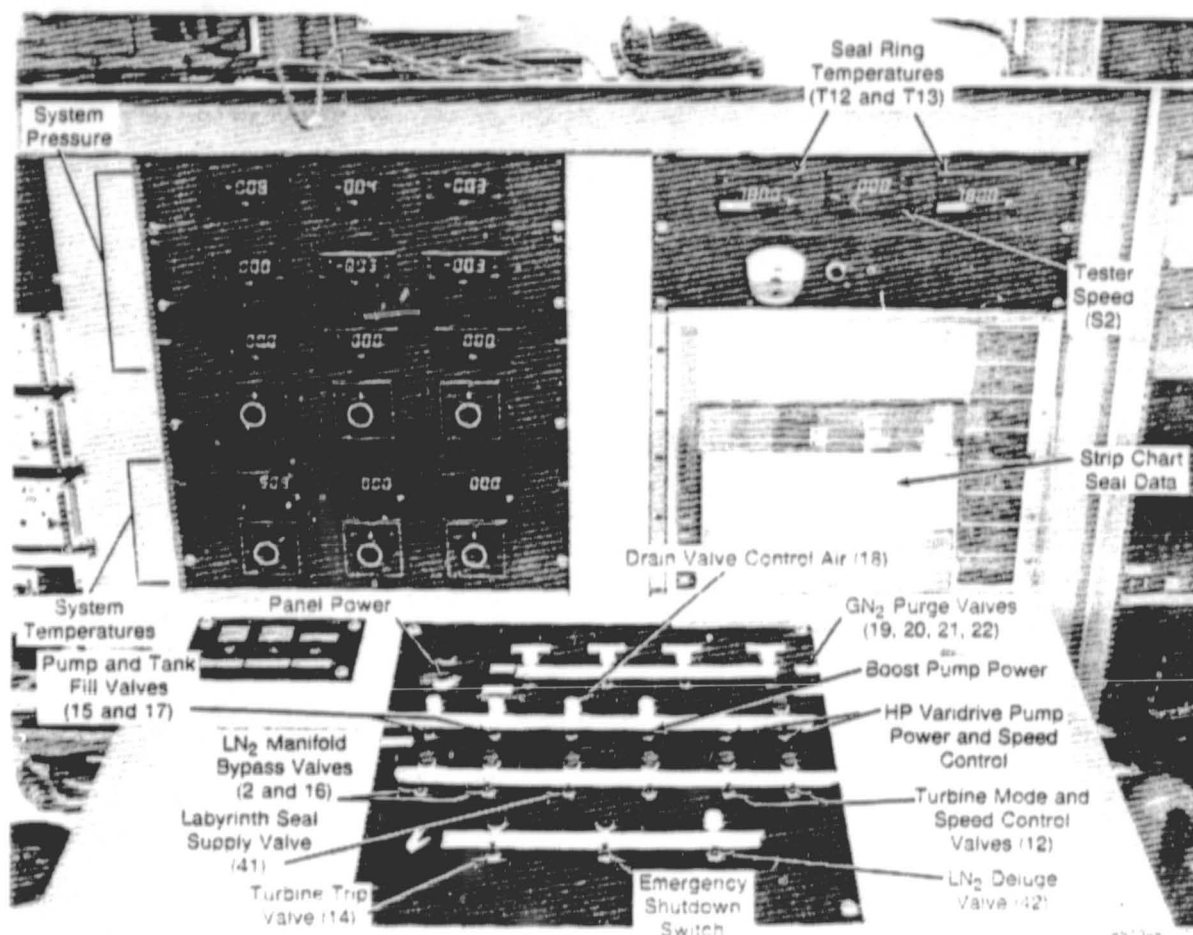
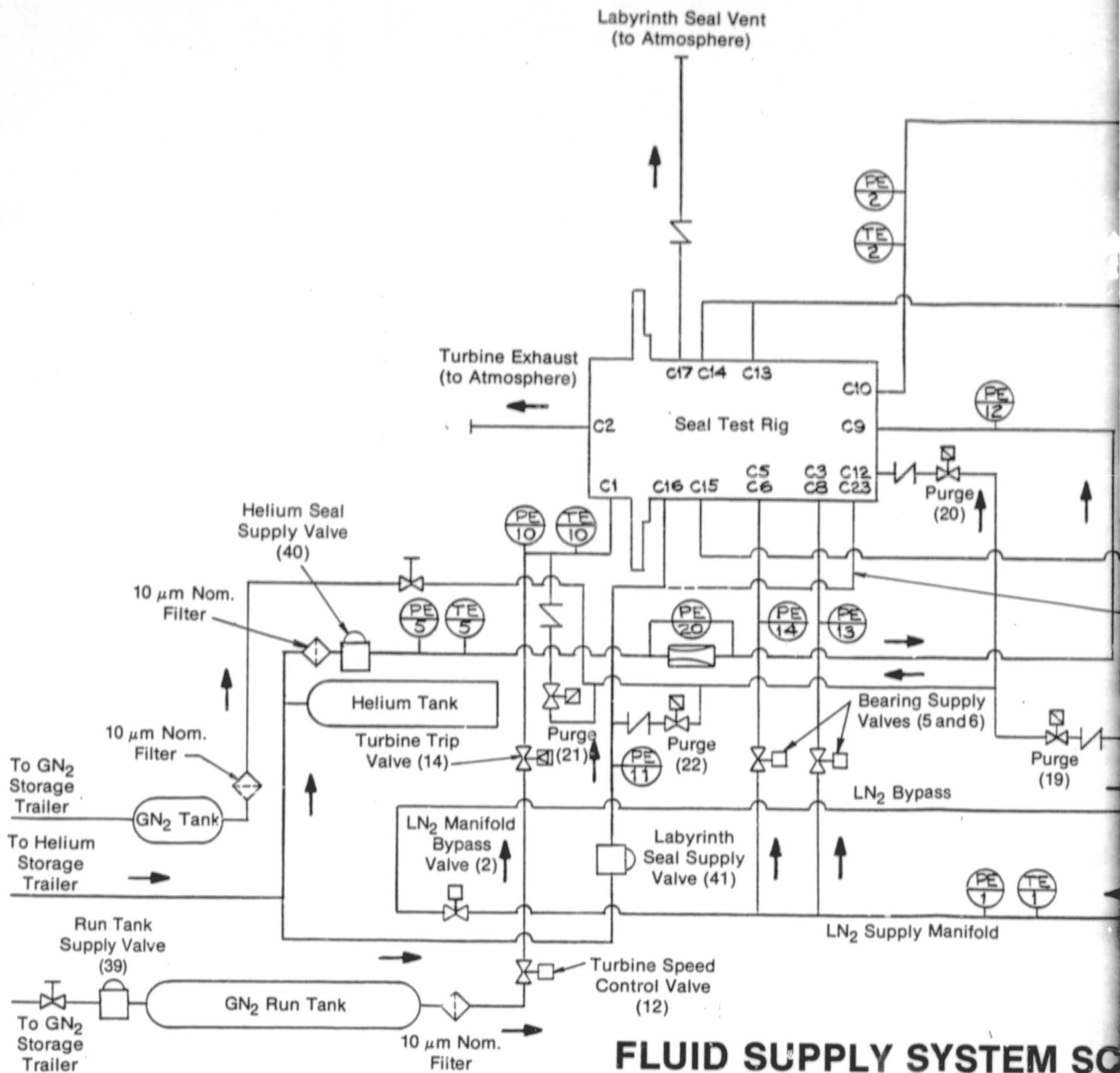


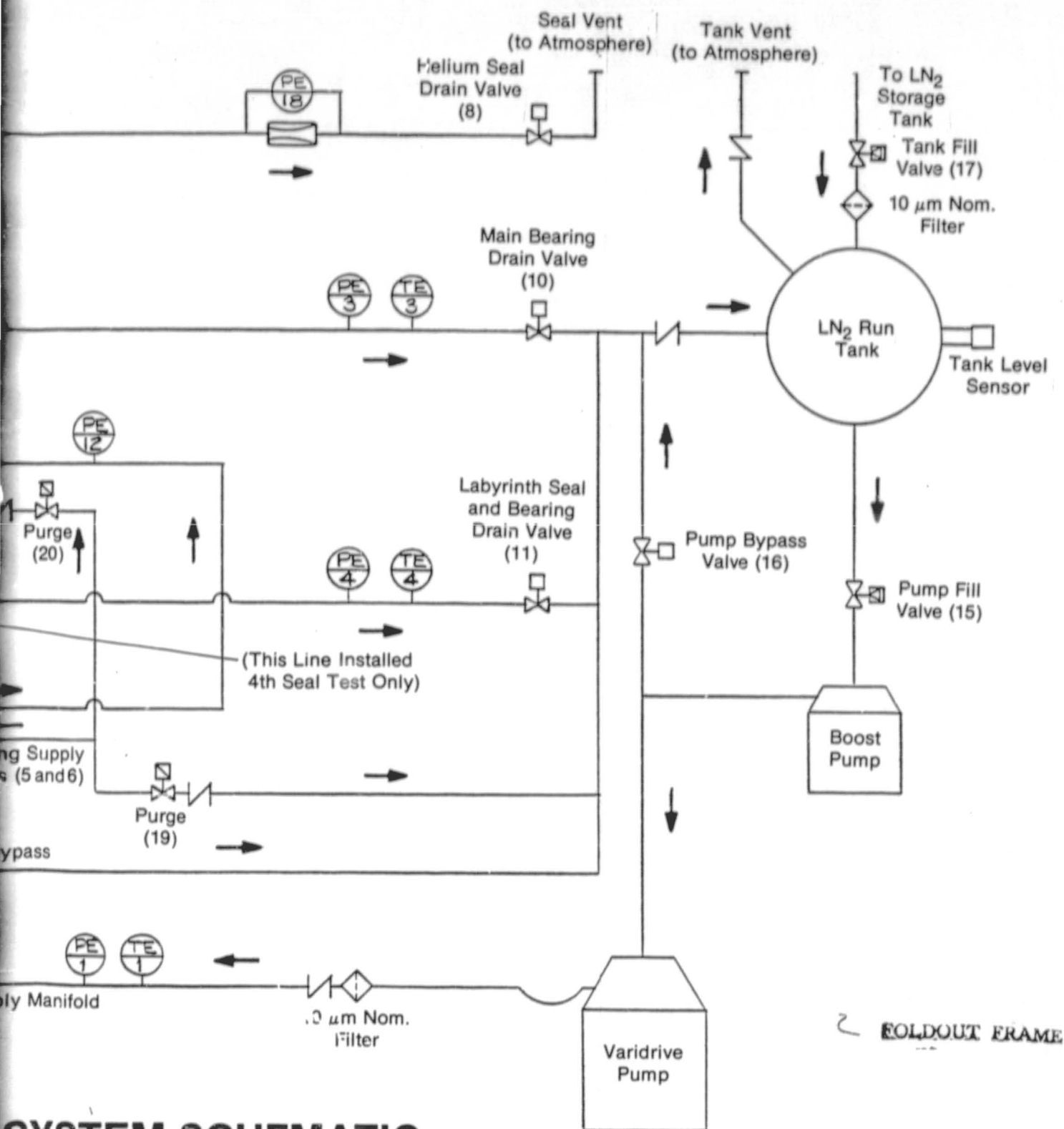
Fig. 7-7 Close-Up View of System Control Panel



FLUID SUPPLY SYSTEM SC

FOLDOUT FRAME

Fig. 7-8 Fluid Supply System Schematic



SYSTEM SCHEMATIC

PRECEDING PAGE BLANK NOT FILMED

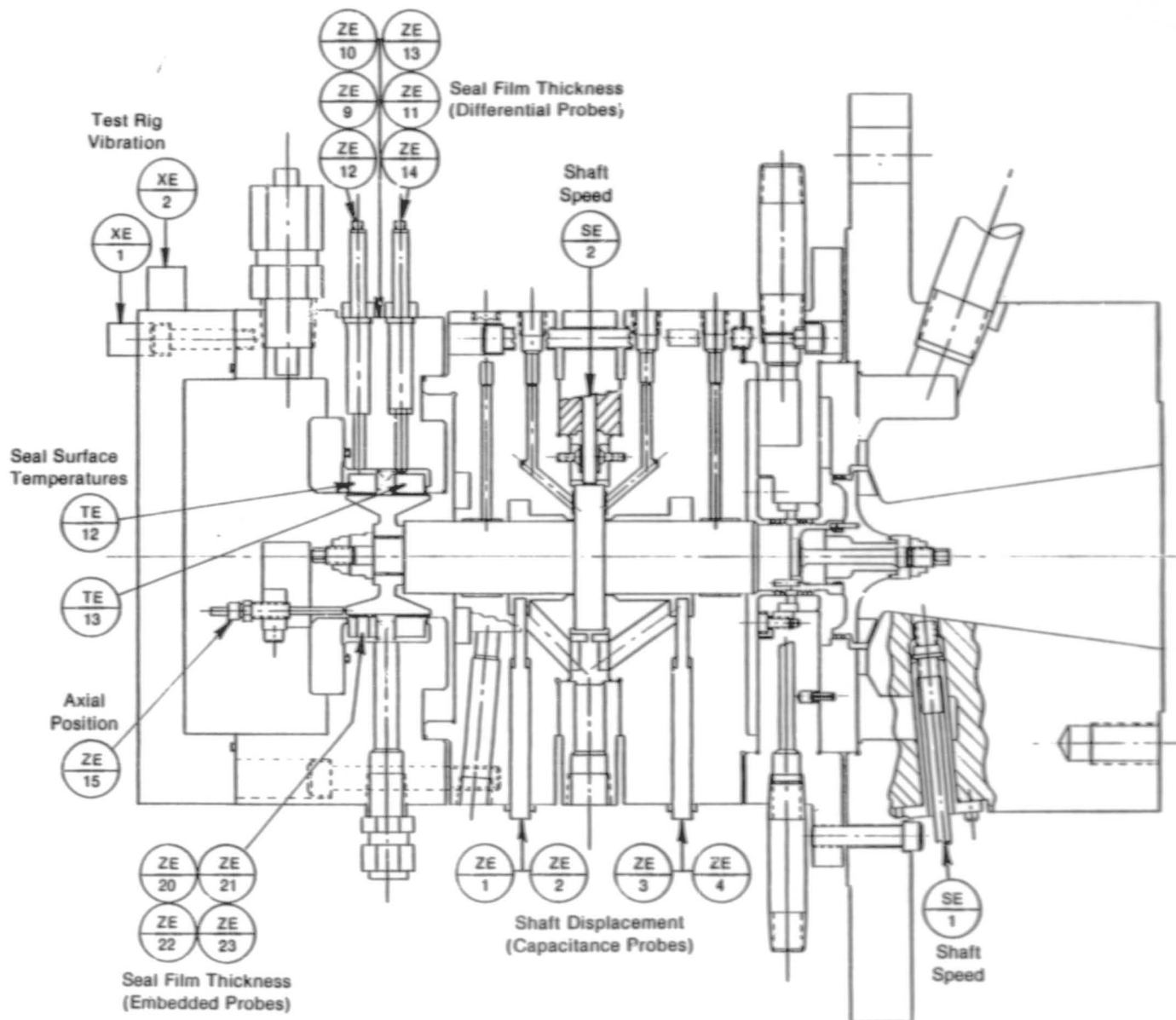


Fig. 7-9 Test Rig Instrumentation

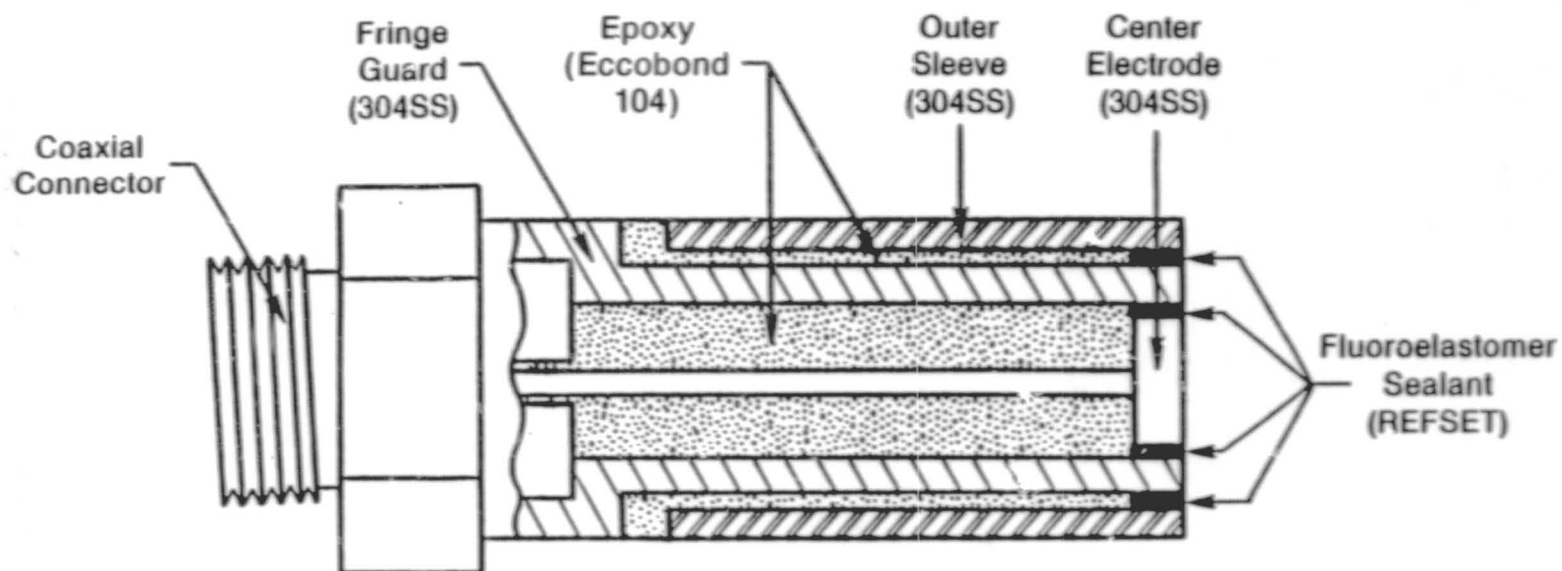


Fig. 7-10 Capacitance Probe Construction

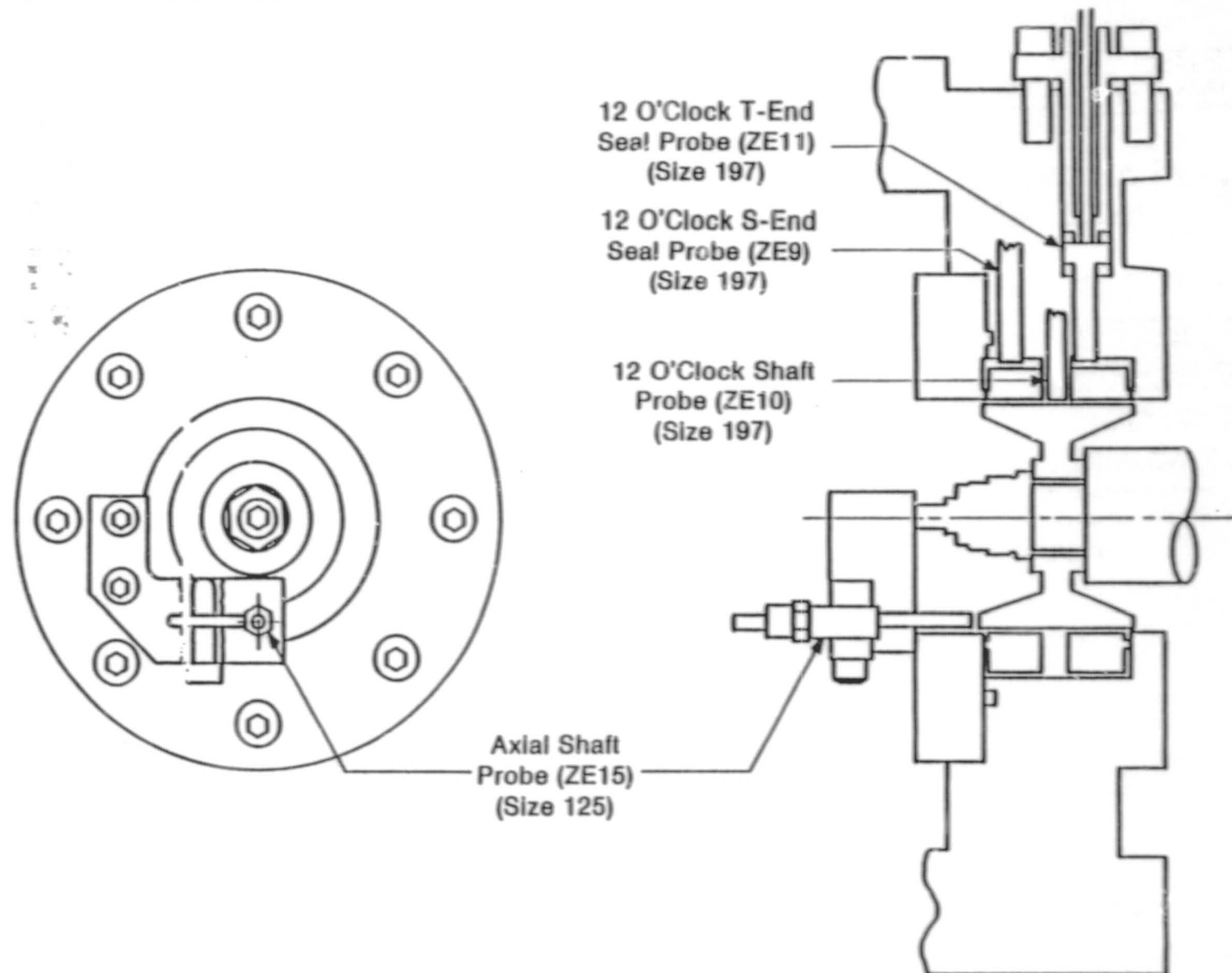
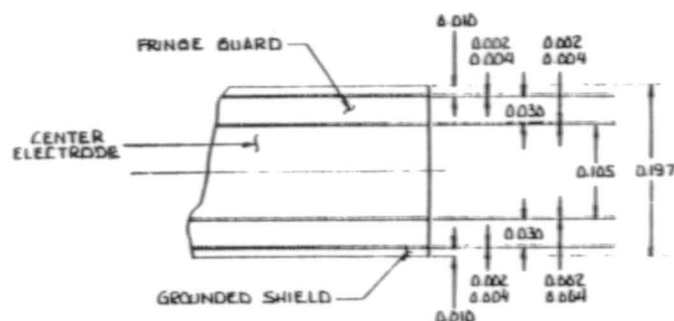
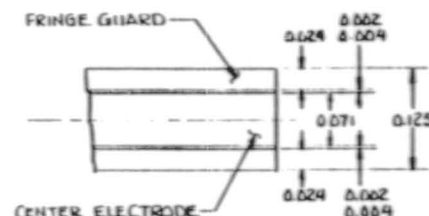


Fig. 7-11 50-mm Helium Seal Probe Configuration

REVISIONS		C 700C052		A	
REV	DESCRIPTION	DATE	BY		
A	ISSUED	17 JAN 83	C. B. Ball		

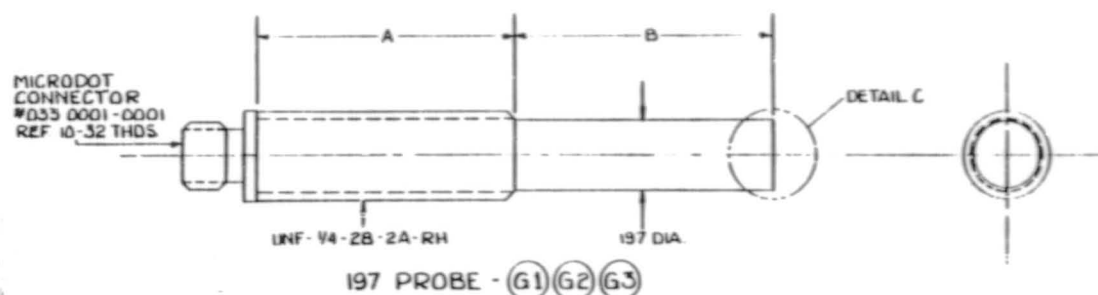


DETAIL C
(SCALE 8/1)

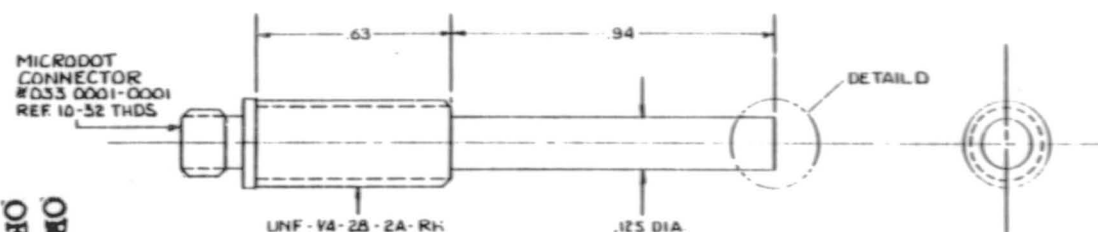


DETAIL D
(SCALE 8/1)

	DIMENSION A	DIMENSION B	MATERIAL
G1	1.00	1.25	AISI 304 STAINLESS STEEL
G2	0.88	0.19	INCONEL 600
G3	0.88	0.84	INCONEL 600
G4	—	—	INCONEL 600



197 PROBE - (G1) (G2) (G3)



125 PROBE - (G4)

NOTES:

1. SURROUNDING FLUID - LOX, LN2, AIR
2. TEMPERATURE RANGE - +100°F TO -350°F
3. UNLESS SPECIFICALLY EXCEPTED ALL MATERIAL MUST BE OXYGEN COMPATIBLE
4. PRESSURE RANGE - 0 TO 250 PSIG (ΔP TIP TO CONNECTOR)
5. USE REFSET - RL 3788 COATING SOLUTION AND/OR RL 3550 POTTING COMPOUND TO CEMENT PARTS TOGETHER. ALTERNATELY USE URALITE 3130 OR LOW TEMP EPOXY FOR CEMENT AND SEAL EXPOSED SURFACES WITH REFSET RL 3788 COATING COMPOUND.
6. G4 FRINGE GUARD EXPOSED FROM TIP TO THREADED SECTION.

Figure 4-3

UNLESS OTHERWISE SPECIFIED DIMENSIONS ARE IN INCHES TOLERANCES ON:			DRAWN <i>R. H. Hines</i> 4/10/83		
DECIMALS	FRACTIONS	ANGLES	CHECK	DATE	
XXX ±	±	±	DATE	17 JAN 83	
ALL ±	ALL SURFACES	✓	ANALYSIS		
BREAK SHARP CORNERS AND REMOVE BURRS			MATERIALS	TITLE SPECIFICATIONS CAPACITANCE PROBES - LOX SEAL & SHAFT PROBES	
MATERIAL			REF. DIMS	CODE IDENT NO. SIZE	
SEE TABLE			PROL. DIMS	26741 C 700C052	
TREATMENT			QUALITY CONTROL	DATE 17 JAN 83 BY 4/1	

Fig. 7-12 Capacitance Probes, LOX Seal, and Shaft Probes Configurations

MTI-21271

ORIGINAL PAGE IS
OF POOR QUALITY

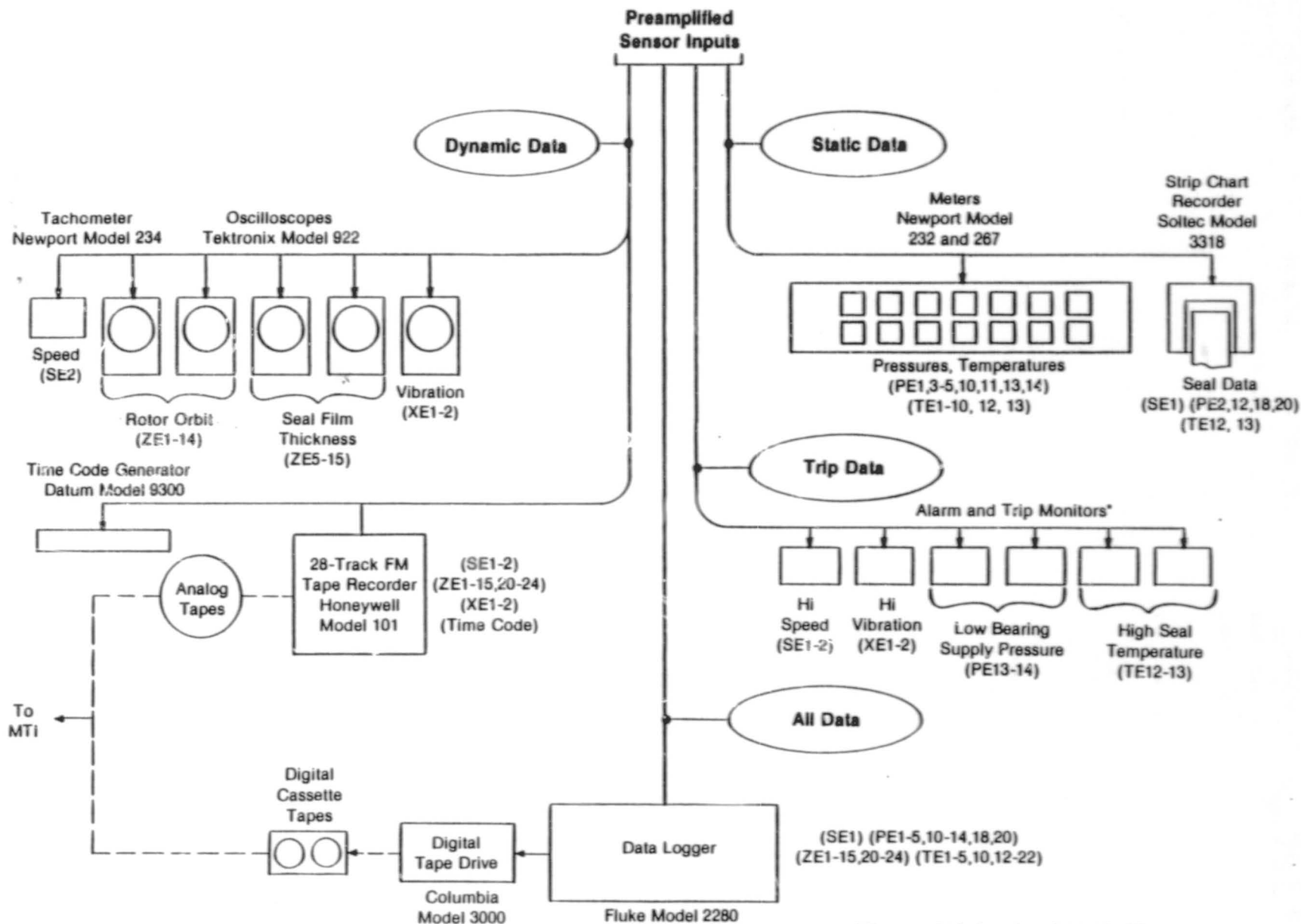


Fig. 7-13 Simplified Schematic of Data Acquisition Equipment

TABLE 7-1

INSTRUMENTATION MATRIX

Sensor Codes			Location	Measurement	Trip Level	Remarks
Ident.	Location	Test				
ZE1	T	A	(1) Jnl.Brg., S-End	Rad. Shaft Displace.		
ZE2			Horiz.			
ZE3			Jnl.Brg., S-End			
ZE4			Vert.			
ZE9		1-3	(2) Otb. Seal Ring	Helium Seal Film Thick.		Differential Method
ZE10			12 o'clock			
ZE11			Seal Runner, 12 o'clock			
ZE12			Inb. Seal Ring			
ZE13			12 o'clock			
ZE14			Otb. Seal Ring, 3 o'clock			
ZE15			Seal Runner, 3 o'clock			
ZE16		A	Inb. Seal Ring, 3 o'clock			
ZE20		4	Seal Cavity, Axial Dir.	Axial Shaft Displace.		Direct Method
ZE21			Otb. Seal Ring,	Helium Seal Film Thick.		(embedded probes)
ZE22			10 o'clock			
ZE23			Otb. Seal Ring,			
SE1	T	A	12 o'clock			
SE2			Otb. Seal Ring, 4 o'clock			
XE1			Otb. Seal Ring, 6 o'clock			
XE2						
PE1	T	A	Turbine Wheel	Shaft Speed	8,042 rad/s (77K rpm)	
PE2			Thrust Runner		High Alarm	
PE3			Seal Housing, Axial Dir.	Vibration	1.0 G peak,	
PE4			Seal Housing, Vert. Dir.		High Alarm	
PE5	E		LN ₂ Supply Manifold	Pressure		
PE6			Otb. Helium Seal Drain			
PE7			Main Brg. Drain			
PE8			Brg./Laby. Seal Drain			
PE9			Helium Supply Manifold			
PE10			Turbine Inlet			
PE11			Laby. Seal Supply			
PE12			Helium Seal Supply			
PE13			Jnl.Brg. Supply		3.45 MPa (500 psig)	
PE14			Thrust Brg. Supply		Low Alarm	
PE15			Otb. Hel. Seal Drain Flow			
PE16			Hel. Seal Supply Flow			
TE1			LN ₂ Supply Manifold	Temperature		
TE2			Otb. Helium Seal Drain			
TE3			Main Brg. Drain			
TE4			Brg./Laby. Seal Drain			
TE5			Helium Supply Manifold			
TE6	T	1-3	Jnl.Brg. Recess, S-End			
TE7			Jnl.Brg. Recess, T-End			
TE8			Thrust Brg. Recess,			
TE9			S-End			
TE10			Thrust Brg. Recess,			
TE11	E	A	T-End			
TE12			Turbine Inlet			
TE13			Laby. Seal Supply			
TE14	T		Otb. Helium Seal Ring		4°C (40°F)	
TE15			Inb. Helium Seal Ring		High Alarm	

(1) S-End refers to Seal End of Test Rig.
T-End refers to Turbine End of Test Rig.

(2) Clock positions are references to viewing Test Rig from Seal End.

TABLE 7-2

MTI ACCUMEASURETM SYSTEM 1000
REQUIREMENTS AND SPECIFICATIONS

Requirements

Probes: (22) All Special Design

Amplifiers: (11) AS1023-PA Probe Amplifiers
(1) AS1041-SA Summing Amplifiers
(2) AS1032-MD Analog Display Unit

Housings: (2) AS1011-H Instrument Housings

Specifications

Probe Amplifier (AS1023-PA)

Linearity: $\pm 0.3\%$ of Range, 10-100% Range
(25-ft Cable)

Frequency Response: 3 db at 5 kHz

Output Noise: 40 mv Peak-to-Peak at Full Scale

Probe Voltage: 5 V rms Maximum

Output Signal: ± 10 V dc, 100-ohm Output Resistance

Summing Amplifier (AS1050-SA)

No. of Channels: Two Channels Summing to One Output

Gain: Unit $\pm 0.1\%$

Output Signal: ± 10 V dc

Analog Display Unit (AS1032-MD)

Meter: 0-100% Vertical Scale

Accuracy: 2%

8.C TEST PLAN FOR THE RAYLEIGH-STEP, HELIUM BUFFER SEAL

The program called for the testing of the following two types and sizes of seals:

1. 50-mm and 20-mm spiral-groove LOX face seals
2. 50-mm and 20-mm Rayleigh-step, helium buffer floating ring seals.

Due to budgetary constraints, only the 50-mm helium seals were tested. In accordance with the final test plan, four seal packages were installed and tested.

8.1 Test Description

Four types of tests were to be conducted on the seal packages consisting of:

1. Normal steady-state demonstration test runs
2. Acceleration test runs
3. Test runs with axial runout built into the LOX seal mating ring
4. Test runs with axial motion imposed on the shaft

All runs were to be conducted in LN₂ and repeated in LOX after verifying the operational integrity of the test rig and seal package. Because the testing was cut back to include only the helium seals, several of the above program features were eliminated. The test runs imposing axial runout and externally applied axial motion were eliminated because the motion was not relevant to the operation of the helium seals which are sensitive only to shaft motion in the radial direction. Secondly, because the seal working fluid was helium, the use of LOX to energize the test rig bearings was not necessary. Thus, LN₂ was used instead, eliminating the need to repeat runs and greatly reducing the risk of fire.

8.1.1 Steady-State Tests

These tests were planned to prove the basic operational ability of the seals. This provided the opportunity to test the seal's endurance and to exper-

imentally examine the parametric relationships governing actual performance. The former addressed the specific program objective which requires one hour of cumulative test time on each of three seals with at least one half of the total test time at a shaft speed of 7329 rad/s (70,000 r/min) and a supply pressure of 1379 kPa absolute (200 psia). The latter provided the necessary basis to verify the theoretical analyses used in the design stage, also a requirement of the program.

While the design requirements of 1379 kPa absolute (200 psia) supply pressure and 7329 rad/s (70,000 r/min) shaft speed were clearly the operational goals of the testing, preliminary operation at lower speeds and pressures was necessary to gain a clear understanding of the mechanisms at work and to minimize the risk of damage either to the seals or the test rig. Thus, the testing was conducted in a step-by-step manner proceeding from relatively safe operating points to conditions more and more demanding of the seals. Figure 8-1* shows the seal operating map which illustrates a typical sequence of test points.

The principal test variables were helium supply pressure, speed, inboard drain pressure, and outboard drain pressure. Their selection is discussed below:

1. Helium Supply Pressure. A full range of supply pressures was planned for each speed going from a minimum of slightly over the inboard drain pressure, about 517 kPa absolute (75 psia) to the full design pressure of 1379 kPa absolute (200 psia). The progression of supply pressures generally went from low to high at given operating speeds. As the test speeds increased, so did both the minimum and maximum value of the supply pressures.
2. Speed. Because low speeds do not favor the development of good hydrodynamic films, the minimum dwell speed was arbitrarily set at 3665 rad/s (35,000 r/min). During all starts the tester was to be quickly brought up to this speed before steady-state operation was attempted. The speed was

*Figures are presented consecutively, beginning on page 8-14.

then to be increased in increments of 524 rad/s (5000 r/min), taking data at each dwell point up to the design speed of 7329 rad/s (70,000 r/min).

In practice, dynamic problems in the tester restricted safe operation to between 4712 rad/s (45,000 r/min) and 5235 rad/s (50,000 r/min). Thus, for the first three seal sets 3665 rad/s (35,000 r/min), 4118 rad/s (40,000 r/min) and 4712 rad/s (45,000 r/min) were selected as the primary dwell speeds. Because of test rig modifications, it was hoped that the fourth seal test would achieve higher speeds. Actual operation did extend to 5968 rad/s (57,000 r/min); however, higher speeds were precluded by a seal failure.

3. Inboard Drain Pressure. Since the helium flowing through the inboard seal mixed with the adjacent LN₂ bearing leakage flow, its pressure was the same as the main bearing drain of the test rig and was thus dependent on test rig operation. Actual values were 517 kPa absolute (75 psia) although variations of ± 35 kPa (5 psia) were observed. After the addition of the labyrinth seal prior to the fourth seal test, the drain pressure was boosted to 637 kPa absolute (92 psia) because of the need to maintain an intermediate pressure in the newly created cavity.

Lacking arbitrary control of the inboard drain pressure posed several problems. The principal concern was that it limited the minimum supply pressure that could be applied. From Figure 8-1, it is easily seen that the range of drain pressures clearly eliminated most of the "safe" region for lower test speeds forcing most of the operation into the "high friction" region. Secondly, while the frictional forces were a function of the absolute supply pressure, the leakage flows were more closely associated with the pressure drop across the seal. The high drain pressure thus presented a built-in imbalance resulting in a high-friction, low-flow condition at any supply pressure.

4. Outboard Drain Pressure. The helium exiting the outboard seal went to a separate, independently controlled drain. The pressure drop across this seal could thus be controlled to the same value as the inboard seal or increased up to the gage pressure of the supply. The latter would tend to

increase the flow and more closely approximate the operating conditions envisioned during the design. Thus, it was planned to increment the outboard drain pressure from 517 kPa absolute (75 psia) to 103 kPa absolute (15 psia) during the testing. This permitted the study of a much wider range of outboard seal flow conditions than could be achieved with the inboard seal.

8.1.2 Acceleration Tests

These tests were planned to demonstrate the ability of the seals to survive repeated start-ups at high rates of acceleration with full supply pressure applied at the start of the run. The program required two seal sets to be subjected to at least 50 starts each at an average rate of 152 m/s^2 (500 ft/s^2).

Because of the tester dynamics problem, the acceleration runs which were conducted on the second and third seal sets were terminated between 4188 and 4712 rad/s (40,000 and 45,000 r/min.) All starts were at a nominal rate of 500 ft/s^2 resulting in an acceleration time of about 0.7 to 0.8 s. The acceleration tests were conducted after the completion of the steady-state runs.

The helium supply pressures applied during the fast starts were increased over the course of the two test series. The first series conducted on Seal Set No. 2 were at a pressure of 931 kPa absolute (135 psia). Those on the third seal set were done at several pressures progressing from 1069 to 1482 kPa absolute (155 to 215 psia).

The planned operating scheme consisted of switching on the solenoid operated trip valve (14), accelerating the test rig and then switching the valve off using an overspeed circuit. This resulted in a controlled acceleration followed immediately by a coastdown.

Because the acceleration runs would be very brief, no steady-state data could be taken to assess the condition of the seals to determine if any damage had taken place. Thus, periodic conventional starts were planned to allow the tester to run for a period of 45 min and achieve steady state conditions.

8.2 Test Schedules

Tables 8-1 to 8-6* present the test schedules describing the steady-state runs for Seal Sets No. 1 - No. 4 and the acceleration tests for Seal Sets No. 2 and No. 3.

The test schedules were based on several important considerations: (1) the final test plan (2) the results of the test rig checkout tests and (3) the results of the ongoing seal tests. The final schedule for each seal set was written just before the test and tailored to the latest test results. This was done to maximize the experimental yield and minimize the risk of damage to both the seals and the test rig. Some changes were also made during the actual testing. These consisted primarily of eliminating data points at conditions of high vibration although several other insitu modifications were also implemented.

8.3 Test Procedures

8.3.1 Preparation of Test Rig at MTI

All test rig parts were checked for dimensional and material conformity in accordance with MTI's quality assurance program. All test seal parts were given a complete dimensional inspection by Stein Seal Company at their facilities in Philadelphia, PA. The inspection reports are fully documented and available for NASA review.

The test rig was completely assembled including the instrumentation and the 50-mm helium seals to make sure there were no problems with anticipated fitting of parts. The rig was then disassembled, cleaned, reassembled, crated, and shipped to the test lab.

*Tables are presented consecutively, beginning on page 8-17.

8.3.2 Preparation of Test Facility and Test Rig at Wyle Laboratories

A test site was prepared including all test loop components, transducers, control room, and connections to the required fluid storage facilities. An area for the test rig assembly, inspection, and parts storage was also set up. All test loop instrumentation was calibrated in accordance with the procedure in Section 8.3.5 prior to installation in the test loop and at various times during the course of the testing. All test loop components were thoroughly cleaned. The tester was then assembled in the test loop. All equipment was thoroughly checked out and debugged, including verifying all instrument connections to the control room and exercising all controls.

8.3.3 Test Facility Operating Procedures

During the design and checkout of the test facility, a detailed operating procedure was developed. This covered all steps from initial energizing of the facility to the point of establishing stable minimum speed operation, and from the point the test rig was shut down to the final shutdown of the facility. The procedure during the runs was covered by the individual test schedules. The operating procedure follows:

1. Open LN₂ supply line (# 62)
2. Pressurize main LN₂ storage tank to 0.17 MPa (25 psig) (# 61)
3. Open LN₂ run tank fill valve* (# 17, # 45)
4. Verify tank filling.
5. Record GN₂ trailer pressure
6. Record GHe trailer pressure
7. Record GN₂ shop supply pressure
8. Record vapor bulb pressure 0.21 MPa (30 psig)
9. Lock off vapor bulbs.
10. Record flow meter sizes
11. Open GN₂ shop supply valve to manifold (#58)

*A,B indicates valve to be operated. Valve A is principal valve; Valve B, where applicable, controls action of Valve A.

12. Verify control panel switches in pre-test position
13. Activate control panel using key switch
14. Verify main alarm indicator light is in trip mode
15. Set all motorized regulators and valves with momentary switches to pre-test conditions
16. Verify transducers zeroed and B-nuts torqued
17. Verify transducer isolation valves open
18. Turn on and verify operation of all instruments at test site
19. Verify all alarms are in latching mode
20. Open and verify purges: labyrinth seal supply, LN₂ manifold, test seal cavity, turbine.
21. Open pump fill solenoid valve (#15, #44)
22. Close pump bypass pressure control valve (#16)
23. Close LN₂ supply manifold bypass pressure control valve (#2, #23)
24. Allow 15 min. for purge of LN₂ manifold and tester
25. Verify deluge hand valve (#52) closed
26. Verify GN₂ turbine run tank is at 0 psig
27. Perform ambient accelerometer tap check
28. Verify manual turbine speed control regulator (#31) is at zero pressure
29. Verify turbine control valve (#12) and turbine trip valve (#14) are closed
30. Verify power plug disconnected from turbine trip solenoid (#29)
31. Verify GN₂ run tank regulator (#39, #34) closed
32. Verify GN₂ supply trailers (2 each) are open
33. Slowly pressurize GN₂ turbine run tank to 100 psig using hand regulator (#34) on dome loader (#39)
34. Verify no flow to turbine
35. Verify GHe supply pressure regulator #25 is fully closed
36. Slowly open GHe ullage and verify no flow to P5 or P11
37. Open GHe supply from trailers
38. Close purge labyrinth seal supply and purge test seal cavity.
39. Open labyrinth seal supply (#41, #24) until P11 is MPa (10 psig).
40. Turn on hydraulic breaker and pump.
41. Verify hydraulic supply pressure is 0.52 MPa (75 psig)
42. Open GHe supply regulator (#40, #25) until P5 is 0.28 MPa (40 psig)
43. Start Soltec recorder
44. Adjust GHe manual control (Z) pot until P12 is 0.21 MPa (30 psig)

45. Verify P12 = 0.21 MPa (30 psig)
46. Verify LN₂ run tank full
47. Close purge solenoid (3) LN₂ manifold
48. Verify tank level control setting
49. Fully open pump bypass valve (#16) and verify
50. Fully open LN₂ supply manifold bypass valve (#2, #23)
51. Close valves #5 and #6
52. Clear test pad area
53. Turn on boost pump breaker
54. Start boost pump
55. Increase LN₂ supply manifold pressure P1 to 0.28 MPa (40 psig) using pump bypass pressure control valve (#16).
56. Verify no fluid leaks
57. When T1 is less than -185°C (-301°F), begin cool down of tester by opening valves #5 and #6
58. Verify tester chilldown, record T6, T7, T8, and T9.
59. Perform a cold turbine torque check
60. Perform a cold accelerometer tap check
61. Close pump bypass pressure control valve (#16) completely
62. Verify varidrive speed control at minimum
63. Verify turbine trip solenoid valve switch is closed
64. Verify turbine trip solenoid valve (#14, #29) is closed
65. Increase setting of labyrinth seal supply regulator (#24) on dome loader (#41) until P11 is 0.52 MPa (75 psig)
66. Turn on varidrive breaker
67. Clear test pad area
68. Start varidrive
69. Fully close bypass valve #2
70. Increase varidrive speed to set P1 to 1. MPa (150 psig)
71. Increase pressure in GN₂ turbine run tank to 2.41 MPa (350 psig) using hand regulator (#34) on dome loader (#39)
72. Verify no flow to turbine
73. Increase GHe manifold P5 to 1.04 MPa (150 psig)
74. Open drain valves air supply valve (#18)
75. Verify controller #68 and #69 at proper pressure
76. Verify that P2 = P3 psig

77. Verify that $P_{12} = P_2 + 0.21 \text{ MPa}$ (30 psig)
78. Perform cold turbine torque check
79. Plug in power lead to turbine trip solenoid
80. Clear test pad area
81. Slowly increase varidrive speed to bring P_1 to 4.14 MPa (600 psig)
82. Verify P_{13} and P_{14} are at least 3.80 MPa (550 psig)
83. Verify P_2 , P_3 and P_4 are at their proper pressures
84. Verify P_6 , P_7 , P_8 , P_9 are at their proper pressures
85. Zero capacitance probe amplifiers
86. Verify Honeywell tape recorder ready
87. Verify Fluke data logger and Columbia digital recorder ready with normal scan group sequence
88. Start data logger/digital recorder
89. Verify all test personnel ready
90. Verify turbine control mode switch set to center-off position
91. Reset all alarms except turbine trip
92. Verify alarms are set by observing main alarm indicator light
93. Set manual speed control valve (#26) to minimum
94. Verify manual speed control pressure is zero
95. Verify auto speed control potentiometer set to provide minimum speed
96. Verify auto speed control pressure is zero
97. Announce "ready to start"
98. Start Honeywell recorder
99. Switch turbine trip solenoid to ON position
100. Switch turbine speed control mode to manual and slowly increase manual control pressure until turbine starts to rotate
101. Verify S_1 and S_2 operation
102. Using manual speed control switch, ramp speed to 3665 rad/s (35,000 r/min)
103. Verify manual control pressure are equal
104. Switch turbine control mode to auto
105. Using auto speed control potentiometer, adjust turbine speed to 3665 rad/s (35,000 r/min)
106. Verify stable operation
107. Adjust GHe manual control (Z) pot for 0.0 VDC
108. Increase P_5 to 2.41 MPa (350 psig)

109. Follow scheduled test plan
110. Adjust GHe manual control (Z) pot for 0.5 VDC
111. Turn turbine trip solenoid (#14, #25) off
112. Turn turbine control mode switch to center-off position.
113. Open purge solenoid (2) turbine
114. Set manual speed control valve (#26) to minimum
115. Allow all recorders to run until speed reaches zero
116. Switch Honeywell recorder and data logger/digital recorder off
117. Decrease varidrive speed to minimum
118. Perform cold turbine torque check
119. Switch varidrive off
120. Switch boost pump off
121. Unplug power lead to turbine trip solenoid
122. Close drain valve air supply solenoid (#18)
123. Verify P2, P3, P4 at zero pressure
124. Decrease setting of labyrinth seal supply regulator (#41, #24) until P11 is 0.06 MPa (10 psig)
125. Verify P12 = 0.21 MPa (30 psig)
126. Verify supply manifold bypass valve (#2, #23) and pump bypass valve (#16) are closed
127. Close pump fill valve (#15, #44) and tank fill valve (#17, #45)
128. Open purge solenoid LN₂ manifold and test seal cavity
129. Adjust GHe manual control (Z) pot until P12 for 0.0 V dc
130. Switch Soltec recorder off
131. Shut down hydraulic system
132. Fully close GN₂ run tank regulator (#39, #34)
133. Fully close labyrinth seal supply regulator (#41, #24)
134. Depressurize GN₂ run tank and verify zero pressure
135. Close GHe supply pressure control regulator (#40, #25)
136. Close GHe supply trailer valve & GHe ullage
137. Open purge solenoid GN₂ seal
138. Return control panel to pretest condition (except for purge valves and bypass valve (#2 and #16))
139. Purge overnight
140. Close all purge solenoids
141. Turn control panel key switch off - remove key

8.3.4 Pre- and Post-Test Inspection and Assembly Procedures

Prior to the testing of each seal set, the test rig was removed from the test facility and taken to the assembly area. Here, under clean conditions, the seal rings and runners were installed. The assembled seal ring clearances were then checked using the capacitance probes by manually moving each ring to the extremes of its motion. These were logged and compared with the previously measured dimensions.

After each test series, the test rig was again taken to the assembly area. The seal assembly was exposed and taken apart in a step-by-step manner. As each piece was taken out, its condition was visually assessed. Also, the seal housing was observed for signs of wear debris and contamination as the disassembly proceeded. When disassembling the seals, after the failures of the first and third seal sets, the seal rings were found to be tight on the runner. To minimize any additional damage due to disassembly, the runner was chilled using LN₂. This caused the runner to contract and the seal rings to loosen allowing them to be easily removed. On site, photographs were taken of the damaged parts. Observations made during testing, assembly and particularly disassembly activities were verbally recorded on a tape recorder and later transcribed in a written test log.

After the parts were returned to MTI in Latham, New York, the bore of the damaged seal rings and the outside diameters of the runners were measured for comparison with the pretest condition. Also, additional photographs were taken of the damaged parts including magnified views.

8.3.5 Instrument Calibration

Equipment used in the acquisition of data was calibrated, evaluated, maintained and controlled to ensure its accuracy, stability and repeatability in accordance with MTI's quality assurance program which is based on MIL-Q-9858A. The evaluation results were documented. The evaluation required was dependent on the type of equipment and its intended use.

8.3.5.1 Commercial Equipment. Commercial equipment for which sufficient information was available relative to its accuracy, stability, and repeatability were not evaluated if used according to established practices. However, the equipment was calibrated and the results documented. Included in this category were all pressure transducers, thermocouples, accelerometers, speed pick-ups, instrument preamplifiers, and readout instrumentation.

8.3.5.2 Special Instrumentation. Specially designed equipment was evaluated. The equipment was checked out prior to actual use by using actual test procedures and conditions to verify the suitability of the equipment for use, adequacy, stability, and repeatability. The capacitance probes used for film thickness and rotor motion measurement fell into this category because of their special size, material and use in cryogenic fluids. Capacitance probe calibration was accomplished by generating a probe gap versus output voltage curve. This established the sensitivity, range and linearity. Gap versus voltage curves were generated for all probes at room temperature in air. Additionally, those probes which were to operate in liquid nitrogen were calibrated in that fluid at atmospheric pressure. Cold calibrations simulated actual operating temperatures and fluid dielectric constants. The ability of the probe to withstand the large temperature transients was tested by repeated immersion in liquid nitrogen after which a visual inspection and both cold and ambient gap versus voltage curves was made.

Calibration procedures, records, and evaluation documentation on data acquisition equipment were maintained. This applies to instruments provided internally by MTI and to instruments provided by the test lab. This information is available to NASA upon request.

8.3.6 Data Reduction

During the testing, data were recorded in three ways: digital tape cassettes, analog magnetic tape, and strip chart recordings.

A Columbia Model 300D digital tape storage system connected directly to a Fluke Model 2280 data logger serially recorded all test data, transducer identification codes, and the time of each data scan. This was the principal

means of recording data throughout the testing. The data logger was triggered to start recording before each test run and continued until after the testing stopped. The approximately 40 transducer signals were completely scanned and recorded every 3 s. Every fifth data scan was additionally printed out on a paper tape to permit preliminary data analyses and provide a back up for the digital cassettes. Figure 8-2 shows a typical scan.

The tape cassettes were returned to MTI after the test series for computerized reduction. The tape cassettes were played back through an identical tape storage system and into MTI's IBM 4341 mainframe computer. The data were filed and output generated in various tabular and graphical forms for analysis and comparison with theoretical predictions. In several cases, theoretical relationships were simultaneously plotted with the experimental results. Figure 8-3 shows a typical computer generated plot of this format.

Analog magnetic tapes and strip chart recordings provided additional documentation of test data. Whereas the data logger sampled each signal every 3 s, data were continuously recorded on parallel channels on the analog and strip chart recorders. This was necessary to capture key data which varied rapidly during transients such as the acceleration runs. Strip chart recordings were taken of speed, seal supply pressure, drain pressures, flows, and seal temperatures during each run.

Magnetic tape recordings of speed, capacitance probe output, rotor and rig vibration were also made. The tape recordings were reviewed and analyzed to evaluate the dynamic behavior of the seal rings. Oscilloscope photographs were taken for a permanent record.

SEAL OPERATING MAP

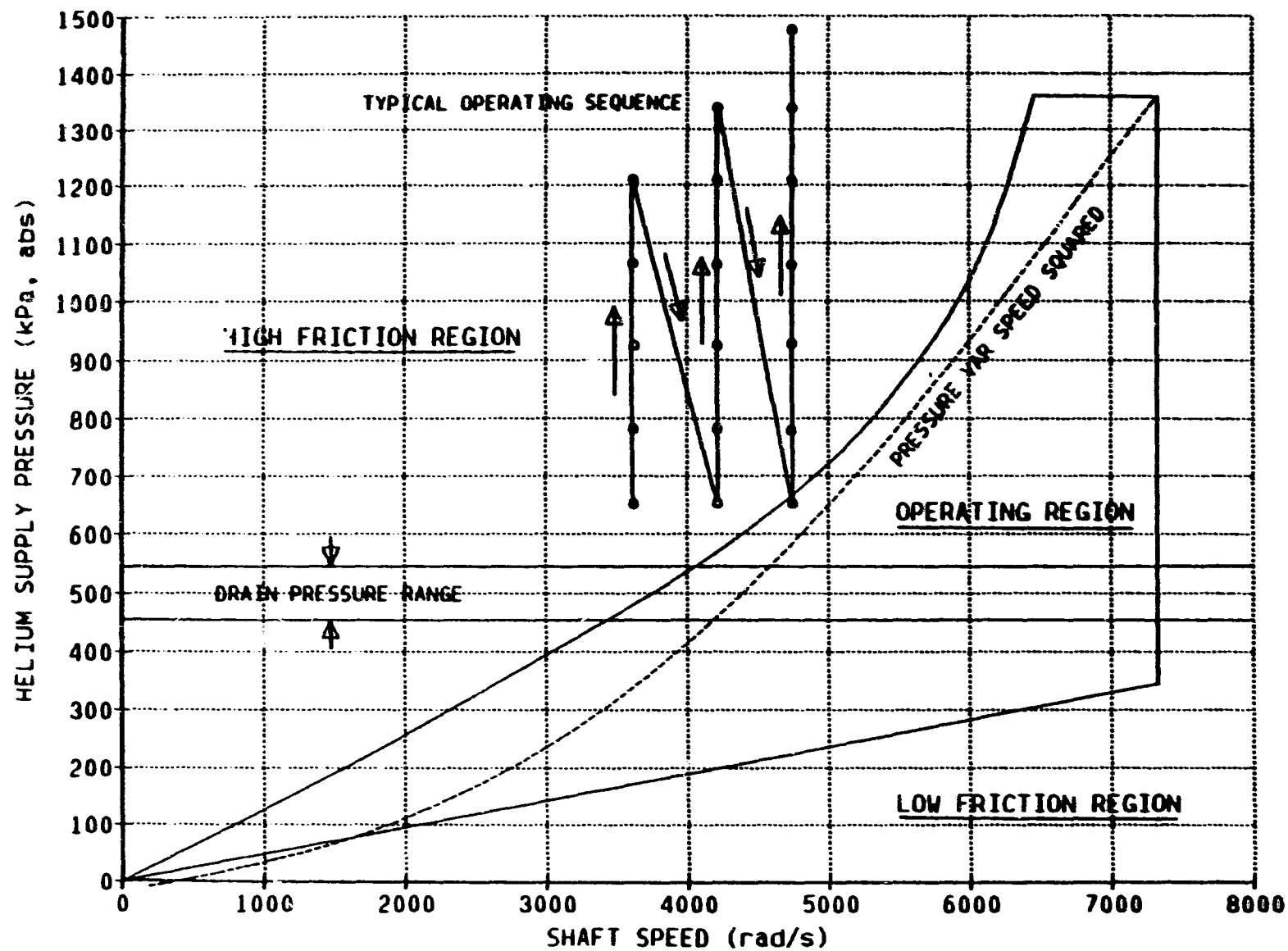


Fig. 8-1 Typical Seal Operating Sequence

BEGIN SCAN GROUP 0 27 NOV 84 13:51:14
FULL DATA SCAN W/ PRINTER

[illegible]

END SCAN GROUP 0 27 NOV 84 13:51:20

STOPPED SINGLE SCAN 27 NOV 84 17:51:23

Fig. 8-2 Typical Data Logger Scan from Seal Test No. 4

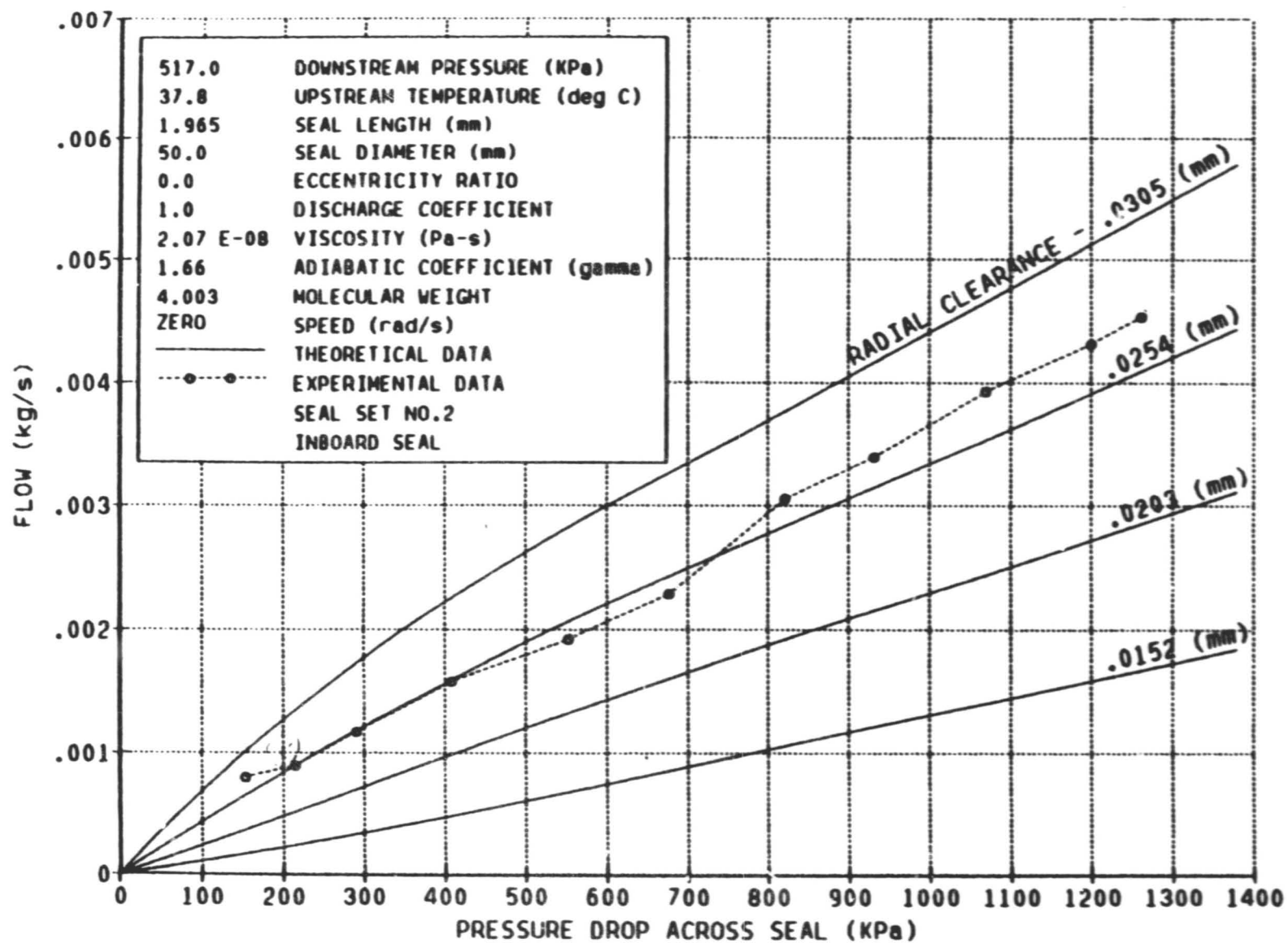


Fig. 8-3 Typical Computer-Generated Plot

TABLE 8-1

SEAL SET NO. 1 STEADY STATE TEST SCHEDULE

Data Point	Shaft Speed rad/s	Helium Supply Pressure (P12) kPa, abs	Outboard Drain Pressure (P2 nom.) kPa, abs	Test Time min.
1	4188	896	517	5
2	↓	793	↓	2
3	↓	724	↓	↓
4	↓	655	↓	↓
5	4188	896	↓	↓
6	4712	896	↓	↓
7	↓	793	↓	↓
8	↓	724	↓	↓
9	↓	655	↓	↓
10	↓	896	↓	↓
11	4712	965	↓	↓
12	5235	965	↓	↓
13	↓	896	↓	↓
14	↓	793	↓	↓
15	↓	724	↓	↓
16	↓	655	↓	↓
17	↓	965	↓	↓
18	5235	1034	↓	↓
19	5759	1034	↓	↓
20	↓	931	↓	↓
21	↓	793	↓	↓
22	↓	655	↓	↓
23	↓	1034	↓	↓
24	5759	1138	↓	↓
25	6202	1138	↓	↓
26	↓	1034	↓	↓
27	↓	931	↓	↓
28	↓	793	↓	↓
29	↓	1138	↓	↓
30	↓	1241	↓	↓
31	6282	1344	↓	↓
32	6806	1344	↓	↓

TABLE 8-1 (Cont'd)

Data Point	Shaft Speed rad/s	Helium Supply Pressure (P12) kPa, abs	Outboard Drain Pressure (P2 nom.) kPa, abs	Test Time min.
33	6806	1241	517	2
34	↓	1138	↓	↓
35	↓	1034	↓	↓
36	↓	931	↓	↓
37	↓	793	↓	↓
38	↓	1344	↓	↓
39	6806	1482	↓	↓
40	7329	1482	↓	↓
41	↓	1241	↓	↓
42	↓	1206	↓	↓
43	↓	1069	↓	↓
44	↓	931	↓	↓
45	↓	793	↓	↓
46	↓	1482	↓	↓
47	↓	1620	↓	↓
48	7329	1482	↓	30
49	6282	1241	↓	as needed
50	5235	1034	↓	as needed
51	4188	896	↓	as needed
52	-0-	896	517	as needed

TABLE 8-2

SEAL SET NO. 2 STEADY STATE TEST SCHEDULE

Data Point	Shaft Speed rad/s	Helium Supply Pressure (P12) kPa, abs	Outboard Drain Pressure (P2 nom.) kPa, abs	Test Time min.
1	3665	724	517	5
2		655		2
3		586		
4		793		
5		862	517	
6		862	310	
7		793		
8		724		
9		655		
10		586	310	
11		586	103	
12		655		
13		724		
14		793		
15		862	103	
16	3665	862	517	
17	4188	862		
18		793		
19		724		
20		655		
21		931	517	
22		931	310	
23		793		
24		793		
25		724	310	
26		655		
27		655	103	
28		724		
29		793		
30		862		
31		931	103	
32	4188	931	517	
33	4712	931		

TABLE 8-2 (Cont'd)

Data Point	Shaft Speed rad/s	Helium Supply Pressure (P12) kPa, abs	Outboard Drain Pressure (P2 nom.) kPa, abs	Test Time min.
34	4712	1000	517	2
35	↓	862	↓	↓
36	↓	793	↓	↓
37	↓	724	↓	↓
38	↓	655	517	↓
39	↓	655	310	↓
40	↓	724	↓	↓
41	↓	793	↓	↓
42	↓	862	↓	↓
43	↓	931	310	1
44	↓	931	103	↓
45	↓	862	↓	↓
46	↓	793	↓	↓
47	↓	724	↓	↓
48	↓	655	103	↓
49	4712	931	517	↓
50	5235	931	↓	↓
51	↓	1000	↓	↓
52	↓	862	↓	↓
53	↓	793	↓	↓
54	↓	724	517	↓
55	↓	724	310	↓
56	↓	793	↓	↓
57	↓	862	↓	↓
58	↓	931	↓	↓
59	↓	1000	310	↓
60	↓	1000	103	↓
61	↓	931	↓	↓
62	↓	862	↓	↓
63	↓	793	↓	↓
64	↓	724	103	↓
65	5235	931	517	↓

TABLE 8-2 (Cont'd)

Data Point	Shaft Speed rad/s	Helium Supply Pressure (P12) kPa, abs	Outboard Drain Pressure (P2 nom.) kPa, abs	Test Time min.
66	5759	931	517	1
67	↓	1000	↓	↓
68		1069	517	
69		862	310	
70		862	↓	
71		931	310	
72		1000	↓	
73		1069	103	
74		862	↓	
75		862	103	
76		931	↓	
77		1000	103	
78	5759	1069		1

TABLE 8-3

SEAL SET NO. 3 STEADY STATE TEST SCHEDULE

Data Point	Shaft Speed rad/s	Helium Supply Pressure (P12) kPa, abs	Outboard Drain Pressure (P2 nom.) kPa, abs	Test Time min.
1	3665	655	517	5
2		793		2
3		931		
4		1069		
5		1206	517	
6		655	310	
7		793		
8		931		
9		1069		
10		1206	310	
11		655	103	
12		793		
13		931		
14		1069		
15	3665	1206	103	
16	4188	655	517	
17		793		
18		931		
19		1069		
20		1206		
21		1344	517	
22		655	310	
23		793		
24		931		
25	4188	1069	310	
26		1206		
27		1344		
28		655	103	
29		793		
30		931		
31		1069		
32		1206		

TABLE 8-3 (Cont'd)

Data Point	Shaft Speed rad/s	Helium Supply Pressure (P12) kPa, abs	Outboard Drain Pressure (P2 nom.) kPa, abs	Test Time min.
33	4188	1344	103	2
34	4712	793	517	
35	↓	931	↓	
36		1069		
37		1206		
38		1344		
39		1482	517	
40		793	310	
41		931	↓	
42		1069		
43		1206		
44		1344		
45		1482	310	
46		793	103	
47		931	↓	
48		1069		
49		1206		
50	↓	1344		
51	4712	1482	103	
52	5235	793	517	
53	↓	931	↓	
54		1069		
55		1206		
56		1344	↓	
57		1482	517	
58		793	310	
59		931	↓	
60		1069		
61		1206		
62		1344		
63		1482	310	
64	↓	793	103	2
65	5235	931	103	
66	↓	1069	↓	
67		1206		
68		1344	↓	
69	5235	1482	103	2

TABLE 8-4

SEAL SET NO. 4 STEADY STATE TEST SCHEDULE

Data Point	Shaft Speed rad/s	Helium Supply Pressure (P12) kPa, abs	Outboard Drain Pressure (P2 nom.) kPa, abs	Test Time min.
1	3665	827	517	3
2	4183	↓	↓	2
3	4712	↓	↓	↓
4	5235	827	↓	↓
5	5759	965	↓	↓
6	6282	1103	↓	↓
7	6806	1241	↓	↓
8	7329	1379	↓	2
9	↓	1379	↓	90
10	↓	1241	↓	2
11	↓	1103	↓	↓
12	↓	965	↓	↓
13	↓	827	517	↓
14	↓	1379	310	↓
15	↓	1241	↓	↓
16	↓	1103	↓	↓
17	↓	965	↓	↓
18	↓	827	310	↓
19	↓	1379	103	↓
20	↓	1241	↓	↓
21	↓	1103	↓	↓
22	↓	965	↓	↓
23	7329	827	103	↓
24	6282	1379	517	↓
25	↓	1241	↓	↓
26	↓	1103	↓	↓
27	↓	965	↓	↓
28	↓	827	517	↓
29	↓	1379	310	↓
30	↓	1241	↓	↓
31	↓	1103	↓	↓
32	↓	965	↓	↓
33	↓	827	310	↓

TABLE 8-4 (Cont'd)

Data Point	Shaft Speed rad/s	Helium Supply Pressure (P12) kPa, abs	Outboard Drain Pressure (P2 nom.) kPa, abs	Test Time min.
34	6282	1379	103	2
35	↓	1241	↓	↓
36	↓	1103	↓	↓
37	↓	965	↓	↓
38	↓	827	103	↓
39	5235	1379	517	↓
40	↓	1241	↓	↓
41	↓	1103	↓	↓
42	↓	965	↓	↓
43	↓	827	517	↓
44	↓	1379	310	↓
45	↓	1241	↓	↓
46	↓	1103	↓	↓
47	↓	965	↓	↓
48	↓	827	310	↓
49	↓	1379	103	↓
50	↓	1241	↓	↓
51	↓	1103	↓	↓
52	↓	965	↓	↓
53	5235	827	103	↓
54	4188	1379	517	↓
55	↓	1241	↓	↓
56	↓	1103	↓	↓
57	↓	965	↓	↓
58	↓	827	517	↓
59	↓	1379	310	↓
60	↓	1241	↓	↓
61	↓	1103	↓	↓
62	↓	965	↓	↓
63	↓	837	310	↓
64	↓	1379	103	↓
65	↓	1241	103	↓
66	4188	1103	103	2
67	↓	965	↓	↓
68	↓	827	103	↓

TABLE 8-5

SEAL SET NO. 2 ACCELERATION TEST SCHEDULE

Run No.	Acceleration Rate		Max. Speed rad/s	Supply Pressure, (P12) kPa, abs.	Drain Pressure (P2) kPa, abs	Test Time min.
	H - High	L - Low				
1-5	H		4188	931	517	1
6	L					5
7-11	H					1
12	L					5
13-17	H					1
18	L					5
19-23	H					1
24	L					5
25-29	H					1
30	L					5
31-35	H					1
36	L					5
37-46	H					1
47	L					5
48-57	H					1
58	L					5

9.0 REFERENCES

1. Shapiro, W., Walowit, J., Jones, H.F. "Interim Report: LOX Turbopump Seals Performance Analysis Verification Analysis, Design of Spiral-Groove Seals." MTI Report 83TR5, prepared for NASA/LeRC, September 1982.
2. Shapiro, W., Artiles, A., Jones, H.F. "Interim Report: LOX Turbopump Seals Performance Analysis Verification Analysis, Design of Floating-Ring, Rayleigh-Step, Helium Buffer Seals." MTI Report 83TR6, prepared for NASA/LeRC, October 1982.
3. Shapiro, W., Dunne, J., Hamm, R. "Interim Report: LOX Turbopump Seals Performance Analysis Verification Analysis, Design of Seal Test Rig." MTI Report 83TR14, prepared for NASA/LeRC, January 1983.
4. Hamm, R., Shapiro, W. "Final Test Plan: LOX Turbopump Seals Performance Analysis Verification." prepared for NASA/LeRC, November 1982.
5. Burcham, R. E., and Boynton, J. L. "Small High-Speed, Self-Acting Shaft Seals for Liquid Rocket Engines." NASA CR 135167, RI/RD77-195, July 1977, prepared for NASA/LeRC, by Rockwell International, Rocketdyne Div., Contract NAS3-17769.
6. Artiles, A., Walowit, J., and Shapiro, W. "Analysis of Hybrid, Fluid-Film Journal Bearings with Turbulence and Inertia Effects." ASME Publication, Advances in Computer-aided Bearing Design, 1982, p. 25.
7. Artiles, A., Shapiro, W., Jones, H.F. "Design Analysis of Rayleigh-Step, Floating Ring Seals." ASLE Transactions, Vol. 27, October 1984, p. 321-331.
8. Shapiro, W., Walowit, J., Jones, H.F. "Analysis of Spiral-Groove Face Seals for Liquid Oxygen." ASLE Transactions, Vol. 27, Number 3, July 1984, p. 177-188.

9. Muijderman, E. A. "Spiral-Groove Bearings." Phillips Technical Library, New York: Springer-Verlag Inc., 1966.
10. Elrod, H. G. and Ng, C. W. "A Theory of Turbulent Films and Its Application to Bearings." ASME Trans., Journal of Lubrication Technology, July 1967.

APPENDIX A

FLOW THROUGH HELIUM SEAL INCLUDING
INERTIA EFFECTS

NOMENCLATURE

A	=	Annular cross section area of seal
C	=	Radial clearance
C_D	=	Discharge coefficient
l	=	Seal length
p_a	=	Downstream ambient pressure
p_i	=	Intermediate pressure immediately downstream of inlet
p_{ci}	=	Intermediate pressure at which flow becomes choked
p_s	=	Inlet pressure to seal region
R	=	Gas constant
T_i	=	Intermediate absolute temperature
T_s	=	Absolute temperature of inlet gas
v	=	Fluid velocity
ϵ	=	Seal eccentricity ratio
γ	=	Ratio of specific heats of gas
μ	=	Fluid viscosity
ρ	=	Fluid density

PRECEDING PAGE BLANK NOT FILMED

There are two regions of flow to be considered over the sealing land:

- (1) An inlet region where the flow is strictly inertial and is treated as an orifice.
- (2) A land region where both inertial and viscous effects are considered.

The unknown is the intermediate pressure between these two regions.

In the inlet zone, the flow is described by an orifice equation:

$$q = AC_D \left(\frac{2\gamma}{\gamma-1} \right)^{1/2} \frac{p_s}{\sqrt{RT_s}} \bar{p}_i^{\frac{1}{\gamma}} \left(1 - \bar{p}_i^{\frac{\gamma-1}{\gamma}} \right)^{1/2} \quad (1)$$

where $\bar{p}_i = p_i/p_s$

$$\bar{p}_{ci} = \frac{p_{ci}}{p_s} = \left(\frac{2}{\gamma+1} \right)^{\frac{\gamma}{\gamma-1}} \quad (2)$$

If $\bar{p}_i < \bar{p}_{ci}$, set $\bar{p}_i = \bar{p}_{ci}$ (choked inlet)

In the film region the following equations apply:

$$\frac{dp}{dx} + \rho v \frac{dv}{dx} = - \frac{12\mu l}{C^2 (1 + \frac{3}{2} \epsilon^2)} v \quad (3)$$

$$q = \rho v A, \quad \rho = p/RT \quad (4)$$

$$\frac{dp}{dx} + \left(\frac{q}{A} \right)^2 \frac{d}{dx} \left(\frac{1}{\rho} \right) = - \frac{12\mu l}{C^2 (1 + \frac{3}{2} \epsilon^2)} \frac{q}{\rho A} \quad (5)$$

$$\frac{d}{dx} \left[\int \rho dp \right] - \left(\frac{q}{A} \right)^2 \frac{d}{dx} (\ln \rho) = - \frac{12 \mu l}{C^2 (1 + \frac{3}{2} \epsilon^2)} \frac{q}{A} \quad (6)$$

$$\rho = \frac{p_1}{RT_1} \frac{\gamma-1}{\gamma} p^{1/\gamma} \quad (7)$$

$$\frac{\gamma}{1+\gamma} \frac{p_1}{RT_1} \frac{\gamma-1}{\gamma} \left(p_1^{\frac{\gamma+1}{\gamma}} - p_a^{\frac{\gamma+1}{\gamma}} \right) - \left(\frac{q}{A} \right)^2 \frac{1}{\gamma} \ln \left(\frac{p_1}{p_a} \right) = \frac{12 \mu l}{C^2 (1 + \frac{3}{2} \epsilon^2)} \frac{q}{A} \quad (8)$$

$$\frac{2\gamma}{1+\gamma} \frac{\bar{p}_1}{\bar{T}_1} \frac{\gamma+1}{\gamma} \left(\bar{p}_1^{\frac{\gamma+1}{\gamma}} - \bar{p}_a^{\frac{\gamma+1}{\gamma}} \right) - \frac{2RT_s}{\gamma} \left(\frac{q}{Ap_s} \right)^2 \ln \frac{\bar{p}_1}{\bar{p}_a} = \frac{24 \mu l RT_s}{p_s^2 C^2 (1 + \frac{3}{2} \epsilon^2)} \frac{q}{A} \quad (9)$$

$$q_o = \frac{p_s^2 C^2 (1 + \frac{3}{2} \epsilon^2) A}{24 \mu l RT_s}, \quad \bar{q} = \frac{q}{q_o}, \quad \beta = 2 RT_s \left(\frac{q_o}{Ap_s} \right)^2 \quad (10)$$

$$\frac{2\gamma}{\gamma+1} \frac{\bar{p}_1}{\bar{T}_1} \frac{\gamma-1}{\gamma} \left(\bar{p}_1^{\frac{\gamma+1}{\gamma}} - \bar{p}_a^{\frac{\gamma+1}{\gamma}} \right) - \frac{\beta \bar{q}}{\gamma} \ln \left(\frac{\bar{p}_1}{\bar{p}_a} \right) = \bar{q} \quad (11)$$

where $\bar{T}_1 = T_1/T_s$

Choking will occur at $\frac{d\bar{q}}{d\bar{p}_a} = 0$

Differentiate above equations with respect to \bar{p}_a , set $d\bar{q}/d\bar{p}_a = 0$, solve for \bar{p}_a and call the value to obtained \bar{p}_c .

$$\bar{p}_c = \left[\frac{\beta \bar{q}}{2\gamma} \frac{\bar{T}_1}{\bar{p}_1^{\frac{\gamma+1}{\gamma}}} \right] \frac{\gamma}{1+\gamma} \quad (12)$$

If $\bar{p}_a < \bar{p}_c$, set $\bar{p}_a = \bar{p}_c$ (choked flow)

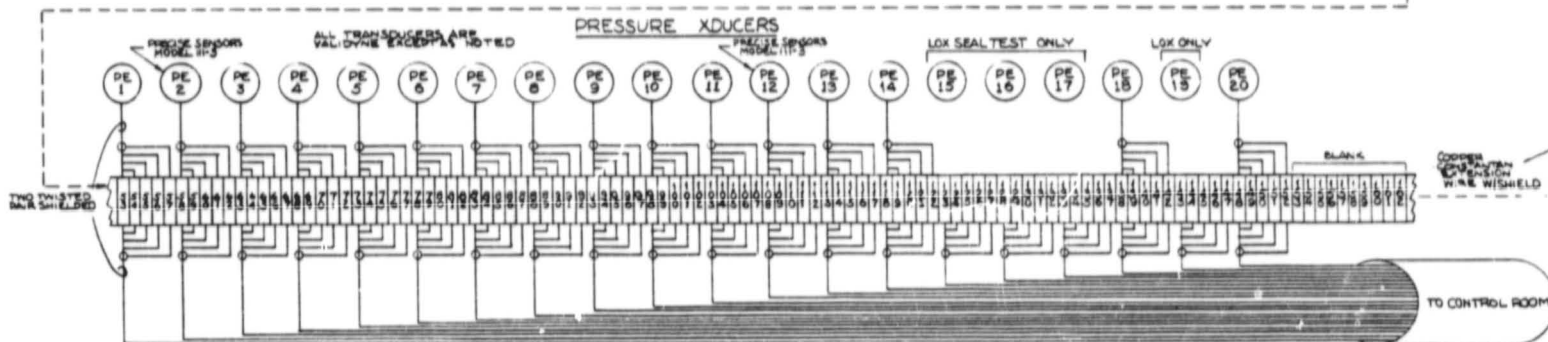
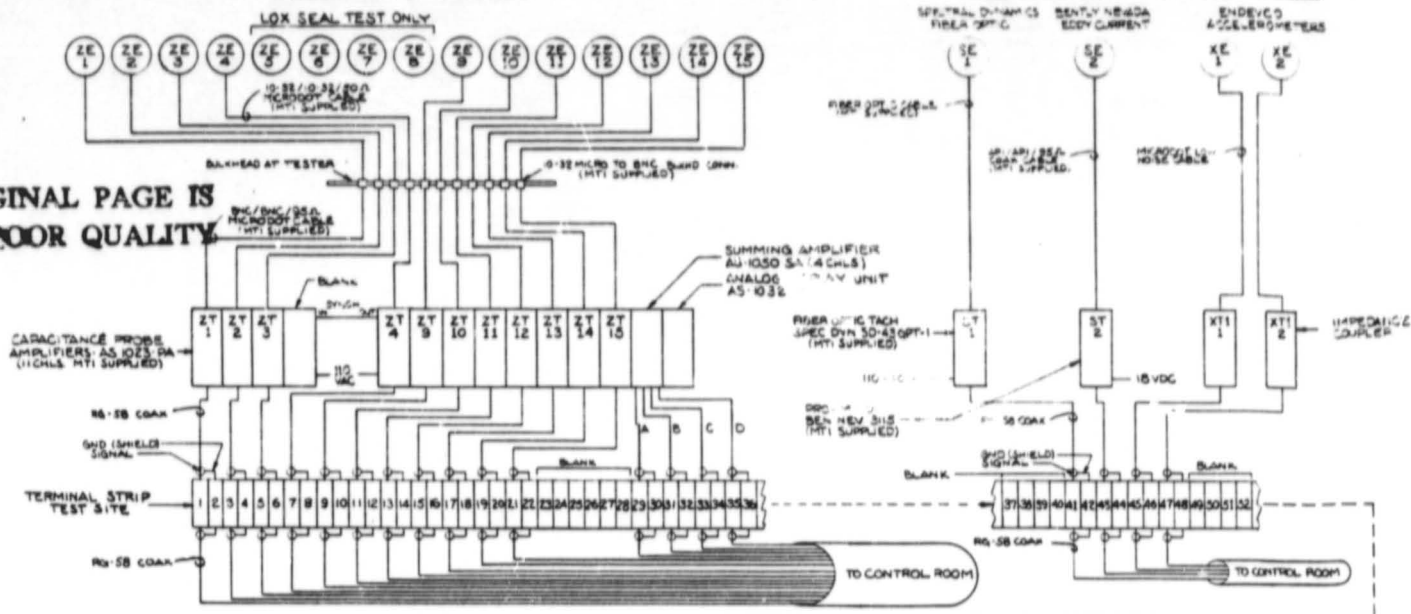
For isothermal flow, set $\gamma = 1$ in equations (11), (12).

The flow through the inlet region is equated to the flow in the film region and the intermediate pressure \bar{p}_1 is solved for numerically.

APPENDIX B

INSTRUMENTATION SCHEMATICS

VIBRATION INDEXES



CONDITIONED SIGNAL TEST
TO READOUTS (SEE SH

FOLDOUT FRAME

ADUCERS

VCO
PROBES

KE
2

KT1
2 IMPEDANCE
COUPLER

CONTROL ROOM

ORIGINAL PAGE IS
OF POOR QUALITY

2 EOLDOUT FRAME

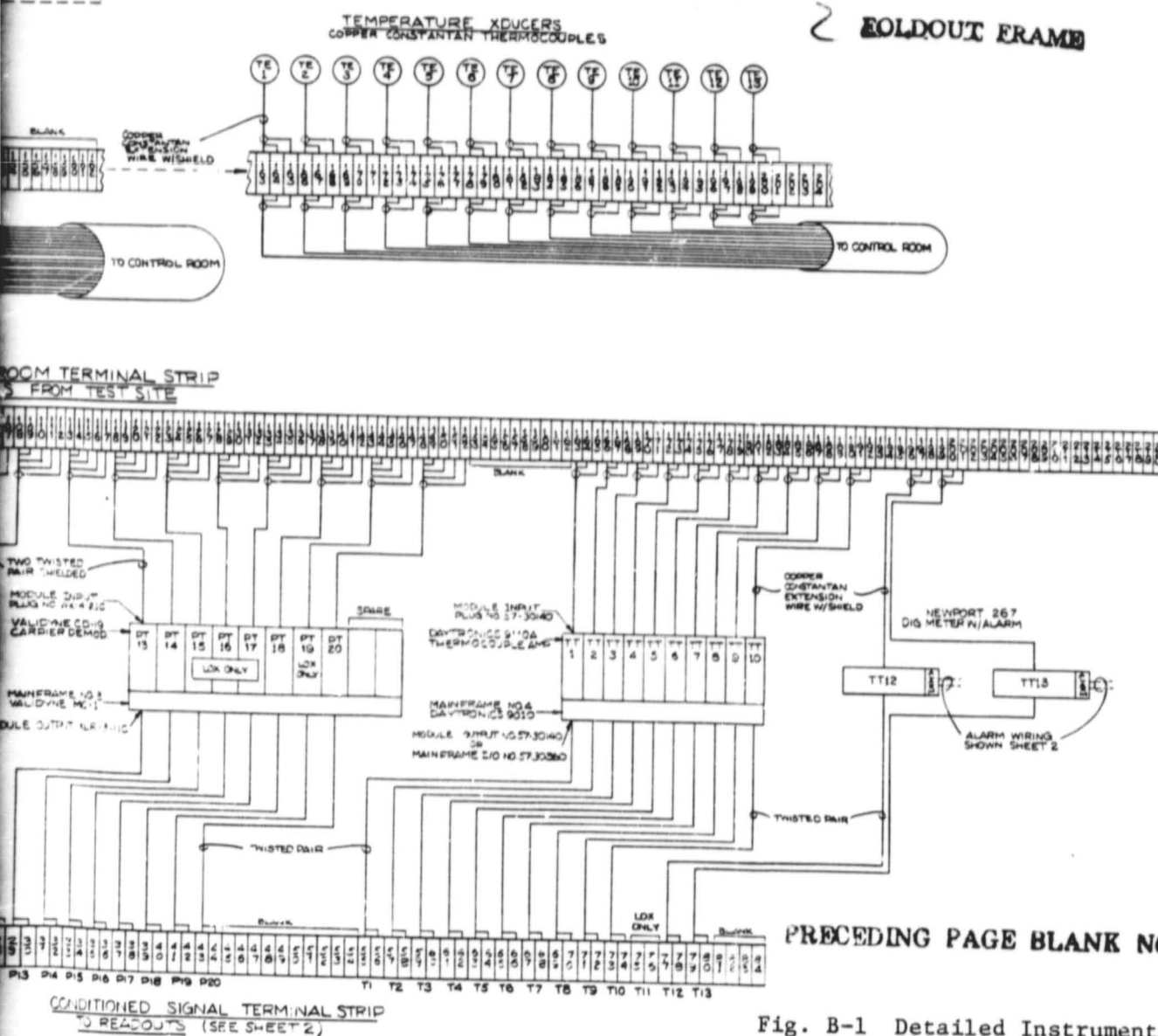


Fig. B-1 Detailed Instrumentation Schematic -
Sensors and Preamplifiers

DYNAMIC SIGNAL PATCH PANEL

X1 X2 X3 X4 X5 X6 X7 X8 X9 X10 X11 X12 X13 X14 X15 X16 X17 X18 X19 X20 X21 X22 X23 X24 X25 X26 X27 X28 X29 X30 X31 X32 X33 X34 X35 X36 X37 X38 X39 X40 X41 X42 X43 X44 X45 X46 X47 X48 X49 X50 X51 X52 X53 X54 X55 X56 X57 X58 X59 X60 X61 X62 X63 X64 X65 X66 X67 X68 X69 X70 X71 X72 X73 X74 X75 X76 X77 X78 X79 X80 X81 X82 X83 X84 X85 X86 X87 X88 X89 X90 X91 X92 X93 X94 X95 X96 X97 X98 X99 X100

SHAFT RADIAL MOTION

SEAL END
OSCILLOSCOPE
X1V2 XY

TURBINE END
OSCILLOSCOPE
X1V4 XY

MTI WILL SUPPLY
ALL OSCILLOSCOPES

SEAL FILM THICKNESS

SEAL END
OSCILLOSCOPE
X1A/B XY

TURBINE END
OSCILLOSCOPE
X1C/D XY

CABLES TO SCOPES & METER
DIRECT FROM PATCH PANEL NOT
FEED AS SHOWN HERE

TESTER VIBRATION

OSCILLOSCOPE
X1I/E XY
X1I/S

NEWPORT 23A
DIG. FREQ. METER
512

CONDITIONED SIGNAL TERMINAL STRIP

P1 P2 P3 P4 P5 P6 P7 P8 P9 P10 P11 P12 P13 P14 P15 P16 P17 P18 P19 P20 P21 P22 P23 P24 P25 P26 P27 P28 P29 P30 P31 P32 P33 P34 P35 P36 P37 P38 P39 P40 P41 P42 P43 P44 P45 P46 P47 P48 P49 P50 P51 P52 P53 P54 P55 P56 P57 P58 P59 P60 P61 P62 P63 P64 P65 P66 P67 P68 P69 P70 P71 P72 P73 P74 P75 P76 P77 P78 P79 P80 P81 P82 P83 P84 P85 P86 P87 P88 P89 P90 P91 P92 P93 P94 P95 P96 P97 P98 P99 P100

PRESSURES & FLOWS

NEWPORT 232
DIG. METER
P11

NEWPORT 232
DIG. METER W/ALARM
P16

NEWPORT 232
DIG. METER
P15

NEWPORT 232
DIG. METER W/ALARM
P17

NEWPORT 232
DIG. METER W/ALARM
P18

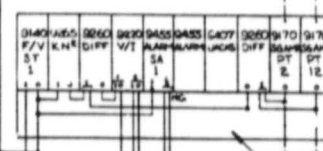
NEWPORT 232
DIG. METER W/ALARM
P19

DATUM
TIME CODE GENERATOR

HONEYWELL 101
PMMAGNETIC RECORDER
ZR

**ORIGINAL PAGE IS
OF POOR QUALITY**

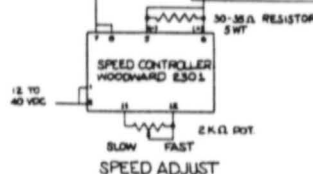
CONTROL LOOP AMPLIFIERS
MAINFRAME NO. 1 DAYTRONICS 5010



**MAINFRAME NO. 5
VALDYNE MC-1**



NEWPORT 232
DIG. METER
TTT
INPUTS & OUTPUTS
SHOWN SHEET 1



THIS WIRING INTERNAL TO MAINFRAME
SEE MANUALS FOR DETAILS

RS-232 INTERFACE CABLE

COLUMBIA 5000
DIGITAL RECORDER
(MTI SUPPLIED)

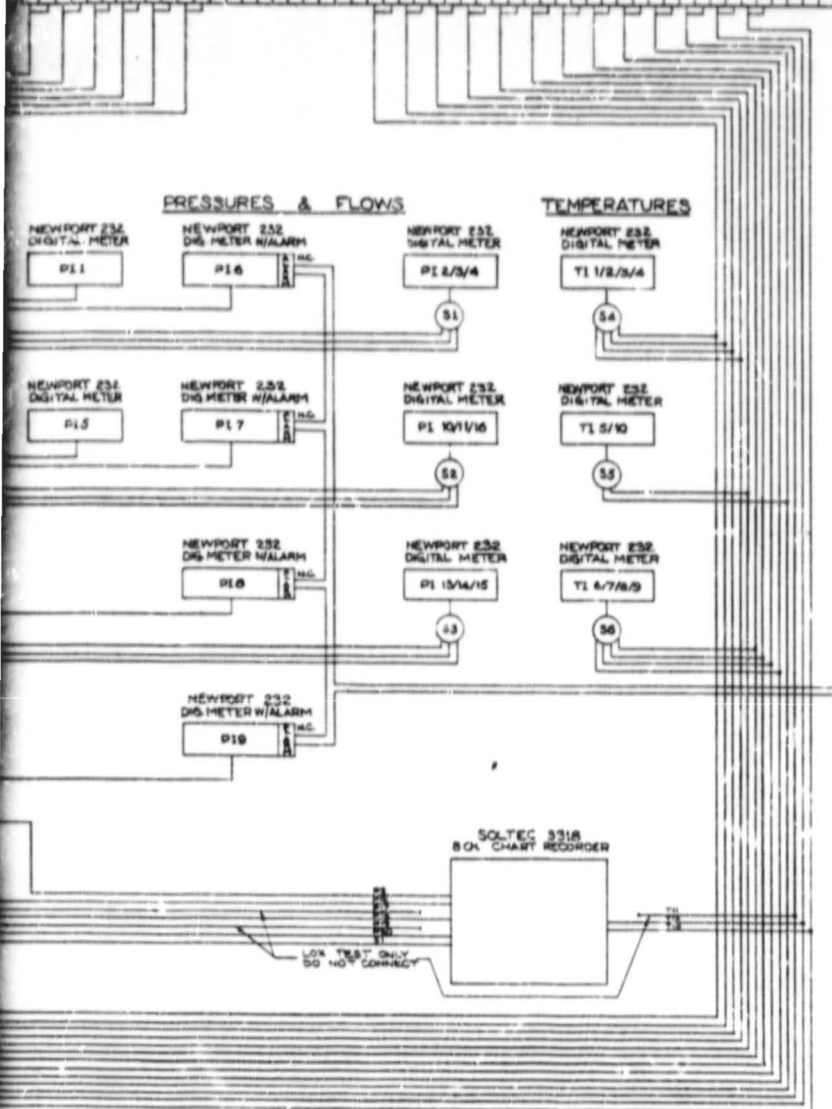
FLUKE 2280
DATA LOGGER

CONDITIONED SIGNAL TERMINAL STRIP

CONTROL ROOM TERM. STRIP

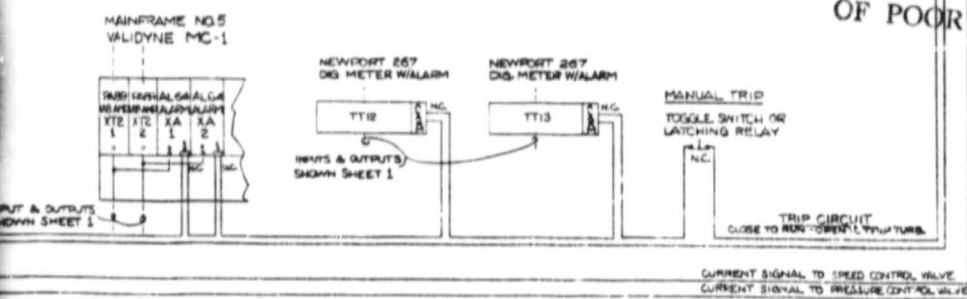
P15	P16	P17	P18	P19	NC	BLANK	T1	T2	T3	T4	T5	T6	T7	T8	T9	T10	T11	T12	T13	BLANK
1	2	3	4	5	6	7	8	9	10	11	12	13	14	15	16	17	18	19	20	21

FOR	FOR	FOR	FOR	FOR	FOR	FOR	FOR	FOR	FOR	FOR	FOR	FOR	FOR	FOR	FOR	FOR	FOR	FOR	FOR	FOR
1	2	3	4	5	6	7	8	9	10	11	12	13	14	15	16	17	18	19	20	21



END
DATE
Feb. 22, 1988

ORIGINAL PAGE IS
OF POOR QUALITY



THIS WIRING INTERNAL TO MAINFRAME
SEE MANUALS FOR DETAILS

PRECEDING PAGE BLANK NOT FILMED

Fig. B-2 Detailed Instrumentation Schematic -
Indicating and Recording Instruments